SURFACE ENHANCED RAMAN SCATTERING: NEW THEORETICAL APPROACHES, MATERIALS AND STRATEGIES

EDITED BY: Ivano Alessandri and John Lombardi
PUBLISHED IN: Frontiers in Chemistry

frontiers Research Topics

ISSN 1664-8714
ISBN 978-2-88963-553-5
DOI 10.3389/978-2-88963-553-5

About Frontiers

Frontiers is more than just an open-access publisher of scholarly articles: it is a pioneering approach to the world of academia, radically improving the way scholarly research is managed. The grand vision of Frontiers is a world where all people have an equal opportunity to seek, share and generate knowledge. Frontiers provides immediate and permanent online open access to all its publications, but this alone is not enough to realize our grand goals.

Frontiers Journal Series

The Frontiers Journal Series is a multi-tier and interdisciplinary set of open-access, online journals, promising a paradigm shift from the current review, selection and dissemination processes in academic publishing. All Frontiers journals are driven by researchers for researchers; therefore, they constitute a service to the scholarly community. At the same time, the Frontiers Journal Series operates on a revolutionary invention, the tiered publishing system, initially addressing specific communities of scholars, and gradually climbing up to broader public understanding, thus serving the interests of the lay society, too.

Dedication to Quality

Each Frontiers article is a landmark of the highest quality, thanks to genuinely collaborative interactions between authors and review editors, who include some of the world's best academicians. Research must be certified by peers before entering a stream of knowledge that may eventually reach the public - and shape society; therefore, Frontiers only applies the most rigorous and unbiased reviews.
Frontiers revolutionizes research publishing by freely delivering the most outstanding research, evaluated with no bias from both the academic and social point of view. By applying the most advanced information technologies, Frontiers is catapulting scholarly publishing into a new generation.

What are Frontiers Research Topics?

Frontiers Research Topics are very popular trademarks of the Frontiers Journals Series: they are collections of at least ten articles, all centered on a particular subject. With their unique mix of varied contributions from Original Research to Review Articles, Frontiers Research Topics unify the most influential researchers, the latest key findings and historical advances in a hot research area! Find out more on how to host your own Frontiers Research Topic or contribute to one as an author by contacting the Frontiers Editorial Office: researchtopics@frontiersin.org

SURFACE ENHANCED RAMAN SCATTERING: NEW THEORETICAL APPROACHES, MATERIALS AND STRATEGIES

Topic Editors:
Ivano Alessandri, University of Brescia, Italy
John Lombardi, City College of New York (CUNY), United States

Citation: Alessandri, I., Lombardi, J., eds. (2020). Surface Enhanced Raman Scattering: New Theoretical Approaches, Materials and Strategies. Lausanne: Frontiers Media SA. doi: 10.3389/978-2-88963-553-5

Table of Contents

frontiers in Chemistry

EDITORIAL
published: 04 February 2020
doi: 10.3389/fchem.2020.00063

Editorial: Surface Enhanced Raman Scattering: New Theoretical Approaches, Materials and Strategies

Ivano Alessandri [1,2,3]* *and John R. Lombardi* [4]*

[1] Unit of Research of Brescia, Department of Information Engineering, INSTM, Brescia, Italy, [2] Department of Information Engineering, Brescia, Italy, [3] Unit of Brescia, CNR-INO, Brescia, Italy, [4] Chemistry and Biochemistry Department, City College New Yok, New York, NY, United States

Keywords: SERS (surface enhanced Raman scattering), Raman sensing, SERS theory, non-plasmonic SERS forensics, food analysis, biodiagnostics, cultural heritage

Editorial on the Research Topic

Surface Enhanced Raman Scattering: New Theoretical Approaches, Materials and Strategies

OPEN ACCESS

Edited and reviewed by:
Huangxian Ju,
Nanjing University, China

****Correspondence:***
Ivano Alessandri
ivano.alessandri@unibs.it
John R. Lombardi
jlombardi@ccny.cuny.edu

Specialty section:
This article was submitted to Analytical Chemistry, a section of the journal Frontiers in Chemistry

Received: *07 January 2020*
Accepted: *20 January 2020*
Published: *04 February 2020*

Citation:
Alessandri I and Lombardi JR (2020) Editorial: Surface Enhanced Raman Scattering: New Theoretical Approaches, Materials and Strategies. Front. Chem. 8:63. doi: 10.3389/fchem.2020.00063

The development of surface-enhanced Raman scattering (SERS) has gone hand-in-hand with that of nanotechnology, oscillating between great expectations associated with high sensitivity, which can be extended down to single molecule detection, and frustrating disappointments, originating from low reproducibility of data. This latter critical issue is inherently entangled with the local enhancement of the electromagnetic field, which forms the basis of plasmon-assisted SERS and still prevents its full implementation in analytical chemistry.

In recent years, significant progress has been reported that promises to bring SERS to the forefront of sensing and advanced diagnostics. Several research groups demonstrated that dielectrics can be suitably engineered to achieve non-plasmonic enhanced Raman scattering, reducing invasiveness and increasing reproducibility of SERS experiments (Alessandri, 2013; Alessandri and Lombardi, 2016; Bontempi et al., 2018).

New theoretical models, encompassing plasmonic and non-plasmonic systems, have been developed (Lombardi and Birke, 2014; Roelli et al., 2016; Frizyuk et al., 2018). In parallel, the urgent need for operational SERS-based analysis in complex environments and real-life conditions stimulated the application of multivariate methods to Raman data analysis, opening the door to machine- and deep-learning approaches that are entering the areas of sensing and analytical chemistry on a large scale (Chen et al., 2019; Fan et al., 2019).

This Special Issue includes 16 contributions (1 review, 1 minireview, and 14 research papers) that touch several aspects of SERS, ranging from theory and modeling to analytical applications of both plasmonic and non-plasmonic systems.

In a full review paper, Zou et al. summarized some of the most recent advances in the use of naked and oxide-coated silver nanorods for SERS purposes, giving an overview of their synthesis and applications in different sectors of sensing (food, environment, biological molecules, and gas).

A special focus on the latest developments of shell isolated nanoparticle-enhanced Raman spectroscopy (SHINERS) was reported in the minireview by Krajczewski and Kudelski.

Zhang et al. reported on the simultaneous enhancement of fluorescence emission and Raman scattering achieved by gold-silver nanoalloys coated by silica shells, which opens exciting perspectives for the development of portable devices. Silver nanostars were utilized by de Almeida et al. to classify different types of Portuguese wines on the basis of SERS data processed by principal components analysis. Further specific examples of analytical SERS were treated in research papers dedicated to advanced diagnostics in art, forensics, drug analysis, and biosensing.

Cesaratto et al. described an innovative sample pretreatment based on the use of nitric acid for detecting aniline and xanthene dyes in microscopic specimens of various masterpieces, including a nineteenth-century silk fabric, paper cut-outs by Matisse, Van Gogh's Irises, and Japanese woodblock prints.

Kolhatkar et al. proposed a new method for revealing latent fingermarks based on the combination of SERS and plasmonic luminescence, which exploits the preferential deposition of gold nanoparticles on the biological components of the fingermarks. Another important field that intersects forensics and analytical chemistry is represented by detection of illicit drugs and pharmaceutical compounds. Farquharson et al. provided a detailed SERS library for 39 most common drugs, including opioids, cannabinoids, amphetamines, fentanyl and derived compounds, benzodiazepines, and other psychoactive small molecules. Similar molecules were compared and analyzed on the basis of their chemical structure, pointing out unique Raman bands that can be utilized for identifying and distinguish similar compounds and the modifications to the Raman spectra that can be caused by pH, medium, and the use of different type of metals as enhancers. Muhamadali et al. demonstrated the detection of novel psychoactive substances (methcathinones, aminoindanes, diphenidines, and synthetic cannabinoids) in complex mixtures. Principal component analysis of the SERS data enabled the extension of the detection limit, as well as direct analysis from biological fluids.

In the field of biodiagnostics, Capocefalo et al. synthesized and tested SERS-based nanosensors that are able to discriminate between healthy and cancer cells by measuring their extracellular pH.

Saveleva et al. demonstrated that polycaprolactone fibers coated by porous $CaCO_3$ and Ag nanoparticles can selectively adsorb different biological molecules, playing as SERS-active platform for detection of low and high molecular weight molecules.

Finally, Yue et al. utilized nuclear-targeted gold nanorod Raman nanoprobes to investigate *in situ* the dynamic intranuclear molecular changes of a murine melanoma cell line treated with a photosensitizer and irradiated with visible laser (650 nm) in a typical photodynamic therapy experiment, revealing protein degradation and DNA fragmentation.

In the area of theory of SERS, Mueller and Reich presented a model for the plasmonic enhancement mechanism of SERS based on perturbation theory. This model treats SERS as higher-order Raman scattering, allowing the optical absorption cross-section to be calculated and compared with experimental data. This approach clarifies the role of different scattering channels in the case of enhancement factors below 10^3.

In another research paper, Aranda et al. re-examined the mother of all SERS experiments, i.e., pyridine adsorbed on silver electrodes, to discuss on the use of DFT for modeling the effect of the electrode potential in SERS experiments.

Kim et al. investigated the mechanism of chemical enhancement in non-plasmonic SERS, by testing the Raman response of molecular probes with significant differences in HOMO-LUMO energy gap (4-MPY, 4-MBA, 4-ATP) deposited either on nanostructured (ZnO, GaN) and 2D (WS_2) semiconductors and excited at different laser wavelengths (488, 514.5, 532, and 632.8 nm). This study shows that the charge transfer from the valence band of the semiconductor to the LUMO of the analyte is the main contribution to the chemical enhancement and can be exploited to maximize the sensitivity of non-plasmonic SERS experiments. This type of charge transfer can be directly controlled by doping, as remarked by Li et al. with an experiment that monitored the variation of Raman intensity of 4-MBA as a function of the Ga content in ZnO nanoparticles utilized as SERS substrates.

In another paper, Ji et al. reported non-plasmonic SERS with ZrO_2 by direct exploitation of charge transfer, which demonstrates the importance of controlling surface states and extended the results reported by Bontempi et al. on zirconia resonators (Bontempi et al., 2017).

The Editors suggest that such a rich palette of examples, encompassing a large variety of themes, explores the essential features of the multi-faceted scenario of research on SERS, and will serve to guide and inspire future research in the field.

AUTHOR CONTRIBUTIONS

IA and JL wrote the manuscript.

REFERENCES

Alessandri, I. (2013). Enhancing Raman scattering without plasmons: unprecedented sensitivity achieved by TiO_2 shell-based resonators. *J. Am. Chem. Soc.* 135, 5541–5544. doi: 10.1021/ja401666p

Alessandri, I., and Lombardi, J. R. (2016). Enhanced Raman scattering with dielectrics. *Chem. Rev.* 116, 14921–14981. doi: 10.1021/acs.chemrev.6b00365

Bontempi, N., Vassalini, I., and Alessandri, I. (2018). All-dielectric core/shell resonators: from plasmon-free SERS to multimodal analysis. *J. Raman Spectr.* 49, 943–953. doi: 10.1002/jrs.5330

Bontempi, N., Vassalini, I., Danesi, S., and Alessandri, I. (2017). ZORRO: zirconium oxide resonators for all-in-one Raman and whispering-gallery-mode optical sensing. *Chem. Commun.* 53, 10382–10385. doi: 10.1039/C7CC06357A

Chen, X., Xie, L., He, Y., Guan, T., Zhou, X., Wang, B., et al. (2019). Fast and accurate decoding of Raman spectra-encoded suspension arrays using deep learning. *Analyst* 144, 4312–4319. doi: 10.1039/c9an00913b

Fan, X., Ming, W., Zeng,. H., Zhang, Z., and Lu,. H. (2019). Deep learning-based component identification for the Raman spectra of mixtures. *Analyst* 144, 1789–1798. doi: 10.1039/c8an02212g

Frizyuk, K., Hasan, M., Krasnok, A., Alù, A., and Petrov, M. (2018). Enhancement of Raman scattering in dielectric nanostructures with electric and magnetic Mie resonances. *Phys. Rev. B.* 97:085414. doi: 10.1103/PhysRevB.97.085414

Lombardi, J. R., and Birke, R. L. (2014). Theory of surface-enhanced Raman scattering in semiconductors. *J. Phys. Chem. C.* 118, 11120–11130. doi: 10.1021/jp5020675

Roelli, P., Galland, C., Piro, N., and Kippenberg, T. J. (2016). Molecular cavity optomechanics as a theory of plasmon-enhanced Raman scattering. *Nat. Nanaotechnol.* 11, 164–169. doi: 10.1038/NNANO.2015.264

Conflict of Interest: The authors declare that the research was conducted in the absence of any commercial or financial relationships that could be construed as a potential conflict of interest.

frontiers in Chemistry

ORIGINAL RESEARCH
published: 28 January 2019
doi: 10.3389/fchem.2018.00665

Investigating Dynamic Molecular Events in Melanoma Cell Nucleus During Photodynamic Therapy by SERS

Jing Yue[1], Lijia Liang[1], Yanting Shen[1], Xin Guan[2], Jing Zhang[1], Zhiyuan Li[3], Rong Deng[1], Shuping Xu[1]*, Chongyang Liang[2]*, Wei Shi[3] and Weiqing Xu[1]

[1] State Key Laboratory of Supramolecular Structure and Materials, Institute of Theoretical Chemistry, Jilin University, Changchun, China, [2] Institute of Frontier Medical Science, Jilin University, Changchun, China, [3] Key Lab for Molecular Enzymology and Engineering of Ministry of Education, Jilin University, Changchun, China

Photodynamic therapy (PDT) involves the uptake of photosensitizers by cancer cells and the irradiation of a light with a specific wavelength to trigger a series of photochemical reactions based on the generation of reactive oxygen, leading to cancer cell death. PDT has been widely used in various fields of biomedicine. However, the molecular events of the cancer cell nucleus during the PDT process are still unclear. In this work, a nuclear-targeted gold nanorod Raman nanoprobe combined with surface-enhanced Raman scattering spectroscopy (SERS) was exploited to investigate the dynamic intranuclear molecular changes of B16 cells (a murine melanoma cell line) treated with a photosensitizer (Chlorin e6) and the specific light (650 nm). The SERS spectra of the cell nucleus during the PDT treatment were recorded *in situ* and the spectroscopic analysis of the dynamics of the nucleus uncovered two main events in the therapeutic process: the protein degradation and the DNA fragmentation. We expect that these findings are of vital significance in having a better understanding of the PDT mechanism acting on the cancer cell nucleus and can further help us to design and develop more effective therapeutic platforms and methods.

Keywords: Ce6, cell nucleus, real-time, photodynamic therapy, surface-enhanced Raman spectroscopy

Edited by:
John Lombardi,
City College of New York (CUNY),
United States

Reviewed by:
Chih-Ching Huang,
National Taiwan Ocean University,
Taiwan
Wei-Lung Tseng,
National Sun Yat-sen University,
Taiwan

****Correspondence:***
Shuping Xu
xusp@jlu.edu.cn
Chongyang Liang
liang@jlu.edu.cn

Specialty section:
This article was submitted to
Analytical Chemistry,
a section of the journal
Frontiers in Chemistry

Received: *26 October 2018*
Accepted: *21 December 2018*
Published: *28 January 2019*

Citation:
Yue J, Liang L, Shen Y, Guan X,
Zhang J, Li Z, Deng R, Xu S, Liang C,
Shi W and Xu W (2019) Investigating
Dynamic Molecular Events in
Melanoma Cell Nucleus During
Photodynamic Therapy by SERS.
Front. Chem. 6:665.
doi: 10.3389/fchem.2018.00665

INTRODUCTION

Over the last few decades, photodynamic therapy (PDT) has emerged as a new and significant therapeutic strategy for various diseases especially in cancer therapy and has been approved for cancer treatments in the clinic (Voon et al., 2014; Han et al., 2015; Sun et al., 2017). Compared with conventional cancer therapy strategies, PDT possesses noticeable merits including high controllability, target selectivity, localized damage and weak side effects. The treatment involves three key components: photosensitizer (PS), light and reactive oxygen species (ROS). The PSs used in PDT are usually non-invasive without light irradiation (Agostinis et al., 2011; Wang et al., 2013). Once there is a light with the appropriate wavelength, ROS especially singlet oxygen will generate, which can induce tumor death (Fan et al., 2016) since excess ROS can damage crucial biological macromolecules, including proteins, lipids, nucleic acids, and carbohydrates(Liu et al., 2012; Abrahamse and Hamblin, 2016).

Also, ROS can induce a series of stress reactions if generated in high amounts. In early stages, the cells will activate the survival mechanism for self-defense or repair from injury. However, if the stress is so severe that cells can't protect themselves, the activation of death mechanisms will begin (Soriano et al., 2017). How cancer cells respond to the stressing situation depends on the cell types, the PS types and the level of ROS. In order to have deep understanding on the mechanisms of the PDT-induced cell death, many strategies have been used. Among them, cell viability tests (MTT and WST-1, etc.) and flow cytometry are the most common-used methods for PDT effect estimation in most literatures (Hodgkinson et al., 2017; Veloso et al., 2017; Yang et al., 2017). For instance, Soriano et al. used the MTT assay, Hoechst staining and nuclear morphology analysis to compare the photodynamic effects of two different PSs on non-tumoral and tumoral breast epithelial cell lines (Soriano et al., 2017). They found that most tumoral cells died from necrosis or apoptosis while non-tumoral cells died from necrosis mostly. These methods can only tell us the final therapeutic results by the ratio of living/dead cells, however, they can't provide any information about how PDT induced cell death. Currently, the response mechanisms of cells exposed to PDT have many different versions but are crucial either for learning the medical PDT therapeutic strategy or for understanding the cell self-defense process.

Surface-enhanced Raman spectroscopy (SERS) is a nearly non-invasive and powerful label-free analysis tool that can provide detailed fingerprint spectral information of cells, tissues and can achieve detection *in situ* (Kneipp et al., 2008; Qian and Nie, 2008; Kuku et al., 2017; Laing et al., 2017). In addition, SERS has inherent advantages of high sensitivity and real-time monitoring of complex and dynamic changes of analytes, which make it appropriate in multiplex biological processes (Kang et al., 2014; Ali et al., 2016; Kircher, 2016). On account of these superiorities, SERS has been widely used for *in situ* exploration of the structural information of intracellular molecules, as well as the dynamic changes of cells in response to some external stimuli, such as photo treatments and chemical drugs (Cialla-May et al., 2017; Kairdolf et al., 2017; Zheng et al., 2018). In previous work, we only found one paper reported by da Silva et al. (Veloso et al., 2017) who employed the direct SERS strategy to investigate cancer cell death caused by PDT. However, they adopted a destructive sample pre-treatment process in which all groups of the PDT-treated cells had been frozen in liquid nitrogen and then ground and stirred to obtain the liquid and homogeneous solutions for SERS detections. This pre-treatment fully destructed the cell framework and functional domains. While, SERS is sensitive to the molecular vibration, both the molecular structure and the localized environment can affect the obtained SERS signals and final results analysis. Additionally, although analyzing the changes of molecular information after the PDT treatment can provide some information about treatment effect, tracing the dynamic molecular events of the cell during the PDT treatment process is much more significant for understanding response mechanisms.

As the control center of cells, the cell nucleus plays important roles in metabolism, growth and differentiation. It is also the main site of genetic materials. A strategy for the *in-situ* SERS detection of cell nuclei has been developed, in which the plasmon-based nanoparticles are required to pre-incubate with cells and the Raman signals of intracellular components closely adjacent to these nanoparticles can be measured (Oyelere et al., 2007; Xie et al., 2009; Huefner et al., 2013). This *in situ* intranuclear SERS exploration method provides new access for the deeper study of cell biophysical processes from the cell nucleus aspect. Also, it provides a possible way to disclose the intracellular response toward external stimuli, particularly during cancer treatments (Austin et al., 2013; Liang et al., 2015; Deng et al., 2017; Shen et al., 2018).

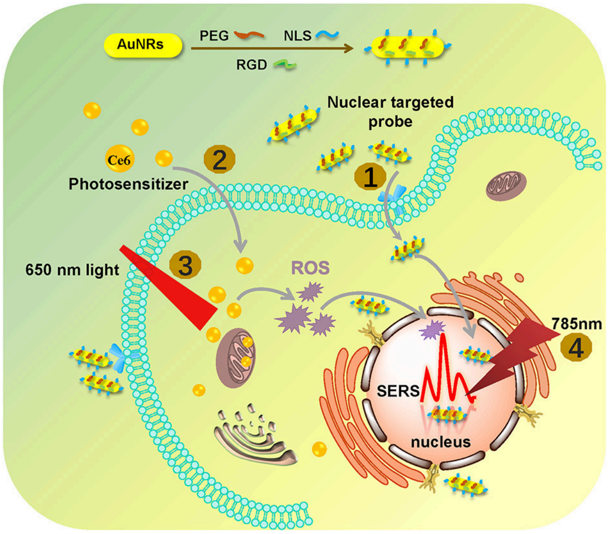

FIGURE 1 | The procedures of monitoring the changes of the nuclear signal after photodynamic therapy by SERS spectroscopy with the AuNR-based nucleus-targeted nanoprobes. ①-④ correspond to the pre-loading of the targeting nanoprobes to the cell nucleus, the internalization of PS in the cell, the irradiation of Ce6 to produce ROS, and the SERS measurement of a cell nucleus.

In this work, by using the SERS technique combined with a nuclear-targeted gold nanorods (AuNRs) probe, we tracked the dynamics of the nucleus during the PDT treatment (as shown in **Figure 1**). A murine melanoma cell line (B16 cell) was selected as a proof of concept to evaluate its response behaviors during the PDT treatment. First, we modified the partial surface of AuNRs with the targeting peptides (cancer cell-specific targeted peptide and nuclear localization signal peptide) which can specially identify cancer cells and then deliver these nanoprobes to the nucleus accurately (①). Then Chlorin e6 (Ce6) as the PS was used for the PDT treatment of B16 cells (②), irradiated with a 650 nm light (③). Finally, the *in situ* SERS spectra of the nucleus during PDT treatment were recorded (④) and analyzed. This work mainly focused on exploring how the biomolecules of a cancer cell nucleus respond to PDT treatment by SERS spectroscopy, which is helpful for better understanding the PDT mechanism and further developing effective therapeutic approaches. The novelty of this work can be summarized as two aspects: (1) this is the first time to explore the acting mechanism of PDT on a cell nucleus based on the spectral information on nuclear components, and (2) it also the first one to monitor PDT with SERS *in situ*.

EXPERIMENTAL

Fabrication of Nuclear-Targeted Nanoprobes

First of all, AuNRs with a plasmonic absorption maximum of 753 nm (aspect ratio of about 4.4) which were stabilized by cetyltrimethylammonium bromide (CTAB) were synthesized. The details were shown in Supporting information. Ultraviolet–visible (UV–vis) spectroscopy, transmission electron microscopy (TEM) and dynamic light scattering (DLS) spectroscopy were employed to measure the plasmonic property, size, morphology, and zeta potential of the obtained AuNRs.

Then, AuNRs were modified by methoxy poly(ethylene glycol)-thiol (mPEG-SH) (MW = 5,000), nuclear localization signal (NLS) peptide, and a cancer-cell-specific targeted peptide (RGD) in one step. To quantify the number of peptides on a single AuNR, the calibration curve from the standards and the fluorescence of free FITC-labeled NLS before and after the reaction with AuNRs were required, as shown in **Figure S1**. According to the calibration curve (**Figure S1b**), the average number of NLS on a single AuNR is calculated as about 1100. The RGD on the surface of AuNRs was kept as the same dose ratio as NLS.

Location of Nanoprobes in Nucleus

In order to confirm the targeting ability of the prepared nanoprobes, the cells grown on a slide glass for 24 h were incubated with fluorescein isothiocyanate (FITC)-labeled nuclear-targeted nanoprobes AuNRs-PEG-NLS-RGD (0.1 nM) prepared by linking FITC-tagged NLS (5.0 mM, 12 μL) on the surface of AuNRs (1.34 nM, 10 mL) for 24 h and next stained by Hoechst 33342 (excited by a 405 nm Laser, 10 μg/mL) for 15 min to highlight the cell nucleus. After that, a FV1000 confocal fluorescence microscope (Olympus) was used to confirm the location of the prepared nanoprobes.

In addition, the specific targeting effects of AuNRs-PEG-NLS-RGD were also evidenced by a self-built platform integrated with both fluorescence microscope (IX71, Olympus) and dark-field microscope (Olympus).

Cell Culture

Murine melanoma cell line (B16 cells) were grown in Roswell Park Memorial Institute 1640 medium (RPMI 1640, Invitrogen) supplemented with 10% fetal bovine serum (FBS). The cells were maintained at 37°C in a humidified environment with 5% of CO_2.

Photosensitizer (Ce6) Preparation and Treatment of B16 Cells

In the dark, the photosensitizer Ce6 was dissolved in PBS in which oxygen was removed and we achieved a Ce6 solution with a concentration of 12 μM. B16 cells that had been planted on Quartz coverslips were cultured with the nanoprobes for 12 h, and then they were treated with the prepared Ce6 solution for 12 h. After that, cells were irradiated with an LED lamp (650 nm) at an energy density of 18 mW/cm^2 for different lengths of time (0 to 5 min). Then cells were washed three times with phosphate-buffered saline (PBS) and fixed by 4% paraformaldehyde for next use.

In vitro Cytotoxicity

In vitro cytotoxicity of AuNRs-PEG-NLS-RGD and Ce6 were assessed by the WST-1 (2-(4-Iodophenyl)-3-(4-nitrophenyl)-5-(2,4-disulfophenyl)-2H-tetrazolium, monosodium salt) assay. B16 cells were firstly grown in two 96-well plates in the RPMI Medium 1640 (1640, Thermo Fisher Scientific) containing 10% fetal bovine serum (FBS) at 37°C in a 5% CO_2 incubator for 24 h. Then B16 cells in one 96-well plate were incubated with fresh culture medium containing 0.1 nM of AuNRs-based nanoprobes for another 24 h, and another 96-well was incubated with fresh culture medium containing different concentrations of Ce6 for the second 24 h. Afterwards, we added 20 μL of the WST-1 solution into each well and incubated them for 2 h continuously. At last, the absorption intensity of each well was measured at 450 nm by a microplate reader (Tecan Sunrise). We used B16 cells incubated with the standard cell culture medium for cell viability evaluation as the control group.

Intracellular ROS Generation Assay

In order to detect the PDT-induced intracellular ROS, a 2, 7-dichlorofuorescin diacetate (DCFH-DA) probe was employed. DCFH-DA probe (10 μM) can monitor the generation of the intracellular ROS owing to a fluorescent turn-on chromogenic reaction from DCFH-DA to dichlorofluorescein (DCF) after undergoing intracellular deacetylation upon ROS-mediated oxidation. The B16 cells cultured in a Petri dish (1 × 10^5) were co-cultured with nanoprobes (0.1 nM) and Ce6 (1.2 μM) for 12 h. After removing unbound NPs with PBS, the cells were incubated with 10 μM DCFH-DA at 37°C for 30 min. After that, cells were exposed to a 650 nm lamp (18 mW/cm^2) for 1 min. Finally, the fluorescence of DCF was measured at 488 nm by using confocal fluorescence microscope.

Apoptosis/Necrosis Assay

To further illustrate that PDT mediated the apoptosis of B16 cells, apoptosis/necrosis assay was applied by the flow cytometry combined with the Annexin V-APC/ 7-aminoactinomycinD (7-AAD). Annexin-VPC was used to differentiate apoptotic cells because of its strong affinity to phosphatidylserine serine on the outer membrane of apoptotic cells. And 7-AAD is generally excluded from live cells. After cultured for 24 h, cells were cultured with AuNRs-PEG-NLS-RGD and Ce6 for 12 h. After PDT, the cells in the suspension and the petri dish were collected. Finally, 100 μL of cells were stained with the Annexin V-APC for 7 min, 7-aminoactinomycinD (7-AAD) for 3 min and then 400 μL of PBS was added. Finally, the suspension was measured by the FACSCalibur (BD Biosciences, USA).

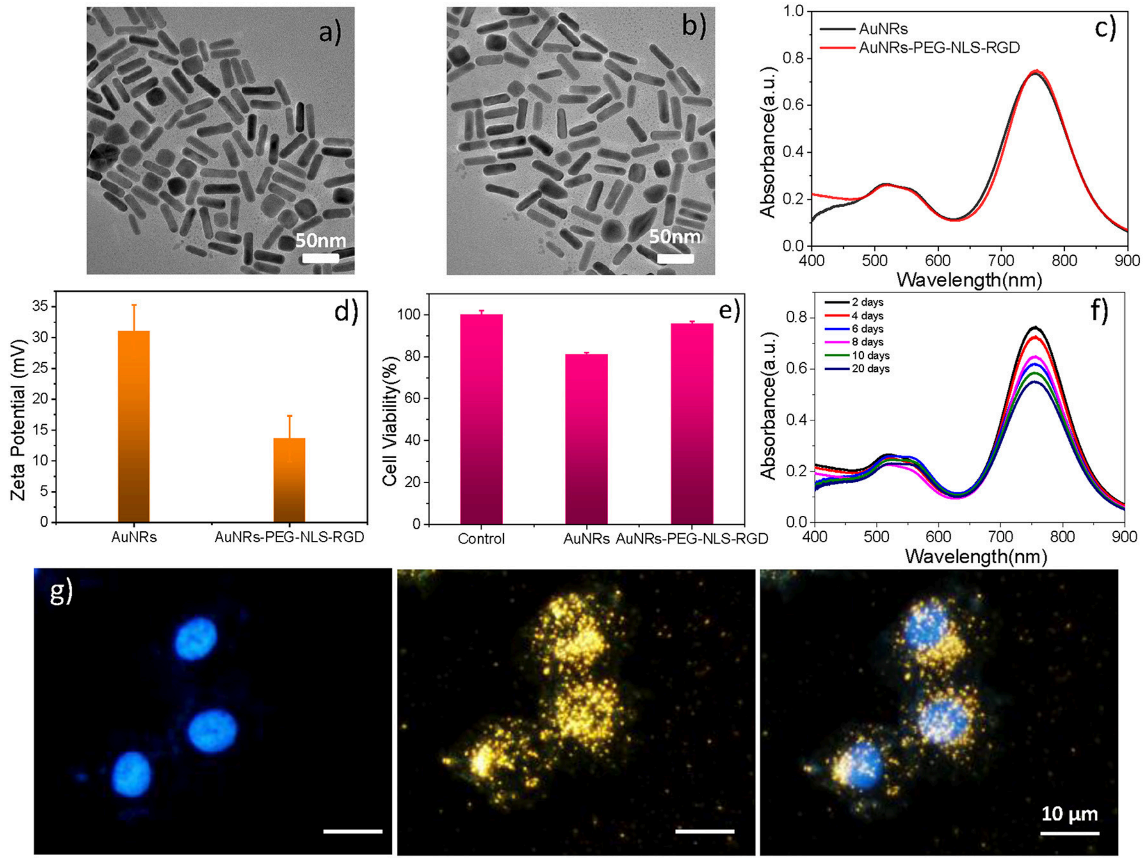

FIGURE 2 | A TEM image of **(a)** AuNRs and **(b)** AuNRs-PEG-NLS-RGD. **(c)** UV–vis spectra of AuNRs and AuNRs-PEG-NLS-RGD. **(d)** Zeta potential of AuNRs and AuNRs-PEG-NLS-RGD. **(e)** Cell viabilities of B16 cells incubated with 0.1 nM of AuNRs and AuNRs-PEG-NLS-RGD for 24 h. **(f)** Uv-vis spectra of AuNRs-PEG-NLS-RGD nanoprobes after storage at 4°C for 20 days. **(g)** Fluorescent, dark-field and merged images of B16 cells incubated with AuNRs-PEG-NLS-RGD for 12 h from left to right.

SERS Detection of B16 Cell Nucleus

As mentioned above, B16 cells cultured already on quartz coverslips for 24 h were incubated with fresh culture medium containing of 0.1 nM nanoprobes and 1.2 μM Ce6 for another 12 h. Then cells were irradiated with the LED lamp (650 nm) at an energy density of 18 mW/cm^2 for 0, 1, 3, and 5 min, respectively. After treatment, they were washed three times with PBS, fixed with 4% paraformaldehyde for 20 min, and then sealed for SERS detections. SERS detections were performed by a confocal Raman system (LabRAM Aramis, Horiba Jobin Yvon) with a 785 nm laser as the excitation source. The laser (with about 20 mW power on the sample) was directed into a microscope and focused on the sample by a 50 × 0.75 NA objective lens. All spectrums were obtained in a 30 s collection time with two accumulations. And the data was analyzed using NGSLabSpec and Origin 9.0.

RESULTS AND DISCUSSION

Synthesis of Nuclear-Targeted Nanoprobes

In order to obtain molecular fingerprint information of the cell nucleus by SERS spectroscopy, a plasmon-based, nuclear-targeted nanoprobe is required and its SERS enhancement capacity should be high enough to achieve high-quality intranuclear spectra. Here, a targeting AuNR-based nanoprobe with the surface functionalization of RGD and NLS was prepared. Firstly, AuNRs were synthesized according to the seed-mediated growth method (Nikoobakht and El-Sayed, 2003; Sau and Murphy, 2004). To prevent aggregation and further improve the biocompatibility of the nanoprobes, mPEG-SH was conjugated to the surface of AuNRs. Next, RGD (CGGGPKKKRKGC) and NLS (GGVKRKKKPGGC) *via* the covalent linking between gold and the thiol group of cysteine (bold in the peptide sequence of NLS and RGD) to enrich the nanoprobe with the cancer cell selectivity and the nuclear-targeted ability. RGD can selectively recognize cancer cells *via* binding with the $\alpha v\beta 6$ or αv integrins on the cell surface. NLS has a crucial sequence (KRKKK), which can deliver the nanoprobes to the cell nucleus through the nuclear pores.

As shown in **Figure 2a**, the AuNRs with an aspect ratio of about 4.4 (40 × 9 nm) were obtained. After surface modifications, the AuNR-based nuclear targeting nanoprobe (**Figure 2b**) keeps monodisperse and the size has no notable change compared with the bare AuNRs. Their plasmonic bands red shifts from 753 to 756 nm when AuNRs modifying with PEG, NLS and RGD (**Figure 2c**). And the zeta potential of AuNRs also show a decrease of 17 mV (from 31 to 14 mV, **Figure 2d**). In addition, considering that the AuNRs might affect cell metabolism and proliferation, the cell incubation concentration of nanoprobes was evaluated by the WST-1 assay, which is as low as 0.1 nM, indicating almost no toxicity to B16 cells (**Figure 2e**). Moreover, we further proved that the nanoprobe has acceptable stability after storage at 4°C for 20 days (**Figure 2f**) through Uv-vis spectroscopy. The decrease of absorbance might result from the colloidal deposition of a small amount of the AuNRs.

Targeting the AuNRs-based nanoprobes to purpose positions is the precondition for exploring the information of the intranuclear components. Our previous studies have demonstrated the targeting ability of the AuNRs-based nanoprobes in cancer cells [Soma gastric cancer cell: SGC-7901 (Liang et al., 2015) and liver cancer cell: HepG2 (Deng et al., 2017; Shen et al., 2018)] through dark-field and fluorescence images (Liang et al., 2015), high-resolution three-dimensional (3D) images, and bio-TEM images (Shen et al., 2018). Here, to prove the targeting effects of the AuNRs-PEG-NLS-RGD for the cell nucleus of the murine melanoma cell line (B16, having a smaller size of about 13 μm than HepG2 and SGC-7901), the dark-field and fluorescent images of cells were also taken. Under the dark-field irradiation, these nanoprobes produce strong scattering due to their plasmonic feature, while the cell nuclei had been stained with a nucleus-specific dye (Hoechst 33342, 10 μg/mL) that gives a blue color. It can be found from **Figure 2g** that most nanoprobes are distributed in the regions of the cell nuclei due to the dark-field/fluorescent merged images. Additionally, we compared three kinds of AuNRs including AuNRs-PEG, AuNRs-PEG-NLS, and AuNRs-PEG-RGD, incubating them with B16 cells, respectively, to verify the nuclear targeting feature of our nanoprobes, as shown in **Figure S2**. By comparing AuNRs-PEG-RGD and AuNRs-PEG-NLS, most of the AuNRs-PEG-NLS probes entered into the cell nucleus, which illustrates the nucleus-targeting ability of the NLS peptide. To further prove that the nanoprobes can enter the cell nucleus with the help of RGD and NLS, we labeled the NLS with a dye (fluorescein isothiocyanate, FITC) to display the locations of nanoprobes under the fluorescence microscopic imaging (IX71, Olympus) (**Figure S3**) and we measured the fluorescence spectrum of AuNRs-RGD-NLS (FITC), as shown in **Figure S4**. It can be observed that the fluorescence signal is still visible although the quenching exists. Besides, the fluorescent images of cells incubated with AuNRs-RGD-NLS (FITC) nanoprobes further prove their fluorescent activity. The green shows the distribution of nanoprobes, while the blue represents the cell nucleus. It can be seen that two colors overlap to a large extent, indicating that the nanoprobes have been delivered to the nucleus successfully. We further quantitated the amount of nanoprobes internalized into each B16 cell due to the plasmonic absorption of AuNRs *via* UV-vis spectroscopy, and the number is calculated as about 2,820 AuNRs per cell (see Part 2.5 in **Supplementary Material**).

PDT-Dominating Treatment for B16 Cells

As one of three key components of PDT, PS endows the role of producing ROS. In this study, Ce6 is used as PS for treating B16 cells (**Figure S5C**), which is a porphyrin derivate (its structure is shown in **Figure S5A**). Ce6 has two strong absorption bands at 402 and 655 nm (**Figure S5B**). Thus, a 650 nm light-emitting diode (LED) array with a power density of 18 mW/cm^2 (**Figure S5D**) was chosen for matching the long-wavelength band of Ce6. The cell culture time of Ce6 in B16 cells was evaluated as 12 h, which allows for the largest accumulation of Ce6 in cells (**Figure S6**). As shown in **Figure 3a**, as the concentration increased, there was no significant increase in toxicity without light irradiation, which means the Ce6 has negligible damage to B16 cells However, once they were exposed to the 650 nm light, cell viability decreases significantly with the Ce6 concentration increasing. When the treated concentration reaches 1.2 μM, the cell viability is only 22.5%. While, the survival rate of cell didn't further decrease even treated with higher dose. Therefore, the concentration of Ce6 for B16 cells is optimized as 1.2 μM by the WST-1 assay.

In order to verify that the photosensitizers (Ce6) can enter into the cancer cell and produce ROS under the irradiation of

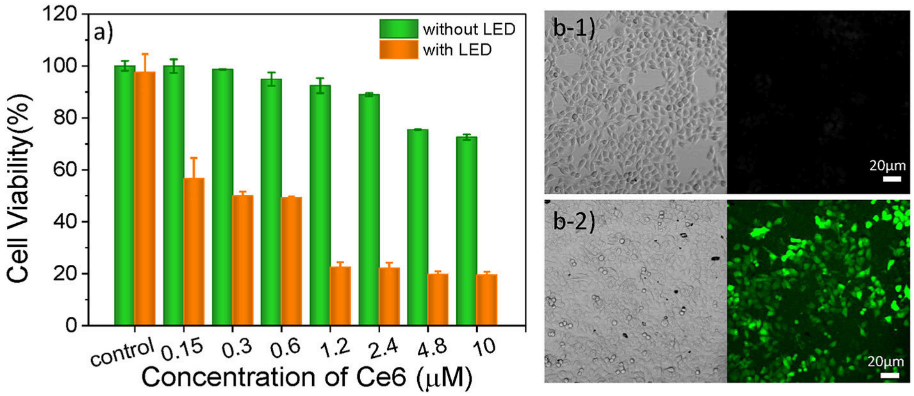

FIGURE 3 | (a) Cell viabilities of B16 cells incubated with Ce6 under different concentrations for 12 h before and after the irradiation of a 650 nm lamp (18 mW/cm^2) for 5 min. Bright-field and confocal fluorescent images of Ce6 (1.2 μM) treated B16 cells stained with DCFH-DA (10 μM) before **(b1)** and after **(b2)** they were treated with 650 nm LED (18 mW/cm^2) for 1 min.

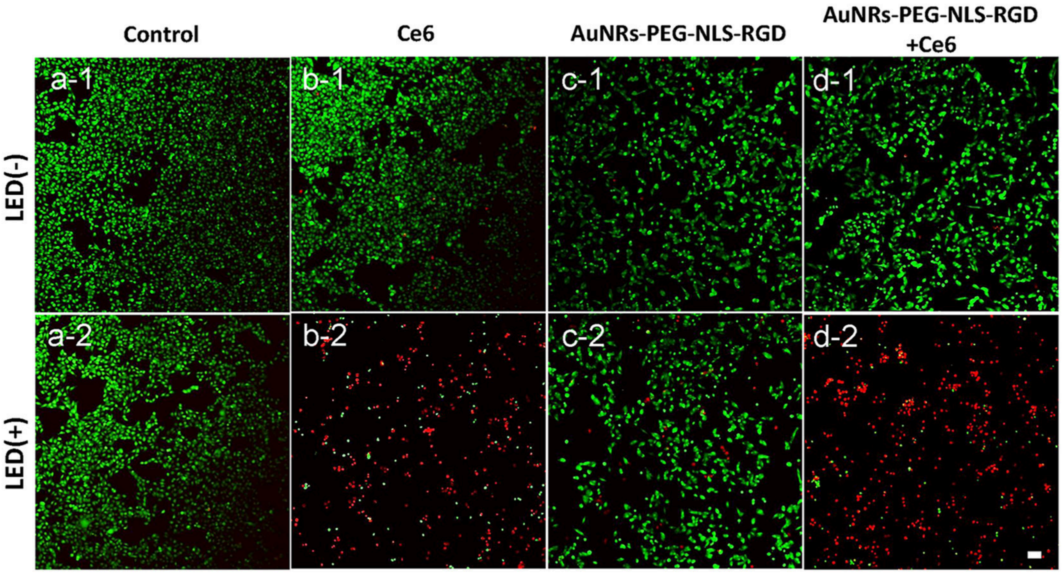

FIGURE 4 | Confocal fluorescent images of B16 cells after they were incubated with Ce6 **(b)** and AuNRs-PEG-NLS-RGD **(c)** and AuNRs-PEG-NLS-RGD + Ce6 **(d)**, without (1) and with (2) the irradiation of a 650 nm lamp (18 mW/cm^2) for 5 min, while the cells without and with the light irradiation were used as the control samples **(a)**. Cells were stained with Calcein-AM (green) and PI (red) for distinguishing the living and dead cells. The scale bar is 20 μm.

650 nm LED, the 2, 7-dichlorofuorescin diacetate (DCFH-DA) probe that can monitor the generation of the intracellular ROS was used to evaluate the pharmaceutical effect of Ce6, owing to a fluorescent turn-on chromogenic reaction from DCFH-DA to dichlorofluorescein (DCF) after undergoing intracellular deacetylation upon ROS-mediated oxidation. **Figure 3b** shows the confocal fluorescent images of the DCFH-DA (10 μM) stained B16 cells that had been treated with Ce6 (1.2 μM) before and after they were exposed to a 650 nm lamp for 1 min. There is no obvious fluorescence signal before the light irradiation. After irradiating the cells for 1 min, obvious green fluorescence displays, proving the generation of ROS inside the PDT-treated cells (**Figure 3b2**). It can also be observed that many small bubbles appeared in cells and the morphology of cells became a nearly spherical shape compared those in **Figure 3b1**) that show a spindle shape, indicating the joint influence of the Ce6 (1.2 μM) and that the light irradiation (18 mW/cm^2, 1 min) is enough for inducing these B16 cells dying.

To further assess the effect of PDT treatment, confocal fluorescence microscopy was used to visually analyze cell viability with PDT treatment. These cells were stained with propidium iodide (PI, red) and Calcien-AM (green), respectively, which can distinguish dead and living cells. As shown in **Figures 4a1,a2**, the light can produce no damage to B16 cells. Similarly, if the cells were treated with Ce6 only, no dead cells were observed (**Figure 4b1**). When cells were exposed to Ce6 (a final concentration of 1.2 μM) and 650 nm light for 5 min (18 mW/cm^2) simultaneously, we can find that a lot of cells were dead (**Figure 4b2**), which agrees with the results obtained by the WST-1 assay (**Figure 3a**). As we all know, AuNRs have good light-heat conversion efficiency and they will produce very high local temperature under the irradiation of light with a specific wavelength to induce cell death. Therefore, to identify whether there is a photothermal therapy (PTT) effect in our system, the images of B16 cells were cultured with the AuNRs-PEG-NLS-RGD nanoprobes (with a final concentration of 0.1 nM), and results with and without light exposure were obtained. The results show that AuNRs-PEG-NLS-RGD probes show no obvious toxicity to cells (**Figure 4c1**). Even after light irradiation, only a few dead cells were observed in **Figure 4c2**, indicating that cell death caused by the PTT can be ignored. Also, compared with PDT treatment (**Figure 4b2**), there is not much difference for cells treated with PDT and AuNRs-PEG-NLS-RGD probes at the same time, (**Figures 4d1,d2**) confirming that the therapeutic effect is dominated by the PDT in present system.

Nuclear Dynamic Changes Revealed by SERS

As in the above discussion, we can obtain the therapeutic effect of the PDT treatment by WST-1 method. Confocal florescence imaging technique can also distinguish and analyze the dead and live cells visually by choosing the specific dyes. However, limited information during the dynamic treatment process can be known. So, we used SERS to reveal the molecular events of the cell nucleus during treatment. Before SERS detection of cells, to demonstrate whether there is obvious interference of the Ce6 on the SERS detection of the cell nucleus, we compared the Raman spectra and SERS spectra of Ce6 with SERS spectra of the nucleus. As shown in **Figure 5A**, by comparison, we can find that neither Raman spectra nor SERS spectra of Ce6 interferes with SERS detection of B16 cell nucleus.

In addition, to verify whether the SERS signals of targeted peptides on the nanoprobes would interfere in the results

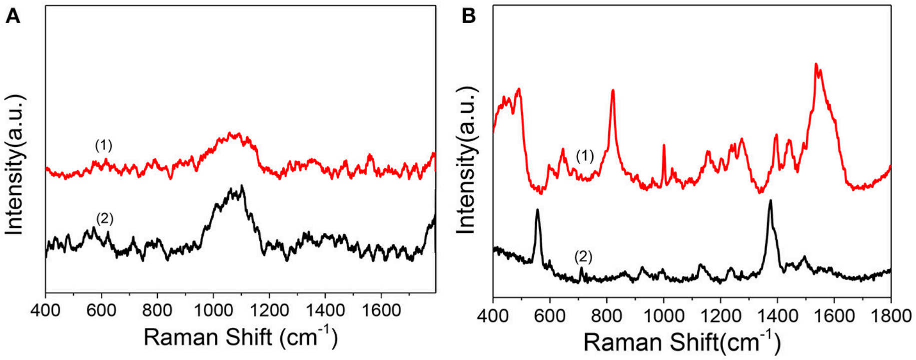

FIGURE 5 | (A) Raman spectrum (1) and SERS spectrum of Ce6 solution (2) measured after mixing AuNRs (0.3 mL, 0.1 nM) with the Ce6 solution (0.3 mL, 1.2 μM). **(B)** (1) SERS spectrum of B16 cell nucleus with the enhancement of nuclear targeting nanoprobes (0.1 nM). (2) SERS spectrum of 1.0 nM of nuclear targeting nanoprobes.

analysis of intranuclear components, we measured the SERS spectrum of the nuclear targeting probes (**Figure 5B** bottom curve). When the spectrum is compared with the nuclear SERS spectrum (**Figure 5B** top curve), despite several overlaps, most peaks are different, which indicates these nanoprobes have little interference in the spectral analysis of intranuclear biomolecules. This is consistent with our previous studies that the SERS spectra of the PEG, RGD, and NLS on the AuNRs are identifiable and distinguishable before and after they were in the cell nucleus (Liang et al., 2015; Deng et al., 2017; Shen et al., 2018).

With the aim of understanding the therapeutic mechanism of PDT, we monitored the dynamics of intranuclear components by SERS. Before the experiment, we measured the SERS spectra of several proteins and DNA, such as bovine serum albumin (BSA) and calf thymus DNA (the data were not given). The spectra suggested that the signal we measured in B16 cells came from proteins and DNA rather than small molecules. Then, to assess the reproducibility of the obtained SERS spectra, the SERS spectra of B16 cells treated with the AuNRs-PEG-NLS-RGD nanoprobes were recorded. There are five intranuclear SERS spectra shown in **Figure 6A**, which demonstrates better reproducibility of the SERS spectra. Besides, the SERS spectra of the B16 cell nucleus, which were co-cultured only with the AuNRs-PEG-NLS-RGD nanoprobes and then irradiated with a 650 nm LED array (18 mW/cm^2) for 0, 1, 3, and 5 min, respectively, were acquired (**Figure 6B**). Apparently, the characteristic peaks are almost unchanged with the increase of the illumination time. These results demonstrate that the molecular information of the cell nucleus has no obvious changes when the cells were only treated with nuclear-targeted nanoprobes or light if the PS is absent.

Afterward, B16 cells were incubated with nanoprobes and Ce6 in turn for 12 h each and then treated with a 650 nm LED array (18 mW/cm^2) for the same time as mentioned above. The time-dependent SERS spectra and possible molecular events of the nuclear components were obtained, as shown in **Figure 6C**. These spectra were collected mainly from the definite spots where the nanoprobes were accumulated.

Each spectrum is an average spectrum of 150 spectra from six cells to reduce the differences between cells and provide convincing repeatability (**Figure S7** shows the data of another batch). **Table 1** summarizes the band assignments of the main components of the B16 cell nucleus in the SERS spectra of **Figure 6C**. The band at 602 cm^{-1} represents the -S-S- vibration of proteins. It can be seen from the spectrum that its intensity decreases with the increase of treatment time and reaches a minimum at 5 min, demonstrating the disruption of disulphide bonds and the denaturation of the protein tertiary structure. At the same time, we can see that the intensity of the Raman band at 1,001 cm^{-1}, which is attributed to the respiration vibration of the phenylalanine in protein (Sau and Murphy, 2004) decreases at the irradiation time of 1 min, while it increases significantly at 3 min and arrives in the lowest after 5 min light irradiation. The apparent enhancement of peak intensity symbolizes the beginning of cell apoptosis (Ali et al., 2016). We hypothesize that the decrease of intensity may be due to the oxidation of phenylalanine to L-tyrosine under the action of ROS and enzyme, which further explains why the peak at 829 cm^{-1} (belonging to L-tyrosine) appears at 1 min light irradiation. Grune et al. (Kang et al., 2012) pointed out that amino acid residues, including tyrosine in proteins, are important reaction targets because of their active reactivity. They always become the primary targets of oxidative attacks on proteins. Thus, in the present study, the peak intensity at 829 cm^{-1} gradually increases with the increase of time as a result of PDT.

Cellular biology discloses that when cells are stimulated by ROS, apoptosis inducing factor (AIF) is released from the mitochondria, then transferred into the cytoplasm and then into the nucleus, causing the DNA within the nucleus to agglutinate and break into fragments, inducing apoptosis (Grune et al., 2001). In the present study, at 5 min, a new band appears at 1,232 cm^{-1} (attributable to the C-N stretch, peptide bond), it is possible that the peptide bonds exposed to the surface of AuNRs. Bands at 820 and 1,391 cm^{-1}, corresponding to O-P-O vibration of DNA backbone, gradually disappear with the increase of treatment time. This backbone structure leads the DNA base pairs exposing

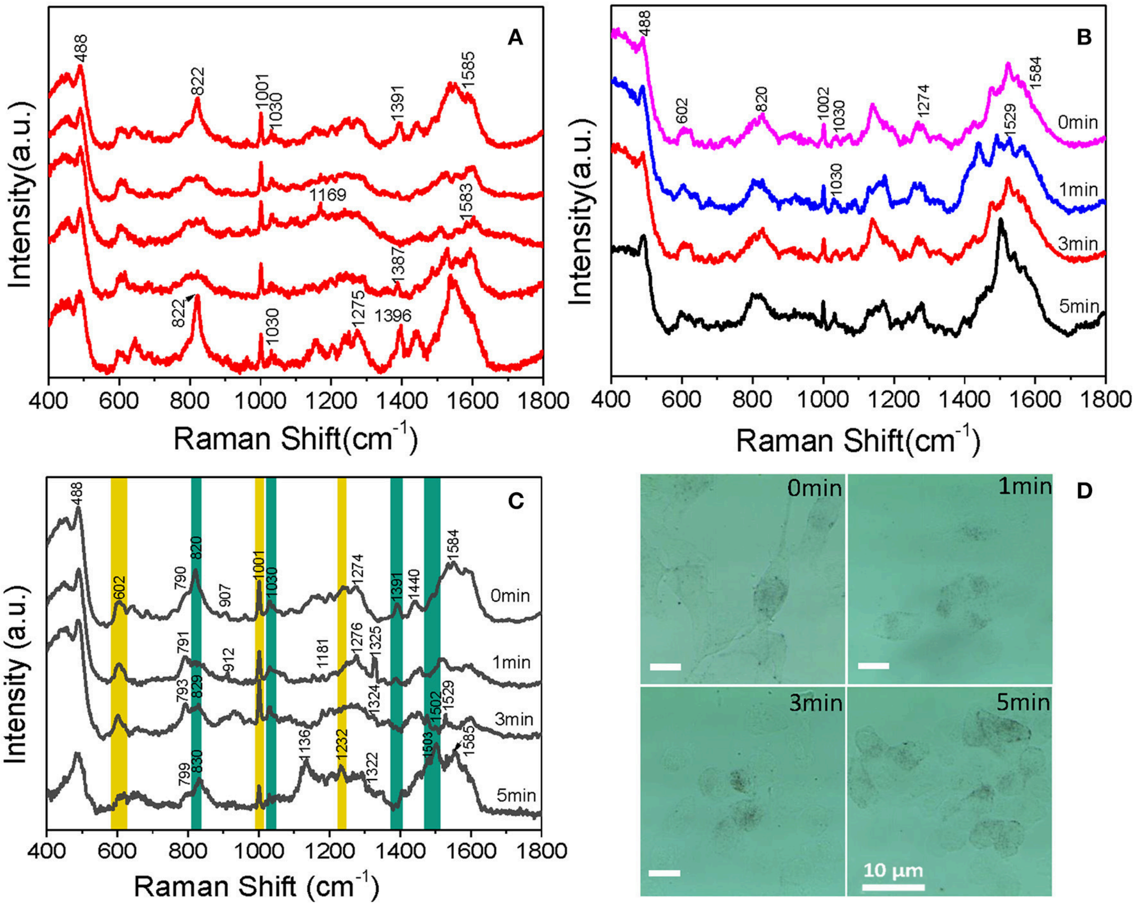

FIGURE 6 | Intranuclear SERS spectra of **(A)** five B16 cells cultured with 0.1 nM AuNRs-PEG-NLS-RGD for 12 h, **(B)** cells cultured with 0.1 nM of AuNRs-PEG-NLS-RGD for 12 h and then treated with 650 nm LED (18 mW/cm^2) for 0, 1, 3, and 5 min, respectively and **(C)** B16 cells cultured with 0.1 nM AuNRs-PEG-NLS-RGD and 1.2 μM Ce6 for 12 h and then treated with 650 nm LED (18 mW/cm^2) for 0, 1, 3, and 5 min, respectively. **(D)** Bright-field images of B16 cells cultured with 0.1 nM AuNRs-PEG-NLS-RGD and 1.2 μM of Ce6 for 12 h and then treated with 650 nm LED (18 mW/cm^2) for 0, 1, 3, and 5 min, respectively.

to the surface of AuNRs or closer to AuNRs, which is the reason why the intensities of the bands at 1,503 and 1,529 cm^{-1} belonging to the DNA base pair increase. Meanwhile, a decrease in the intensity of the band at 1,030 cm^{-1} is observed, which represents the C-O vibration in DNA, and further proves DNA fragmentation. The 1,529 cm^{-1} peak decreases at 5 min, which is mainly because guanine is the most easily oxidized base by singlet oxygen among the four bases of nucleic acid (Buchko et al., 1995). In addition to the orderly changes in peak intensities, Raman shifts of several bands also vary regularly. For example, peaks at 790 and 907 cm^{-1} shifts to higher wavenumbers. Since they represent DNA and protein, all these variations in Raman band intensity and shift suggest that DNA and protein in the nucleus of B16 cells has been destroyed and cell apoptosis occurs during the treatment of Ce6.

Beyond that, the process of Ce6 acting on B16 cells can also be researched by sustained cell deformation, a visualization process displayed on bright-field images (**Figure 6D**). Since B16 cells are adhere-wall cultured, we can see that there are many long filaments around individual cells and the shape of cells is fusiform before the treatment. After incubation with AuNRs-PEG-NLS-RGD, Ce6 and light irradiation, the morphology of B16 cells gradually shrank and eventually turned into a small spherical shape. At the same time, the adherence of cells gradually reduced, which caused them to float in the culture medium when they approached apoptosis. This visual process demonstrates that, with the prolongation of the action time of Ce6 in the body, Ce6 performs its damaging action gradually.

Apart from the SERS spectra of nucleus during PDT treatment processes, we investigated that the dynamic changes of intranuclear biomolecules treated with phorbol myristate acetate (PMA, 1 μg/mL), a membrane-permeable ROS generation stimulus (Bellavite, 1988), to further explore whether PMA will produce the same PDT effect as Ce6. SERS spectra of cell nuclei were recorded after they were treated with PMA for 1 and 2 h. As anticipated, we observed similar changes in peak intensities at 602, 820, 1,236, and 1,389 cm^{-1} (**Figure S8**). This observation is consistent with the above changes obtained from the treatment of Ce6 and confirms the therapeutic effect of the photosensitizer Ce6.

TABLE 1 | The band assignment of the SERS spectra of the main components in B16 cell nucleus.

Raman Shift(cm^{-1})				Assignments		
0 min	**1 min**	**3 min**	**5 min**	**Carbohydrate**	**DNA**	**Protein**
488	488	488	488	Mannitose		
602	602	602	602			-S-S-
820	-	-	-		O-P-O stretch	
-	829	829	830			Tyrosine
907	912	-	-			C-C
1,001	1,001	1,001	1,001			Phenylalanine ring breath
1,030	1,031	1,032	1,030		C-O stretch	
-	1,181	1,180	1,181			C-N stretch
-	-	-	1,232			Amide III
1,391	1,390	-	-		O-P-O stretch	
-	-	1,502	1,503		A	
-	-	1,529	1,531		G	

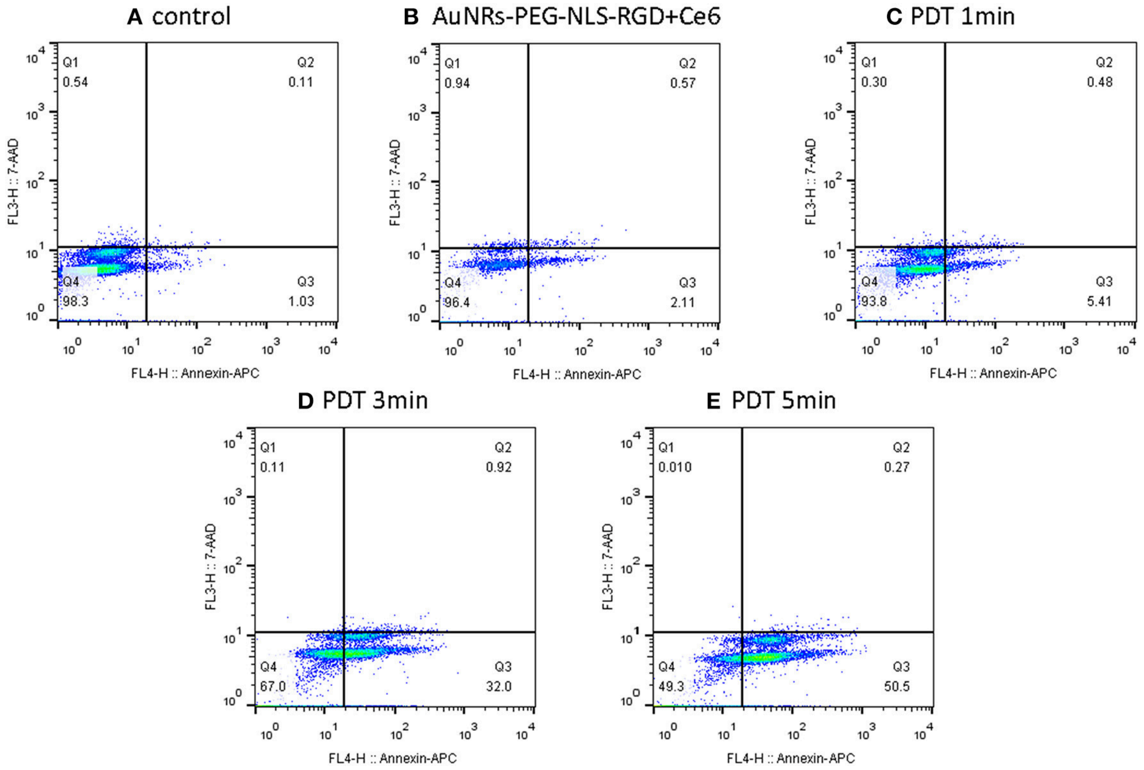

FIGURE 7 | Flow cytometry (apoptosis/necrosis assay) for the B16 cells treated with nanoprobes and Ce6 before **(B)** and after light irradiation with different time **(C–E)**, while the B16 cells without any treatment was used as a control **(A)**. Cells were labeled with Annexin V-APC and 7-aminoactinomycinD (7-AAD) and measured by the FACSCalibur (BD Biosciences, USA). Q1- Q4 indicate necrosis, late apoptosis, early apoptosis and viable, respectively.

PDT-Induced Apoptosis Revealed by Flow Cytometry

In addition to the SERS spectra, the effect of PDT was confirmed by the apoptosis/necrosis assay in which cells were labeled with Annexin V-APC and 7-aminoactinomycinD (7-AAD) and then the fluorescence intensity was examined by flow cytometry. It should be noted that the fluorescence emission bands of either Annexin V-APC or 7-AAD can effectively avoid the emission interference from Ce6. As shown in **Figure 7**, by comparing the control sample (B16 cells) and the B16 cells plus Ce6 before light irradiation, more and more apoptotic cells experiencing the PDT gradually appear in the Q3 phase that indicates an apoptosis-dominating physiological process, when the PDT strength increases as the irradiation time. These data well support the conclusion that the B16 cells undergo the way of apoptosis, which agrees with the above SERS results that the drastic changes of DNA and proteins in the cell nucleus were observed during this apoptotic process.

CONCLUSIONS

SERS was successfully employed to monitor the dynamics of the murine melanoma cell nucleus during the PDT process. The nuclear targeted nanoprobes with significant SERS enhancement ability, specific targeting and excellent biocompatibility were designed and used for SERS measurements of the cell nucleus. With the assistance of targeting nanoprobes, the time-dependent SERS spectra along the course of the PDT treatment were achieved and the events of proteins and DNA molecules in the nucleus of cancer cells were disclosed. The apoptotic experience of a cell nucleus during the PDT was obtained and described. From this, we can conclude that the photosensitizer Ce6 may interfere with cell reproduction and induce cell apoptosis during PDT treatment, which has been proved by the data of flow cytometry. We believe that SERS tracing real-time cellular dynamic molecular changes of cancer cells in cell level during the PDT process will help with understanding the underlying molecular mechanisms in photodynamic cancer cell death.

AUTHOR CONTRIBUTIONS

JY, LL, YS, SX, CL, and WX: designed research; JY, XG, and ZL: performed research; JY, LL, JZ, YS, and RD: analyzed data; CL and WS: provided the cell culture conditions; JY, LL, and SX: wrote the paper. All authors have approved the final version of the manuscript.

ACKNOWLEDGMENTS

This work was supported by the National Natural Science Foundation of China Grant Nos. 21873039, 21573087, and 21573092. We thank Mr. Xiangyuan Liu from Changchun Xiangyuan Sci. & Tec. Co (www.ccyxtech.cn) for supporting a 650 nm lamp.

SUPPLEMENTARY MATERIAL

The Supplementary Material for this article can be found online at: https://www.frontiersin.org/articles/10.3389/fchem.2018.00665/full#supplementary-material

REFERENCES

Abrahamse, H., and Hamblin, M. R. (2016). New photosensitizers for photodynamic therapy. *Biochem. J.* 473, 347–364. doi: 10.1042/BJ20150942

Agostinis, P., Berg, K., Cengel, K. A., Foster, T. H., Girotti, A. W., Gollnick, S. O., et al. (2011). Photodynamic therapy of cancer: an update. *CA Cancer J. Clin.* 61, 250–281. doi: 10.3322/caac.20114

Ali, M. R., Wu, Y., Han, T., Zang, X., Xiao, H., Tang, Y., et al. (2016). Simultaneous time-dependent surface-enhanced Raman spectroscopy, metabolomics, and proteomics reveal cancer cell death mechanisms associated with gold nanorod photothermal therapy. *J. Am. Chem. Soc.* 138, 15434–15442. doi: 10.1021/jacs.6b08787

Austin, L. A., Kang, B., and El-Sayed, M. A. (2013). A new nanotechnology technique for determining drug efficacy using targeted plasmonically enhanced single cell imaging spectroscopy. *J. Am. Chem. Soc.* 135, 4688–4691. doi: 10.1021/ja4011145

Bellavite, P. (1988). The superoxide-forming enzymatic system of phagocytes. *Free Radic. Biol. Med.* 4, 225–261. doi: 10.1016/0891-5849(88)90044-5

Buchko, G., Wagner, J. R., Cadet, J., Raoul, S., and Weinfeld, M. (1995). Methylene blue-mediated photooxidation of 7,8-dihydro-8-oxo-2-deoxyguanosine. *Biochim. Biophys. Acta* 1263, 17–24. doi: 10.1016/0167-4781(95)00078-U

Cialla-May, D., Zheng, X. S., Weber, K., and Popp, J. (2017). Recent progress in surface-enhanced Raman spectroscopy for biological and biomedical applications: from cells to clinics. *Chem. Soc. Rev.* 46, 3945–3961. doi: 10.1039/C7CS00172J

Deng, R., Qu, H., Liang, L., Zhang, J., Zhang, B., Huang, D., et al. (2017). Tracing the therapeutic process of targeted aptamer/drug conjugate on cancer cells by surface-enhanced Raman scattering spectroscopy. *Anal. Chem.* 89, 2844–2851. doi: 10.1021/acs.analchem.6b03971

Fan, W., Huang, P., and Chen, X. (2016). Overcoming the Achilles' heel of photodynamic therapy. *Chem. Soc. Rev.* 45, 6488–6519. doi: 10.1039/C6CS00616G

Grune, T., Klotz, L., Gieche, J., Rudeck, M., and Sies, H. (2001). Protein oxidation and proteolysis by the nonradical oxidants singlet oxygen or peroxynitrite. *Free Radic. Biol. Med.* 30, 1243–1253. doi: 10.1016/S0891-5849(01)00515-9

Han, K., Wang, S., Lei,Q., Zhu, J., and Zhang, X. (2015). Ratiometric biosensor for aggregation-induced emission-guided precise photodynamic therapy. *ACS Nano* 9, 10268–10277. doi: 10.1021/acsnano.5b04243

Hodgkinson, N., Kruger, C. A., Mokwena, M., and Abrahamse, H. (2017). Cervical cancer cells (HeLa) response to photodynamic therapy using a zinc phthalocyanine photosensitizer. *J. Photochem. Photobiol. B* 177, 32–38. doi: 10.1016/j.jphotobiol.2017.10.004

Huefner, A., Kuan, W. L., Barker, R. A., and Mahajan, S. (2013). Intracellular SERS nanoprobes for distinction of different neuronal cell types. *Nano Lett.* 13, 2463–2470. doi: 10.1021/nl400448n

Kairdolf, B. A., Qian, X., and Nie, S. (2017). Bioconjugated nanoparticles for biosensing, *in vivo* imaging, and medical diagnostics. *Anal. Chem.* 89, 1015–1031. doi: 10.1021/acs.analchem.6b04873

Kang, B., Austin, L. A., and El-Sayed, M. A. (2012). Real-time molecular imaging throughout the entire cell cycle by targeted plasmonic-enhanced Rayleigh/Raman spectroscopy. *Nano Lett.* 12, 5369–5375. doi: 10.1021/nl3027586

Kang, B., Austin, L. A., and El-Sayed, M. A. (2014). Observing real-time molecular event dynamics of apoptosis in living cancer cells using nuclear-targeted plasmonically enhanced Raman nanoprob. *ACS Nano* 8, 4883–4892. doi: 10.1021/nn500840x

Kircher, M. F. (2016). How can we apply the use of surfaceenhanced Raman scattering nanoparticles in tumor imaging? *Nanomedicine* 12, 171–174. doi: 10.2217/nnm-2016-0385

Kneipp, J., Kneipp, H., and Kneipp, K. (2008). SERS–a single-molecule and nanoscale tool for bioanalytics. *Chem. Soc. Rev.* 37, 1052–1060. doi: 10.1039/b708459p

Kuku, G., Altunbek, M., and Culha, M. (2017). Surface-enhanced Raman scattering for label-free living single cell analysis. *Anal. Chem.* 89, 11160–11166. doi: 10.1021/acs.analchem.7b03211

Laing, S., Jamieson, L. E., Faulds, K., and Graham, D. (2017). Surface-enhanced Raman spectroscopy for *in vivo* biosensing. *Nat. Rev. Chem.* 1:0060. doi: 10.1038/s41570-017-0060

Liang, L., Huang, D., Wang, H., Li, H., Xu, S., Chang, Y., et al. (2015). *In situ* surface-enhanced Raman scattering spectroscopy exploring molecular changes of drug-treated cancer cell nucleus. *Anal. Chem.* 87, 2504–2510. doi: 10.1021/ac504550w

Liu, K., Liu, X., Zeng, Q., Zhang, Y., Tu, L., Liu, T., et al. (2012). Covalently assembled NIR nanoplatform for simultaneous fluorescence imaging and photodynamic therapy of cancer cells. *ACS Nano* 6, 4054–4062. doi: 10.1021/nn300436b

Nikoobakht, B., and El-Sayed, M. A. (2003). Preparation and growth mechanism of gold nanorods (NRs) using seed-mediated growth method. *Chem. Mater.* 15, 1957–1962. doi: 10.1021/cm020732l

Oyelere, A. K., Chen, P. C., Huang, X., El-Sayed, I. H., and El-Sayed, M. A. (2007). Peptide-conjugated gold nanorods for nuclear targeting. *Bioconjugate Chem.* 18, 1490–1497. doi: 10.1021/bc070132i

Qian, X. M., and Nie, S. M. (2008). Single-molecule and single-nanoparticle SERS: from fundamental mechanisms to biomedical applications. *Chem. Soc. Rev.* 37, 912–920. doi: 10.1039/b708839f

Sau, T. K., Murphy, C. J. (2004). Seeded high yield synthesis of short Au nanorods in aqueous solution. *Langmuir* 20, 6414–6420. doi: 10.1021/la049463z

Shen, Y., Liang, L., Zhang, S., Huang, D., Deng, R., Zhang, J., et al. (2018). Organelle-targeting gold nanorods for macromolecular profiling of subcellular organelles and enhanced cancer cell killing. *ACS Appl. Mater. Interfaces* 10, 7910–7918. doi: 10.1021/acsami.8b01320

Soriano, J., Mora-Espí, I., Alea-Reyes, M. E., Perez-Garcia, L., Barrios, L., Ibanez, E., et al. (2017). Cell death mechanisms in tumoral and non-tumoral human cell lines triggered by photodynamic treatments: apoptosis, necrosis and parthanatos. *Sci. Rep.* 7:41340. doi: 10.1038/srep41340

Sun, Q., You, Q., Pang, X., Tan, X., Wang, J., Liu, L., et al. (2017). A photoresponsive and rod-shape nanocarrier: single wavelength of light triggered photothermal and photodynamic therapy based on AuNRs-capped and Ce6-doped mesoporous silica nanorods. *Biomaterials* 122, 188–200. doi: 10.1016/j.biomaterials.2017.01.021

Veloso, A. B., Longo, J. P. F., Muehlmann, L. A., Tollstadius, B. F., Souza, P. E. N., Azevedo, R. B., et al. (2017). SERS investigation of cancer cells treated with PDT: quantification of cell survival and follow-up. *Sci. Rep.* 7:7175. doi: 10.1038/s41598-017-07469-1

Voon, S. H., Kiew, L. V., Lee, H. B., Lim, S. H., Noordin, M. I., Kamkaew, A., et al. (2014). *In vivo* studies of nanostructure-based photosensitizers for photodynamic cancer therapy. *Small* 10, 4993–5013. doi: 10.1002/smll.201401416

Wang, C., Cheng, L., and Liu, Z. (2013). Upconversion nanoparticles for photodynamic therapy and other cancer therapeutics. *Theranostics* 3, 317–330. doi: 10.7150/thno.5284

Xie, W., Wang, L., Zhang, Y., Su, L., Shen, A., Tan, J., et al. (2009). Nuclear targeted nanoprobe for single living cell detection by surface-enhanced Raman scattering. *Bioconjugate Chem.* 20, 768–773. doi: 10.1021/bc800469g

Yang, D., Gulzar, A., Yang, G., Gai, S., He, F., Dai, Y., et al. (2017). Au nanoclusters sensitized black TiO2-x nanotubes for enhanced photodynamic therapy driven by near-infrared light. *Small* 13:1703007. doi: 10.1002/smll.201703007

Zheng, X. S., Jahn, I. J., Weber, K., Cialla-May, D., and Popp, J. (2018). Label-free SERS in biological and biomedical applications: recent progress, current challenges and opportunities. *Spectrochim Acta A Mol. Biomol. Spectrosc.* 197, 56–77. doi: 10.1016/j.saa.2018.01.063

Conflict of Interest Statement: The authors declare that the research was conducted in the absence of any commercial or financial relationships that could be construed as a potential conflict of interest.

ORIGINAL RESEARCH
published: 04 March 2019
doi: 10.3389/fchem.2019.00105

Recent Advances on the Analysis of Polychrome Works of Art: SERS of Synthetic Colorants and Their Mixtures With Natural Dyes

*Anna Cesaratto, Marco Leona and Federica Pozzi**

Department of Scientific Research, The Metropolitan Museum of Art, New York, NY, United States

The development and application of proper sample pretreatments is often a key step toward the successful analysis of dyes used as artists' materials by surface-enhanced Raman spectroscopy (SERS). Complexation of the organic colorants with metal ions to dye fabrics and produce lake pigments, as well as undesired interactions with other matrix components such as substrate, binding media, fillers, and extenders, are just some of the issues that typically complicate dye identification in minute samples from invaluable artworks and museum objects. These concerns may be addressed by using, prior to SERS analysis, *ad-hoc* sample pretreatments that, in addition to increasing the technique's sensitivity, favorably affect its selectivity toward certain molecules or molecular classes. The present work describes a newly developed sample pretreatment based on the use of nitric acid that has proven crucial for the successful detection of aniline and xanthene dyes–the first synthetic organic colorants to be used in printing and painting, among other art forms–in microscopic samples from works of art such as a 19th-century silk fabric, paper cut-outs by Henri Matisse, Vincent Van Gogh's *Irises*, and Japanese woodblock prints. This treatment promotes the hydrolysis of the dye-metal bond in mordant dyes or lake pigments, resulting in a more efficient adsorption of the dye molecules on the SERS-active substrate and, hence, enabling the acquisition of high-quality spectra. In the case of synthetic colorants, this method shows advantages over hydrolysis with hydrofluoric acid–a procedure previously established for the analysis of red lakes prepared from natural dyes. The nitric acid treatment presented here may be integrated into a multi-step methodology that, by exploiting differences in solubility of various dyes and lake pigments, has enabled for the first time to successfully characterize intentional mixtures of natural and synthetic colorants of the xanthene and anthraquinone molecular classes, i.e., eosin Y and carmine, in a selection of Japanese prints of the Meiji era. The present study paves the way for the systematic identification of synthetic dyes in objects of artistic and archeological interest, even when they are present in mixtures with natural organic colorants.

Keywords: SERS, synthetic dyes, dye mixtures, sample pretreatments, nitric acid, artworks, cultural heritage

Edited by:
Ivano Alessandri,
Università degli Studi di Brescia, Italy

Reviewed by:
Philippe Colomban,
Centre National de la Recherche Scientifique (CNRS), France
Giuseppe Egidio De Benedetto,
University of Salento, Italy
Maurizio Becucci,
Università degli Studi di Firenze, Italy

****Correspondence:***
Federica Pozzi
federica.pozzi@metmuseum.org

Specialty section:
This article was submitted to Analytical Chemistry, a section of the journal Frontiers in Chemistry

Received: *02 November 2018*
Accepted: *11 February 2019*
Published: *04 March 2019*

Citation:
Cesaratto A, Leona M and Pozzi F (2019) Recent Advances on the Analysis of Polychrome Works of Art: SERS of Synthetic Colorants and Their Mixtures With Natural Dyes. Front. Chem. 7:105. doi: 10.3389/fchem.2019.00105

INTRODUCTION

In the last decade, surface-enhanced Raman spectroscopy (SERS) has conquered a crucial role in the detection and identification of organic colorants in works of art, especially in cases when sample size concerns prevent the use of separation techniques such as liquid chromatography (Casadio et al., 2010a, 2016; Pozzi and Leona, 2015; Pozzi et al., 2016a). As most dyes were traditionally complexed with metal ions for use in painting and textile dyeing, the application of hydrolysis pretreatments prior to SERS analysis has significantly increased the chances of successful identification of unknowns. SERS experiments on lake pigments and mordant dyes initially relied on extractions in strong acids or alkali (Leona, 2005; Chen et al., 2006; Leona et al., 2006; Whitney et al., 2006). Sulfuric and hydrochloric acids (H_2SO_4 and HCl) have been also used in more recent instances (Oakley et al., 2012; Mayhew et al., 2013; Roh et al., 2016) for the SERS analysis of indigo and Prussian blue, as well as yellow dyes and lake pigments in oil paint, with successful results. However, despite their high yield, such methods have been shown to often result in the disruption of the matrix, leading to the formation of degradation products that inhibit the dye-nanoparticles interaction and interfere with the analysis (Leona et al., 2006; Brosseau et al., 2009a; Bruni et al., 2010). To circumvent this issue, researchers have proposed gentler extraction procedures, and non-extractive *in-situ* hydrolysis methodologies that, while still enabling dye detection and identification in most cases, do not cause as severe a degradation of the substrate and analyte itself. These alternative methods, sometimes tailored to the sample color (Bruni et al., 2011; Pozzi et al., 2012a), typically involve removal of the dye using milder extracting reagents, such as combinations of weaker acids, organic solvents, and chelating agents (Leona et al., 2006; Brosseau et al., 2009a; Bruni et al., 2011). In some instances, researchers have followed experimental protocols in which samples are just briefly exposed to room temperature acid vapor instead of being immersed in heated solutions (Leona and Lombardi, 2007). Among the latter, a hydrolysis treatment based on the use of hydrofluoric acid (HF) has proven successful for the ultrasensitive detection of lake pigments obtained from natural dyes (Leona et al., 2006). In this procedure, briefly exposing the sample to HF vapor causes the dye-metal bond of lake pigments and mordant dyes to hydrolyze. The dye molecules are thus released into the aqueous silver colloid used as SERS-active substrate and, being water soluble, adsorb efficiently onto the nanoparticles' surface, resulting in a significant enhancement of the signal intensity without disruption of the dyes' molecular structure. Following presentation of the HF hydrolysis, its advantages and drawbacks have been systematically studied in series of samples removed from a wide variety of art objects (Pozzi et al., 2012b). In the subsequent years, this methodology has been validated as a fundamental step for the analysis of red lakes of natural origin (Pozzi et al., 2013a, 2014), although applications to the characterization of flavonoid-based yellow lakes (Cesaratto et al., 2016), weld-dyed silk fibers (Jurasekova et al., 2008; Corredor et al., 2009), and aniline-dyed textiles (Woodhead et al., 2016) have also been reported. This pretreatment was shown to be necessary even when using laser ablation (LA)-SERS, which entails an otherwise dry procedure, for the analysis of red lake-containing paint layers in cross sections (Cesaratto et al., 2014) and yellow lakes (Cesaratto et al., 2016).

As highlighted in a recent paper on the topic (Casadio et al., 2016), the application of SERS to the analysis of synthetic organic colorants in works of art has not been fully investigated yet. To fill this gap, the present work focuses specifically on aniline and xanthene dyes, which are characterized by a strong fluorescence in the visible range that often obscures the inherently weaker Raman signal. These colorants have high SERS cross sections and their SERS spectra are well-known, which makes them ideal candidates for the development and testing of new methodological approaches. Moreover, aniline and xanthene dyes are of particular interest as they were the first synthetic organic colorants to be widely used in printing and painting, among other art forms. The spectrum of crystal violet was first presented in the early developmental stages of the SERS technique (Jeanmaire and Van Duyne, 1977), and an assignment of its most distinctive bands was carried out a decade ago by means of density functional theory (DFT) (Cañamares et al., 2008). Rhodamine 6G has been used for single-molecule experiments (Kneipp et al., 1997; Nie and Emory, 1997), while rhodamine B as a tag in biosensors (Fang et al., 2008). Also, the SERS spectrum of eosin Y has been studied in depth (Narayanan et al., 1994; Whitney et al., 2006; Greeneltch et al., 2012), while phloxine has received only minor attention (Narayanan et al., 1996).

Despite the abundant work on reference synthetic dyes available in the literature, examples of SERS identification of these materials in museum objects are still rare (Brosseau et al., 2009b; Cesaratto et al., 2016; Woodhead et al., 2016). The hierarchical complexity of samples removed from artworks makes the identification of their coloring components not always straightforward. The possible aging of the materials under study and their chemical interactions with the support, binding media, and other matrix components such as fillers, extenders, and any additional pigments may complicate the analysis and subsequent data interpretation, and so does the use of colorants in their "laked" or "mordanted" form and not as free dyes. All these factors need to be accounted for when SERS analysis of natural and synthetic dyes in art-related samples is attempted. In this context, the present work aims to further expand a relatively recent study on anthraquinone lake pigments and textile dyes (Pozzi et al., 2012b) by focusing on sample pretreatments specifically tailored to the characterization of aniline (crystal/methyl violet and rosaniline/pararosaniline) and xanthene (rhodamine B, rhodamine 6G, eosin Y, and phloxine) colorants in samples from art objects. Case studies presented include the SERS analysis of aniline dyes in purple paper cut-outs by Henri Matisse and in a 19th-century silk fabric, and the characterization of xanthene dyes and lakes in a selection of pink Matisse cut-outs, in Vincent Van Gogh's *Irises*, and in Japanese woodblock prints. Our study shows that, unlike dyed paper, SERS of aniline dyes on fabrics generally requires a sample pretreatment, and that, similarly, xanthene dyes and lakes display a significant SERS enhancement when treated with a nitric acid (HNO_3) solution. Remarkably, application of this sample pretreatment has enabled to obtain, for the first time, great results from the SERS analysis of eosin Y and phloxine in actual works of art.

Furthermore, the introduction of an additional stage in the two-step SERS procedure previously proposed by some of the authors (analysis of the sample as is and upon HF hydrolysis) (Pozzi et al., 2012b), i.e., hydrolysis with HNO_3, has enabled the successful characterization of eosin-carmine binary mixtures in a selection of Japanese woodblock prints of the Meiji era. Interestingly, this represents the first instance in which an intentional combination of natural and synthetic dyes that do not naturally occur in mixtures has been attested in historical samples. The analytical procedure employed exploits both differences in solubility between the dyes and lake pigments present in the samples, as well as other factors such as pH and the choice of aggregating agents, enabling to selectively detect one component of the mixture over another.

While SERS has been deemed valuable for its high sensitivity and for the little sample preparation needed prior to analysis, its ability to resolve mixtures of colorants, especially if belonging to different molecular classes, has not been fully explored yet (Pozzi and Leona, 2015). This is a rather substantial problem, as plant and insect dyes are often found as complex mixtures of naturally occurring products and, even when dealing with single-component dyes such as synthetics, the possibility of intentional mixtures on the artist's or paint supplier's part cannot be ruled out (Kirby and White, 1996). Unlike chromatographic techniques such as high-performance liquid chromatography (HPLC), SERS is not able to separate the different species present in a mixture for individual detection and quantification. Moreover, surface chemistry factors may lead to the preferential adsorption of one dye over another onto the nanoparticles surface, resulting in skewed spectroscopic data. To date, various studies have examined the contribution of individual mixture components to the SERS spectra for a few selected cases of closely related dye molecules: among the reds, alizarin and purpurin (Snowden et al., 2004; Whitney et al., 2007); alizarin and lac dye (Whitney et al., 2007); alizarin and carminic acid (Murcia-Mascarós et al., 2005); various binary mixtures of the above-mentioned anthraquinone colorants and brazilwood (Pozzi et al., 2016b); and, among the yellows, luteolin and apigenin (Corredor et al., 2009; Cesaratto et al., 2016). To overcome the lack in separation capabilities, a few preliminary studies have explored the coupling of SERS with thin layer chromatography (TLC) to resolve and characterize mixtures of alizarin, purpurin, and carminic acid (Brosseau et al., 2009b), the alkaloid chromophores of the *Peganum Harmala* plant extract (Pozzi et al., 2013b), and the components of ballpoint pen inks (Geiman et al., 2009). Furthermore, TLC-SERS was applied to the study of four constituents of the first synthetic dye, mauve (Cañamares et al., 2014). More recently, an online hyphenated system combining HPLC with photodiode array (PDA) and SERS detection was proven suitable to provide a detailed electronic and vibrational characterization of natural dyes in mixtures (Zaffino et al., 2016). It is worth noting that both TLC-SERS and HPLC-SERS entail extraction of the dye components from the sample, which greatly limits the applicability of the technique to artworks and irreplaceable objects due to the relatively large amount of specimen required. However, due to the issues discussed above, successful applications of regular SERS to the detection of dye mixtures in samples from art objects are also quite infrequent. Examples in the literature include the analysis of cochineal and brazilwood mixtures in historical textile samples (Idone et al., 2013); the simultaneous identification of madder and cochineal in red lake samples from paintings by Pierre-Auguste Renoir and Édouard Manet (Pozzi et al., 2014); and the characterization of a mixture of rhodamine B and rhodamine 6G in a pink pastel from Mary Cassatt's pastel box (Brosseau et al., 2009b). Yet, to date, the simultaneous SERS detection and identification of non-closely related dyes in samples from artworks has never been accomplished. Therefore, the results reported here represent a great advancement in the field, and may serve as a reference when the SERS technique is used for the study of synthetic dyes in modern and contemporary art objects.

MATERIALS AND METHODS

Reference Materials and Artworks

Rosaniline was obtained from Eimer and Amend. Pararosaniline, crystal violet, rhodamine 6G, and eosin Y were purchased from Sigma Aldrich. Methyl violet was obtained from Fluka Chemical Corp. Rhodamine B was purchased from Fischer Scientific. Phloxine was obtained from Acros Organics. Microscopic samples of roughly equivalent size were removed from several works of art, as described in **Table 1**. Samples studied include: paper fibers from a collection of gouache paper samples from Henry Matisse's cut-out paintings (The Museum of Modern Art, New York); paper fibers from a polychrome print, *Ladies Sewing* (*Kijo saiho no zu*), by Adachi (Shosai) Ginko (1887, The Metropolitan Museum of Art, New York, accession number JP3272); paper fibers from a collection of ten late Edo-early Meiji woodblock Japanese prints (1860-1898, private collection); paint samples from Vincent Van Gogh's *Irises* (1890, The Metropolitan Museum of Art, New York, accession number 58.187).

Silver Colloid Preparation

A monodisperse colloidal suspension of silver nanoparticles was synthesized by microwave-supported glucose reduction of silver sulfate in the presence of sodium citrate as a capping agent. Details on the synthetic procedure and physicochemical properties of this type of colloids (Leona, 2009), as well as a comparison with other silver substrates used for SERS in the cultural heritage field (Pozzi and Leona, 2015; Pozzi et al., 2016a), are reported elsewhere in the literature. Silver nanoparticles produced by this microwave-assisted methodology have $\lambda_{max} = 401$ nm, FWHM $= 50$ nm, and a narrow nanoparticle size range of 3–10 nm, leading to great efficiency, high stability over time, and reproducible SERS results. A 5x-concentrated colloid, obtained by centrifuging 1 mL of nanoparticle suspension and replacing 950 μL of the supernatant with 150 μL of 18 MΩ water, was used for all analyses reported in this work.

TABLE 1 | List of samples analyzed by SERS in the present study.

Samples	Art objects	Artistic techniques	SERS characterization
Violet 1 bis	Henri Matisse's cut-outs	Gouache on paper	Faded crystal/methyl violet
Violet 4	Henri Matisse's cut-outs	Gouache on paper	Highly faded crystal/methyl violet and/or rosaniline/pararosaniline
Purple silk	Nineteenth-century silk fabric	Dyed silk	Faded crystal/methyl violet
M1	Henri Matisse's cut-outs	Gouache on paper	Rhodamine B
M4	Henri Matisse's cut-outs	Gouache on paper	Rhodamine B and 6G
R5	Henri Matisse's cut-outs	Gouache on paper	Eosin Y
P/R3	Henri Matisse's cut-outs	Gouache on paper	Phloxine
VG1	Vincent Van Gogh's *Irises*	Oil painting	Eosin Y
Various	Japanese woodblock prints	Polychrome prints	Eosin Y and carmine

The sample names, art objects from which the samples were removed, artistic techniques, and dyes identified are indicated.

Sample Pretreatments and SERS Procedure

Three different SERS procedures have been used, as schematically illustrated in **Figure 1**. These three methodologies, all carried out at room temperature, may be combined into a multi-step approach and applied in sequence to the same sample. In the first step, the sample is placed on a polyethylene holder and analyzed as is, after being covered with a 2 μL drop of colloid and 0.4 μL of 0.5 M KNO_3 to induce nanoparticle aggregation. Following acquisition of a SERS spectrum, the colloid droplet is removed with a micropipette or let evaporate. In the second step, the sample is treated with 1 μL of 1% HNO_3 aqueous solution, and a 2 μL drop of colloid is then dropcasted onto the sample. Upon acquisition of a SERS spectrum, the colloid droplet is again removed or let evaporate. In the third and last step, the sample is exposed to HF vapor for 5 min in a closed microvial (Leona et al., 2006), and a SERS spectrum is acquired upon addition of colloid and 0.5 M KNO_3. In the latter step, the HF-containing microreactor is prepared by placing as little as 10 μL of acid at the bottom every 4–5 days, greatly reducing the risks associated with the use of this reagent. Moreover, it is worth highlighting that, besides promoting the hydrolysis of the dye-metal bond in mordant dyes and lake pigments, the HNO_3 simultaneously acts as an aggregant for the silver nanoparticles, thus enabling to combine into a single step what, in most cases, has been accomplished in two separate phases of the analytical protocol through the use of different chemicals. In addition to a longstanding and well-documented use of nitrate ions in SERS to activate silver colloids by inducing nanoparticle aggregation, the selection of HNO_3 finds reason in the fact that, as previously discussed, other strong acids such as HCl have been reported to cause an excessive disruption of the host material or competition for the adsorption onto the metal surface (Leona et al., 2006; Bruni et al., 2010), ultimately preventing dye detection and identification.

Instrumentation

A Bruker Senterra Raman instrument equipped with a charge-coupled device (CCD) detector was used to acquire the SERS spectra, exciting the specimens at 488 and 633 nm by means of solid state laser and He-Ne lasers, respectively. The laser beam was focused through a 20x long working distance microscope objective just below the surface of the silver nanoparticle droplet. The laser power at the sample was kept below 0.2 mW ($\lambda_{exc} = 488$ nm) and 1 mW ($\lambda_{exc} = 633$ nm) to avoid thermal damage. The spectra reported in this article were acquired with a resolution of about 3–5 cm^{-1}, integrating the signal two times for 15 s each.

RESULTS AND DISCUSSION

All the dyes examined in this work, with the exception of rhodamines, have been characterized by means of a solid state laser providing excitation at 488 nm. This wavelength is typically the most suitable to produce high-quality SERS spectra, as it matches both the silver colloids' plasmon resonance and most red dyes' optical absorption, leading to a significant increase in the technique's sensitivity (Leona, 2009). Among the synthetic colorants identified in the present study, only rhodamines were found to yield better SERS results when excited at 633 nm using a He-Ne laser, likely because, in this case, the resonance between the laser excitation and the dyes' optical absorption–shifted toward higher wavelengths, i.e., around 500–550 nm–plays a more crucial role toward a successful analysis compared to other factors, including resonance with the nanoparticles' absorption maximum. Unless otherwise specified, all the spectra in this article are shown without modifying their relative intensities, in order to enable an easy and effective comparison of the results obtained using the three methodologies described above (sample not treated, sample treated with HNO_3 solution, and sample treated with HF vapor). Illegible spectra that displayed very low relative enhancements have been multiplied by a certain factor to help in inspection; such factor is reported in the corresponding graphs for clarity. Three spectra were typically collected from each sample to ensure reproducibility of the results in terms of band position. In each graph, the reference spectra of commercial pure dyes and lake pigments, appearing as dashed lines, are reported along with those collected from the art samples investigated to provide evidence of the colorants identified. Wavenumbers of the main peaks are marked in the figures to facilitate visual examination. Usually, spectra acquired without any pretreatment and after hydrolysis with HNO_3 and

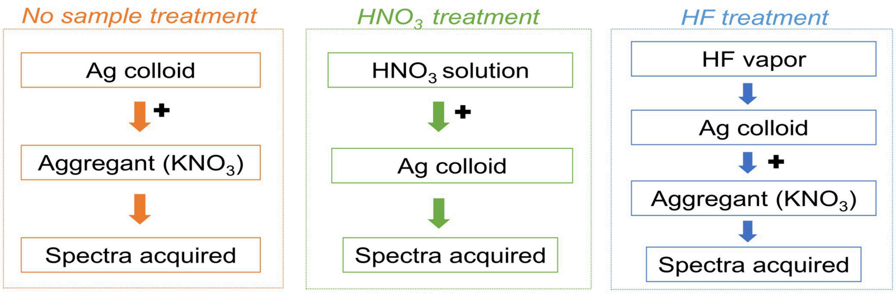

FIGURE 1 | Sample treatments used for the SERS analysis reported in this study.

HF are enclosed in the same graph, to make the effects of the various methodologies easier to compare.

Aniline Dyes

Crystal/Methyl Violet and Rosaniline/Pararosaniline

SERS investigation of some of the samples removed from Henry Matisse's purple cut-outs show the presence of aniline dyes. It is worth noting that the SERS spectra of crystal/methyl violet and rosaniline/pararosaniline are respectively identical (Geiman et al., 2009; Cesaratto et al., 2017). A definitive assignment of the symmetry and normal modes of the spectrum of crystal violet can be found in the literature (Cañamares et al., 2008). As explained in a recent article, SERS spectra of crystal/methyl violet are highly dependent on the level of photo-degradation of the material under study (Cesaratto et al., 2017). In particular, the SERS spectrum of crystal violet assumes some of the characteristic features of pararosaniline as a result of the progressive N-demethylation induced by light exposure. Accordingly, Matisse's cut-out sample Violet 1 bis shows the typical signals of faded crystal/methyl violet–materials that can be easily detected even without sample treatments (**Figure 2A**); in this case, in fact, application of the HNO_3 hydrolysis did not affect the SERS signal intensity. On the other hand, the HF treatment slightly enhanced the signal but, at the same time, it also altered the relative ratio of peaks at 1589 and 1622 cm^{-1}. As such ratio is indicative of the material's photo-induced fading level (Cesaratto et al., 2017), this factor must be taken into consideration when selecting the most suitable treatment for samples that are likely to contain aniline dyes.

Compared with the latter, Matisse's cut-out sample Violet 4, identified as highly faded crystal/methyl violet or rosaniline/pararosaniline, displays a different behavior (**Figure 2B**). In this case, the hydrolysis with HNO_3 was found to improve the otherwise weak SERS signal. The higher fading levels exhibited by the dyes contained in this sample may be responsible for the lower spectral quality observed when the specimen is not treated prior to SERS analysis. Interestingly, the ratio of peaks at 1589 and 1622 cm^{-1} appeared to remain overall stable regardless of the sample treatments applied. Based on these data, a hypothesis may be put forward that aniline colorants on paper may have been used here as free dyes; therefore, successful characterization can be accomplished even without sample pretreatments, while HNO_3 might help enhance the signal in case of highly degraded samples, as also observed in a study of Japanese woodblock prints recently published (Cesaratto et al., 2017).

Contrarily to what was observed on the Matisse cut-out samples, SERS analysis of crystal/methyl violet in a 19th-century silk fabric was only possible upon treatment with acids. As shown in **Figure 3**, when the sample is treated with HNO_3, the signal-to-noise ratio drastically increases, making even the small features that are characteristic of these dyes clearly detectable. Our observations regarding the necessity of a sample pretreatment for aniline-dyed textiles are in accordance with experimental results presented in a recent paper by Woodhead et al. (2016). Even if both the HF and HNO_3 treatments enabled dye identification by hydrolyzing the dye-mordant complex, the latter method was found to be more effective and less time consuming than the HF hydrolysis. Indeed, as already suggested by one of the authors (Pozzi et al., 2012b), the HF might cause the silk proteins to be released into solution and interfere with dye adsorption onto the silver nanoparticles, resulting in a significant signal broadening and deterioration of the SERS spectra.

Xanthene Dyes and Lakes

Rhodamine

Various dyes belonging to the xanthene group are responsible for the bright pink color shades of a second selection of paper cut-outs by Henri Matisse examined in this work. An assignment of the observed peaks for rhodamine 6G and B is reported in the literature (Jensen and Schatz, 2006; Lin et al., 2015). SERS spectra of rhodamine-containing samples, i.e., M1 and M4 (**Figure 4**), were acquired by means of a 633 nm laser. This excitation wavelength quenches the fluorescence background arising from the unadsorbed dye molecules more effectively than other shorter laser emissions and, due to resonance effects, greatly enhances rhodamine B's and 6G's characteristic peaks at 619 and 613 cm^{-1}, respectively, making conclusive identification easier. This is especially useful when the two dyes are present in a mixture, as in sample M4 (**Figure 4B**). As shown in **Figure 4**, the application of the HNO_3 treatment was crucial to produce a clean spectrum of rhodamine B from sample M1. Without treatment, this sample does not show any characteristic bands ascribable to the colorant, while the spurious signals of citrate ions from the silver colloid

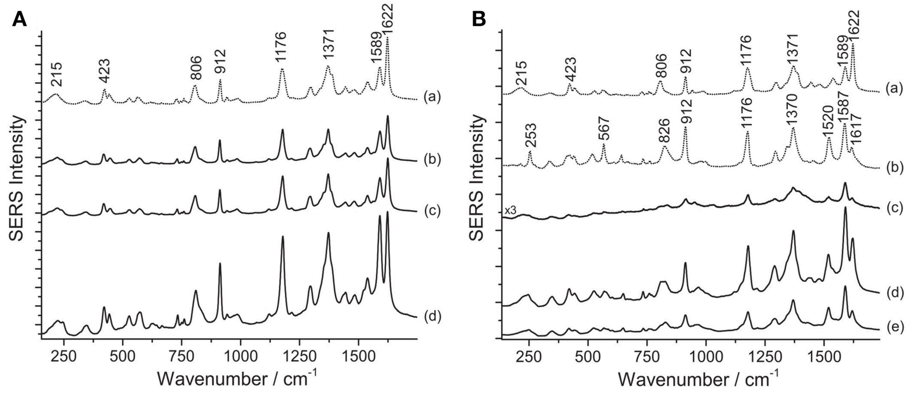

FIGURE 2 | SERS spectra of aniline dyes from some of Matisse's paper cut-outs ($\lambda_{\text{exc}} = 488$ nm). **(A)** Spectrum of reference crystal/methyl violet (a) compared with spectra acquired from sample Violet 1 bis without any treatment (b), after HNO_3 treatment (c), and after HF treatment (d). **(B)** Spectra of reference crystal/methyl violet (a) and pararosaniline (b) compared with spectra acquired from sample Violet 4 without any treatment (c), after HNO_3 treatment (d), and after HF treatment (e). Signals of faded crystal/methyl violet are detected at 215, 423, 806, 912, 1176, 1371, 1589, and 1622 cm^{-1}, while signals of highly faded crystal/methyl violet or pararosaniline are detected at 215, 253, 423, 567, 806, 826, 912, 1176, 1370, 1520, 1589, and 1622 cm^{1}.

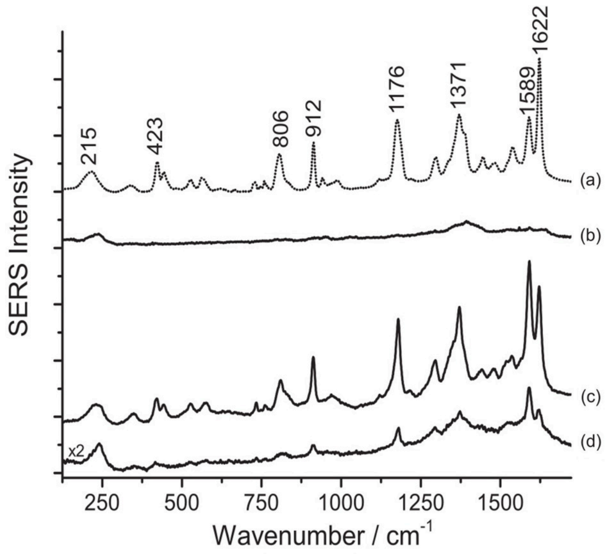

FIGURE 3 | SERS spectra of a nineteenth-century purple silk fabric ($\lambda_{\text{exc}} =$ 488 nm). Spectrum of reference crystal/methyl violet (a) compared with spectra acquired from the dyed silk sample without any treatment (b), after HNO_3 treatment (c), and after HF treatment (d). Signals of faded crystal/methyl violet are detected at 215, 423, 806, 912, 1176, 1371, 1589, and 1622 cm^{-1}.

are present along with those of the dye upon HF hydrolysis. Similarly, the rhodamine B and rhodamine 6G mixture in M4 requires a sample pretreatment with HNO_3 to enhance the dyes signal over the citrate bands. It is worth noting that, in the latter case, the sample gives rise to a SERS spectrum, albeit weak and dominated by citrate bands, even when it is not pretreated. In the spectrum shown in **Figure 4B**, the band at 1362 cm^{-1} is a combination of two signals at 1364 cm^{-1} (rhodamine B) and 1358 cm^{-1} (rhodamine 6G), while the band at 1509 cm^{-1} is a combination of peaks at 1511 cm^{-1} (rhodamine B) and 1507 cm^{-1} (rhodamine 6G), respectively. In the past, the use of mixtures of rhodamine B and 6G as artists' materials has already been confirmed by SERS in a pink pastel from a pastel box belonging to Mary Cassatt from the Boston Museum of Fine Arts (Brosseau et al., 2009b). The spectra shown in the above-mentioned article are characterized by strong peaks attributed to citrate, consistently with the fact that the sample had not been treated prior to SERS analysis.

According to the results obtained from analysis with X-ray fluorescence (XRF) spectroscopy, rhodamine B in sample M1 is present as a phosphorus (P)–molybdenum (Mo)–tungsten (W) lake, as it is common in commercial formulations of the pigment. The acidic conditions reached when using HNO_3 appear to be ideal to induce the hydrolysis of the rhodamine lake, making the free colorant available for adsorption onto the silver nanoparticles. Based on XRF data, however, it is not possible to determine whether rhodamine was used in sample M4 in the form of a lake pigment, while the SERS results obtained after the first analytical step (no hydrolysis) seem to indicate that at least a fraction of the dye molecules are solubilized in the colloidal droplet and able to adsorb onto the SERS substrate. However, the detection of citrate peaks in spectra collected without hydrolysis indicates that the adsorption process was inefficient and/or incomplete. For both samples, the HNO_3 treatment induces the release of the free dye molecules and promotes most efficiently their adsorption on the SERS-active surface, resulting in the complete replacement of the citrate bands previously observed in the spectra with the dye signals. On the other hand, the results obtained for M1 and M4 upon HF hydrolysis seem to point toward an incomplete substitution of the citrate ions with the dye molecules on the nanoparticles surface.

Eosin Y and Phloxine

Results from SERS analysis suggest that Matisse extensively used eosin Y and phloxine to produce a bright pink color shade often observed in some of his cut-out paintings. An assignment of the normal modes of the spectrum of eosin Y can be found in the literature (Greeneltch et al., 2012). These two closely related dyes display a similar response toward the different sample treatments. Indeed, in both cases, the use of HNO_3 proved essential to achieve dye identification, as can be clearly observed for sample R5, containing eosin Y, and sample P/R3, consisting of phloxine (**Figure 5**). When samples are analyzed as is, a strong fluorescence emission arises, which might be ascribable to the unsuccessful adsorption of the dye on the SERS substrate. Similarly, the HF-treated samples give rise to a highly fluorescent background, in which even the main peaks at ~1330 and ~1620 cm^{-1} are barely visible.

As previously reported in the literature, in the present work, too, SERS analysis played a key role in shedding light on the original appearance of works of art that have undergone severe fading overtime. SERS of a sample removed from Van Gogh's *Irises*, in The Met's holdings, revealed the presence of eosin Y, suggesting that the currently white painting background may have been, in the artist's original intention, of a bright pink hue. Similarly to some of the samples discussed above, the dye, in this case, could be only identified upon HNO_3 treatment, as shown in **Figure 6**.

One key difference may be noticed in spectra of eosin-containing untreated samples reported in **Figures 5**, **6**: while Matisse's cut-outs show a strong fluorescent background, the eosin lake found in Van Gogh's sample gives rise to a weak SERS signal and poor signal-to-noise ratio. In the latter spectrum, however, a weak peak at 1620 cm^{-1} can be actually detected, which might be related to the few free dye molecules present in the sample as residues from the laking process. The observation of a high fluorescence emission in Matisse's cut-out samples and absence of it in the Van Gogh paint specimen might suggest that eosin Y and phloxine are present as free dyes in the first

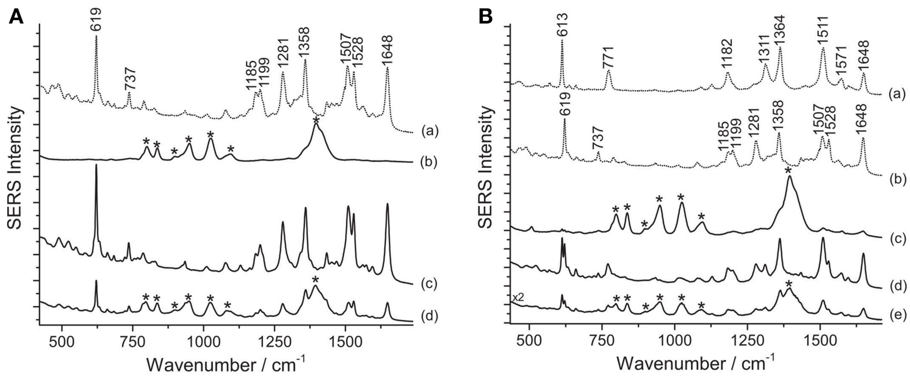

FIGURE 4 | SERS spectra of xanthene dyes from some of Matisse's paper cut-outs ($\lambda_{exc} = 633$ nm). **(A)** Spectrum of reference rhodamine B (a) compared with spectra acquired from sample M1 without any treatment (b), after HNO_3 treatment (c), and after HF treatment (d). **(B)** Spectra of reference rhodamine 6G (a) and rhodamine B (b) compared with spectra acquired from sample M4 without any treatment (c), after HNO_3 treatment (d), and after HF treatment (e). Signals of rhodamine B are detected at 619, 737, 1185, 1199, 1281, 1358, 1507, 1528, and 1648 cm^{-1}, while signals of a mixture of rhodamine B and rhodamine 6G are detected at 613, 619, 737, 771, 1182, 1199, 1281, 1311, 1362 (combination band), 1509 (combination band), 1528, and 1648 cm^{-1}. Spurious bands due to citrate are marked with an asterisk.

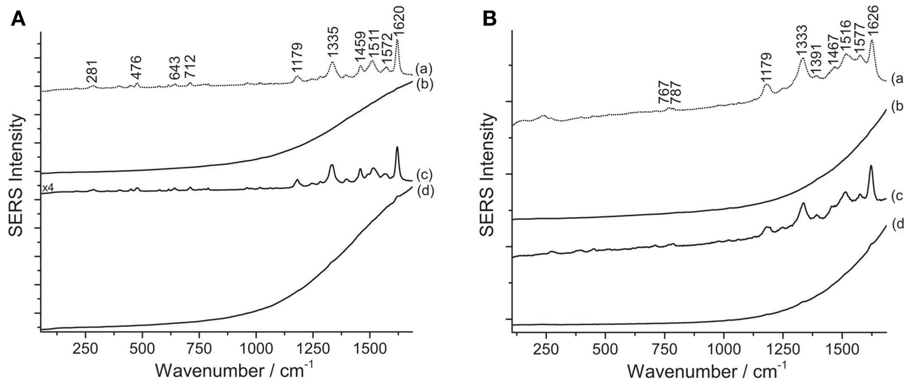

FIGURE 5 | SERS spectra of xanthene dyes from some of Matisse's paper cut-outs ($\lambda_{exc} = 488$ nm). **(A)** Spectrum of reference eosin Y (a) compared with spectra acquired from sample R5 without any treatment (b), after HNO_3 treatment (c), and after HF treatment (d). **(B)** Spectrum of reference phloxine (a) compared with spectra acquired from sample P/R3 without any treatment (b), after HNO_3 treatment (c), and after HF treatment (d). Signals of eosin Y are detected at 281, 476, 643, 712, 1179, 1335, 1459, 1511, 1572, and 1620 cm^{-1}, while signals of phloxine are detected at 767, 787, 1179, 1333, 1391, 1467, 1516, 1577, and 1626 cm^{-1}.

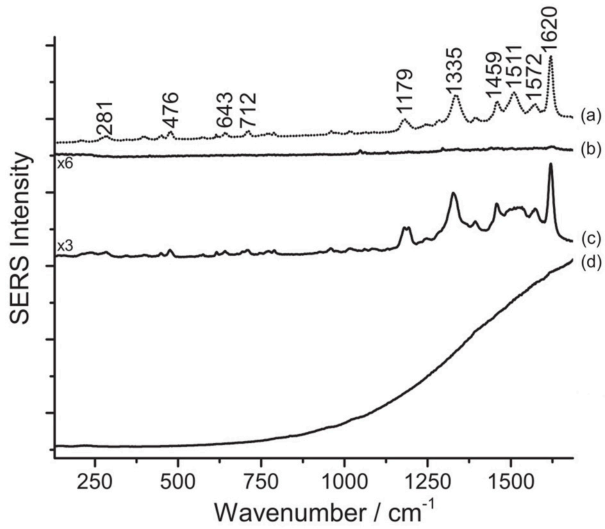

FIGURE 6 | SERS spectra of an eosin lake from Van Gogh's *Irises* (λ_{exc} = 488 nm). Spectrum of reference eosin (a) compared with spectra acquired from the Van Gogh paint sample without any treatment (b), after HNO_3 treatment (c), and after HF treatment (d). Signals of eosin Y are detected at 281, 476, 643, 712, 1179, 1335, 1459, 1511, 1572, and 1620 cm^{-1}.

(for which XRF could not determine if metal ions were used as mordants) or that, at least, a portion of the colorant was not complexed. It may be hypothesized that the dye molecules may have entered the aqueous solution of the colloidal droplet, but did not properly adsorb on the nanoparticles; as an alternative, the dyes may have reacted with the matrix in which they are embedded, making them unavailable for solubilization and adsorption onto the SERS-active substrate. On the other hand, the great results obtained upon treatment with HNO_3 are likely achieved thanks to the acidic environment provided by the acid that favors the dye adsorption on the metal surface. As regards the Van Gogh sample, it is well-known that eosin Y has been used as a lead (Pb) lake pigment by the artist, as indicated by normal Raman and scanning electron microscopy/energy-dispersive X-ray (SEM/EDX) spectroscopy (Centeno et al., 2017). In the first step of the analysis (no treatment), it was found that, when in the form of a water-insoluble lake, eosin Y cannot enter the aqueous solution of the colloidal droplet due to its scarce solubility in the medium. In the second step (hydrolysis with HNO_3), an intense SERS signal is collected, indicating that the dye-metal bond has been completely hydrolyzed by the acid, leading to the preferential adsorption of the free dye molecules onto the silver nanoparticles. In the third step (hydrolysis with HF), the HF is able to hydrolyze the dye-metal complex in the lake pigment, although the overall chemical conditions do not enable a complete adsorption of the dye molecules on the SERS-active substrate. This results in a SERS spectrum in which the main signals of eosin Y are barely visible over a strong fluorescent background that is due to the presence, in solution, of some free dye molecules that were not adsorbed on the silver surface. To the best of the authors' knowledge, the results reported above represent the first instances in which eosin Y and phloxine are identified in actual art objects by SERS. In the past, FT-Raman spectroscopy has been used for the characterization of phloxine in José Gaudalupe Posada prints (Casadio et al., 2010b). The SERS identification of eosin Y in the Van Gogh sample opens up new frontiers for the study of eosin-containing faded paintings for which only minimally invasive sampling is allowed (Burnstock et al., 2005).

Xanthene-Anthraquinone Mixtures

Eosin Y and Carmine

As a final step of the present study, samples removed from red areas of ten Japanese prints of the Meiji era (1877-1898) were analyzed with SERS following the three-step procedure presented in this work. One of the prints examined is shown in **Figure 7**. It was noticed at first that, without acidic pretreatment, samples from such prints yield poor SERS data, characterized by a highly fluorescent background, and no specific peaks. On the other hand, hydrolysis with HNO_3 leads to the preferential adsorption of eosin Y over carmine on the silver nanoparticles, as shown in **Figure 8**. The SERS spectra collected correlate well with previously published data of eosin Y (Narayanan et al., 1994; Whitney et al., 2006; Greeneltch et al., 2012). In particular, based on the classification reported by Whitney et al. (2006), eosin Y could be present in the samples from the Japanese prints as a free acid; in our spectra, only the peak at 1016 cm^{-1} is ascribable to the disodium salt, even if it is not one of the most characteristic for this specific form. In principle, the presence of eosin Y in its free acid form is in accordance with the fact that normal Raman spectra acquired on the same areas as those sampled for SERS are characterized by an intense fluorescence signal arising from the dye (Whitney et al., 2006). Nevertheless, the fluorescent background could also originate from the other materials present in the sample, such as additional dyes and pigments, starch, and/or the paper itself. Interestingly, after HF hydrolysis, the typical signals of carmine are also detected in the SERS spectrum (**Figure 8**). An assignment of the normal modes for carminic acid, the main coloring molecule of cochineal and carmine lakes, may be found in the literature (Cañamares et al., 2006).

The pH reached by treating the samples with a 1% HNO_3 aqueous solution is evidently not sufficient to break the chemical bond between carminic acid and its substrate in the lake used by the printer, while eosin Y, more soluble in the medium, can be more easily detected. On the other hand, as the HF treatment was originally designed to hydrolyze anthraquinone-based lake pigments (Pozzi et al., 2012b), the corresponding SERS spectrum shows a strong signal for carminic acid that, as expected, is predominant compared to that of eosin Y. In the spectrum obtained upon HF hydrolysis, reported in **Figure 8**, the signals of both carminic acid and eosin Y can be identified. Compared to spectra acquired after hydrolysis with HNO_3, the signals of eosin Y decrease visibly following HF treatment, as can be noted comparing spectra (c) and (d). In the absence of other studies on Japanese printmakers' practices, it is not clear if, in these cases, eosin Y and carminic acid were used as free dyes or as lakes. Experimental evidence gathered from the prints, in particular an intense signal for aluminum detected by SEM/EDX for cochineal-colored samples, suggests that cochineal might have been used

FIGURE 7 | Adachi (Shosai) Ginko, *Ladies Sewing (Kijo saiho no zu)*, dated to September 3rd of 1887. Reproduced with permission of the Metropolitan Museum of Art, New York, accession number JP3272.

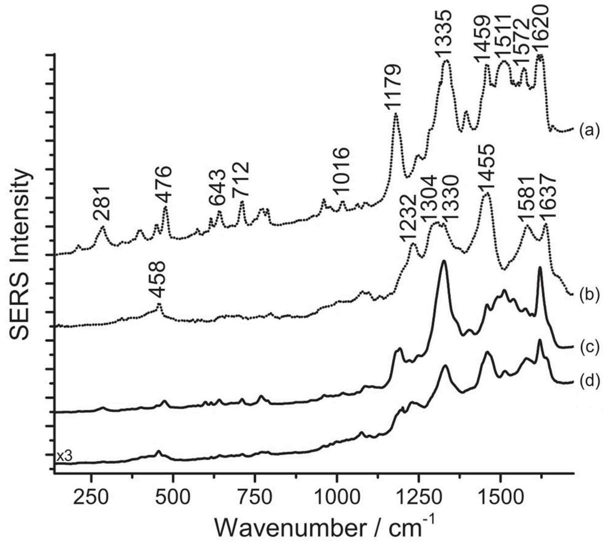

FIGURE 8 | SERS spectra of a mixture of eosin Y and carmine in Japanese woodblock prints (λ_{exc} = 488 nm). Spectrum of reference eosin Y (a) and carmine lake (b) compared with spectra acquired from the print sample after HNO_3 treatment (c), and after HF treatment (d). In spectrum (c), signals of eosin Y are detected at 281, 476, 643, 712, 1016, 1179, 1335, 1459, 1511, 1572, and 1620 cm^{-1}. In spectrum (d), signals of carmine lake are detected at 458, 1232, 1330 (combination band), 1455, 1581, and 1637 cm^{-1}, while some signals of eosin Y are also detected at 281, 476, 643, 712, 1179, 1332 (combination band), 1511, and 1620 cm^{-1}.

as an aluminum lake. Results from SERS analysis following the three-step procedure described here confirmed that cochineal is indeed found as a lake pigment (Leona, 2009; Pozzi et al., 2012b); indeed, free carminic acid is rather soluble in water and, if present, would adsorb rapidly onto the silver nanoparticles in the first step, producing a legible SERS response, while in the present case analysis of the untreated samples gave no results. As for eosin Y, lead, typically used to produce eosin lakes in Europe (Eastaugh et al., 2004), was rarely detected. Based on the absence of lead and other elements that may have been used as laking substrates in the XRF data, it is possible to hypothesize that, in our case, eosin Y was used as a free dye by the Japanese printmaker. Accordingly to what was previously stated, the high fluorescence detected when the samples are not treated seems to indicate the presence of eosin Y as a free dye in the material examined. However, the use of a mixture of the dye along with the corresponding lake pigment cannot be excluded. In both cases, the HNO_3 treatment enables an efficient interaction between the silver nanoparticles and the dye molecules, resulting in the best and most consistent analytical results.

As a final remark, the experiments performed showed that different results are obtained when the step order, in particular steps 2 and 3, is inverted. Indeed, to accomplish detection of eosin successfully, it is crucial to carry out the HNO_3 hydrolysis before treatment with HF. When the latter is used first, the carmine lake is hydrolyzed and free carminic acid is brought into solution. Likely due to the two molecules' differences in terms of solubility and affinity for the metal substrate, carminic acid then competes with eosin for adsorption onto the silver nanoparticles, resulting in the anthraquinone signals becoming predominant in the SERS spectrum.

CONCLUSIONS

In the present study, three SERS approaches for the selective detection and conclusive identification of synthetic dyes in samples from artworks were evaluated and compared, i.e., SERS on silver nanoparticles without any preliminary sample treatment, upon hydrolysis with HNO_3, and after treatment with HF. These three methodologies may be conveniently incorporated into a three-step analytical procedure, in which they can be performed in sequence on the same microscopic sample upon physical removal or evaporation of the colloidal droplet after each step.

The synthetic dyes examined in this work, belonging to the aniline and xanthene molecular classes, show a high fluorescence emission in the visible range of the electromagnetic spectrum, which often obscures the intrinsically weaker Raman signal, and are therefore ideal candidates for SERS. Being good SERS scatterers, these colorants have been used in previous studies to test innovative methodological approaches of interest to the biology and forensic science fields. In addition, aniline and xanthene dyes are greatly relevant to cultural heritage research, as it is attested by the fact that they were the first synthetic organic colorants to be widely used in printing and painting, among other art forms. Their extensive occurrence as artists' materials and the lack of reliable, minimally invasive identification methods to date prompted the authors to design a SERS procedure specifically tailored to their detection and characterization in samples removed from works of art and objects of archaeological and historical significance.

The present study shows that aniline dyes on paper give rise to good quality SERS spectra even without pretreating the sample, although hydrolysis with HNO_3 may help improve the signal-to-noise ratio in spectra from highly degraded specimens. In the case of silk dyed with crystal/methyl violet, treatment of the sample with acids was crucial to induce the hydrolysis of the dye-mordant complex; HNO_3 was found to be more effective than HF for this purpose.

When dealing with xanthene dyes and lakes, the application of a HNO_3 pretreatment step is highly recommended. When xanthenes are present as free dyes, the use of HNO_3 enables the efficient adsorption of the dye molecules onto the SERS-active substrate, resulting in a significant enhancement of the SERS signal combined with the complete suppression of colloid-related citrate peaks (for rhodamine) and background fluorescence (for eosin Y and phloxine). In the case of xanthene lakes, the main purpose of using the HNO_3 is to hydrolyze the dye-metal complex in the lake pigment and release the free dye molecules for adsorption onto the nanoparticles surface.

Interestingly, it was found that pretreating the sample with two different acids (HNO_3 and HF) in sequence is key to the selective detection and identification of non-closely related dyes in mixtures. In this context, the present study reports, for the first time, an instance in which a multi-step SERS approach was applied to the characterization of mixtures of colorants belonging to the xanthene and anthraquinone molecular classes, i.e., eosin Y and carmine, in actual artworks. The occurrence of natural and synthetic dyes in combination cannot be ruled out when examining works by modern and contemporary artists whose studio practice is still unknown or under investigation. In these cases, the introduction of an additional step based on the use of HNO_3 in the SERS procedure, which only requires a few additional minutes compared to the two-step methodology presented by some of the authors in an earlier article, was found to be essential to reveal such mixtures.

DATA AVAILABILITY

The datasets generated for this study are available on request to the corresponding author.

AUTHOR CONTRIBUTIONS

AC carried out most of the experimental work and drafted the paper. FP helped with the experimental work and actively contributed to the preparation and submission of the manuscript. ML offered guidance and supervision throughout the project.

ACKNOWLEDGMENTS

The authors would like to thank Chris McGlinchey and Ana Martins, The Museum of Modern Art, for providing the Matisse samples; Henry D. Smith II, Columbia University, for offering access to the Japanese woodblock prints; and Silvia Centeno and Charlotte Hale, The Metropolitan Museum of Art, for providing the Van Gogh sample.

REFERENCES

Brosseau, C. L., Gambardella, A., Casadio, F., Grzywacz, C. M., Wouters, J., and Van Duyne, R. P. (2009a). *Ad-Hoc* surface-enhanced raman spectroscopy methodologies for the detection of artist dyestuffs: thin layer chromatography-surface enhanced raman spectroscopy and *in situ* on the fiber analysis. *Anal. Chem.* 81, 3056–3062. doi: 10.1021/ac802761v

Brosseau, C. L., Rayner, K. S., Casadio, F., Grzywacz, C. M., and Van Duyne, R. P. (2009b). Surface-enhanced raman spectroscopy: a direct method to identify colorants in various artist media. *Anal. Chem.* 81, 7443–7447. doi: 10.1021/ac901219m

Bruni, S., Guglielmi, V., and Pozzi, F. (2010). Surface-Enhanced Raman Spectroscopy (SERS) on silver colloids for the identification of ancient textile dyes: tyrian purple and madder. *J. Raman Spectrosc.* 41, 175–180. doi: 10.1002/jrs.2456

Bruni, S., Guglielmi, V., Pozzi, F., and Mercuri, A. M. (2011). Surface-enhanced Raman Spectroscopy (SERS) on Silver colloids for the identification of ancient textile dyes. part ii: pomegranate and sumac. *J. Raman Spectrosc.* 42, 465–473. doi: 10.1002/jrs.2736

Burnstock, A., Lanfear, I., van den Berg, K. J., Carlyle, L., Hendriks, E., and Kirby, J. (2005). "A Comparison of the Fading and Surface Deterioration of Red Lake Pigments in Six Paintings by Vincent van Gogh with Artificially Aged Paint Reconstructions," in *14th Triennial Meeting, The Hague, 12-16 September 2005: Preprints (ICOM Committee for Conservation) Triennial Meeting of the ICOM Committee for Conservation*. London: James and James.

Cañamares, M. V., Chenal, C., Birke, R. L., and Lombardi, J. R. (2008). DFT, SERS, and single-molecule SERS of crystal violet. *J. Phys. Chem. C* 112, 20295–20300. doi: 10.1021/jp807807j

Cañamares, M. V., Garcia-Ramos, J. V., Domingo, C., and Sanchez-Cortes, S. (2006). Surface-enhanced raman scattering study of the anthraquinone red pigment carminic acid. *Vibr. Spectrosc*. 40, 161–167. doi: 10.1016/j.vibspec.2005.08.002

Cañamares, M. V., Reagan, D. A., Lombardi, J. R., and Leona, M. (2014). TLC-SERS of mauve, the first synthetic dye. *J. Raman Spectrosc*. 45, 1147–1152. doi: 10.1002/jrs.4508

Casadio, F., Daher, C., and Bellot-Gurlet, L. (2016). Raman spectroscopy of cultural heritage materials: overview of applications and new frontiers in instrumentation, sampling modalities, and data processing. *Top. Curr. Chem*. 374:62. doi: 10.1007/s41061-016-0061-z

Casadio, F., Leona, M., Lombardi, J. R., and Van Duyne, R. P. (2010a). Identification of organic colorants in fibers, paints, and glazes by surface enhanced raman spectroscopy. *Acc. Chem. Res*. 43, 782–791. 10.1021/ar100019q

Casadio, F., Mauck, K., Chefitz, M., and Freeman, R. (2010b). Direct identification of early synthetic dyes: FT-raman study of the illustrated broadside prints of José Gaudalupe Posada (1852–1913). *Appl. Phys*. 100, 885–899. doi: 10.1007/s00339-010-5668-2

Centeno, S. A., Hale, C., Car,ò, F., Cesaratto, A., Shibayama, N., Delaney, J., et al. (2017). Van Gogh's *irises* and *roses*: the contribution of chemical analyses and imaging to the assessment of color changes in the red lake pigments. *Her. Sci*. 5:18. doi: 10.1186/s40494-017-0131-8

Cesaratto, A., Leona, M., Lombardi, J. R., Comelli, D., Nevin, A., and Londero, P. (2014). Detection of organic colorants in historical painting layers using UV laser ablation surface-enhanced raman microspectroscopy. *Angew. Chem. Int. Ed*. 53, 14373–14377. doi: 10.1002/anie.201408016

Cesaratto, A., Lombardi, J. R., and Leona, M. (2017). Tracking photo-degradation of triarylmethane dyes with surface-enhanced raman spectroscopy. *J. Raman Spectrosc*. 48, 418–424. doi: 10.1002/jrs.5056

Cesaratto, A., Londero, P., Shibayama, N., Lombardi, J. R., and Leona, M. (2016). Fourier filtering ultraviolet laser ablation SERS for the analysis of yellow lakes. *Microchem. J*. 126, 237–242. doi: 10.1016/j.microc.2015.12.018

Chen, K., Leona, M., Vo-Dinh, K.-C., Yan, F., Wabuyele, M. B., and Vo-Dinh, T. (2006). Application of Surface-Enhanced Raman Scattering (SERS) for the identification of anthraquinone dyes used in works of art. *J. Raman Spectrosc*. 37, 520–527. doi: 10.1002/jrs.1426

Corredor, C., Teslova, T., Cañamares, M. V., Chen, Z., Zhang, J., Lombardi, J. R., et al. (2009). Raman and Surface-Enhanced Raman spectra of chrysin, apigenin and luteolin. *Vibr. Spectrosc*. 49, 190–195. doi: 10.1016/j.vibspec.2008.07.012

Eastaugh, N., Walsh, V., Chaplin, T., and Siddall, R. (2004). *Pigment Compendium*. A Dictionary of Historical Pigments. Oxford: Elsevier Butterworth-Heinemann.

Fang, C., Agarwal, A., Buddharaju, K. D., Khalid, N. M., Salim, S. M., Widjaja, E., et al. (2008). DNA detection using nanostructured SERS substrates with rhodamine B as raman label. *Biosens. Bioelectron*. 24, 216–221. doi: 10.1016/j.bios.2008.03.032

Geiman, I., Leona, M., and Lombardi, J. R. (2009). Application of raman spectroscopy and surface-enhanced raman scattering to the analysis of synthetic dyes found in ballpoint pen inks. *J. Forensic Sci*. 54, 947–952. doi: 10.1111/j.1556-4029.2009.01058.x

Greeneltch, N. G., Davis, A. S., Valley, N. A., Casadio, F., Schatz, G. C., Van Duyne, R. P., et al. (2012). Near-Infrared Surface-Enhanced Raman Spectroscopy (NIR-SERS) for the identification of eosin Y: theoretical calculations and evaluation of two different nanoplasmonic substrates. *J. Phys. Chem. A* 116, 11863–11869. doi: 10.1021/jp3081035

Idone, A., Gulmini, M., Henry, A.-I., Casadio, F., Chang, L., Appolonia, L., et al. (2013). Silver colloidal pastes for dye analysis of reference and historical textile fibers using direct, extractionless, non-hydrolysis surface-enhanced raman spectroscopy. *Analyst* 138, 5895–5903. doi: 10.1039/c3an00788j

Jeanmaire, D. L., and Van Duyne, R. P. (1977). Surface raman spectroelectrochemistry: part I. heterocyclic, aromatic, and aliphatic amines adsorbed on the anodized silver electrode. *J. Electroanal. Chem. Interf. Electrochem*. 84, 1–20. doi: 10.1016/S0022-0728(77)80224-6

Jensen, L., and Schatz, G. C. (2006). Resonance raman scattering of rhodamine 6G as calculated using time-dependent density functional theory. *J. Phys. Chem. A* 110, 5973–5977. doi: 10.1021/jp0610867

Jurasekova, Z., Domingo, C., Garcia-Ramos, J. V., and Sanchez-Cortes, S. (2008). *In situ* detection of flavonoids in weld-dyed wool and silk textiles by surface-enhanced raman scattering. *J. Raman Spectrosc*. 39, 1309–1312. doi: 10.1002/jrs.2053

Kirby, J., and White, R. (1996). The Identification of Red Lake Pigment Dyestuffs and a Discussion of Their Use. In National Gallery Technical Bulletin, ed. Diana Davies and Jan Green, 17: 56–80. London: National Gallery Publications Limited.

Kneipp, K., Wang, Y., Kneipp, H., Perelman, L. T., Itzkan, I., Dasari, R. R., et al. (1997). Single molecule detection using Surface-Enhanced Raman Scattering (SERS). *Phys. Rev. Lett*. 78, 1667–1670. doi: 10.1103/PhysRevLett.78.1667

Leona, M. (2005). "Sub-Nanogram Level Identification of Alizarin by Surface-Enhanced Raman Scattering," in *Proceedings Volume of the Sixth Infrared and Raman Users Group Conference*, ed. M. Picollo, Florence: Il Prato.

Leona, M. (2009). Microanalysis of organic pigments and glazes in polychrome works of art by surface-enhanced resonance raman scattering. *Proc. Natl. Acad. Sci. U.S.A*. 106, 14757–14762. doi: 10.1073/pnas.0906995106

Leona, M., and Lombardi, J. R. (2007). Identification of berberine in ancient and historical textiles by surface-enhanced raman scattering. *J. Raman Spectrosc*. 38, 853–858. doi: 10.1002/jrs.1726

Leona, M., Stenger, J., and Ferloni, E. (2006). Application of Surface-Enhanced Raman scattering techniques to the ultrasensitive identification of natural dyes in works of art. *J. Raman Spectrosc*. 37, 981–992. doi: 10.1002/jrs.1582

Lin, S., Hasi, W.-L.-J., Lin, X., Han, S., Lou, X.-T., Yang, F., et al. (2015). Rapid and sensitive SERS Method for determination of rhodamine B in chili powder with paper-based substrates. *Anal. Methods* 7, 5289–5294. doi: 10.1039/C5AY00028A

Mayhew, H. E., Fabian, D. M., Svoboda, S. A., and Wustholz, K. L. (2013). Surface-Enhanced raman spectroscopy studies of yellow organic dyestuffs and lake pigments in oil paint. *Analyst* 138, 4493–4499. doi: 10.1039/c3an00611e

Murcia-Mascarós, S., Domingo, C., Sanchez-Cortes, S., Cañamares, M. V., and Garcia-Ramos, J. V. (2005). Spectroscopic identification of alizarin in a mixture of organic red dyes by incorporation in Zr-Ormosil. *J. Raman Spectrosc*. 36, 420–426. doi: 10.1002/jrs.1315

Narayanan, V. A., Stokes, D. L., and Vo-Dinh, T. (1994). Vibrational spectral analysis of eosin Y and erythrosin B-intensity studies for quantitative detection of the dyes. *J. Raman Spectrosc*. 25, 415–422. doi: 10.1002/jrs.1250250607

Narayanan, V. A., Stokes, D. L., and Vo-Dinh, T. (1996). Vibrational spectra of the industrial dyes cresyl fast violet, phloxine B and saffron. Intensity study by surface-enhanced raman spectroscopy. *Analusis* 24, 1–5.

Nie, S., and Emory, S. R. (1997). Probing single molecules and single nanoparticles by surface-enhanced raman scattering. *Science* 275, 1102–6. doi: 10.1126/science.275.5303.1102

Oakley, L. H., Fabian, D. M., Mayhew, H. E., Svoboda, S. A., and Wustholz, K. L. (2012). Pretreatment strategies for SERS analysis of indigo and prussian blue in aged painted surfaces. *Anal. Chem*. 84, 8006–8012. doi: 10.1021/ac301814e

Pozzi, F., Jan van den Berg, K., Fiedler, I., and Casadio, F. (2014). A systematic analysis of red lake pigments in french impressionist and post-impressionist paintings by Surface-Enhanced Raman Spectroscopy (SERS). *J. Raman Spectrosc*. 45, 1119–1126. doi: 10.1002/jrs.4483

Pozzi, F., and Leona, M. (2015). Surface-enhanced raman spectroscopy in art and archaeology. *J. Raman Spectrosc*. 47, 67–77. doi: 10.1002/jrs.4827

Pozzi, F., Lombardi, J. R., Bruni, S., and Leona, M. (2012b). Sample treatment considerations in the analysis of organic colorants by surface-enhanced raman scattering. *Anal. Chem*. 84, 3751–3757. 10.1021/ac300380c.

Pozzi, F., Poldi, G., Bruni, S., De Luca, E., and Guglielmi, V. (2012a). Multi-Technique characterization of dyes in ancient kaitag textiles from caucasus. *Anthropol. Sci*. 4, 185–197. doi: 10.1007/s12520-012-0092-5

Pozzi, F., Porcinai, S., Lombardi, J. R., and Leona, M. (2013a). Statistical methods and library search approaches for fast and reliable identification of dyes using Surface-Enhanced Raman Spectroscopy (SERS). *Anal. Methods* 5, 4205–12. doi: 10.1039/c3ay40673c

Pozzi, F., Shibayama, N., Leona, M., and Lombardi, J. R. (2013b). TLC-SERS study of syrian rue (*Peganum Harmala*) and its main alkaloid constituents. *J. Raman Spectrosc*. 44, 102–107. doi: 10.1002/jrs.4140

Pozzi, F., Zaleski, S., Casadio, F., Leona, M., Lombardi, J. R., and Van Duyne, R. P. (2016a). "Surface-Enhanced Raman Spectroscopy: Using Nanoparticles to Detect Trace Amounts of Colorants in Works of Art," in *Nanoscience and Cultural Heritage,* eds. Ph. Dillmann, L. Bellot-Gurlet, and I. Nenner (Atlantis Press) 161–204. doi: 10.2991/978-94-6239-198-7_6

Pozzi, F., Zaleski, S., Casadio, F., and Van Duyne, R. P. (2016b). SERS discrimination of closely related molecules: a systematic study of natural red dyes in binary mixtures. *J. Phys. Chem. C*. 120, 21017–21026. doi: 10.1021/acs.jpcc.6b03317

Roh, J. Y., Matecki, M. K., Svoboda, S. A., and Wustholz, K. L. (2016). Identifying pigment mixtures in art using SERS: a treatment flowchart approach. *Anal. Chem*. 88, 2028–2032. doi: 10.1021/acs.analchem.6b00044

Snowden, M. J., Shadi, I. T., Chowdhry, B. Z., Snowden, M. J., and Withnall, R. (2004). Semi-quantitative analysis of alizarin and purpurin by Surface-Enhanced Resonance Raman Spectroscopy (SERRS) using silver colloids. *J. Raman Spectrosc*. 35, 800–807. doi: 10.1002/jrs.1199

Whitney, A. V., Casadio, F., and Van Duyne, R. P. (2007). Identification and characterization of artists' red dyes and their mixtures by Surface-Enhanced Raman Spectroscopy. *Appl. Spectrosc*. 61, 994–1000. doi: 10.1366/000370207781745838

Whitney, A. V., Van Duyne, R. P., and Casadio, F. (2006). An innovative Surface-Enhanced Raman Spectroscopy (SERS) method for the identification of six historical red lakes and dyestuffs. *J. Raman Spectrosc*. 37, 993–1002. doi: 10.1002/jrs.1576

Woodhead, A. L., Cosgrove, B., and Church, J. S. (2016). The purple coloration of four late 19th century silk dresses: a spectroscopic investigation. *Spectrochim. Acta Part A* 154, 185–192. doi: 10.1016/j.saa.2015.10.024

Zaffino, C., Bedini, G. D., Mazzola, G., Guglielmi, V., and Bruni, S. (2016). Online coupling of high-performance liquid chromatography with surface-enhanced raman spectroscopy for the identification of historical dyes. *J. Raman Spectrosc*. 47, 607–615. doi: 10.1002/jrs.4867

Conflict of Interest Statement: The authors declare that the research was conducted in the absence of any commercial or financial relationships that could be construed as a potential conflict of interest.

frontiers in Chemistry

ORIGINAL RESEARCH
published: 19 March 2019
doi: 10.3389/fchem.2019.00144

Investigation of the Charge-Transfer Between Ga-Doped ZnO Nanoparticles and Molecules Using Surface-Enhanced Raman Scattering: Doping Induced Band-Gap Shrinkage

Peng Li[1,2], *Xiaolei Wang*[1,2], *Xiaolei Zhang*[1,2], *Lixia Zhang*[2], *Xuwei Yang*[2] *and Bing Zhao*[1,2]*

[1] *State Key Laboratory of Supramolecular Structure and Materials, College of Chemistry, Jilin University, Changchun, China,*
[2] *College of Chemistry, Jilin University, Changchun, China*

OPEN ACCESS

Edited by:
Ivano Alessandri,
Università degli Studi di Brescia, Italy

Reviewed by:
Nicolò Bontempi,
Catholic University of Sacred Heart, Italy
Guo Lin,
Beihang University, China

***Correspondence:**
Bing Zhao
zhaob@jlu.edu.cn

Specialty section:
This article was submitted to Analytical Chemistry, a section of the journal Frontiers in Chemistry

Received: *16 January 2019*
Accepted: *27 February 2019*
Published: *19 March 2019*

Citation:
Li P, Wang X, Zhang X, Zhang L, Yang X and Zhao B (2019) Investigation of the Charge-Transfer Between Ga-Doped ZnO Nanoparticles and Molecules Using Surface-Enhanced Raman Scattering: Doping Induced Band-Gap Shrinkage. Front. Chem. 7:144. doi: 10.3389/fchem.2019.00144

Semiconductor nanomaterial is a kind of important enhancement substrate in surface-enhanced Raman scattering (SERS), and the charge-transfer (CT) process contributes dominantly when they are used as the enhancement substrate for SERS. Doping has significant effect on the CT process of semiconductor nanomaterials. Yet till now, none attempts have been made to explore how doping affects the CT process between the semiconductor and probe molecules. For the first time, this paper investigates the effect of gallium (Ga) doping on the CT process between ZnO nanoparticles and 4-mercaptobenzoic acid (4-MBA) monolayer. In this paper, a series of Ga-doped ZnO nanoparticles (NPs) with various ratio of Ga and Zn are synthesized and their SERS performances are studied. The study shows that the doped Ga can cause the band gap shrinkage of ZnO NPs and then affect the CT resonance process form the valence band (VB) of ZnO NPs to the LUMO of 4-MBA molecules. The band gap of Ga-doped ZnO NPs is gradually narrowed with the increasing doping concentration, and a minimum value (3.16 eV) is reached with the Ga and Zn ratio of 3.8%, resulting in the maximum degree of CT. This work investigates the effects of doping induced band gap shrinkage on CT using SERS and provides a new insight on improving the SERS performance of semiconductor NPs.

Keywords: charge-transfer, Ga-doped ZnO, SERS, 4-MBA, band gap shrinkage

INTRODUCTION

The interfacial charge-transfer (CT) process between a substrate and an adsorbed molecule is an interesting phenomenon which has attached extensive research. The CT process has a wide range of applications in interface chemistry (Osako et al., 2018), catalytic chemistry (Thang et al., 2018), electronic devices (Liu et al., 2018), solar cells (Yadav et al., 2018), photoelectrochemistry (Chen et al., 2018), and so on. Therefore, it is vital to conduct an in-depth investigation of the CT process, which may provide us better understanding and thus expand its applications in various fields.

Surface-enhanced Raman scattering (SERS) is a forceful method for studying the CT between adsorbed molecule monolayer and the substrate (Wang et al., 2011; Li et al., 2018; Yu et al., 2018). As is well-known, the emergence of SERS phenomenon is inseparable from enhancement substrates. With the development of relevant researches, SERS active nanomaterials have been extended from noble metals, such as Au, Ag, and so on, to semiconductor nanomaterials (NMs) (Fleischmann et al., 1974; Tian et al., 2002; Biju et al., 2008; Shen et al., 2008; Alessandri and Lombardi, 2016). Many semiconductor NMs such as TiO_2 (Yamada and Yamamoto, 1983), ZnO (Wang et al., 2009), NiO (Yamada et al., 1982), InAs/GaAs (Quagliano, 2004), CdS (Wang et al., 2007b), ZnS (Wang et al., 2007a) *etc*., have been demonstrated to exhibit good SERS activities. In comparison with metal substrates, semiconductor NMs have additional optical and electrical properties, which enable them to display remarkable CT enhancement and catalytic abilities (Lombardi and Birke, 2009; Han et al., 2017). As we all know, for the vast majority of semiconductors, their localized surface plasmon resonance is located in the infrared region. That is to say, when semiconductor NMs was used as enhancement substrate, SERS is mainly generated through the CT enhancement mechanism (Lombardi and Birke, 2007), so the SERS performance of semiconductor NMs is a powerful tool to investigate the CT process between the semiconductor NMs and adsorbed molecules.

The CT process between the adsorbed molecules and the substrate is closely related to the size and morphology of semiconductor NMs (Musumeci et al., 2009; Tang et al., 2012; Lamberti et al., 2015). Moreover, doping is also a very important factor for the CT process when semiconductor NMs are used as the SERS substrate. Our group have reported that the SERS performance of TiO_2 nanoparticles (NPs) can be improved by Fe^{3+}, Co^{2+}, Ni^{2+} doping (Yang et al., 2011, 2014; Xue et al., 2013a), and the improvements were attributed to the formation of abundant doping (defects) levels in the band gap of TiO_2 NPs. Dual functional Ta-doped electrospun TiO_2 nanofibers with enhanced photocatalysis and SERS activity for detection of organic compounds were synthesized by Singh et al. (2017) The generation of Ti^{3+} defects from Ta^{5+} doping, which acted as an intermediate state for TiO_2 to methylene blue molecules electron transfer, was used to explain the enhanced SERS activity of their obtained products. Effects of Mn^{2+}, Zn^{2+}, and Mg^{2+} doping on SERS properties of TiO_2 NPs were also studied by our group (Yang et al., 2010; Xue et al., 2012a, 2013b), it was found that an appropriate amount of metal ions dopant enriched the surface states and improved the photo-generated carrier separation efficiency. SERS characteristics of Co^{2+} doped ZnO (Xue et al., 2012b) and Mn^{2+} doped CuO (Prakash et al., 2016) were also investigated, the influences of dopant were attributed to the increasing of defects and the ferromagnetic ordering, respectively. To date, most studies about the effect of metal doping semiconductor on SERS (CT process) focused on the change of surface state level or content of defects, however, the impact of doping induced band gap shrinkage on the CT process between semiconductor NPs and molecules have never been reported. For the first time, this paper investigates the effect of doping induced band gap shrinkage on the CT between semiconductor NPs and molecules.

Due to some unmatched properties in photoelectric and magnetism, ZnO is widely used in medicine and health care, food industry, varistor, antivirus, gas sensitive elements, and photocatalysis (Zhang et al., 2009; Cushen et al., 2012; Nohynek and Dufour, 2012; Hassan et al., 2013; Lang et al., 2014; Wang et al., 2014) etc. ZnO is also an important enhancement substrate in SERS study because of its wide band gap. Numerous SERS studies around ZnO NPs have been carried out. The size-dependent effect of ZnO NPs for SERS signal (Sun et al., 2007) and ZnO/PATP(p-aminothiophenol)/Ag assemblies (Sun et al., 2008) was investigated, the SERS enhancement mechanism for ZnO was attributed to the CT enhancement mechanism. The influence of contact variation in ZnO-molecules-metal system (Mao et al., 2012), fabrication of one-dimensional ZnO/4-MPy/Ag assemblies (Hu et al., 2010), contribution of ZnO to CT induced SERS in Au/ZnO/PATP assembly (Yang et al., 2008) and so on have been reported. Above all, the investigation about CT process between ZnO NPs and adsorbed molecules is necessary in view of the wide applications of ZnO NPs. Here we study the effect of doping induced band gap shrinkage on CT process between ZnO NPs and molecules. The band gap of ZnO NPs is altered by doping gallium (Ga) into ZnO NPs, the ionic radius of Ga^{3+} ions (0.062 nm) is less than the Zn^{2+} ions (0.074 nm), so the Ga^{3+} ions are soluble in the ZnO matrix.

In this work, a range of Ga-doped ZnO NPs with various ratio Ga and Zn and 4-MBA@ZnO (Ga-doped ZnO) system are obtained. The actual ratios of Ga and Zn in the Ga-doped ZnO NPs are confirmed by ICP measurement. Then it is determined that the degree of crystallinity and particles size of Ga-doped ZnO NPs can be affected by the ratio of Ga and Zn according to XRD, Raman, and TEM characterizations. Moreover, it is found that the band gap of NPs shrinks as the ratio of Ga and Zn increases. The effect of Ga doping on the CT process between ZnO NPs and 4-MBA monolayer is investigated using SERS. The modest amount of doped Ga can enhance the degree of CT between ZnO and 4-MBA monolayer compared to the pure ZnO NPs. The change of CT is mainly due to the size dependence effect and the band-gap shrinkage effect. The doped Ga causes the band gap shrinkage of ZnO and then affects the CT resonance process from the valence band (VB) of ZnO NPs to the LUMO of 4-MBA molecules. This work conducts an in-depth investigation on the effects of doping induced band gap shrinkage on CT using SERS and provides a new insight on improving the SERS performance of semiconductor NPs.

EXPERIMENTAL SECTION

Chemicals

4-Mercaptobenzoic acid (4-MBA) and Gallium(III) nitrate hydrate were purchased from Sigma-Aldrich and used without further purification. All other chemicals were acquired from Beijing Chemical Reagent Factory and used without further purification. The distilled and deionized water from a Milli-Q-plus system with the resistivity >18.0 MΩ was used in aqueous solution.

Synthesis of ZnO and Ga-Doped ZnO NPs

ZnO and Ga-doped ZnO NPs were synthesized as follows. In short, 40 mL of 0.5 mol/L NaOH solution was slowly added dropwise into 100 mL of 0.1 mol/L $Zn(Ac)_2$ solutions under vigorous stirring in order to produce the $Zn(OH)_2$ precipitate. Subsequently, 1.2 g of NH_4HCO_3 powder was added. After stirring for 30 min, a semitransparent zinc carbonate hydroxide colloid was obtained. Then the colloid was centrifuged and rinsed three times with purified water and absolute ethyl alcohol in alternation and dried at 80°C. Thus, the precursor of a small crystallite $Zn_5(CO_3)_2(OH)_6$ was formed. Then, the as-prepared precursor was calcined at 550°C for 2 h to obtain the ZnO NPs.

The synthetic methods of Ga-doped ZnO NPs is similar with what we described above. The difference is that there is an opportune amount of $Ga(NO_3)_3$ (0.0003, 0.0005, 0.0007, 0.0009, 0.002, 0.004, 0.006, 0.008, and 0.01 mol/L, respectively) was added to the $Zn(Ac)_2$ solutions to obtain Ga-doped ZnO NPs with difference ratio of Ga and Zn.

Adsorption of Probing Molecules

ZnO and Ga-doped ZnO NPs surface-modified by molecules were obtained as follows: 20 mg of ZnO and Ga-doped ZnO nanocrystals were dispersed in 20 mL of 4-MBA (1×10^{-3} M) ethanol solution and the mixture was stirred for 6 h. Then, the precipitate was centrifuged and rinsed with absolute ethyl alcohol twice. ZnO and Ga-doped ZnO nanocrystals modified by 4-MBA were obtained.

Sample Characterization

The crystal structure of ZnO sample was determined by X-ray diffraction (XRD) using a Siemens D5005 X-ray powder diffractometer with a Cu Kα radiation source at 40 kV and 30 mA. X-ray photoelectron spectra (XPS) were obtained by using a Thermo ESCALAB 250 spectrometer with an Mg Ka excitation (1253.6 eV). Elemental analysis was carried out by ICP-AES with an Agilent 725 spectrometer. The UV-Vis DRS spectra were recorded on a Shimadzu UV-3600 spectrophotometer. Transmission electron microscopy (TEM) images were taken using a JEM-2100F high-resolution transmission electron microscopy operating at 200.0 kV. Raman spectra acquired at ambient pressure were obtained by using a Horiba-Jobin Yvon LabRAM ARAMIS system with the resolution of ca. 4 cm^{-1}; The 633 nm radiation from a 20 mW air-cooled HeNe narrow bandwidth laser was used as exciting source. The laser beam was focused onto a spot with a diameter of approximately 1 µm using an objective microscope with a magnification of 50×. The Raman band of the silicon wafer at 520.7 cm^{-1} was used to calibrate the spectrometer. Data acquisition was the result of two times 30 s accumulations for the 4-MBA molecules absorbed on ZnO (Ga-doped ZnO) NPs.

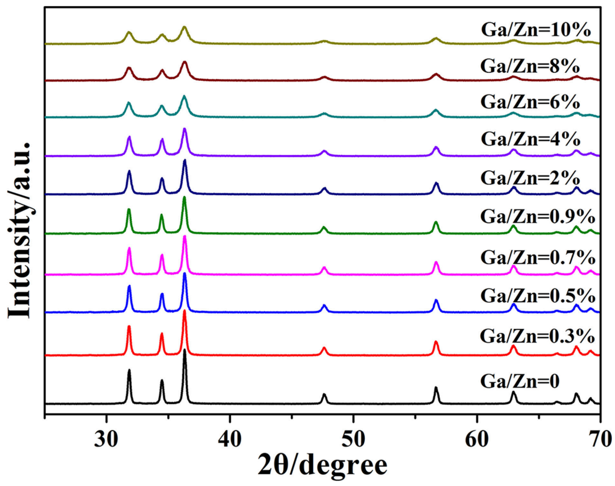

FIGURE 1 | XRD spectra of ZnO and Ga-doped ZnO NPs with different ratio of Ga and Zn.

RESULTS AND DISCUSSION

Measurement of XRD

The XRD patterns of Ga-doped ZnO NPs with different ratio of Ga and Zn are shown in **Figure 1**. All the diffraction peaks of pure and doped ZnO are the characteristic peak of hexagonal wurtzite ZnO (JCPDS36-1451). No characteristic peaks corresponding to Ga or Ga_2O_3 are observed in the diffraction patterns, which is because the concentration of gallium is too low for those impurities to be detected by the XRD instrument. **Figure S1** demonstrates the relationship between full width at half maximum (FWHM) of the peak (101) and the ratio of Ga and Zn : the intensity of the peak decreases and the FWHM is increased with the ratio of Ga and Zn increasing. All these results indicate that the Ga is doped into ZnO successfully and the crystallinity of Ga-doped ZnO NPs is decreased with the increasing doping ratio. The diameter of Ga-doped ZnO NPs (0–10%) are 35.4, 30.1, 27.4, 26.2, 25.0, 22.6, 19.0, 14.4, 13.5, and 12.9 nm, respectively, calculated using Scherrer's formula (Swamy et al., 2006) based XRD data.

Measurement of XPS and ICP

According to the XPS spectra which is shown in **Figure S2A**, we can observe that all samples show similar characteristics as the pure ZnO spectra. However, in terms of **Figure S2B**, the relevant peaks of Ga-dopant (Ga $2p_{1/2}$ and Ga $2p_{3/2}$ located at 1117.9 and 1144.8 eV, respectively) can be observed when the spectra is magnified in the approximate range of 1110–1150 eV, moreover, the intensities of Ga-dopant-related peaks increases with the Ga concentration increasement. **Figure S2C** shows the XPS spectra of $Zn_{3/2}$ and $Zn_{1/2}$ for pure and doped ZnO NPs, and the two peaks are observed at 1021.7 and 1044.7 eV, respectively, the data is consistent with the binding energy of Zn-O (Sano et al., 2002; Jin et al., 2009).

All the description about the ratio of Ga and Zn used previously is the initial ratio, the ICP test is conducted in order

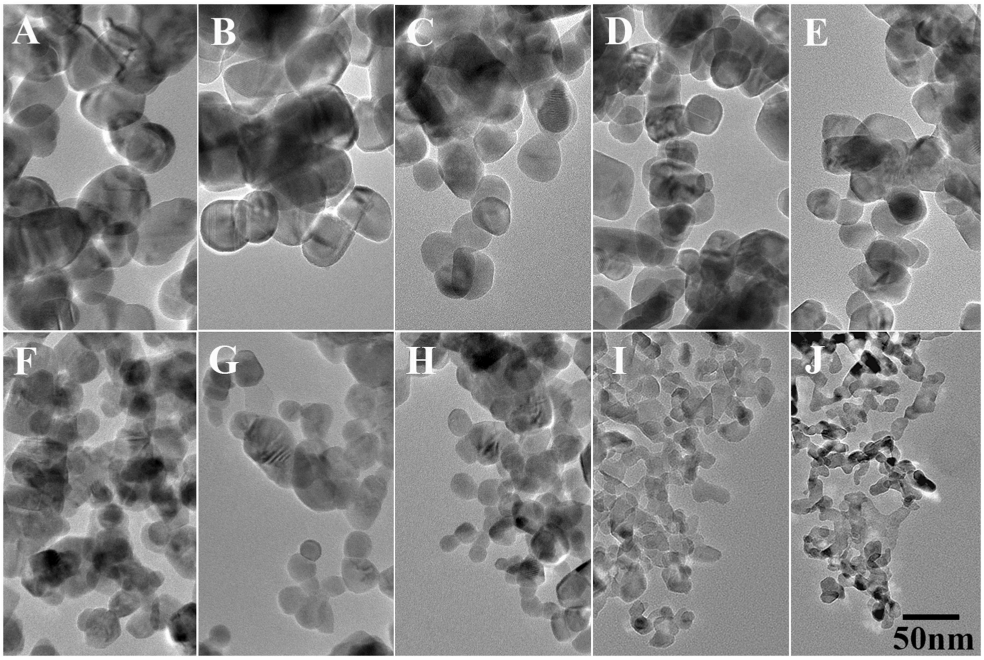

FIGURE 2 | TEM images of Ga-doped ZnO NPs: **(A–J)** represent the initial ratio of 0, 0.3, 0.5, 0.7, 0.9, 2, 4, 6, 8, and 10% for the Ga-doped ZnO NPs, respectively. The bar is 50 nm, and it is common to all images.

to determine the actual Ga and Zn ratio of doped ZnO NPs. The results (initial ratio 0–10%) are 0, 0.29, 0.39, 0.56, 0.66, 1.4, 2.7, 3.8, 5.0, and 6.1%, respectively. It is clear that the results of quantitative analysis from ICP is similar with the initial ratio in the low doping ratio and a significant discrepancy appears when the initial ratio is higher than 0.9%. The reason for this phenomenon is that the vast majority of Ga is doped into the lattice of ZnO at low doping ratio, and a portion of Ga is not introduced into ZnO when the content of Ga is too high. Above all, the XPS measurement proves that the Ga is doped into ZnO successfully and the actual ratio of Ga and Zn is determined by ICP.

Measurement of TEM Images and UV-vis Spectra

Figure 2 shows the TEM images of pure and doped ZnO NPs, all the NPs are spherical and the diameters decreases with the increased Ga/Zn ratio. The particle sizes of the NPs are determined as approximate 51.4, 44.3, 35.7, 31.4, 28.6, 25.7, 22.9, 15.7, 14.3, and 12.9 nm, which are a little different from the value calculated from XRD. Such difference occurs due to the fact that the calculation results of XRD are based on the assumption that the materials are all signal crystals, and the measured values from TEM represent the size of nanoparticles which consist of one or multiple single crystal. However, the tendency of size change coincided with the result of XRD, evidencing that the particle diameter decreases as the doping concentration increases.

The effect of doped gallium on the optical properties of ZnO is investigated via UV-vis absorption spectroscopy. The optical absorption spectra are shown in **Figure 3A**. The steep drop of the absorption at about 378 nm is assigned to the CT process between valence band (VB) and conduction band (CB). Besides, all the absorption edge of Ga-doped ZnO NPs have a red shift compared to the pure ZnO and the maximal absorption edge appeared at the initial ratio of 6%. The phenomenon is attributed to the effect of doping on the carrier density. The band gap of ZnO NPs was calculated according to the absorption edge. Due to the fact that ZnO has a direct inter-band transition (Mahdhi et al., 2015) and on the basis of practical fact and theoretical calculation, the band gap of ZnO can be obtained through the Tuac's relation (Tauc, 1968; You and Hua, 2012):

$$A(h\nu) = \mathrm{B}(\mathrm{h}\nu - \mathrm{E_g})^{1/2} \qquad (1)$$

where A is the absorbance, $h\nu$ is the energy of the incident photon and E_g is the band gap. The band gap is determined by plotting $(Ah\nu)^2$ vs. $h\nu$ and extrapolating the straight-line portion to the energy axis, the plots are shown in **Figure 3B** and the numerical values of E_g (0–10%) are 3.24, 3.22, 3.21, 3.20, 3.19, 3.18, 3.17, 3.16, 3.20, and 3.21 eV, respectively. According to this figure, with the increasement in doping concentration, the band gap of Ga-doped ZnO is first shrinked and down to the minimum value at the initial ratio of 6%, then increased. It should be noted that all the band gap of Ga-doped ZnO is less than the pure ZnO. Generally, there are two well-known theories about the changes of band gap of semiconductors: Burstein-Moss (BM) effect (Burstein, 1954; Moss, 1954) and band gap renormalization (BGR) effect (Dou et al., 1997; Jeon et al., 2011). The former is always related to the widening of the band gap and the

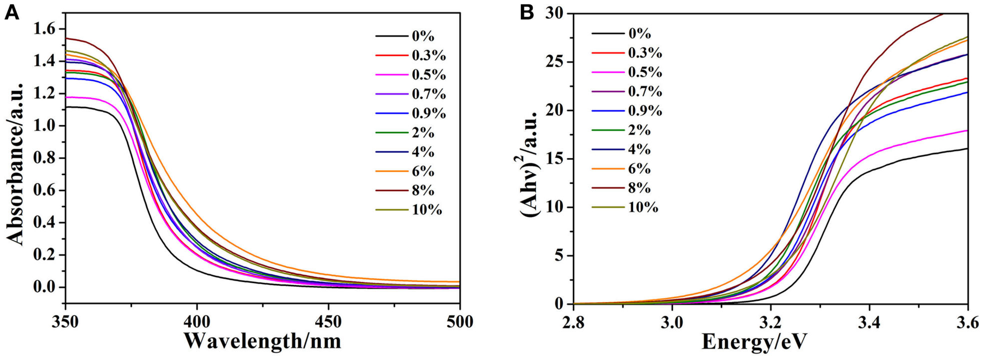

FIGURE 3 | (A) The optical absorption spectra of pure and doped ZnO NPs, **(B)** Relationship between $(Ah\nu)^2$ and photon energy ($h\nu$) for Ga-doped ZnO NPs.

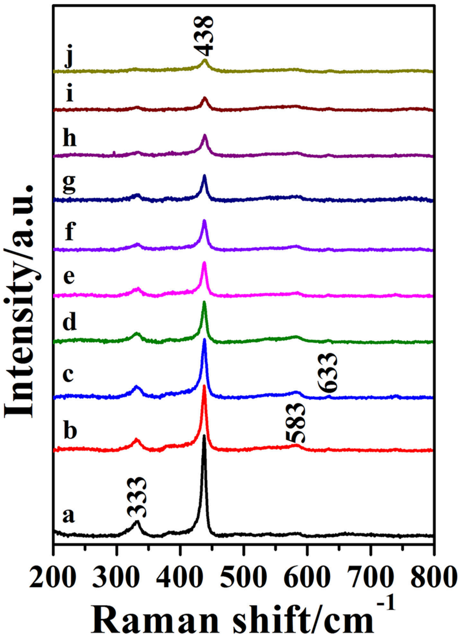

FIGURE 4 | The Raman spectra of Ga-doped ZnO NPs with various initial ratio of Ga and Zn(from a to j): 0, 0.3, 0.5, 0.7, 0.9, 2, 4, 6, 8, and 10%.

latter is in connection with the shrinking-effect. The BGR effect is dominant in our system, the electron-impurity interactions, exchange interactions, and electron-electron Coulomb within the CB resulted in the shrinkage of the host band gap.

Raman Spectra of ZnO and Ga-Doped ZnO NPs

The Raman spectra of pure and doped ZnO NPs are shown in **Figure 4**, all the Raman peaks are the characteristic peaks of hexagonal wurtzite structure. The ZnO NPs with hexagonal wurtzite phase possess $C_{6v}{}^4$ (P63/mc) space group and are simple single axial crystals. Only the optical phonon in the center of Brillouin zone is related to the first-order Raman scattering for perfect ZnO single crystal. In the point-group theory, the optical phonon modes are classified as $\Gamma_{opt} = A_1+2B_1+E_1+2E_2$, the A_1 and E_1 are split into transverse optical (TO) and longitudinal optical (LO) on account of they are polar modes. In all the phonon modes, A_1 and E_1 modes have Raman and infrared active, and that E_2 modes only have Raman active, B_1 modes are silent. According to the group theory and **Figure 4**, the peak at 333 cm^{-1} is the E_2(high)-E_2(low) mode and this mode is related to the multi-phonon scattering process. The strongest peak located at 438 cm^{-1} is the E_2(high) mode. This is the characteristic peak of the wurtzite phase and its intensity is associated with the crystallinity of ZnO; the weak peak at 583 cm^{-1} is assigned to the A_1(LO)-E_1(LO) mode and the E_1 vibrational mode is concerned with defects such as oxygen vacancy, zinc interstitial and the complex-defect and so on. The origin of another weak peak at 633 cm^{-1} is uncertain although it has been reported in ZnO films (Bundesmann et al., 2003; Shinde et al., 2011). Above all, all the peaks together prove the pure and doped ZnO NPs as hexagonal wurtzite phase, moreover, their crystallinity decrease with the ratio of Ga and Zn increasing, judging by the changes of E_2(high) modes. All the results are consistent with the results of XRD and TEM.

SERS Spectra of 4-MBA Adsorbed on Pure and Ga-Doped ZnO NPs

The SERS spectra of 4-MBA adsorbed on pure and Ga-doped ZnO NPs are obtained as shown in **Figure 5A**, all the peaks are the characteristic peaks of 4-MBA adsorbed on ZnO NPs and coincides with the reported results from literature (Sun et al., 2007). The strong peaks located at 1,594 cm^{-1} and 1,078 cm^{-1} can be attributed to υ_{8a} (a1) and υ_{12} (a1) aromatic ring characteristic vibrations, respectively. It is worth mentioning that there is an irregular change in the peak position of 1,078 cm^{-1}, the reason for this is attributed to the effect of the vibration mode of ZnO at 1,069 cm^{-1} (see the **Figure S3**). Other weak peaks such as 1,148 (υ_{15},b2) and 1,180 (υ_9,a1) cm^{-1} are corresponded to the C-H deformation modes and agree well with the literature data (Sun et al., 2007; Xue et al., 2012b). The Raman shifts and assignments of the peaks are listed in **Table 1**. Moreover, it can be certified was that the 4-MBA molecules are bonded to

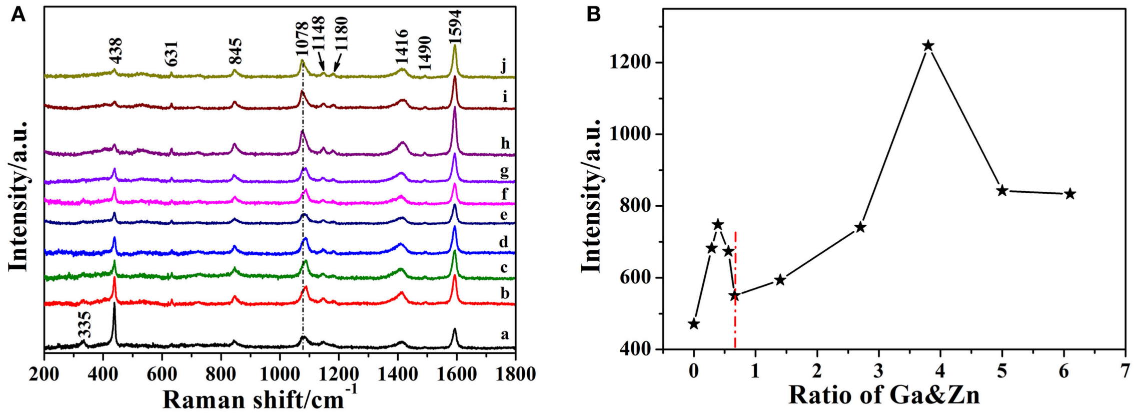

FIGURE 5 | (A) SERS spectra of 4-MBA adsorbed on Ga-doped ZnO NPs with various initial ratio of Ga and Zn(from a to j): 0, 0.3, 0.5, 0.7, 0.9, 2, 4, 6, 8, and 10%. **(B)** The relationship between the intensity of the 1,594 cm^{-1} peak and the actual ratio of Ga and Zn for Ga-doped ZnO NPs.

the surface of ZnO (Ga-doped ZnO) by sulfhydryl; comparing the Raman spectrum of bulk 4-MBA with the SERS of 4-MBA adsorbed on ZnO NPs, the peaks at 913 cm^{-1} of 4-MBA powder disappeared when the molecules are adsorbed on the surface of ZnO. The relational graph between the intensity of the 1,594 cm^{-1} peak and the actual ratio of Ga and Zn is plotted and shown in **Figure 5B**, and an interesting phenomenon is observed. With the actual ratio increasing, the intensity increases to a first maximum value when the actual ratio is 0.39%, then the intensity decreases and down to the minimum value when the actual ratio is 0.66%. Interestingly, the intensity increases again and the second maximum value appears at the actual ratio of 3.8%. The reason for this phenomenon will be discussed in the next section. Moreover, to estimate and compare the enhancement ability of Ga-doped ZnO NPs with various ratio of Ga and Zn, the magnitude of the enhancement factor (EF) is calculated (see the **Supporting Information**). The EF of pure and Ga-doped (6%, initial ratio) ZnO NPs are 3.29×10^3 and 8.13×10^3, respectively, obviously demonstrating that doping Ga into ZnO NPs can significantly improve the enhancement ability of ZnO NPs. In other words, the degree of CT between ZnO NPs and 4-MBA monolayer is improved due to the Ga doping into ZnO NPs. The Ga doping induced band gap shrinkage can enhance the CT process between ZnO NPs and 4-MBA. The EF of Ga-doped ZnO NPs with other ratio is also calculated and is shown in the **Table S1**.

TABLE 1 | Raman Shifts and Assignments of 4-MBA molecule adsorbed on ZnO (Ga-doped ZnO) NPs.

Raman (bulk)	SERS (on ZnO)	Assignment
1,596	1,594	υCC,8a(a1)
1,451	1,490	υCC+δCH
1,405	1,416	υCOO–
1,182	1,180	υCH,9(a1)
	1,148	υCH,15(b2)
1,098	1,078	υCC,12(a1)
913		δCSH,9b(b2)
813	845	δOCO

δ = *bend or deformation;* ν = *stretch.*

Enhancement Mechanism and the Effect of Doped Ga on CT of ZnO NPs

It is well-known that there are two main mechanisms widely accepted to interpret SERS: EM and CM. The former is related to the surface plasmon resonance (SPR) of the substrate, while the CT process is required for the latter. As we mentioned in the Introduction, the CT enhancement mechanism contributes to our system dominantly. In this system, the CT process occurs between ZnO NPs and the adsorbed 4-MBA molecules. All the possible CT resonance process in our ZnO-molecules system are shown in **Figure 6A**. The numerical values are referenced from literature data, such as: the highest occupied molecular orbit (HOMO) and the lowest unoccupied molecular orbit (LUMO) level of 4-MBA molecule are −8.48 and −3.85 eV (Yang et al., 2009), respectively; the CB and the VB level of ZnO NPs are −1.9 and −5.2 eV (Xue et al., 2012b), respectively. In addition, the Roman numerals in the figure represent different types of CT resonance: I is the exciton resonance of ZnO (Ga-doped ZnO) NPs; II is the molecule resonance of 4-MBA; III, IV, V, VI are the photon induced CT resonance from matches energy level between ZnO NPs and 4-MBA molecules. The excitation energy required when the process of exciton resonance (I) and molecule resonance (II) takes place is 3.3 and 4.63 eV, respectively. However, the excitation energy provided by 633 nm laser is only 1.96 eV. Therefore, the two processes of CT resonance are ruled out due to the provided energy is far less than the amount of energy needed. Likewise, the photon induced CT resonance between the HOMO level of 4-MBA molecules and the CB of ZnO NPs is impossible to happen owing to the process needs 6.58 eV. According to the literature data, the surface state level of ZnO NPs is located at −3.5 eV (Xue et al., 2012b) approximately, the energy needed for the excited transition of electrons in the VB of ZnO NPs to surface state level (V) and the LUMO orbit of 4-MBA molecules (IV) are 1.7 and 1.35 eV, respectively. The

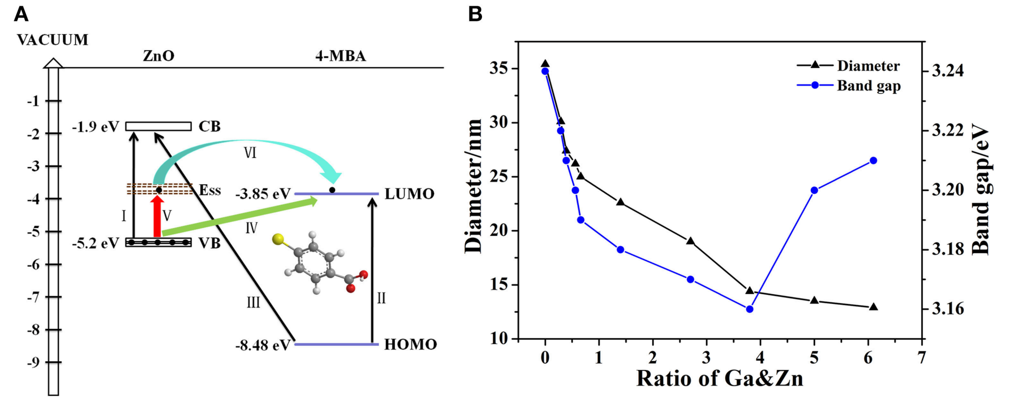

FIGURE 6 | **(A)** All the possible CT resonance process in ZnO-molecules system, **(B)** The relationship between diameter, band gap and the actual ratio of Ga and Zn for Ga-doped ZnO NPs.

laser excitation energy is enough for the two photon-induced CT resonance process. With respect to the process that the electrons in the surface state level of ZnO injected into LOMO level of molecules (VI), it is occurred by oneself due to the LUMO level of 4-MBA molecules was slightly below the surface state level of ZnO NPs.

When it comes to the effect of doped Ga on CT of ZnO NPs, there are two changes on the properties of ZnO NPs: particle size and band gap. Correspondingly, there are two main factors that can affect the enhance ability of ZnO NPs for SERS: size dependence effect and band-gap shrinkage effect. **Figure 6B** shows the relationship between diameter, band gap and the actual ratio of Ga and Zn for Ga-doped ZnO NPs. Combined with **Figures 5B**, **6B**, we think the size dependence effect is predominant when the actual ratio of Ga and Zn is below 0.66% and the strongest SERS signal is obtained when the diameter of Ga-doped ZnO NPs is 27.4 nm. The variation of the intensity of SERS signal on the particle size of ZnO derives from the resonance effect between the level of ionized receptor-exciton complex on the surface and the frequency of incident light. Moreover, the result we obtained is consistent with the conclusion that the maximum SERS signal appeared when the crystal size is 27.7 nm for pure ZnO NPs (Sun et al., 2007). When the actual doping ratio increases over 0.66%, the band-gap shrinkage effect becomes the predominant factor to affect the SERS performance (degree of CT) of ZnO NPs. The maximum shrinkage of bang gap is 0.08 eV in all the doping ratios, so the CT resonance process of I, II, III (described in **Figure 6A**) are still forbidden. However, the photon induced CT resonance (IV, V, VI) can be influenced by the decrease of band gap, thus promoting the CT process. The gap between VB and the surface state level of ZnO is decreased, and the gap between VB of ZnO and the LUMO level of molecules is also reduced. Therefore, the excited transition of electrons in the VB of ZnO to surface state level (V) or the LUMO level of molecules (IV) are much easier, hence the SERS performance (degree of CT) of ZnO is improved and a stronger SERS signal can be obtained. Besides, due to the decreases of gap between surface state level of ZnO NPs and the LUMO of 4-MBA molecules, the efficiency of electrons in the surface state level of ZnO injected into LUMO level of molecules (VI) is raised. Above all, the improvement of SERS signal (degree of CT) is because the photon induced CT resonance (IV, V, VI) is enhanced due to band-gap shrinkage effect. Moreover, the reliability of the schematic diagram of the possible CT resonance process in our ZnO-molecules system can also be testified by the SERS spectra obtained at excitations of 532 and 785 nm, the data is shown in **Figure S5**.

CONCLUSIONS

In summary, we synthesized a series of Ga-doped ZnO NPs with various ratio of Ga and Zn by a simple method and obtained the 4-MBA@ZnO system by modifying ZnO used 4-MBA molecules. The XRD and TEM measurements are carried out, the particle size diminishes gradually with the increasing ratio of Ga and Zn. When Ga is introduced into ZnO, the degree of crystallinity is decreased according to the results from XRD and Raman. Moreover, a Ga doping induced band gap shrinkage occurs: the band gap of Ga-doped ZnO narrows with the ratio of Ga and Zn increasing, and the band gap is down to the minimum value (3.16 eV) when the actual ratio of Ga and Zn is 3.8%. The last but not the least, the SERS performance (degree of CT) of Ga-doped ZnO NPs is investigated, and the doped Ga is found to enhance the intensity of SERS signal because it can cause the band gap shrinkage and then affect the CT resonance process. The band gap shrinkage can promote the photon induced CT resonance process, the electrons in the VB of ZnO NPs were excited transition to surface state level of ZnO NPs and then injected into the LUMO level of molecules, or that the electrons in the VB of ZnO NPs were directly excited transition into the LUMO level of molecules. In conclusion, this work is not only beneficial for in-depth understanding of the effect of doping on CT resonance process between adsorbed molecules and semiconductor, but also provides a new insight on improving the SERS performance of semiconductor NMs.

DATA AVAILABILITY

All datasets generated for this study are included in the manuscript and/or the supplementary files.

AUTHOR CONTRIBUTIONS

PL performed the experiments and analyzed the date with help from BZ, XY, XW, XZ, and LZ. PL wrote and revised the manuscript with input from all authors. All authors read and approved the manuscript.

FUNDING

The research was supported by the National Natural Science Foundation (Grants 21773080 and 21711540292) of P. R. China; and the Development Program of the Science and Technology of Jilin Province (20190701003GH).

SUPPLEMENTARY MATERIAL

The Supplementary Material for this article can be found online at: https://www.frontiersin.org/articles/10.3389/fchem.2019.00144/full#supplementary-material

REFERENCES

Alessandri, I., and Lombardi, J. R. (2016). Enhanced Raman scattering with dielectrics. *Chem. Rev.* 116, 14921–14981. doi: 10.1021/acs.chemrev.6b00365

Biju, V., Itoh, T., Anas, A., Sujith, A., and Ishikawa, M. (2008). Semiconductor quantum dots and metal nanoparticles: syntheses, optical properties, and biological applications. *Anal. Bioanal. Chem.* 391, 2469–2495. doi: 10.1007/s00216-008-2185-7

Bundesmann, C., Ashkenov, N., Schubert, M., Spemann, D., Butz, T., Kaidashev, E., et al. (2003). Raman scattering in ZnO thin films doped with Fe, Sb, Al, Ga, and Li. *Appl. Phys. Lett.* 83, 1974–1976. doi: 10.1063/1.1609251

Burstein, E. (1954). Anomalous optical absorption limit in InSb. *Phys. Rev.* 93:632. doi: 10.1103/PhysRev.93.632

Chen, X., German, L., Bong, J., Yu, Y., Starr, M., Qin, Y., et al. (2018). Decoupling the charge collecting and screening effects in piezotronics-regulated photoelectrochemical systems by using graphene as the charge collector. *Nano Energy* 48, 377–382. doi: 10.1016/j.nanoen.2018.03.066

Cushen, M., Kerry, J., Morris, M., Cruz-Romero, M., and Cummins, E. (2012). Nanotechnologies in the food industry–recent developments, risks and regulation. *Trends. Food Sci. Tech.* 24, 30–46. doi: 10.1016/j.tifs.2011.10.006

Dou, Y., Fishlock, T., Egdell, R., Law, D., and Beamson, G. (1997). Band-gap shrinkage in n-type-doped CdO probed by photoemission spectroscopy. *Phys. Rev. B* 55:R13381. doi: 10.1103/PhysRevB.55.R13381

Fleischmann, M., Hendra, P. J., and McQuillan, A. J. (1974). Raman spectra of pyridine adsorbed at a silver electrode. *Chem. Phys. Lett.* 26, 163–166. doi: 10.1016/0009-2614(74)85388-1

Han, X. X., Ji, W., Zhao, B., and Ozaki, Y. (2017). Semiconductor-enhanced Raman scattering: active nanomaterials and applications. *Nanoscale* 9, 4847–4861.doi: 10.1039/C6NR08693D

Hassan, J., Mahdi, M., Chin, C., Abu-Hassan, H., and Hassan, Z. (2013). A high-sensitivity room-temperature hydrogen gas sensor based on oblique and vertical ZnO nanorod arrays. *Sensor. Actua. B Chem.* 176, 360–367. doi: 10.1016/j.snb.2012.09.081

Hu, H., Song, W., Ruan, W., Wang, Y., Wang, X., Xu, W., et al. (2010). Fabrication of one-dimensional ZnO/4-Mpy/Ag assemblies and their spectroscopic studies. *J. Colloid. Interf. Sci.* 344, 251–255. doi: 10.1016/j.jcis.2009.12.061

Jeon, J.-W., Jeon, D.-W., Sahoo, T., Kim, M., Baek, J.-H., Hoffman, J. L., et al. (2011). Effect of annealing temperature on optical band-gap of amorphous indium zinc oxide film. *J. Alloy. Compd.* 509, 10062–10065. doi: 10.1016/j.jallcom.2011.08.033

Jin, Y., Cui, Q., Wen, G., Wang, Q., Hao, J., Wang, S., et al. (2009). XPS and Raman scattering studies of room temperature ferromagnetic ZnO: Cu. *J. Phys. D Appl. Phys.* 42:215007. doi: 10.1088/0022-3727/42/21/215007

Lamberti, A., Virga, A., Chiadò, A., Chiodoni, A., Bejtka, K., Rivolo, P., et al. (2015). Ultrasensitive Ag-coated TiO_2 nanotube arrays for flexible SERS-based optofluidic devices. *J. Mater. Chem. C* 3, 6868–6875. doi: 10.1039/C5TC01154J

Lang, X., Chen, X., and Zhao, J. (2014). Heterogeneous visible light photocatalysis for selective organic transformations. *Chem. Soc. Rev.* 43, 473–486. doi: 10.1039/C3CS60188A

Li, P., Wang, X., Li, H., Yang, X., Zhang, X., Zhang, L., et al. (2018). Investigation of charge-transfer between 4-mercaptobenzoic acid monolayer and TiO_2 nanoparticles under high pressure using surface-enhanced Raman scattering. *Chem. Commun.* 54, 6280–6283. doi: 10.1039/C8CC01850B

Liu, Q., Dong, G., Chen, Q., Guo, J., Xiao, Y., Delplancke-Ogletree, M.-P., et al. (2018). Charge-transfer kinetics and cyclic properties of inorganic all-solid-state electrochromic device with remarkably improved optical memory. *Sol. Energ. Mat. Sol. C* 174, 545–553. doi: 10.1016/j.solmat.2017.09.012

Lombardi, J. R., and Birke, R. L. (2007). Time-dependent picture of the charge-transfer contributions to surface enhanced Raman spectroscopy. *J. Chem. Phys.* 126:244709. doi: 10.1063/1.2748386

Lombardi, J. R., and Birke, R. L. (2009). A unified view of surface-enhanced Raman scattering. *Acc. Chem. Res.* 42, 734–742. doi: 10.1021/ar800249y

Mahdhi, H., Ayadi, Z. B., Gauffier, J., Djessas, K., and Alaya, S. (2015). Effect of sputtering power on the electrical and optical properties of Ca-doped ZnO thin films sputtered from nanopowders compacted target. *Opt. Mater.* 45, 97–103. doi: 10.1016/j.optmat.2015.03.015

Mao, Z., Song, W., Xue, X., Ji, W., Li, Z., Chen, L., et al. (2012). Interfacial charge-transfer effects in semiconductor–molecule–metal structures: influence of contact variation. *J. Phys. Chem. C* 116, 14701–14710. doi: 10.1021/jp304051r

Moss, T. (1954). The interpretation of the properties of indium antimonide. *Proc. Phys. Soc. B* 67, 775–782. doi: 10.1088/0370-1301/67/10/306

Musumeci, A., Gosztola, D., Schiller, T., Dimitrijevic, N. M., Mujica, V., Martin, D., et al. (2009). SERS of semiconducting nanoparticles (TiO_2 hybrid composites). *J. Am. Chem. Soc.* 131, 6040–6041. doi: 10.1021/ja808277u

Nohynek, G. J., and Dufour, E. K. (2012). Nano-sized cosmetic formulations or solid nanoparticles in sunscreens: a risk to human health? *Arch. Toxicol.* 86, 1063–1075. doi: 10.1007/s00204-012-0831-5

Osako, K., Matsuzaki, K., Susaki, T., Ueda, S., Yin, G., Yamaguchi, A., et al. (2018). Direct observation of interfacial charge transfer between rutile TiO_2 and ultrathin CuO_x film by visible-light illumination and its application for efficient photocatalysis. *ChemCatChem* 10, 3666–3670. doi: 10.1002/cctc.201800669

Prakash, O., Kumar, S., Singh, P., Deckert, V., Chatterjee, S., Ghosh, A., et al. (2016). Surface-enhanced Raman scattering characteristics of CuO: Mn/Ag heterojunction probed by methyl orange: effect of Mn^{2+} doping. *J. Raman Spectrosc.* 47, 813–818. doi: 10.1002/jrs.4904

Quagliano, L. G. (2004). Observation of molecules adsorbed on III-V semiconductor quantum dots by surface-enhanced Raman scattering. *J. Am. Chem. Soc.* 126, 7393–7398. doi: 10.1021/ja031640f

Sano, M., Adaniya, T., Fujitani, T., and Nakamura, J. (2002). Oxidation of a Zn-deposited Cu (1 1 1) surface studied by XPS and STM. *Surf. Sci.* 514, 261–266. doi: 10.1016/S0039-6028(02)01639-4

Shen, C. M., Hui, C., Yang, T. Z., Xiao, C. W., Tian, J. F., Bao, L. H., et al. (2008). Monodisperse noble-metal nanoparticles and their surface enhanced Raman scattering properties. *Chem. Mater.* 20, 6939–6944. doi: 10.1021/cm800882n

Shinde, S., Deshmukh, A., Date, S., Sathe, V., and Adhi, K. (2011). Effect of Ga doping on micro/structural, electrical and optical properties of pulsed laser deposited ZnO thin films. *Thin Solid Films* 520, 1212–1217. doi: 10.1016/j.tsf.2011.06.094

Singh, N., Prakash, J., Misra, M., Sharma, A., and Gupta, R. K. (2017). Dual functional Ta-doped electrospun TiO_2 nanofibers with enhanced photocatalysis and SERS detection for organic compounds. *ACS Appl. Mater. Interfaces* 9, 28495–28507. doi: 10.1021/acsami.7b07571

Sun, Z., Wang, C., Yang, J., Zhao, B., and Lombardi, J. R. (2008). Nanoparticle metal– semiconductor charge transfer in ZnO/PATP/Ag assemblies by surface-enhanced raman spectroscopy. *J. Phys. Chem. C* 112, 6093–6098. doi: 10.1021/jp711240a

Sun, Z., Zhao, B., and Lombardi, J. R. (2007). ZnO nanoparticle size-dependent excitation of surface Raman signal from adsorbed molecules: observation of a charge-transfer resonance. *Appl. Phys. Lett.* 91:221106. doi: 10.1063/1.2817529

Swamy, V., Muddle, B. C., and Dai, Q. (2006). Size-dependent modifications of the Raman spectrum of rutile TiO_2. *Appl. Phy. Lett.* 89:163118. doi: 10.1063/1.2364123

Tang, H., Meng, G., Huang, Q., Zhang, Z., Huang, Z., and Zhu, C. (2012). Arrays of cone-shaped ZnO nanorods decorated with Ag nanoparticles as 3D surface-enhanced Raman scattering substrates for rapid detection of trace polychlorinated biphenyls. *Adv. Funct. Mater.* 22, 218–224. doi: 10.1002/adfm.201102274

Tauc, J. (1968). Optical properties and electronic structure of amorphous Ge and Si. *Mater. Res. Bull.* 3, 37–46. doi: 10.1016/0025-5408(68)90023-8

Thang, H. V., Tosoni, S., and Pacchioni, G. (2018). Evidence of charge transfer to atomic and molecular adsorbates on ZnO/X (111)(X= Cu, Ag, Au) ultrathin films. Relevance for Cu/ZnO Catalysts. *ACS Catal.* 8, 4110–4119. doi: 10.1021/acscatal.7b03896

Tian, Z.-Q., Ren, B., and Wu, D.-Y. (2002). Surface-enhanced Raman scattering: from noble to transition metals and from rough surfaces to ordered nanostructures. *J. Phys. Chem. B* 106, 9463–9483. doi: 10.1021/jp0257449

Wang, X., She, G., Xu, H., Mu, L., and Shi, W. (2014). The surface-enhanced Raman scattering from ZnO nanorod arrays and its application for chemosensors. *Actuat. B Chem.* 193, 745–751. doi: 10.1016/j.snb.2013.11.097

Wang, X., Shi, W., She, G., and Mu, L. (2011). Using Si and Ge nanostructures as substrates for surface-enhanced Raman scattering based on photoinduced charge transfer mechanism. *J. Am. Chem. Soc.* 133, 16518–16523. doi: 10.1021/ja2057874

Wang, Y., Ruan, W., Zhang, J., Yang, B., Xu, W., Zhao, B., et al. (2009). Direct observation of surface-enhanced Raman scattering in ZnO nanocrystals. *J. Raman Spectrosc.* 40, 1072–1077. doi: 10.1002/jrs.2241

Wang, Y., Sun, Z., Hu, H., Jing, S., Zhao, B., Xu, W., et al. (2007a). Raman scattering study of molecules adsorbed on ZnS nanocrystals. *J. Raman Spectrosc.* 38, 34–38. doi: 10.1002/jrs.1570

Wang, Y., Sun, Z., Wang, Y., Hu, H., Zhao, B., Xu, W., et al. (2007b). Surface-enhanced Raman scattering on mercaptopyridine-capped CdS microclusters. *Spectrochim. Acta A* 66, 1199–1203. doi: 10.1016/j.saa.2006.06.008

Xue, X., Ji, W., Mao, Z., Li, Z., Ruan, W., Zhao, B., et al. (2012a). Effects of Mn doping on surface enhanced Raman scattering properties of TiO_2 nanoparticles. *Spectrochim. Acta A* 95, 213–217. doi: 10.1016/j.saa.2012.04.101

Xue, X., Ji, W., Mao, Z., Zhao, C., Zhao, B., and Lombardi, J. R. (2013b). Simultaneous enhancement of phonons modes with molecular vibrations due to Mg doping of a TiO_2 substrate. *RSC Adv.* 3, 20891–20895. doi: 10.1039/c3ra43780a

Xue, X., Ruan, W., Yang, L., Ji, W., Xie, Y., Chen, L., et al. (2012b). Surface-enhanced Raman scattering of molecules adsorbed on Co-doped ZnO nanoparticles. *J. Raman Spectrosc.* 43, 61–64. doi: 10.1002/jrs.2988

Xue, X. X., Ji, W., Mao, Z., Li, Z. S., Guo, Z. N., Zhao, B., et al. (2013a). SERS study of Co-doped TiO_2 nanoparticles. *Chem. Res. Chin. Univ.* 29, 751–754. doi: 10.1007/s40242-013-3051-5

Yadav, P., Alotaibi, M. H., Arora, N., Dar, M. I., Zakeeruddin, S. M., and Grätzel, M. (2018). Influence of the nature of a cation on dynamics of charge transfer processes in perovskite solar cells. *Adv. Funct. Mater.* 28:1706073. doi: 10.1002/adfm.201706073

Yamada, H., and Yamamoto, Y. (1983). Surface enhanced Raman scattering (SERS) of chemisorbed species on various kinds of metals and semiconductors. *Surf. Sci.* 134, 71–90. doi: 10.1016/0039-6028(83)90312-6

Yamada, H., Yamamoto, Y., and Tani, N. (1982). Surface-enhanced raman scattering (SERS) of adsorbed molecules on smooth surfaces of metals and a metal oxide. *Chem. Phys. Lett.* 86, 397–400. doi: 10.1016/0009-2614(82)83531-8

Yang, L., Jiang, X., Ruan, W., Zhao, B., Xu, W., and Lombardi, J. R. (2009). Adsorption study of 4-MBA on TiO_2 nanoparticles by surface-enhanced Raman spectroscopy. *J. Raman Spectrosc.* 40, 2004–2008. doi: 10.1002/jrs.2358

Yang, L., Jiang, X., and Yang, M. (2011). Improvement of surface-enhanced Raman scattering performance for broad band gap semiconductor nanomaterial (TiO_2): strategy of metal doping. *Appl. Phys. Lett.* 99:111114. doi: 10.1063/1.3638467

Yang, L., Qin, X., Gong, M., Jiang, X., Yang, M., Li, X., et al. (2014). Improving surface-enhanced Raman scattering properties of TiO_2 nanoparticles by metal Co doping. *Spectrochim. Acta A* 123, 224–229. doi: 10.1016/j.saa.2013.12.087

Yang, L., Ruan, W., Jiang, X., Zhao, B., Xu, W., and Lombardi, J. R. (2008). Contribution of ZnO to charge-transfer induced surface-enhanced Raman scattering in Au/ZnO/PATP assembly. *J. Phys. Chem. C* 113, 117–120. doi: 10.1021/jp8074095

Yang, L., Zhang, Y., Ruan, W., Zhao, B., Xu, W., and Lombardi, J. R. (2010). Improved surface-enhanced Raman scattering properties of TiO_2 nanoparticles by Zn dopant. *J. Raman Spectrosc.* 41, 721–726. doi: 10.1002/jrs.2511

You, Z., and Hua, G. (2012). Electrical, optical and microstructural properties of transparent conducting GZO thin films deposited by magnetron sputtering. *J. Alloy. Compd.* 530, 11–17. doi: 10.1016/j.jallcom.2012.03.078

Yu, Z., Yu, W., Xing, J., Ganeev, R. A., Xin, W., Cheng, J., et al. (2018). Charge transfer effects on resonance-enhanced raman scattering for molecules adsorbed on single-crystalline perovskite. *ACS Photonics* 5, 1619–1627. doi: 10.1021/acsphotonics.8b00152

Zhang, Q., Dandeneau, C. S., Zhou, X., and Cao, G. (2009). ZnO nanostructures for dye-sensitized solar cells. *Adv. Mater.* 21, 4087–4108. doi: 10.1002/adma.200803827

Conflict of Interest Statement: The authors declare that the research was conducted in the absence of any commercial or financial relationships that could be construed as a potential conflict of interest.

frontiers in Chemistry

ORIGINAL RESEARCH
published: 17 April 2019
doi: 10.3389/fchem.2019.00245

Direct Observation of Enhanced Raman Scattering on Nano-Sized ZrO_2 Substrate: Charge-Transfer Contribution

Peng Ji[1,2], Zhe Wang[2], Xiaohong Shang[1], Yu Zhang[2], Yikuan Liu[2], Zhu Mao[1] and Xiumin Shi[2]*

[1] School of Chemistry and Life Science, Changchun University of Technology, Changchun, China, [2] College of Chemical Engineering, Changchun University of Technology, Changchun, China

Direct observation of the surface-enhanced Raman scattering (SERS) of molecules adsorbed on nano-sized zirconia (ZrO_2) substrates was first reported without the need for the addition of metal particles. It was found that ZrO_2 nanoparticles can exhibit unprecedented Raman signal enhancements on the order of 10^3 for the probe molecule 4-mercaptobenzoic acid (4-MBA). The dramatic effect of the calcination temperature on the ZrO_2 nanoparticles was also investigated. The ZrO_2 nanoparticles with the particle diameter of 10.5 nm, which were prepared by calcination at a temperature of 500°C, have the highest SERS activity. A comparison between the experimental and calculation results indicates that charge transfer (CT) effects dominate the surface enhancement. The plentiful surface state of ZrO_2 active substrate that is beneficial to CT resonance occurs between molecules and ZrO_2 to produce a SERS effect. The CT process depends, to a large extent, on the intrinsic properties of the modifying molecules and the surface properties of the ZrO_2. This is a new SERS phenomenon for ZrO_2 that will expand the application of ZrO_2 to microanalysis and is beneficial for studying the basic properties of both ZrO_2 and SERS.

Keywords: raman, SERS, ZrO_2, charge-transfer, nanoparticle

OPEN ACCESS

Edited by:
John Lombardi,
City College of New York (CUNY),
United States

Reviewed by:
Hui Xu,
Ludong University, China
Lingxin Chen,
Yantai Institute of Coastal Zone
Research (CAS), China

Correspondence:
Xiumin Shi
shixiumin@ccut.edu.cn

Specialty section:
This article was submitted to
Analytical Chemistry,
a section of the journal
Frontiers in Chemistry

Received: *22 January 2019*
Accepted: *27 March 2019*
Published: *17 April 2019*

Citation:
Ji P, Wang Z, Shang X, Zhang Y, Liu Y, Mao Z and Shi X (2019) Direct Observation of Enhanced Raman Scattering on Nano-Sized ZrO_2 Substrate: Charge-Transfer Contribution. Front. Chem. 7:245. doi: 10.3389/fchem.2019.00245

INTRODUCTION

The large surface-enhanced Raman scattering (SERS) enhancement observed in metals and semiconductors is explained by the vibrational coupling of various resonances in the molecules of the semiconductor system, such as surface plasmons, excitons, charge transfer (CT), and molecular resonance (Yin et al., 2010; Li et al., 2011; Wang and Chen, 2011; Jiang et al., 2013; Wang et al., 2013, 2014, 2016; Huang et al., 2014; Kadkhodazadeh et al., 2014; Mogensen and Kneipp, 2014; Shiohara et al., 2014; Zhao et al., 2014; Shen et al., 2015; Scott and Carron, 2016; Fu et al., 2019). Because semiconductor materials are widely used in the rapidly developing energy and optoelectronic fields, it is important to investigate the SERS mechanism for semiconductor substrates (Lombardi and Birke, 2014; Alessandri and Lombardi, 2016; Han et al., 2017). Semiconductors that can be used as SERS substrates have been identified, such as TiO_2, ZnO, and CdS. These can amplify the Raman signals of surface-adsorbed organic molecules such as 4-mercaptopyridine (4-MPY) and 4-mercaptobenzoic acid (4-MBA) by more than 100-fold (Sun et al., 2007; Wang et al., 2007; Yang et al., 2008).

Nano-sized zirconium dioxide (ZrO_2) is one of the most important materials for the preparation of nano-ceramics, and it can prepare ceramic components with various functions (Li et al., 2017). It has applications and developments in solid oxide fuel cells, thermal barrier coating materials, catalyst carriers, lubricant additives, medical, gas sensitive, and wear resistant materials (Duan et al., 2017; Gan et al., 2017; Long et al., 2017; Xu et al., 2017; Wang et al., 2019). The brittleness of ceramic materials limits its practical application, and nanoceramics are a strategic way to solve the brittleness of ceramics. However, grain size is the most important factor affecting the performance of nano-ceramics. The decrease of grain size will significantly improve the mechanical properties of materials (Zhang L. et al., 2015). The grain refinement will contribute to the slip between the grains, giving the material plastic behavior. A large number of studies by researchers have shown that the temperature is closely related to the size of ZrO_2 particles, and the transition temperature of ZrO_2 particles below 100 nm can be greatly reduced (Becker et al., 2008). Toughening of ceramics by microcracks and residual stresses generated the conversion of ZrO_2 from a tetragonal phase (t-ZrO_2) to a monoclinic phase (m-ZrO_2). Therefore, the nano-sized ZrO_2 can significantly increase the strength and stress intensity factor of the ceramic, thereby increasing the toughness of the ceramic (De Aza et al., 2002). Nowadays, the application research on nano-sized ZrO_2 has become one of the research hotspots of nano-ceramic new technology. As a new type of high-performance ceramics, the use of highly sensitive SERS technology with *in-situ* characterization advantages to study the size effect of nano-sized ZrO_2 is expected to promote the better performance of nano-ceramic materials to enable the emergence of new properties and functions.

In addition, ZrO_2 is a particularly attractive candidate to promote CT enhancement because it has recently been shown that the luminescence effect of ZrO_2 materials is derived from transitions between new and ground state energy levels formed by oxygen vacancies that capture electrons and oxygen vacancies produced by the formed association center (Kralik et al., 1998; Chang and Doong, 2007). Owing to the photoelectric properties of ZrO_2, a CT state is readily formed. Currently, there are no reports on the use of ZrO_2 enhancement to obtain SERS (**Figure 1**).

MATERIALS AND METHODS

Chemicals

Zirconium nitrate pentahydrate was obtained from Tianjin Guangfu Fine Chemical Research Institute; triethylamine was obtained from XiLong Chemical Co., Ltd.; CTAB were obtained from China Huishi Biochemical Reagent Co., Ltd. 4-Mercaptobenzoic acid (4-MBA), 4-Mercaptopyridine (4-Mpy), and P-aminothiophenol (PATP) were purchased from Sigma-Aldrich. The other chemicals are analytically pure without further purification.

Synthesis of ZrO_2 Nanoparticles

The synthesis of ZrO_2 was followed the procedure below (Zhou et al., 2006). First, at room temperature and in a 500 mL round-bottomed flask, mix and dissolve 17.44 g Zirconium Nitrate and 2.95 g Hexadecyl trimethyl ammonium Bromide in 180 mL deionized water. The hydrolysis was carried out with slight stirring. Stirring was continued for about 20 min until a clear sol was obtained. 22.615 mL Triethylamine was added in the solution under rough stirring. The mixture was kept at 75°C for 8 h in the round-bottomed flask. The sol-gel production was dried at 82°C for 48 h. This was the last step after drying the product, eluted with ethanol for 48 h in a Soxhlet extraction. The product was calcined in a muffle furnace for 2 h to obtain ZrO_2 nanoparticles at different temperatures (450–650°C).

Adsorption of Probing Molecules

The surface modification of ZrO_2 nanocrystals is obtained as follows: 10 mL 4-MBA ethanol solution concentration 1×10^{-3} M was used to dissolve 20 mg of ZrO_2 nanocrystals. The mixture was stirred at room temperature for 4 h and then centrifuged. The 4-MBA molecules that did not adsorb were subsequently removed by rinsing the precipitate with absolute deionized water and ethanol once more. ZrO_2 Nanoparticles that modify by 4-MBA and PATP are similar to 4-MBA.

Sample Characterization

The crystal structure of the ZrO_2 sample was determined by X-ray diffraction using a Rikagu Smartlab X-ray powder diffractometer with 0.15406 nm. The electronic absorption spectra were recorded on a Cary5000 UV-vis spectrophotometer. Raman spectra were obtained with Horiba HR Evolution Raman spectroscopy. The 532 nm radiation from an air-cooled argon ion laser was used as the exciting source. The morphology of ZrO_2 nanoparticles was characterized by the JEM-2000EX TEM instrument. A Thermofisher Escalab 250XI X-ray photoelectron spectroscopy (XPS) was applied to investigate the elemental composition and the surface electronic valence state for UPS.

RESULTS AND DISCUSSION

ZrO_2 Phonon Modes (XRD & Raman)

Zirconia has three low-pressure structural phases. With increasing temperatures, zirconia changes from a monoclinic phase (m-ZrO_2) to a tetragonal phase (t-ZrO_2), eventually becoming a cubic phase (Zheng et al., 2009). The monoclinic phase (space group C5 2 h or P21/c) is thermodynamically stable at temperatures of <1400 K. At around 1400 K, the t-ZrO_2 transition (space group D15 4 h or P42/nmc) is stable until 2570 K, and is a slightly distorted form of the cubic structure (Heuer et al., 1982). In this study, the size of the ZrO_2 nanoparticles was controlled by adjusting the calcination temperature to change the surface defect state of the nanoparticles to obtain a stronger SERS signal of the surface substance. This is verified by UV-vis spectra of ZrO_2 nanoparticles with different calcination temperature, see **Figure S1**.

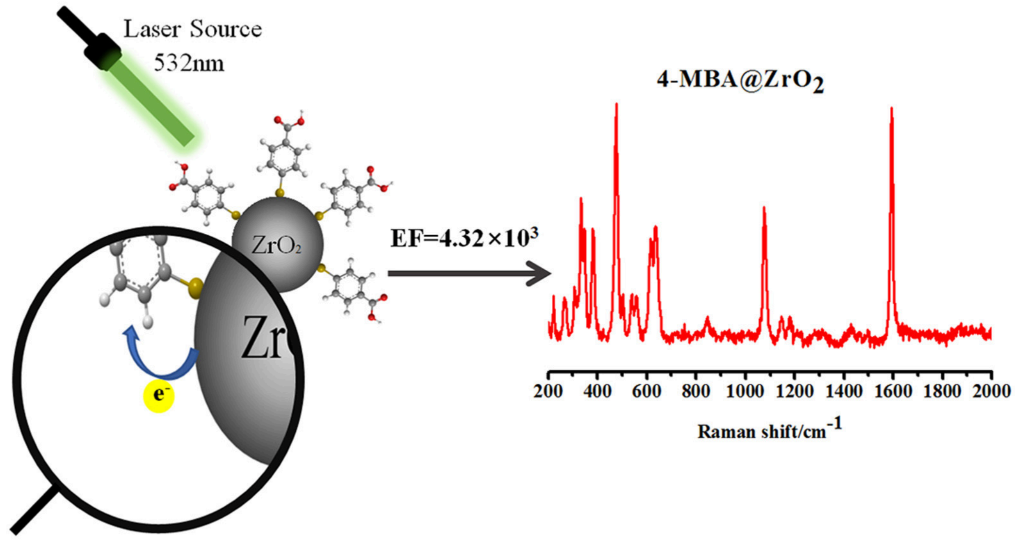

FIGURE 1 | Schematic representation of ZrO_2 nanoparticles with the organic molecule 4-MBA.

Increase in Nanoparticle Size With Increasing Calcination Temperature

Figure 2A shows the XRD patterns of ZrO_2 nanoparticles calcined at different temperatures. The m-ZrO_2 is the dominant phase in these ZrO_2 nanoparticles. Almost all of the diffraction peaks are comparable to the standard data and are remarkably sharp, indicating the purity and high crystallinity of the synthesized ZrO_2 material. It can be observed that as the calcination temperature increases from 450 to 650°C, the XRD pattern becomes narrower and the sample crystallinity increases. The diameters of the ZrO_2 nanoparticles calcined at 450, 500, 550, 600, and 650°C were calculated from the full width at half-maximum using the Scherrer equation. The calculated diameters of the zirconia nanoparticles were 8.1, 10.5, 11.1, 15.5, and 17.6 nm, respectively. Thus, it can be seen that the grain size increases with increasing calcination temperature. The wide XRD peak is attributed to a very small particle size, which is also demonstrated by the transmission electron microscopy (TEM) results (**Figure S2**). As the calcination temperature increases from 450 to 650°C, both of the crystallinity and grain size of the ZrO_2 sample gradually increases. As shown in **Figure S3**, the XRD patterns show that the ZrO_2 nanoparticles calcined at 500°C primarily exhibit m-ZrO_2 (PDF card: 13-307), and there is extremely little t-ZrO_2 present (PDF card: 88-1007).

Nanoparticles Primarily Exist in the m-Phase

ZrO_2 samples were prepared through the sol-gel method and characterized using Raman spectroscopy (**Figure 2B**). The Raman shift characteristics reflect the energy level change in the specific vibration of the molecules. Tetragonal zirconia has six active vibrational modes (see Equation 1): B1g, Eg, B1g, Eg, A1g, and Eg (Zhao and Vanderbilt, 2002). Monoclinic zirconia has 18 Raman-active vibrational modes (see Equation 2).

$$\Gamma_{vib}{}^{t} = A1g + 2B1g + 3Eg \quad (1)$$

$$\Gamma_{vib}{}^{m} = 9Ag + 9Bg \quad (2)$$

From the Raman spectra and scattering data (see **Figure 2B**), it can be seen that the composition of the synthesized ZrO_2 is a mixture of t-ZrO_2 and m-ZrO_2, with a greater proportion of monoclinic phase. Comparing the Raman spectra, it is observed that the prepared ZrO_2 nanoparticles had an Eg vibrational mode at 265 cm^{-1} corresponding to the tetragonal phase. The remaining peaks occurred at 221 cm^{-1} (Bg), 309 cm^{-1} (Bg), 332 cm^{-1} (Bg), 345 cm^{-1} (Ag), 380 cm^{-1} (Ag), 476 cm^{-1} (Ag), 503 cm^{-1} (Bg), 539 cm^{-1} (Bg), 558 cm^{-1} (Ag), 613 cm^{-1} (Bg), and 635 cm^{-1} (Ag) are the vibration modes of m-ZrO_2 (Carlone, 1992). **Figure 2B** shows that the 11 active vibrational modes correspond well with the monoclinic phase. This indicates that m-ZrO_2 is dominant and the crystallization is relatively good. This point is consistent with the results observed using XRD; however, compared to the XRD patterns, the Raman spectra can reflect the difference in the crystallinity of ZrO_2 caused by different calcination temperatures with greater sensitivity.

Size-Dependent of SERS

ZrO_2 is an n-type semiconductor, and thus the surface of ZrO_2 nanoparticles are rich in oxygen vacancy defects (Navio et al., 2001). To study the effect of the calcination temperature of ZrO_2 on the SERS enhancement, SERS spectra of 4-MBA adsorbed on ZrO_2 nanoparticles calcined at different temperatures were obtained, as shown in **Figure 3**. The Raman spectra obtained for ZrO_2 nanoparticles at varying calcination temperatures can be used to explore the role of surface defects on the CT mechanism. For calcination temperatures in excess of 500°C, as the zirconia

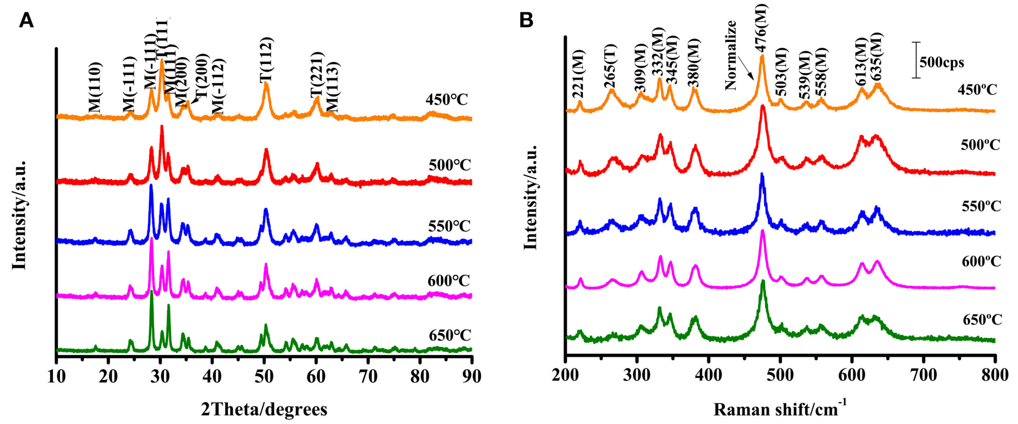

FIGURE 2 | (A) XRD patterns of ZrO_2 nanoparticles with different calcination temperature; **(B)** Raman spectra of ZrO_2 with different calcination temperature with excitation 532 nm.

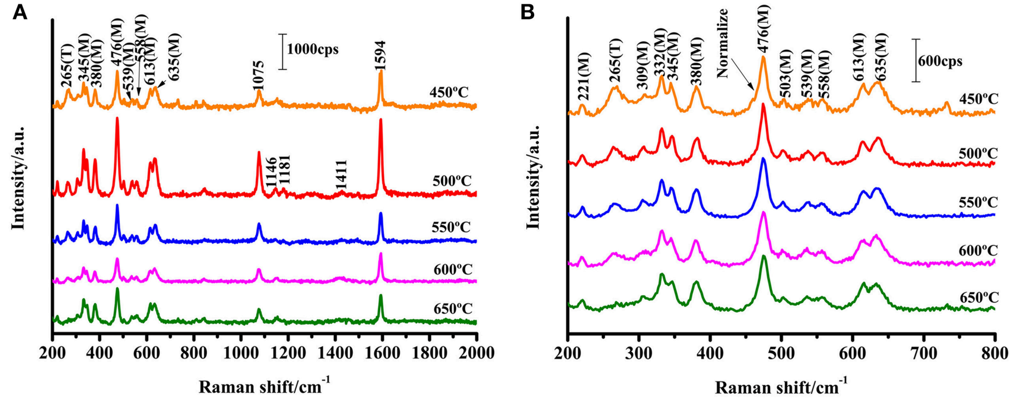

FIGURE 3 | SERS spectra of 4-MBA adsorbed on ZrO_2 nanoparticles with different calcination temperature with 532 nm excitation. **(B)** Is a magnification of **(A)** in the range of 200-800 cm^{-1}.

calcination temperature increases, the crystallinity also increases, resulting in a decrease in the surface defect content of the ZrO_2 nanoparticles (**Figure 2A**). This is also the reason for the decrease in CT effects of the ZrO_2 molecules. Therefore, it can be seen from **Figure 3** that at temperatures above 500°C, the SERS signal of zirconia decreases with increasing temperatures. This indicates that in the process of ZrO_2 molecular CT, the surface defects play an important role and a rich surface state favors the ZrO_2-to-molecule CT process.

The structural characteristics of the ZrO_2 nanostructures are analyzed by TEM techniques, as shown in **Figure S2**. Based on the results, the crystalline sizes of all of the nanoparticles are ≈10 nm in diameter, which is similar to the results obtained from the XRD patterns through calculation with the Scherrer equation. The results indicate that the size of the ZrO_2 nanoparticles increases with increasing calcination temperature. This indicates that the calcination temperature has a significant effect on the size of the nanoparticles. The optical properties of the ZrO_2 nanoparticles were further analyzed by means of UV-Vis spectra.

Calculation of the Surface Enhancement Factor (EF)

The surface enhancement factor (EF) was calculated for the 4-MBA adsorbed on ZrO_2 nanoparticles at an excitation of 532 nm. The assignment of each of the strong peaks in the Raman spectrum is listed in **Table S1**. The ν (C-C) ring breathing mode (∼1,594 cm^{-1}) was selected to calculate the EF of ZrO_2 nanoparticles. The EF calculation formula is shown in Equation (3):

$$\mathrm{EF} = \frac{I_{surf} N_{Bulk}}{I_{Bulk} N_{Surf}} \tag{3}$$

where I represents the corresponding intensity of the selected peak, and N represents the number of molecules observed by the laser spot; N_{Bulk} is the number of bulk 4-MBA molecules under laser irradiation, N_{Surf} is the number of 4-MBA molecules involved in the surface modification of ZrO_2, I_{Surf} is the intensity of a vibrational mode in the SERS, and I_{Bulk} is the intensity in the conventional Raman spectra of the same mode. From the area of the laser spot (∼1.3 μm^2) and the focus penetration depth of the laser (∼10 μm), the volume of the solid sample can be calculated. Based on the density (1.5 $g \cdot cm^{-3}$) and volume of 4-MBA, N_{Bulk} was calculated to be 7.61×10^{10}. Assuming that a single layer of ZrO_2 nanoparticles are uniformly covered with a square centimeter of sediment, the number density is estimated to be 9.07×10^{11} particles/cm^2 based on the XRD (according to the XRD results, the average diameter of the zirconia nanoparticles was 10.5 nm), as shown in **Figure 2A**. Using the laser spot size and the boundary density of the adsorbing molecules on the surface of the nanoparticles (∼0.5 nmol/cm^2), N_{Surf} can be calculated as 6.15×10^6. From the observed spectra, the ratio of intensities $I_{Surf}/I_{Bulk} = 1765.42/5051.69 = 0.349$ can be obtained. Substituting the obtained values for these variables into Equation 3, the EF value is calculated as 4.32×10^3.

An enhancement (by a factor ∼3) of the Bg and Ag ZrO_2 phonon modes at 330 and 475 cm^{-1}, respectively, was also observed. This enhancement is similar to the enhancement mechanism for the normal mode of the molecule. The results show that an EF of more than 10^3 is achieved for 4-MBA on ZrO_2 nanoparticles. It has not previously been reported that SERS signals are observed on the surface of ZrO_2, but the results are similar to the EF for other semiconductor nanoparticles that have been reported previously.

CT Mechanism

a1 and b2 Modes of 4-MBA

The SERS signal of a near-monolayer of 4-MBA adsorbed on the surface of ZrO_2 nanoparticles was observed (the excess of 4-MBA on the surface was washed away with a solvent). **Figure 4** shows the Raman spectra for the bulk 4-MBA and a solution dissolved in ethanol (0.1 mol/L), as well as the enhanced Raman spectrum of 4-MBA on a ZrO_2 substrate. The only difference between the conventional Raman spectroscopy and SERS samples is the amount of 4-MBA molecules: in the former, a large number of pure 4-MBA molecules are present, while the latter utilizes a monolayer of 4-MBA molecules present only on the ZrO_2 substrate. All of the other test conditions and procedures are the same. A distinct 4-MBA signal was observed on the ZrO_2 substrate with clear Raman peaks at 1075, 1146, 1181, and 1594 cm^{-1}. However, because SERS modifies the surface selection rules, there is a significant difference in the relative intensities of the peaks observed for the 4-MBA molecule in the Raman and SERS spectra. The bulk 4-MBA spectrum is mainly dominated by the fully symmetric a1 vibration mode, while the SERS spectrum for 4-MBA exhibits a strong contribution of the asymmetric b2 mode (1146 cm^{-1}).

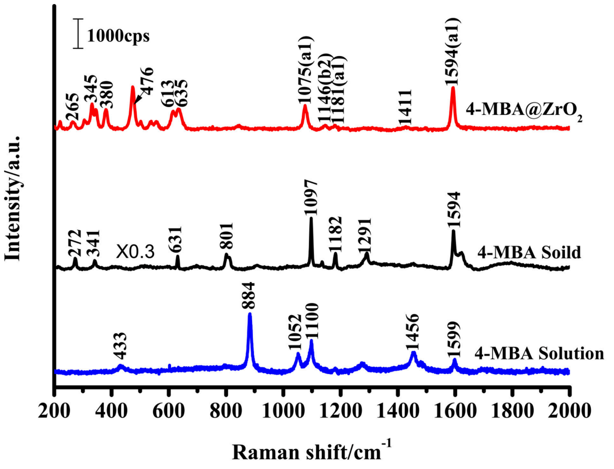

FIGURE 4 | Raman spectra of 4-MBA adsorbed on ZrO_2 nanoparticles, 4-MBA solid, and 4-MBA solution (0.1 mol/L in ethanol) with 532 nm excitations.

The Raman peak at 1075 cm^{-1} is attributed to aromatic ring vibration with a C-S stretching mode (ν12a, a1), while at approximately 1,594 cm^{-1} the Raman peak is assigned to the aromatic ring breathing mode (ν8a, b2). As shown in **Figure 4**, the Raman spectrum for 4-MBA adsorbed on the surface of zirconia nanoparticles was strongly enhanced compared to the conventional Raman spectrum for 4-MBA, and the Raman shift was significantly different from that of the bulk Raman spectrum. The spectrum of the 4-MBA adsorbed on the surface of zirconia nanoparticles exhibits a weak peak at 1146 cm^{-1} (ν15, b2) in the SERS spectrum (attributed to the C-H deformation vibrational mode), which is generally considered to be due to the Herzberg-Teller contribution that produces enhanced CT effects. The SERS spectrum of 4-MBA on the surface of ZrO_2 is almost identical to that observed on the surface of ZrO_2 and TiO_2 in the literature. We also calculated the value of P_{CT}, which was calculated through the expression which was defined as "$P_{CT} = R/(1 + R)$" for the degree of charge transfer($R = I_{b2}/I_{a1}$). As shown in **Figure S4**, the P_{CT} of 4-MBA is near 0.5 at the excitation wavelengths of 532, 633, and 785 nm. It was observed that the degree of charge transfer increases with the increase of laser energy.

Direction of CT Effects

There are two main ways to explain the enhancement mechanism of the SERS effect: chemical mechanisms (CT) and electromagnetic mechanisms (EM). Chemical enhancement (CE) is a resonance-like Raman process. It is generated by chemical adsorption interactions between the substrate and the adsorbed molecules and photoinduced charge transfer, resulting in an increase in the polarizability and an increase in the distribution number of the adsorbed molecules in the excited state. The electromagnetic mechanisms (EM) is caused by an increase in the local electric field induced by the laser on the surface of the nanoparticles (Kadkhodazadeh et al., 2014; Mogensen and Kneipp, 2014). According to the literature, for most semiconductor materials, the surface plasmon resonance frequency is in the infrared region, away from the excitation wavelength (532 nm) used to obtain the SERS phenomenon in this study (Wang et al., 2009; Xue et al., 2012). Therefore, the SERS enhancement of ZrO_2 in this work does not include EM contributions, but mainly contributes to CE contributions. In **Figure 4**, the SERS spectrum of 4-MBA exhibit a non-totally symmetric b2 mode at 1146 cm^{-1}. As the CT mechanism is a resonance Raman-like process, the charge transfers occurred between the ZrO_2 nanocrystals and 4-MBA molecules. When the organic molecules and semiconductor are in contact with each other, a reasonable charge distribution will exist around the interface within a very short time. A new electronic state then forms at the interface.

To determine the direction of charge transfer in the 4-MBA–ZrO_2 complex, Gaussian 09 was used to calculate the highest occupied molecular orbital (HOMO) and lowest unoccupied molecular orbital (LUMO) of 4-MBA molecules adsorbed on ZrO_2 nanoparticles, as shown in **Figure 5A**. In the 4-MBA-modified ZrO_2 system, the HOMO and LUMO for the 4-MBA occur at −6.75 and −1.33 eV, respectively. Thus, the CT between ZrO_2 and the adsorbed 4-MBA molecule may occur as shown in **Figure 5B**. In these experiments, when irradiated under a 532 nm (ca. 2.33 eV) laser, the excited electrons of the ZrO_2 conduction band (CB) migrate to the LUMO of the adsorbed molecules. This is a reasonable CT model to explain the SERS of ZrO_2 modified by 4-MBA.

Zhao et al. reported the use of UV-Vis diffuse reflectance spectroscopy (DRS; **Figure S5**) (Zhang X. et al., 2015) and ultraviolet photoelectron spectroscopy (UPS; **Figure S6**) to calculate the HOMO and LUMO of the substrate and probe molecules. This can be calculated with Equation 4:

$$W = h\nu - \Delta E \tag{4}$$

The value of $h\nu$ is 21.22 eV, and thus the valence band (VB) of ZrO_2 is calculated to occur at −5.19 eV. The band gap of ZrO_2 is 4.95 eV, and the CB of ZrO_2 is situated at −1.97 eV. As shown in **Figure 5B**, in the ZrO_2 system modified by 4-MBA, the HOMO of the 4-MBA is at −6.24 eV and the LUMO is at −1.68 eV. Therefore, considering the relative band structure of the ZrO_2 system with 4-MBA, the CT direction between the ZrO_2 and 4-MBA determined by the theoretical calculations and UPS results is consistent, i.e., the CT occurs from the zirconium dioxide to the 4-MBA molecules.

SERS Spectra of the ZrO_2 Surface Modified by 4-MBA, 4-MPY, and PATP

To illuminate that the enhancement mechanism of a ZrO_2 surface modified by 4-MBA is the CT mechanism, the following experiment was performed. The surface of ZrO_2 nanoparticles were modified with different thiophenol-related molecules (4-MPY and PATP), as shown in **Figure 6A**. In addition, these thiophenol-based molecules possess functional groups on the benzene ring, such as C-COOH, N, or C-NH_2. The electron attracting ability of these functional groups on the benzene ring occurs in the order of C-COOH (4-MBA) > N (4-MPY) > C-NH_2 (PATP). **Figure 6A** shows the SERS spectra for 4-MBA, 4-MPY, and PATP adsorbed on ZrO_2 nanoparticles. The results clearly show that the intensities decrease in the order of 4-MBA > 4-MPY > PATP. This is in agreement with the previous estimations.

As the probe molecules have almost the same Raman cross-sections, the experimental results described above are not due

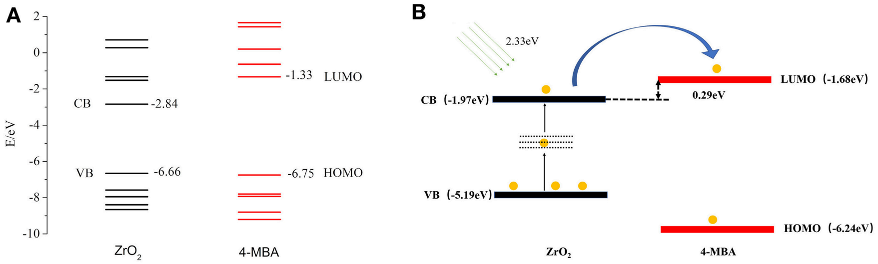

FIGURE 5 | (A) The molecular orbital illustrations of the 4-MBA molecule and ZrO_2 nanoparticles from calculations by Gaussian 09. **(B)** The schematic energy-level diagram at a ZrO_2/4-MBA molecule interfaces, and also the position of the HOMO and the LUMO of 4-MBA and the position of CB and VB of ZrO_2 nanoparticles.

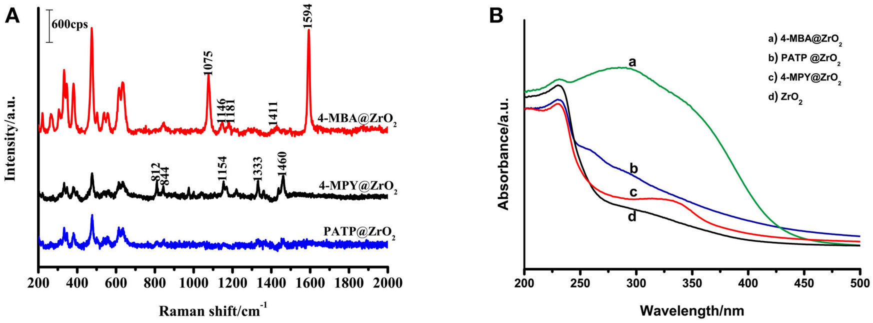

FIGURE 6 | (A) SERS spectra of 4-MBA, PATP, 4-MPY adsorbed on ZrO_2 nanoparticles; **(B)** UV-vis spectra of ZrO_2 nanoparticles and 4-MBA, PATP, 4-MPY adsorbed on ZrO_2 nanoparticles.

to different Raman cross-sections of the molecules. The SERS spectra effect is consistent with the ability of the mercapto-pair to attract electrons. These results indicate a correlation between the SERS signal and the ZrO_2-to-molecula CT. This suggests that for ZrO_2 nanoparticles surface-modified by other molecules, the primary enhancement mechanism is the CT mechanism. The stronger the electron-withdrawing groups in the molecules bonded on the surface of ZrO_2, the greater the ability of ZrO_2 for molecular CT will be, and a stronger SERS signal on the ZrO_2 will be observed.

Comparisons of the optical properties of ZrO_2 nanoparticles modified by molecules with those of pure ZrO_2 were carried out by using UV-Vis spectroscopy (**Figure 6B**). It is clear that the adsorption of organic molecules has a significant influence on the absorption spectrum of ZrO_2. It was observed that the typical ZrO_2 direct band gap adsorbs organic molecules with different degrees of narrowing and widening.

Figure S5 shows the spectra of ZrO_2 nanoparticles surface-modified by 4-MBA, 4-MPY, and PATP, as well as pure ZrO_2 nanoparticles monitored with room temperature UV-vis DRS. Using the Kubelka–Munk function, the bandgap energy of the pure ZrO_2 and molecule-modified ZrO_2 were calculated based on the photon energy $[(\alpha E)^2]$ function. The resulting band energy is 4.95 eV (250 nm) for the pure ZrO_2 nanoparticles, 3.22 eV (385 nm) for the 4-MBA-modified ZrO_2, 4.88 eV (254 nm) for the 4-MPY-modified ZrO_2, and 4.91 eV (253 nm) for the PATP-modified ZrO_2. The interaction between the adsorbed molecules and the ZrO_2 nanoparticle substrate resulted in these shifts. The transformation may be due to the interaction of the nanoparticles with probe molecules. The observed shift shows that the bandgap of the 4-MBA–ZrO_2 system has a lower optical transition energy than that of pure ZrO_2 due to the CT transition. The 4-MBA–ZrO_2 system has the lowest optical transition energy, which explains why the ZrO_2 modified by 4-MBA has the strongest SERS effect.

CONCLUSION

This study first observed that the SERS spectrum can be obtained on the surface of ZrO_2. The results show that the SERS spectrum of 4-MBA on ZrO_2 is mainly due to the contribution of the CT mechanism, and the intrinsic properties of the adsorbed molecules and the surface properties of the semiconductor have a significant effect on SERS. The plentiful surface state of the ZrO_2 active substrate is beneficial for the occurrence of CT resonance between molecules and the ZrO_2 to produce a SERS effect. The results show that the ZrO_2 nanoparticles prepared through the sol-gel method at a calcination temperature of 500°C exhibit the strongest SERS effect on the surface-adsorbed probe molecules. This study demonstrates for the first time that ZrO_2 can be used as a Raman enhancement substrate material, breaking through the limitations of the precious metal substrates used in traditional SERS technology, and further broadening the application of semiconductor oxides as substrate materials for SERS detection. Also, the SERS study on the size effect of nano-sized ZrO_2 is expected to promote the better performance of nano-ceramic materials to enable the emergence of new properties and functions.

AUTHOR CONTRIBUTIONS

XiuS designed the experiment. PJ conducted experiments and characterization. ZW funded some of the subject experiments. XiaS assisted in the theoretical simulation. YZ and YL participated in the discussion. PJ, XiuS, and ZM wrote the manuscript together.

FUNDING

This work is supported by the Jilin Province Science and Technology Research Project (No. 20150204024GX) and the National Natural Foundation of China (No.21503021 and No.51673030).

SUPPLEMENTARY MATERIAL

The Supplementary Material for this article can be found online at: https://www.frontiersin.org/articles/10.3389/fchem.2019.00245/full#supplementary-material

REFERENCES

Alessandri, I., and Lombardi, J. R. (2016). Enhanced raman scattering with dielectrics. *Chem. Rev.* 116, 14921–14981. doi: 10.1021/acs.chemrev.6b00365

Becker, J., Hald, P., Bremholm, M., Pedersen, J. S., Chevallier, J., Iversen, S. B., et al. (2008). Critical size of crystalline ZrO2 nanoparticles synthesized in near- and supercritical water and supercritical isopropyl alcohol. *ACSnano* 2, 1058–1068. doi: 10.1021/nn7002426

Carlone, C. (1992). Raman spectrum of zirconia-hafnia mixed crystals. *Phys. Rev. B* 45, 2079–2084. doi: 10.1103/physrevb.45.2079

Chang, S., and Doong, R. (2007). Interband transitions in Sol–Gel-Derived ZrO_2 films under different calcination conditions. *Chem. Mater.* 19, 4804–4810. doi: 10.1021/cm070606n

De Aza, A. H., Chevalier, J., Fantozzi, G., Schehl, M., and Torrecillas, R. (2002). Crack growth resistance of alumina, zirconia andzirconia toughened alumina ceramics for joint prostheses. *Biomaterials* 23, 937–945. doi: 10.1016/S0142-9612(01)00206-X

Duan, H., Unno, M., Yamada, Y., and Sato, S. (2017). Adsorptive interaction between 1,5-pentanediol and Mgo-Modified ZrO_2 catalyst in the vapor-phase dehydration to produce 4-Penten-1-Ol. *Appl. Cataly. A Gen.* 546, 96–102. doi: 10.1016/j.apcata.2017.07.048

Fu, X., Wang, Y., Liu, Y., Liu, H., Fu, L., Wen, J., et al. (2019). A graphene oxide/gold nanoparticle-based amplification method for SERS immunoassay of cardiac troponin I. *Analyst* 144, 1582–1589. doi: 10.1039/c8an02022a

Gan, X., Yu, Z., Yuan, K., Xu, C., Wang, X., Zhu, L., et al. (2017). Preparation of a CeO_2-nanoparticle thermal radiation shield coating on ZrO_2 fibers Via a hydrothermal method. *Ceram. Int.* 43, 14183–14191. doi: 10.1016/j.ceramint.2017.07.161

Han, X. X., Ji, W., Zhao, B., and Ozaki, Y. (2017). Semiconductor-enhanced raman scattering: active nanomaterials and applications. *Nanoscale* 9, 4847–4861. doi: 10.1039/c6nr08693d

Heuer, A. H., Claussen, N., , Kriven, W. M., and Ruhle, M. (1982). Stability of tetragonal ZrO2 particles in ceramic matrices. *J. Am. Ceram. Soc.* 65, 643–650. doi: 10.1111/j.1151-2916.1982.tb09946.x

Huang, Y. F., Zhang, M., Zhao, L. B., Feng, J. M., Wu, D. Y., Ren, B., et al. (2014). Activation of oxygen on gold and silver nanoparticles assisted by surface plasmon resonances. *Angew. Chem. Int. Edn.* 53, 2353–2357. doi: 10.1002/ange.201310097

Jiang, L., You, T., Yin, P., Shang, Y., Zhang, D., Guo, L., et al. (2013). Surface-enhanced raman scattering spectra of adsorbates on Cu(2)O nanospheres: charge-transfer and electromagnetic enhancement. *Nanoscale* 5, 2784–2789. doi: 10.1039/c3nr33502j

Kadkhodazadeh, S., de Lasson, J. R., Beleggia, M., Kneipp, H., Wagner, J. B., and Kneipp, K. (2014). Scaling of the surface plasmon resonance in gold and silver dimers probed by eels. *J. Phys. Chem. C.* 118, 5478–5485. doi: 10.1021/jp500288s

Kralik, B., Chang, E. K., and Louie, S. G. (1998). Structural properties and quasiparticle band structure of zirconia. *Phys. Rev. B.* 57:7027. doi: 10.1103/physrevb.57.7027

Li, J., Chen, L., Lou, T., and Wang, Y. (2011). Highly sensitive SERS detection of As3+ ions in aqueous media using glutathione functionalized silver nanoparticles. *ACS Appl. Mater. Interfaces* 3, 3936–3941. doi: 10.1021/am200810x

Li, X., Xu, Y., Mao, X., Zhu, Q., Xie, J., Feng, M., et al. (2017). Investigation of optical, mechanical, and thermal properties of ZrO_2-Doped Y_2O_3 transparent ceramics fabricated by Hip. *Ceram. Int.* 44, 1362–1369. doi: 10.1016/j.ceramint.2017.08.204

Lombardi, J. R., and Birke, R. L. (2014). Theory of surface-enhanced raman scattering in semiconductors. *J. Phys. Chem. C* 118, 11120–11130. doi: 10.1021/jp5020675

Long, D., Niu, M., Tan, L., Fu, C., Ren, X., Xu, K., et al. (2017). Ball-in-Ball ZrO_2 nanostructure for simultaneous Ct imaging and highly efficient synergic microwave ablation and tri-stimuli-responsive chemotherapy of tumors. *Nanoscale* 9, 8834–8847. doi: 10.1039/c7nr02511d

Mogensen, K. B., and Kneipp, K. (2014). Size-dependent shifts of plasmon resonance in silver nanoparticle films using controlled dissolution: monitoring the onset of surface screening effects. *J. Phys. Chem. C* 118, 28075–28083. doi: 10.1021/jp505632n

Navio, J., Hidalgo, M., Colon, G., Botta, S., and Litter, M. (2001). Preparation and physicochemical properties of ZrO_2 and Fe/ZrO_2 prepared by a Sol– Gel Technique. *Langmuir* 17, 202–210. doi: 10.1021/la000897d

Scott, B. L., and Carron, K. T. (2016). Dynamic raman scattering studies of coated gold nanoparticles: 4-mercaptopyridine, 4-mercaptophenol, and benzenethiol. *J. Phys. Chem. C* 120, 20905–20913. doi: 10.1021/acs.jpcc.6b02617

Shen, W., Lin, X., Jiang, C., Li, C., Lin, H., Huang, J., et al. (2015). Reliable quantitative sers analysis facilitated by core–shell nanoparticles with embedded internal standards. *Angew. Chem. Int. Edn.* 54, 7308–7312. doi: 10.1002/ange.201502171

Shiohara, A., Wang, Y., and Liz-Marzán, L. M. (2014). Recent approaches toward creation of hot spots for sers detection. *J. Photochem. Photobiol. C.* 21, 2–25. doi: 10.1016/j.jphotochemrev.2014.09.00

Sun, Z., Zhao, B., and Lombardi, J. R. (2007). ZnO nanoparticle size-dependent excitation of surface raman signal from adsorbed molecules: observation of a charge-transfer resonance. *Appl. Phys. Lett.* 91:221106. doi: 10.1063/1.2817529

Wang, C., Guan, Q., Wu, F., and Wang, H. (2019). A novel Mgo doped Zr0.92y0.08O_2-Î'(8ysz) with NaCl/KCl composite electrolyte for intermediate temperature fuel cells. *Ceram. Int.* 45, 1605–1608. doi: 10.1016/j.ceramint.2018.10.035

Wang, Y., and Chen, L. (2011). Quantum dots, lighting up the research and development of nanomedicine. *Nanomedicine* 7, 385–402. doi: 10.1016/j.nano.2010.12.006

Wang, Y., Ji, W., Sui, H., Kitahama, Y., Ruan, W., Ozaki, Y., et al. (2014). Exploring the effect of intermolecular H-bonding: a study on charge-transfer contribution to surface-enhanced raman scattering of P-mercaptobenzoic acid. *J. Phys. Chem. C* 118, 10191–10197. doi: 10.1021/jp5025284

Wang, Y., Ruan, W., Zhang, J., Yang, B., Xu, W., Zhao, B., et al. (2009). Direct observation of surface-enhanced Raman scattering in ZnO nanocrystals. *J. Raman Spectrosc.* 40, 1072–1077. doi: 10.1002/jrs.2241

Wang, Y., Sun, Z., Wang, Y., Hu, H., Zhao, B., Xu, W., et al. (2007). Surface-enhanced raman scattering on mercaptopyridine-capped CdS microclusters. *Spectrochim. Acta. Part A Mole. Biomol. Spectrosc.* 66, 1199–1203. doi: 10.1016/j.saa.2006.06.008

Wang, Y., Wang, Y., Wang, W., Sun, K., and Chen, L. (2016). Reporter-embedded SERS tags from gold nanorod seeds: selective immobilization of reporter molecules at the tip of nanorods. *ACS Appl. Mater. Interfaces* 8, 28105–28115. doi: 10.1021/acsami.6b04216

Wang, Y., Yan, B., and Chen, L. (2013). SERS tags: novel optical nanoprobes for bioanalysis. *Chem. Rev.* 113, 1391–1428. doi: 10.1021/cr300120g

Xu, S., Xu, Y., Liu, Y., Fang, M., Wu, X., Min, X., et al. (2017). Fabrication and abrasive wear behavior of ZrO_2-SiC-Al_2O_3 ceramic. *Ceram. Int.* 43, 15060–15067. doi: 10.1016/j.ceramint.2017.08.032

Xue, X., Ji, W., Mao, Z., Mao, H., Wang, Y., Wang, X., et al. (2012). Raman investigation of nanosized TiO2: effect of crystallite size and quantum confinement. *J. Phys. Chem. C* 116, 8792–8797. doi: 10.1021/jp2122196

Yang, L., Jiang, X., Ruan, W., Zhao, B., Xu, W., and Lombardi, J. R. (2008). Observation of enhanced raman scattering for molecules adsorbed on Tio$_2$ nanoparticles: charge-transfer contribution. *J. Phys. Chem. C* 112, 20095–20098. doi: 10.1021/jp8074145

Yin, P. G., Jiang, L., You, T. T., Zhou, W., Li, L., and Guo, L. (2010). Surface-enhanced Raman spectroscopy with self-assembled cobalt nanoparticle chains: comparison of theory and experiment. *Phys. Chem.* 12, 10781–10785. doi: 10.1039/c002662j

Zhang, L., Huang, Z., Pan, W., and Krell, A. (2015). High transparency Nd: Y2o3ceramics prepared with La_2O_3 and ZrO_2 additives. *J. Am. Ceram. Soc.* 98, 824–828. doi: 10.1111/jace.13354

Zhang, X., Yu, Z., Ji, W., Sui, H., Cong, Q., Wang, X., et al. (2015). Charge-transfer effect on Surface-Enhanced Raman Scattering (SERS) in an ordered Ag Nps/4-mercaptobenzoic Acid/TiO_2 system. *J. Phys. Chem. C* 119, 22439–22444. doi: 10.1021/acs.jpcc.5b06001

Zhao, L. B., Zhang, M., Huang, Y. F., Williams, C. T., Wu, D. Y., Ren, B., et al. (2014). Theoretical study of plasmon-enhanced surface catalytic coupling reactions of aromatic amines and nitro compounds. *J. Phys. Chem. Lett.* 5, 1259–1266. doi: 10.1021/jz5003346

Zhao, X., and Vanderbilt, D. (2002). Phonons and lattice dielectric properties of zirconia. *Phys. Rev. B.* 65:075105. doi: 10.1103/PhysRevB.65.075105

Zheng, H., Liu, K., Cao, H., and Zhang, X. (2009). L-Lysine-assisted synthesis of ZrO_2 nanocrystals and their application in photocatalysis. *J. Phys. Chem. C* 113, 18259–18263. doi: 10.1021/jp9057324

Zhou, L., Xu, J., Li, X., and Wang, F. (2006). Metal oxide nanoparticles from inorganic sources via a simple and general method. *Mater. Chem. Phys.* 97, 137–142. doi: 10.1016/j.matchemphys.2005.07.062

Conflict of Interest Statement: The authors declare that the research was conducted in the absence of any commercial or financial relationships that could be construed as a potential conflict of interest.

frontiers
in Chemistry

ORIGINAL RESEARCH
published: 24 May 2019
doi: 10.3389/fchem.2019.00368

Expedite SERS Fingerprinting of Portuguese White Wines Using Plasmonic Silver Nanostars

Miguel Peixoto de Almeida[1], **Nicolae Leopold**[2], **Ricardo Franco**[3]* **and Eulália Pereira**[1]

[1] LAQV, REQUIMTE, Departamento de Química e Bioquímica, Faculdade de Ciências da Universidade do Porto, Porto, Portugal, [2] Faculty of Physics, Babeş-Bolyai University, Cluj-Napoca, Romania, [3] UCIBIO, REQUIMTE, Departamento de Química, Faculdade de Ciências e Tecnologia, Universidade NOVA de Lisboa, Caparica, Portugal

Surface-enhanced Raman Spectrosocopy (SERS) is a highly sensitive form of Raman spectroscopy, with strong selectivity for Raman-active molecules adsorbed to plasmonic nanostructured surfaces. Extremely intense Raman signals derive from "hotspots", generally created by the aggregation of a silver nanospheres colloid. An alternative and cleaner approach is the use of anisotropic silver nanoparticles, with intrinsic "hotspots", allowing a more controlled enhancement effect as it is not dependent on disordered nanoparticle aggregation. Here, a simple SERS-based test is proposed for Portuguese white wines fingerprinting. The test is done by mixing microliter volumes of a silver nanostars colloid and the white wine sample. SERS spectra obtained directly from these mixtures, with no further treatments, are analyzed by principal component analysis (PCA), using a dedicated software. Depending on the duration of the incubation period, different discrimination can be obtained for the fingerprinting. A "mix-and-read" approach, with practically no incubation, allows for a simple discrimination between the three white wines tested. An overnight incubation allows for full discrimination between varieties of wine (*Verde* or *Maduro*), as well as between wines from different *Maduro* wine regions. This use of SERS in a straightforward, fast and inexpensive test for wine fingerprinting, avoiding the need for prior sample treatment, paves the way for the development of a simple and inexpensive authenticity assay for wines from specific appellations.

Keywords: silver nanostars, surface-enhanced Raman spectroscopy (SERS), white wine, authenticity test, fingerprinting, principal component analysis (PCA)

Edited by:
Ivano Alessandri,
University of Brescia, Italy

Reviewed by:
Daniel Cozzolino,
RMIT University, Australia
Stefania Federici,
University of Brescia, Italy

***Correspondence:**
Ricardo Franco
ricardo.franco@fct.unl.pt

Specialty section:
This article was submitted to Analytical Chemistry, a section of the journal Frontiers in Chemistry

Received: *14 March 2019*
Accepted: *06 May 2019*
Published: *24 May 2019*

Citation:
de Almeida MP, Leopold N, Franco R and Pereira E (2019) Expedite SERS Fingerprinting of Portuguese White Wines Using Plasmonic Silver Nanostars. Front. Chem. 7:368. doi: 10.3389/fchem.2019.00368

INTRODUCTION

The gold standards for wine characterization are chromatography methods, especially liquid chromatography. Methods such as liquid chromatography coupled to mass spectroscopy (LC–MS) and high-performance liquid chromatography (HPLC) are typically used, and efficient, but preliminary fractionation and purification steps are often needed before any analytical procedure (Carpentieri et al., 2007). Wine phenolic fraction is typically analyzed by these chromatographic methods.

Several techniques were already described for wine discrimination based on the statistical analysis of their outputs (typically spectra). Red wines were analyzed by fluorescence spectroscopy and data analysis by parallel factor analysis (PARAFAC) allowed to distinguish wines from different world regions (e.g., Australia, Chile, Spain, USA) (Airado-Rodríguez et al., 2009). A group of four techniques were compared for the same batch of red wines (from only two different appellations): near infrared spectroscopy (NIR), ultraviolet-visible spectroscopy (UV-Vis), a headspace-mass "artificial nose" and a voltammetric "artificial tongue" (Casale et al., 2010). The best separation, determined by principal component analysis (PCA) and linear discriminant analysis (LDA), was achieved by the spectroscopic techniques, which is excellent, given their speed and ease of use. White wines were also discriminated by MALDI–MS (Rešetar et al., 2016), and by a combination of NIR, MIR and Raman spectroscopies (Teixeira dos Santos et al., 2017).

Phenolic composition is one of the most important quality parameters of wines. This composition is directly related to wine organoleptic characteristics such as color, astringency, and bitterness (Paixão et al., 2007). The resonance condition of phenolic compounds, such as hydroxycinnamic acids, has been analyzed selectively by Raman spectroscopy, using lasers at different wavelengths (Martin et al., 2015). Also by Raman spectroscopy, a complete chemometric analysis was implemented to discriminate different wines from the protected designation of origin of Piemonte (Northwest Italy) in accordance with grape varieties, production area and aging time (Mandrile et al., 2016), or to discriminate between wine variety (Feteasca Regala and Sauvignon Blanc) and geographic origin of Romanian wines. These works are relevant examples of the development of analytical methods for traceability to authenticate the geographical origin of foods, a mandatory requirement in the European Union (Peres et al., 2007; Regulation, 2012).

Surface-enhanced Raman spectroscopy (SERS) is an easy, simple, and rapid spectroscopic detection technique, with the possibility of portable use. Unlike Raman, SERS is selective to molecules adsorbed to metal nanostructures, leading to a drastic increase in the intensity of Raman signals originating from those specifically adsorbed molecules. This leads to molecular fingerprint specificity, high sensitivity, and narrow spectral bandwidth, making SERS highly promising for identifying disease markers from complex mixtures of clinical samples (Sinha et al., 2016), antibiotic-resistant bacteria (Galvan and Yu, 2018; Wang et al., 2018), viruses (Paul et al., 2015), or pathogenic fungi (Witkowska et al., 2018), to name a few examples in the medical area. In food analysis, SERS one-pot analysis is especially interesting in areas where inexpensive assays are necessary. SERS fingerprinting followed by PCA analysis has been successfully applied to discriminate tea varieties (Buyukgoz et al., 2016), for example, but never, to our knowledge, to discriminate wines from different regions.

There are two main varieties of Portuguese wines, namely, *Verde* and *Maduro*. *Verde* wine is typical from Northwest wine region of Portugal (Fraga et al., 2014). Across the remaining territory, *Maduro* wine is essentially produced, original from areas like *Douro* (Northeast) and *Alentejo* (South) wine regions. The main difference between *Verde* and *Maduro* wines is essentially the harvesting time, which is at an earlier stage of maturation for *Verde* wine. Hence the names in Portuguese language, "Verde" meaning "green" and "Maduro" meaning "ripe" (Fraga et al., 2014). This incomplete maturation stage influences the profile of compounds responsible for the organoleptic properties of wine. Between the several *Maduro* wine regions the main differences are due to the climate conditions. For example, *Douro* region has a lower average temperature and higher precipitation levels when compared to the *Alentejo* region (Fraga et al., 2014, 2015; Cunha and Richter, 2016). These factors are expected to influence the chemical composition of wines.

Our main goal was to fingerprint white wines from three different wine regions in Portugal using a simple SERS-based method, that could be ultimately used in a point-of-need assay to authenticate the origin of the particular wine tested. Silver nanostars were used as signal enhancers. Silver nanostars (AgNSs) are probably the most interesting anisotropic nanoparticles for SERS applications. In fact, AgNS superior plasmonic properties and remarkable capacity to form "hotspots", make them ideal substrates for adsorption of Raman-active species. The multiplicity or number of arms, arm's length and resulting global size enables interaction with light across all the visible spectrum, although with higher intensity at the ∼400 nm region (Garcia-Leis et al., 2013). Furthermore, AgNS fulfill all the requirements regarding the typical morphology that favors "hotspots", namely, rough surface, sharp tips, intra- and interparticle nanogaps (Liu et al., 2016). Some of us have already proved the high SERS performance of these particular AgNS, for trace analyte detection on paper substrates (Oliveira et al., 2017).

To avoid laborious and/or costly sample analysis, including pre-treatment processes, spectra were analyzed by PCA, a projection method that provides the best fit of data distribution (Biancolillo and Marini, 2018). This fingerprinting technique is much more expedite than the more common analysis of specific wine components, implying separation and pre-concentration procedures, before applying the sample on SERS substrates (Chen et al., 2016; Li et al., 2016).

Figure 1 depicts our approach to an expedite method for white wine fingerprinting.

MATERIALS AND METHODS

All the reagents were used as purchased, with no further steps of purification. For nanoparticle synthesis, a KD Scientific KDS 200 syringe pump, holding a BD 60 mL plastic syringe was used. Centrifugations were in a Sigma 30K centrifuge, with a 19776H rotor. Ultraviolet-visible spectroscopy (UV-Vis) was performed using a Varian Cary 50 Bio spectrophotometer. Nanoparticle tracking analysis (NTA) was using a Malvern Nanosight NS300 equipped with a 642 nm (red) laser module, by acquisition of 5 videos of 1 min each in static mode. Transmission electron microscopy (TEM) was performed using a Hitachi H8100 transmission electron microscope.

Wine Samples

Portuguese white wine samples were chosen from two different varieties, *Verde* and *Maduro*. From the latter variety, wines

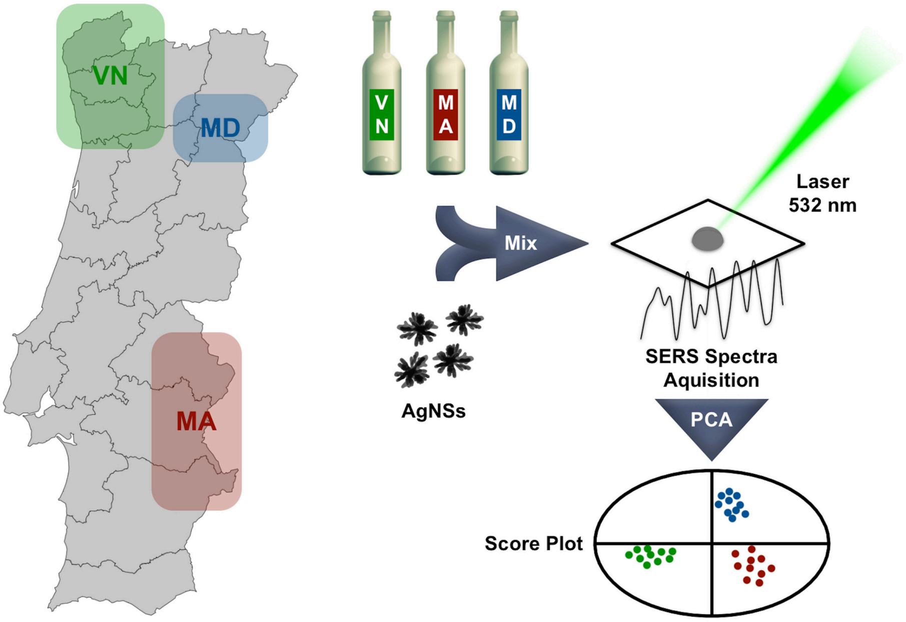

FIGURE 1 | White wine samples from three different wine regions in Portugal are simply mixed with a silver nanostars colloid and incubated. A 532 nm laser is used to obtain the respective SERS spectra, that after principal component analysis (PCA) produces a score plot allowing sample discrimination. The duration of the incubation period is determinant for the obtained results.

from two different regions were tested. One commercial bottle, representative of each wine type was used. The wines were all bottled in 2014. The storage and aging processes of the specific wines are undisclosed, but it is known that *Verde* wine is stored in stainless steel containers, whereas *Maduro* wine is stored in wood barrels. Experimental protocols were applied to two independent samples of each bottle. Each sample was read in 5 different points, in a total of 10 spectra for each wine. The following abbreviations are used to designate the samples under study: *Verde* wine from the *Northwest* region (VN), *Maduro* wine from the *Douro* region (MD), and *Maduro* wine from the *Alentejo* region (MA). Wines were used as direct samples, with no further treatment.

Preparation of Silver Nanostars

Star-shaped silver nanoparticles were synthesized based in the method from Garcia-Leis *et al* (Garcia-Leis et al., 2013). The following reagents were used: silver nitrate 99.9999% (Aldrich), hydroxylamine solution 50% wt. in water 99.999% (Aldrich), sodium hydroxide 98% (Fisher) and trisodium citrate dihydrate 99.0% (Merck). All glassware was previously treated with *aqua regia* and rinsed abundantly with deionized water, followed by ultrapure water (18.2 MΩ·cm at 25°C). All solutions were prepared with ultrapure water.

For the synthesis reaction, 2.5 mL of a 50 mM sodium hydroxide solution (125 μM) and 2.5 mL of a 60 mM hydroxylamine solution (150 μM) were mixed in beaker and, immediately after, 45 mL of a 1 mM silver nitrate solution (45 μM) was added dropwise from a syringe, using a syringe pump at a 45 mL/min injection rate. After 90 s, 500 μl of a 1.5% wt. trisodium citrate (dihydrate) solution was added to the mixture. The reaction vessel was kept protected from light for a 3-h reaction period.

After this 3-h period, the content of the five beakers was mixed and the resultant batch (250 mL) of AgNSs suspension was centrifuged for 12 min at a relative centrifugal force (RCF) of 1,600 g. The pellet was resuspended in ultrapure water (up to 10% of the initial volume) and stored in a glass vial.

Raman and SERS Experiments

Raman and SERS spectra were measured with a Renishaw InVia Raman microscope, coupled with 442 nm 80 mW (He-Cd), 532 nm 200 mW (diode), 633 nm 17 mW (He-Ne), 785/830 nm 300 mW (diode) lasers. Gratings of 1,200 l/mm and 1,800 l/mm were used, the first for 785 nm measurements and the second for 442 nm, 532 nm and 633 nm. The system is equipped with a CCD camera detector, with a 1,040 × 256 resolution. The objective used had a 50x magnification.

Incubation protocol: 1 ml of wine and 100 μl of 0.1 nM AgNS colloid were mixed, followed by overnight incubation. Immediately before Raman/SERS measurements, samples containing nanoparticles were centrifuged for 5 min at RCF 1,600 g, and 99% of the supernatant volume was removed. The pellet rich in AgNS with adsorbed wine components, was dispersed in the remaining supernatant by "up and down" pipetting. From this final volume, 10 μl aliquots for analysis were taken. As a control experiment, Raman and SERS measurements were made of the supernatant fraction, with no detectable signals for any of the measurements.

"Mix-and-read" protocol: 10 µl of wine and 10 µl of 0.1 nM AgNS colloid were mixed and read immediately. No concentration steps were needed for this protocol, since the final volume was already 20 µl. All measurements were also performed in 10 µl aliquots.

Aliquots were placed in a microscope glass slide, wrapped in one layer of commercial-grade aluminum foil. When justifiable, spectra of the external elements to the sample, such as the aluminum foil, were acquired. The aluminum foil is in the origin of some peaks found in spectra collected with 633 nm and 785 nm lasers (**Supplementary Figure 1**), and one of the reasons why data obtained with these lasers was further excluded (see below).

Signal acquisition parameters such as laser power and acquisition time were different for the two protocols, with batches of spectra analyzed together acquired under identical experimental conditions. Number of acquisitions was always two per sample and acquisition times were between 4 and 10 s.

Selection of Laser Line for SERS

In order to choose the appropriate laser line for maximum spectral intensity and resolution, SERS spectra were obtained for the three white wines mixed with AgNS colloid, following the overnight incubation protocol, using four different laser lines: 442, 532, 633, and 785 nm (**Supplementary Figure 2**). Spectra collected with the blue laser line (442 nm), are poorly structured, not allowing an easy fingerprinting of the wine samples. When the 532 nm laser line was used to obtain SERS spectra of this set of samples, it was possible to observe well-defined vibrations that may be helpful to the fingerprinting. Spectra acquired with the near infrared laser (785 nm line) presents sharp peaks, for the MD sample (as also observed for the 633 nm and 532 nm laser lines), but presents broad peaks leading to less defined spectra for the other two samples (MA and VN). A practical difficulty that contributed for the decision to exclude analysis based on the 633 or 785 nm laser lines, was the interference of the sample substrate observed for spectra obtained with these two laser lines (see **Supplementary Figure 1**). In conclusion, spectra obtained with 532 nm laser line are the most structured and, therefore, richer in information, being this one the selected laser line for these SERS studies. Also, using the 532 nm laser line in combination with the 1,800 lines/mm grating, enables the possibility of collecting data, in single measurement mode, in a larger range (∼1,750 units of Raman shift) than 633 or 785 nm laser lines. This lower resolution for the 532 nm laser line does not seem to compromise data quality.

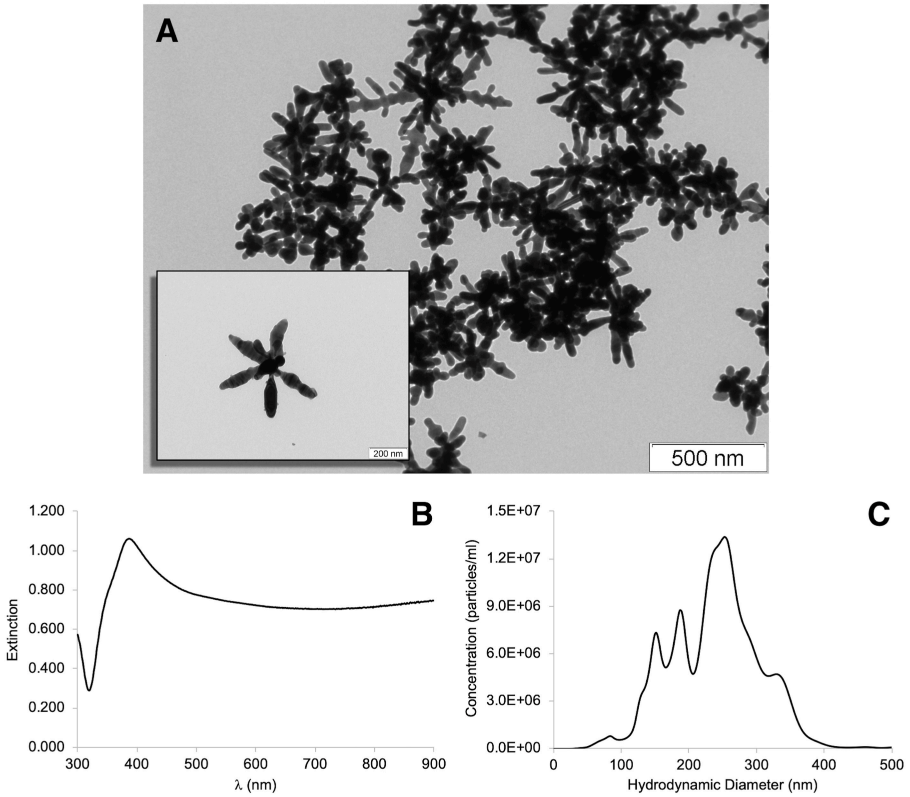

FIGURE 2 | Silver nanostars (AgNS) colloid characterization by **(A)** Transmission Electron Microscopy (TEM) micrographs; **(B)** UV-visible spectrum, and **(C)** hydrodynamic diameter distribution, obtained by Nanoparticle Tracking Analysis (NTA).

Principal Component Analysis

Principal component analysis (PCA) was performed using The Unscrambler® X 10.4.1 (CAMO) software. For PCA analysis, ten spectra were collected per wine sample. Five spectra were collected in five different spots in both duplicates. Before application of PCA, spectra were submitted to data pre-treatment by baseline linear correction (BLC). Spectra were considered in the full range 100-1,800 cm^{-1}.

RESULTS AND DISCUSSION

Silver nanostars characterization was made using Transmission Electron Microscopy (TEM), ultraviolet-visible spectroscopy (UV-Vis) and nanoparticle tracking analysis (NTA) (**Figure 2**). TEM micrographs depicted in **Figure 2A** show star-shaped nanoparticles, with variable tip to tip size consequence of the number, relative position and shape of the arms. Each one of the nanoparticles is noticeably unique. The UV-vis spectrum depicted in **Figure 2B** is a typical spectrum for this type of nanoparticles (Garcia-Leis et al., 2013). Concentration of silver nanostars is typically 0.01 nM after synthesis (on the 50 mL reaction volume). After centrifugation and resuspension into 10% of the initial volume (5 mL), the concentration is 0.1 nM. The hydrodynamic diameter distribution of the synthesized silver nanoparticles was determined by NTA (**Figure 2C**), as average diameter of 217 nm (mode of 253 nm) and a standard deviation (SD) of 69 nm.

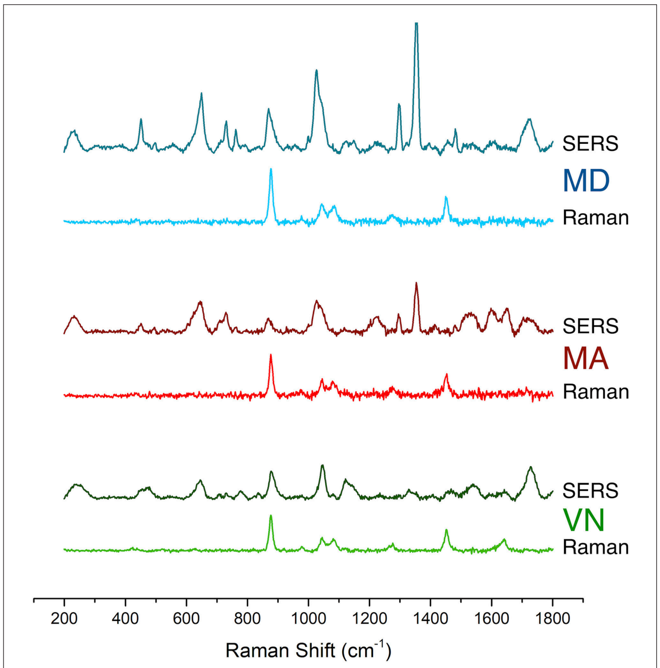

FIGURE 3 | Normal Raman and SERS spectra for the three white wine samples of the *Maduro* (MD and MA) and *Verde* (VA) varieties, acquired using a 532 nm laser line. Spectra were baseline corrected using a polynomial subtraction procedure. Original spectra are in **Supplementary Figure 3**.

Figure 3 presents a comparison of normal Raman and SERS spectra for the three white wine samples, acquired using a 532 nm laser line. It should be pointed out that fluorescence background was removed from Raman and SERS spectra, using a polynomial subtraction procedure (Martin et al., 2015). Interestingly, the fluorescent background was much less intense in the *Verde* wine (VN), that in wines from the *Maduro* variety (MD and MA), suggesting that the *Verde* wine is poorer in fluorescent phenolic compounds when compared to *Maduro* wine. This is a plausible conclusion since the maturation of *Verde* wines is done in stainless steel containers, whereas for the *Maduro* variety, maturation is on oak wood barrels, sometimes with the addition of oak chips (Pérez-Coello et al., 2000; Afonso, 2002; Liberatore et al., 2010). These treatments, to improve aroma quality of the *Maduro* wines, lead to a high content in flavor active compounds, especially of the phenolic (fluorescent) kind.

Raman spectra of all three samples are very similar, with lines that can be attributed to the most abundant components, namely, sugars (namely fructose and glucose) exhibiting vibrations around 1,000–1,100 cm^{-1} (Ilaslan et al., 2015) and ethanol, showing at around 880 cm^{-1} (CC stretching) (Ilaslan et al., 2015; Martin et al., 2015). Another line appears at around 1,465 cm^{-1} in all the normal Raman spectra, that can also be attributed to ethanol, which is obviously found in abundance in wines, as mentioned above (Dolenko et al., 2015).

All SERS spectra obtained in the presence of AgNSs showed a strong enhancement of the Raman lines, with several new lines appearing (**Figure 3**). Also, lines from some groups of the identified molecules in Raman are missing or have very weak intensity, since SERS is a short-distance effect, only molecules close to the nanoparticles experience the strong electromagnetic field of "hotspots". It is also interesting to notice that in contrast with normal Raman, SERS spectra from the three wine samples have notable differences between each other, hinting at an important role for SERS in wine fingerprinting. As SERS spectra are very complex and line attribution is nearly impossible, a statistical analysis by Principal Component Analysis (PCA) was thus applied.

Obtaining such intense and complicated SERS spectra for white wines mixed with citrate-capped AgNS, is probably related to several different types of molecules from the wine sample adsorbing to the surface of the AgNS. An interesting parallelism can be drawn to a study of the adsorption of different varieties of wines on membranes presenting different chemical functionalities (Mierczynska-Vasilev and Smith, 2016). In this study, the authors concluded that amine and carboxyl modified surfaces encourage the adsorption of constituents specifically from white wine as opposed to hydroxyl modified surfaces for rosé wine constituents, and acrylic acid surfaces for red wine. One could speculate that the carboxylic groups from the citrate capping are responsible for the extensive white wine components adsorption, resulting in the observed complexity of SERS spectra.

Another interesting feature observed for SERS spectra when comparing with normal Raman, is the significant fluorescence quenching induced by the AgNS. The presence of fluorescence emission in the normal Raman spectra and its quenching in SERS spectra, by the presence of AgNS, can be observed in the raw

Raman and SERS spectra presented in **Supplementary Figure 3**. This effect was previously observed by some of us when the same type AgNS were adsorbed to an office paper substrate. In fact, the presence of AgNS on the surface of the paper was able to fully quench its intrinsic fluorescence emission, derived from excitation with a 633 nm laser line (Oliveira et al., 2017).

Two different protocols were used for SERS sample preparation, corresponding to different incubation periods, namely, overnight incubation and the "mix-and-read" approach, i.e., without incubation. Our rationale is based in the plausible adsorption process of the wine chemical components to the surface of the AgNS. In a process reminiscent of protein corona formation around metal nanoparticles, it is expected that wine chemical components with high abundance are firstly adsorbed on the surface, and over the time, they are replaced by components with lower concentration but higher affinity (Rahman et al., 2013). These lower concentration components, in the case of wine, are probably highly specific for each wine label, allowing fine fingerprinting.

SERS spectra of the three wine samples under study, after simple mixing with the AgNS colloid, with no further treatments, are presented in **Figure 4** for two different incubation periods. SERS spectra of samples that were incubated overnight (**Figure 4A**) show in general, much less resolution compared to SERS spectra of samples read immediately after the addition of silver nanostars (**Figure 4B**). On the other hand, comparing the three different wine samples for each incubation protocol, a better differentiation between samples is apparent for samples that were incubated overnight, compared to "mix-and-read" samples. In fact, the spectra of "mix-and-read" samples are individually very well-resolved, but look similar to each other, hinting at common and abundant wine components being the main contribution to the observed SERS signals.

In order to obtain the best fit for SERS data distribution and establish the principles of a fingerprinting method for the white wine samples, a statistical analysis of the SERS spectra was performed using PCA. This is the technique of choice for the intended data analysis, allowing compression of the data dimensionality at the same time reducing to a minimum the loss of information (Biancolillo and Marini, 2018). This analysis generates score plots which can highlight possible trends in the data, presence of clusters or of an underlying structure. Principal Components will have positive or negative scores on these plots and are directly correlated in the loadings plot with spectral regions with positive or negative loadings, respectively.

The score plot and loadings resulting from the PCA analysis with baseline linear correction (BLC) pre-treatment, of SERS spectra obtained by the overnight incubation protocol, are depicted in **Figure 5**. In the score plot, three data clusters are clearly distinguishable, corresponding to the three different wines. Furthermore, distinction between *Verde* and *Maduro*

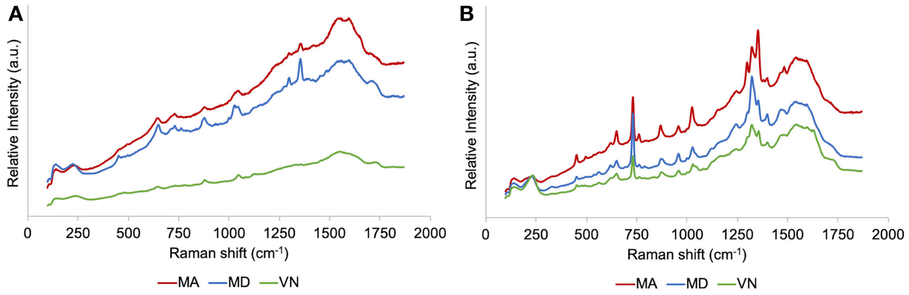

FIGURE 4 | SERS spectra for the three white wine samples acquired using a 532 nm laser line. Two different protocols for sample preparation, corresponding to different incubation times, were used after mixing the AgNS colloid with the wine samples: **(A)** Overnight incubation, and **(B)** "mix-and-read" approach.

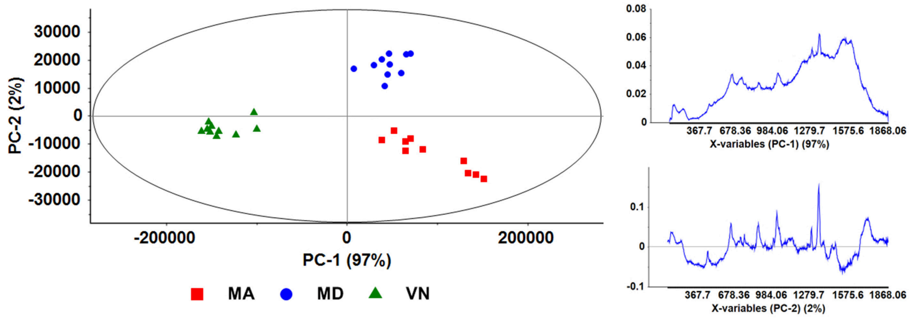

FIGURE 5 | Scores plot depicting PC-1 and PC-2 (left); and loadings plots (right) for both Principal Components, PC-1 (top), and PC-2 (bottom). These plots are for SERS spectra obtained from samples prepared following the overnight incubation protocol, with data pre-treatment by BLC.

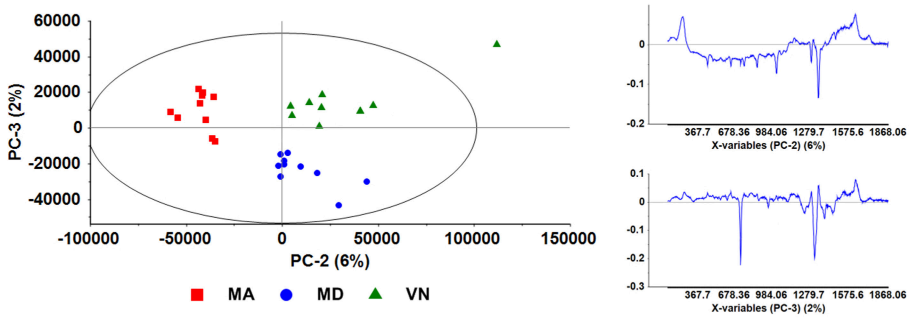

FIGURE 6 | Scores plot depicting PC-2 and PC-3 (left); and loadings plots (right) for both Principal Components, PC-2 (top), and PC-3 (bottom). These plots are for SERS spectra obtained from samples prepared following the "mix-and-read" protocol, with data pre-treatment by BLC.

wines is possible from this plot, since it is related to principal component 1 (PC-1, horizontal axis), which has a 97% weight. In fact, *Verde* wine (VN) is clustered in the negative section of the score plot, while both *Maduro* wines (MD and MA) cluster on the positive section. The loading plot of PC-1 (**Figure 5**, bottom left), is an all-positive spectrum with a baseline that increases in intensity toward the high frequency region of the spectrum, an indication of sample fluorescence. This seems to be an important characteristic of *Maduro* wines, as these present a positive score for PC-1. This conclusion agrees with the hypothesis that the *Verde* wine is poorer in fluorescent phenolic compounds compared to wines from the *Maduro* variety.

The second principal component from the score plot of **Figure 5** (PC-2, vertical axis, 2% weight) seems to essentially distinguish between the two regions of *Maduro* wine, with MD and MA clustering on the positive and negative sections of the PC-2 axis, respectively.

In data obtained for "mix-and-read" protocol, PCA analysis with data pre-treatment by BLC, shows a very important weight (91%) for PC-1. However, the samples score points are quite dispersed across the PC-1 axis, being both in positive and negative regions. It is nevertheless possible to recognize groups organized in the horizontal axis, so PC-2 seems to distinguish the three wines (**Supplementary Figure 4**).

We then decided to produce a score plot of PC-2 (horizontal axis, 6%) vs. PC-3 (vertical axis, 2%) in order to evaluate its usefulness for the white wine samples discrimination (**Figure 6**). In spite of these principal components 2 and 3 presenting only a total weight of 8% of the total SERS data, their score plot clearly isolates three groups corresponding to the three white wines under analysis, thus allowing the intended discrimination between white wine samples.

This is a notorious case in which PC-1 loses relevance and PC-3 helps to differentiate wines. This is in line with what it was already discussed for this approach, specifically the determinant role of abundant and common wine compounds in the SERS signal. These common and abundant compounds are probably the main contributor for PC-1 in this case of the "mix-and-read" protocol, leading to a high distribution across the PC-1 axis and its high weight.

It is worth mentioning that applying the same PCA analysis to Raman spectra, gave no results as to discrimination of any of the three samples. PCA analysis was tried in the raw spectra and also using two types of data pre-treatment, namely BLC and SNV, in all cases with no discrimination results (data not shown).

In conclusion, the use of AgNS for wine fingerprinting by SERS was proven possible with these three wines. When a AgNS colloid is incubated with wine samples, SERS spectra obtained using two different incubation protocols, corresponding to two different incubation periods, allowed discrimination between white wines from two different Portuguese varieties (*Verde* and *Maduro*) as well as between wines of the Maduro variety from two different wine regions (*Alentejo* and *Douro*).

SERS signals derive from the adsorption of wine chemical compounds to the surface of the nanoparticles. These compounds exchange with AgNS capping agent, citrate and presumably become new capping agents. A capping agent is as close as possible to any nanoparticle surface, so the new capping comprised by wine-derived molecules will be greatly enhanced by AgNSs hotspots.

Either AgNS are functionalized quickly by the most abundant compounds in wine, that should be quite transversal to every wine, or they act as regular Raman enhancers, i.e., without direct conjugation, with sample components being under the influence of the hotspots electromagnetic field. This also will privilege the most abundant compounds, given the higher probability to be found in higher quantity near the hotspots.

It important to notice that a typical "mix-and-read" approach can be misleading, probably due to the emphasis given to abundant compounds in wine, that are not so specific from wine to wine. If long incubation periods of AgNS with the wine samples (e.g., 20 h) are used, wine compounds with higher affinity to silver surfaces will replace the abundant compounds. These low quantity compounds are probably more characteristic of each wine.

However, since the objective of this work was to find a fast, yet effective, method for wine fingerprinting, the "mix-and-read" protocol should be considered. If the weight of the most abundant species is somehow discarded (e.g., ignoring PC-1), it is possible to fully achieve the objective of obtaining results in a facile and expedite way.

Work is underway to add more wine samples in order to validate this method in a larger range. This will confirm the need of using a protocol focused in high affinity compounds or if a fast protocol is suitable for the purpose. Additional wine samples from more regions will also be analyzed, and besides different regions, different wine years can also be tested as a discrimination factor. With data from different years, it will be also possible to evaluate if there are some tendencies regarding a possible convergence or divergence of wine properties from different regions due to climate changes (Cunha and Richter, 2016).

DATA AVAILABILITY

All datasets generated for this study are included in the manuscript and/or the **Supplementary Files**.

AUTHOR CONTRIBUTIONS

All the authors contributed equally to experiment planning. MA was responsible for experiment execution. MA and RF wrote the manuscript with contributions from EP and NL.

FUNDING

The authors are grateful to Fundação para a Ciência e a Tecnologia (MCTES funds) and European Union (European Social Fund and European Regional Development Fund), for financial support through grants UID/QUI/50006/2019 and POCI-01-0145-FEDER-007265 (LAQV-REQUIMTE), UID/Multi/04378/2019 and POCI-01-0145-FEDER-007728 (UCIBIO-REQUIMTE), EXPL/CTM-NAN/0754/2013 and PTDC/CTM-NAN/2912/2014, all from COMPETE and COMPETE 2020 programs, grant NORTE-01-0145-FEDER-000011, from NORTE 2020 program, and fellowship SFRH/BD/95983/2013 (to MA), from POCH program, all programs from QREN (COMPETE) or Portugal 2020 (all others) partnership agreements. NL acknowledges support from a grant of the Romanian Ministry of Research and Innovation, CCCDI-UEFISCDI, project number PN-III-P1-1.2-PCCDI-2017-0056, within PNCDI III.

ACKNOWLEDGMENTS

TEM images of the silver nanostars used in this work, were collected by Dr. Pedro Quaresma at Electron Microscopy Laboratory (MicroLab) of the Instituto Superior Teìcnico, Universidade de Lisboa, Portugal.

SUPPLEMENTARY MATERIAL

The Supplementary Material for this article can be found online at: https://www.frontiersin.org/articles/10.3389/fchem.2019.00368/full#supplementary-material

REFERENCES

Afonso, V. L. G. (2002). Sensory descriptive analysis between white wines fermented with oak chips and in barrels. *Food Sci.* 67, 2415–2419. doi: 10.1111/j.1365-2621.2002.tb09563.x

Airado-Rodríguez, D., Galeano-Díaz, T., Durán-Merás, I., and Wold, J. P. (2009). Usefulness of fluorescence excitation-emission matrices in combination with PARAFAC, as fingerprints of red wines. *J. Agricul. Food Chem.* 57, 1711–20. doi: 10.1021/jf8033623

Biancolillo, A., and Marini, F. (2018). Chemometric methods for spectroscopy-based pharmaceutical analysis. *Front. Chem.* 6:576. doi: 10.3389/fchem.2018.00576

Buyukgoz, G. G., Soforoglu, M., Basaran Akgul, N., and Boyaci, I. H. (2016). Spectroscopic fingerprint of tea varieties by surface enhanced Raman spectroscopy. *J. Food Sci. Technol.* 53, 1709–1716. doi: 10.1007/s13197-015-2088-5

Carpentieri, A., Marino, G., and Amoresano, A. (2007). Rapid fingerprinting of red wines by MALDI mass spectrometry. *Anal. Bioanal. Chem.* 389, 969–982. doi: 10.1007/s00216-007-1476-8

Casale, M., Oliveri, P., Armanino, C., Lanteri, S., and Forina, M. (2010). NIR and UV-vis spectroscopy, artificial nose and tongue: comparison of four fingerprinting techniques for the characterisation of Italian red wines. *Anal. Chim. Acta.* 668, 143–148. doi: 10.1016/j.aca.2010.04.021

Chen, M., Yang, H., Rong, L., and Chen, X. (2016). A gas-diffusion microfluidic paper-based analytical device (μPAD) coupled with portable surface-enhanced Raman scattering (SERS): facile determination of sulphite in wines. *Analyst* 141, 5511–5519. doi: 10.1039/C6AN00788K

Cunha, M., and Richter, C. (2016). The impact of climate change on the winegrape vineyards of the *Portuguese Douro* region. *Clim. Change.* 138, 239–251. doi: 10.1007/s10584-016-1719-9

Dolenko, T. A., Burikov, S. A., Dolenko, S. A., Efitorov, A. O., Plastinin, I. V., Yuzhakov, V. I., et al. (2015). Raman spectroscopy of water-ethanol solutions: the estimation of hydrogen bonding energy and the appearance of clathrate-like structures in solutions. *J. Phys. Chem. A.* 119, 10806–10815. doi: 10.1021/acs.jpca.5b06678

Fraga, H., Malheiro, A. C., Moutinho-Pereira, J., and Santos, J. A. (2014). Climate factors driving wine production in the Portuguese Minho region. *Agricul. Forest Meteorol.* 185, 26–36. doi: 10.1016/j.agrformet.2013.11.003

Fraga, H., Santos, J. A., Moutinho-Pereira, J., Santos, J. A., Silvestre, J., Eiras-Dias, J., et al. (2015). Statistical modelling of grapevine phenology in Portuguese wine regions: observed trends and climate change projections. *J. Agricult. Sci.* 154, 795–811. doi: 10.1017/s0021859615000933

Galvan, D. D., and Yu, Q. (2018). Surface-enhanced raman scattering for rapid detection and characterization of antibiotic-resistant bacteria. *Adv. Healthc Mater.* 7:e1701335. doi: 10.1002/adhm.201701335

Garcia-Leis, A., Garcia-Ramos, J. V., and Sanchez-Cortes, S. (2013). Silver nanostars with high SERS performance. *J. Phys. Chem. C.* 117, 7791–7795. doi: 10.1021/jp401737y

Ilaslan, K., Boyaci, I. H., and Topcu, A. (2015). Rapid analysis of glucose, fructose and sucrose contents of commercial soft drinks using Raman spectroscopy. *Food Control.* 48, 56–61. doi: 10.1016/j.foodcont.2014.01.001

Li, M., Zhao, Y., Cui, M., Wang, C., and Song, Q. (2016). SERS-active Ag nanostars substrates for sensitive detection of ethyl carbamate in wine. *Anal. Sci.* 32, 725–728. doi: 10.2116/analsci.32.725

Liberatore, M. T., Pati, S., Nobile, M. A. D., and Notte, E. L. (2010). Aroma quality improvement of Chardonnay white wine by fermentation and ageing in barrique on lees. *Food Res. Int.* 43, 996–1002. doi: 10.1016/j.foodres.2010.01.007

Liu, K., Bai, Y., Zhang, L., Yang, Z., Fan, Q., Zheng, H., et al. (2016). Porous Au-Ag nanospheres with high-density and highly accessible hotspots for SERS analysis. *Nano Lett.* 16, 3675–3681. doi: 10.1021/acs.nanolett.6b00868

Mandrile, L., Zeppa, G., Giovannozzi, A. M., Rossi, A. M. (2016). Controlling protected designation of origin of wine by Raman spectroscopy. *Food Chem.* 211, 260–267. doi: 10.1016/j.foodchem.2016.05.011

Martin, C., Bruneel, J. L., Guyon, F., Médina, B., Jourdes, M., Teissedre, P. L., Guillaume, F. (2015). Raman spectroscopy of white wines. *Food Chem.* 181, 235–240. doi: 10.1016/j.foodchem.2015.02.076

Mierczynska-Vasilev, A., Smith, P. A. (2016). Adsorption of wine constituents on functionalized surfaces. *Molecules (Basel, Switzerland)* 21:1394. doi: 10.3390/molecules21101394

Oliveira, M. J., Quaresma, P., de Almeida., M. P., Araújo, A., Pereira, E., et al. (2017). Office paper decorated with silver nanostars - an alternative cost effective platform for trace analyte detection by SERS. *Sci. Rep.* 7:2480. doi: 10.1038/s41598-017-02484-8

Paixão, N., Perestrelo, R., Marques, J., Câmara, J. (2007). Relationship between antioxidant capacity and total phenolic content of red, rosé and white wines. *Food Chem.* 105, 204–214. doi: 10.1016/j.foodchem.2007.04.017

Paul, A. M., Fan, Z., Sinha, S. S., Shi, Y., Le, L., Bai, F., et al. (2015). Bioconjugated gold nanoparticle based SERS probe for ultrasensitive identification of mosquito-borne viruses using raman fingerprinting. *J. Phys. Chem. C Nanomater. Interfaces*. 119, 23669–23775. doi: 10.1021/acs.jpcc.5b07387

Peres, B., Barlet, N., Loiseau, G., Montet, D. (2007). Review of the current methods of analytical traceability allowing determination of the origin of foodstuffs. *Food Control* 18, 228–235. doi: 10.1016/j.foodcont.2005.09.018

Pérez-Coello, M. S., Sáchez, M. A., García, E., González-Viñas, M. A., Sanz, J., Cabezudo, M. D. (2000). Fermentation of white wines in the presence of wood chips of american and French Oak. *J. Agricult. Food Chem.* 48, 885–889 doi: 10.1021/jf990884+

Rahman, M., Laurent, S., Tawil, N., Yahia, L. H., Mahmoudi, M. (2013). “Nanoparticle and Protein Corona,” in *Protein-Nanoparticle Interactions: The Bio-Nano Interface. Springer Series in Biophysics,* eds M. Rahman, S. Laurent, N. Tawil, L. H. Yahia, M. Mahmoudi (Berlin: Springer Berlin Heidelberg), 21–44.

Regulation (2012). *Regulation (Eu) No 1151/2012 Of the European Parliament And Of the Council of 21 November 2012 on quality schemes for agricultural products and foodstuffs*. Official Journal of the European Union.

Rešetar, D., Marchetti-Deschmann, M., Allmaier, G., Katalini,ć, J. P., Kraljević Pavelić, S. (2016). Matrix assisted laser desorption ionization mass spectrometry linear time-of-flight method for white wine fingerprinting and classification. *Food Control* 64, 157–164. doi: 10.1016/j.foodcont.2015.12.035

Sinha, S. S., Jones, S., Pramanik, A., Ray, P. C. (2016). Nanoarchitecture Based SERS for biomolecular fingerprinting and label-free disease markers diagnosis. *Acc. Chem. Res.* 49, 2725–2735. doi: 10.1021/acs.accounts.6b00384

Teixeira dos Santos, C. A., Páscoar, R. N. M. J., Sarraguça, M. C., Porto, A. L. S., Cerdeira, A. L., González-Sáiz, J. M., et al. (2017). Merging vibrational spectroscopic data for wine classification according to the geographic origin. *Food Res. Int.* 102, 504–510 doi: 10.1016/j.foodres.2017.09.018

Wang, K., Li, S., Petersen, M., Wang, S., Lu, X. (2018). Detection and characterization of antibiotic-resistant bacteria using surface-enhanced raman spectroscopy. *Nanomaterials (Basel)*. 8:E762. doi: 10.3390/nano8100762

Witkowska, E., Jagielski, T., Kaminska, A. (2018). Genus- and species-level identification of dermatophyte fungi by surface-enhanced Raman spectroscopy. *Spectrochim. Acta A Mol. Biomol. Spectrosc.* 192, 285–290. doi: 10.1016/j.saa.2017.11.008

Conflict of Interest Statement: The authors declare that the research was conducted in the absence of any commercial or financial relationships that could be construed as a potential conflict of interest.

frontiers in Chemistry

REVIEW
published: 04 June 2019
doi: 10.3389/fchem.2019.00376

Ag Nanorods-Based Surface-Enhanced Raman Scattering: Synthesis, Quantitative Analysis Strategies, and Applications

Sumeng Zou[1], **Lingwei Ma**[2], **Jianghao Li**[1], **Yuehua Liu**[1], **Dongliang Zhao**[3] and **Zhengjun Zhang**[4*]

[1] State Key Laboratory of New Ceramics and Fine Processing, School of Materials Science and Engineering, Tsinghua University, Beijing, China, [2] Institute for Advanced Materials and Technology, University of Science and Technology Beijing, Beijing, China, [3] Department of Functional Material Research, Central Iron and Steel Research Institute, Beijing, China, [4] Key Laboratory of Advanced Materials (MOE), School of Materials Science and Engineering, Tsinghua University, Beijing, China

OPEN ACCESS

Edited by:
John Lombardi,
City College of New York (CUNY),
United States

Reviewed by:
Hui Xu,
Ludong University, China
Chih-Ching Huang,
National Taiwan Ocean University, Taiwan
Xianming Kong,
Liaoning Shihua University, China

***Correspondence:**
Zhengjun Zhang
zjzhang@tsinghua.edu.cn

Specialty section:
This article was submitted to Analytical Chemistry, a section of the journal Frontiers in Chemistry

Received: 14 February 2019
Accepted: 08 May 2019
Published: 04 June 2019

Citation:
Zou S, Ma L, Li J, Liu Y, Zhao D and Zhang Z (2019) Ag Nanorods-Based Surface-Enhanced Raman Scattering: Synthesis, Quantitative Analysis Strategies, and Applications. Front. Chem. 7:376. doi: 10.3389/fchem.2019.00376

Surface-Enhanced Raman Scattering (SERS) is a powerful technology that provides abundant chemical fingerprint information with advantages of high sensitivity and time-saving. Advancements in SERS substrates fabrication allow Ag nanorods (AgNRs) possess superior sensitivity, high uniformity, and excellent reproducibility. To further promote AgNRs as a promising SERS substrate candidate to a broader application scope, oxides are integrated with AgNRs by virtue of their unique properties which endow the AgNRs-oxide hybrid with high stability and recyclability. Aside from SERS substrates fabrication, significant developments in quantitative analysis strategies offer enormous approaches to minimize influences resulted from variations of measuring conditions and to provide the reasonable data analysis. In this review, we discuss various fabrication approaches for AgNRs and AgNRs-oxide hybrids to achieve efficient SERS platforms. Then, we introduce three types of strategies which are commonly employed in chemical quantitative analysis to reach a reliable result. Further, we highlight SERS applications including food safety, environment safety, biosensing, and vapor sensing, demonstrating the potential of SERS as a powerful and promising technique. Finally, we conclude with the current challenges and future prospects toward efficient SERS manipulations for broader real-world applications.

Keywords: AgNRs-based substrates, SERS, synthesis, quantitative analysis strategy, detections, applications

INTRODUCTION

Surface-Enhanced Raman Scattering (SERS) is a promising analytical tool which provides identification and quantitative information of chemicals at trace levels based on their specific molecular vibrational fingerprints. Benefited from enormous advantages, such as non-destructive, high sensitivity, and time-saving, SERS was employed in several fields, including biosensing, food safety, environment safety, heterogeneous catalysis, and disease diagnosis, etc. (Zhao et al., 2015; Han et al., 2016; Chinnakkannu Vijayakumar et al., 2017; Tan et al., 2017; Kim et al., 2018). Therefore, SERS has attracted a lot of interests and many efforts have been devoted to develop ideal SERS substrates.

Generally, it is recognized that Raman signal enhancement is attributed to electromagnet enhancement (EM) and chemical enhancement (CM) (Kambhampati et al., 1998; Xu et al., 2000; Ding et al., 2017). EM is the dominant contributor originated from collective oscillation of localized surface plasmon resonance (LSPR) in metallic particles which are mainly coinage metals (Au, Ag, and Cu) (Willets and Van Duyne, 2007; Ding et al., 2016; Cardinal et al., 2017). Considering the correlation of LSPR to particles' shapes and sizes, thriving researches in substrate fabrications were focused on exploring SERS performance of particles with various shapes, such as nanospheres, nanorods, nanowires, nanoprisms, and nanocubes (Yang et al., 2015; Zhou et al., 2015; Chook et al., 2017; Ke et al., 2017; Wang et al., 2017). Among these, AgNRs proves to be a powerful SERS substrate candidate because it integrates the merit of the highest plasmonic resonance quality factor provided by Ag with the advantage of the tunable localized surface plasmon resonance (LSPR) peaks offered by the nature of nanorods (Rycenga et al., 2011; Li et al., 2017). Despite the rational preparation of AgNRs to realize its optimal SERS performance, intrinsic shortcomings of Ag nanoparticles including sensitivity degradation in severe measuring conditions and short shelf life still remain (Mai et al., 2012; Nuntawong et al., 2013; Bachenheimer et al., 2017). Moreover, the one-time use property of AgNRs makes substrates expensive which indicates the need to develop recyclable SERS substrates. These issues greatly restrict utilization of SERS as a universal technique. Fortunately, recent studies have shown that combining Ag nanoparticles with oxide was able to overcome these barriers by the virtue of unique properties of oxides (Kong et al., 2012; Wolosiuk et al., 2014; Chong et al., 2015).

On the other hand, considering that the appropriate analysis strategy is of crucial importance and the prerequisite to reach reliable chemical quantitative determinations, enormous quantitative analysis strategies were developed to minimize influences arising from variations of measuring conditions in order to obtain reliable data and further to provide the reasonable data analysis approach (Shen et al., 2015; Subaihi et al., 2016).

In this review, we cover the developments in AgNRs synthesis through oblique angle deposition method (OAD) to acquire sensitive, uniform, and reproducible SERS substrates. Then, approaches for AgNRs-oxide substrates preparation are introduced to achieve accurate control for the thickness of the oxide and to gain improvements in stability and recyclability with the merits of oxides. After surveying the recent progress in fabrication of AgNRs and AgNRs-oxide hybrids, in order to reach reliable SERS determinations, we then discuss three types of strategies which are commonly employed for chemical quantitative analysis: (1) external and internal method, (2) standard addition method, (3) multivariate data analysis. Later, to provide a clear understanding for readers, we further highlight SERS applications in the fields of food safety, environment safety, biosensing, and vapor sensing. At the end, we conclude with the challenges and potential opportunities in future SERS platform designs and utilizations.

SYNTHESIS AND PROPERTIES OF AGNRS-BASED NANOSTRUCTURES

Synthesis of AgNRs

High uniformity, superior sensitivity, and excellent reproducibility are always the most important targets for substrates preparations to allow SERS as a promising technique. Among numerous fabrication methods for AgNRs, oblique angle deposition (OAD) has been proved to be a straightforward approach to fabricate uniform and reproducible AgNRs which could also hold outstanding SERS sensitivity (Šubr et al., 2015). As shown in **Figure 1A**, OAD is a physical vapor deposition technique in which the incident vapor flux is deposited at a large incident angle θ (>70°) with respect to the substrate normal and Ag nanostructures with various morphologies and thicknesses can be readily obtained by simple control of the deposition angle and time (Liu et al., 2010; Ma et al., 2017). Specifically, substrates morphologies are dominated by a combination of atom shadowing effect and surface adatom diffusion effect (Negri and Dluhy, 2013). Taking account of the importance of AgNRs array's morphology on their SERS performance, critical parameters, such as incidence angle, temperature, and rotate rate during deposition process should be considered for optimizing SERS efficiency of substrates.

Slanted AgNRs is one of the commonest substrates fabricated by OAD technique, and their growth angle is expected to be positively correlated with the incident angle. Studies have shown that AgNRs tends to be well-separated and obtain stronger SERS sensitivity at larger deposition angle (Liu et al., 2010; Gao et al., 2018; Liao et al., 2018). Specifically, as shown in **Figure 1B**, Liu et al. further demonstrated that the enhancement factor (EFs) increases almost 1 order of magnitude as the deposition angle increases 2° by comparing EFs of AgNRs with similar length (Liu et al., 2010). Moreover, temperature exerts an impact on nanostructures' morphologies by influencing adatom diffusion. Hence, more considerations on temperature are required in nanostructure fabrication procedures, especially for materials with low melting temperature, such as Ag. Our group studied the effect of temperature on the morphology and SERS performance of AgNRs (Zhou et al., 2008). As shown in **Figures 1C,D**, well-separated AgNRs were obtained at a lower temperature, leading the better SERS performance. Singh et al. reported the cost-effective finding that AgNRs holding the maximum SERS sensitivity can be fabricated using less amount of Ag source at a lower temperature (Singh et al., 2012). In addition, the influence of rotate rate on the substrates morphology was investigated which showed that the formation of vertical nanorods were favorable at a higher rotation rate of substrate holder (Jen et al., 2015). Besides these experiment results, a simple hemisphere model was proposed to offer a theoretical route for analyzing the impact of crucial experiment factors in OAD method, such as incidence angle, incidence rate, substrate temperature, and substrate rotation rate on the morphology of nanostructures (Zhou et al., 2011b).

Although adjustments on the experiment conditions are able to provide straight AgNRs with the optimal SERS performance, the disadvantage that limited hotspots are generated in straight

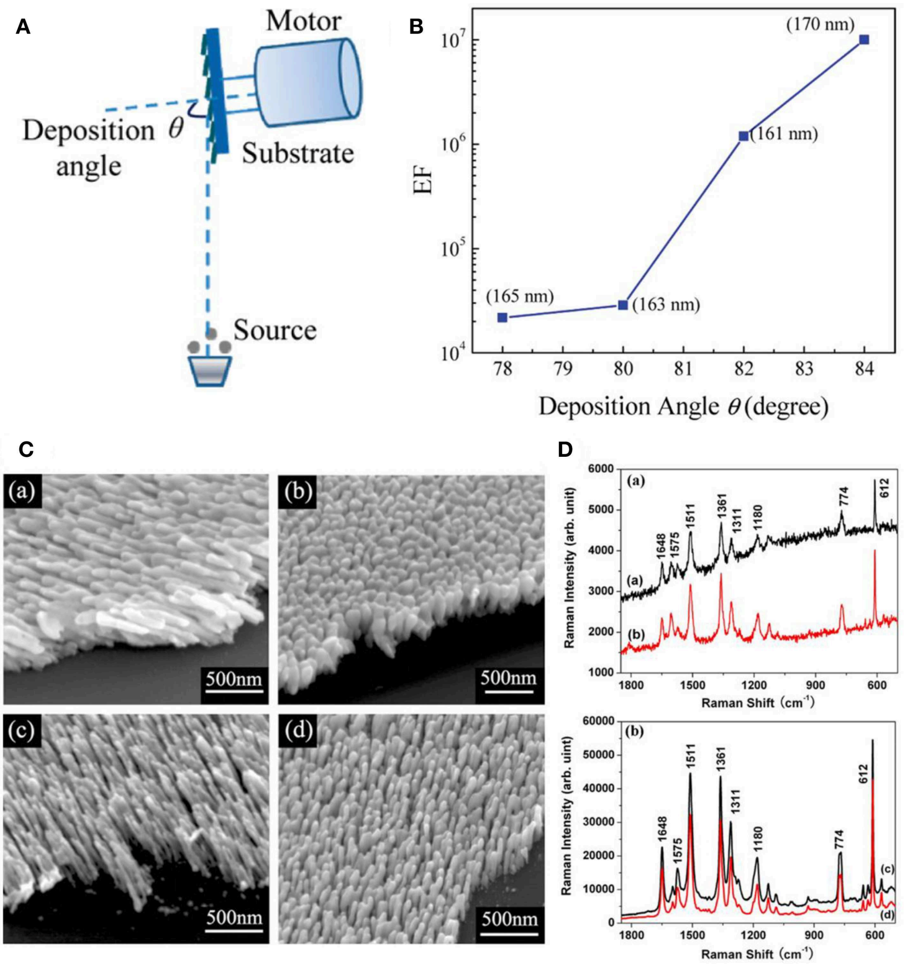

FIGURE 1 | (A) Schematic illustration of nanostructure fabrication via OAD. **(B)** SERS enhancement factor of AgNRs as a function of deposition angle with nanorods length fixed at 165 nm. Reprinted with permission from Liu et al. (2010) Copyright (2010) ACS publications. **(C)** SEM images of AgNRs deposited (a) at 120°C without substrate rotation; (b) at 120°C and substrate rotation at 0.2 rpm; (c) at −40°C without substrate rotation; (d) at −40°C and substrate rotation at 0.2 rpm; **(D)** SERS spectra of R6G on (a) joined AgNRs shown in **C** (a,b); and **(b)** separated AgNRs shown in **C** (c,d). Reprinted with permission from Zhou et al. (2008). Copyright (2008) IOP Publishing.

AgNRs still restricts the improvement in the substrate sensitivity. Therefore, more corners or curvatures are expected to be introduced within AgNRs array because they are regard as the hotspots which hold the extremely high electromagnetic field (Li et al., 2017). Recently, our group has been focused on the fabrication of multifold AgNRs via OAD in order to gain stronger SERS response. As shown in **Figures 2A,C**, AgNRs with multiple bends were successfully fabricated. Typically, after the fabrication of the first arm followed by a short cooling, the substrates holder was azimuthally rotated a certain angle to start deposition of the next arm. The numerical simulation was employed to compare EFs of V-shape and straight AgNRs with the same length, and the result (**Figure 2B**) showed that V-shape AgNRs exhibited stronger EFs in almost 90% cases under a 785 nm laser (Li et al., 2018). SERS performance of AgNRs as a function of the arm number N ($N \geq 3$) was also investigated. As illustrated in **Figure 2D**, SERS response elevated rapidly with the increase of the arm number N when $N \leq 5$ and the rate of enhancement slows down toward a plateau as N increases continuously (Zhou et al., 2011a). This trend should attributed to the combination result of "hotspots" amount, excitation light intensity reached to the "hot spot" layer, and optical absorbance of arm layers.

Synthesis of AgNRs-Oxide Hybrid Composites

Despite advances in optimizing AgNRs fabrications and their SERS performances, fatal drawbacks that come from intrinsic properties of AgNRs, such as susceptible to severe measuring conditions including high temperature, etchant solutions, and oxidants, still remain a problem to be addressed (Park and Day, 1986; Alarifi et al., 2011; Nuntawong et al., 2013). Therefore, SERS substrates combine high sensitivity with great stability are desirable toward real life applications. On the other hand, the high cost of AgNRs substrates and one-time use only property

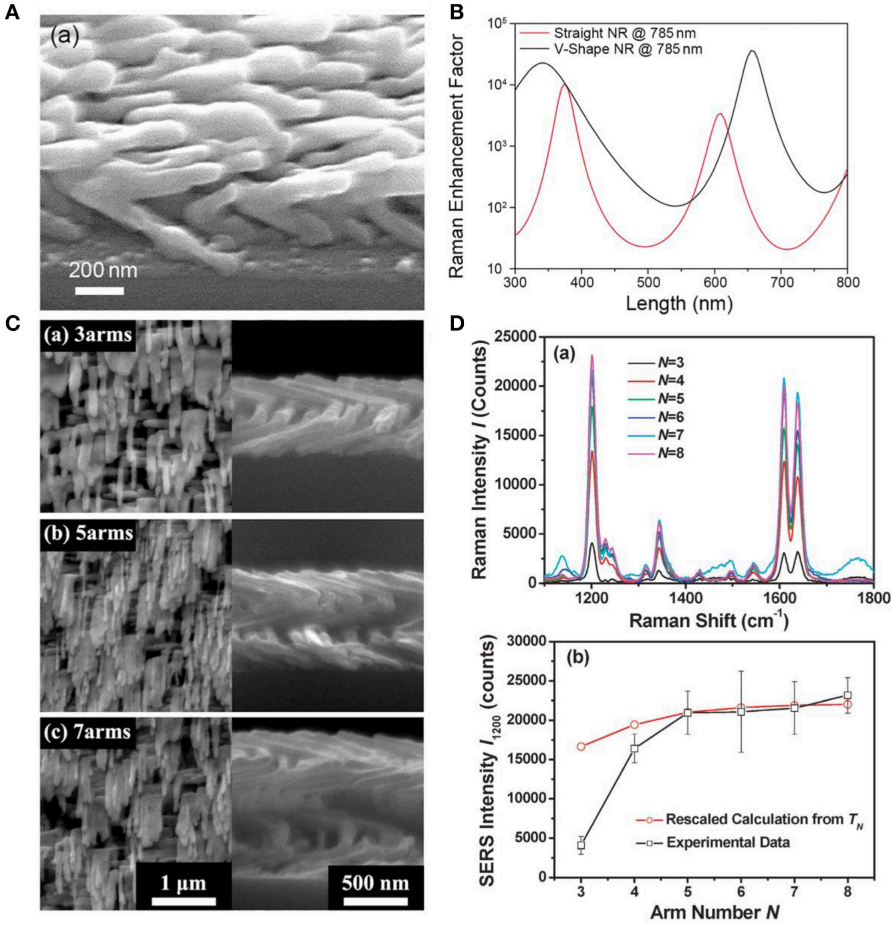

FIGURE 2 | (A) SEM image of the V-shaped AgNRs fabricated by the GLAD method. **(B)** Numerical simulations of Raman EFs for the V-shaped AgNR and the straight AgNR as a function of AgNRs total length under a 785 nm laser. Reproduced with permission from Li et al. (2018). Copyright (2018) RSC publications. **(C)** SEM images of helical AgNRs with arm number at (a) $N = 3$, (b) $N = 5$, and (c) $N = 7$. **(D)** (a) SERS spectra of trans-1,2-bis (4-pyridyl) ethylene on helical AgNRs with various arm numbers. (b) Plots of experimental peak intensities (□) and calculations (○) as a function of arm number *N*. Reprinted with permission from Zhou et al. (2011a). Copyright (2011) RSC publications.

hinder the widespread utilization of SERS technique. Given that incorporating AgNRs with oxides may bring unique properties to substrates by virtue of oxides (Li et al., 2017), in this section, we present the progress that have been made on the manipulation of AgNRs-oxides to achieve high stability and recyclability.

Oxide Coating

Although the oxide coating serves as a protective layer for AgNRs, the simultaneously increased distance between the plasmoinc active materials and analytes could lead to decreased EM enhancement for analytes. According to the studies, Raman signals of analytes within several nanometers from the plasmonic active materials are effectively boosted (Cardinal et al., 2017). Hence, precisely controlling the thickness of oxide coating is of significant importance to gain excellent SERS performance. Sol-gel method and atomic layer deposition (ALD) method are two approaches that are commonly employed to realize controllable thickness of oxide on AgNRs.

Sol-gel method provides a facile way to synthesis ultrathin oxide layer, such as TiO_2 and SiO_2 (Song et al., 2012; Du et al., 2014, 2015). Taking SiO_2 layer synthesis as an example, first, ethanol, DI water, $NH_3 \cdot H_2O$, and tetraethyl orthosilicate (TEOS) were mixed successively in a certain volume proportion to gain the SiO_2 sol–gel precursor. Later, AgNRs modified with citric groups was added to this SiO_2 sol–gel precursor solution and the thickness of SiO_2 was readily controlled by changing the reaction time. Finally, the resultant AgNRs-oxide was removed from the solution once the reaction completes, followed by washing steps. Song et al. demonstrated that the uniform and porous SiO_2 layer could be formed on individual AgNRs through this method (Song et al., 2012). As shown in **Figure 3A**, uniform SiO_2 layers were successfully coated on AgNRs and a linear function between SiO_2 layer thickness and the reaction time was further verified. However, in sol-gel method, SERS signals of citrate can be detected on prepared AgNRs-SiO_2 substrates, resulting in the possible interference to the analytes detections.

On the other hand, ALD strategy serves as an effective way for oxide coating on AgNRs with desired thickness through self-limiting surface reactions (Wiedmann et al., 2012). Taking Al_2O_3 as an example, ALD process primarily contains these steps: (1) AgNRs were placed into an ALD deposition chamber with trimethyl-aluminum (TMA, maintained at 150°C) and water (maintained at 40°C) as precursors. (2) TMA was pulsed into the chamber for 20ms followed by 10s nitrogen purging. (3) Later, water was pulsed into the chamber for 10 ms followed by 20 s nitrogen purging. Then, the uniform and ultrathin oxide layer with various thicknesses could be obtained by repeating the cycle times of step (2) and (3). HRTEM images of AgNRs coated by Al_2O_3 layer with different ALD cycles were shown in **Figure 3B**, and uniform Al_2O_3 layers were formed on AgNRs with its thickness increased linearly vs. the cycle time (Ma et al., 2015b). Besides, a few pinholes could be observed on AgNRs-Al_2O_3 with 1 ALD cycle time which disappeared as cycle times increased.

The two approaches mentioned above both demonstrate the possibility of fabricating ultrathin oxide with acceptable sacrifice in sensitivity and the linear correlations between oxide layer thickness and the reaction time/cycle time were further established which imply the potential to fabricate reproducible and sensitive AgNRs-oxide as the SERS platform (John et al., 2010; Song et al., 2012). Following these advancements, fascinating properties of AgNRs-oxide in aspects of stability and recyclability were explored with the aim to expand SERS to a broader application scope.

Stability

Up to date, a library of diverse findings were reported in the field of the stability improvement for AgNRs through oxide coating, and they are usually in three aspects: (1) temporal stability, (2) chemical stability, and (3) thermal stability.

Temporal stability

As shelf-time stability is the fundamental concern toward practical utilizations of SERS substrates, therefore, the mechanism for signal degradation of AgNRs in the ambient was studied by many researchers, leading a consensus that contaminants including sulfur, hydrocarbons, and oxygen were responsible for the SERS signals damping (Nuntawong et al., 2013; Bachenheimer et al., 2017). To pursue long temporal stability of substrates, Ag nanoparticles coated with oxides were estimated as SERS substrates. In the presence of the oxide layer, the contaminants diffusions from the air to the surface of AgNRs are effectively suppressed, resulting in great temporal stability improvement for substrates (Wolosiuk et al., 2014; Ma et al., 2015b; Zhao et al., 2016; Nguyen et al., 2017). For example, Nguyen et al. demonstrated that the thin shell of silica (∼1.5 nm) enabled SERS activity of Ag@SiO_2 nanocubes maintained at ∼90% over 12 weeks (Nguyen et al., 2017). Moreover, Ma et al. investigated the SERS sensitivity of AgNRs-Al_2O_3 with different thicknesses as a function of the storage time (Ma et al., 2015b). As shown in **Figure 4A**, the Al_2O_3 layers with different thicknesses were fabricated by simply adjusting their cycle times of ALD. SERS response of AgNRs wrapped by 1 cycle Al_2O_3 layer decreased ∼18% after 50 days in air, and SERS sensitivity of AgNRs coated with two or more Al_2O_3 cycles kept at the same level.

Chemical stability

The poor chemical stability of AgNRs in solutions mainly comes from their vulnerability to acids, halides and other etching chemicals that may impose the structural deterioration. To overcome this issue, chemical stabilities of Ag-oxides have been estimated by many researchers. For example, Du et al. reported that the oxide could serve as the anti-corrosion protective layer for Ag nanoplates and effectively retain their plasmonic property in salts, buffer, and oxidant solutions (NaCl, PBS, and H_2O_2) (Du et al., 2014). Ma et al. proved that 1 ALD cycle of Al_2O_3 layer was efficient to keep the morphology and SERS performance of AgNRs in NaCl solution (30 mM, 3 h) and H_2O_2 solution (2.2%, 0.5 h) (Ma et al., 2016a). Moreover, Hou et al. investigated the acid tolerance of AgNRs-HfO_2 by immersing them into 10 mM HCl solution. As shown in **Figure 4B**, AgNRs suffered from violent corrosion by HCl. In contrast, the morphology and SERS performance of AgNRs-HfO_2 remained the same, demonstrating the potential of AgNRs-HfO_2 substrate to be utilized in acid solution (Hou et al., 2016).

Thermal stability

As SERS performances of substrates are highly correlated with their shapes and sizes, it is vital to preserve their geometric shape during detection conditions especially for low melting temperature materials, such as silver. Studies demonstrated that dramatic morphologies changes and devastating sensitivity degradation were observed on Ag nanoparticle substrates under high temperature and enhanced thermal stability could be effectively obtained by integrating oxides into SERS substrates (Mai et al., 2012; Pinkhasova et al., 2013; Lou et al., 2014; Ma et al., 2015b). For example, Lou et al. proved that capping TiO_2 layer on AgNRs via PVD effectively protected AgNRs morphology up to at least 100°C (**Figure 5A**) (Lou et al., 2014). As shown in **Figure 5B**, they found that AgNRs started to coarsen once the TiO_2 layer was no longer present under high temperature. Besides, the uniform oxide layer coated on AgNRs not only proves the effectiveness to improve substrates thermal stability, but also shows the potential to further enhance the thermal stability of substrates by increasing the oxide layer thickness. For example, as shown in **Figures 5C,D**, both the morphology and SERS performance of AgNRs coated by one cycle of Al_2O_3 layer started to change when the temperature reached to 300°C, while that of AgNRs coated by two cycles of Al_2O_3 layer remained the same even at 400°C (Ma et al., 2015b).

Recyclability

Although remarkable advancements in integrating oxide with AgNRs for the purpose of stability improvement, the cost of substrates emerges as another non-negligible issue which could limit the commercial utilization of SERS technique. To overcome this problem, the physical approaches including solvent washing and heat treatment as well as the chemical approach, such as photocatalysis were usually employed toward realizing substrates recyclability (Lin et al., 2012; Hou et al., 2015b; Ma et al., 2015a;

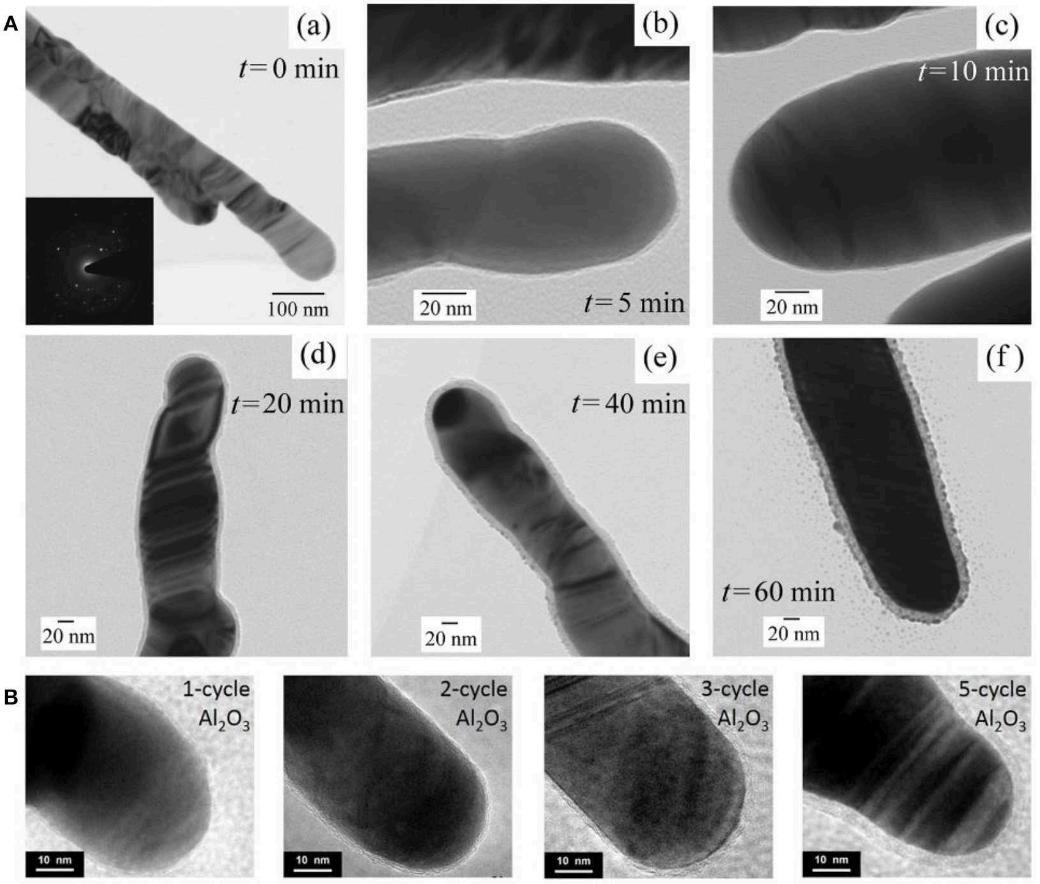

FIGURE 3 | (A) HRTEM images of AgNRs coated by SiO_2 as function of time by sol-gel method. (a) 0 min, (b) 5 min, (c) 10 min, (d) 20 min, (e) 40 min, (f) 60 min. Reprinted with permission from Song et al. (2012). Copyright (2012) ACS publications. **(B)** HRTEM images of AgNRs coated by Al_2O_3 with ALD cycles of 1, 2, 3, and 5. Reproduced with permission from Ma et al. (2015b).

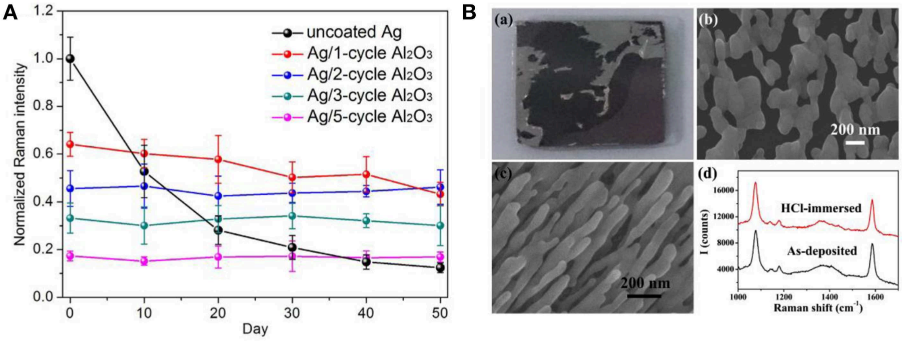

FIGURE 4 | (A) Normalized Raman intensities of methylene blue at 1,622 cm^{-1} on AgNRs and AgNRs coated by various layers Al_2O_3 vs. storage time. Reproduced with permission from Ma et al. (2015b). **(B)** Morphologies and SERS performance of AgNRs and AgNRs-HfO_2 after immersing into 10 mM HCl. (a) Images of AgNRs array on wafer. (b) SEM images of AgNRs. (c) SEM images of AgNRs-HfO_2 array. (d) SERS spectra of 1×10^{-5} M 4-Mercaptobenzoic acid obtained from AgNRs-HfO_2 before and after 10 mM HCl treatment. Reproduced with permission from Hou et al. (2016).

Weng et al., 2016; Botta et al., 2018b). For AgNRs substrates, due to its susceptibility to heat and UV illumination, solvent washing becomes the common approach to remove adsorbed molecules from substrates. For example, Botta et al. examined the feasibility of reusing AgNRs through a simple de-ionized water washing (Botta et al., 2018b). They found that analytes molecules could be

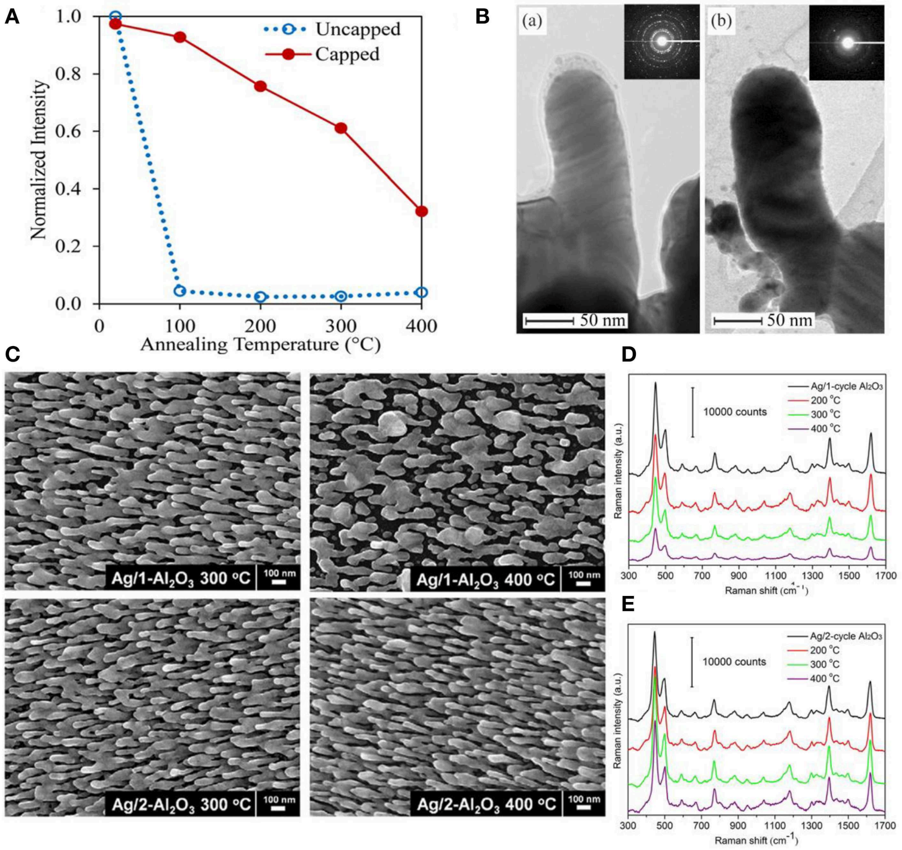

FIGURE 5 | (A) Normalized SERS intensity on capped and uncapped AgNRs as a function of annealing temperature. **(B)** TEM images of TiO_2 capped AgNRs after annealing at (a) 100°C for 10 min and (b) 200°C for 10 min. Reproduced with permission from Lou et al. (2014). Copyright (2014) AIP Publishing. **(C)** SEM images of AgNRs coated with Al_2O_3 layers at elevated temperatures. SERS spectra of methylene blue on AgNRs coated with 1 cycle Al_2O_3 layer **(D)** and 2 cycle Al_2O_3 layers **(E)** at elevated temperatures. Reproduced with permission from Ma et al. (2015b).

completely rinsed off from substrates and almost similar Raman signals re-appeared after analytes re-adsorbing on the substrates in the first three adsorption-desorption cycles. However, the reusability of AgNRs was found lost at the fourth repeated runs. Beside the solvent washing approach to remove analytes from substrates which should be universal to SERS substrates, the recyclability of AgNRs-oxide through heat treatment and photodegradation was investigated by our group. Ma et al. estimated the reusability of AgNRs-HfO_2 through heat treatment (Ma et al., 2016b). As shown in **Figure 6A**, no Raman signatures of MB was observed after AgNRs-HfO_2 were treated at 250°C for 30s which indicates their successful detachment from AgNR-HfO_2 substrates. Later, MB signatures re-appeared on substrates through re-adsorbing without losing its intensity for as many as 30 repeated cycles, indicating super reusability of AgNRs-HfO_2 through heat treatment by virtue of its robustness and thermal stability. Moreover, reusability of substrates obtained through photodegradation of analytes was estimated. AgNRs-TiO_2 was employed due to the self-cleaning property of TiO_2(Ma et al., 2015a). As shown in **Figure 6B**, AgNRs wrapped by 3 cycles of TiO_2 layer via ALD proved to be recyclable within 4 repeated runs by UV-illumination, and no damage on SERS sensitivity was observed. Moreover, Fe_2O_3-Ag hybrid was also demonstrated as the reusable SERS substrates to be recycled 5 times without losing its sensitivity with the aid of visible light (Weng et al., 2016).

QUANTITATIVE ANALYSIS STRATEGY

Benefitting from the advancements in the field of substrates fabrication, SERS substrates that possess numerous superior properties, such as excellent sensitivity, reproducibility, stability, and cost saving, have been successfully engineered. This has driven the thriving research in the field of quantitative analysis strategies to achieve reasonable and accurate SERS measurement. These strategies include: (1) external and internal method; (2) standard addition method; (3) multivariate data analysis.

External and Internal Method

External method is a straightforward approach for quantitative analysis which is based on the relationship between analytes concentration and its characteristic peak intensity/peak area. At submonolayer concentration, a linear correlation was always

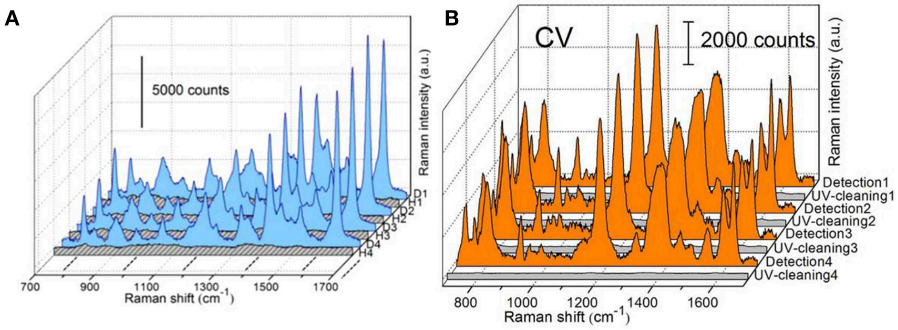

FIGURE 6 | (A) SERS spectra of methylene blue (MB) on AgNRs-HfO$_2$ during the repeated "detection (D)—heating (H)" process. Reproduced with permission from Ma et al. (2016b). Copyright (2016) ACS publications. **(B)** SERS spectra of crystal violet (CV) adsorbed on AgNRs-TiO$_2$ during the repeated "detection-UV cleaning" process. Reproduced with permission from Ma et al. (2015a).

observed and thereby established as the standard curve which was utilized to predict analytes concentration (Zhu et al., 2016; Rekha et al., 2018). However, SERS intensities can be interfered with many factors in practical SERS measurements, such as laser power variations and environmental changes, leading an unreliable result (Bell and Sirimuthu, 2008). Therefore, the internal method was proposed to minimize the interference effect. In this method, an internal standard (IS) was introduced into the measurement system, generating its SERS signals with which SERS signals of analytes were able to calibrate. For example, Ren's group employed the characteristic band of phosphate backbone as the internal standard signal to calibrate signals from each base of DNA in order to achieve a reliable determination for DNA structure (Xu et al., 2015). Moreover, embedding internal standard molecules into core-shell nanoparticles emerges as another strategy to effectively correct the signal fluctuations of targets and this strategy proved to be efficient to provide reliable results by many researchers (Joshi et al., 2014; Shen et al., 2015).

Standard Addition Method

The external and internal method depend on the well-established standard curve and a similar chemical component in the detection system as the standard solution is required to achieve accurate prediction of analytes. However, in practical applications, it is often hard to gain a prior knowledge concerning the testing solution which enables standard curve acquisition a difficult task. To overcome this problem, the standard additional method (SAM) was combined to the SERS analysis (Hidi et al., 2016; Westley et al., 2017). To utilize SAM, a series of analytes solutions with different concentrations were added into the sample whose composition is unknown. At trace levels, a linear correlation between the spiked analyte amount (x) and its characteristic peak/area intensity (y) should be observed which can be expressed as $y = mx + b$. In this equation, b represents the intensity of analytes initially existed in the sample and m is an indicator of intensity increment rate due to the addition of analytes. Conceptionally, the numerical value of m can be deduced from the linear relationship between the intensity increment of analytes with respect to its original value and the addition amount, and the numerical value of b is easily obtained by SERS measurement before the addition of analytes into the sample. Therefore, the initial amount of analytes in the sample can be obtained by the numerical value of b divided by m. For example, through establishing the correlation between the intensity increment and the addition amount, Zou et al. accurately predicted concentration of 2-naphthalenethiol (2-NaT) in the prepared binary solution (**Figure 7A**), and further employed this method for pollutants determinations in water (Zou et al., 2018). Westley et al. utilized this method to quantify uric acid in urine samples and compared results with high performance liquid chromatography (HPLC). As shown in **Figure 7B**, a good agreement was observed, indicating the reliability of this method (Westley et al., 2017).

Multivariate Date Analysis

Quantitative analysis strategies mentioned above use some characteristic peaks of analytes, which may fail to predict analytes concentrations in the case when peaks are overlapped and thereby make the accurate intensity acquisition a difficult task. This situation is common especially in multi-component systems. Therefore, more sophisticated algorithms were developed to allow multivariate date analysis by exploiting the whole spectrum or a subset of the spectral features.

Principle component analysis (PCA) is a well-established chemometrics strategy for multivariate data analysis with principles to reduce the dimensionality of multivariate data and to preserve most of the valuable variance (Goodacre et al., 2018). The spectra data are converted into a set of loadings and scores and the first score (PC1) contains the most natural variance of the data followed by the one which is of less importance. Based on the PCA scores, PCA is widely employed to differentiate different molecules in the field of biosensing (Shanmukh et al., 2008; Chen et al., 2012, 2016; Botta et al., 2018a). For example, Shanmukh et al. demonstrated that three different respiratory syncytial virus strains were able to be differentiated by PCA using their PCA scores as shown in **Figure 8A** (Shanmukh

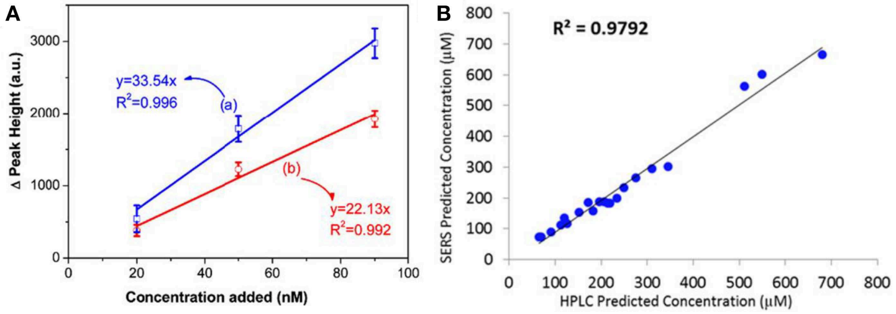

FIGURE 7 | (A) Linear correlation between Raman peak intensity increment at (a) 365 cm^{-1}, (b) 1379 cm^{-1} with the addition amount of 2-NaT ranging from 20 to 90 nM. Reproduced with permission from Zou et al. (2018). **(B)** The plot of comparison between results obtained from HPLC and SERS with the aid of SAM. Reproduced with permission from Westley et al. (2017). Copyright (2017) ACS publications.

et al., 2008). Recently, our group proposed a simple way to estimate compositions for binary and ternary chemical mixtures employing PCA and SERS (Hou et al., 2015a). As differences between the chemical compositions adsorbed on substrates and that in solution was neglected which is not suitable for most cases, we modified that method in order to provide a general route for the compositional analysis by considering the difference in chemicals' adsorption abilities in trace level solution (Zou et al., 2017). A standard mixture sample was introduced as the reference from which the adsorption kinetic factor of each component was obtained. Thus, predictions by PCA can be corrected by using these adsorption kinetic factors to eliminate the composition discrepancies between the substrates and the solution. As shown in **Figure 8B**, predictions for compositions in ternary solution were closer to their real value. Furthermore, the validity of this approach was demonstrated in binary, ternary, and quadruple chemical mixtures at trace level with the relative error of around 5%.

Partial least squares regression (PLSR) is another widely used chemometrics strategy for SERS analysis (Luo et al., 2016). In PLSR modeling process, intensities of all characteristic peaks were utilized and the redundant information would be eliminated by PCA. For example, Hou et al. reported quantitative analysis for single and binary food antiseptics by this strategy (Hou et al., 2016). Based on the regression relationship between potassium sorbate (PS) concentration and their corresponding SERS spectra, concentrations estimated by PLSR model were close to their actual value (**Figure 8C**). PLSR model was further employed for PS determinations in the binary solution of PS and sodium benzoate (SB). As shown in **Figure 8D**, predicted PS concentration values were around their actual values regardless of the different concentrations of SB in the measuring sample which contains the same concentration of PS.

APPLICATIONS

Advances in fabrications of Ag nanorods-based SERS substrates and the developments of quantitative analysis strategies have enabled SERS as a powerful technique to be utilized in various field. Herein, we highlight some SERS applications in the field of food safety, environment safety, biosensing, and vapor sensing.

Food Safety

Advantages of SERS, such as high sensitivity and easy operation have made it a powerful and promising technique for chemical detections in the field of food safety, such as beverages, pesticides, dairy production, and oil and so forth (Chen et al., 2015; Hou et al., 2016; Han et al., 2017; Roy et al., 2017; Jiang et al., 2018; Tian et al., 2018; Yao et al., 2018). For example, AgNRs substrate was employed for the rapid identification of gutter oil through capsaicin detection based on SERS (Tian et al., 2018). **Figure 9A** shows SERS spectra of the corn oil, extract liquor from corn oil which contains capsaicin, and capsaicin. The Raman bands from the extract liquor were similar to that of capsaicin, and distinct spectra differences between the corn oil and capsaicin were observed. Moreover, AgNRs substrate was employed to detect capsaicin in three gutter oils and **Figure 9B** shows their SERS spectra. Characteristic bands of capsaicin (807 and 1,264 cm^{-1}) were clearly observed in gutter oils which demonstrates the potential to quantify capsaicin in gutter oil. Han et al. reported a detection limit of 0.3 mg/L for sodium saccharin by SERS (Han et al., 2017). They further employed SERS to detect the sodium saccharin in four soft drinks (sprite, cola, fanta, and schweppes) which were pre-extracted by ethyl acetate and obvious signals attributed to the sodium saccharin could be observed. Then, they estimated the ability of SERS to detect sodium saccharin in these four soft drinks with results far below the national standard, indicating the potential of SERS in practical applications. However, these detections rely on the analytes adsorbed from the solution to the surface of substrates, which are hard to be adopted for pesticide determinations on fruits and vegetables. Therefore, Jiang et al. developed an approach to allow SERS measurements on curved surfaces (Jiang et al., 2018). As shown in **Figure 9C**, analytes were transferred from the surface of apple to the surface of AgNRs-Al_2O_3 through the transparent and adhesive tapes. A high extraction efficiency of analytes (91.6%) was achieved in this way and evident SERS spectra of tetramethylthiuram (TMTD) extract from various vegetables and fruits can be observed in **Figure 9D**.

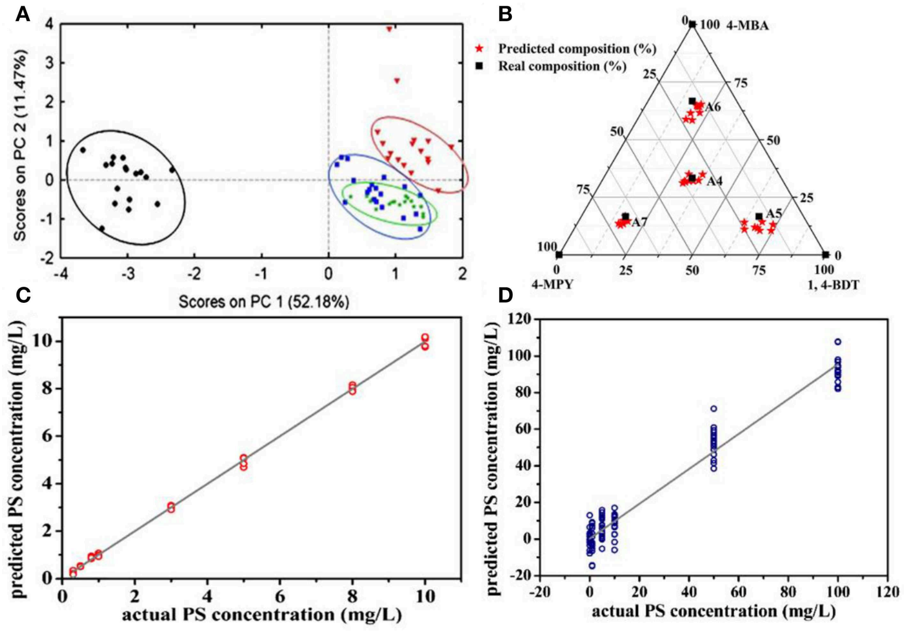

FIGURE 8 | (A) The plot of PCA scores obtained from SERS spectra of four different respiratory syncytial virus strains. Reproduced with permission from Shanmukh et al. (2008). Copyright (2008) Springer Nature. **(B)** The plot of real compositions of component in ternary solution vs. that obtained by correcting PCA predictions. Reproduced with permission from Zou et al. (2017). **(C)** The plot of PS concentration predicted by the PLSR model vs. their actual concentration. **(D)** The plot of PS concentration in binary solution predicted by the PLSR model vs. their actual concentration. Reproduced with permission from Hou et al. (2016).

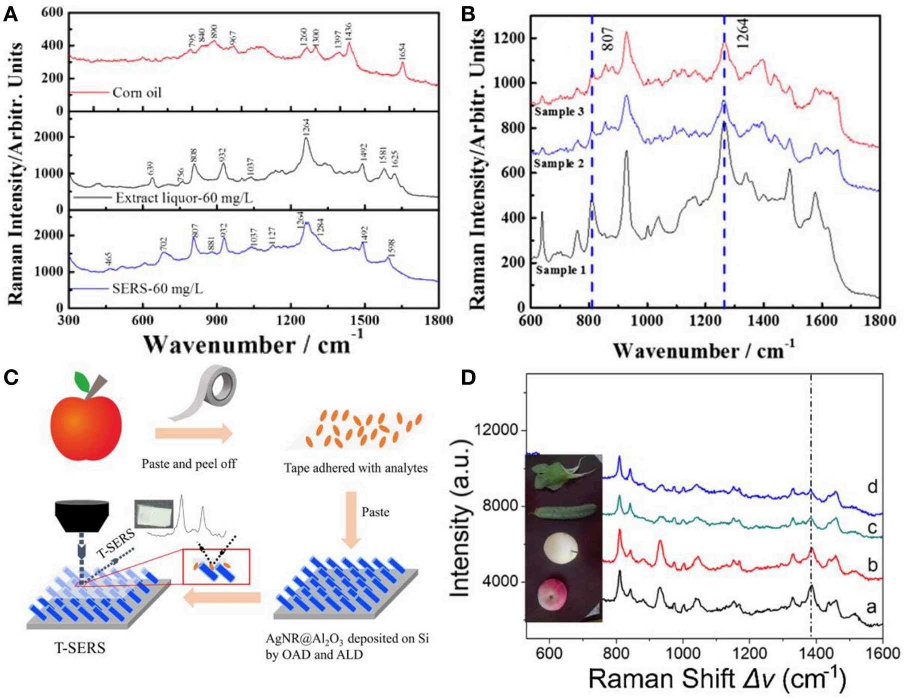

FIGURE 9 | (A) SERS spectra of corn oil, the extract liquor from corn oil by methanol, and capsaicin. **(B)** SERS spectra of the extract liquor from gutter oil samples. Reproduced with permission from Tian et al. (2018). Copyright (2018) John Wiley and Sons. **(C)** Schematic representation for pesticide extracted from the curved samples. **(D)** SERS spectra of TMTD extracted from different fruits and vegetables. Reproduced with permission from Jiang et al. (2018). Copyright (2018) ACS publications.

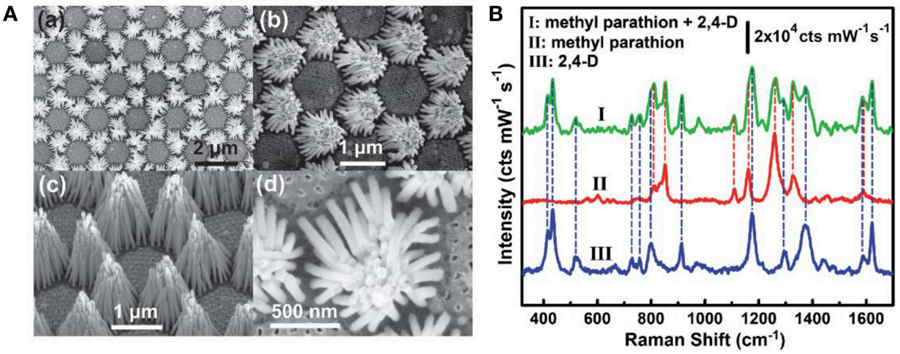

FIGURE 10 | (A) SEM images of AgNRs bundle arrays. (a,b) Top views with different magnifications. (c) Side view. (d) Enlarged top view of a single AgNRs bundle. **(B)** SERS spectra of methyl parathion and 2,4-dichlo-rophenoxyacetic acid. Reproduced with permission from Zhu et al. (2016). Copyright (2016) John Wiley and Sons.

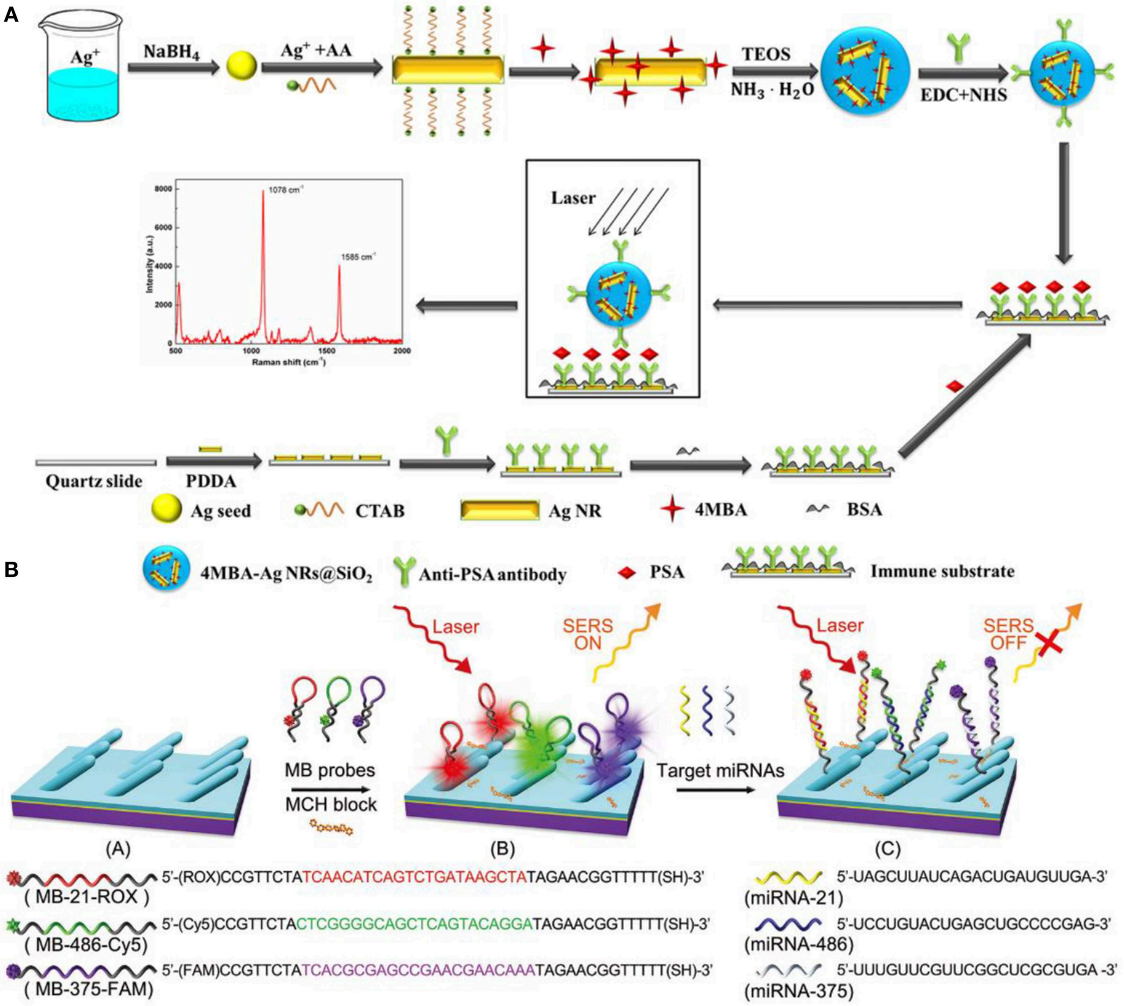

FIGURE 11 | (A) Schematic illustration of the preparation for SERS-based immunoassay protocol. Reproduced with permission from Lai et al. (2015). Copyright (2015) RSC publications. **(B)** Schematic illustration of the preparation and measuring protocol for multiple miRNAs sensor. Reproduced with permission from Song et al. (2016). Copyright (2016) RSC publications.

Environment Safety

Environment pollutions pose great challenges to human health nowadays and many of these pollutants at trace levels are able to be rapidly detected on SERS platforms, such as the phosphates, metal ions, and phenolic compounds, and so forth (Ma et al., 2014; Ji et al., 2015; Zhu et al., 2016; Song et al., 2017; Wang et al., 2018; Li et al., 2019). For example, Zhu et al. fabricated a hierarchically ordered AgNRs array on the Au/Cu substrate through the binary template assisted electrodeposition method (Zhu et al., 2016). On the substrates, AgNRs bundles were hexagonally organized with each bundle consisting of 30–45 AgNRs. With the aid of the capillary force, small gaps were formed between adjacent AgNRs (**Figure 10A**) which created the high density of hotspots and exhibited about 10^8 enhancement factor. Later, they estimated the ability of this chip to detect multiple pollutants in water and a mixture of methyl parathion (0.3×10^{-6} M) and 2,4-dichlo-rophenoxyacetic acid (2, 4-D) (2×10^{-6} M) was employed as the model molecules. As shown in **Figure 10B**, simultaneous detection of two analytes was achieved by observing different characteristic peaks of them which indicates SERS as a promising candidate in detection multiple organic pollutants in real world. Moreover, Song et al. developed a SERS sensor for Hg^{2+} in which AgNRs was modified with a single-strand oligonucleotide probe comprising of fifteen thymines (T) with a Cy5 dye labeled on the 3′-end and a thiol group at the 5′-end (Song et al., 2017). In the absence of Hg^{2+}, the oligonucleotide probes were in flabby state, allowing the closest distance between the Cy5 dye and AgNRs and generating the strongest SERS signals. Upon Hg^{2+} addition, this single-strand oligonucleotide probe transformed into double stranded complex with the formation of T-Hg^{2+}-T pairs, and this would keep the Cy5 dye away from AgNRs and decrease its SERS intensity.

Biosensing

As SERS provides abundant information in the molecular vibrational spectra with high sensitivity, it emerges as a powerful tool for biomolecules detections and diseases diagnosis (Lai et al., 2015; Chen et al., 2016; Song et al., 2016; Botta et al., 2018a; Zong et al., 2018). Immunoassays have been widely used for protein detections combining SERS. For example, Lai et al. utilized a sandwich immunoassay configuration which is composed of the immune probes/target protein/immune substrate to detect prostate-specific antigen (PSA) (Lai et al., 2015) (**Figure 11A**). In their work, silica-coated AgNRs aggregates with 4-mercaptobenzoic acid (4-MBA) molecules and AgNRs on slide substrates were both prepared and functionalized with anti-prostate specific antigen (anti-PSA) antibody to act as the immune probe and immune substrate, respectively. The sandwich detection system formed in the presence of PSA which remarkably boost the SERS intensity of 4-MBA molecules. Based on the correlations between PSA at different concentrations and characteristic SERS signals of 4-MBA, a limit of detection of 0.3 fg/ml was obtained. Moreover, the immunoassay protocol also exhibits good selectivity.

SERS also proves to be a powerful candidate in human diseases diagnosis. For example, Song et al designed a sensor for simultaneous detections of multiple cancer-related miRNAs in which AgNRs was modified with specific hairpin-shaped molecular beacons (MBs) (Song et al., 2016). As shown in **Figure 11B**, three kinds of MBs that contained different Raman reporter dyes and were complementary to miRNA-21, miRNA-486, miRNA-375 were prepared and modified on AgNRs via thiol group, leading the strongest specific SERS signals. After blocking the available regions for molecules on AgNRs by Mercaptohexanol (MCH), the sensor was employed for simultaneous detections of miRNA-21/486/375. Based on the signal reduction due to hybridization between MBs and the target analytes, the sensor exhibits excellent sensitivity and good specificity for the target analytes. Furthermore, because miRNA-21/486/375 were regarded as lung cancer-related biomarkers, the sensor was further utilized in patients' serum to achieve early detection of lung cancer. Ultra-sensitivity was obtained with the limits of detection of the three miRNAs are 393, 176, and 144 aM. Chen et al. reported the direct detection of malaria infected red blood cells by SERS (Chen et al., 2016). In their work, they observed distinct spectral differences between normal red blood cells (RBCs) and plasmodium falciparum infected RBCs (iRBCs) which were further analyzed by PCA to better illustrate the surface protein evolution for iRBC at different stages. In addition, the limit of detection for RBCs and iRBCs was measured in practical considerations and the ultimate sensitivity of a single cell can be reached based on the experiment results and theoretical calculation.

Vapor Sensing

SERS can also expand its utilization from the aquatic environment to the vapor phase which should find applications in chemical sensing for volatile organic chemicals and explosives (Shah et al., 2013; Kreno et al., 2014; He et al., 2015; Ma et al., 2016b; Oh et al., 2018). Ma et al. designed a real-time gas sensing platform for 2-naphthalenethiol (2-NaT) and 2-mercaptopyridine (2-MPy) employing AgNRs-HfO_2 substrates (Ma et al., 2016b). As shown in **Figure 12A**, 2-NaT and 2-MPy were dissolved in ethanol with various compositions which resulted in the different compositions of gas. AgNRs-HfO_2 was placed into the sealed chamber and analytes in gas phase were carried by N_2 gas to flow through the substrates. After exposure to 2-NaT gas for 40 min, SERS spectra of 20 ppb 2-NaT could be observed on substrates as shown in **Figure 12B**. Moreover, the mixture vapor gas of 2-NaT (600 ppb) and 2-MPy (600 ppb) was successfully recognized utilizing this platform which indicates its effectiveness for detections of vapor molecules. Similarly, Shah et al. reported a strategy for vapor detection of 4-aminobenzenethiol (4-ABT) (Shah et al., 2013). Due to the highly volatile of 4-ABT and its thiol group, 4-ABT vapor for different exposure times were successful detected on AgNRs. However, some molecules are weakly adsorbed on plasmonic materials, making it a difficult task to detect them. Thus, various molecules modifications on plasmonic materials were explored by researchers, such as metal–organic frameworks and thiol compounds (Lee et al., 2019). For example, Oh et al fabricated AgNRs and functionalized it with propanethiol (Oh et al., 2018). Due to the physical adsorption of benzene molecules

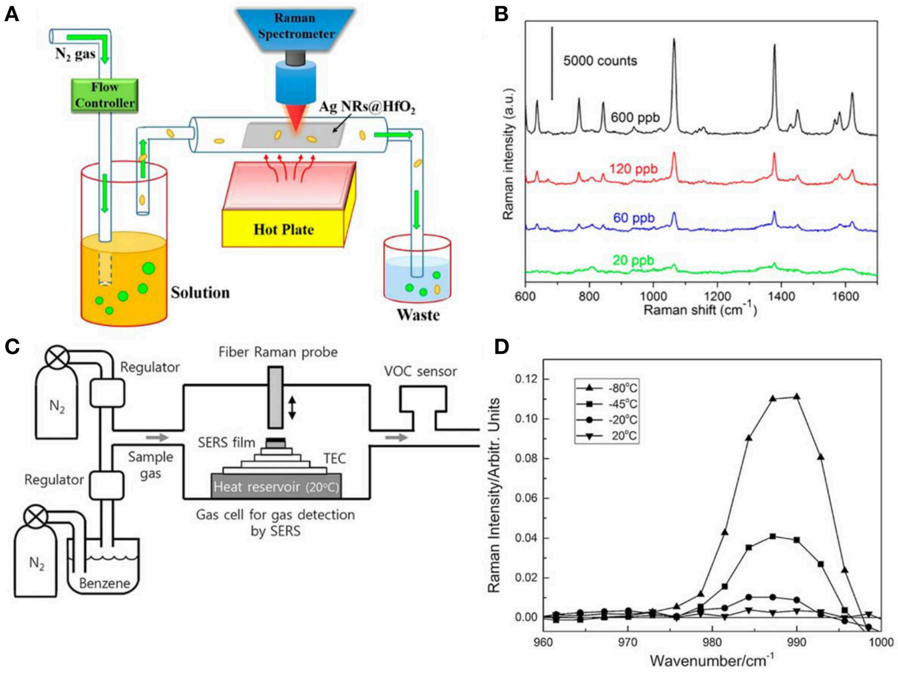

FIGURE 12 | (A) Schematic illustration of real time SERS-based vapor sensing platform. **(B)** SERS spectra of 2-naphthalenethiol with various concentrations employing platform shown in **(A)** after 40 min gas flow. Reproduced with permission from Ma et al. (2016b). Copyright (2016) ACS publications. **(C)** Schematic illustration of the platform integrated with thermoelectric cooler (TEC) for benzene vapor detection. **(D)** SERS spectra of benzene gas with concentration of 34 ppm from modified AgNRs at different temperature. Reproduced with permission from Oh et al. (2018). Copyright (2018) John Wiley and Sons.

to propanethiol, SERS spectra of benzene in vapor phase were successfully observed on substrates and the detection ability of this sensor was found ∼1 ppm at room temperature with 120 s acquisition time. To further decrease the limit of detection, they designed a SERS-based benzene gas detection apparatus in which thermoelectric cooler was integrated for the purpose of deep cooling of substrates (**Figure 12C**). SERS spectra of benzene gas with concentration of 34 ppm were obtained from modified AgNRs at different temperatures. As shown in **Figure 12D**, lower temperature for substrates enhanced Raman intensity of benzene obviously. They further found that sensitivity of the gas sensor for benzene greatly improved from ppm to ppb level when the substrate was cooled down from room temperature to −80°C, and they attributed this great sensitivity improvement to the enhancement of the amount of gas adsorption resulted from the cooling effect of substrates.

CONCLUSIONS AND PERSPECTIVE

In this review, we introduce advancements in AgNRs preparation through OAD technique that help guide rational manipulation of SERS substrates to acquire superior sensitivity, high uniformity, and excellent reproducibility. Considering the intrinsic fatal drawbacks of AgNRs, our review covers approaches to integrate oxides with AgNRs with the aim to endow SERS substrates with better stability and recyclability and to allow SERS technique be suitable for a broader application scope. Moreover, accompanied by these significant progress in substrates fabrications, three different quantitative analysis strategies were developed and we discuss them in detail to gain a reasonable and accurate data analysis. Furthermore, we highlight SERS applications in the fields of food safety, environment safety, biosensing, and vapor sensing, demonstrating the potential of SERS as a versatile and promising technique.

Although remarkable progress have been made on substrates to pursue better SERS performance and various quantitative analysis strategies were established to obtain reliable results, many challenges still remain to be addressed. First, despite that thriving researches in substrates manipulation enable the realization of improved SERS sensitivity down to even single-molecule level, single molecule detection sensitivity in complex matrix especially the biological system remains challenging. Trapping the molecules of interest to the hotspots by surface modification of substrates emerges as a promising strategy to solve this issue as it can simultaneously enhance SERS detection sensitivity and avoid incorrect SERS information brought by the interference molecules. However, effective surface modification approaches are still limited. Therefore, further advancement in the surface modification to precisely control analytes close to the hotspots are expected.

The bi-functional hybrid that incorporating catalysts (Au, Pd) with AgNRs-based substrates combines the merits of the abundant molecules information brought by SERS and catalytic activities provided by the catalyst, enabling it as a promising platform to monitor catalytic reactions *in situ* and to elucidate the catalytic mechanism. However, current studies related to this field are mainly focused on the hybrids manipulations to obtain optimized SERS sensitivity and catalytic activity, and SERS monitoring for catalytic reactions are limited to only a few model systems, such as reduction of 4-nitrothiophenol to 4-aminothiophenol and oxidation of 4-aminothiophenol to trans-4,4′-dimercaptoazobenzene. Therefore, more catalytic reactions monitored by SERS need to be explored to help uncover the reaction mechanism and to fully exploit the potential of bifunctional hybrid systems. Moreover, while employing SERS as a tool to monitor dynamic processes including catalytic reactions and biological processes, high time resolution is of great importance to provide detailed information about the process, especially for reactions occurred at a time scale of ms or dynamic SERS measurement of a living cell. Thus, more efforts are needed to improve the time resolution of SERS technology.

AUTHOR CONTRIBUTIONS

SZ and ZZ wrote the manuscript. LM, JL, YL, and DZ provided critical feedback and helped revision of the manuscript.

ACKNOWLEDGMENTS

The authors are grateful to the financial support from the National Natural Science Foundation of China (Grant No. 51761145045 and No. 51572148) and the Tsinghua University Initiative Scientific Research Program.

REFERENCES

Alarifi, H., Hu, A., Yavuz, M., and Zhou, Y. N. (2011). Silver nanoparticle paste for low-temperature bonding of copper. *J. Electron. Mater.* 40, 1394–1402. doi: 10.1007/s11664-011-1594-0

Bachenheimer, L., Scherzer, R., Elliott, P., Stagon, S., Gasparov, L., and Huang, H. (2017). Degradation mechanism of Ag nanorods for surface enhanced Raman spectroscopy. *Sci. Rep.* 7:16282. doi: 10.1038/s41598-017-16580-2

Bell, S. E. J., and Sirimuthu, N. M. S. (2008). Quantitative surface-enhanced Raman spectroscopy. *Chem. Soc. Rev.* 37:1012. doi: 10.1039/b705965p

Botta, R., Chindaudom, P., Eiamchai, P., Horprathum, M., Limwichean, S., Chananonnawathorn, C., et al. (2018a). Tuberculosis determination using SERS and chemometric methods. *Tuberculosis (Edinb).* 108, 195–200. doi: 10.1016/j.tube.2017.12.008

Botta, R., Eiamchai, P., Horprathum, M., Limwichean, S., Chananonnawathorn, C., Patthanasettakul, V., et al. (2018b). Investigation of silver nanorods as reusable SERS-active substrates for trace level detection of 2-MIB volatile organic compound. *Sens. Actuat. B Chem.* 271, 122–127. doi: 10.1016/j.snb.2018.05.110

Cardinal, M. F., Vander Ende, E., Hackler, R. A., McAnally, M. O., Stair, P. C., Schatz, G. C., et al. (2017). Expanding applications of SERS through versatile nanomaterials engineering. *Chem. Soc. Rev.* 46, 3886–3903. doi: 10.1039/c7cs00207f

Chen, F., Flaherty, B. R., Cohen, C. E., Peterson, D. S., and Zhao, Y. (2016). Direct detection of malaria infected red blood cells by surface enhanced Raman spectroscopy. *Nanomedicine* 12, 1445–1451. doi: 10.1016/j.nano.2016.03.001

Chen, J., Huang, Y.-W., and Zhao, Y. (2015). Detection of polycyclic aromatic hydrocarbons from cooking oil using ultra-thin layer chromatography and surface enhanced Raman spectroscopy. *J. Mater. Chem. B* 3, 1898–1906. doi: 10.1039/c4tb01632g

Chen, Y., Chen, G., Zheng, X., He, C., Feng, S., Chen, Y., et al. (2012). Discrimination of gastric cancer from normal by serum RNA based on surface-enhanced Raman spectroscopy (SERS) and multivariate analysis. *Med. Phys.* 39, 5664–5668. doi: 10.1118/1.4747269

Chinnakkannu Vijayakumar, S., Venkatakrishnan, K., and Tan, B. (2017). SERS active nanobiosensor functionalized by self-assembled 3D nickel nanonetworks for glutathione detection. *Acs Appl. Mater. Interfaces* 9, 5077–5091. doi: 10.1021/acsami.6b13576

Chong, X., Zhao, B., Li, R., Ruan, W., and Yang, X. (2015). Photocatalytic degradation of rhodamine 6G on Ag modified TiO_2 nanotubes: surface-enhanced Raman scattering study on catalytic kinetics and substrate recyclability. *Colloid Surf. A* 481, 7–12. doi: 10.1016/j.colsurfa.2015.04.021

Chook, S. W., Yau, S. X., Chia, C. H., Chin, S. X., and Zakaria, S. (2017). Carboxylated-nanoncellulose as a template for the synthesis of silver nanoprism. *Appl. Surf. Sci.* 422, 32–38. doi: 10.1016/j.apsusc.2017.05.242

Ding, S.-Y., Yi, J., Li, J.-F., Ren, B., Wu, D.-Y., Panneerselvam, R., et al. (2016). Nanostructure-based plasmon-enhanced Raman spectroscopy for surface analysis of materials. *Nat. Rev. Mater.* 1:16021. doi: 10.1038/natrevmats.2016.21

Ding, S. Y., You, E. M., Tian, Z. Q., and Moskovits, M. (2017). Electromagnetic theories of surface-enhanced Raman spectroscopy. *Chem. Soc. Rev.* 46, 4042–4076. doi: 10.1039/c7cs00238f

Du, P., Jing, P., Li, D., Cao, Y., Liu, Z., and Sun, Z. (2015). Plasmonic Ag@oxide nanoprisms for enhanced performance of organic solar cells. *Small* 11, 2454–2462. doi: 10.1002/smll.201402757

Du, P., Ma, L., Cao, Y., Li, D., Liu, Z., Wang, Z., et al. (2014). Stable Ag@oxides nanoplates for surface-enhanced Raman spectroscopy of amino acids. *Acs Appl. Mater. Interfaces* 6, 8853–8858. doi: 10.1021/am501637d

Gao, R., Zhang, Y., Zhang, F., Guo, S., Wang, Y., Chen, L., et al. (2018). SERS polarization-dependent effects for an ordered 3D plasmonic tilted silver nanorod array. *Nanoscale* 10, 8106–8114. doi: 10.1039/c8nr01198b

Goodacre, R., Graham, D., and Faulds, K. (2018). Recent developments in quantitative SERS: moving towards absolute quantification. *TrAC Trends Anal. Chem.* 102, 359–368. doi: 10.1016/j.trac.2018.03.005

Han, C., Yao, Y., Wang, W., Qu, L., Bradley, L., Sun, S., et al. (2017). Rapid and sensitive detection of sodium saccharin in soft drinks by silver nanorod array SERS substrates. *Sens. Actuat. B Chem.* 251, 272–279. doi: 10.1016/j.snb.2017.05.051

Han, Q., Zhang, C., Gao, W., Han, Z., Liu, T., Li, C., et al. (2016). Ag-Au alloy nanoparticles: synthesis and *in situ* monitoring SERS of plasmonic catalysis. *Sens. Actuat. B Chem.* 231, 609–614. doi: 10.1016/j.snb.2016.03.068

He, X., Wang, H., Li, Z., Chen, D., Liu, J., and Zhang, Q. (2015). Ultrasensitive SERS detection of trinitrotoluene through capillarity-constructed reversible hot spots based on ZnO-Ag nanorod hybrids. *Nanoscale* 7, 8619–8626. doi: 10.1039/c4nr07655a

Hidi, I. J., Jahn, M., Weber, K., Bocklitz, T., Pletz, M. W., Cialla-May, D., et al. (2016). Lab-on-a-chip-surface enhanced Raman scattering combined with the standard addition method: toward the quantification of nitroxoline in spiked human urine samples. *Anal. Chem.* 88, 9173–9180. doi: 10.1021/acs.analchem.6b02316

Hou, M., Huang, Y., Ma, L., and Zhang, Z. (2015a). Compositional analysis of ternary and binary chemical mixtures by surface-enhanced Raman scattering at trace levels. *Nanoscale Res. Lett.* 10:437. doi: 10.1186/s11671-015-1142-6

Hou, M., Huang, Y., Ma, L., and Zhang, Z. (2015b). Sensitivity and reusability of SiO_2 NRs@ Au NPs SERS substrate in trace monochlorobiphenyl detection. *Nanoscale Res. Lett.* 10:444. doi: 10.1186/s11671-015-1147-1

Hou, M., Huang, Y., Ma, L., and Zhang, Z. (2016). Quantitative analysis of single and mix food antiseptics basing on SERS spectra with PLSR method. *Nanoscale Res. Lett.* 11:296. doi: 10.1186/s11671-016-1507-5

Jen, Y. J., Chan, S., Huang, J. W., Jheng, C. Y., and Liu, W. C. (2015). Self-shadowing deposited pure metal nanohelix arrays and SERS application. *Nanoscale Res. Lett.* 10:498. doi: 10.1186/s11671-015-1205-8

Ji, W., Song, W., Tanabe, I., Wang, Y., Zhao, B., and Ozaki, Y. (2015). Semiconductor-enhanced Raman scattering for highly robust SERS sensing: the case of phosphate analysis. *Chem. Commun.* 51, 7641–7644. doi: 10.1039/c5cc02395e

Jiang, J., Zou, S., Ma, L., Wang, S., Liao, J., and Zhang, Z. (2018). Surface-enhanced Raman scattering detection of pesticide residues using transparent adhesive tapes and coated silver nanorods. *Acs Appl. Mater. Interfaces* 10, 9129–9135. doi: 10.1021/acsami.7b18039

John, J. F., Mahurin, S., Dai, S., and Sepaniak, M. J. (2010). Use of atomic layer deposition to improve the stability of silver substrates for *in situ*, high-temperature SERS measurements. *J. Raman Spectrosc.* 41, 4–11. doi: 10.1002/jrs.2395

Joshi, P., Zhou, Y., Ahmadov, T. O., and Zhang, P. (2014). Quantitative SERS-based detection using Ag–Fe_3O_4 nanocomposites with an internal reference. *J. Mater. Chem. C* 2, 9964–9968. doi: 10.1039/c4tc01550a

Kambhampati, P., Child, C. M., Foster, M. C., and Campion, A. (1998). On the chemical mechanism of surface enhanced Raman scattering: experiment and theory. *J. Chem. Phys.* 108, 5013–5026. doi: 10.1063/1.475909

Ke, Y., Meng, G., Huang, Z., and Zhou, N. (2017). Electrosprayed large-area membranes of Ag-nanocubes embedded in cellulose acetate microspheres as homogeneous SERS substrates. *J. Mater. Chem. C* 5, 1402–1408. doi: 10.1039/C6TC04579K

Kim, W., Lee, S. H., Ahn, Y. J., Lee, S. H., Ryu, J., Choi, S. K., et al. (2018). A label-free cellulose SERS biosensor chip with improvement of nanoparticle-enhanced LSPR effects for early diagnosis of subarachnoid hemorrhage-induced complications. *Biosens. Bioelectron.* 111, 59–65. doi: 10.1016/j.bios.2018.04.003

Kong, X., Yu, Q., Zhang, X., Du, X., Gong, H., and Jiang, H. (2012). Synthesis and application of surface enhanced Raman scattering (SERS) tags of Ag@SiO_2 core/shell nanoparticles in protein detection. *J. Mater. Chem.* 22:7767. doi: 10.1039/c2jm16397g

Kreno, L. E., Greeneltch, N. G., Farha, O. K., Hupp, J. T., and Van Duyne, R. P. (2014). SERS of molecules that do not adsorb on Ag surfaces: a metal-organic framework-based functionalization strategy. *Analyst* 139, 4073–4080. doi: 10.1039/c4an00413b

Lai, W., Zhou, J., Liu, Y., Jia, Z., Xie, S., Petti, L., et al. (2015). 4MBA-labeled Ag-nanorod aggregates coated with SiO_2: synthesis, SERS activity, and biosensing applications. *Anal. Methods* 7, 8832–8838. doi: 10.1039/c5ay01886b

Lee, H. K., Lee, Y. H., Koh, C. S. L., Phan-Quang, G. C., Han, X., Lay, C. L., et al. (2019). Designing surface-enhanced Raman scattering (SERS) platforms beyond hotspot engineering: emerging opportunities in analyte manipulations and hybrid materials. *Chem. Soc. Rev.* 48, 731–756. doi: 10.1039/c7cs00786h

Li, C., Peng, Y., Wang, H., Liang, A., and Jiang, Z. (2019). A nanosol SERS method for quantitative analysis of trace potassium based on aptamer recognition and silver nanorod catalysis of Ag(I)-glucose reaction. *Sens. Actuat. B Chem.* 281, 53–59. doi: 10.1016/j.snb.2018.10.079

Li, J., Fan, Y., Xue, X., Ma, L., Zou, S., Fei, Z., et al. (2018). Fabrication and simulation of V-shaped Ag nanorods as high-performance SERS substrates. *Phys. Chem. Chem. Phys.* 20, 25623–25628. doi: 10.1039/c8cp05533e

Li, J.-F., Zhang, Y.-J., Ding, S.-Y., Panneerselvam, R., and Tian, Z.-Q. (2017). Core–shell nanoparticle-enhanced Raman spectroscopy. *Chem. Rev.* 117, 5002–5069. doi: 10.1021/acs.chemrev.6b00596

Liao, Y., Huang, J., Huang, X., and Jiang, S. (2018). Morphological and near-field properties of silver columnar thin film for surface-enhanced Raman scattering. *J. Nanosci. Nanotechnol.* 18, 2803–2810. doi: 10.1166/jnn.2018.14539

Lin, Y., Bunker, C. E., Fernando, K. A., and Connell, J. W. (2012). Aqueously dispersed silver nanoparticle-decorated boron nitride nanosheets for reusable, thermal oxidation-resistant surface enhanced Raman spectroscopy (SERS) devices. *ACS Appl. Mater. Interfaces* 4, 1110–1117. doi: 10.1021/am201747d

Liu, Y. J., Chu, H. Y., and Zhao, Y. P. (2010). Silver nanorod array substrates fabricated by oblique angle deposition: morphological, optical, and SERS characterizations. *J. Phys. Chem. C* 114, 8176–8183. doi: 10.1021/jp1001644

Lou, B., Elliott, P., Stagon, S., and Huang, H. (2014). Enhanced thermal stability of Ag nanorods through capping. *Appl. Phys. Lett.* 26:241. doi: 10.1063/1.4902829

Luo, H., Huang, Y., Lai, K., Rasco, B. A., and Fan, Y. (2016). Surface-enhanced Raman spectroscopy coupled with gold nanoparticles for rapid detection of phosmet and thiabendazole residues in apples. *Food Control* 68, 229–235. doi: 10.1016/j.foodcont.2016.04.003

Ma, L., Huang, Y., Hou, M., Li, J., Xie, Z., and Zhang, Z. (2016a). Pinhole-containing, subnanometer-thick Al_2O_3 shell-coated Ag nanorods as practical substrates for quantitative surface-enhanced Raman scattering. *J. Phys. Chem. C* 120, 606–615. doi: 10.1021/acs.jpcc.5b11043

Ma, L., Huang, Y., Hou, M., Xie, Z., and Zhang, Z. (2015a). Ag nanorods coated with ultrathin TiO_2 shells as stable and recyclable SERS substrates. *Sci. Rep.* 5:15442. doi: 10.1038/srep15442

Ma, L., Huang, Y., Hou, M., Xie, Z., and Zhang, Z. (2015b). Silver nanorods wrapped with ultrathin Al_2O_3 layers exhibiting excellent SERS sensitivity and outstanding SERS stability. *Sci. Rep.* 5:12890. doi: 10.1038/srep12890

Ma, L., Li, J., Zou, S., and Zhang, Z. (2017). Ag nanorods-oxide hybrid array substrates: synthesis, characterization, and applications in surface-enhanced Raman scattering. *Sensors* 17:1895. doi: 10.3390/s17081895

Ma, L., Wu, H., Huang, Y., Zou, S., Li, J., and Zhang, Z. (2016b). High-performance real-time SERS detection with recyclable Ag nanorods@HfO_2 substrates. *ACS Appl. Mater. Interfaces* 8, 27162–27168. doi: 10.1021/acsami.6b10818

Ma, P., Liang, F., Wang, D., Yang, Q., Ding, Y., Yu, Y., et al. (2014). Ultrasensitive determination of formaldehyde in environmental waters and food samples after derivatization and using silver nanoparticle assisted SERS. *Microchim. Acta* 182, 863–869. doi: 10.1007/s00604-014-1400-9

Mai, F. D., Yang, K. H., Liu, Y. C., and Hsu, T. C. (2012). Improved stabilities on surface-enhanced Raman scattering-active Ag/Al_2O_3 films on substrates. *Analyst* 137, 5906–5912. doi: 10.1039/c2an35829h

Negri, P., and Dluhy, R. A. (2013). Ag nanorod based surface-enhanced Raman spectroscopy applied to bioanalytical sensing. *J. Biophotonics* 6, 20–35. doi: 10.1002/jbio.201200133

Nguyen, M. K., Su, W. N., Chen, C. H., Rick, J., and Hwang, B. J. (2017). Highly sensitive and stable Ag@SiO_2 nanocubes for label-free SERS-photoluminescence detection of biomolecules. *Spectrochim. Acta A Mol. Biomol. Spectrosc.* 175, 239–245. doi: 10.1016/j.saa.2016.12.024

Nuntawong, N., Eiamchai, P., Wong-ek, B, Horprathum, M., Limwichean, K., Patthanasettakul, V., et al. (2013). Shelf time effect on SERS effectiveness of silver nanorod prepared by OAD technique. *Vacuum* 88, 23–27. doi: 10.1016/j.vacuum.2012.08.006

Oh, M.-K., De, R., and Yim, S-Y. (2018). Highly sensitive VOC gas sensor employing deep cooling of SERS film. *J. Raman Spectrosc.* 49, 800–809. doi: 10.1002/jrs.5355

Park, H. S., and Day, D. E. (1986). Corrosion of evaporated Ag films on glass by saturated water vapor. *Solar Energy Mater.* 13, 351–365. doi: 10.1016/0165-1633(86)90083-3

Pinkhasova, P., Chen, H., Verhoeven, M. W. G. M., Sukhishvili, S., and Du, H. (2013). Thermally annealed Ag nanoparticles on anodized aluminium oxide for SERS sensing. *RSC Adv.* 3:17954. doi: 10.1039/c3ra43808b

Rekha, C. R., Nayar, V. U., and Gopchandran, K. G. (2018). Synthesis of highly stable silver nanorods and their application as SERS substrates. *J. Sci.* 3, 196–205. doi: 10.1016/j.jsamd.2018.03.003

Roy, A., Sahoo, R., Chowdhury, J., Bhattacharya, T. S., Agarwal, R., and Pal, T. (2017). Directional growth of Ag nanorod from polymeric silver cyanide: a potential substrate for concentration dependent SERS signal enhancement leading to melamine detection. *Spectrochim. Acta A Mol. Biomol. Spectrosc.* 183, 402–407. doi: 10.1016/j.saa.2017.04.074

Rycenga, M., Cobley, C. M., Zeng, J., Li, W., Moran, C. H., Zhang, Q., et al. (2011). Controlling the synthesis and assembly of silver nanostructures for plasmonic applications. *Chem. Rev.* 111, 3669–3712. doi: 10.1021/cr100275d

Shah, P., Ju, D., Niu, X., and Sarangan, A. M. (2013). Vapor phase sensing using metal nanorod thin films grown by cryogenic oblique angle deposition. *J. Sensors* 2013, 1–6. doi: 10.1155/2013/823041

Shanmukh, S., Jones, L., Zhao, Y. P., Driskell, J. D., Tripp, R. A., and Dluhy, R. A. (2008). Identification and classification of respiratory syncytial virus (RSV) strains by surface-enhanced Raman spectroscopy and multivariate statistical techniques. *Anal. Bioanal. Chem.* 390, 1551–1555. doi: 10.1007/s00216-008-1851-0

Shen, W., Lin, X., Jiang, C., Li, C., Lin, H., Huang, J., et al. (2015). Reliable quantitative SERS analysis facilitated by core-shell nanoparticles with embedded internal standards. *Angew. Chem. Int. Ed.* 54, 7308–7312. doi: 10.1002/anie.201502171

Singh, J. P., Lanier, T. E., Zhu, H., Dennis, W. M., Tripp, R. A., and Zhao, Y. (2012). Highly sensitive and transparent surface enhanced Raman scattering substrates made by active coldly condensed Ag nanorod arrays. *J. Phys. Chem. C* 116, 20550–20557. doi: 10.1021/jp305061s

Song, C., Chen, J., Abell, J. L., Cui, Y., and Zhao, Y. (2012). Ag-SiO_2 core-shell nanorod arrays: morphological, optical, SERS, and wetting properties. *Langmuir* 28, 1488–1495. doi: 10.1021/la203772u

Song, C., Yang, B., Zhu, Y., Yang, Y., and Wang, L. (2017). Ultrasensitive sliver nanorods array SERS sensor for mercury ions. *Biosens. Bioelectron.* 87, 59–65. doi: 10.1016/j.bios.2016.07.097

Song, C. Y., Yang, Y. J., Yang, B. Y., Sun, Y. Z., Zhao, Y. P., and Wang, L. H. (2016). An ultrasensitive SERS sensor for simultaneous detection of multiple cancer-related miRNAs. *Nanoscale* 8, 17365–17373. doi: 10.1039/c6nr05504d

Subaihi, A., Almanqur, L., Muhamadali, H., AlMasoud, N., Ellis, D. I., Trivedi, D. K., et al. (2016). Rapid, accurate, and quantitative detection of propranolol in multiple human biofluids via surface-enhanced Raman scattering. *Anal. Chem.* 88, 10884–10892. doi: 10.1021/acs.analchem.6b02041

Šubr, M., Petr, M., Peksa, V., Kylián, O., Hanuš, J., and Procházka, M (2015). Ag nanorod arrays for SERS: aspects of spectral reproducibility, surface contamination, and spectral sensitivity. *J. Nanomater.* 2015, 1–7. doi: 10.1155/2015/729231

Tan, M. J., Hong, Z.-Y., Chang, M.-H., Liu, C.-C., Cheng, H.-F., Loh, X. J., et al. (2017). Metal carbonyl-gold nanoparticle conjugates for highly sensitive SERS detection of organophosphorus pesticides. *Biosens. Bioelectron.* 96, 167–172. doi: 10.1016/j.bios.2017.05.005

Tian, K., Wang, W., Yao, Y., Nie, X., Lu, A., Wu, Y., et al. (2018). Rapid identification of gutter oil by detecting the capsaicin using surface enhanced Raman spectroscopy. *J. Raman Spectrosc.* 49, 472–481. doi: 10.1002/jrs.5306

Wang, S., Zou, S., Yang, S., Wu, H., Jia, J., Li, Y., et al. (2018). HfO_2-wrapped slanted Ag nanorods array as a reusable and sensitive SERS substrate for trace analysis of uranyl compounds. *Sens. Actuat. B Chem.* 265, 539–546. doi: 10.1016/j.snb.2018.03.062

Wang, Y., Yang, Y., Sun, Y., Quan, B., Li, Y., Gu, C., et al. (2017). Rapidly fabricating large-scale plasmonic silver nanosphere arrays with sub-20 nm gap on Si-pyramids by inverted annealing for highly sensitive SERS detection. *RSC Adv.* 7, 11578–11584. doi: 10.1039/c6ra28517a

Weng, X., Feng, Z., Guo, Y., Feng, J.-J., Hudson, S. P., Zheng, J., et al. (2016). Recyclable SERS substrates based on Fe_2O_3-Ag hybrid hollow microspheres with crumpled surfaces. *N. J. Chem.* 40, 5238–5244. doi: 10.1039/c6nj00473c

Westley, C., Xu, Y., Thilaganathan, B., Carnell, A. J., Turner, N. J., and Goodacre, R. (2017). Absolute quantification of uric acid in human urine using surface enhanced Raman scattering with the standard addition method. *Anal. Chem.* 89:2472. doi: 10.1021/acs.analchem.6b04588

Wiedmann, M. K., Jackson, D. H. K., Pagan-Torres, Y. J., Cho, E., Dumesic, J. A., and Kuech, T. F. (2012). Atomic layer deposition of titanium phosphate on silica nanoparticles. *J. Vac. Sci. Technol. A* 30:01A134. doi: 10.1116/1.3664097

Willets, K. A., and Van Duyne, R. P. (2007). Localized surface plasmon resonance spectroscopy and sensing. *Annu. Rev. Phys. Chem.* 58, 267–297. doi: 10.1146/annurev.physchem.58.032806.104607

Wolosiuk, A., Tognalli, N. G., Martínez, E. D., Granada, M., Fuertes, M. C., Troiani, H., et al. (2014). Silver nanoparticle-mesoporous oxide nanocomposite thin films: a platform for spatially homogeneous SERS-active substrates with enhanced stability. *ACS Appl. Mater. Interfaces* 6, 5263–5272. doi: 10.1021/am500631f

Xu, H., Aizpurua, J., Kall, M., and Apell, P. (2000). Electromagnetic contributions to single-molecule sensitivity in surface-enhanced raman scattering. *Phys. Rev. E* 62:4318. doi: 10.1103/physreve.62.4318

Xu, L. J., Lei, Z. C., Li, J., Zong, C., Yang, C. J., and Ren, B. (2015). Label-free surface-enhanced Raman spectroscopy detection of DNA with single-base sensitivity. *J. Am. Chem. Soc.* 137, 5149–5154. doi: 10.1021/jacs.5b01426

Yang, A.-Q., Wang, D., Wang, X., Han, Y., Ke, X.-B., Wang, H.-J., et al. (2015). Rational design of Au nanorods assemblies for highly sensitive and selective SERS detection of prostate specific antigen. *RSC Adv.* 5, 38354–38360. doi: 10.1039/c5ra01322d

Yao, Y., Wang, W., Tian, K., Ingram, W. M., Cheng, J., Qu, L., et al. (2018). Highly reproducible and sensitive silver nanorod array for the rapid detection of Allura Red in candy. *Spectrochim. Acta A Mol. Biomol. Spectrosc.*195, 165–171. doi: 10.1016/j.saa.2018.01.072

Zhao, H., Jin, J., Tian, W., Li, R., Yu, Z., Song, W., et al. (2015). Three-dimensional superhydrophobic surface-enhanced Raman spectroscopy substrate for sensitive detection of pollutants in real environments using an oil-water separation system. *J. Mater. Chem. A* 3, 4330–4337. doi: 10.1039/C4TA06590E

Zhao, M., Guo, H., Liu, W., Tang, J., Wang, L., Zhang, B., et al. (2016). Silica cladding of Ag nanoparticles for high stability and surface-enhanced Raman spectroscopy performance. *Nanoscale Res. Lett.* 11:403. doi: 10.1186/s11671-016-1604-5

Zhou, M., Lin, M., Wang, Y., Guo, X., Guo, X., Peng, L., et al. (2015). Organic-free synthesis of ultrathin gold nanowires as effective SERS substrates. *Chem. Commun.* 51, 11841–11843. doi: 10.1039/C5CC03974F

Zhou, Q., He, Y., Abell, J., Zhang, Z., and Zhao, Y. (2011a). Surface-enhanced Raman scattering from helical silver nanorod arrays. *Chem. Commun.* 47, 4466–4468. doi: 10.1039/c0cc05465h

Zhou, Q., Li, Z., Ni, J., and Zhang, Z. (2011b). A simple model to describe the rule of glancing angle deposition. *Mater. Trans.* 52, 469–473. doi: 10.2320/matertrans.M2010342

Zhou, Q., Li, Z., Yang, Y., and Zhang, Z. (2008). Arrays of aligned, single crystalline silver nanorods for trace amount detection. *J. Phys. D Appl. Phys.* 41:152007. doi: 10.1088/0022-3727/41/15/152007

Zhu, C., Meng, G., Zheng, P., Huang, Q., Li, Z., Hu, X., et al. (2016). A hierarchically ordered array of silver-nanorod bundles for surface-enhanced Raman scattering detection of phenolic pollutants. *Adv. Mater.* 28, 4871–4876. doi: 10.1002/adma.201506251

Zong, C., Xu, M., Xu, L. J., Wei, T., Ma, X., Zheng, X. S., et al. (2018). Surface-enhanced Raman spectroscopy for bioanalysis: reliability and challenges. *Chem. Rev.* 118, 4946–4980. doi: 10.1021/acs.chemrev.7b00668

Zou, S., Hou, M., Li, J., Ma, L., and Zhang, Z. (2017). Semi-quantitative analysis of multiple chemical mixtures in solution at trace level by surface-enhanced Raman Scattering. *Sci. Rep.* 7:6186. doi: 10.1038/s41598-017-06543-y

Zou, S., Ma, L., Li, J., Xie, Z., Zhao, D., Ling, Y., et al. (2018). Quantification of trace chemicals in unknown complex systems by SERS. *Talanta* 186, 452–458. doi: 10.1016/j.talanta.2018.04.095

Conflict of Interest Statement: The authors declare that the research was conducted in the absence of any commercial or financial relationships that could be construed as a potential conflict of interest.

frontiers in Chemistry

MINI REVIEW
published: 04 June 2019
doi: 10.3389/fchem.2019.00410

Shell-Isolated Nanoparticle-Enhanced Raman Spectroscopy

*Jan Krajczewski and Andrzej Kudelski**

Faculty of Chemistry, University of Warsaw, Warsaw, Poland

In 2010, Tian et al. reported the development of a new, relatively sensitive method of the chemical analysis of various surfaces, including buried interfaces (for example the surfaces of solid samples in a high-pressure gas or a liquid), which makes it possible to analyze various biological samples *in situ*. They called their method shell-isolated nanoparticle-enhanced Raman spectroscopy (SHINERS). SHINERS spectroscopy is a type of surface-enhanced Raman spectroscopy (SERS) in which an increase in the efficiency of the Raman scattering is induced by plasmonic nanoparticles acting as electromagnetic resonators that locally significantly enhance the electric field of the incident electromagnetic radiation. In the case of SHINERS measurements, the plasmonic nanoparticles are covered by a very thin transparent protective layer (formed, for example, from various oxides such as SiO_2, MnO_2, TiO_2, or organic polymers) that does not significantly damp surface electromagnetic enhancement, but does separate the nanoparticles from direct contact with the probed material and keeps them from agglomerating. Preventing direct contact between the metal plasmonic structures and the analyzed samples is especially important when biological samples are investigated, because direct interaction between the metal nanoparticles and various biological molecules (e.g., peptides) may lead to a change in the structure of those biomolecules. In this mini-review, the state of the art of SHINERS spectroscopy is briefly described.

Keywords: shell-isolated nanoparticle-enhanced Raman spectroscopy, surface-enhanced Raman spectroscopy, core-shell nanoparticles, SHINERS, SERS

OPEN ACCESS

Edited by:
Ivano Alessandri,
University of Brescia, Italy

Reviewed by:
Jian-Feng Li,
Xiamen University, China
Lingxin Chen,
Yantai Institute of Coastal Zone Research (CAS), China

****Correspondence:***
Andrzej Kudelski
akudel@chem.uw.edu.pl

Specialty section:
This article was submitted to Analytical Chemistry, a section of the journal Frontiers in Chemistry

Received: *25 February 2019*
Accepted: *20 May 2019*
Published: *04 June 2019*

Citation:
Krajczewski J and Kudelski A (2019) Shell-Isolated Nanoparticle-Enhanced Raman Spectroscopy. Front. Chem. 7:410. doi: 10.3389/fchem.2019.00410

INTRODUCTION

When nanoparticles formed from metals with a negative real and small positive imaginary dielectric constant (for example, nanoparticles of gold or silver) interact with electromagnetic radiation, a collective oscillation of surface conduction electrons called surface plasmons is induced (Aroca, 2006). The excitation of surface plasmons significantly affects the intensity of the electric field in the proximity of the illuminated plasmonic nanoparticles—a very large enhancement of the electromagnetic field may be induced in some places in the proximity of the illuminated plasmonic nanostructures (Wei et al., 2018). This electric field enhancement leads to a significant increase in the efficiency of a number of optical processes for molecules in the proximity of the plasmonic nanostructures, such as: fluorescence (Touahir et al., 2010; Wang et al., 2012), phosphorescence (Meng et al., 2018), second harmonic generation (Brolo et al., 2002), Raman scattering (Brolo et al., 2002; Wang et al., 2013; Zhang et al., 2014), Raman optical activity (Osinska et al., 2010), hyper-Raman scattering (Hulteen et al., 2006), coherent anti-Stokes Raman scattering (Brolo et al., 2002), and infrared absorption (Imae and Torii, 2000). From the practical point of view, what is most important is the enhancement of the efficiency of Raman scattering generation induced by the plasmonic systems–this effect is called surface-enhanced Raman scattering (SERS). A very interesting kind of SERS spectroscopy developed in 2010 by Tian et al. is known as shell-isolated nanoparticle-enhanced Raman spectroscopy—SHINERS (Li et al., 2010). In this method, plasmonic nanoparticles are covered with a very thin protective layer, and the core-shell structures obtained are deposited on the surface under study. The plasmonic cores of the deposited nanoparticles induce a large local enhancement in the intensity of the electric field, which, as in standard SERS measurements, leads to a significant increase in the efficiency of the Raman signal generation. The deposited ultrathin protective layer only slightly dampers the electromagnetic enhancement, but also prevents the nanoparticles from coming into direct contact with the probed material, and from agglomerating. Preventing direct contact between the metallic plasmonic resonators and the surfaces being investigated is especially important when biological samples are analyzed, because direct interaction between the metal plasmonic structures and various biological molecules (e.g., peptides) may lead to a change in the structure of the biomolecules. The SHINERS spectroscopy developed by Tian et al. seems be a very useful tool for analyzing the surfaces of various materials, even in *in situ* conditions, which is a big advantage both economically and scientifically. For example, by depositing SHINERS nanoresonators on living cells, one can record *in situ* the Raman spectrum dominated by the contribution from the species present in the outermost part of the cells of various organisms (Li et al., 2010; Kołataj et al., 2017). The principles of SHINERS measurements are presented in **Figure 1**. In this mini-review, we briefly present current advances in the synthesis of SHINERS nanoresonators (both plasmonic cores and protective layers), and new applications of SHINERS spectroscopy.

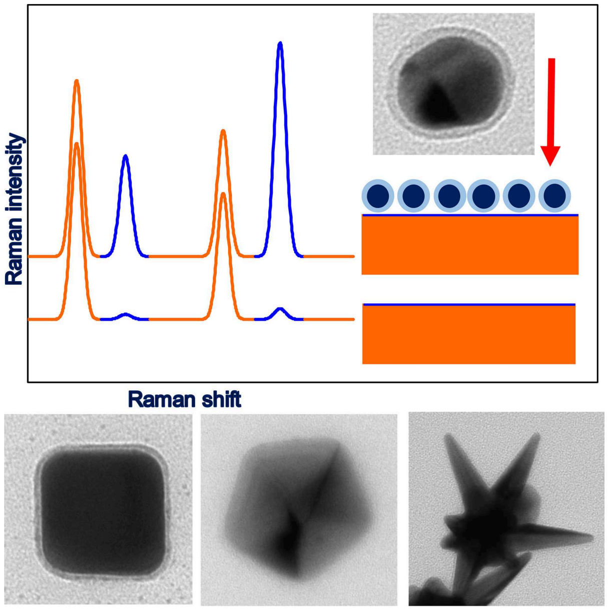

FIGURE 1 | Upper part: illustration of the principles of SHINERS measurements, lower part: example TEM images of anisotropic SHINERS nanoresonators (cubic-Ag@MnO_2, decahedral-Ag@SiO_2, star-Au@SiO_2).

SYNTHESIS OF PLASMONIC CORES FOR SHINERS NANORESONATORS

The first SHINERS experiments were carried out using, as plasmonic cores, spherical gold nanoparticles synthesized by the standard citrate method (Li et al., 2010, 2011a,b; Butcher et al., 2012). In 2012, Tian et al. (Uzayisenga et al., 2012) and Kudelski and Wojtysiak (2012) carried out the first SHINERS measurements using silver rather than gold nanoresonators, and showed that, in some cases, the use of silver plasmonic cores allows for a significant increase in the sensitivity of the SHINERS measurements. The silver plasmonic cores for the first SHINERS measurements were also spherical and were synthesized using the standard citrate method (Kudelski and Wojtysiak, 2012; Uzayisenga et al., 2012). Recently, also bimetallic plasmonic core-shell structures have been applied as cores of SHINERS nanoresonators (Lin et al., 2015).

As has been shown in many theoretical simulations, the highest field enhancement is induced in sharp structures on the surface of the illuminated plasmonic nanoparticles. Therefore, it is well-known that an effective method of increasing the efficiency of the enhancement of the intensity of the electric field in the plasmonic nanoparticles is to form on their surfaces various sharp structures, such as apexes and edges (Kottmann et al., 2001; Kudelski, 2009). Moreover, for anisotropic nanoparticles, the wavenumber of the radiation that induces the surface plasmon resonance can be changed in a significantly broader frequency range than for spherical nanostructures. Due to higher activity in the SERS measurements, and because it is easier to change the condition of the surface plasmon resonance, anisotropic plasmonic nanostructures having the shape of a cube, rod, dipyramide, decahedral, or star have been tested as plasmonic cores of SHINERS nanoresonators. As expected, when anisotropic plasmonic nanoparticles containing many sharp apexes and edges are used as SHINERS nanoresonators, the intensity of the measured Raman signal is significantly greater than in the case of experiments carried out using spherical plasmonic nanoparticles having roughly the same size and produced from the same amount of plasmonic material. For example, in the case of nanoparticles having the shape of a decahedron or dipyramid, the increase in SERS activity is equal to about one order of magnitude (Kołataj et al., 2017, 2018).

Anisotropic plasmonic nanostructures can be often synthesized using relatively simple chemical methods. For example, gold nanorods and dipyramids can be obtained using what is known as seed mediated growth synthesis (Quyan et al., 2014). In this process, anisotropic nanoparticles are formed as a result of the growth (achieved by a reduction of the metal precursor, for example $HAuCl_4$, by a weak reducing agent like ascorbic acid) of initially spherical seeds in solutions containing various surfactants. Silver decahedrons are usually obtained by photochemical synthesis (Kołataj et al., 2018). Anisotropic plasmonic nanoparticles can be also synthetized using various compounds that are selectively adsorbed on various crystalline facets. For example, a reduction of silver ions in hot dimethylformamide in the presence of polyvinylpyrrolidone leads to the formation of silver nanodecahedrons (Gao et al., 2006), while a reduction of silver ions in hot ethylene glycol in the presence of sulfide ions leads to the formation of silver nanocubes (Siekkinen et al., 2006)—all these kinds of nanoparticles have been tested as plasmonic cores for SHINERS nanoresonators (Quyan et al., 2014; Kołataj et al., 2018).

Another interesting kind of plasmonic cores for SHINERS nanoresonators are hollow nanostructures, which exhibit in many cases plasmonic properties superior to analogous solid nanoparticles (Sun et al., 2003; Huschka et al., 2011). For example, for hollow spherical gold nanostructures the position of the plasmonic band can be changed (by changing the diameter of the nanoparticle and the thickness of the shell) in a significantly broader wavelength range than for solid spherical gold nanoparticles (Sun et al., 2003; Huschka et al., 2011). The significant achievable red-shift of the plasmon band for hollow gold nanoparticles facilitates various biomedical applications of such nanostructures, because it makes it possible to tune the position of the plasmonic band to the transparent window of typical biological tissues (800–1,200 nm) (Hirsch et al., 2003; Prodan et al., 2003). Therefore, SHINERS nanoresonators containing hollow plasmonic cores are especially useful for experiments in which red or infrared radiation must be used.

In 2015, Abdulrahman et al. (2015) reported the first example of SHINERS measurements using hollow silver and hollow gold nanoparticles as plasmonic cores of SHINERS nanoresonators. Similar to SHINERS nanoresonators containing anisotropic cores, SHINERS nanoresonators containing hollow plasmonic cores are in many cases significantly more efficient than solid nanostructures of a similar size—especially when it is possible to significantly change the frequency of the surface plasmon resonance for the synthesized systems (Abdulrahman et al., 2015).

FORMATION OF THE PROTECTIVE LAYER

As mentioned in the introduction, in order to obtain SHINERS nanoresonators, the plasmonic cores have to be covered with a dielectric protective layer. Protective layers are typically formed from various oxides such as SiO_2, MnO_2, TiO_2, or ZrO_2. However, in some cases, organic polymers or carbon shells are also used. Nowadays, the cores of SHINERS nanoresonators are often covered with an silica layer, which is usually formed by the decomposition of Na_2SiO_3 or tetraethyl orthosilicate. Deposition of a nanometric silica layer by the decomposition of Na_2SiO_3 is usually carried out using the procedure proposed by Mulvaney et al. (2003). Briefly speaking, to a sol of metal nanoparticles (Ag or Au), an Na_2SiO_3 solution acidified with HCl is added, and the reaction mixture is kept for a relatively long time (even up to 6 days) under stirring. In the case of the deposition of silica on highly anisotropic nanoparticles, their surfaces are often protected by a layer formed from alkanethiols, for example, from 16-mercaptohexadecanoic acid (Mulvaney et al., 2003).

A silica layer can be also formed by the catalyzed by ammonia or amines (like dimethylamine) decomposition of tetraethyl orthosilicate. This reaction is carried out in organic solvents such as isopropanol (Krajczewski et al., 2018b) or ethanol (Kobayashi et al., 2005). The thickness of the silica shells formed depends on the initial concentration of the tetraethyl orthosilicate added. An important advantage of this method is the short time required to deposit even a thick SiO_2 layer—usually only *ca.* 15 min.

A serious drawback of silica protective layers is their low durability in some solutions, for example, solutions having a high or low pH. Therefore, for SHINERS investigations in alkali media, Tian et al. suggested using Au@MnO_2 nanoresonators (Liu et al., 2012). Layers of MnO_2 on gold cores have been deposited by a reduction of $KMnO_4$ by $K_2C_2O_4$ carried out in the presence of Au nanoparticles in a solution with a pH of 9.5 (Liu et al., 2012). The thickness of the MnO_2 layer formed can be controlled by changing the concentration of $KMnO_4$. To deposit an MnO_2 layer on silver cores, the above procedure has to be slightly modified—silver cores dissolve themselves in such a reaction mixture (Abdulrahman et al., 2016). In order to deposit MnO_2 layer on Ag cores, the reduction of $KMnO_4$ by $K_2C_2O_4$ has to be carried out at a higher pH (optimally at pH equal to *ca.* 12) (Abdulrahman et al., 2016).

SHINERS nanoresonators protected by ZrO_2 layers are significantly more stable in acidic and alkaline solutions than nanoresonators protected by SiO_2 shells. Moreover, since zirconia has an exceptionally large refractive index, the deposition of a ZrO_2 layer significantly shifts the frequency of the plasmon resonance. A zirconia layer is usually deposited by the decomposition of zirconium (IV) isopropoxide (Krajczewski et al., 2018a).

SHINERS nanoresonators can be also protected by carbon or the polymer layers. To form carbon shells, Yang et al. deposited p-mercaptobenzoic acid on the surface of silver nanoparticles and then carbonized the deposited organic layer in a concentrated solution of sulphuric acid. TEM analysis of the nanostructures obtained showed that, after this procedure, the silver cores are covered by a carbon layer with a thickness of about 2 nm (Yang et al., 2011). SHINERS nanoresonators protected by a layer of polydopamine have been synthesized by Ye et al. (2017). Polydopamine layers on gold cores were formed by the self-polymerization of dopamine, and the thickness of the layer can be controlled by changing the dopamine concentration.

An important problem in the synthesis of SHINERS nanoresonators is how to control the thickness of the protective layer. If the layer is too thin, pin-holes are more likely to appear. However, increasing the thickness of the protective layer deposited on the SHINERS nanoresonators leads to a decrease in their SERS activity [the achievable SERS enhancement decreases as a function of r^{-10} with increasing distance from the plasmonic nanoparticle (Stiles et al., 2008)]. More details on the dependence of the efficiency of SHINERS nanoresonators in enhancing in the efficiency of Raman scattering on the thickness of a deposited layer is given by Stiles et al. (2008).

EXAMPLE APPLICATIONS OF SHINERS SPECTROSCOPY

SHINERS spectroscopy has been used to detect and determine the concentration of many various chemical compounds or biological objects. One of the first systems analyzed using SHINERS spectroscopy was the skin of an orange fruit contaminated with methyl parathion (Li et al., 2010). The SHINERS detection of methyl parathion (an efficient insecticide) is based on the observation of the appearance of its characteristic Raman band at 1,350 cm^{-1}. The first SHINERS detection of methyl parathion was carried out using $Au@SiO_2$ nanoparticles; later, another nanoresonators were also used, for example $Ag@SiO_2$ (Kudelski and Wojtysiak, 2012), hollow–$Ag@SiO_2$ (Abdulrahman et al., 2015), and $Ag@MnO_2$ nanoparticles (Abdulrahman et al., 2016). Another pesticide detected using SHINERS spectroscopy was thiram (Kołataj et al., 2018). The limit of detection of thiram on a tomato skin using SHINERS spectroscopy was estimated as 0.9 ng/cm^2 (Kołataj et al., 2018).

Other important compounds that can be detected using SHINERS spectroscopy are nitrites. Nitrite ions (NO_2^-) pose a serious hazard to human health (Ralt, 2009) and the environment (Chung et al., 2004), and therefore, the US Environmental Protection Agency established a maximum contaminant level allowed for nitrite ions in drinking water (equal to 1 mg/L) (Zhang et al., 2013). Nitrite ions do not produce strong Raman spectra. Also, the addition of gold nanoparticles does not lead nitrite ions producing strong SERS spectra. However, it has been shown that nitrite ions can be detected by using them in the diazotization of p–nitroaniline in acid media. Diazotization leads to a coupling reaction and to the formation of azo dye, which has a very large cross-section for Raman scattering. The azo dye formed exhibits strong SHINERS spectra, meaning that nitrite ions can be detected indirectly using the SHINERS technique on the basis of the intensity of the Raman signal of the azo dye (Zhang et al., 2013). The limit of detection was estimated as 0.07 mg/L (Zhang et al., 2013). The method described has been successfully applied for the analysis of real samples of drinking water, tap water, and mineral water. Importantly, this method exhibits high selectivity against nitrite ions.

SHINERS measurements could be applied to detect illegal food additives, like melamine (Yang et al., 2017). Application of $Ag@SiO_2$ allows to detect melamine in milk samples with good reproducibility, ultrahigh sensitivity, and high stability in a wide concentration range (0.1–5 ppm).

An interesting class of SHINERS nanoresonators is nanoresonators containing organic shells. For example, gold cores coated by poly(2-aminothiophenol) (PAT) have been used to detect trinitrotoluen (Qian et al., 2012). Due to the strong electron-withdrawing effect of the nitro group, trinitrotoluen forms Meisenheimer complexes with the amino groups which come from PAT deposited on gold nanoparticles (see **Figure 2**).

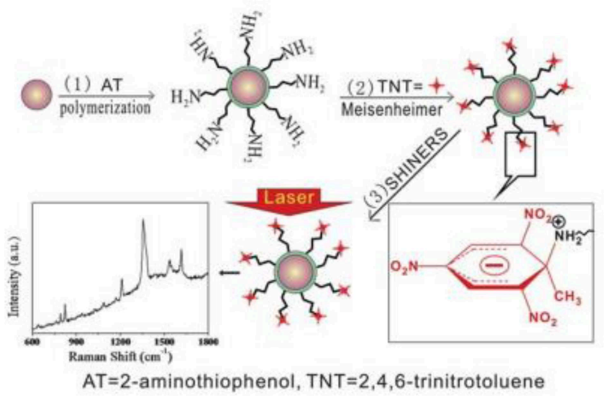

FIGURE 2 | General scheme of the formation of Meisenheimer complexes between molecules of trinitrotoluen and Au@PAT nanoparticles (Qian et al., 2012). The formation of Meiseinheimer complexes makes it possible to detect trinitrotoluen molecules using SHINERS spectroscopy. Reproduced with permission from Royal Society of Chemistry, 2012.

The formation of Meisenheimer complexes is observed even when traces of trinitrotoluen are present in the gas phase. The detection of trinitrotoluen is based on measuring the intensity of the characteristic Raman bands of the complex formed (Qian et al., 2012). The sensor described exhibits high selectivity because the presence in the analyzed sample of dinitrotoluene, nitrophenol, nitrobenzene, or toluene does not generate any significant Raman signal.

Gold SHINERS nanoresonators covered by polydopamine have been used for the label-free and quantitative detection of benzotriazole, an important corrosion inhibitor, by utilizing a presumed π-π stacking interaction (Ye et al., 2017). A broad linear range from 10^{-4} to 10^{-8} M was achieved with a limit of detection of 1 nM. The limit of detection of benzotriazole using SHINERS spectroscopy is about 200 times lower than the maximum allowable level of benzotriazole in water, and is also significantly lower than that of some modern methods such as gas chromatography coupled with mass spectrometry, liquid chromatography, and fluorescence (Ye et al., 2017).

SHINERS measurements could be applied to monitored some catalytic reactions (Hartman et al., 2018; Wang et al., 2019), for example, oxidation of methanol and formic acid (Wang et al., 2018). Also the mechanism of CO oxidation could be investigated using SHINERS spectroscopy (Zhang et al., 2017a). In a case of reduction of p–nitrothiophenol to p–aminothiophenol by sodium borohydride carried out in a liquid phase SHINERS nanoparticles demonstrate the bifunctionality as SERS nanoresonators and nanocatalyst (Zhang et al., 2017b). SHINERS is also one of the novel and promising techniques for electrochemical surface science, which can be relatively easy carried out in aqueous solutions (Xu et al., 2018).

Another promising field of application of SHINERS nanomaterials is the detection of various biochemical compounds and the analysis of biological samples. For example, it has been reported that, when SHINERS nanoresonators are deposited on various cells, it is possible to differentiate, on the basis of the measured SHINERS spectra, between normal and pathologically-changed cancer cells (Liang et al., 2014; Zheng et al., 2014). Kast et al. (2008) also showed that pathologically-changed tissues exhibit slightly different SHINERS spectra, which makes it possible to identify various types of cancer.

Due to their non-toxicity and high biocompatibility SHINERS nanoresonators could be sometimes applied for detection of biomolecules *in vivo*. For example, Au@SiO_2 nanoparticles have been used to investigate the silica nano-biointeraction inside eukaryotic cells *in situ* (Drescher et al., 2014). Ag@SiO_2 nanoparticles could selectively enhance Raman signal of cytochrome c, while, due to the very weak interaction with the target molecule, the important properties of this protein are not affected (Sivanesan et al., 2012). Also secondary structures of proteins could be investigated by SHINERS method (Wang et al., 2012). Therefore, SHINERS spectroscopy is very promising tool for non-invasive optical analysis of biomolecular processes.

SUMMARY

In this mini-review, we briefly presented recent advances in the synthesis of SHINERS nanoresonators (both plasmonic cores and protective layers) and some typical applications of SHINERS spectroscopy in chemical and biochemical analysis. We hope that these examples convince readers that SHINERS spectroscopy is a sensitive tool useful in the chemical analysis of various surfaces, including surfaces of biological objects in *in situ* conditions.

AUTHOR CONTRIBUTIONS

All authors listed have made a substantial, direct and intellectual contribution to the work, and approved it for publication.

ACKNOWLEDGMENTS

This work was financed out of funds of the National Science Centre, Poland, No. 2017/25/B/ST5/01997.

REFERENCES

Abdulrahman, H. B., Kołataj, K., Lenczewski, P., Krajczewski, J., and Kudelski, A. (2016). MnO_2-protected silver nanoparticles: New electromagnetic nanoresonators for Raman analysis of surfaces in basis environment. *Appl. Surf. Sci.* 388, 480–485. doi: 10.1016/j.apsusc.2016.01.262

Abdulrahman, H. B., Krajczewski, J., Aleksandrowska, D., and Kudelski, A. (2015). Silica-protected hollow silver and gold nanoparticles: new material for Raman analysis of surfaces. *J. Phys. Chem. C* 119, 20030–20038. doi: 10.1021/acs.jpcc.5b03556

Aroca, R. (2006). *Surface-Enhanced Vibrational Spectroscopy*. Chichester: John Wiley & Sons Ltd.

Brolo, A. G., Germain, P., and Hager, G. (2002). Investigation of the adsorption of L-cysteine on a polycrystalline silver electrode by surface-enhanced Raman scattering (SERS) and surface-enhanced second harmonic generation (SESHG). *J. Phys. Chem. B* 106, 5982–5987. doi: 10.1021/jp025650z

Butcher, D. P., Boulos, S. P., Murphy, C. J., Ambrosio, R. C., and Gewirth, A. A. (2012). Face-dependent shell-isolated nanoparticle enhanced Raman spectroscopy of 2,2ctrode by surface-enhanced Raman scat*J. Phys. Chem. C* 116, 5128–5140. doi: 10.1021/jp211884s

Chung, J. C., Chou, S. S., and Hwang, D. F. (2004). Changes in nitrate and nitrite content of four vegetables during storage at refrigerated and ambient temperatures. *Food Addit. Contam.* 21, 317–322. doi: 10.1080/02652030410001668763

Drescher, D., Zeise, I., Traub, H., Guttmann, P., Seifert, S., Büchner, T., et al. (2014). *In situ* characterization of SiO_2 nanoparticle biointeractions using bright silica. *Adv. Funct. Mater.* 24, 3765–3775. doi: 10.1002/adfm.201304126

Gao, Y., Jiang, P., Song, L., Wang, J. X., Liu, L. F., Ciu, D. F., et al. (2006). Studies on silver nanodecahedrons synthesized by PVP-assisted N,N-dimethylformamide (DMF) reduction. *J. Cryst. Growth* 289, 376–380. doi: 10.1016/j.jcrysgro.2005.11.123

Hartman, T., Wondergem, C. S., and Weckhuysen, B. M. (2018). Practical guidelines for shell-isolated nanoparticle-enhanced Raman spectroscopy of heterogeneous catalysts. *Chem. Phys. Chem.* 19, 2461–2467. doi: 10.1002/cphc.201800509.

Hirsch, L. R., Jackson, J. B., Lee, A., Halas, N. J., and West, J. L. (2003). A whole blood immunoassay using gold nanoshells. *Anal. Chem.* 75, 2377–2381. doi: 10.1021/ac0262210

Hulteen, J. C., Young, M. A., and Van Duyne R. P. (2006). Surface-enhanced hyper-Raman scattering (SEHRS) on Ag film over nanosphere (FON) electrodes: surface symmetry of centrosymmetric adsorbates. *Langmuir* 22, 10354–10364. doi: 10.1021/la0612264

Huschka, R., Zuloaga, J., Knight, M. W., Brown, L. V., Nordlander, P., and Halas, N. J. (2011). Light-induced release of DNA from gold nanoparticles: nanoshells and nanorods. *J. Am. Chem. Soc.* 133, 12247–12255. doi: 10.1021/ja204578e

Imae, T., and Torii, H. (2000). *In situ* investigation of molecular adsorption on Au surface by surface-enhanced infrared absorption spectroscopy. *J. Phys. Chem. B* 104, 9218–9224. doi: 10.1021/jp001592a

Kast, R. E., Serhatkulu, G. K., Cao, A., Pandya, A. K., Dai, H., Thakur, J. S., et al. (2008). Raman spectroscopy can differentiate malignant tumors from normal breast tissue and detect early neoplastic changes in a mouse model. *Biopolymers* 89, 235–241. doi: 10.1002/bip.20899

Kobayashi, Y., Katakami, H., Mine, E., Nagao, D., Konno, M., and Liz-Marzán, L. M. (2005). Silica coating of silver nanoparticles using a modified Stober method. *J. Colloid Interface Sci.* 15, 392–396. doi: 10.1016/j.jcis.2004.08.184

Kołataj, K., Krajczewski, J., and Kudelski, A. (2017). Silver nanoparticles with many sharp apexes and edges as efficient nanoresonators for shell-isolated nanoparticle-enhanced Raman spectroscopy. *J. Phys. Chem. C* 121, 12383–12391. doi: 10.1021/acs.jpcc.7b02695

Kołataj, K., Krajczewski, J., and Kudelski, A. (2018). Dipyramidal-Au@SiO_2 nanostructures: New efficient electromagnetic nanoresonators for Raman spectroscopy analysis of surfaces. *Appl. Surf. Sci.* 456, 932–940. doi: 10.1016/j.apsusc.2018.06.208

Kottmann, J. P., Martin, O. J. F., Smith, D. R., and Schultz, S. (2001). Dramatic localized electromagnetic enhancement in plasmon resonant nanowires. *Chem. Phys. Lett.* 341, 1–6. doi: 10.1016/S0009-2614(01)00171-3

Krajczewski, J., Abdulrahman, H. B., Kołataj, K., and Kudelski, A. (2018a). Zirconium(IV) oxide: New coating material for nanoresonators for shell-isolated nanoparticle-enhanced Raman spectroscopy. *Spectrochim. Acta A* 193, 480–485. doi: 10.1016/j.saa.2017.12.064

Krajczewski, J., Kołataj, K., Pietrasik, S., and Kudelski, A. (2018b). Silica-covered star-shaped Au-Ag nanoparticles as new electromagnetic nanoresonators for Raman characterisation of surfaces. *Spectrochim. Acta A* 193, 1–7. doi: 10.1016/j.saa.2017.11.060

Kudelski, A. (2009). Raman spectroscopy of surfaces. *Surf. Sci.* 603, 1328–1334. doi: 10.1016/j.susc.2008.11.039

Kudelski, A., and Wojtysiak, S. (2012). Silica-covered silver and gold nanoresonators for Raman analysis of surfaces of various materials. *J. Phys. Chem. C* 116, 16167–16174. doi: 10.1021/jp304409x

Li, J. F., Anema, J. R., Yu, Y. C., Yang, Z. L., Huang, Y. F., Zhou, X. S., et al. (2011a). Core–shell nanoparticle based SERS from hydrogen adsorbed on a rhodium(111) electrode. *Chem. Commun.* 47, 2023–2025. doi: 10.1039/C0CC04049E

Li, J. F., Ding, S. Y., Yang, Z. L., Bai, M. L., Anema, J. R., Wang, X., et al. (2011b). Extraordinary enhancement of Raman scattering from pyridine on single crystal Au and Pt electrodes by shell-isolated Au nanoparticles. *J. Am. Chem. Soc.* 133, 15922–15925. doi: 10.1021/ja2074533

Li, J. F., Huang, Y. F., Ding, Y., Yang, Z. L., Li, S. B., Zhou, X. S., et al. (2010). Shell-isolated nanoparticle-enhanced Raman spectroscopy. *Nature* 464, 392–395. doi: 10.1038/nature08907

Liang, L., Zheng, C., Zhang, H., Xu, S., Zhang, Z., Hu, C., et al. (2014). Exploring type II microcalcifications in benign and premalignant breast lesions by shell-isolated nanoparticle-enhanced Raman spectroscopy (SHINERS). *Spectrochim. Acta A* 132, 397–402. doi: 10.1016/j.saa.2014.04.147

Lin, M., Wang, Y., Sun, X., Wang, W., and Chen, L. (2015). "Elastic" property of mesoporous silica shell: for dynamic surface enhanced Raman scattering ability monitoring of growing noble metal nanostructures via a simplified spatially confined growth method. *ACS Appl. Mater. Interfaces* 7, 7516–7525. doi: 10.1021/acsami.5b01077

Liu, X. D., Uzayisenga, V., Li, J. F., Fang, P. P., Wu, D. Y., Ren, B., et al. (2012). Synthesis of ultrathin and compact Au@MnO_2 nanoparticles for shell-isolated nanoparticle-enhanced Raman spectroscopy (SHINERS). *J. Raman. Spectrosc.* 23, 40–45. doi: 10.1002/jrs.3007

Meng, M., Zhang, F. L., Yi, J., Lin, L. H., Zhang, C. L., Bodappa, N., et al. (2018). Shell-isolated nanoparticle-enhanced phosphorescence. *Anal. Chem.* 90, 10837–10842. doi: 10.1021/acs.analchem.8b02109

Mulvaney, S. P., Musick, M. D., Keating, C. D., and Natan, M. J. (2003). Glass-coated, analyte-tagged nanoparticles: A new tagging system based on detection with surface-enhanced Raman scattering. *Langmuir* 19, 4784–4790. doi: 10.1021/la026706j

Osinska, K., Pecul, M., and Kudelski, A. (2010). Circularly polarized component in surface-enhanced Raman spectra. *Chem. Phys. Lett.* 496, 86–90. doi: 10.1016/j.cplett.2010.07.002

Prodan, E., Nordlander, P., and Halas, N. J. (2003). Electronic structure and optical properties of gold nanoshells. *Nano Lett.* 3, 1411–1415. doi: 10.1021/nl034594q

Qian, K., Liu, H., Yang, L., and Liu, J. (2012). Functionalized shell-isolated nanoparticle-enhanced Raman spectroscopy for selective detection of trinitrotoluene. *Analyst* 137, 4644–4646. doi: 10.1039/c2an35947b

Quyan, T. T. B., Chang, C. C., Su, W. N., Uen, Y. H., Pan, L. J., Lin, J. Y., et al. (2014). Self-focusing Au@SiO_2 nanorods with rhodamine 6G as highly sensitive SERS substrate for carcinoembryonic antigen detection. *J. Mater. Chem. B* 2, 629–636. doi: 10.1039/C3TB21278E

Ralt, D. (2009). Does NO metabolism play a role in the effects of vegetables in health? Nitric oxide formation via the reduction of nitrites and nitrates. *Med. Hypotheses.* 73, 794–796. doi: 10.1016/j.mehy.2009.03.049

Siekkinen, A. R., McLellan, J. M., Chen, J., and Xia, Y. (2006). Rapid synthesis of small silver nanocubes by mediating polyol reduction with a trace amount of sodium sulfide or sodium hydrosulfide. *Chem. Phys. Lett.* 432, 491–496. doi: 10.1016/j.cplett.2006.10.095

Sivanesan, A., Kozuch, J., Khoa Ly, H., Kalaivani, G., Fischer, A., and Weidinger, I. M. (2012). Tailored silica coated Ag nanoparticles for non-invasive surface enhanced Raman spectroscopy of biomolecular targets. *RSC Adv.* 2, 805–808. doi: 10.1039/C1RA00781E

Stiles, P. L., Dieringer, J. A., Shah, N. C., and Van Duyne, R. P. (2008). Surface-enhanced Raman spectroscopy. *Annu. Rev. Anal. Chem.* 1, 601–626. doi: 10.1146/annurev.anchem.1.031207.112814

Sun, Y., Mayers, B., and Xia, Y. (2003). Metal nanostructures with hollow interiors. *Adv. Mater.* 15, 641–646. doi: 10.1002/adma.200301639

Touahir, L., Jenkins, A. T. A., Boukherroub, R., Gouget-Laemmel, A. C., Chazalviel, J. N., Peretti, J., et al. (2010). Surface plasmon-enhanced fluorescence spectroscopy on silver based SPR substrates. *J. Phys. Chem. C* 114, 22582–22589. doi: 10.1021/jp107402r

Uzayisenga, V., Lin, X. D., Li, L. M., Anema, J. R., Yang, Z. L., Huang, Y. F., et al. (2012). Synthesis, characterization, and 3D-FDTD simulation of Ag@SiO_2 nanoparticles for shell-isolated nanoparticle-enhanced Raman spectroscopy. *Langmuir* 28, 9140–9146. doi: 10.1021/la3005536

Wang, Y., Chen, L., and Liu, P. (2012). Biocompatible triplex Ag@SiO_2@mTiO_2 core–shell nanoparticles for simultaneous fluorescence-SERS bimodal imaging and drug delivery. *Chem. Eur. J.* 18, 5935–5943. doi: 10.1002/chem.201103571

Wang, Y., Yan, B., and Chen, L. (2013). SERS tags: novel optical nanoprobes for bioanalysis. *Chem. Rev.* 113, 1391–1428. doi: 10.1021/cr300120g

Wang, Y. H., Liang, M. M., Zhang, Y. J., Chen, S., Radjenovic, P., Zhang, H., et al. (2018). Probing interfacial electronic and catalytic properties on well-defined surfaces by using *in situ* Raman spectroscopy. *Angew. Chem. Int. Ed.* 57, 11257–11261. doi: 10.1002/anie.201805464

Wang, Y. H., Wei, J., Radjenovic, P., Tian, Z. Q., and Li, J. F. (2019). *In<underline >situ* analysis of surface catalytic reactions using shell-isolated nanoparticle-enhanced Raman spectroscopy. *Anal. Chem.* 91, 1675–1685. doi: 10.1021/acs.analchem.8b05499

Wei, Y., Li, L., Sun, D., Zhu, Y., and Tian, G. (2018). The effect of silica shell on the surface enhanced Raman scattering and fluorescence with Ag nanoparticles: a three-dimensional finite element method investigation. *Opt. Commun.* 427, 426–432. doi: 10.1016/j.optcom.2018.06.086

Xu, J., Zhang, Y. J., Yin, H., Zhong, H. L., Su, M., Tian, Z. Q., et al. (2018). Shell-isolated nanoparticle-enhanced Raman and fluorescence spectroscopies: synthesis and applications. *Adv. Optical Mater.* 6:1701069. doi: 10.1002/adom.201701069

Yang, D., Xia, L., Zhao, H., Hu, X., Liu, Y., Li, J., et al. (2011). Preparation and characterization of an ultrathin carbon shell coating a silver core for shell-isolated nanoparticle-enhanced Raman spectroscopy. *Chem. Commun.* 47, 5873–5875. doi: 10.1039/C0CC05749E

Yang, J. L., Yang, Z. W., Zhang, Y. J., Ren, H., Zhang, H., Xu, Q. C., et al. (2017). Quantitative detection using two-dimension shell-isolated nanoparticle film. *J. Raman Spectrosc.* 48, 919–924. doi: 10.1002/jrs.5151

Ye, W., Huang, H., Yang, W., Wang, X., Ren, C., Hu, Q., et al. (2017). Ultrathin polydopamine film coated gold nanoparticles: a sensitive, uniform, and stable SHINERS substrate for detection of benzotriazole. *Analyst* 142, 3459–3467. doi: 10.1039/C7AN00675F

Zhang, H., Wang, C., Sun, H. L., Fu, G., Chen, S., Zhang, Y. J., et al. (2017a). *In situ* dynamic tracking of heterogeneous nanocatalytic processes by shell-isolated nanoparticle-enhanced Raman spectroscopy. *Nat. Commun.* 8:15447. doi: 10.1038/ncomms15447

Zhang, H., Zhang, X. G., Wei, J., Wang, C., Chen, S., Sun, H. L., et al. (2017b). Revealing the role of interfacial properties on catalytic behaviors by *in situ* surface-enhanced Raman spectroscopy. *J. Am. Chem. Soc.* 139, 10339–10346. doi: 10.1021/jacs.7b04011

Zhang, K., Hu, Y., and Li, G. (2013). Diazotization-coupling reaction-based selective determination of nitrite in complex samples using shell-isolated nanoparticle-enhanced Raman spectroscopy. *Talanta* 116, 712–718. doi: 10.1016/j.talanta.2013.07.019

Zhang, W., Wang, Y., Sun, X., Wang, W., and Chen, L. (2014). Mesoporous titania based yolk–shell nanoparticles as multifunctional theranostic platforms for SERS imaging and chemo-photothermal treatment. *Nanoscale* 6, 14514–14522. doi: 10.1039/c4nr04864d

Zheng, C., Liang, L., Xu, S., Zhang, H., Hu, C., Bi, L., et al. (2014). The use of Au@SiO_2 shell-isolated nanoparticle-enhanced Raman spectroscopy for human breast cancer detection. *Anal. Bioanal. Chem.* 406, 5425–5432. doi: 10.1007/S00216-014-7967-5

Conflict of Interest Statement: The authors declare that the research was conducted in the absence of any commercial or financial relationships that could be construed as a potential conflict of interest.

frontiers in Chemistry

ORIGINAL RESEARCH
published: 05 June 2019
doi: 10.3389/fchem.2019.00423

Theoretical Approaches for Modeling the Effect of the Electrode Potential in the SERS Vibrational Wavenumbers of Pyridine Adsorbed on a Charged Silver Surface

Daniel Aranda, Samuel Valdivia, Juan Soto, Isabel López-Tocón, Francisco J. Avila and Juan C. Otero**

Andalucía Tech, Unidad Asociada CSIC, Departamento de Química Física, Facultad de Ciencias, Universidad de Málaga, Málaga, Spain

Vibrational wavenumbers of pyridine adsorbed on a silver electrode have been correlated to the calculated ones from different theoretical approaches based on DFT methods. The vibrational tuning caused by the electrode potential has been simulated by means of pyridine-silver clusters with different densities of charge or, alternatively, under applied external electric fields. Both methodologies predict correctly a qualitative red-shift of the vibrational wavenumbers at negative potentials. As a result, harmonic frequency calculations performed at the B3LYP/LanL2DZ level of theory by using a linear $[Ag_nPy]^q$ complex model with different densities of charge ($q_{eff} = q/n$) have exhibited the best agreement with the experimental observations although the tuning amplitudes are overestimated. Electric fields calculations are unable to account for subtle details observed in the spectra related to the differentiated chemical nature of the metal-molecule bond at positive or negative potentials with respect to the potential of zero charge of the electrode.

Keywords: SERS, Raman, pyridine, electrode potential, DFT, vibrational wavenumbers, vibrational Stark effect

Edited by:
John Lombardi,
City College of New York (CUNY),
United States

Reviewed by:
Joydeep Chowdhury,
Jadavpur University, India
Kubilay Balci,
Istanbul University, Turkey

Correspondence:
Francisco J. Avila
avila@uma.es
Juan C. Otero
jc_otero@uma.es

Specialty section:
This article was submitted to Analytical Chemistry, a section of the journal Frontiers in Chemistry

Received: *15 March 2019*
Accepted: *22 May 2019*
Published: *05 June 2019*

Citation:
Aranda D, Valdivia S, Soto J, López-Tocón I, Avila FJ and Otero JC (2019) Theoretical Approaches for Modeling the Effect of the Electrode Potential in the SERS Vibrational Wavenumbers of Pyridine Adsorbed on a Charged Silver Surface. Front. Chem. 7:423. doi: 10.3389/fchem.2019.00423

INTRODUCTION

Surface-enhanced Raman Scattering (SERS) is one of the most powerful techniques to get insight into the complex electronic structure of molecules bonded to charged metals (Weaver et al., 1985; Wolkow and Moskovits, 1992; Szekeres and Kneipp, 2019). These metal-molecule hybrid systems are involved in many scientific fields like electrochemistry or heterogeneous catalysis but they are also related to the electrical transport through single molecule junctions or are part of electronic devices for solar energy conversion. All of these scientific areas are controlled by the overall electronic structure of the metal-adsorbate complex whose chemical and physical properties can be, in many cases, tuned continuously by applying electric potentials.

The main characteristic of SERS is the huge enhancement of the Raman signal, but the spectra show very often changes in the relative intensities as well as in the vibrational wavenumbers of the bands which are modified by the electric potential in electrochemical SERS experiments. Changes in the intensities are related to the enhancement mechanism or mechanisms acting in each particular experiment (plasmonic, charge-transfer resonances, etc.) (Aroca, 2006; Kneipp et al., 2006; Le Ru and Etchegoin, 2008).

But the shifts between the Raman and the SERS wavenumbers of a molecule are not dependent on these mechanisms being restricted to the ground electronic structure of the metal-molecule surface complex. Pyridine (Py) is mainly bonded to a metal atom by charge donation from the lone pair of the nitrogen to vacant orbitals of the metal. In the case of this molecule the weak chemical adsorption modifies slightly the structure of the adsorbate in such a way that the aromatic ring becomes stronger given that the donated charge has non-bonding character. As a consequence, the SERS wavenumbers of the ring vibrations of pyridine should be blue-shifted which respect to the Raman ones. This behavior allows for deducing the orientation of the adsorbate with respect to a macroscopic electrode (Soto et al., 2002) without resorting to the involvement of any SERS enhancement mechanism which is a controversial question (Moskovits, 2013; Aranda et al., 2018).

In the case of electrochemical SERS experiments, the electrode potential controls the strength of the metal-molecule bond. More positive potentials induce more positive excess of charge on the electrode, favoring charge donation from the pyridine to the metal, strengthening the ring (Avila et al., 2011a) and shifting the wavenumbers of the ring vibrations toward the blue. On the contrary, negative potentials reduces the strength of the complex and the corresponding wavenumbers should be red-shifted. This dependence of the vibrational wavenumbers observed from the electrochemical interfaces on the applied electrode potential is called usually vibrational Stark effect. For pyridine adsorbed on a silver electrode, this effect has been previously discussed by Johansson (Johansson, 2005).

Besides the effect of the electrode potential, the vibrational wavenumbers are affected by the interaction with the environment. Previous studies have shown that the wavenumber of ring breathing vibration changes with the molar fraction (Schlücker et al., 2001; Tukhvatullin et al., 2010; Kalampounias et al., 2015), demonstrating that even weak solute-solvent interactions can perturbate the electronic structure of the solute, as is observed in the experiments. When a molecule is adsorbed on electrodes these interactions change and can have a non-negligible role (Kelly et al., 2016) but the theoretical quantification of their effects in the vibrational wavenumbers remains a challenge.

This work deals with the comparative study of the performance of different theoretical methodologies for modeling the dependence of the vibrational wavenumbers of pyridine adsorbed on a charged silver interface. The experimental results obtained from SERS spectra are compared with the calculated shifts by assuming three different approaches (**Figure 1**): model $[Ag_nPy]^q/q_{eff}$, a pyridine bonded to linear metal clusters with different densities of charge q_{eff}; model $[Ag_2Py]^0/\overrightarrow{E}$, a pyridine bonded to a dimer neutral cluster in the presence of an external electric field and, for the sake of comparison, model $Py/\overrightarrow{E}$, the isolated molecule subjected to electric fields. Additionally, solvent effects have been considered for the different systems studied. The aim of this work is to discuss the accuracy of different theoretical approaches for predicting the vibrational wavenumber shifts of molecules bonded to metals in charged interfaces in order to know the effect of the adsorption and the electric potentials in the overall electronic structure of metal-molecule hybrids.

MATERIALS AND METHODS

The SERS Measurements

Electrochemical SERS spectra have been recorded using a three electrodes cell controlled by a CH model 600E potentiostat, with a platinum counter electrode, an Ag/AgCl/KCl (sat.) reference electrode to which all the electrode potentials are referred to, and a pure silver working electrode. This latter was polished with 0.30 and 0.05 µm alumina (Buëhler) and electrochemically activated by using a 0.1 M KCl aqueous solution as electrolyte by maintaining the electrode potential at −0.5 V, and then subjecting it to seven 2 s pulses at +0.6 V in order to produce the necessary surface roughness for SERS enhancement.

Pyridine was purified by distillation in vacuum and a 0.1/0.1 M aqueous solution of pyridine/KCl was used to record the SERS spectra. The water of the solutions was of Milli-Q quality (resistivity over 18 MΩcm).

Raman and SERS spectra have been recorded with 1 cm^{-1} resolution by using a Renishaw Invia micro-Raman spectrometer and the excitation line of 514.5 nm from an Ar^+ gas laser. The microscope has an adapted objective (f: 30 mm) to work in macro conditions. To avoid overheating during the measurement of Raman spectra neutral density filters with an optical throughput of 0.5 and 1% were used and the laser power at the sample position was 0.1 and 5 mW, respectively.

DFT Calculations

Electronic structure calculations were performed using Density Functional Theory (DFT) as implemented in the Gaussian09 package (Frisch et al., 2010). Three different functionals B3LYP (Becke, 1993; Stephens et al., 1994), PW91 (Perdew et al., 1996) and M06-HF (Zhao and Truhlar, 2006) have been checked in combination with several basis sets. The LanL2DZ (Hay and Wadt, 1985a,b,c) effective core potential was selected for silver atoms, whereas for pyridine the same LanL2DZ pseudopotential (DV95V, Dunning and Hay, 1977), 6-31G(d) (Ditchfield et al., 1971), and 6-311G(d,p) (Krishnan et al., 1980; McLean and Chandler, 1980) basis sets have been also tested.

B3LYP and PW91 functionals usually provide accurate vibrational wavenumbers, whose shifts caused by the adsorption is the main focus of this work. The long-range corrected M06-HF functional is less reliable in computing vibrational wavenumbers as it remarkably overestimates them. Nevertheless, this method should be expected to return more reliable energy values for some particular cases than the non-corrected functionals like B3LYP (Avila et al., 2011a), and we also used it in this study considering that it was previously used to quantify the presence of metal-to-molecule charge transfer resonances in similar systems.

Solvent effects were taken into account using the PCM (Polarizable Continuum Model, Tomasi et al., 2005) model as implemented in Gaussian 09 with standard parameters. The main drawback of implicit models is that they cannot reproduce properly specific interactions like hydrogen bonding, but they are

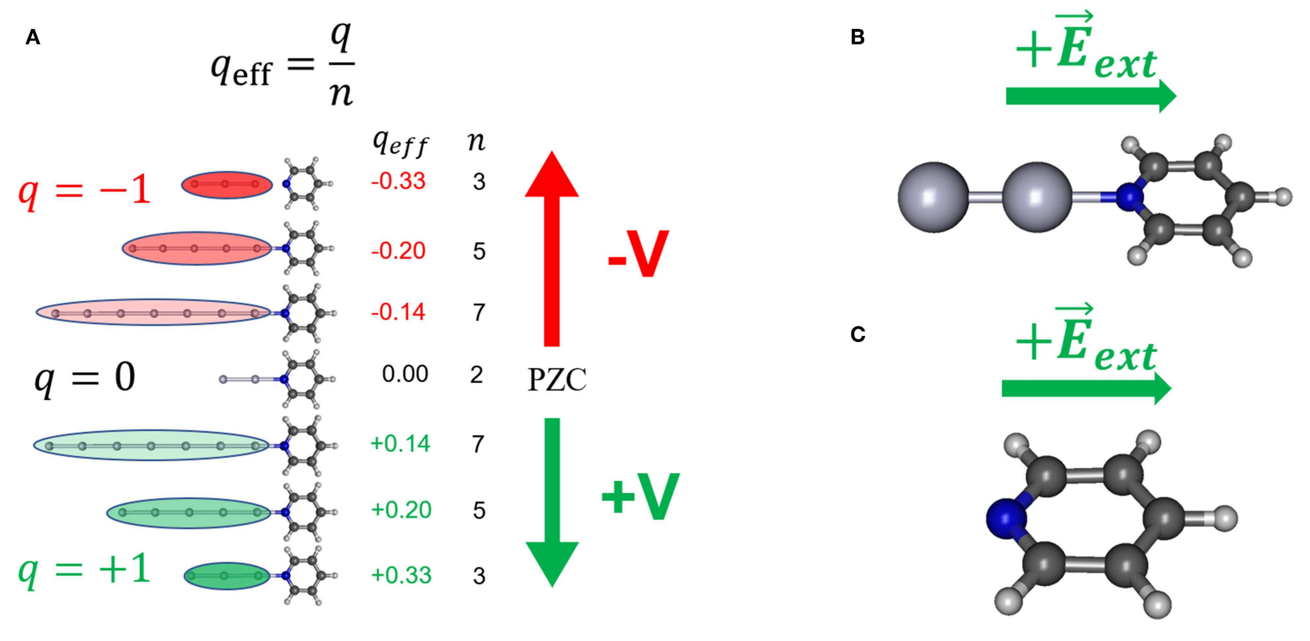

FIGURE 1 | Some of the theoretical models used in simulating the effect of the electrode potential on the electronic structure of adsorbate; **(A)** the $[Ag_nPy]^q/q_{\text{eff}}$ model; **(B)** the $[Ag_2Py]^0/\vec{E}$ model; **(C)** the model $Py/\vec{E}$.

expected to be small for chemically adsorbed pyridine since the nitrogen atom is not available for hydrogen bonding.

The effect of the electrode potential has been modeled in the calculations by assuming two different approaches briefly described below: charged metal clusters and external electric fields. The electrode potential tunes the surface excess of charge of the electrode. Consequently, it modifies also the ionic structure of the electrolyte part of the double layer which can be simulated by means of an electric field. Both factors, metal charges and external electric fields, modify the electronic structure of the metal-molecule hybrid and therefore, shift the vibrational wavenumbers of the adsorbate.

The Charged Metal Cluster Models

In order to model the effect of the metal excess of charge on the metal-molecule surface complex $[Ag_nPy]^q$ systems formed by linear metal clusters with different sizes ($n = 2, 3, 5, 7$) and charges ($q = 0$ for $n = 2$, and $q = \pm 1$ a.u. for odd n) (**Figure 1A**) have been used. These complexes allow for defining the effective density of charge of the cluster as $q_{\text{eff}} = q/n$ (atomic units) which ranges from +0.33 to −0.33 a.u. in this series. Previous studies indicate that this range of q_{eff} can be correlated with electrochemical SERS results recorded from 0.0 to −1.5 V (Román-Pérez et al., 2014a; Roman-Perez et al., 2015).

q_{eff} is the average density of charge of the cluster and is the microscopic analogous of the macroscopic surface excess of charge of a metal, $q^{'}$ (C/cm^2), which is more or less linearly tuned by the electrode potential. In this way, the neutral Ag_2 cluster with $q = 0$ would simulate the case of pyridine adsorbed on a neutral metal surface, i.e., at the potential of zero charge of the electrode ($\mathbf{V}_{\text{PZC.}}$) Therefore, positively charged clusters ($[Ag_nPy]^{+1}$, $q_{\text{eff}} > 0$) should correspond to electrode potentials more positive than $\mathbf{V}_{\text{PZC}}$ (+**V**) whereas negative clusters ($[Ag_nPy]^{-1}$, $q_{\text{eff}} < 0$) simulate potentials more negative that $\mathbf{V}_{\text{PZC}}$ (−**V**). For a polycrystalline silver electrode $\mathbf{V}_{\text{PZC}}$ lies in the range of −0.8 to −0.9 V (Hupp et al., 1983; Chen and Otto, 2005). For convenience, the potential of −0.7 V has been considered as the $\mathbf{V}_{\text{PZC}}$ of the rough silver electrode given that is the center of the experimental range of potentials scanned in this work.

A rough metal surface shows a lot of different local structures at an atomic scale where a single molecule can be bonded. This gives an unaffordable range of possibilities for the geometries of the surface complex, each of them having different properties and specific interactions. To avoid selecting arbitrarily one of them we have considered the simplest case where pyridine is bonded to a terminal atom of the linear cluster through the nitrogen atom. In spite of its simplicity, this model has proved its usefulness in analyzing the complex behavior in the SERS spectra of benzene-like molecules, which have been considered in our previous works (Arenas et al., 2002; Avila et al., 2011a,b and references therein).

The External Electric Field Models

An alternative and widely used strategy consist of simulating the effect of the electrode potential by means of external electric fields $\vec{E}_{ext}$ applied, in this case, to isolated pyridine (model $Py/\vec{E}$, **Figure 1C**) or to the neutral $[Ag_2Py]^0$ complex (model $[Ag_2Py]^0/\vec{E}$, **Figure 1B**) by using the FIELD keyword in Gaussian 09 calculations. Fields has been imposed by assuming a single component perpendicular to the surface along the symmetry axis of the molecule. It is important to clearly define the sign of $\overrightarrow{E}_{ext}$ by considering the criterium of the particular computer program used (Aranda et al., 2017). The sign of $\overrightarrow{E}_{ext}$ has been selected in such a way that positive fields ($+\overrightarrow{E}$) polarize the negative electronic cloud of the adsorbate toward the electrode and, therefore, it corresponds to positive potentials or positive excess of charge on the metal ($+\mathbf{V}$). Calculated wavenumbers of pyridine at zero-field are those of the isolated molecule, but they must be correlated to the experimental ones recorded in the SERS at $\mathbf{V}_{PZC}$ which are perturbed by the chemical adsorption on a neutral metal surface simulated through the neutral $[Ag_2Py]^0$ complex. However, a comparison between the results of the simple linear model $[Ag_2Py]^0/\overrightarrow{E}$ and model $[Ag_{20}Py]^0/\overrightarrow{E}$, where pyridine is bonded to tetrahedral Ag_{20}^0 cluster (Zhao et al., 2005; Zhao and Chen, 2013), will be presented in order to discuss the effect of the cluster size and geometry.

The selection of the range of applied $\overrightarrow{E}_{ext}$ to reproduce the electrochemical SERS experiments recorded from 0 to −1.4 V is not trivial. This approach has been very frequently used in the earlier similar studies. For instance, Mohammadpour et al. (2017) used an asymmetric range of $120 \cdot 10^{-4}$ a.u. by using a planar-triangular Ag_6^0 cluster to reproduce the trends observed on the SERS intensities of pyridine recorded by us on silver in the range −0.5 to −1.2 V. Zhao and Chen (2013) studied pyridine on a gold electrode modeled as a Au_{20} tetrahedral cluster using a range of $\pm 10 \cdot 10^{-4}$ a.u. in order to reproduce the SERS intensities focused in the 1,000 cm^{-1} region. Differently from the others, in this study we screened a larger range of the applied external electricity field $\Delta \overrightarrow{E}_{ext} = \pm 120 \cdot 10^{-4}$ a.u. to have an overall view on its effect on the fundamental bands observed in the spectra of pyridine.

Correlating Parameters of Theoretical Models With the Electrode Potential

The calculation results have indicated that, at the B3LYP/LanL2DZ level of theory, the effect of the electric field applied in the range of $\pm 120 \cdot 10^{-4}$ a.u. on the calculated properties of silver-pyridine complex models is comparable to those calculated of the charged silver-pyridine models with $\Delta q_{\text{eff}} \pm 0.33$ a.u. For instance, the injected charge from pyridine to the metal in the extreme negative case amounts to −0.072 and −0.071 a.u. in the models $[Ag_2Py]^0/\overrightarrow{E}$, with $\overrightarrow{E}_{ext} = -120 \cdot 10^{-4}$ a.u., and $[Ag_nPy]^q/q_{\text{eff}}$, with $q_{\text{eff}} = -0.33$ a.u., respectively. In turn, values of −0.268 and −0.273 a.u. are obtained at the positive side with $\overrightarrow{E}_{ext} = +120\ 10^{-4}$ a.u. and $q_{\text{eff}} = +0.33$ a.u., respectively. The difference between the stability of the metal-molecule surface complex between the most negative and the most favorable positive potentials can be estimated by comparing the relative energies of the systems of both models at the extreme values of the respective ranges, giving $\Delta E_{\pm}$ of 46.33 and 45.75 Kcal/mol for models $[Ag_2Py]^0/\overrightarrow{E}$ and $[Ag_nPy]^q/q_{\text{eff}}$, respectively. Furthermore, the only available explanation so far of the huge energy gain ($G = \Delta E_{CT}/\Delta V$ up to 3–5 eV/V, Otto et al., 1984; Cui et al., 2010; Aranda et al., 2017) observed in SERS when the electrode potential ($\mathbf{V}$) tunes the energies of the metal-to-molecule charge transfer states (E_{CT}) requires that the usual range of experimental electrode potentials $\Delta\mathbf{V} = \mathbf{V}_+ - \mathbf{V}_- = 1.5$ V is again correlated to the calculated E_{CT} energies of $[Ag_nPy]^q/q_{\text{eff}}$ complexes with $q_{\text{eff}} = +0.33$ and −0.33 a.u. From the two $[Ag_3Py]^{\pm 1}$ systems a value of $\Delta E_{CT} = 3.63$ eV is obtained, while the model $[Ag_2Py]^0/\overrightarrow{E}$ provides an estimation of only 1.99 eV from $\Delta \overrightarrow{E}_{ext} = \pm 120 \cdot 10^{-4}$ a.u. This is a lack of the electric field approach given that ΔE_{CT} is too small to account for the experimental energy gain (Aranda et al., 2017).

Finally, the strong selective enhancement of mode 9a in the SERS of pyridine recorded at very negative electrode potentials (see **Figure 2** and **Supplementary Figure S1**) can be only explained on the basis of a Raman resonance process up to intracluster electronic excitations in the case of the most negatively charged $[Ag_nPy]^{-1}$ complexes (Roman-Perez et al., 2015). This means that the experimental conditions at −1.2 or −1.4 V can be only reproduced by theoretical models with $q_{\text{eff}} = -0.33$ a.u.

The previous discussion in which the experimental and theoretical parameters are related to one other allows for correlating the respective ranges of the experimental and theoretical parameters, such as electrode potential ($\Delta\mathbf{V} = 1.5$), charge ($\Delta q_{\text{eff}} = \pm 0.33$ a.u.) and electric fields ($\Delta \overrightarrow{E}_{ext} = \pm 120 \cdot 10^{-4}$ a.u.).

Wavenumber Shifts Arising From the Molecular Adsorption

To study the changes of the electronic structure of the adsorbate, the wavenumber shift $\Delta\upsilon_i(V)$ of each vibrational mode i at a particular potential V has been computed as follows:

$$\Delta\upsilon_i(V) = \upsilon_i(V) - \upsilon_i(Ref)$$

Where $\upsilon_i(V)$ is the absolute wavenumber of the mode i at the potential V and $\upsilon_i(Ref)$ is the wavenumber of the mode i in the selected reference conditions. This work focuses on the adsorption phenomenon, so the experimental data of pure liquid pyridine have been selected as a reference. Therefore, $\Delta\upsilon_i(V)$ contains adsorption and solvation effects, the strength of the adsorption being modulated by the electrode potential. In the case of theoretical results, $\mathbf{V}$ is simulated by q_{eff} or $\overrightarrow{E}_{ext}$ and the reference was the calculated wavenumbers for a single pyridine molecule in a pyridine PCM environment, while water parameters has been used for solvent correction in the PCM calculations of silver-pyridine complexes.

RESULTS AND DISCUSSION

The effect of the adsorption on a neutral surface will be discussed firstly by comparing the wavenumbers of liquid pyridine with those of the SERS at −0.7 V and these results will be compared with the theoretical calculations carried out with and without solvent corrections. Thereafter, the effect of the electrode potential on the wavenumber shifts will be discussed by comparing the experimental data with three sets of calculations carried out under different approaches: effect of the charge of

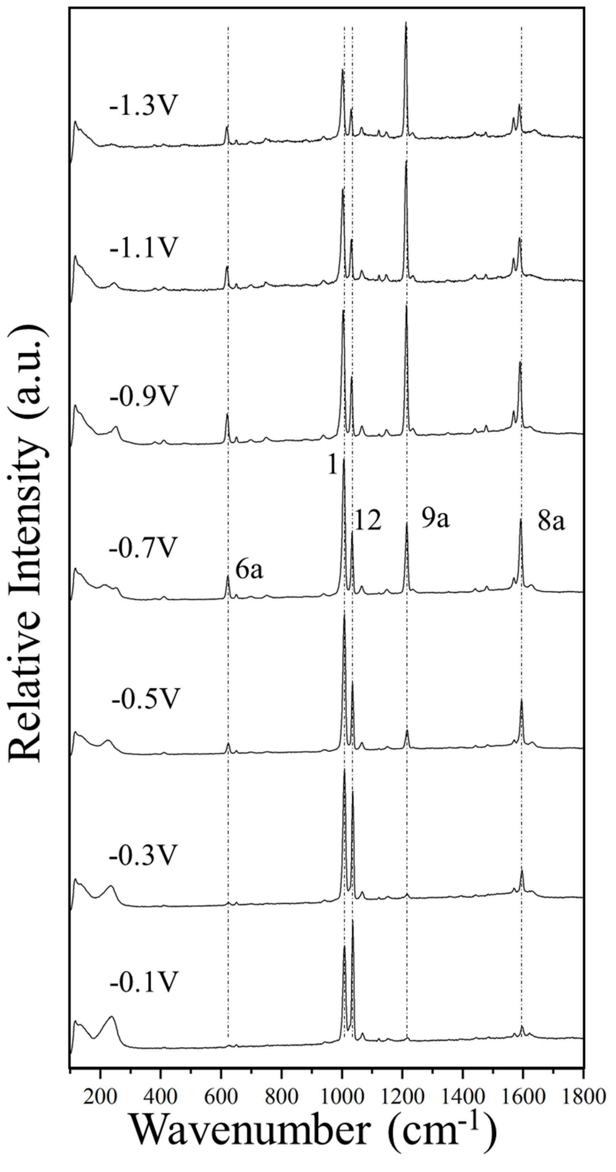

FIGURE 2 | The SERS spectra of pyridine (0.1 M) adsorbed on silver, recorded at different electrode potentials by using a laser source of 514.5 nm wavelength.

the metal clusters (model $[Ag_nPy]^q/q_{eff}$), effect of electric fields in a complex where a molecule is adsorbed on the Ag_2^0 neutral cluster (model $[Ag_2Py]^0/\vec{E}$) and effect of electric fields in the wavenumbers of an isolated pyridine (model $Py/\vec{E}$).

The Experimental SERS Spectra of Pyridine

Figure 2 and **Supplementary Figure S1** show the potential-dependent SERS of pyridine adsorbed on silver electrode, on steps of 0.2 V and 0.1 V, respectively. Some vertical dotted lines have been added to the main SERS bands corresponding to the totally symmetric modes 6a, 1, 12, 9a, and 8a recorded at around 622, 1,006, 1,034, 1,215, and 1,592 cm^{-1}, respectively.

The wavenumbers of the strongest SERS bands measured in the complete set of spectra recorded in steps of 0.1 V are reported in the **Supplementary Table S1**. The experimental $\Delta\upsilon_i(V)$ selected by Johansson (2005) of only an electrochemical SERS spectrum for pyridine are very similar to our results obtained at the most positive potentials of 0 or −0.1 V.

The general trend is that for potentials more positive than −0.5 V the respective wavenumbers remains almost constant, while they are quasi-linearly red-shifted as the potential is made more negative. Some exceptions are the vibrational modes 18a and 6b of 1,067 and 650 cm^{-1}, respectively, which are almost insensitive to the potential.

The Changes Occurred at the Vibrational Modes of Pyridine Depending on the Molecular Adsorption on a Neutral Surface

As previously pointed, the experimental conditions corresponding to the potential of charge zero has been assigned to the SERS recorded at $\mathbf{V}_{PZC} = -0.7$ V. **Figure 3** compares experimental $\Delta\upsilon_i$ obtained from the pure liquid Raman and the SERS recorded at this potential with the calculated $\Delta\upsilon_i$ from isolated pyridine and for the $[Ag_2Py]^0$ complex at the B3LYP/LanL2DZ level of theory, both with and without considering solvent effects with PCM. As can be seen, the harmonic frequency calculations produce results well agreeing with the observed general trend despite they are carried out by using a rather simple complex model $[Ag_2Py]^0$.

The experimental results (**Figure 3B**) show large and positive shifts for the strong SERS modes 6a, 1, and 8a (+18, +13, and +10 cm^{-1}, respectively), and a small blue-shift for mode 12 (+1.2 cm^{-1}). All other vibrations show moderate or small red-shifts, showing mode 19a the largest displacement (−5 cm^{-1}). Pyridine vibrations can be classified in different types according to the nature and the amount of the wavenumber shifts: type I for A_1 vibrational modes mainly localized on the ring (6a, 1, 8a, and 12), type II for A_1 modes involving hydrogen motion or ring deformations (19a, 9a, and 18a) and finally type III for the B_2 symmetry modes 8b and 6b. Animations of each fundamental can be found on **Supplementary Material**.

Harmonic frequency calculations of the $[Ag_2Py]^0$ complex predict a blue-shift for all the vibrations (**Figure 3A**), the most sensitive ones to the adsorption being type I in agreement with the experimental results. However, $\Delta\upsilon_i$ for mode 12 is overestimated and the negative shifts of type II and III are not well-reproduced. PCM results improve the agreement with the experiment. The large blue-shifts for type I, are preserved and remain overestimated. Types II and III now show negative displacements, except for vibration 19a. Generally speaking, PCM methodology reduces the large shifts predicted by the DFT calculations as previously detected (Brewer and Aikens, 2010). From the results of the five strongest SERS fundamentals (type I plus mode 9a) an overestimation of 50% is obtained for the calculated shifts: $\Delta\upsilon_{calc} = 1.5\ \Delta\upsilon_{exp}$.

Very similar behavior is observed with the PW91 functional, while M06-HF predictions are somewhat worse (**Supplementary Figure S2**). Generally speaking, B3LYP seems

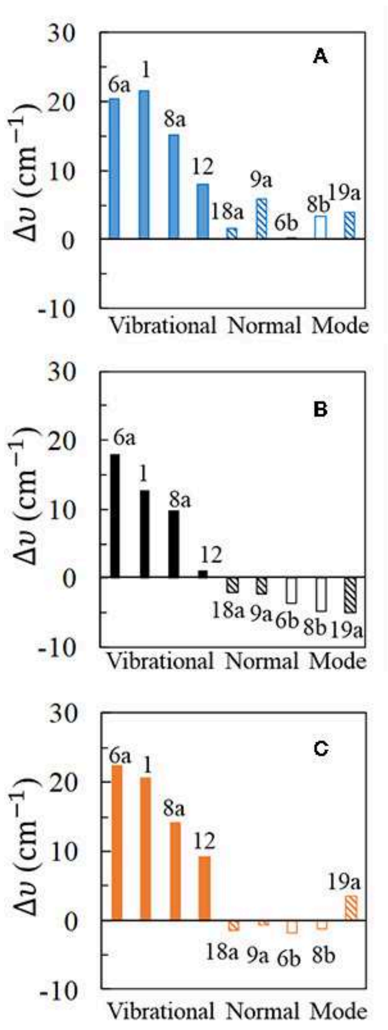

FIGURE 3 | Wavenumber shifts ($\Delta\upsilon$) determined for the most representative normal modes of pyridine: **(A,C)** show the shifts calculated at B3LYP/LanL2DZ level of theory for the $[Ag_2Py]^0$ complex model in vacuum and for the $[Ag_2Py]^0$ complex model in water environment where the solvent effects are taken into account by using the PCM (solvent = water), respectively; **(B)** shows the experimental shifts when an electrode potential of $\mathbf{V}_{PZC} = -0.7$ V is used in the SERS measurement.

to be the most reliable one amongst the three compared functionals. It should be noted that the experimental shifts in **Figure 3B** are dependent on the rather arbitrary potential selected as $\mathbf{V}_{PZC}$ and the agreement between calculated and experimental results could be improved if a more negative SERS spectra than −0.7 V would have been chosen as reference.

For completeness, three different basis sets for pyridine have been checked in combination with the three functionals: D95V (LanL2DZ), 6-31G(d), and 6-311G(d,p), respectively, and the corresponding results can be compared by examining **Figure 3** and **Supplementary Figures S2–S4**. As can be seen, 6-31G(d) and 6-311G(d,p) results are very similar, improving both the predictions obtained with the smaller LanL2DZ basis set. All the calculated shifts for the most characteristic type I modes are reduced, in agreement with the experimental results, as well as the relative amount of $\Delta\upsilon_i$ for vibrations 6a and 1. Finally, B3LYP and PW91 shifts calculated with the 6-31G(d) basis set for pyridine are negative for the weaker type II and III set of bands in the PCM calculations. However, the red-shift of −5.0 cm^{-1} observed for mode 19a still remains not well-reproduced.

The Changes Occurred at the Vibrational Modes of Pyridine Depending on the Electrode Potential

The tuning of the wavenumbers by the electrode potential is discussed in this section being mainly restricted to the behavior of the five strongest SERS bands which corresponds to type I vibrations plus mode 9a.

Once the molecule is adsorbed, the vibrational wavenumbers are tuned by the electrode potential in such a way that positive potentials favors charge donation from pyridine to the metal and, therefore, the surface complex becomes stronger and the bands are blue-shifted. This tuning of the experimental wavenumbers $\Delta\upsilon_V$ originated by the applied potential is referred to the absolute SERS wavenumbers recorded in the reference spectrum at −0.7 V as:

$$\Delta\upsilon_V = \upsilon_V - \upsilon_{PZC\ =\ -0.7\ V}$$

Figure 4 shows the $\Delta\upsilon_V$ values for the main set of vibrational modes (type I plus mode 9a). As can be seen, the amplitude of the tuning for the most shifted ones (modes 8a and 6a) among them ranges from +6 to +10 cm^{-1}. All of them show the expected behavior and are red-shifted as the electrode potential is more negative. It has to be stressed that a SERS spectrum recorded at a particular potential can contain contributions from an ensemble of molecules bonded to a distribution of local sites characterized by different densities of charge. Therefore, the height and width of a SERS band contain heterogeneous contributions from different molecules bonded to an unknown distribution of atomic sites of the rough electrode surface, each one of them being characterized by a particular excess of charge. This causes smoothing of the experimental dependence of the wavenumbers on the potential. The wavenumbers are more or less insensitive to the potential at the most positive values (0.0 to −0.4 V) showing a very small or near zero slope (region A in **Figure 4**). This is a rather surprising result given that the silver-pyridine complex should be strengthened as the density of charge of the metal increases and, therefore, the corresponding wavenumbers should be continuously blue-shifted. This behavior can be also seen in the case of pyrazine in spite of the smaller number of potentials scanned (Soto et al., 2002). Region B show the expected behavior with a rather linear positive slope, while the most negative potentials also show again a reduced slope (region C). This behavior of region C is probably due to the desorption of pyridine at very negative potentials. The relative intensities of the SERS bands observed at the potentials of −1.1, −1.2, and −1.3 V remain almost constant (**Figure 2** and **Supplementary Figure S1**), indicating that the limit of the most negative potential which can enable to keep the metal-molecule binding has been surpassed. Potentials more negative

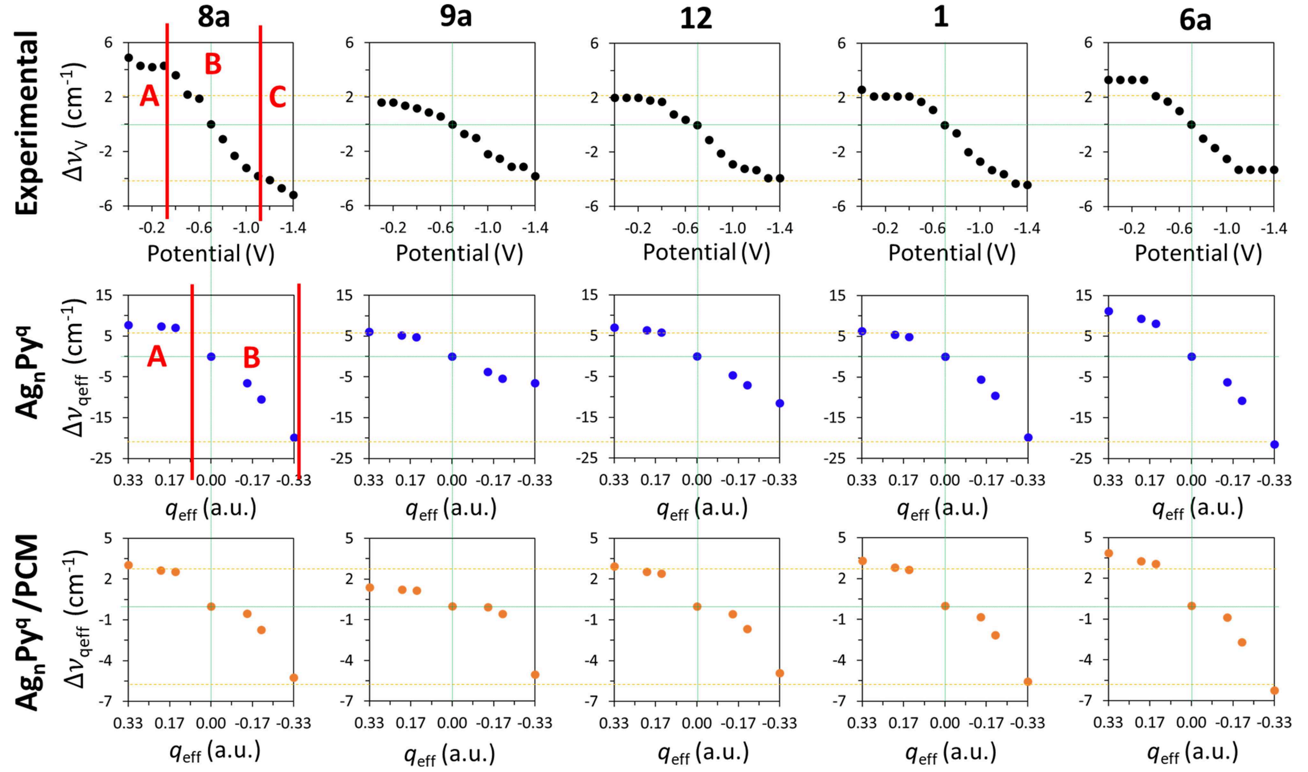

FIGURE 4 | Comparison of the wavenumbers shifts observed in the SERS spectra of pyridine which are tuned by the electrode potential with those calculated at the B3LYP/LanL2DZ level of theory for the $[Ag_nPy]^q$ complex models with different q_{eff} in vacuum and in solvent environments by using the PCM (solvent = water).

than such limit produce the dissociation of the surface complex and, therefore, the spectra of region C could be produced by the same kind of very weak complexes whose number is being diminished as the electrode potential is even more negative. The absolute intensities of the SERS become weaker at these potentials, but the relative intensities of the bands are not affected once such negative limit is reached.

The Results Obtained From the $[Ag_nPy]^q$ Cluster Model

The shifts observed at the experimental vibrational wavenumbers of pyridine $\Delta\upsilon_V$ which are tuned by the applied potential, and those calculated for the $[Ag_nPy]^q$ model complexes at the B3LYP/LanL2DZ level of theory by taking $[Ag_2Py]^0$ as a reference, are shown in **Figure 4**.

$$\Delta\upsilon_{qeff} = \upsilon_{[Ag_nPy]^q} - \upsilon_{[Ag_2Py]^0}$$

As can be observed, the general behavior of the dependence of the wavenumbers on q_{eff} agrees qualitatively very well with the experimental results. While the largest shifts are obtained for the vibrational modes 8a and 6a in the calculations, the shifts predicted for the modes 9a, 12, and 1 are smaller as observed in the experimental measurements. The relative slopes obtained from the wavenumbers calculated for these five vibrational modes exhibit a good agreement with those obtained from the observed wavenumbers. All $\Delta\upsilon_{qeff}$ are more or less constant for positive densities of charge ($q_{\text{eff}} > 0$), so reproducing the characteristics of the experimental region A. This could be related to the previously described bi-modal behavior of the electronic structure of complexes formed by organic molecules (A) bonded to charged metal clusters (M^q) (Román-Pérez et al., 2014a). In the case of charged adsorbates like the isonicotinate anion this effect is very striking, and the structure of complexes formed with positive clusters are almost insensitive to q_{eff}, while the properties of complexes in neutral ($q_{\text{eff}} = 0$) or negative ($q_{\text{eff}} < 0$) cases are very dependent on the electrode density of charge. In the first case, a strong (attractive) chemisorbed hybrid species is formed (A^--M^+) and its electronic structure is almost insensitive to the electrode potential. In the second case (A^--M^0 and A^--M^-) the physisorbed (repulsive) complex is weak and its properties can be smoothly tuned by the charge of the metal. Pyridine is a neutral molecule and can be considered as a case of physisorption in all the potential range (Avila et al., 2011a). Therefore, this duality should be less evident in pyridine than in cases of charged adsorbates, but the experimental and calculated results point to a minor but significant change in the chemical nature of silver-pyridine hybrids at positive or negative/neutral charges of the metallic surface.

The $[Ag_3Py]^{-1}$ is the most negative case where the complex is almost dissociated as previously reported with M06-HF calculations (Avila et al., 2011a) and marks the negative limit of region B in **Figure 2**. This explains why the B3LYP/LanL2DZ calculated wavenumbers at the corresponding value of $q_{\text{eff}} = -0.33$ a.u. are very similar to those of the isolated pyridine.

Although a qualitative agreement between $\Delta\upsilon_V$ and $\Delta\upsilon_{qeff}$ is found in **Figure 4**, the calculated amplitudes of the effect of the excess of charge of the metal on the wavenumbers of this set of five vibrations are strongly overestimated by B3LYP/LanL2DZ calculations (-28, -13, -19, -26, and -33 cm^{-1}) with respect to the SERS results (-10, -5 -6, -6, and -7 cm^{-1}): $\Delta\upsilon_{qeff} = 3.5\ \Delta\upsilon_V$. PCM calculations reduce significantly this discrepancy. This may be because the metal cluster is also inside the cavity and the counter charges located around the metal in the PCM calculations diminish the effect of q_{eff} of the respective clusters. The amplitudes calculated by considering the effect of the solvent are only overestimated by about 20%: $\Delta\upsilon_{qeff} = 1.2\ \Delta\upsilon_V$. Unfortunately, this numerical improvement is not accomplished by appropriate dependences on q_{eff}. PCM is unable to account for the differentiated behavior of the experimental shapes of this set of five fundamentals (**Figure 4**). Now all vibrations show almost the same shape and amplitude, and only the positive part of the curve of mode 9a differs slightly from the remaining ones. Moreover, a discontinuity can be appreciated in the results for the neutral complex $[\text{Ag}_2\text{Py}]^0$ indicating that the PCM method does not modify the properties of charged species in a similar way than the neutral ones.

Concerning the dependence of the results on the level of theory, the three functionals predict similar behaviors, although a poorer performance can be seen in the case of M06-HF. With respect to the basis set size, the very large $\Delta\upsilon_{qeff}$ values provided for this model $[\text{Ag}_n\text{Py}]^q/q_{\text{eff}}$ with the LanL2DZ basis are slightly reduced by using the 6-31G(d) or 6-311G(d,p) basis for the pyridinic atoms. As an example, **Supplementary Figure S5** compares the experimental $\Delta\upsilon_V$ and the B3LYP calculated $\Delta\upsilon_{qeff}$ using three different basis sets, LanL2DZ, def2-TZVPP (Weigend and Ahlrichs, 2005) and LanL2DZ/6-31G(d), respectively. As can be seen, B3LYP/LanL2DZ and def2-TZVPP calculations look like very similar and all of them overestimate the amount of the tuning (slopes and amplitudes) of the electrode potential. The $[\text{Ag}_n\text{Py}]^q$ complexes become even more repulsive at the B3LYP/LanL2DZ/6-31G(d) level and dissociates in the case of $q_{\text{eff}} = -0.33$ a.u. giving a very large N-Ag distance at the end of the geometry optimization process. This is the cause of the anomalous values shown by modes 9a and 12 while vibrations 8a, 1, and 6a are well-behaved.

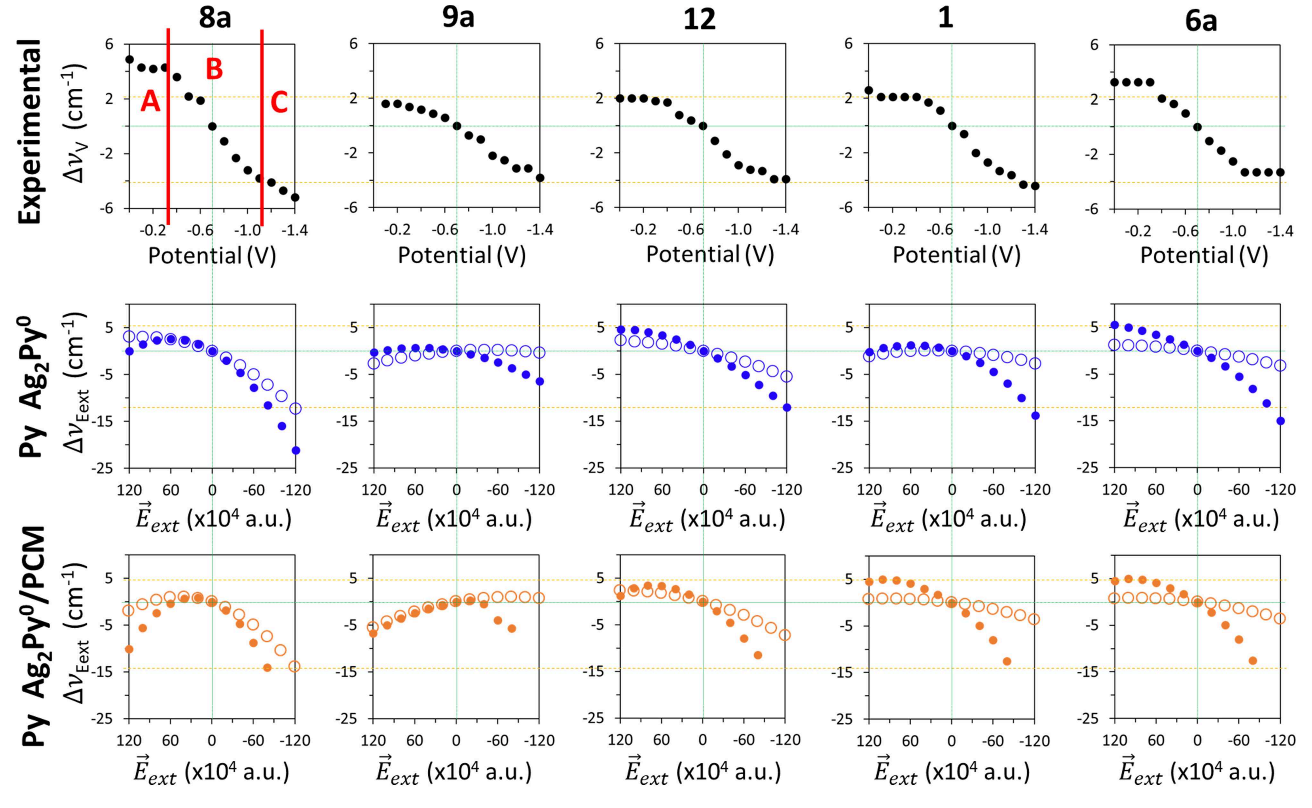

FIGURE 5 | Comparison of the wavenumbers shifts observed in the SERS spectra of pyridine which are tuned by the electrode potential with those calculated at the B3LYP/LanL2DZ level of theory by applying external electric fields for the isolated pyridine (empty circles) and for the $[\text{Ag}_2\text{Py}]^0$ complex model (full circles) in vacuum and in solvent environments by using the PCM (solvent = water).

The Results Obtained From the Py/$\overrightarrow{E}$ and $[Ag_2Py]^0$/ $\overrightarrow{E}$ Models

External electric fields polarize the electronic cloud of a molecule along the direction of the field with respect to the equilibrium structure. **Figure 5** show the effect of $\overrightarrow{E}_{ext}$ in the calculated B3LYP/D95V (LanL2DZ) wavenumber shifts $\Delta\upsilon_{\overrightarrow{E}_{ext}}$ for isolated pyridine (empty circles):

$$\Delta\upsilon_{\overrightarrow{E}_{ext}} = \upsilon_{Py,\ \overrightarrow{E}_{ext}} - \upsilon_{Py,\ \overrightarrow{E}_{ext}\ =0}$$

As can be seen, all the five discussed modes are smoothly shifted in the ±120·10^{-4} a.u. range of fields with a curved shape resembling parabolic sections. These curves are not symmetric with respect to $\overrightarrow{E}_{ext} = 0$ a.u. because pyridine is not centrosymmetric like benzene or pyrazine, being this behavior much more evident in the case of mode 8a, which shows the largest amplitude amounting to -15 cm^{-1}. The tuning of the wavenumbers by the field in the case of the remaining modes 1, 12, 6a, and 9a is smaller (around -5 cm^{-1}), but the trend is just the opposite to the expected one in the case of vibration 9a. In the same **Figure 5** (full circles) the calculated values for the $[Ag_2Py]^0$ complex can be also compared:

$$\Delta\upsilon_{\overrightarrow{E}_{ext}} = \upsilon_{[Ag_2Py]^0,\ \overrightarrow{E}_{ext}} - \upsilon_{[Ag_2Py]^0,\ \overrightarrow{E}_{ext}=0}$$

The presence of the Ag_2^0 cluster makes the electronic density of pyridine much more polarizable resulting in a larger sensitivity of the wavenumbers to the field. The amplitudes are increased up to -21, -6, -17, -14, and -21 cm^{-1} for the respective 8a, 9a, 12, 1, and 6a modes, and the parabolic trend is more evident, especially in the cases of vibrations 8a, 9a, and 1 which show a maximum at +60 10^{-4} a.u. Once again, the amplitude of the predicted tuning is overestimated with respect to the experimental results and the behavior is similar regardless the functional or the basis set used.

Any improvement can be seen in the PCM results also shown in **Figure 5**. The curvature is now more evident, notably in the case of mode 8a, vibration 9a shows two differentiated and unexpected change of trend before and after of +20 10^{-4} a.u. and the $[Ag_2Py]^0$ complex dissociates at fields more negative than -80 10^{-4} a.u. Therefore, electric field calculations do not reproduce well the observed results given that neither the experimental region A, with near zero slope, nor region B, with a linear dependence, can be distinguished. Moreover, the curved profiles do not allow for quantifying the dependence on the field by means of a single numerical slope.

A similar assessment can be applied to the results obtained for the effect of electric fields in the case of pyridine bonded to a larger tetrahedral Ag_{20}^0 complex. Two different geometries have been studied with the molecule bonded to a vertex (V-complex) or to the center of a face (S-complex) (**Supplementary Figure S6**). B3LYP/LanL2DZ results for these systems can be compared to the experimental SERS results and the calculated shifts for model $Ag_2Py^0/\overrightarrow{E}$ in **Supplementary Figure S6**. Full optimization of the geometries of both $Ag_{20}Py^0$ hybrids have the problem that pyridine losses the original orientation at negative fields when the metal-molecule bond is too weak and breaks. In this circumstance, the dipole of pyridine is realigned along the strong negative field, migrates to another site or dissociates, depending on the particular complex and the field strength. Anyway, the general behavior shown by the two large complexes $[Ag_{20}Py]^0$ and the simpler $[Ag_2Py]^0$ system looks like very similar.

Concerning the remaining A_1 (19a and 18a) and B_2 (8b and 6b) fundamentals all of them are very weak in SERS and the respective wavenumbers show a little dependence on the electrode potential, in rough agreement with the corresponding B3LYP/LanL2DZ results (**Supplementary Figure S6**). It should be stressed that both B_2 bands do not show the blue-shift theoretically predicted from the wavenumbers calculated at negative electrode potentials. This behavior of pyridine differs from the one reported for the SERS spectra of pyrazine (Soto et al., 2002), at which both the observed and calculated wavenumbers indicate a blue-shift. The interested reader can reach a complete set of the figures (**Supplementary Figures S8–S28**) presented in this study in the **Supplementary** section where the observed wavenumber shifts $\Delta\upsilon_i(V)$ are compared with those calculated at the different levels of theory.

CONCLUDING REMARKS

This work discusses the dependence on the applied electrode potential of the vibrational wavenumbers of pyridine adsorbed on a metal surface in the light of calculation results obtained at different levels of theory. The experimental results have indicated small but significant shifts for the wavenumbers of some respective bands observed in the SERS spectra of a pyridine-silver interface. The effect of the electrode potential has been considered in the DFT calculations by means of pyridine-silver $[Ag_nPy]^q$ complexes with different densities of charge (q_{eff}) or by applying external electric fields to a neutral $[Ag_2Py]^0$ complex. The dependence of the results with the functional (B3LYP, PW91 and M06-HF) the basis set size (LanL2DZ and combined LanL2DZ/6-31G(d) or LanL2DZ/6-311G(d,p) sets for silver/pyridine atoms, respectively) has been discussed. B3LYP and PW91 provide similar results while M06-HF shows a poorer performance. Larger basis set does not improve the quality of the predictions as well as the size of the metal cluster in models using electric fields, given that $[Ag_{20}Py]^0$ complexes add nothing to predictions derived from the simple $[Ag_2Py]^0$ hybrid. As a conclusion, it does not seem worth the use of more realistic models of the metal surface in the theoretical estimations of the here discussed properties.

Although these conclusions, based on the linear $[Ag_nPy]^q$ complex models which are applied at the B3LYP/LanL2DZ level of theory, need to be confirmed also for the other similar molecular systems, they have shown that the simple model used here satisfactorily reproduce the shifts observed at the vibrational wavenumbers of the pyridine-silver complexes. Moreover, this model is also able to account for the small or near zero slope of the experimental tuning of the wavenumbers at positive electrode potentials (region A) as well as for the linear red-shift observed at more negative potentials than $\mathbf{V}_{PZC}$ (region B). However, theoretical predictions are overestimated and need to be numerically corrected. Summarizing, DFT calculations on the properties of linear $[Ag_nPy]^q$ complexes have proved once again its usefulness for understanding complex SERS results like the enhancement of selective in-plane enhancement fundamentals of aromatic molecules under charge transfer (Avila et al., 2011b) or plasmon-like (Roman-Perez et al., 2015) resonant processes, the effect of the symmetry of the surface complex in the SERS selection rules (Centeno et al., 2006, 2012), the dual electronic structure of charged molecules bonded to charged metals (Román-Pérez et al., 2014b), the activity of the out-of-plane bands in SERS (Aranda et al., 2018), the huge energy gain of the electrode potential in tuning the energies of the charge transfer states (Román-Pérez et al., 2014a) or the wavenumber shifts of the vibrations under adsorption on neutral or charged metal surfaces.

DATA AVAILABILITY

The raw data supporting the conclusions of this manuscript will be made available by the authors, without undue reservation, to any qualified researcher.

AUTHOR CONTRIBUTIONS

DA, SV, JS, and FA carried out DFT calculations. IL-T recorded the SERS spectra. JO and FA coordinated and designed the research. All authors contributed to write the sections of the manuscript and to revise it, read and approved the submitted version.

FUNDING

The authors thanks financial support from Spanish Ministerio de Economía y Competitividad (Project CTQ2015-65816-R). FA thanks university of Malaga for contract E-29-2018-0016654.

ACKNOWLEDGMENTS

The authors thanks to the Supercomputing and Bioinnovation Center (University of Malaga) for computational resources and Rafael Larrosa for technical support. The authors also acknowledge University of Malaga for financial support to publication fees.

SUPPLEMENTARY MATERIAL

The Supplementary Material for this article can be found online at: https://www.frontiersin.org/articles/10.3389/fchem.2019.00423/full#supplementary-material

REFERENCES

Aranda, D., Román-Pérez, J., López-Tocón, I., Soto, J., Avila, F., and Otero, J. C. (2017). Comment on "Elucidation of charge-transfer SERS selection rules by considering the excited state properties and the role of electrode potential" by M. Mohammadpour, M. H. Khodabandeh, L. Visscher and Z. Jamshidi, Phys. Chem. Chem. Phys., 2017, 19, 7833. *Phys. Chem. Chem. Phys.* 19, 27888–27891. doi: 10.1039/C7CP03075D

Aranda, D., Valdivia, S., Avila, F. J., Soto, J., Otero, J. C., and López-Tocón, I. (2018). Charge transfer at the nanoscale and the role of the out-of-plane vibrations in the selection rules of surface-enhanced Raman scattering. *Phys. Chem. Chem. Phys.* 20, 29430–29439. doi: 10.1039/c8cp05623d

Arenas, J. F., Soto, J., López Tocón, I., Fernández, D. J., Otero, J. C., and Marcos, J. I. (2002). The role of charge-transfer states of the metal-adsorbate complex in surface-enhanced Raman scattering. *J. Chem. Phys.* 116:7207. doi: 10.1063/1.1450542

Aroca, R. (2006). *Surface-Enhanced Vibrational Spectroscopy*. West Sussex: John Wiley & Sons Ltd.

Avila, F., Fernandez, D. J., Arenas, J. F., Otero, J. C., and Soto, J. (2011a). Modelling the effect of the electrode potential on the metal–adsorbate surface states: relevant states in the charge transfer mechanism of SERS. *Chem. Commun.* 47, 4210–4212. doi: 10.1039/C0CC05313A

Avila, F., Ruano, C., Lopez-Tocon, I., Arenas, J. F., Soto, J., and Otero, J. C. (2011b). How the electrode potential controls the selection rules of the charge transfer mechanism of SERS. *Chem. Commun.* 47, 4213–4215. doi: 10.1039/C0CC05314G

Becke, A. D. (1993). Density-functional thermochemistry. III. The role of exact exchange. *J. Chem Phys.* 98, 5648–5653. doi: 10.1063/1.464913

Brewer, K. E., and Aikens, C. M. (2010). TDDFT investigation of surface-enhanced Raman scattering of HCN and CN^- on Ag_{20}. *J. Phys. Chem. A* 144, 8858–8863. doi: 10.1021/jp1025174

Centeno, S. P., López-Tocón, I., Arenas, J. F., Soto, J., and Otero, J. C. (2006). Selection rules of the charge transfer mechanism of surface-enhanced Raman scattering: the effect of the adsorption on the relative intensities of pyrimidine bonded to silver nanoclusters. *J. Phys. Chem. B* 110, 14916–14922. doi: 10.1021/jp0621373

Centeno, S. P., López-Tocón, I., Roman-Perez, J., Arenas, J. F., Soto, J., and Otero, J. C. (2012). Franck–condon dominates the surface-enhanced Raman scattering of 3-methylpyridine: propensity rules of the charge-transfer mechanism under reduced symmetry. *J. Phys. Chem. C* 116, 23639–23645. doi: 10.1021/jp307015a

Chen, Y.-X., and Otto, A. (2005). Electronic effects in SERS by liquid water. *J. Raman Spectrosc.* 36:6–7. doi: 10.1002/jrs.1335

Cui, L., Wu, D.-Y., Wang, A., Ren, B., and Tian, Z.-Q. (2010). Charge-transfer enhancement involved in the SERS of adenine on Rh and Pd demonstrated by ultraviolet to visible laser excitation. *J. Phys. Chem. C* 114, 16588–16595. doi: 10.1021/jp1055717

Ditchfield, R., Hehre, W. J., and Pople, J. A. (1971). Self-consistent molecular orbital methods. 9. Extended Gaussian-type basis for molecular-orbital studies of organic molecules. *J. Chem. Phys.* 54, 724–728. doi: 10.1063/1.1674902

Dunning, T. H. Jr., and Hay, P. J. (1977). *Modern Theoretical Chemistry*. New York, NY: H. F. Schaefer III.

Frisch, M. J., Trucks, G. W., Schlegel, H. B., Scuseria, G. E., Robb, M. A., Cheeseman, J. R., et al. (2010). *Gaussian 09, Revision C. 01*. Wallingford, CT: Gaussian Inc.

Hay, P. J., and Wadt, W. R. (1985a). *Ab initio* effective core potentials for molecular calculations. Potentials for the transition metal atoms Sc to Hg. *J. Chem. Phys.* 82, 270–283. doi: 10.1063/1.448799

Hay, P. J., and Wadt, W. R. (1985b). *Ab initio* effective core potentials for molecular calculations. Potentials for main group elements Na to Bi. *J. Chem. Phys.* 82, 284–298. doi: 10.1063/1.448800

Hay, P. J., and Wadt, W. R. (1985c). *Ab initio* effective core potentials for molecular calculations. Potentials for K to Au including the outermost core orbitals. *J. Chem. Phys.* 82, 299–310. doi: 10.1063/1.448975

Hupp, J. T., Larkin, D., and Weaver, M. J. (1983). Specific adsorption of halide and pseudohalide ions at electrochemically roughened versus smooth silver-aqueous interfaces. *Surf. Sci.* 125, 429–451. doi: 10.1016/0039-6028(83)90576-9

Johansson, P. (2005). Illustrative direct *ab initio* calculations of surface Raman spectra. *Phys. Chem. Chem. Phys.* 7, 475–482. doi: 10.1039/B415535A

Kalampounias, A. G., Tsilomelekis, G., and Boghosian, S. (2015). Vibrational dephasing and frequency shifts of hydrogen-bonded pyridine-water complexes. *Spectrochim. Acta A Mol. Biomol. Spectrosc.* 135, 31–38. doi: 10.1016/j.saa.2014.06.156

Kelly, J. T., McClellan, A. K., Joe, L. V., Wright, A. M., and Lloyd, L. T. (2016). Competition between hydrophilic and argyrophilic interactions in surface enhanced Raman spectroscopy. *ChemPhysChem* 17, 2782–2786. doi: 10.1002/cphc.201600678

Kneipp, K., Moskovits, and, M., and Kneipp, H. (2006). *Surface-Enhanced Raman Scattering: Physics and Applications*. New York, NY: Springer.

Krishnan, R., K., Binkley, J. S., Seeger, R., and Pople, J. A. (1980). Self-consistent molecular orbital methods. XX. Basis set for correlated wave-functions. *J. Chem. Phys.* 72, 650–654. doi: 10.1063/1.438955

Le Ru, E., and Etchegoin, P. (2008). *Principles of Surface-Enhanced Raman Spectroscopy and Related Plasmonic Effects*. Amsterdam: Elsevier.

McLean, A. D., and Chandler, G. S. (1980). Contracted Gaussian-basis sets for molecular calculations. 1. 2nd row atoms, Z=11-18. *J. Chem. Phys.* 72, 5639–5648. doi: 10.1063/1.438980

Mohammadpour, M., Khodabandeh, M. H., Visscher, L., and Jamshidi, Z. (2017). Elucidation of charge-transfer SERS selection rules by considering the excited state properties and the role of electrode potential. *Phys. Chem. Chem. Phys.* 19, 7833–7843. doi: 10.1039/C6CP07585A

Moskovits, M. (2013). Persistent misconceptions regarding SERS. *Phys. Chem. Chem. Phys.* 15, 5301–5311. doi: 10.1039/C2CP44030J

Otto, A., Billmann, J., Eickmans, J., Ertürk, U., and Pettenkofer, C. (1984). The "adatom model" of SERS (surface enhanced Raman scattering): the present status. *Surf. Sci.* 138, 319–338. doi: 10.1016/0039-6028(84)90251-6

Perdew, J. O., Burke, K., and Wang, Y. (1996). Generalized gradient approximation for the exchange-correlation hole of a many-electron system. *Phys. Rev. B* 54, 16533–16539. doi: 10.1103/PhysRevB.54.16533

Román-Pérez, J., Centeno, S. P., López-Ramírez, M. R., Arenas, J. F., Soto, J., López-Tocón, I., et al. (2014b). On the dual character of charged metal–molecule hybrids and the opposite behaviour of the forward and reverse CT processes. *Phys. Chem. Chem. Phys.* 16, 22958–22361. doi: 10.1039/C4CP03984J

Roman-Perez, J., López-Tocón, I., Castro, J. L., Arenas, J. F., Soto, J., and Otero, J. C. (2015). The electronic structure of metal–molecule hybrids in charged interfaces: surface-enhanced Raman selection rules derived from plasmon-like resonances. *Phys. Chem. Chem. Phys.* 17, 2326–2329. doi: 10.1039/C4CP04724A

Román-Pérez, J., Ruano, C., Centeno, S. P., López-Tocón, I., Arenas, J. F., Soto, J., et al. (2014a). Huge energy gain in metal-to-molecule charge transfer processes: a combined effect of an electrical capacitive enhancement in nanometer-size hot spots and the electronic structure of the surface complex. *J. Phys. Chem. C* 118, 2718–2725. doi: 10.1021/jp412231w

Schlücker, S., Singh, R. K., Asthana, B. P., Popp, J., and Kiefer, W. (2001). Hydrogen-bonded pyridine-water complexes studied by density functional theory and Raman spectroscopy. *J. Phys. Chem. A* 105, 9983–9989. doi: 10.1021/jp0122272

Soto, J., Fernández, D. J., Centeno, S. P., López Tocón, I., and Otero, J. C. (2002). Surface orientation of pyrazine adsorbed on silver from the surface-enhanced Raman scattering recorded at different electrode potentials. *Langmuir* 18, 3100–3104. doi: 10.1021/la010489p

Stephens, P. J., Devlin, F. J., Chabalowski, C. F., and Frisch, M. J. (1994). *Ab initio* calculations of vibrational absorption and circular dichroism spectra using density functional force fields. *J. Phys. Chem.* 98, 11623–11627. doi: 10.1021/j100096a001

Szekeres, G. P., and Kneipp, J. (2019). SERS probing of proteins in gold nanoparticle agglomerates. *Front. Chem.* 7:30. doi: 10.3389/fchem.2019.00030

Tomasi, J., Mennucci, B., and Cammi, R. (2005). Quantum mechanical continuum solvation models. *Chem. Rev.* 105, 2999–3093. doi: 10.1021/cr9904009

Tukhvatullin, F. H., Hudayberdiev, B. G., Jumabaev, A., Hushvaktov, H. A., and Absanov, A. A. (2010). Aggregation of molecules in liquid pyridine and its solutions: Raman spectra and quantum-chemical calculations. *J. Mol. Liq.* 155, 67–70. doi: 10.1016/j.molliq.2010.05.015

Weaver, M. J., Farquharson, S., and Tadayyoni, M. A. (1985). Surface enhancement factors for Raman scattering at silver electrodes. Role of adsorbate-surface interactions and electronic structure. *J. Chem. Phys.* 82, 4867–4874. doi: 10.1063/1.448657

Weigend, F., and Ahlrichs, R. (2005). Balanced basis sets of split valence, triple zeta valence and quadruple zeta valence quality for H to Rn: Design and assessment of accuracy. *Phys. Chem. Chem. Phys.* 7, 3297–3305. doi: 10.1039/B508541A

Wolkow, R. A., and Moskovits, M. (1992). A comparative study of the electron energy loss spectrum and the surface-enhance Raman spectrum of benzene adsorbed on silver. *J. Chem. Phys.* 96, 3966–3980. doi: 10.1063/1.461899

Zhao, L., Jensen, L., and Schatz, G. C. (2005). Pyridine-Ag_{20} cluster: a model system for studying surface-enhanced Raman scattering. *J. Am. Chem. Soc.* 128, 2911–2917. doi: 10.1021/ja0556326

Zhao, X., and Chen,. M. (2013). DFT study on the influence of electric field on surface-enhanced Raman scattering from pyridine-metal complex. *J. Raman. Spectrosc.* 45, 62–67. doi: 10.1002/jrs.4422

Zhao, Y., and Truhlar, D. G. (2006). Density functional for spectroscopy: no long-range self-interaction error, good performance for rydberg and charge-transfer states, and better performance on average than B3LYP for ground states. *J. Phys. Chem. A* 110, 13126–13130. doi: 10.1021/jp066479k

Conflict of Interest Statement: The authors declare that the research was conducted in the absence of any commercial or financial relationships that could be construed as a potential conflict of interest.

ORIGINAL RESEARCH
published: 07 June 2019
doi: 10.3389/fchem.2019.00413

Exploring the Potentiality of a SERS-Active pH Nano-Biosensor

*Angela Capocefalo[1], Daisy Mammucari[1], Francesco Brasili[2], Claudia Fasolato[1,3], Federico Bordi[1], Paolo Postorino[1] and Fabio Domenici[2]**

[1] Dipartimento di Fisica, Sapienza Università di Roma, Rome, Italy, [2] Dipartimento di Scienze e Tecnologie Chimiche, Università di Roma Tor Vergata, Rome, Italy, [3] Dipartimento di Fisica e Geologia, Università di Perugia, Perugia, Italy

The merging of the molecular specificity of Raman spectroscopy with the extraordinary optical properties of metallic nanoarchitectures is at the heart of Surface Enhanced Raman Spectroscopy (SERS), which in the last few decades proved its worth as powerful analytical tool with detection limits pushed to the single molecule recognition. Within this frame, SERS-based nanosensors for localized pH measurements have been developed and employed for a wide range of applications. Nevertheless, to improve the performances of such nanosensors, many key issues concerning their assembling, calibration and stability, that could significantly impact on the outcome of the pH measurements, need to be clarified. Here, we report on the detailed characterization of a case study SERS-active pH nanosensor, based on the conjugation of gold nanoparticles with the pH-sensitive molecular probe 4-mercaptobenzoic acid (4MBA). We analyzed and optimized all the aspects of the synthesis procedure and of the operating conditions to preserve the sensor stability and provide the highest responsiveness to pH. Exploiting the dependence of the SERS spectrum on the protonation degree of the carboxylic group at the edge of the 4MBA molecules, we derived a calibration curve for the nanosensor. The extrapolated working point, i.e., the pH value corresponding to the highest sensitivity, falls at pH 5.6, which corresponds to the pKa value of the molecule confined at the nanoparticle surface. A shift of the pKa of 4MBA, observed on the molecules confined at the nanostructured interface respect to the bulk counterpart, unveils the opportunity to assembly a SERS-based pH nanosensor with the ability to select its working point in the sensitivity region of interest, by acting on the nanostructured surface on which the molecular probe is confined. As a proof-of-concept, the nanosensor was successfully employed to measure the extracellular pH of normal and cancer cells, demonstrating the capability to discriminate between them.

Keywords: SERS, pH sensor, plasmonics, gold nanoparticles, biosensing, extracellular pH, cancer cells

Edited by:
Ivano Alessandri,
University of Brescia, Italy

Reviewed by:
Wei-Lung Tseng,
National Sun Yat-sen University, Taiwan
Chih-Ching Huang,
National Taiwan Ocean University, Taiwan

***Correspondence:**
Fabio Domenici
fabio.domenici@uniroma2.it

Specialty section:
This article was submitted to Analytical Chemistry, a section of the journal Frontiers in Chemistry

Received: *14 March 2019*
Accepted: *20 May 2019*
Published: *07 June 2019*

Citation:
Capocefalo A, Mammucari D, Brasili F, Fasolato C, Bordi F, Postorino P and Domenici F (2019) Exploring the Potentiality of a SERS-Active pH Nano-Biosensor. Front. Chem. 7:413. doi: 10.3389/fchem.2019.00413

INTRODUCTION

In the last decades, the advances in the field of plasmonics enabled to tailor and enhance electromagnetic fields at the subwavelength scale, with a wide range of applications spreading from electronics to biomedicine (Stockman et al., 2018). The opportunity to exploit the nanoscale localization of such intense fields to push the sensitivity of traditional vibrational spectroscopies has raised a great deal of interest around surface enhanced spectroscopies (Camden et al., 2008; Lal et al., 2008). In this context, a relevant position is occupied by Surface Enhanced Raman Spectroscopy (SERS) which, benefiting of the highest signal enhancement [10^6-10^9 orders of magnitude (Le Ru et al., 2007)], allows to overcome the intrinsic limit of low intensity of Raman spectroscopy and hence has emerged as one of the most widely used technique in biosensing (Cialla et al., 2014). Recent advances in SERS-based detection methods involve the development of novel chips for immunoassays with enhanced sensitivity and specificity for the study of protein affinity (Chuong et al., 2017) and for the identification of pathogens based on the nucleic acid recognition (Dougan and Faulds, 2012). Beyond the application as ultrasensitive spectroscopy, SERS turned out to be an invaluable technique capable to actively and selectively interact with complex biological systems, including cells and tissues (Fasolato et al., 2016; Cialla-May et al., 2017); (Kneipp, 2017).

In this context, colloidal noble metal nanoparticles play a central role thanks to their high surface-to-volume ratio and to their ease of synthesis and functionalization in different environmental conditions, which make them a versatile platform to develop SERS-active chemical sensors (Yeh et al., 2012). In particular, by employing weak acids as reporter molecule and gold or silver nanoparticles as enhancing scaffold, it has been possible to develop pH sensors capable to convey the SERS potential in providing localized and molecular specific information (Bishnoi et al., 2006; Lawson et al., 2014; Gühlke et al., 2015; Williams et al., 2016). The development of tools for the evaluation of pH at the nanoscale enables to obtain information on small sample volumes, e.g., microfluidic devices or even single cells (Jamieson et al., 2015; Puppulin et al., 2018). In the latter framework, alterations of the local pH of cellular compartments could have dramatic effects on cells and organelles, encouraging the occurrence of diseases. Furthermore, the extracellular pH of cancer cells is expected to be more acidic with respect to that of healthy ones (Webb et al., 2011).

Despite the broad scientific landscape involving the employment of SERS-based pH sensors, many key issues concerning their assembling, calibration and stability, that could significantly affect the precision and accuracy of the pH measurements, need to be clarified.

Here we report on the detailed characterization of a SERS-active pH nanosensor based on the conjugation of gold nanoparticles (AuNPs) with the pH-sensitive molecular probe 4-mercaptobenzoic acid (4MBA), a benzene derivative with a thiol group, which covalently binds to the AuNPs surface, and a carboxylic acid in the opposite position. This molecule is particularly suitable to realize a SERS sensor since the protonation degree of the carboxyl moiety acts as pH indicator (Michota and Bukowska, 2003; Li et al., 2015) that, combined with the strong SERS cross section typical of benzene-derived molecules, results in a spectrum sensible even to weak pH variations (Bishnoi et al., 2006; Williams et al., 2016). Moreover, the orientation with respect to the thiol group provides minimized steric hindrance and maximum exposure outwards of the carboxylic moiety in comparison with other carboxyl-modified benzoic acid derivatives. This allows for a more packed coverage of AuNPs by 4MBA and therefore for a more efficient response to pH variations. With specific reference to the biological application of measuring the cellular pH, the choice of employing of AuNPs as plasmonic scaffold ensures higher chemical stability and biocompatibility with respect to different SERS-active metals such as silver (Wang et al., 2012).

Based on the analyses of the case study of the 4MBA-AuNPs nanosensor, the final purpose of the present work is to develop a systematic and general protocol for the characterization and employment of a nansosensor in different environments. To this aim, all the underlying aspects of the synthesis procedure and of the operating conditions have been analyzed and rationalized to provide the highest sensitivity to pH variations and to preserve the sensor stability. In particular, we focused on the colloidal stability of the system, a crucial parameter for measurements in liquid environment, and on its photostability, identifying a variability range of the measurement parameters to reduce the radiation-induced molecule degradation. All the spectral modifications, directly and indirectly associated to pH variations, have been analyzed and discussed to achieve a close control on all the aspects involved in the measurement.

In the perspective of obtaining a fine tuning of the nanosensor features, particular emphasis has been placed in analyzing the acidic properties of the molecular probe conjugated to the AuNPs in terms of the pKa value. Three calibration curves have been provided in terms of relative intensity of selected pH-dependent SERS bands as a function of the pH and the dynamic range of sensitivity of the nanosensor was identified. The suitability of the 4MBA-AuNPs pH nanosensor for biological applications was demonstrated by measuring the extracellular pH of two cellular models: keratinocyte HaCaT and melanoma SK-Mel5 human skin cells. The possibility to discriminate between the two types of cells highlights a great potential for future diagnosis applications.

MATERIALS AND METHODS

Nanosensor Assembling

AuNPs with nominal diameter of 60 nm stabilized by a citrate capping were purchased from Ted Pella Inc. 4MBA and all the other chemicals involved in sample preparation were purchased from Sigma-Aldrich and used without further purification.

The pH nanosensor employed in this study consists of a core-shell system made up of colloidal AuNPs functionalized by a layer of 4MBA. The molecular functionalization, sketched in **Figure S1A**, was performed by adding 5 μL of an ethanol solution of 4MBA (0.1 mg/mL) to the water-dispersed colloids stock solution. We employed a large excess of 4MBA molecules to obtain a full coverage of the AuNP (Fasolato et al., 2014), which based on steric hindrance considerations can be esteemed to $\sim 2 \times 10^4$ molecules per AuNP. In this way it was possible to ensure the stability of the colloidal dispersion and to maximize the SERS cross section of the nanosensor. In addition, a high coverage of the AuNPs prevents the molecule degradation that might be induced by the interaction of the carboxyl moiety with the gold surface (Michota and Bukowska, 2003), as discussed in detail in section Nanosensor Assembling and Stability. The solution was incubated for 3 h at room temperature and the excess of unbound 4MBA was removed by 24 h dialysis against Milli-Q water, under continuous gentle stirring, using a filter with a cutoff of 50 kDa. A careful characterization was performed after each step and at the end of the functionalization by UV-Visible absorption spectroscopy and Dynamic Light Scattering (DLS).

UV-Visible Absorption Spectroscopy

The molecular functionalization of AuNPs with 4MBA has been checked by monitoring the absorption peak corresponding to the Localized Surface Plasmon Resonance (LSPR) of the AuNPs by UV-Visible absorption spectroscopy. Being the LSPR very sensitive to the dielectric environment, information on the coverage can be inferred from the observed wavelength shift. Measurements were performed employing a double beam Jasco V-570 Uv/Vis/NIR spectrophotometer, with a resolution of 0.1 nm in the UV-Vis region and 0.5 nm in the NIR region.

Dynamic Light Scattering

Size and ζ-potential distributions of the water dispersed 4MBA-AuNPs were characterized by Dynamic Light Scattering (DLS). Measurements were performed employing a Malvern NanoZetaSizer apparatus equipped with a 5 mW HeNe laser (Malvern Instruments Ltd, UK) in quasi-backscattering detection, i.e., the scattered light was collected at an angle of 173°. In order to obtain the size distributions, the measured autocorrelation functions were analyzed by the CONTIN algorithm. ζ-potential measurements were performed adopting the Phase Analysis Light Scattering technique of the same Malvern NanoZetaSizer apparatus, by employing a palladium electrode dip cell ZEN 1002 (Malvern, UK). The measured electrophoretic mobility values μ_e were converted into the ζ-potential using the Smoluchowski relation $\zeta = \mu_e\eta/\varepsilon$, where ε is the solvent permittivity and η its viscosity.

Cell Culture

The cell lines employed in the experiments were obtained from Interlab Cell Line Collection (Istituto Nazionale per la Ricerca sul Cancro, Genoa, Italy) and kindly provided by the Molecular Medicine Department of Sapienza University of Rome. Non-tumorigenic human keratinocyte (HaCaT) and tumorigenic human skin melanoma (SK-Mel5) cell lines were grown, respectively, in Dulbecco's Modified Eagle Medium (DMEM; Euroclone, Life Science Division, GB, Pero, Italy) and Minimum Essential Medium (MEM; Euroclone). All media were supplemented with 1% penicillin/streptomycin, 10% fetal bovine serum and 2 mM L-Glutamine (Euroclone). MEM was also supplemented with 1% non-essential amino acids and 1% Na pyruvate. Before experiments cells were plated onto a glass coverslip deposited in a cell culture Petri dish and then incubated at 37°C under 5% CO_2.

Raman Micro-spectroscopy and SERS Measurements

4MBA-AuNPs samples for Raman measurements were prepared as sketched in **Figure S1B**. A droplet of the solution was deposited on a glass coverslip and dried at room temperature. A representative optical microscopy image of the so obtained substrate, showing self-assembled clusters with micrometric size, is also shown in **Figure S1B**. SERS measurements were performed in liquid as sketched in **Figure S1C**, by exposing the dried substrate to solutions with pH adjusted to the desired value. Preliminary stability and reversibility tests have been performed in a broad pH range, spanning between pH 2 and pH 12. SERS measurements of the cellular samples were performed by superimposing a SERS substrate with 4MBA-AuNPs onto a glass coverslip with the cells cultured according to section Cell Culture, as sketched in **Figure S9**. For each sample at least 10 spectra have been collected.

Raman and SERS measurements were performed employing a Horiba HR-Evolution microspectrometer, equipped with a 15 mW He–Ne laser (632.8 nm wavelength) and a set of neutral power attenuating filters. The spectrometer is coupled with a confocal microscope equipped with a set of objectives at different magnification. In the experiments a 50× −0.50 NA objective (laser spot diameter 1.5 µm) was employed for SERS measurements in liquid and a 100× −0.8 NA objective (laser spot diameter 1 µm) was employed for dried samples. A 600 lines/mm diffraction grating ensures a spectral resolution of 3 cm^{-1}. The spectrometer is equipped with an automatic mapping stage with sub-micrometric precision (∼0.3 µm).

All the spectra are here presented after a calibration of the Raman shift frequencies obtained by exploiting the emission spectrum of a neon lamp and a polynomial baseline subtraction performed using LabSpec software. To improve the signal-to-noise ratio, the spectra shown in **Figure 3** and **Figure S5** have been slightly smoothed using a FFT filter procedure (2 points of window). The frequencies of the main Raman and SERS bands were estimated by a fitting procedure performed using Origin 8.1 software.

RESULTS AND DISCUSSION

Nanosensor Assembling and Stability

In this paragraph we report on all the aspects concerning the fabrication and characterization of the nanosensor with special focus on the colloidal stability, pivotal to refine the performances in liquid environment, and on the chemical alterations that might occur in the molecular probe due to the laser illumination.

The employed nanosensor consists of a plasmonic core made of 60 nm AuNPs conjugated with 4MBA, according to the protocol described in section Nanosensor Assembling. Briefly, as sketched in **Figure S1A**, the spontaneous S-Au functionalization reaction between the thiol group of the 4MBA and the AuNPs surface was carried out in aqueous solution and thereafter the assembled 4MBA-AuNPs were purified to remove unbound molecules.

The functionalization procedure was monitored by UV-Vis absorption and Raman spectroscopies. Being related to the presence of 4MBA, both the absorption bands in the UV region (Guo et al., 2012) and the redshift of ∼4 nm of the LSPR of the AuNPs (LSPR at 533 nm for bare AuNPs), driven by the change

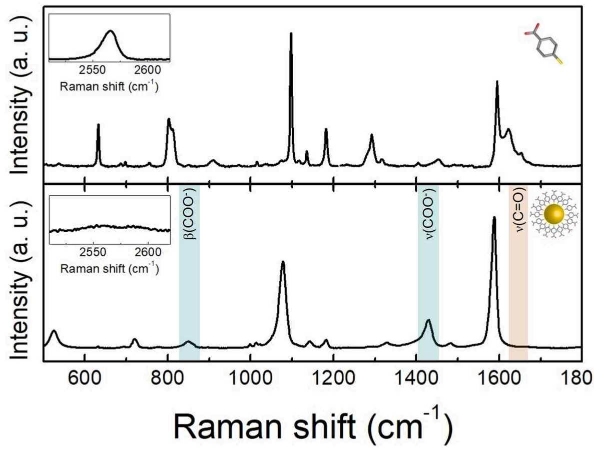

FIGURE 1 | Raman spectrum of bulk 4MBA (top) and SERS spectrum of 4MBA conjugated to AuNPs and dried onto a glass slide (bottom). The peaks of the pH-dependent bands in the SERS spectrum are highlighted: β(COO^-) and ν(COO^-) in blue and ν(C=O) in red. The spectral region of the ν(SH) band is reported in the insets. The disappearance of the corresponding peak in the SERS spectrum witnesses a successful functionalization of the AuNPs by S-Au covalent binding.

TABLE 1 | Peak assignment of the main Raman and SERS bands of the spectra reported in **Figure 1** according to Michota and Bukowska (2003), Varnholt et al. (2014), Li et al. (2015) and Williams et al. (2016).

Peak assignment	Raman shift (cm^{-1})	SERS frequency (cm^{-1})
S-Au	–	228
ν(CS)	–	525
ν_{6b}	632	631
β(CO_2) + ν(CS)	686	–
ν_{4b} + γ(CCC)	–	720
ν_{10a}	801	–
ν_{17b} + ω(CO_2)	812	–
β(COO^-)	–	849
β(SH)	915	–
ring deformation	–	1,011
ν_{12} – ring breathing	1,098	1,076
ν_{19b} + ν(CS)	1,116	–
ν_{9a}	1,135	–
ν($CCOO^-$) + ν(CS)	–	1,143
β(CH)	–	1,183
ν_3	1,292	–
ν(COO^-)	–	1,428
ν_{8a} – ring breathing	1,594	1,586
ν(C=O)	1,620	1,710
ν(SH)	2,565	–

Greek letters indicate the vibrational modes: ν, stretching; β, bending; ω, wagging; γ, out-of-plane vibration. Benzene modes are reported according to the Wilson notation (Wilson, 1934). The rows highlighted in light blue identify the bands whose intensity increases with pH, while the one whose intensity decreases with pH is highlighted in light red. The band corresponding to the S-Au and ν(SH) vibrations, used to assess the functionalization of AuNPs with 4MBA, are highlighted in gray.

in the dielectric environment at the AuNPs surface (Mock et al., 2003), are indicative of the effective conjugation. The absorption spectrum of the 4MBA-AuNPs in comparison with that of the bare AuNPs is reported in **Figure S2**.

The Raman spectra of 4MBA-AuNPs and bulk 4MBA, both deposited on a glass slide are shown in **Figure 1**. The complete assignment of the main Raman and SERS bands is reported in **Table 1**.

The SERS spectrum of 4MBA-AuNPs is characterized by two intense bands at 1,076 and 1,586 cm^{-1}, corresponding to the vibrations of the aromatic ring of the molecule (Michota and Bukowska, 2003), both redshifted with respect to their Raman counterpart. It is known that a relaxation of Raman selection rules occurs when molecules are in proximity to a metal surface, under near-field illumination: this can cause the appearance, in the SERS spectra, of bands that are hindered in the conventional Raman spectra (Moskovits and Suh, 1984; Le Ru et al., 2008, 2011). For analogous reasons, frequency shifts can take place as a result of molecule-metal charge transfer phenomena (Osawa et al., 1994). The successful functionalization by S-Au covalent binding is witnessed by the appearance of the band at 228 cm^{-1} (see **Figure S3**), corresponding to the gold-sulfur vibration (Varnholt et al., 2014) and by the concomitant vanishing of the band at 2,565 cm^{-1}, showed in the insets of **Figure 1**, corresponding to the thiol S-H stretching vibration (Fasolato et al., 2014). Furthermore, the disappearance of the latter peak certifies that all the molecules concurring to the SERS signal are covalently bound to the AuNPs.

The bands that are sensitive to pH variations are those related to the carboxylic moiety at the edge of the 4MBA molecule, i.e., the bending and stretching vibrations β(COO^-) and ν(COO^-) at 849 and 1,428 cm^{-1}, and the weak band at 1,710 cm^{-1} corresponding to the ν(C=O) stretching vibration (Li et al., 2015; Williams et al., 2016). The first two bands arise when the carboxylic groups are in the deprotonated form, in basic environment; while the ν(C=O) band appears more intense in acidic condition, when the moiety is protonated. In the SERS spectrum of **Figure 1**, the bands corresponding to COO^- vibrations are prominent, suggesting that most of the carboxylic residues of the 4MBA-AuNPs deposited after the functionalization are in the deprotonated form.

Moving into the issues concerning the actual applicability of the nanosensor, we analyzed the stability of the 4MBA-AuNPs colloidal dispersion by DLS measurements, in terms of size distribution and ζ-potential, and by UV-Visible absorption spectroscopy at varying the pH of the solution. The combined measurements allowed to correlate the aggregation of the system, which occurs upon pH variations due to the related changes in the 4MBA-AuNPs surface charge, with its optical response. The ζ-potential of particles in solution, which is proportional to their average surface charge, is a well-established indicator of the stability of a colloidal dispersion, quantifying the electrostatic repulsion between like-charged particles (Bhattacharje, 2016).

Size and ζ-potential results are shown in **Figure 2**, where a remarkable pH-dependence is clearly observed for both the

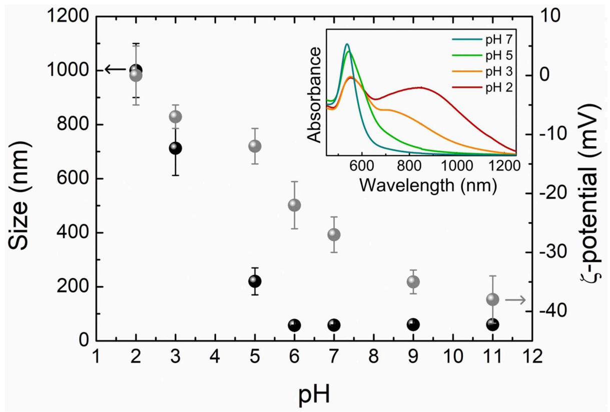

FIGURE 2 | Size (black) and ζ-potential (gray) of 4MBA-AuNPs obtained by DLS measurements as a function of the pH of the solution. The error bars represent the standard deviations of the measured size and ζ-potential distributions. In the inset are reported selected UV-Visible absorption spectra.

quantities. At basic pH and down to pH 6, the absolute value of the ζ-potential is high enough ($-38\,\text{mV} < \zeta < -22\,\text{mV}$) to prevent the 4MBA-AuNPs aggregation, with size distributions centered on that of single AuNPs. Starting from pH 5, the ζ-potential decreases in modulus and the colloids form aggregates whose dimensions increase with lowering the pH. At pH values lower than 3, 4MBA-AuNPs aggregates reach a micrometric size and could precipitate, as the ζ-potential approaches zero. Notice that the ζ-potential shows the highest slope, corresponding to the maximum sensitivity of the surface charge of the nanosensor with respect to pH variations, in the region between pH 5 and pH 6. Since the 4MBA-AuNPs surface charge basically depends on the protonation degree of the exposed carboxyl moieties, this finding strongly suggests that the working point of the SERS-active nanosensor lies in the same pH range. For the same reason, at pH > 9 the ζ-potential remains essentially unchanged, pointing out that all the carboxylic groups are in the deprotonated form. In these conditions the average number N of 4MBA molecules bound to each AuNP is equal to the number of elementary charges on the surface of each 4MBA-AuNPs colloids. This allows to validate the geometrical esteem of the 4MBA coverage ($N \sim 2 \times 10^4$ molecules per AuNP) using the electrophoretic mobility value (see section Dynamic Light Scattering) measured at pH 11. By employing the Hückel relation it is possible to derive a value for the effective charge Q_{eff} of the colloids and compare it to that obtained independently from N using the model of Aubouy for spherical particles (Aubouy et al., 2003; Bordi et al., 2006). The good accordance between the two values ($Q_{eff} = -90 \pm 10e$ and $Q_{eff} = -94e$, where e is the elementary charge) ascertains the reliability of the esteem herein provided.

Selected absorption spectra corresponding to the DLS measurements are reported in the inset of **Figure 2**. The resonance frequency of the LSPR is strongly influenced by the aggregation of the nanoparticles, leading to the substantial shift and broadening of the plasmons absorption peak due to the coupling among the single particle plasmonic modes of adjacent nanoparticles (Halas et al., 2011). The optical response of the samples changes coherently with the measured aggregation trends. Noteworthy, starting from pH 5, inter-particle plasmonic modes appear at higher wavelength with respect to the LSPR of non-aggregated colloids and the associated absorption band progressively broadens toward the infrared spectral region with the lowering of the pH. These modifications in the shape, amplitude and frequency of the plasmon resonance could critically affect the outcome of the SERS measurement, resulting in possible variations of the spectral enhancement at a given excitation wavelength (Trautmann et al., 2018).

It is therefore evident that the pH of the environment has an impact on the colloidal stability of the nanosensor. The plasmon resonance modifications that occur upon nanoparticles aggregation could compromise the plasmonic efficiency of the enhancing SERS scaffold. Moreover, the precipitation of the sensor upon aggregation at low pH could restrict the range of pH values that allows reliable measurements. Such issues have to be taken into account for properly controlling and interpreting the measurements in liquid environment. The approach adopted in this work to obtain a SERS enhancement independent on the pH of the solution relies in the self-assembly of the 4MBA-AuNPs in micrometric clusters onto glass slides, as shown in **Figure S1B**. Such aggregates show a stable plasmonic absorption band in the red spectral region (Fasolato et al., 2014; Domenici et al., 2016). The related SERS enhancement is therefore not affected by a different coupling between plasmonic modes upon aggregation, but only by dimensional scale effects of the cluster size which can be overcome by a normalization procedure respect to the intensity of selected pH-independent bands, as discussed below.

Proceeding on this line, a necessary step is to tackle the issue of the nanosensor photostability, and the associated reproducibility of the SERS response. Indeed repeated, extended illumination could cause a degradation of the molecule. Specifically, 4MBA molecules are known to be subject to decarboxylation, i.e., the loss of the carboxylic moiety, as a result of the interaction with plasmonic-active surfaces (Zong et al., 2014; Williams et al., 2016). The occurrence of this phenomenon is recognized in the spectra by the appearance of two new peaks at 996 and 1,019 cm^{-1} (**Figure S4**), which are attributable to the benzene monosubstituted thiophenol (Michota and Bukowska, 2003). The two bands are mainly related to the ring out-of-plane and in-plane deformations, respectively (see **Table S1**) (Fontana et al., 2013).

Since the loss of the carboxylic moiety directly affects the nanovector sensitivity to pH variations, we carried out a study with the aim of identifying the experimental conditions to minimize the decarboxylation process. SERS spectra of the 4MBA-AuNPs deposited on glass slides at varying the illumination time and the laser intensity are shown in **Figure 3**, over the spectral region where are located the spectral markers of decarboxylated 4MBA.

When comparing the reported spectra, a clear dependence of the decarboxylation process on the laser intensity can be recognized. Noticeable, at 0.56 kW/cm^2 the loss of the carboxylic group does not occur, even upon repeated measurements (**Figure 3A**). At 5.6 kW/cm^2, the thiophenol peaks appear already

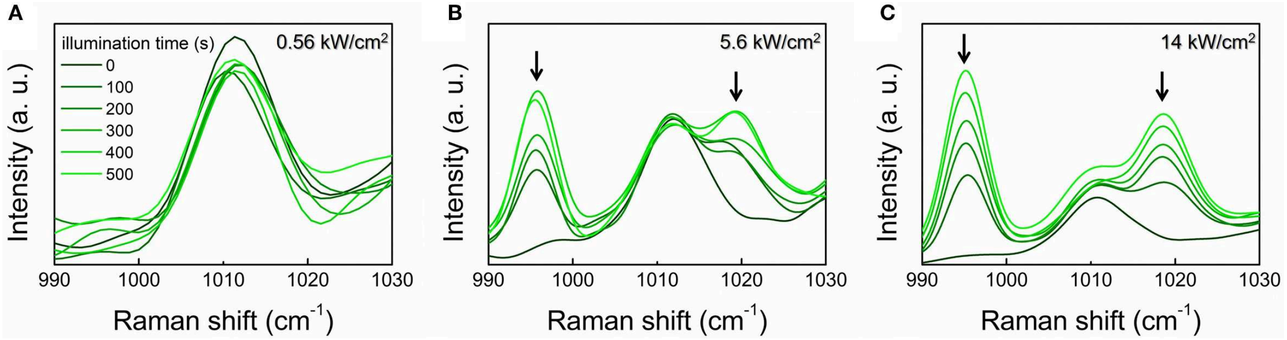

FIGURE 3 | SERS spectra of 4MBA-AuNPs deposited on glass slides over the 990–1,030 $\mathrm{cm^{-1}}$ spectral range. The onset of the spectral markers of the irradiation-induced decarboxylation at 996 and 1,019 $\mathrm{cm^{-1}}$ (highlighted by the arrows) is well-evident. The spectra were acquired at varying the illumination time with laser intensity of 0.56 $\mathrm{kW/cm^2}$ **(A)**, 5.6 $\mathrm{kW/cm^2}$ **(B)** and 14 $\mathrm{kW/cm^2}$ **(C)**. A FFT filter smoothing was applied to the spectra.

after 100 s illumination (**Figure 3B**). The observed phenomenon is ascribed to plasmon-derived "hot" electrons extracted from the nanoparticle upon plasmon excitation. These are transferred to the molecule, where they promote the decarboxylation reaction which is also accelerated by the local increase of temperature (Zong et al., 2014).

To deepen the investigation on the decarboxylation phenomenon, we acquired SERS spectra by exposing 4MBA-AuNPs to acidic and basic solutions, as reported in **Figure S5**. A dependence on the pH of the solution appears evident. In particular, for acidic pH the decarboxylation threshold is shifted to higher laser intensities. This effect is mainly ascribed to the orientation of the 4MBA molecules with respect to the AuNPs surface. At basic pH, indeed, 4MBA preferentially adopts a flat configuration when adsorbed on the surface (Ho and Lee, 2015), promoting the interaction of the deprotonated carboxylic moiety with the gold surface and in turn the plasmon-induced decarboxylation. At acidic pH, on the other hand, the molecules stand upright with respect to the surface, and the carboxylic group is further away from the metal surface.

Having reached a control on the experimental issues concerning the applicability of the nanosensor, in the next section we provide a detailed study of the pH-dependent 4MBA-AuNPs SERS spectra with the final aim of obtaining a calibration of the nanosensor.

SERS Responsiveness to pH Variations and Calibration of the Nanosensor

The analyses reported in the previous section were aimed to the optimization of the experimental conditions for both the synthesis and the employment of the 4MBA-AuNPs sensor. Here we investigate the SERS response to pH variations of the assembled nanosensor, with the purpose to determine its dynamic range of sensitivity. Proceeding from this, a thorough study concerning the acidic properties of the molecule has been conducted to explore the possibility to obtain a modulation of the working point of the nanosensor.

A preliminary test of the sample responsiveness has been provided by sequentially immersing the nanosensor to solutions with extreme pH values. The results, corresponding to cyclic measurements performed at pH 3 and pH 10 are reported in **Figure S6**. The features of the spectra show a good responsiveness of the sensor and a high reproducibility for consecutive measurements. In any case, to avoid the presence of salt residues affecting the SERS spectrum (Sun et al., 2015), after each measurement and before the exposure to the next solution, the substrate was rinsed with pure water.

As starting point for the nanosensor calibration, spectra of 4MBA-AuNPs deposited on a glass slide and exposed to solutions at different pH were acquired. Selected SERS spectra are reported in **Figure 4**. To better visualize the spectral differences, and to compensate possible effects of the number of molecules concurring to the SERS signal as well as of the SERS enhancement due to the non-homogeneous morphology of the clusters, which affects the signal intensity, all the spectra shown are normalized to the pH-independent integrated intensity of the peak at 1,586 $\mathrm{cm^{-1}}$, ascribed to the aromatic ring breathing mode. Only a slight redshift of the peak upon pH increase can be observed, attributable to the coupling with the stretching mode of the carboxyl, more intense in case of deprotonated 4MBA (Liu et al., 2013). Notice that the intensity of the peak at 1,076 $\mathrm{cm^{-1}}$, also ascribed to the benzene ring, is automatically normalized.

Clear modifications appear in the spectra upon pH variations from the acidic to the basic pH (from red to blue in the figure). The more pronounced are those occurring in the peaks corresponding to the $\beta(\mathrm{COO^-})$ and $\nu(\mathrm{COO^-})$ bending and stretching modes and to the $\nu(\mathrm{C{=}O})$ stretching. As mentioned above, the first two are related to the progressive deprotonation of the 4MBA molecules at high pH that results in a progressive increase in the intensity of the bands related to the $\mathrm{COO^-}$ group vibrations. On the contrary, with lowering pH, the number of the protonated carboxylic groups COOH increases, resulting in the appearance of the band at 1,710 $\mathrm{cm^{-1}}$ which becomes more intense at the lower pH values.

In order to actually employ the 4MBA-AuNPs as nanosensor for pH measurements, we analyzed the SERS spectra to construct suitable calibration curves. To this end, we calculated the integrated intensities I of the above-mentioned pH-dependent peaks in the normalized spectra highlighted in **Figure 4**. The

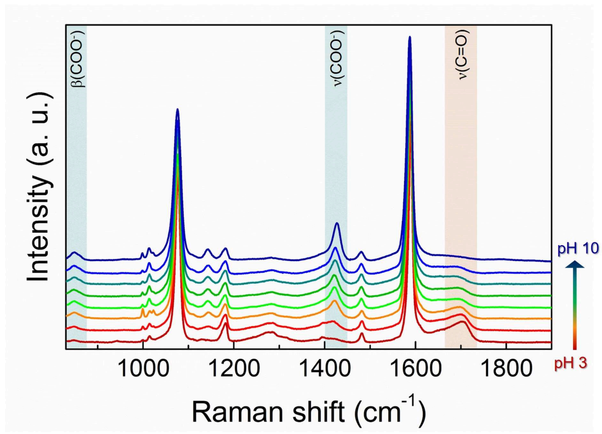

FIGURE 4 | Representative SERS spectra of 4MBA-AuNPs exposed to solutions at different pH. The peaks corresponding to the vibrations of the carboxylic group are highlighted, in the deprotonated (β(COO$^-$) and ν(COO$^-$), in blue) and protonated case (ν(C=O) in red), respectively.

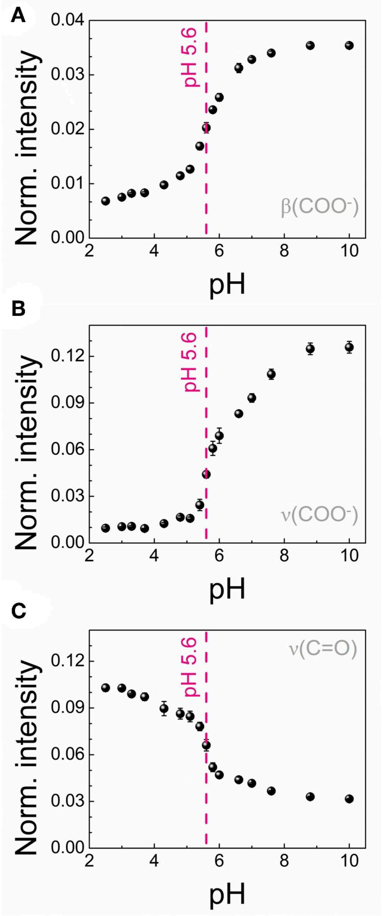

FIGURE 5 | Calibration curves for the 4MBA-AuNPs nanosensor obtained for three different pH-dependent SERS bands: β(COO$^-$) bending mode at 849 cm^{-1} **(A)**, ν(COO$^-$) stretching mode at 1,428 cm^{-1} **(B)** and ν(C=O) stretching mode at 1,710 cm^{-1} **(C)**. In all the graphs the region of maximum sensitivity respect to pH variations has been indicated.

three calibration curves obtained, reported in **Figure 5**, show a sigmoidal-like trend, in line with those reported in literature for similar systems (Wang et al., 2012; Lawson et al., 2014; Jamieson et al., 2015). For each curve we determined the working point of the nanosensor, namely the pH value corresponding to the highest sensitivity $\left|\frac{dI}{dpH}\right|$, at pH 5.6, in good agreement with the range identified by ζ-potential measurements. The maximum sensitivity values are 0.017, 0.091, and 0.065 for β(COO$^-$), ν(COO$^-$), and ν(C=O), respectively. Therefore, amongst all the three curves analyzed, the one which gives the highest sensitivity to pH variations is that derived from the COO$^-$ stretching mode (**Figure 5B**).

With reference to other similar pH nanosensors reported in literature (Jamieson et al., 2015; Wei et al., 2016; Williams et al., 2016; Puppulin et al., 2018), showing a region of sensitivity in the pH range 7–8, the sharp working range identified for our nanoscale pH sensor turns out to be more suitable for monitoring pH-dependent biological processes on single cells. In fact, variations of cellular pH are generally identified at pH values between 5 and 7 (Casey et al., 2010). Going to analyze the chemical aspects in detail, the working range extrapolated from the SERS calibration curves corresponds to the dissociation constant, namely the pKa, of the indicator employed as probe (Wencel et al., 2014). Moreover, the confinement of molecules at nanostructured interfaces could affect their acidic properties, depending on the surface curvature (Leopold et al., 2002; Wang et al., 2011; Koivisto et al., 2016). To deepen this aspect, we performed a standard acid-base titration curve on the bulk 4MBA molecule, reported in **Figure S8**, obtaining a pKa of 4.2 pH units for the carboxylic acid. The SERS-based calibration curve and the ζ-potential measurements, instead, highlight a weakening of the acidic properties of the 4MBA when bound to the plasmonic nanostructure. Since the deactivation of the thiol moiety upon conjugation with the AuNPs does not affect the acidic properties of the system, as discussed in section Acid-Base Titration of the Bulk 4MBA of **Supplementary Material**, the observed pKa shift is attributable only to the confinement of 4MBA molecules on the nanostructured surface. Interestingly, this latter aspect points out the possibility of modulating the pKa value of the nanosensor by acting on the properties of the nanostructured surface on which the molecular probe is confined.

The overall modifications that occur in the SERS spectra depending on the pH, not only supply the information that can be used to determine the nanosensor performances but provide unique molecular and stereochemical information which are related as well to the pH variation. With reference to **Figure 4**, it is possible to notice the appearance of a further peak moving to basic pH, centered at 1,143 cm^{-1}, mainly assigned to the ν(CCOO$^-$) stretching mode (Liu et al., 2013). Moreover, a modification of the shape of the ν(COO$^-$) peak at ∼1,400 cm^{-1} is observed with increasing pH. This is due to the increasing weight of a second component of the band, centered at ∼1,380 cm^{-1}, related to the vibrations at lower energy of the COO$^-$ groups that are interacting with the metallic surface. The

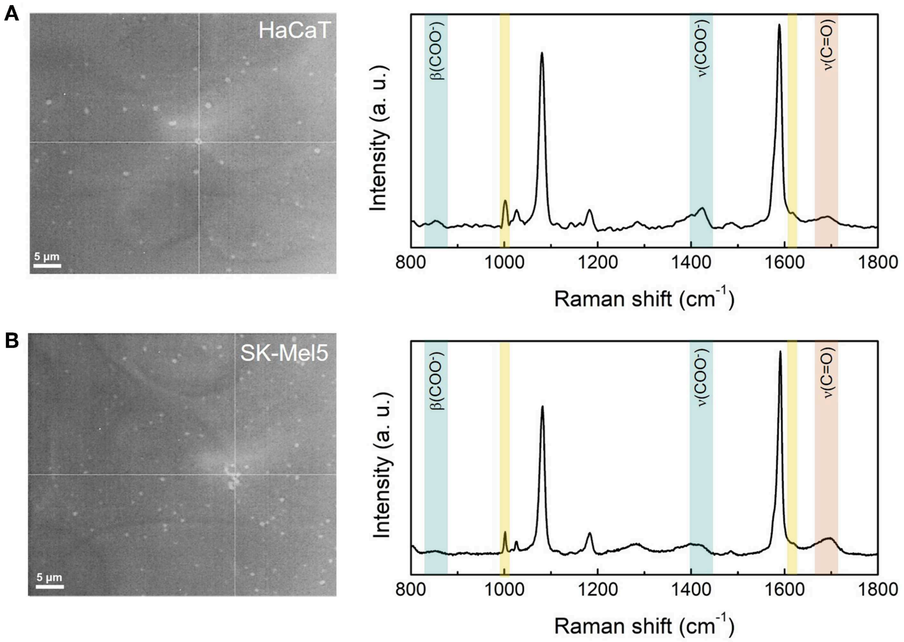

FIGURE 6 | Optical microscope images and SERS spectra of HaCaT **(A)** and SK-Mel5 **(B)** cells exposed to the nanosensor. The bright spots are the 4MBA-AuNPs clusters assembled onto the glass coverslip superimposed to the cells. The grids in the images identify the spatial point corresponding to the SERS spectra. The pH-dependent SERS peaks are highlighted in blue (β(COO-) and ν(COO-)) and in red (ν(C=O)), while the spectral markers of the cell (Phenylalanine at 1,000 and 1,610 cm^{-1}) are highlighted in yellow.

parallel orientation of the 4MBA molecules with respect to the AuNPs surface, resulting in the COO$^-$ group being closer to the gold interface, is in fact favored at higher pH (Michota and Bukowska, 2003) due to the negative charge of the carboxylate. This effect is reflected also in the appearance of a band at 720 cm^{-1}, assigned to the γ(CCC) out-of-plane ring vibrations, also index of flat-oriented 4MBA molecules (Ho and Lee, 2015) (see **Figure S7**).

The great deal of information that can be inferred over the whole fingerprint region reduces considerably the presence of artifacts that might occur with potentiometric methods or paper-based sensors (Khan et al., 2017).

Nanosensor Application: *In vitro* pH Detection of Living Cells

The calibration curves obtained for 4MBA-AuNPs point out that the dynamic working range of the nanosensor lies in the pH range 5–7, suggesting a high reliability for pH measurements at the single cell level. Therefore, as a proof-of-concept to demonstrate the actual applicability of our SERS-active pH nanosensor we measured the extracellular pH (pH$_e$) of two clinically relevant human skin cell lines: normal HaCaT and cancer SK-Mel5. The pH$_e$, being involved in cell progression, differentiation and proliferation (Sun et al., 2015), is an important parameter that allows to discriminate unhealthy cells from healthy ones (Neri and Supuran, 2011). Indeed, cancer cells lead to an acidification of the extracellular milieu due to their enhanced glucose metabolism (Neri and Supuran, 2011; Damaghi et al., 2013).

According to section Cell Culture, the cells were cultured on a glass coverslip and, for the SERS measurements, the cells were put in contact with the nanosensor by superimposing a second glass coverslip with the 4MBA-AuNPs previously assembled, as sketched in **Figure S9**. **Figure 6** shows two optical microscopy images of the HaCaT and SK-Mel5 cells where the 4MBA-AuNPs clusters are clearly visible. Corresponding SERS spectra collected on the cells are also shown in **Figure 6**, right side.

The SERS spectra of the 4MBA-AuNPs in contact with the cells do not show spectral distortions and are in excellent agreement with the 4MBA-AuNPs spectra reported in the previous sections. Noteworthy, the peaks corresponding to the ring vibrations of Phenylalanine, at 1,000 and 1,610 cm^{-1} (see **Table S2** for the complete peak assignment), can be clearly identified due to the huge Raman and SERS cross section of this amino acid (Cialla et al., 2014). The two peaks can be hence considered as cellular spectral markers (see **Figure S10**), certifying that the pH nanosensor is effectively in contact with the cells. For each sample, the integrated intensities of the pH-dependent SERS bands in the normalized spectra, according to section SERS Responsiveness to pH Variations and Calibration of the Nanosensor, have been determined to extrapolate the pH$_e$ from the calibration curves. The obtained results for each of the three bands are reported in **Table 2**, together with the standard deviations.

The distributions of the obtained pH values point out that our 4MBA-AuNPs nanosensor yields a good esteem of the pH$_e$ (Casey et al., 2010) and, even better, it is suitable to discriminate between normal and cancer cells. In fact, for each

TABLE 2 | Estimated pH_e values for the normal HaCaT and cancer SK-Mel5 cell lines, extrapolated from the SERS spectra.

	$\beta(COO^-)$	$\nu(COO^-)$	$\nu(C{=}O)$
HaCaT	7.0 ± 0.4	7.4 ± 0.7	6.5 ± 0.9
SK-Mel5	5.6 ± 0.2	6.3 ± 0.6	5.6 ± 0.2

of the pH-dependent SERS bands, the measured pH_e of the cancer SK-Mel5 cells results to be more acidic respect to that of the normal HaCaT cells. Analyzing in detail the obtained pH_e values, the $\nu(COO^-)$ peak systematically yields a slightly higher pH value if compared with the $\beta(COO^-)$ and the $\nu(C{=}O)$ peaks. This can be ascribed to the superimposition with the band corresponding to the CH_2 deformation of the cell membrane lipids. Since the SERS probe is located in proximity of the cell membrane, the spectral contribution of this band results convoluted to that of the $\nu(COO^-)$ band, leading to a slight overestimation of the integrated intensity. Concerning the spectral region in which are located the other two pH-dependent SERS bands, at 853 cm^{-1} it is only present a narrow and not intense peak, ascribed to the Tyrosine ring breathing and, at higher frequencies, the amide I band at 1,660 cm^{-1} is usually suppressed in SERS spectra (Kurouski et al., 2013). These considerations implies that the $\beta(COO^-)$ and the $\nu(C{=}O)$ peaks are not affected by the spectral contribution of the cells and allow to obtain a measurement of the pH_e from the average of the values reported in **Table 2**, which is equal to 6.8 ± 0.5 for the HaCaT and to 5.6 ± 0.1 for the SK-Mel5 cells. More in general, the derivation of three different calibration curves for the pH evaluation based on the SERS measurement allows to choose the most appropriate, addressing issues associated with the superimposition of spectral band of the sample and of the probe.

Based on these evidences, we can conclude that our 4MBA-AuNPs pH nanosensor is effectively suitable to perform localized pH measurements on single cells and, even more appealing, it has the potential to distinguish between normal and cancer cells.

CONCLUSIONS

In this work we have presented a detailed study of a SERS-active pH nanosensor made of AuNPs conjugated with the pH-sensitive molecular probe 4MBA, aimed to improve the reliability and accuracy of pH measurements at the nanoscale, providing a thorough characterization of the 4MBA-AuNPs performances in different measurement conditions.

Special focus has been paid to the reproducibility of the SERS response by analyzing how the colloidal properties of the nanosensor could affect the plasmonic efficiency of the SERS enhancing scaffold. Moreover, the experimental condition to minimize the laser-induced degradation of the molecular probe have been identified as well as at varying the pH of the environment.

The calibration of the nanosensor was performed in terms of the intensities of selected pH-dependent SERS bands, identifying the dynamic range of sensitivity centered in the pH range 5–7. The detailed analysis of the whole SERS fingerprint allowed to identify highly correlated spectroscopic markers which provide robust reliability to the measurements.

The comprehensive study of the acidic properties of the molecular probe allowed to reveal a shift of the molecule pKa at the interface of the plasmonic nanostructure. This last finding points out the opportunity to assemble a pH nanosensor with the ability to select its working point in the sensitivity region of interest, depending on the properties (e.g., curvature, material, additional ligand, position of the carboxyl substituent, etc.) of the nanostructured surface on which the molecular probe is confined.

The experimental efforts conducted in this work allowed to successfully employ the 4MBA-AuNPs nanosensor to detect the extracellular pH of normal HaCaT and cancer SK-Mel5 cells, proving the capability of the nanosensor to discriminate between the two cell types. The overall results presented in this work pave the way for realizing efficient SERS-active microplate substrates suitable for biomedical applications, offering the possibility to perform localized pH measurements at sub-cellular level.

DATA AVAILABILITY

All datasets generated for this study are included in the manuscript and/or the **Supplementary Files**.

AUTHOR CONTRIBUTIONS

FD designed the research and work coordination. PP and FeB provided the equipment. AC and DM performed the research. AC, DM, FrB, CF, PP, and FD analyzed data. AC, FrB, and FD wrote the manuscript. All authors reviewed the manuscript.

FUNDING

This research was funded by INAIL, under the agreement BRIC 2016 ID 41.

ACKNOWLEDGMENTS

We are grateful to Dr. Sabrina Giantulli for her technical support with cell culture treatments.

SUPPLEMENTARY MATERIAL

The Supplementary Material for this article can be found online at: https://www.frontiersin.org/articles/10.3389/fchem.2019.00413/full#supplementary-material

REFERENCES

Aubouy, M., Trizac, E., and Bocquet, L. (2003). Effective charge versus bare charge: an analytical estimate for colloids in the infinite dilution limit. *J. Phys. A Math. General* 36:5835. doi: 10.1088/0305-4470/36/22/302

Bhattacharje, S. (2016). DLS and zeta potential—What they are and what they are not? *J. Controlled Release* 235, 337–351. doi: 10.1016/j.jconrel.2016.06.017

Bishnoi, S. W., Rozell, C. J., Levin, C. S., Gheith, M. K., Johnson, B. R., Johnson, D. H., et al. (2006). All-optical nanoscale pH meter. *Nano Lett.* 6, 1687–1692. doi: 10.1021/nl060865w

Bordi, F., Cametti, C., Sennato, S., Paoli, B., and Marianecci, C. (2006). Charge renormalization in planar and spherical charged lipidic aqueous interfaces. *J. Phys. Chem. B* 110, 4808–4814. doi: 10.1021/jp055821a

Camden, J. P., Dieringer, J. A., Zhao, J., and Van Duyne, R. P. (2008). Controlled plasmonic nanostructures for surface-enhanced spectroscopy and sensing. *Accounts Chem. Res.* 41, 1653–1661. doi: 10.1021/ar800041s

Casey, J. R., Grinstein, S., and Orlowski, J. (2010). Sensors and regulators of intracellular pH. *Nat. Rev. Mol. Cell Biol.* 11:50. doi: 10.1038/nrm2820

Chuong, T. T., Pallaoro, A., Chaves, C. A., Li, Z., Lee, J., Eisenstein, M., et al. (2017). Dual-reporter SERS-based biomolecular assay with reduced false-positive signals. *Proc. Natl. Acad. Sci. U.S.A.* 114, 9056–9061. doi: 10.1073/pnas.1700317114

Cialla, D., Pollok, S., Steinbrücker, C., Weber, K., and Popp, J. (2014). SERS-based detection of biomolecules. *Nanophotonics* 3, 383–411. doi: 10.1515/nanoph-2013-0024

Cialla-May, D., Zheng, X. S., Weber, K., and Popp, J. (2017). Recent progress in surface-enhanced Raman spectroscopy for biological and biomedical applications: from cells to clinics. *Chem. Soc. Rev.* 46, 3945–3961. doi: 10.1039/C7CS00172J

Damaghi, M., Wojtkowiak, J. W., and Gillies, R. J. (2013). pH sensing and regulation in cancer. *Front. Physiol.* 4:370. doi: 10.3389/fphys.2013.00370

Domenici, F., Fasolato, C., Mazzi, E., De Angelis, L., Brasili, F., Mura, F., et al. (2016). Engineering microscale two-dimensional gold nanoparticle cluster arrays for advanced Raman sensing: an AFM study. *Colloids Surfaces A Physicochem. Eng. Aspects* 498, 168–175. doi: 10.1016/j.colsurfa.2016.03.043

Dougan, J. A., and Faulds, K. (2012). Surface enhanced Raman scattering for multiplexed detection. *Analyst* 137, 545–554. doi: 10.1039/C2AN15979A

Fasolato, C., Domenici, F., Sennato, S., Mura, F., De Angelis, L., Luongo, F., et al. (2014). Dimensional scale effects on surface enhanced Raman scattering efficiency of self-assembled silver nanoparticle clusters. *Appl. Phys. Lett.* 105:073105. doi: 10.1063/1.4893373

Fasolato, C., Giantulli, S., Silvestri, I., Mazzarda, F., Toumia, Y., Ripanti, F., et al. (2016). Folate-based single cell screening using surface enhanced Raman microimaging. *Nanoscale* 8, 17304–17313. doi: 10.1039/C6NR05057C

Fontana, J., Livenere, J., Bezares, F. J., Caldwell, J. D., Rendell, R., and Ratna, B. R. (2013). Large surface-enhanced Raman scattering from self-assembled gold nanosphere monolayers. *Appl. Phys. Lett.* 102:201606. doi: 10.1063/1.4807659

Gühlke, M., Heiner, Z., and Kneipp, J. (2015). Combined near-infrared excited SEHRS and SERS spectra of pH sensors using silver nanostructures. *Phys. Chem. Chem. Phys.* 17, 26093–26100. doi: 10.1039/C5CP03844H

Guo, H. B., He, F., Gu, B., Liang, L., and Smith, J. C. (2012). Time-dependent density functional theory assessment of UV absorption of Benzoic Acid derivatives. *J. Phys. Chem. A* 116, 11870–11879. doi: 10.1021/jp3084293

Halas, N. J., Lal, S., Chang, W. S., Link, S., and Nordlander, P. (2011). Plasmons in strongly coupled metallic nanostructures. *Chem. Rev.* 111, 3913–3961. doi: 10.1021/cr200061k

Ho, C., and Lee, S. (2015). SERS and DFT investigation of the adsorption behavior of 4-mercaptobenzoic acid on silver colloids. *Colloids Surfaces A Physicochem. Eng. Aspects* 474, 29–35. doi: 10.1016/j.colsurfa.2015.03.004

Jamieson, L. E., Jaworska, A., Jiang, J., Baranska, M., Harrison, D. J., and Campbell, C. J. (2015). Simultaneous intracellular redox potential and pH measurements in live cells using SERS nanosensors. *Analyst* 140, 2330–2335. doi: 10.1039/C4AN02365J

Khan, M. I., Mukherjee, K., Shoukat, R., and Dong, H. (2017). A review on pH sensitive materials for sensors and detection methods. *Microsystem Technol.* 23, 4391–4404. doi: 10.1007/s00542-017-3495-5

Kneipp, J. (2017). Interrogating cells, tissues, and live animals with new generations of surface-enhanced Raman scattering probes and labels. *ACS Nano* 11, 1136–1141. doi: 10.1021/acsnano.7b00152

Koivisto, J., Chen, X., Donnini, S., Lahtinen, T., Häkkinen, H., Groenhof, G., et al. (2016). Acid-base properties and surface charge distribution of the water-soluble Au102(pMBA)44 nanocluster. *J. Phys. Chem. C* 120, 10041–10050. doi: 10.1021/acs.jpcc.6b00922

Kurouski, D., Postiglione, T., Deckert-Gaudig, T., Deckert, V., and Lednev, I. K. (2013). Amide I vibrational mode suppression in surface (SERS) and tip (TERS) enhanced Raman spectra of protein specimens. *Analyst* 138, 1665–1673. doi: 10.1039/c2an36478f

Lal, S., Grady, N. K., Kundu, J., Levin, C. S., Lassiter, J. B., and Halas, N. J. (2008). Tailoring plasmonic substrates for surface enhanced spectroscopies. *Chem. Soc. Rev.* 37, 898–911. doi: 10.1039/b705969h

Lawson, L. S., Chan, J. W., and Huser, T. (2014). A highly sensitive nanoscale pH-sensor using Au nanoparticles linked by a multifunctional Raman active reporter molecule. *Nanoscale* 6, 7971–7980. doi: 10.1039/C3NR06277E

Le Ru, E. C., Blackie, E., Meyer, M., and Etchegoin, P. G. (2007). Surface enhanced Raman scattering enhancement factors: a comprehensive study. *J. Phys. Chem. C* 111, 13794–13803. doi: 10.1021/jp0687908

Le Ru, E. C., Meyer, M., Blackie, E., and Etchegoin, P. G. (2008). Advanced aspects of electromagnetic SERS enhancement factors at a hot spot. *J. Raman Spectroscopy* 39, 1127–1134. doi: 10.1002/jrs.1945

Le Ru, E. C., Meyer, S. A., Artur, C., Etchegoin, P. G., Grand, J., Lang, P., et al. (2011). Experimental demonstration of surface selection rules for SERS on flat metallic surfaces. *Chem. Commun.* 47, 3903–3905. doi: 10.1039/c1cc10484e

Leopold, M. C., Black, J. A., and Bowden, E. F. (2002). Influence of gold topography on carboxylic acid terminated self-assembled monolayers. *Langmuir* 18, 978–980. doi: 10.1021/la011683e

Li, R., Lv, H., Zhang, X., Liu, P., Chen, L., Cheng, J., et al. (2015). Vibrational spectroscopy and density functional theory study of 4-mercaptobenzoic acid. *Spectrochim. Acta Part A Mol. Biomol. Spectroscopy* 148, 369–374. doi: 10.1016/j.saa.2015.03.132

Liu, Y., Yuan, H., Fales, A. M., and Vo-Dinh, T. (2013). pH-sensing nanostar probe using surface enhanced Raman scattering (SERS): theoretical and experimental studies. *J. Raman Spectroscopy* 44, 980–986. doi: 10.1002/jrs.4302

Michota, A., and Bukowska, J. (2003). Surface-enhanced Raman scattering (SERS) of 4-mercaptobenzoic acid on silver and gold substrates. *J. Raman Spectroscopy* 34, 21–25. doi: 10.1002/jrs.928

Mock, J. J., Smith, D. R., and Schultz, S. (2003). Local refractive index dependence of plasmon resonance spectra from individual nanoparticles. *Nano Lett.* 3, 485–491. doi: 10.1021/nl0340475

Moskovits, M., and Suh, J. S. (1984). Surface selection rules for surface-enhanced Raman spectroscopy: calculations and application to the surface-enhanced Raman spectrum of phthalazine on silver. *J. Phys. Chem.* 88, 5526–5530. doi: 10.1021/j150667a013

Neri, D., and Supuran, C. T. (2011). Interfering with pH regulation in tumours as a therapeutic strategy. *Nat. Rev. Drug Discovery* 10:767. doi: 10.1038/nrd3554

Osawa, M., Matsuda, N., Yoshii, K., and Uchida, I. (1994). Charge transfer resonance Raman process in surface-enhanced Raman scattering from p-aminothiophenol adsorbed on silver: Herzberg-Teller contribution. *J. Phys. Chem.* 98, 12702–12707. doi: 10.1021/j100099a038

Puppulin, L., Hosogi, S., Sun, H., Matsuo, K., Inui, T., Kumamoto, Y., et al. (2018). Bioconjugation strategy for cell surface labelling with gold nanostructures designed for highly localized pH measurement. *Nat. Commun.* 9:5278. doi: 10.1038/s41467-018-07726-5

Stockman, M. I., Kneipp, K., Bozhevolnyi, S. I., Saha, S., Dutta, A., Ndukaife, J., et al. (2018). Roadmap on plasmonics. *J. Opt.* 20:043001. doi: 10.1088/2040-8986/aaa114

Sun, F., Zhang, P., Bai, T., Galvan, D. D., Hung, H., Zhou, N., et al. (2015). Functionalized plasmonic nanostructure arrays for direct and accurate mapping extracellular pH of living cells in complex media using SERS. *Biosensors Bioelectronics* 73, 202–207. doi: 10.1016/j.bios.2015.05.060

Trautmann, S., Richard-Lacroix, M., Dathe, A., Schneidewind, H., Dellith, J., Fritzschea, W., et al. (2018). Plasmon response evaluation based on image-derived arbitrary nanostructures. *Nanoscale* 10, 9830–9839. doi: 10.1039/C8NR02783H

Varnholt, B., Oulevey, P., Luber, S., Kumara, C., Dass, A., and Bürgi, T. (2014). Structural information on the Au–S interface of thiolate-protected gold clusters: a Raman spectroscopy study. *J. Phys. Chem. C* 118, 9604–9611. doi: 10.1021/jp502453q

Wang, D., Nap, R. J., Lagzi, I., Kowalczyk, B., Han, S., Grzybowski, B. A., et al. (2011). How and why nanoparticle's curvature regulates the apparent pKa of the coating ligands. *J. Am. Chem. Soc.* 133, 2192–2197. doi: 10.1021/ja108154a

Wang, F., Widejko, R. G., Yang, Z., Nguyen, K. T., Chen, H., Fernando, L. P., et al. (2012). Surface-enhanced raman scattering detection of pH with silica-encapsulated 4-mercaptobenzoic acid-functionalized silver nanoparticles. *Anal. Chem.* 84, 8013–8019. doi: 10.1021/ac3018179

Webb, B. A., Chimenti, M., Jacobson, M. P., and Barber, D. L. (2011). Dysregulated pH: a perfect storm for cancer progression. *Nat. Rev. Cancer* 11, 671–677. doi: 10.1038/nrc3110

Wei, H., Willner, M. R., Marr, L. C., and Vikesland, P. J. (2016). Highly stable SERS pH nanoprobes produced by co-solvent controlled AuNP aggregation. *Analyst* 141, 5159–5169. doi: 10.1039/C6AN00650G

Wencel, D., Abel, T., and McDonagh, C. (2014). Optical chemical pH sensors. *Anal. Chem.* 86, 15–29. doi: 10.1021/ac4035168

Williams, A., Flynn, K. J., Xia, Z., and Roger Dunstan, P. (2016). Multivariate spectral analysis of pH SERS probes for improved sensing capabilities. *J. Raman Spectroscopy* 47, 819–827. doi: 10.1002/jrs.4910

Wilson, E. B Jr. (1934). The normal modes and frequencies of vibration of the regular plane hexagon model of the benzene molecule. *Phys. Rev.* 45:706. doi: 10.1103/PhysRev.45.706

Yeh, Y. C., Creran, B., and Rotello, V. M. (2012). Gold nanoparticles: preparation, properties, and applications in bionanotechnology. *Nanoscale* 4, 1871–1880. doi: 10.1039/C1NR11188D

Zong, Y., Guo, Q., Xu, M., Yuan, Y., Gu, R., and Yao, J. (2014). Plasmon-induced decarboxylation of mercaptobenzoic acid on nanoparticle film monitored by surface-enhanced Raman spectroscopy. *RSC Adv.* 4, 31810–31816. doi: 10.1039/C4RA03512G

Conflict of Interest Statement: The authors declare that the research was conducted in the absence of any commercial or financial relationships that could be construed as a potential conflict of interest.

frontiers in Chemistry

ORIGINAL RESEARCH
published: 13 June 2019
doi: 10.3389/fchem.2019.00440

Latent Fingermark Imaging by Single-Metal Deposition of Gold Nanoparticles and Surface Enhanced Raman Spectroscopy

*Gitanjali Kolhatkar[1], Cédric Parisien[1], Andreas Ruediger[1] and Cyril Muehlethaler[2,3]**

[1] Nanophotonics and Nanoelectronics Group, Institut National de la Recherche Scientifique Énergie-Matériaux-Télécommunication, Varennes, QC, Canada, [2] Department of Chemistry, Biochemistry, and Physics, Université du Québec à Trois-Rivières, Trois-Rivières, QC, Canada, [3] Laboratoire de Recherche en Criminalistique, Université du Québec à Trois-Rivières, Trois-Rivières, QC, Canada

In forensic science, there is a high demand for a technique that allows the revelation of fingermarks invisible to the naked eye as well as the chemical information they contain. Here, we present a feasibility study consisting of using both the luminescence enhanced by surface plasmon of gold nanoparticles, and the surface enhanced Raman spectroscopy signal of fingermark chemical components to image latent fingermarks. A latent fingermark deposited on a transparent glass substrate was visually revealed using single-metal deposition employing gold nanoparticles. The resulting enhanced luminescence was monitored over a developed area of the latent fingermark, displaying light regions of 200–400 μm, corresponding to the fingermark ridges. The Raman signal of the fingermark's chemical components was enhanced into a measurable signal. Imaging those Raman peaks revealed the ridges pattern, attesting to the potential of our method. Since SMD is an end-of-sequence revelation technique for which further enhancement techniques do not exist, this work aims at demonstrating the feasibility of the technique in order to apply it on different systems, able to illuminate a complete surface of a few cm, and thus capable of both detecting contaminants in LFM and imaging features of the size of a complete LFM.

Keywords: surface enhanced Raman spectroscopy, latent fingermarks, gold nanoparticles, single metal deposition, gold luminescence, chemical composition

Edited by:
John Lombardi,
City College of New York,
United States

Reviewed by:
Lai-Kwan Chau,
National Chung Cheng University,
Taiwan
Scott Chadwick,
University of Technology Sydney,
Australia

****Correspondence:***
Cyril Muehlethaler
cyril.muehlethaler@uqtr.ca

Specialty section:
This article was submitted to Analytical Chemistry, a section of the journal Frontiers in Chemistry

Received: *06 November 2018*
Accepted: *28 May 2019*
Published: *13 June 2019*

Citation:
Kolhatkar G, Parisien C, Ruediger A and Muehlethaler C (2019) Latent Fingermark Imaging by Single-Metal Deposition of Gold Nanoparticles and Surface Enhanced Raman Spectroscopy. Front. Chem. 7:440. doi: 10.3389/fchem.2019.00440

INTRODUCTION

Human fingerprints display patterns that are highly selective to each and every individual and remain unchanged throughout their lives, offering an unequaled capacity for identification (Champod et al., 2016). This unique identifier is a powerful tool in forensic science. Fingerprints are composed of friction ridges that are separated into a three level hierarchical order (Jain et al., 2007; Champod et al., 2016). Level 1 refers to the general pattern, Level 2, to minutiae points i.e., endings or bifurcations, and Level 3 includes dimensional attributes like sweat pores and the ridges contours (Hutchins et al., 2013; Champod et al., 2016). Upon contact with an item or a surface with unprotected hands, a person will deposit an image of their fingerprint patterns, referred to as a fingermark (FM), mostly composed of biological secretions and environmental contaminants.

Since such FM is mostly not visible, they are then referred to as latent fingermarks (LFM). LFMs are usually not visible to the naked eye and need to be enhanced for forensic applications (Wei et al., 2016).

The available fingermark development techniques target skin secretions from the eccrine, apocrine and sebaceous glands (Wei et al., 2016). Eccrine secretions are provided by glands located all over the body that can be found in higher density on the palms of the hands and the sole of the feet. They are water-based solutions containing traces of organic compounds and inorganic salts. The apocrine glands can be found in areas such as the armpits and the hair and excrete a viscous milky fluid composed of proteins, carbohydrates, cholesterol, iron, and steroid sulfates. Finally, the sebaceous glands, found in the dermis layer, are associated with body hair and secrete sebum fluids consisting of waxes, squalene and saturated fats (Holder et al., 2011). Those secretions are known as endogenous factors and provide the biological characteristics of an individual, while external contaminations (i.e., cosmetics, food residues) are referred to as exogenous composition factors (Cai et al., 2017). Therefore, in addition to providing the patterns and enabling the identification of an individual, the development of fingermarks can offer information regarding the environment and lifestyle of a person. Indeed, the presence of gunpowder or drugs have been extracted from LFMs (Day et al., 2004; Charlton et al., 2013; Groeneveld et al., 2015; Figueroa et al., 2017).

Several revelation techniques have been explored that exploit the specific binding to skin secretions to provide the contrast. Black powder, cyanoacrylate fuming, and amino acid reagents (Ninhydrin, Indanedione Zinc), are the most favored revelation methods providing the necessary versatility to detect traces on non-porous and porous surfaces. The development techniques are based on a chemical enhancement to increase contrast, but do not allow for the identification of specific endogenous or exogenous components (Lennard, 2014). Specific LFM-related components were monitored using label-free mass spectrometry (MS) detection methods (Musah et al., 2012), such as desorption electrospray ionization (DESI) (Ifa et al., 2008), matrix-assisted laser desorption ionization (MALDI) (Wolstenholme et al., 2009; Bradshaw et al., 2011; Groeneveld et al., 2015), and time-of-flight secondary ion mass spectrometry (TOF-SIMS) (Bailey et al., 2010; Hinder and Watts, 2010; Cai et al., 2017). The photoluminescence of nanoparticles (NPs) such as ZGO:Ga, Mn-ConA (Wang et al., 2017), or that of upconversion NPs with a lysozyme-bonding aptamer (Wang et al., 2014) was exploited to image fingermarks. Successful revelation was also achieved through FTIR (Tahtouh et al., 2005; Ricci et al., 2007), and Raman spectroscopy (Day et al., 2004; Widjaja, 2009; Deng et al., 2012). However, MS techniques are destructive while Raman spectroscopy and other vibrational techniques require long measurement times due to the weak signal of the chemical compounds. This weak signal can also be overshadowed by a substrate background (Figueroa et al., 2017).

To overcome this detection limit and reduce the measurement time, surface enhanced Raman spectroscopy (SERS) has been proposed (Connatser et al., 2010; Cialla et al., 2012; Song et al., 2012; Muehlethaler et al., 2016). This powerful surface-sensitive technique exploits the plasmonic properties of metallic nanostructures, most commonly silver (Ag) or gold (Au), to amplify a Raman signal. This enhancement is obtained by exciting the localized surface plasmon (LSP) of the metallic nanostructures through the collective coherent oscillations of free electrons in a continuous band structure. This LSP has a resonance, known as localized surface plasmon resonance (LSPR), which will enhance a near-field signal that was initially too weak to be detected and make it measurable. Additionally, metallic NPs display a strong luminescence originating from interband transitions caused by the direct radiative recombination of Fermi level electrons with holes from the sp or d bands (Mooradian, 1969). This luminescence will be enhanced by the LSPR, resulting in a measurable emission signal (Mohamed et al., 2000). This technique was employed to image fingermarks by imaging the signal of proteins, enhanced using an antibody Raman probe (Song et al., 2012). Yet, proteins are only a minor component of fingerprint secretions compared to free amino acids or lipids, making it challenging to detect on conventional traces. Besides, revelation techniques exploiting gold and silver NPs, known as multi-metal deposition (MMD) and single-metal deposition (SMD) approaches were introduced in LFM sequences of revelation (Becue et al., 2007; Stauffer et al., 2007; Fairley et al., 2012; Newland et al., 2016). These two-steps techniques consist in using metal NP, either gold (Au) or silver (Ag) to reveal a fingermark independently from its chemical composition and from the substrate porosity. They combine an important sensitivity to a high selectivity, as the NPs will preferentially attach on the fingermark compounds (Mohamed, 2011). The most important advantage of these methods is the universality with which they allow detection on non-porous, semi-porous and porous surfaces. Yet, while MMD and SMD enhance the visual contrast, it is still not sufficient for these techniques to become standard procedures. While the few limitations are continuously being improved (Becue et al., 2012), the nanoparticle layer generally precludes any additional technique to be used, and SMD/MMD are generally seen as end-of-sequence techniques. However, the NPs size, in the 1–100 nm range, is well-adapted for SERS application and likely to provide strong plasmonic resonance and luminescence (Muehlethaler et al., 2016). The possibility to visualize a chemical map of the fingermark might be valuable on difficult substrates (colored or dark), or for poorly revealed traces.

This work demonstrates the potential of combining SMD to SERS imaging to reveal the fingermark patterns. Gold NPs are deposited on a glass substrate presenting a LFM and their luminescence is monitored to reproduce the ridges patterns. In addition, the signal of chemicals composing the LFM, rendered measurable through a SERS effect, is imaged to reconstruct the fingermark. While most studies so far exploited immunoassays with antigen-antibody functionalized probes to produce a SERS signal, our method exploits the nanoparticles-enhancing electromagnetic field to create a chemical contrast with the substrate. By doing so, the substrate contribution is removed, allowing visualization of precise fingermark details with high resolution, irrespective of the substrate color. This simple, non-destructive approach does not require any reagent, and offers an added visualization possibility without any modification of the original SMD revelation. In addition, this approach provides a way to perform fast non-destructive measurements that reveal the LFM patterns as well as endogenous and exogenous chemical information.

MATERIALS AND METHODS

Sample Preparation

The sample consists of standard microscopy glass slides bearing a latent fingermark revealed through SMD (Becue et al., 2007; Stauffer et al., 2007). Natural fingermarks were deposited by the donors, which were asked not to wash their hands for 30 min prior to deposition, and to slightly rub their hands together to ensure distribution of both eccrine and sebaceous secretions. A single depletion was made directly on the glass slide. The revelation was performed by immersing the sample in a succession of baths. First, it was dipped for 2–3 min in H_2O for rinsing to remove undesired contaminations. Second, in a gold nanoparticles (AuNPs) solution. The AuNPs (15–20 nm in diameter) were formed from a prior $HAuCl_4$ and trisodium citrate dihydrate synthesis. The colloids preferentially attach on the fingermark ridges under precise pH conditions (2.5–2.8), which need be controlled. Third, it was rinsed in H_2O to remove the NP that may have attached on the glass substrate itself. It was then plunged in a second solution of $HAuCl_4$ and hydroxylamine hydrochloride ($HONH_2$-HCl) which contributes to reinforcement over the gold already present on the ridges before being rinsed in H_2O (Stauffer et al., 2007). Lastly, the sample was dried in ambient conditions.

SERS Measurements

The luminescence and SERS measurements were performed using linearly polarized TEM_{00} He-Ne laser operating at 632.8 nm and an AIST-NT OmegaScope 1000 equipped with a thermoelectrically cooled CCD detector and Nanofinder 30 Raman spectrometer. The laser beam was focused on the sample through a 0.28 NA Mitutoyo MPlan Apo 10× objective. A laser power of 0.31 mW was used throughout the measurements. A typical spectrum at one pixel point consists of one accumulation of 0.5–1 s integration time. No further post-treatments were realized on the spectra.

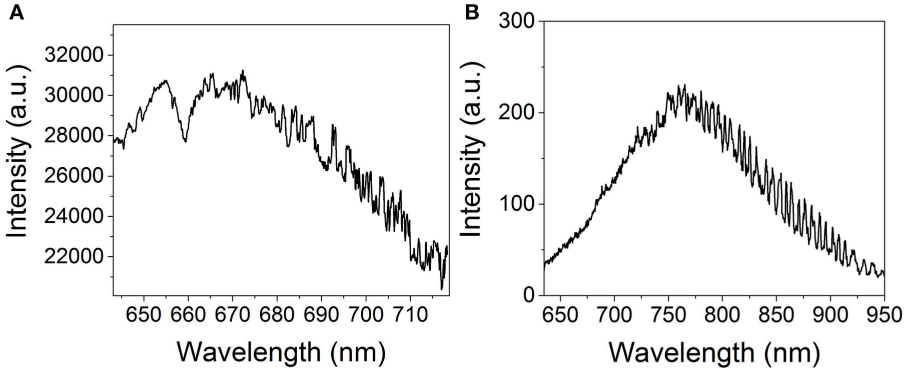

FIGURE 1 | Typical luminescence spectra of **(A)** 15 nm gold nanoparticles and **(B)** the glass substrate on which the fingerprint was revealed.

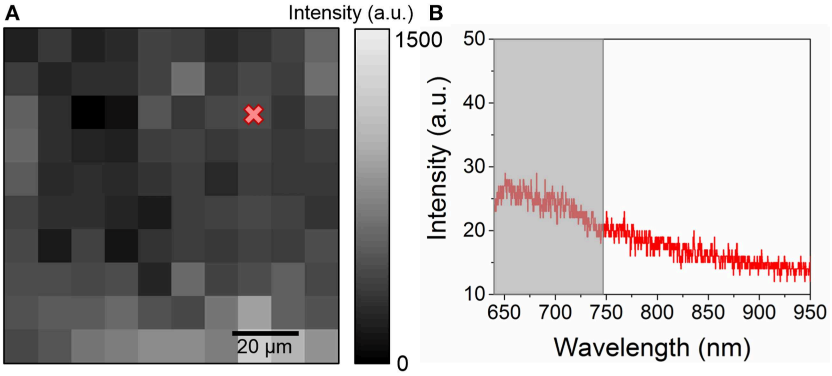

FIGURE 2 | (A) 100 × 100 μm^2 map of the integrated intensity between 640 and 750 nm acquired with a 5 μm spatial resolution on a reference sample consisting of a fingermark on a glass cover slide with no gold NP and **(B)** example of a spectrum obtained from the map. The gray region indicates the integrated intensity range.

RESULTS AND DISCUSSION

The typical luminescence spectra of gold NPs and the glass substrate are presented in **Figure 1**. The glass substrate depicts a wide Gaussian-shaped luminescence centered at ~800 nm. The gold NPs display a relatively narrow Lorentzian-shaped luminescence centered at ~670 nm. This signal corresponds to the luminescence enhanced by the surface plasmon (Zheng et al., 2012). While this luminescence shifts with the radius of the NP, both the glass substrate and the NP luminescence remain in different spectral ranges and can therefore be distinguished. In both cases, the noise observed at higher wavelengths is due to optical etaloning in the CCD detector. Neither of those spectra display any Raman peaks. The luminescence signal was first mapped over a reference sample consisting of a glass cover slide bearing a fingermark and no gold NPs. The map of the integrated intensity (**Figure 2A**) appears homogeneous, with no regions displaying significantly higher intensities. The spectra (**Figure 2B**) exhibit a weak luminescence all over the mapped region. This signal can be attributed to the cover slide.

Fingermarks revealed by SMD on glass substrates in illustrated in **Figure 3**. After the revelation, the ridge are well-defined as indicated by the golden-brown regions with limited background contamination. 100 × 100 μm map of the intensity of the luminescence signal was acquired on a revealed area of the fingermark with a 5 μm spatial resolution, as presented in **Figure 4A**. The light region corresponds to areas covered with gold NPs while the dark regions are attributed to the glass only, as confirmed by the spectra illustrated in **Figure 4B**. The intensities recorded on the map presents a strong gold luminescence, much higher than that of the glass substrate. A SERS effect is also indicated by the presence of Raman peaks on the gold luminescence spectrum at Position 3 (red curve). The peak positions are provided in **Table 1**. They can be linked to functional groups of organic molecules, mainly proteins, lipoproteins, DNA, and aminoacids, as listed in **Table 1**. This is coherent with the chemicals produced by the eccrine, apocrine and sebaceous glands, that are expected to remain after the SMD treatment. Such peaks were not observed on the reference sample presented in **Figure 2**, confirming that the signal is due to an enhancement effect originating from the presence of gold NPs on the fingermark ridges and not to the fingermark alone.

Furthermore, the trace revealed in **Figure 4A** is not uniform, and is much narrower than a typical fingermark ridge (200–400 μm), revealing that the gold NPs tend to form clusters instead of attaching homogeneously on the fingermark ridges. This also suggests that the fingermark chemical constituents were not deposited uniformly on the glass substrate, adding an uncertainty on the revelation. Nevertheless, this indicates that by monitoring the gold luminescence as well as the SERS peaks, the fingermark can be revealed. Furthermore, even in the regions with a strong gold luminescence and a SERS effect, the signal of the glass substrate remains visible. Therefore, the glass spectrum can be used to normalize the spectra for the LFM revelation.

To reconstruct the fingermark pattern (**Figure 5a**), the gold luminescence was mapped over a large region (1,100 × 3,100 μm^2) of the LFM revealed with gold NPs, as illustrated in **Figure 5b**. These dimensions were chosen to display 2–3 ridges. To eliminate intensity variations due to the substrate flatness and changes in the focus, and assuming that the glass signal should remain constant all over the sample surface, the spectra were normalized with respect to the glass luminescence.

FIGURE 3 | Stereomicroscopy image (5× objective) of a complete SMD revealed fingermark on a glass substrate.

The image obtained by this process presents light and dark regions. The dark regions (position 1, **Figure 5b**) display a very low intensity while the light regions (position 2, **Figure 5b**) present a strong gold luminescence signal. The light regions have a width of 200–400 μm, which corresponds to the typical width of ridges. The pattern observed in **Figure 5b** can be correlated with the optical microscopy image acquired in the same region (**Figure 5a**, zoomed-in), where the fingermark revealed by SMD on the glass substrate shows a typical reddish-brown coloration due to the presence of gold NPs on the ridges. We can see that these patterns are not always well-defined, and gold aggregates can be observed between the ridges. This could be due to poor transfer conditions such as smearing, over pressure, under-pressure or double tapping. This could also be caused by the revelation process. Indeed, as the revelation is realized through a series of baths, an overexposure of the fingermark to gold NPs can result in a coloring of the substrate. Brown stains are common as a result of the revelation. In addition, the revelation technique can produce dashed or dot-like ridges instead of continuous patterns, such as those observed in **Figure 5b** (Becue et al., 2012).

Due to the very high spatial resolution used here as compared to the features dimensions, the image presented is very rich in information, which results in the blurring-like effect obtained here. Each spectrum provides very sensitive results of the pixel it represents due to the SERS enhancement. However, black lines appearing in the ridges run over several pixels, confirming that

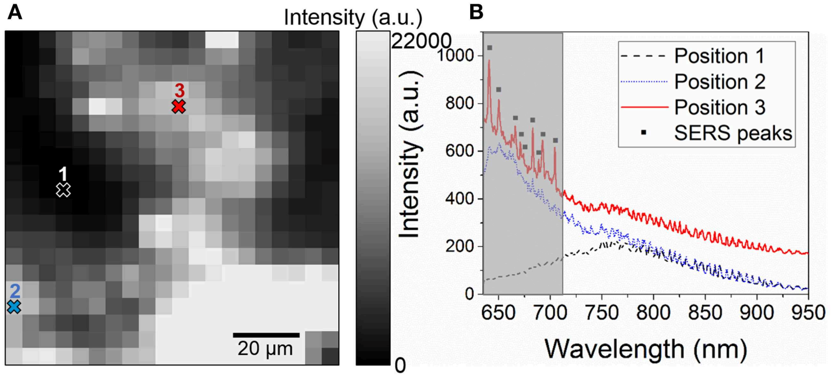

FIGURE 4 | (A) 100 × 100 µm^2 map of the integrated intensity in the 640–710 nm performed on a LFM revealed with gold NPs with a 5 µm spatial resolution and **(B)** Raman spectra acquired at three different positions of the map showing the spectrum of glass (Position 1), a region of the fingerprint with gold NPs (Position 2), and a region with SERS enhancement (Position 3, black squares). The gray region indicates the integrated intensity range.

they are caused by the sample and not due to an artifact. Possible causes are fingermark features, scratches in the glass substrate or sample degradation. Therefore, those marks indicate that we are able to reveal substructures of the LFM. Finally, the black pixels are due to a non-optimized system. Our resolution remains limited by the quality of the fingermark and the revelation technique. Nevertheless, this study attests to the potential of this technique for the visualization of LFMs.

Furthermore, a SERS effect was recorded in the light regions, as shown by the Raman peaks presented in **Figure 5c**, consistently with that of the high resolution map (**Figure 4**). The Raman peaks measured here (black squares), located at 200, 420, 900, 1,160, 1,360, and 1,600 cm^{-1} were also observed in **Figure 4B**. These peaks are not due to etaloning in the CCD. Two peaks measured in **Figure 4B** are not visible here, most likely due to the lower integration time (0.5 s instead of 1 s). The intensity of the peaks were mapped over the same area as that of **Figure 5a** in order to image the hot spots. To do so, the gold luminescence was fitted and subtracted from the spectra in order to obtain the Raman peaks only, as shown in **Figure 5c**, attesting to the accuracy of our fit. The maps of the different Raman peaks are presented in **Figure 6**.

The first two peaks (**Figures 6a,b**), located at ∼200 and 420 cm^{-1}, reveal the most hot spots. Indeed, these two peaks are located close to the maximum of the gold signal, which corresponds to the spectral range enhanced by the LSPR. The maps of these two peaks results in images very similar to that of the gold luminescence. This reveals that the gold luminescence is stronger at the SERS hot spots, and confirms that the gold NPs clusters preferentially form on the secretions.

Regarding the other four Raman peaks' maps (**Figures 6c–f**), the bright spots are very few, and no evident correlation with the gold luminescence can be seen. Yet, all four maps display similar features, indicating that these four chemical components all attached at the same positions. This further reveals that these components are most likely due to fingerprint secretions and not to contaminations. Therefore, this technique allows us to recover not only the general LFM patterns using the gold luminescence but also by imaging the chemical components via SERS measurements. In addition, correlating the positions of the different chemical components provides us with a way to discriminate contaminants from human secretions.

TABLE 1 | Raman peaks recorded on the revealed fingermark and their tentative assignment.

Peak position (cm^{-1})	**Tentative assignment** (Movasaghi et al., 2007)
197	N/A
422	Symmetric stretching Po_4^{3-}
788	Nucleic acid measure
900	C-O-C sugar skeletal
952	CH_3 stretching (proteins α-helix)
1,162	Quinoid ring
1,284	Amide III and CH_2 wagging (glycine + proline)
1,361	Guanine/tryptophan
1,606	Cytosine (NH2), Ring C-C stretch of phenyl, Phenylalanine, tyrosine, C55C (protein)

While it would be interesting to conduct this study on a large region and reveal the complete fingermark, we were not able to perform those measurements due to the limitations of our setup. The map dimension is limited by the stage. In addition, the laser spot employed here has a diameter of ∼3 µm. Therefore, the minimum spatial resolution we can use to accurately map the LFMs is ∼20 µm, which results in longer acquisition times and heavier data files. By using of a lower spatial resolution we would risk missing the LFM features and the resulting map will not be representative of the mark.

The purpose of this study is to understand the phenomenon and verify that SERS and luminescence effects could be observed at the microscopic scale. It also aims at demonstrating the feasibility of the technique in order to apply it on different systems, able to illuminate a complete surface of a few cm and thus better adapted for the imaging of features of the size of a complete LFM.

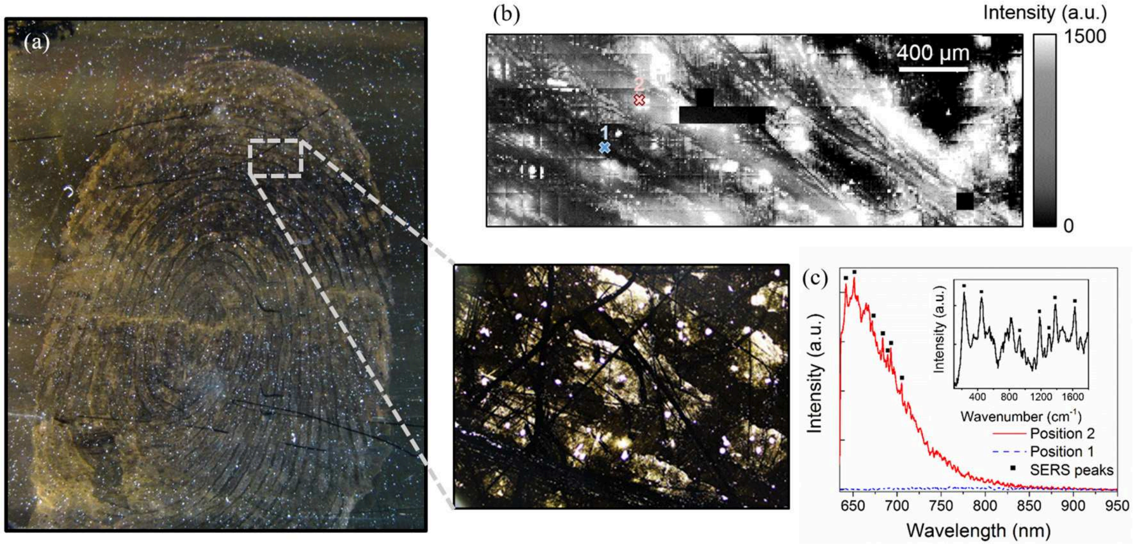

FIGURE 5 | (a) optical dark-field microscopy image (4× objective) of the sample showing three fingermark ridges (golden-brown regions) deposited on a glass substrate (black region), **(b)** 1,100 × 3,100 µm^2 integrated intensity map of the gold luminescence acquired on a region of the fingerprint revealed with gold NP with a spatial resolution of 10 µm, **(c)** Raman spectra taken in a dark region (Position 1) and on a high intensity region (Position 2), revealing SERS peaks (black squares). The inset presents the Raman spectrum obtained at Position 2 after subtracting the gold contribution. All spectra were normalized using the spectrum of the glass substrate.

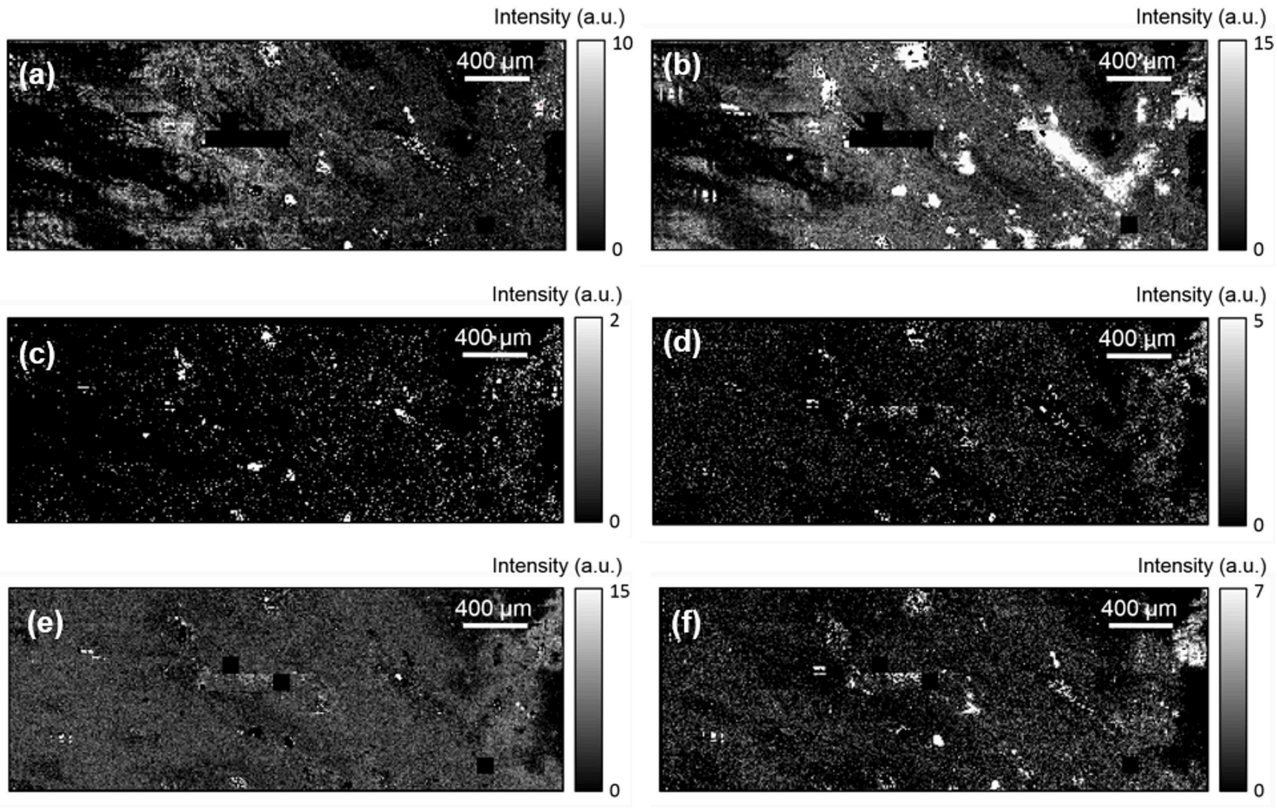

FIGURE 6 | 1,100 × 3,100 µm^2 maps of the SERS peaks located at **(a)** 200 cm^{-1}, **(b)** 420 cm^{-1}, **(c)** 900 cm^{-1}, **(d)** 1,160 cm^{-1}, **(e)** 1,360 cm^{-1}, and **(f)** 1,600 cm^{-1}.

Nevertheless, this study paves the way for LFM studies in forensic science. By combining SMD revelation to SERS measurements, we can visualize the fingermark through gold luminescence and chemically through the secretions' composition and/or contaminants. Also drugs metabolites might be reflected in the SERS signal. Therefore, the SERS effect could potentially be used to identify contaminants such as gun powder residues or drugs, which will be explored in future studies.

CONCLUSION

This paper demonstrates the potential of combining SMD treatments with SERS imaging to reconstruct LFMs. Using gold NPs and the SMD method, the contrast of a LFM deposited on a glass substrate is enhanced to reveal it visually. By monitoring the gold luminescence enhanced by LSPR, we are able to reproduce ridges patterns. In addition, Raman peaks measured on these ridges suggest a SERS enhancement due to the presence of gold NPs. These Raman peaks can be attributed to chemicals produced by the apocrine, eccrine, and sebaceous glands that are not removed by the SMD treatment. Comparison with a reference sample consisting in an unrevealed LFM deposited on a glass cover slide confirms the SERS nature of the signal. By imaging the SERS peaks over the surface of the revealed fingermark, we are able to reconstruct the LFM. Also, correlating different chemical components provides us with a way to discriminate contaminants. The method proposed here will be applied to other systems, better adapted for larger scale imaging, to reveal a complete LFM. This methodology will prove useful for contrast enhancement of LFM on difficult substrates and a combined identification of fingermarks' secretions and/or contaminants. SERS imaging through the gold nanoparticles provides an additional visualization technique for SMD, that is usually an end-of-sequence revelation technique for which further enhancement techniques do not exist.

AUTHOR CONTRIBUTIONS

GK, CP, AR, and CM designed the experiments and were responsible for the results analysis and their interpretation. GK and CP performed the measurements and the data treatment and co-wrote the paper. The project was supervised by CM.

FUNDING

This work was supported by NSERC discovery grant (RGPIN-2014-05024), NSERC strategic partnership grants (506289-2017; 506953-17), Fonds de Recherche du Québec en Nature et Technologies (FRQNT-020-NC-269402).

ACKNOWLEDGMENTS

The authors thank Q. Anseaume and J. Prevost for help with the data acquisition and J. Plathier for his hyperspectral imaging software. GK is grateful for an FRQNT postdoctoral scholarship and AR acknowledges an NSERC discovery grant and two NSERC strategic partnership grants. CM acknowledges a FRQNT support grant for new academics.

REFERENCES

Bailey, M. J., Jones, B. N., Hinder, S., Watts, J., Bleay, S., and Webb, R. P. (2010). Depth profiling of fingerprint and ink signals by SIMS and MeV SIMS. *Nucl. Instrum. Methods Phys. Res. Sect. B* 268, 1929–1932. doi: 10.1016/j.nimb.2010.02.104

Becue, A., Champod, C., and Margot, P. (2007). Use of gold nanoparticles as molecular intermediates for the detection of fingermarks. *Forensic Sci. Int.* 168, 169–176. doi: 10.1016/j.forsciint.2006.07.014

Becue, A., Scoundrianos, A., and Moret, S. (2012). Detection of fingermarks by colloidal gold (MMD / SMD)—beyond the pH 3 limit. *Forensic Sci. Int.* 219, 39–49. doi: 10.1016/j.forsciint.2011.11.024

Bradshaw, R., Wolstenholme, R., Blackledge, R. D., Clench, M. R., Ferguson, L. S., and Francese, S. (2011). A novel matrix-assisted laser desorption/ionisation mass spectrometry imaging based methodology for the identification of sexual assault suspects. *Rapid Commun. Mass Spectrom.* 25, 415–422. doi: 10.1002/rcm.4858

Cai, L., Xia, M. C., Wang, Z., Zhao, Y. B., Li, Z., Zhang, S., et al. (2017). Chemical visualization of sweat pores in fingerprints using GO- enhanced TOF-SIMS. *Anal. Chem.* 89, 8372–8376. doi: 10.1021/acs.analchem.7b01629

Champod, C. J., Lennard, C., Margot, P., and Stoilovic, M. (2016). *Fingerprints and Other Ridge Skin Impressions*. Boca Raton, FL: CRC press. doi: 10.1201/b20423

Charlton, D. T., Bleay, M., and Sears, V. G. (2013). Evaluation of the multimetal deposition process for fingermark enhancement in simulated operational environments. *Anal. Methods* 5, 5411–5417. doi: 10.1039/c3ay40533h

Cialla, D., März, A., Böhme, R., Theil, F., Weber, K., Schmitt, M., et al. (2012). Surface-enhanced Raman spectroscopy (SERS): progress and trends. *Anal. Bioanal. Chem.* 403, 27–54. doi: 10.1007/s00216-011-5631-x

Connatser, R. M., Prokes, S. M., Glembocki, O. J., Schuler, R. L., Gardner, C. W., Lewis, S. A., et al. (2010). Toward surface-enhanced raman imaging of latent fingerprints. *J. Forensic Sci.* 55, 1462–1470. doi: 10.1111/j.1556-4029.2010.01484.x

Day, J. S., Edwards, H. G., Dobrowski, S. A., and Voice, A. M. (2004). The detection of drugs of abuse in fingerprints using Raman spectroscopy I: latent fingerprints. *Spectrochim. Acta Part A Mol. Biomol. Spectrosc.* 60, 563–568. doi: 10.1016/S1386-1425(03)00263-4

Deng, S., Liu, L., Liu, Z., Shen, Z., Li, G., and He, Y. (2012). Line-scanning Raman imaging spectroscopy for detection of fingerprints. *Appl. Opt.* 51, 3701–3706. doi: 10.1364/AO.51.003701

Fairley, C., Bleay, S. M., Sears, V. G., and Nicdaeid, N. (2012). A comparison of multi-metal deposition processes utilising gold nanoparticles and an evaluation of their application to 'low yield' surfaces for finger mark development. *Forensic Sci. Int.* 217, 5–18. doi: 10.1016/j.forsciint.2011.09.018

Figueroa, B., Chen, Y., Berry, K., Francis, A., and Fu, D. (2017). Label-free chemical imaging of latent fingerprints with stimulated raman scattering microscopy. *Anal. Chem.* 89, 4468–4473. doi: 10.1021/acs.analchem.6b04213

Groeneveld, G., de Puit, M., Bleay, S., Bradshaw, R., and Francese, S. (2015). Detection and mapping of illicit drugs and their metabolites in fingermarks by MALDI MS and compatibility with forensic techniques. *Sci. Rep.* 5, 11716. doi: 10.1038/srep11716

Hinder, S. J., and Watts, J. F. (2010). SIMS fingerprint analysis on organic substrates. *Surf. Interface Anal.* 42, 826–829. doi: 10.1002/sia.3497

Holder, E. H., Robinson, L. O., and Laub, J. H. (2011). *The Fingerprint Sourcebook*. Washington, DC: U.S. Dept. of Justice, Office of Justice Programs, National Institute of Justice.

Hutchins, L. A., States, U., and Service, S. (2013). "Identification and Classification, *Encyclopedia of Forensic Sciences 2nd Edn*, eds J. Siegel and P. Saukko (Waltham: Elsevier Inc.; Academic Press).

Ifa, D. R., Manicke, N. E., Dill, A. L., and Cooks, R. G. (2008). Latent fingerprint chemical imaging by mass spectrometry. *Science.* 321, 805. doi: 10.1126/science.1157199

Jain, A. K., Chen, Y., and Demirkus, M. (2007). Pores and ridges : high-resolution fingerprint matching using level 3 features. *IEEE Trans. Pattern Anal. Mach. Intell.* 29, 15–27. doi: 10.1109/TPAMI.2007.250596

Lennard, C. (2014). Fingermark detection and identification : current research efforts. *Aust. J. Forensic Sci.* 46, 293–303. doi: 10.1080/00450618.2013.839743

Mohamed, A. A. (2011). Gold is going forensic. *Gold Bull.* 44, 71–77. doi: 10.1007/s13404-011-0013-x

Mohamed, M. B., Volkov, V., Link, S., and El-Sayed, M. A. (2000). The 'lightning' gold nanorods: fluorescence enhancement of over a million compared to the gold metal. *Chem. Phys. Lett.* 317, 517–523. doi: 10.1016/S0009-2614(99)01414-1

Mooradian, A. (1969). Photoluminescence of metals. *Phys. Rev. Lett.* 22, 185–187. doi: 10.1103/PhysRevLett.22.185

Movasaghi, Z., Rehman, S., and Rehman, I. (2007). Raman Spectroscopy of biological tissues. *Appl. Spectrosc. Rev.* 42, 493–541. doi: 10.1080/05704920701551530

Muehlethaler, C., Leona, M., and Lombardi, J. R. (2016). Review of surface enhanced raman scattering applications in forensic science. *Anal. Chem.* 88, 152–169. doi: 10.1021/acs.analchem.5b04131

Musah, R. A., Cody, R. B., Dane, A. J., Vuong, A. L., and Shepard, J. R. (2012). Direct analysis in real time mass spectrometry for analysis of sexual assault evidence. *Rapid Commun. Mass Spectrom.* 26, 1039–1046. doi: 10.1002/rcm.6198

Newland, T. G., Moret, S., Bécue, A., and Lewis, S. W. (2016). Further investigations into the single metal deposition (SMD II) technique for the detection of latent fingermarks. *Forensic Sci. Int.* 268, 62–72. doi: 10.1016/j.forsciint.2016.09.004

Ricci, C., Bleay, S., and Kazarian, S. G. (2007). Spectroscopic imaging of latent fingermarks collected with the aid of a gelatin tape. *Anal. Chem.* 79, 5771–5776. doi: 10.1021/ac070580j

Song, W., Mao, Z., Liu, X., Lu, Y., Li, Z., Zhao, B., et al. (2012). Detection of protein deposition within latent fingerprints by surface-enhanced Raman spectroscopy imaging. *Nanoscale* 4, 2333–2338. doi: 10.1039/c2nr12030e

Stauffer, E., Becue, A., Singh, K. V., Thampi, K. R., Champod, C., and Margot, P. (2007). Single-metal deposition (SMD) as a latent fingermark enhancement technique : an alternative to multimetal deposition (MMD). *Forensic Sci. Int.* 168, e5–e9. doi: 10.1016/j.forsciint.2006.12.009

Tahtouh, M., Kalman, J. R., Roux, C., Lennard, C., and Reedy, B. J. (2005). The detection and enhancement of latent fingermarks using infrared chemical imaging. *J. Forensic Sci.* 50, 64–72. doi: 10.1520/JFS2004213

Wang, J., Ma, Q., Liu, H., Wang, Y., Shen, H., Hu, X., et al. (2017). Time-gated imaging of latent fingerprints and specific visualization of protein secretions via molecular recognition. *Anal. Chem.* 89, 12764–12770. doi: 10.1021/acs.analchem.7b03003

Wang, J., Wei, T., Li, X., Zhang, B., Wang, J., Huang, C., et al. (2014). Near-infrared-light-mediated imaging of latent fingerprints based on molecular recognition. *Angew. Chem. Int. Ed.* 53, 1616–1620. doi: 10.1002/anie.201308843

Wei, Q., Zhang, M., Ogorevc, B., and Zhang, X. (2016). Recent advances in the chemical imaging of human fingermarks (a review). *Analyst* 141, 6172–6189. doi: 10.1039/C6AN01121G

Widjaja, E. (2009). Latent fingerprints analysis using tape-lift, Raman microscopy, and multivariate data analysis methods. *Analyst* 134, 769–775. doi: 10.1039/B808259F

Wolstenholme, R., Bradshaw, R., Clench, M. R., and Francese, S. (2009). Study of latent fingermarks by matrix-assisted laser desorption/ionisation mass spectrometry imaging of endogenous lipids. *Rapid Commun. Mass Spectrom.* 23, 3031–3039. doi: 10.1002/rcm.4218

Zheng, J., Zhou, C., Yu, M., and Liu, J. (2012). Different sized luminescent gold nanoparticles. *Nanoscale* 4, 4073–4083. doi: 10.1039/c2nr31192e

Conflict of Interest Statement: The authors declare that the research was conducted in the absence of any commercial or financial relationships that could be construed as a potential conflict of interest.

The handling editor declared a past co-authorship with one of the authors CM.

frontiers in Chemistry

ORIGINAL RESEARCH
published: 19 June 2019
doi: 10.3389/fchem.2019.00412

Rapid Detection and Quantification of Novel Psychoactive Substances (NPS) Using Raman Spectroscopy and Surface-Enhanced Raman Scattering

Howbeer Muhamadali[1,2], **Alexandra Watt**[2], **Yun Xu**[1,2], **Malama Chisanga**[2], **Abdu Subaihi**[2,3], **Carys Jones**[2], **David I. Ellis**[2], **Oliver B. Sutcliffe**[4] and **Royston Goodacre**[1,2]*

[1] Department of Biochemistry, Institute of Integrative Biology, University of Liverpool, Liverpool, United Kingdom, [2] School of Chemistry, Manchester Institute of Biotechnology, University of Manchester, Manchester, United Kingdom, [3] Department of Chemistry, University College in Al-Qunfudah, Umm Al-Qura University, Mecca, Saudi Arabia, [4] MANchester DRug Analysis and Knowledge Exchange, Faculty of Science and Engineering, School of Science and the Environment, Manchester Metropolitan University, Manchester, United Kingdom

OPEN ACCESS

Edited by:
Ivano Alessandri,
University of Brescia, Italy

Reviewed by:
Alois Bonifacio,
University of Trieste, Italy
Hui Xu,
Ludong University, China

***Correspondence:**
Royston Goodacre
roy.goodacre@liverpool.ac.uk

Specialty section:
This article was submitted to
Analytical Chemistry,
a section of the journal
Frontiers in Chemistry

Received: 17 March 2019
Accepted: 20 May 2019
Published: 19 June 2019

Citation:
Muhamadali H, Watt A, Xu Y, Chisanga M, Subaihi A, Jones C, Ellis DI, Sutcliffe OB and Goodacre R (2019) Rapid Detection and Quantification of Novel Psychoactive Substances (NPS) Using Raman Spectroscopy and Surface-Enhanced Raman Scattering. Front. Chem. 7:412. doi: 10.3389/fchem.2019.00412

With more than a million seizures of illegal drugs reported annually across Europe, the variety of psychoactive compounds available is vast and ever-growing. The multitude of risks associated with these compounds are well-known and can be life threatening. Hence the need for the development of new analytical techniques and approaches that allow for the rapid, sensitive, and specific quantitative detection and discrimination of such illicit materials, ultimately with portability for field testing, is of paramount importance. The aim of this study was to demonstrate the application of Raman spectroscopy and surface-enhanced Raman scattering (SERS) combined with chemometrics approaches, as rapid and portable techniques for the quantitative detection and discrimination of a wide range of novel psychoactive substances (methcathinone and aminoindane derivatives), both in powder form and in solution. The Raman spectra of the psychoactive compounds provided clear separation and classification of the compounds based on their core chemical structures; *viz*. methcathinones, aminoindanes, diphenidines, and synthetic cannabinoids. The SERS results also displayed similar clustering patterns, with improved limits of detections down to ~2 mM (0.41 g L^{-1}). As mephedrone is currently very popular for recreational use we performed multiplexed quantitative detection of mephedrone (4-methylmethcathinone), and its two major metabolites (nor-mephedrone and 4-methylephedrine), as tertiary mixtures in water and healthy human urine. These findings readily illustrate the potential application of SERS for simultaneous detection of multiple NPS as mixtures without the need for lengthy prior chromatographic separation or enrichment methods.

Keywords: spectroscopy, raman, SERS, drug detection, psychoactive compounds

INTRODUCTION

Novel Psychoactive Substances (NPS) are defined as any substance able to affect a person's mental capability or emotional state (Welter-Luedeke and Maurer, 2016). They have been reported in the earliest of human records, used by healers in primitive medicines with compounds like opium, by priests in religious ceremonies, and in the general population for recreational use with drugs such as nicotine and caffeine.

According to the 2018 report from the United Nations Office on Drugs and Crimes, around 275 million people worldwide have used drugs at least once during 2016, and around 167,750 deaths directly due to drug use have been registered in 2015 (UNODC., 2018). The emergence of hundreds of NPS into various markets, with little to no understanding of their toxicity, pharmacodynamics, and long-term side effects (Tracy et al., 2017), has created a challenge for their detection, identification and quantification, as well as treatment and control efforts. Despite the availability of various detection methods such as: capillary electrophoresis (Nguyen et al., 2015; Saar-Reismaa et al., 2018), immunoassays (Poklis et al., 1993), nuclear magnetic resonance (NMR) spectroscopy (Balayssac et al., 2014), and DNA aptameric sensors (Rauf et al., 2017), the current gold standard techniques for the analysis of such materials are so-called hyphenated methods. These typically involve a combination of prior chromatographic separation techniques coupled to mass spectrometry and include gas or liquid chromatography mass spectrometry (GC-MS, LC-MS) (McKenzie et al., 2018). Despite the accuracy and sensitivity of these techniques, there are some drawbacks, including: not being sufficiently portable, destructive, time-consuming, requiring skilled personnel, and being expensive to run and maintain. Therefore, the use of vibrational techniques such as infrared (Schulz et al., 2004; Risoluti et al., 2016) and Raman spectroscopy (Penido et al., 2016), and surface-enhanced Raman scattering (SERS) (Yu et al., 2018, 2019), has attracted a lot of interest as a reliable alternative (D'Elia et al., 2015) as these physicochemical methods provide a portable (hand-held), rapid and cost-effective solution. In addition to these advantages, these techniques enable on-site quantitative singular or multiplexed detection and identification of xenobiotic compounds such as NPS and their metabolites in human biofluids (Mabbott et al., 2015; Yu et al., 2019).

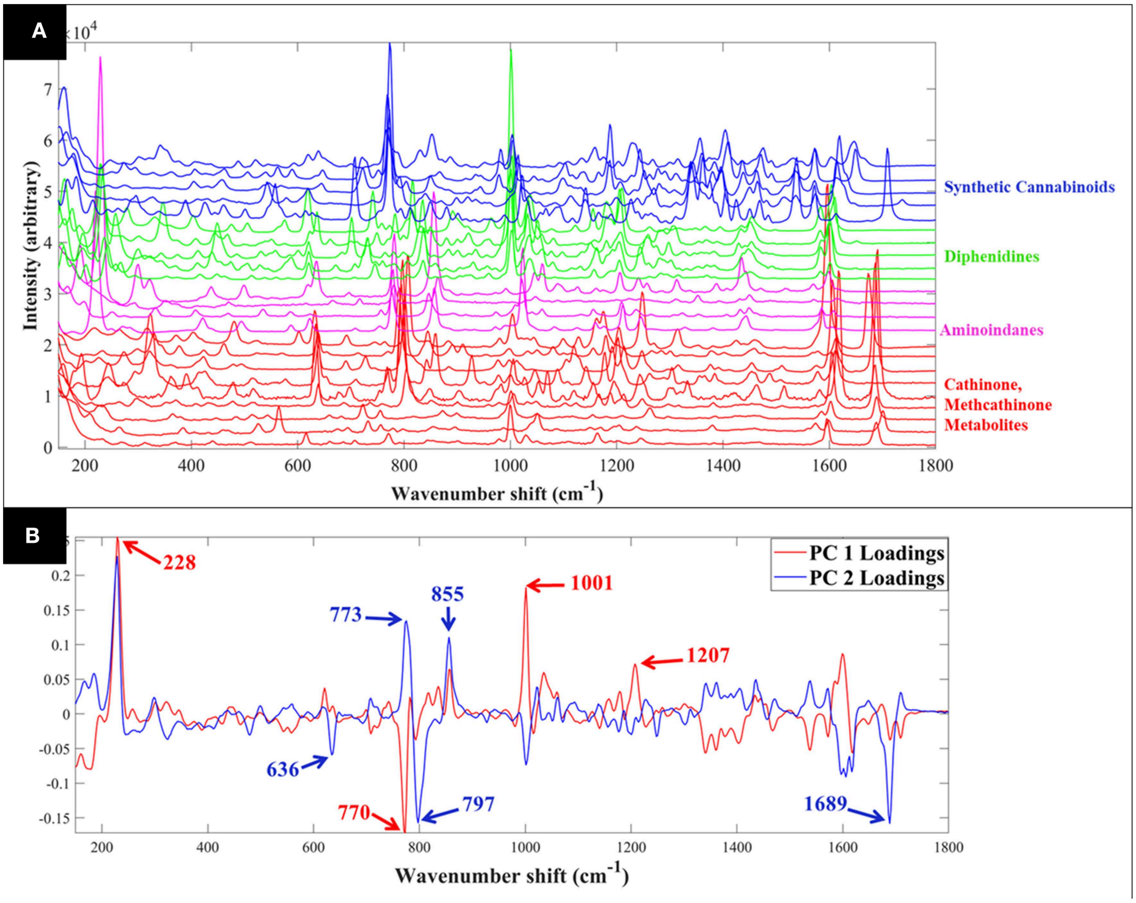

FIGURE 1 | Comparative Raman spectra of all samples collected in solid form **(A)**. PCA loadings plot of the Raman spectral data collected from all samples in solid form **(B)**; this corresponds to the PCA scores plot shown in **Figure 3A**. Different colors represent the compounds with same core structures (methcathinones in red, aminoindanes in purple, diphenidines in green, and synthetic cannabinoids in blue).

Whilst infrared and Raman spectroscopy have been shown to be valuable tools in forensics, including for the analysis of NPS (Jones et al., 2016), providing detailed chemical information, due to their inherent weak signal, these techniques are perceived to lack the required sensitivity for the detection of compounds at low concentrations (Stiles et al., 2008). Therefore, the specificity and selective sensitivity of SERS promotes this approach as a viable alternative method for such applications, allowing the detection, and absolute quantification of trace quantities of target analytes (Goodacre et al., 2018). Several studies in the literature have reported the application of SERS for quantitative detection of various drugs such as: caffeine (Alharbi et al., 2015b), propranolol (Subaihi et al., 2016), 5,6-methylenedioxy-2-aminoindane (MDAI) (Mabbott et al., 2013), codeine (Subaihi et al., 2017), tramadol (Alharbi et al., 2015a), phenothiazine (Ackermann et al., 2007), and amphetamines (Faulds et al., 2002; Dong et al., 2015; Han et al., 2015).

The primary aim of this study was to demonstrate the application of Raman spectroscopy and SERS combined with chemometrics approaches for the quantitative detection and discrimination of a wide range of NPS (methcathinone and aminoindane derivatives), both as powders and in solution. Furthermore, to examine fully the suitability of this approach as a valid alternative to current methods, a secondary aim was to illustrate the detection and quantification of mephedrone (4-methylmethcathinone) and its metabolites (nor-mephedrone and 4-methylephedrine) in a multiplexed system as tertiary mixtures in water and human urine, in order to translate this approach to real-world applications.

MATERIALS AND METHODS

Silver nitrate (99.9% purity), trisodium citrate, and sodium chloride were purchased from Sigma Aldrich (Dorset, United Kingdom). The target compounds (**Table S1**) were synthesized at Manchester Metropolitan University, under UK Home Office license (No. 337201), and obtained as stable, white to off-white powders. To ensure the authenticity of the materials utilized in this study the synthesized samples were structurally characterized and the purity of all samples was confirmed by NMR and GC-MS (>99.5% in all cases). Stock solutions (0.1 M) of the samples (S1–S16) were prepared in de-ionized (DI) water. Samples S17–S23 did not dissolve in water, thus only Raman spectra of the solid (powder) were collected. Sodium chloride stock solution (0.5 M) was prepared by dissolving 0.29 g NaCl in 10 mL of DI water.

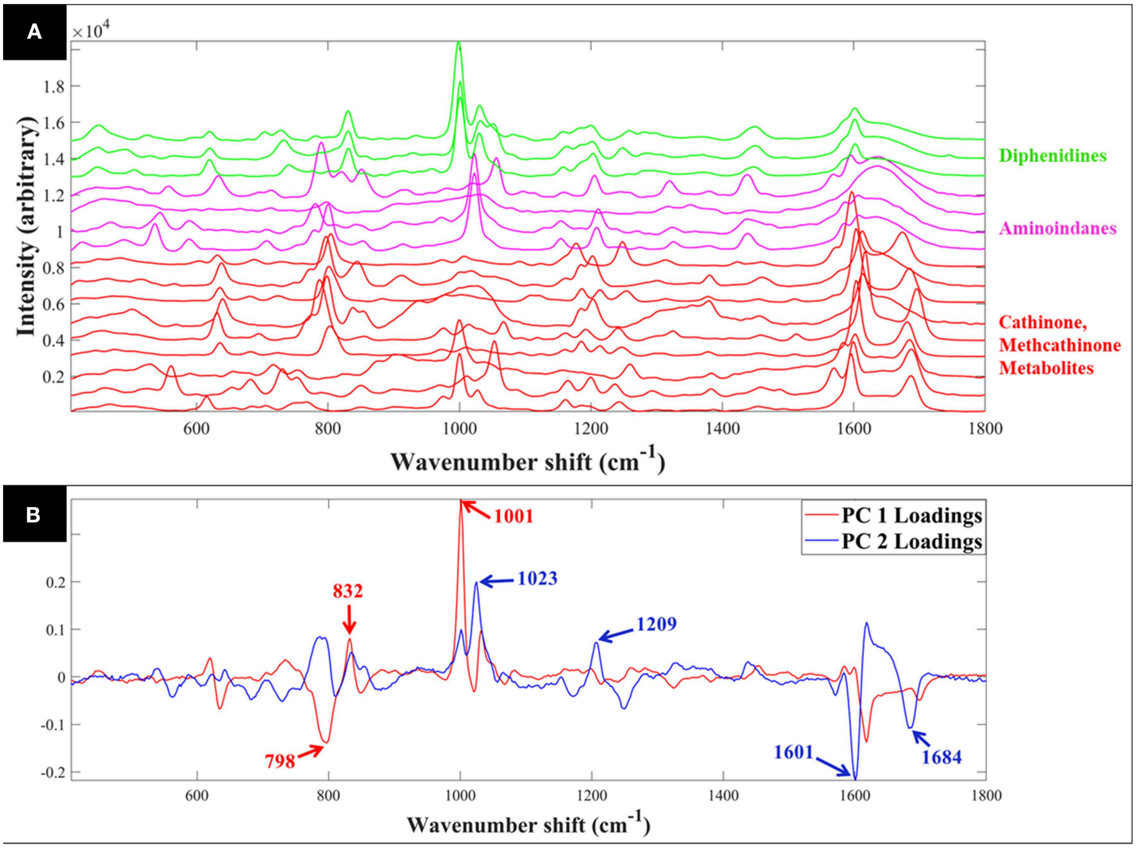

FIGURE 2 | Comparative SERS spectra of all samples collected in aqueous solution **(A)**. PCA loadings plot of the SERS spectral data collected from all samples **(B)**; this corresponds to the PCA scores plot shown in **Figure 4**. Different colors represent the compounds with same core structures (methcathinones in red, aminoindanes in purple, and diphenidines in green).

Mid-stream first morning urine samples were collected in 50 mL Falcon tubes. Samples were briefly kept at ∼4°C immediately following collection, then transported to the laboratory and stored at −80°C within 2 h of collection. Prior to analysis, samples were allowed to thaw, centrifuged at 5,000 *g* for 10 min at 4°C and any pellet removed before being used.

Ethical Approval for collection of urine from a single healthy volunteer was not required and this is in line with local legislation and is also in line with the 1964 Declaration of Helsinki.

Preparation and Characterization of Nanoparticles

All glassware were carefully washed in aqua regia (HNO_3:HCl 1:3) and deionised water and air-dried at room temperature before nanoparticle preparation.

Citrate-reduced Ag colloid was prepared by following the Lee and Meisel (Lee and Meisel, 1982), method. Briefly 90 mg of silver nitrate was dissolved in 500 mL deionised water and heated to boiling. 10 mL of 1% w/v trisodium citrate aqueous solution was then added to the boiling silver nitrate solution, and left stirring for 20 min to stabilize nanoparticle sizes. A color change from colorless to milky green indicated successful synthesis of nanoparticles. The colloids were cooled to room temperature and stored in bottles covered in aluminum foil to prevent light degradation.

Borohydride-reduced Ag colloid (Lee and Meisel, 1982; Zeiri et al., 2002). Silver nitrate (0.104 g) was dissolved in DI water (100 mL). A solution of sodium borohydride (0.057 g) was prepared. Both solutions were cooled separately in ice for 30 min. The ice-cold silver nitrate solution was added dropwise to the sodium borohydride solution with stirring for 20 min. A color change from colorless to a dark milky yellow was observed. Once cool, the flask was wrapped in foil to prevent light degradation.

Silver colloid by hydroxylamine reduction (Leopold and Lendl, 2003). Stock solutions of silver nitrate (0.176 g in 10 mL DI water), sodium hydroxide (0.125 g in 100 mL DI water) and hydroxylamine hydrochloride (1.059 g in 10 mL DI water)

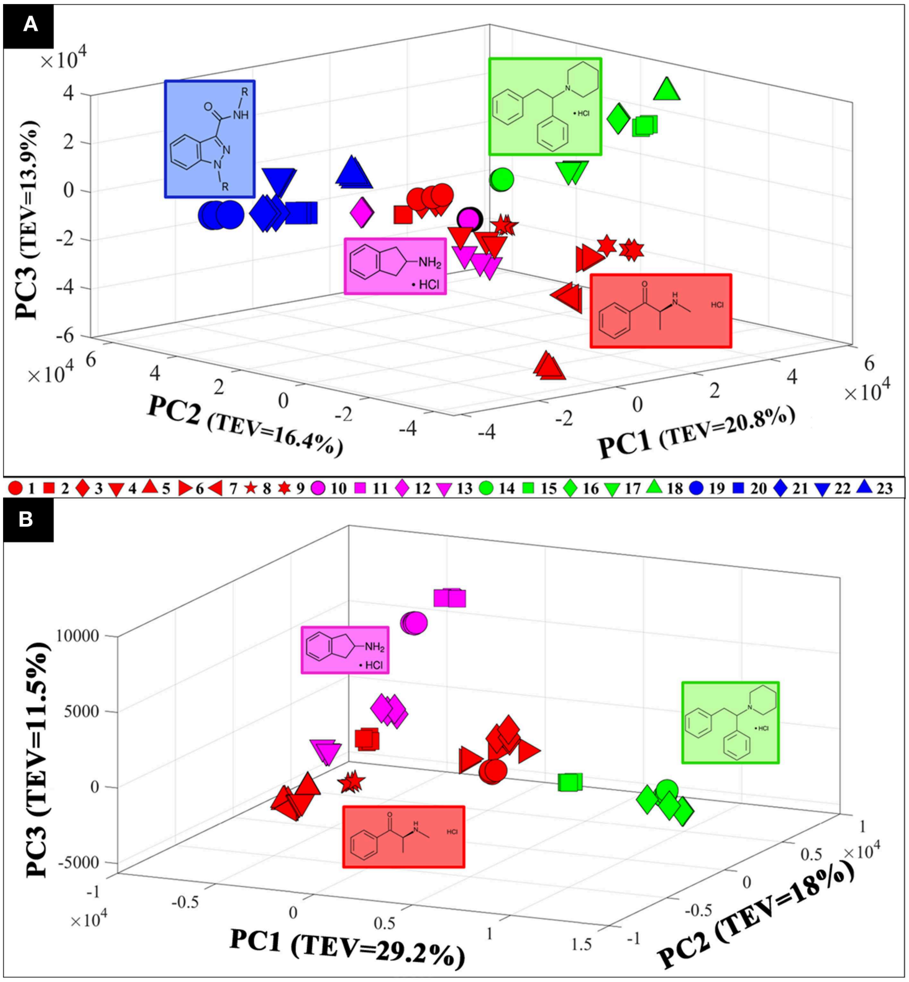

FIGURE 3 | 3D PCA scores plots of the Raman spectral data collected from the samples in solid (powder) **(A)** and aqueous form (0.1 M) **(B)**. Different colors represent the compounds with same core structures (methcathinones in red, aminoindanes in purple, diphenidines in green, and synthetic cannabinoids in blue), while the symbols represent the individual samples analyzed in this study. TEV = total explained variance.

were prepared. Sodium hydroxide solution (20 mL) was added to DI water (158 mL) and the resulting solution heated with stirring. Hydroxylamine hydrochloride solution (2 mL) was then added. In a separate flask, silver nitrate solution (2 mL) was diluted with DI water (20 mL) and added dropwise to the sodium hydroxide solution with stirring. Once addition was complete, the solution was left stirring for 15 min. A color change from colorless to gray/purple was observed. Following this, the suspension was left to cool and wrapped in foil to prevent light degradation.

UV-Vis characterization was carried out by collecting absorbance spectra over a range of 300–800 nm using a Thermo Biomate 5 spectrophotometer (Thermo Fischer Scientific Inc., Massachusetts, USA).

Optimisation of SERS Parameters

For optimization purposes, a stock solution of methcathinone hydrochloride (sample 1) was prepared to test the synthesized nanoparticles and to establish the optimal nanoparticles and conditions (various pH and addition of aggregating agent) for acquiring the most reproducible SERS signal.

Instrumentation

Raman analysis was undertaken using a Renishaw inVia confocal Raman microscope (Renishaw Plc., Gloucestershire, U.K.) equipped with a 785 nm laser. The instrument was calibrated using a silicon plate focused under a ×50 objective, where a static spectrum centered at 520 cm^{-1} for 1 s at 10% power was collected. Spectral data were collected using the WiRE 3.4 software (Galactic Industries Corp. Salem, NH). All spectra were acquired using the laser power adjusted on the sample to ∼28 mW.

SERS spectral data of analyte solutions were collected by mixing 100 μL of sample and 200 μL of the nanoparticle solution in a small glass vial, using Delta Nu Advantage portable Raman spectrometer (Laramie WY, USA) equipped with a 785 nm laser. Power density on the sample was adjusted to ∼60 mW for 20 s, with three SERS spectral acquisitions per sample. All SERS spectra were collected from a minimum of three replicate samples within 100–1,800 cm^{-1} range, immediately after mixing the solutions in the glass vials.

Data Analysis

All Raman and SERS spectra were analyzed using MATLAB software (R2015a) (The Math Works Inc., Natick, USA). Data were baseline corrected using asymmetric least-squares (AsLS) algorithms (Eilers, 2003), using an asymmetry parameter of 0.001 and smoothing parameter of 10,000, and auto-scaled. Principal components analysis (PCA) was carried out to reduce the dimensionality of the data, and scores plots generated to investigate the similarities and differences of spectral features (via loadings plots) of the samples. Partial least squares regression (PLSR) (Geladi and Kowalski, 1986; Gromski et al., 2015) was used to generate a series of multivariate regression models using the spectral data (serial dilutions) of the individual samples. The number of latent variables (PLS factors) were selected using cross validation, with subsequent testing on independent hold out data (test sets).

Multiplexed detection of the target analyte (mephedrone hydrochloride) and its phase I metabolites (nor-mephedrone hydrochloride and 4-methylephedrine hydrochloride) in water and human urine was carried out by generating a set of univariate models via regression of the integrated areas of the discriminatory peaks of interest, against the known concentrations of the analytes.

RESULTS AND DISCUSSION

Raman spectra of all samples collected in solid (S1–S23: **Figure 1A**) and liquid (S1–S16: **Figure 2A**) displayed clear

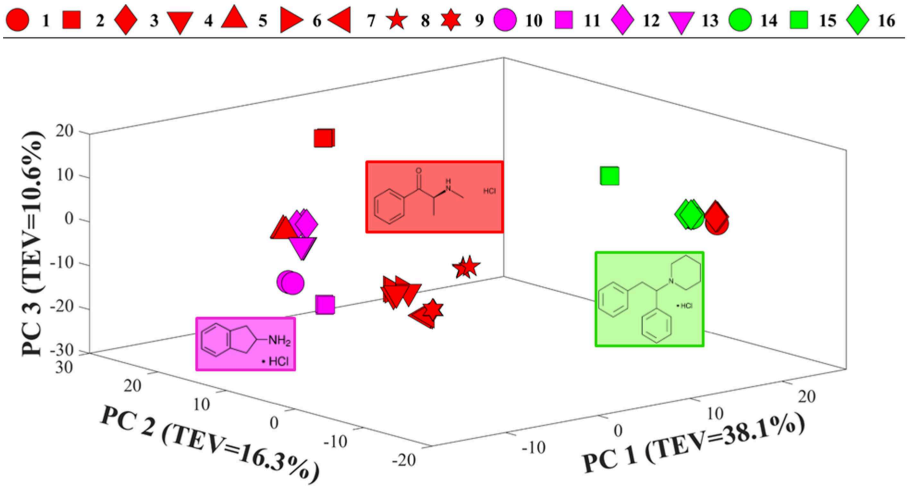

FIGURE 4 | PCA scores plot of all SERS spectral data. Different colors represent the compounds with same core structures (methcathinones in red, aminoindanes in purple, and diphenidines in green), while the symbols represent the individual samples analyzed in this study. TEV = total explained variance.

compound-specific vibrational patterns. Multivariate statistical approaches were applied to characterize and differentiate the samples and to see if these were based on core chemical structural differences. PCA was therefore employed to explore these data further (**Figure 3**). As PCA is an unsupervised learning method any clusters observed would be a natural reflection of any spectral similarities and/or differences. The PCA scores plot of the pre-processed (AsLS and auto-scaled) Raman spectral data collected from the solid (powder) samples (**Figure 3A**) did indeed display a clear separation of the samples according to their core structures. Whilst the diphenidines (samples 14–18) were separated from all other samples according to PC1 axis (**Figure 3A**) with a total explained variance (TEV) of 20.8%, the synthetic cannabinoids were clustered on the positive side of PC2, with a TEV of 16.4%, and away from all other samples. According to the PC1 loadings plot of the solid samples (**Figure 1B**), the most significant vibrational band contributing to the separation of the diphenidines from all other NPS samples was the peak at 1,001 cm^{-1} which can be assigned to aromatic ring breathing/in-plane C-H bending. This is also apparent in the Raman spectra (**Figure 1A**) exhibiting a sharp peak in this region for all the diphenidines, which is perhaps not surprising considering the structure of this group of compounds containing multiple aromatic rings. In addition, the PC2 loadings plot (**Figure 1B**) identified the 773 cm^{-1} peak, corresponding to N-N asymmetric stretching of indazole (Islam et al., 2018), to be the most significant feature discriminating between the synthetic cannabinoids and all other samples.

PCA scores plot of the Raman spectral data collected from the samples in solution (**Figure 3B**) displayed similar clustering patterns, where the diphenidines were again separated from all other samples according to PC1 axis with a TEV of 29.2%, while PC3 allowed for further discrimination of the aminoindanes from methcathinones. The most significant vibrational bands highlighted by the PCA loadings plot (**Figure 2B**) of these samples were also in agreement with those from the solid samples (**Figure 1B**).

In order to establish the required optimal condition for achieving the SERS signal, methcathinone hydrochloride (sample 1) and Rhodamine 6G (0.2 mM) was tested with different nanoparticles (silver borohydride, silver citrate, and silver hydroxylamine reduced) in NaCl as the aggregation agent at a range of pH levels (3, 5, 7, and 9). Comparison of the SERS spectra acquired from the three tested nanoparticles demonstrated that the silver hydroxylamine reduced nanoparticles provided the most reproducible spectra, and that the addition of the aggregation agent did not improve the signal (**Figures S1A–C**, **S2**). Hence, hydroxylamine-reduced Ag nanoparticles without the addition of an aggregation agent was taken forward and employed as the optimum SERS substrate. To determine the optimal pH for SERS analysis, SERS spectra of methcathinone hydrochloride (sample 1) was collected at different pH levels and the results suggested pH 7 as the optimum condition (**Figure S1D**).

Comparison of the SERS spectra of all 16 samples in solution (**Figure S3**) also demonstrated clear vibrational patterns specific to each of the psychoactive compounds. PCA scores plot of these SERS data (**Figure 4**), were consistent with previous Raman findings (**Figure 3**), and allowed for the separation of diphenidines from all other samples according to PC1 axis with 38.1% TEV. Surprisingly, two of the methcathinone samples (1 and 3) also clustered closely with the diphenidines. PC1 loadings plot of these data (**Figure S4**), highlighted the vibrational band at 1,028 cm^{-1} (C-H in plane bending, aromatic stretch) to be the most significant peak distinguishing between the diphenidines and the rest of the samples. This finding also explains the reason for clustering of the two methcathinones (samples 1 and 3) with the diphenidines, as these are the only methcathinone samples which also displayed a strong vibrational band at 1,028 cm^{-1} (**Figure S3**).

In order to determine the limit of detection (LOD) for each of the compounds via SERS, we followed the procedure as described in Clayton et al. (1987), Ortiz et al. (2003). Dilution series of the individual compounds was prepared in water (**Table 1**), and the SERS spectra were collected (**Figure S5**). The PLSR models were built to predict the concentrations of each compound using corresponding SERS spectra. The models were validated using a double cross-validation procedure as described in Westerhuis et al. (2008). The PLSR models displayed acceptable (0.48–0.94) coefficient of determination of validation (Q^2). Based on the predictions of these PLS-R models the estimated LODs varied from the lowest of ~2 mM to the highest of 51 mM for samples 13 and 12, respectively. It is also worth noting that, a comparison of all spectral data collected from the samples in solution displayed clear differences between the Raman and SERS vibrational features and relative intensities, which suggests that the spectra collected from the NPs mixtures are indeed SERS signal.

The above findings clearly demonstrated the potential application of SERS for the detection of various psychoactive drugs using their intrinsic spectral signatures. However, in a

TABLE 1 | Estimated limits of detection (LOD) of all the compounds using SERS.

Sample No.	Conc. range/mM	LOD/mM	Q2 of double-CV
1	50.0–3.1	4.25	0.77
2	25.0–1.6	6.05	0.73
3	100.0–3.1	5.62	0.81
4	50.0–1.6	2.44	0.93
5	50.0–3.1	2.99	0.78
6	100.0–6.3	19.13	0.60
7	50.0–1.6	2.45	0.89
8	100.0–1.6	2.21	0.94
9	100.0–3.1	3.37	0.88
10	100.0–1.6	10.94	0.70
11	50.0–3.1	3.21	0.87
12	100.0–3.1	51.01	0.48
13	50.0–1.6	1.99	0.94
14	25.0–1.6	3.60	0.82
15	25.0–1.6	2.46	0.77
16	100.0–1.6	30.86	0.62

Q2 indicates the prediction-linearity of the PLSR models generated for each of the compounds, from test cross validation samples (i.e., samples not used in the calibration of the PLS models).

real biological system many of these xenobiotic compounds could be metabolized, thus detection of the target compound as well as its metabolites may play a crucial role in monitoring, since these metabolites may still be present after the NPS is no longer detectable. This would also enable a better understanding of the pharmacokinetics and pharmacodynamics of these drugs. To give an example, various studies have reported the potential phase I metabolic pathway of mephedrone

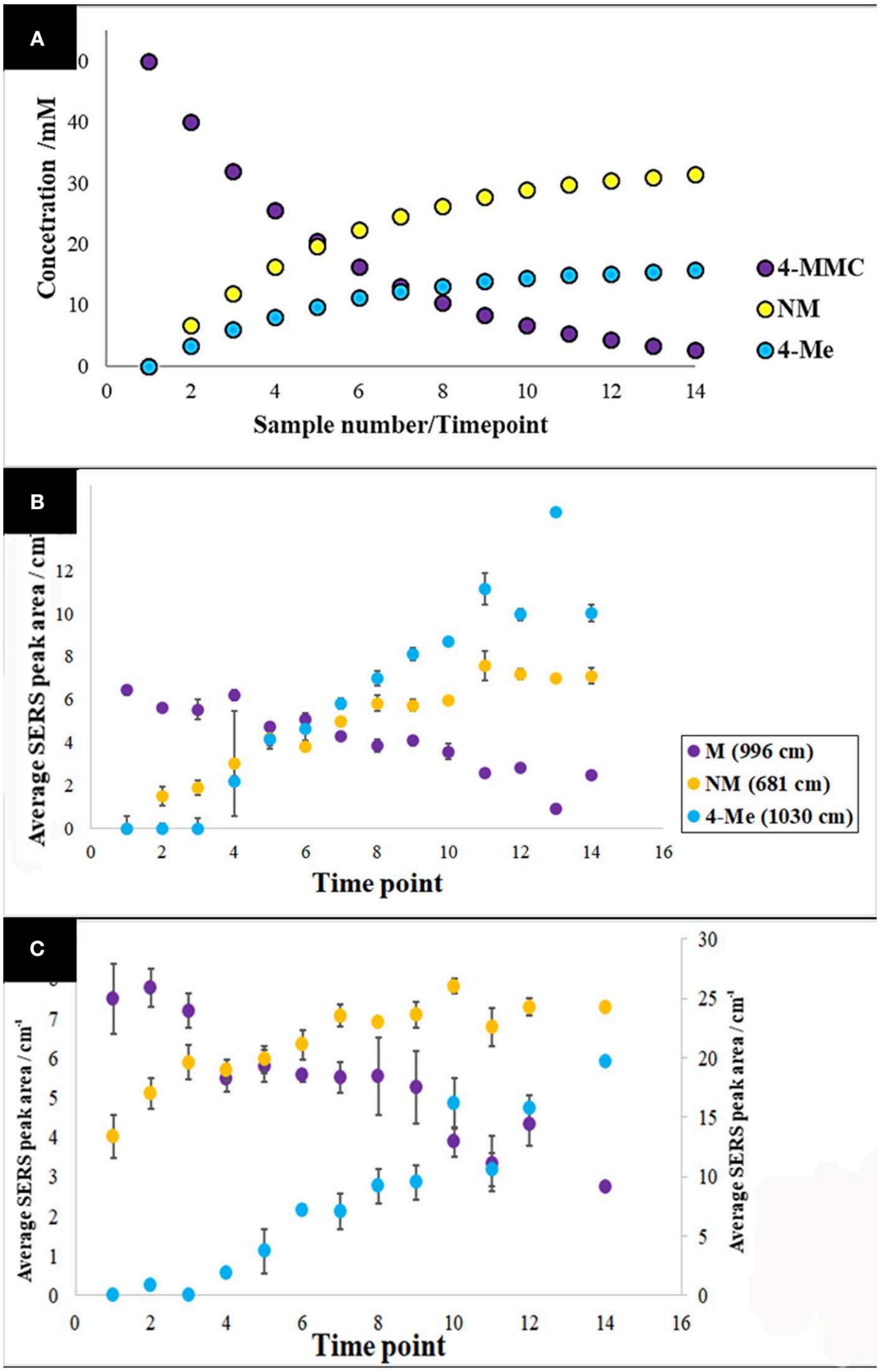

FIGURE 5 | Pharmacokinetic mock-up model for 4-MMC and two of its major metabolites **(A)**. Average metabolite-specific SERS peak areas *vs*. timepoints for the multiplex detection experiment carried out in water **(B)**, and urine **(C)**. The letters 4-MMC, NM, and 4-Me, represent 4-methylmethcathinone, and its metabolites nor-mephedrone and 4-methylephedrine, respectively. The secondary y-axis indicates the detected peak area for NM. Data points presented are average values of three replicates, with error bars indicating the standard deviation.

(4-MMC) as: (i) N-demethylation of the primary amine to form normephedrone; (ii) reduction of the β-keto moiety to the respective alcohol named dihydromephedrone; and (iii) oxidation of the tolyl moiety to the corresponding alcohol, 4-hydroxytolylmephedrone which undergoes further oxidation (Khreit et al., 2013; Pozo et al., 2015; Elbardisy et al., 2019).

As 4-MMC (sample 4) and two of its main metabolites, nor-mephedrone (Sample 7) and 4-methylephedrine (sample 8), were successfully detected in this study with reasonable LOD values (**Table 1**), multiplexed detection of these compounds in both water and urine were investigated. In order to mimic the pharmacokinetics of 4-MMC in a real biological system, and based on the reported findings in the literature (Green et al., 2014; Olesti et al., 2017), it was assumed that metabolism to nor-mephedrone was twice that of the metabolism to 4-methylephedrine throughout the experiment. Two sets of samples were prepared in water and human urine, where the concentration of 4-MMC was decreased while the concentration of nor-mephedrone and 4-methylephedrine were gradually increased to mimic a real-life scenario in a biological system (**Table S2**). Thus, the sample numbers were referred to as time-points to assist such visualization. It is also worth noting that the combined overall concentration of all three compounds in each sample was kept constant.

The specific vibrational bands for each of the metabolites were identified (**Figure S6**), and their corresponding peak areas in both water and urine samples were plotted against time-points (sample numbers) (**Figure 5**). These results clearly displayed the decrease of 4-MMC levels, while its two metabolites exhibited an increasing trend with time. In addition, the known concentration of 4-MMC and its metabolites in the solutions were also plotted against the detected peak areas to examine the linearity of the SERS signal (**Figure 6**). Although the SERS signal of 4-MMC did not display a linear trend at higher concentrations in the urine samples (>13.1 mM) (**Figure 6D**), probably due

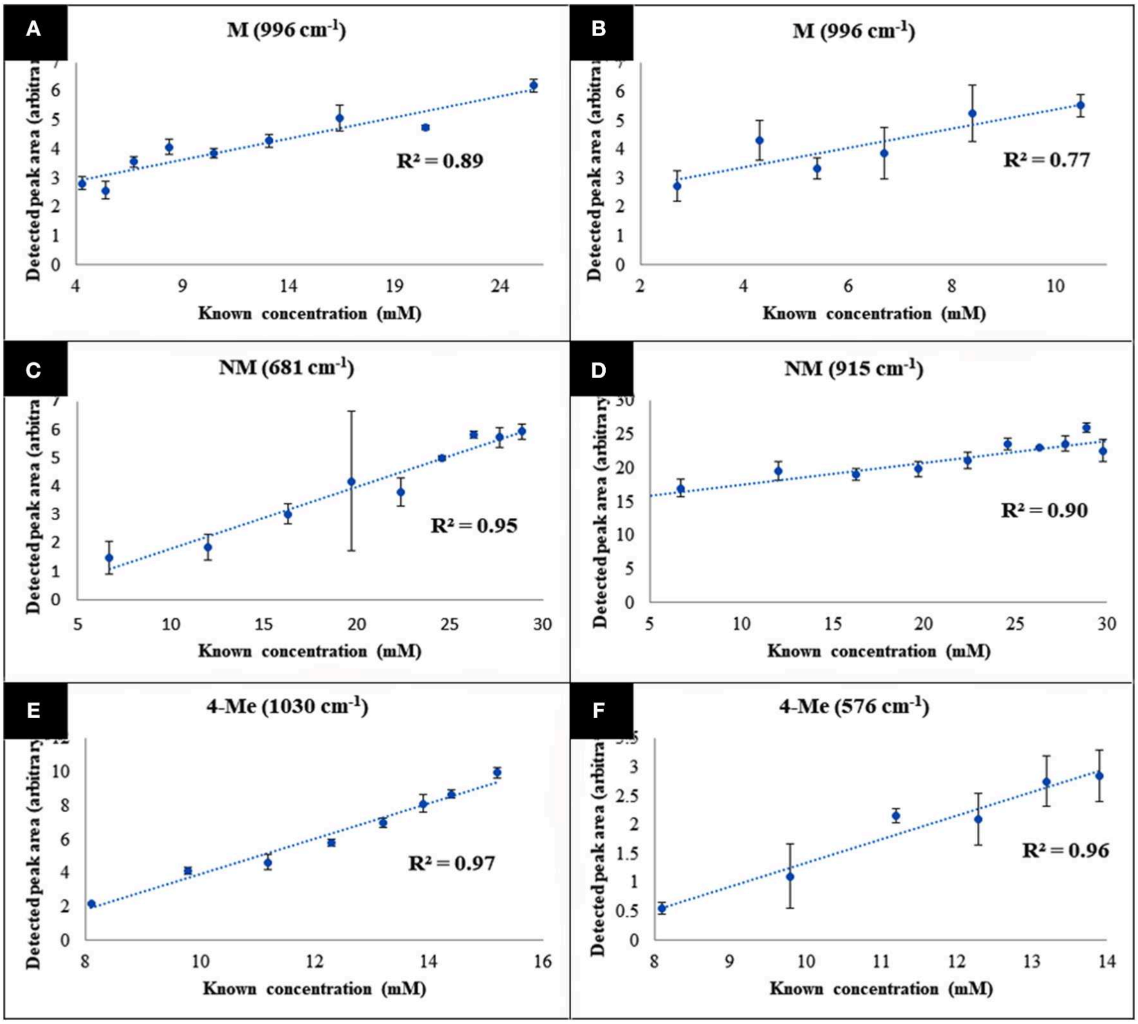

FIGURE 6 | Average metabolite-specific peak areas *vs*. known concentration for the multiplex detection experiment carried out in water **(A–C)**, and urine **(D–F)**. The letters 4-MMC, NM, and 4-Me, represent 4-methylmethcathinone, and its metabolites nor-mephedrone and 4-methylephedrine, respectively. Data points presented are average values of three replicates, with error bars indicating the standard deviation.

to the complexity of the background matrix (urine) causing saturation of the nanoparticles, all other samples exhibited a linear correlation with a correlation coefficient (R^2) in the range of 0.77–0.97.

CONCLUSION

The emergence of NPS, such as cathinones, tryptamines, synthetic cannabinoids, and piperazines, and the vast range of potentially serious side-effects associated with these substances (Hillebrand et al., 2010), illuminates the importance of having rapid, quantitative testing, and detection analytical methods. Thus, the aim of this study was to demonstrate the application of Raman spectroscopy and SERS for quantitative detection and discrimination of a range of NPS as powders and in solution. The detailed and specific vibrational signatures acquired from the Raman and SERS spectral data allowed for clear PCA clustering and separation of the investigated compounds according to their core chemical structures and suggesting that classification would be feasible. To our knowledge this is the first time that multivariate statistics has been applied to Raman or SERS data from NPS that reveal core chemical structures and this may be useful when new NPS are synthesized that have not been detected before as they should cluster with their core structural motif.

The SERS analysis provided LODs mostly ranging between 2.0 and 5.6 mM. Although values in this range are low enough to compare favorably with some techniques currently being used in drug detection, such as microcrystalline testing, they are perhaps not low enough to compare with the current gold standard laboratory techniques such as GC-MS. However, SERS does have the advantage of providing accurate and reliable data rapidly (1 min sample analysis time), with the considerable bonus of the potential of using portable and handheld technologies that could be deployed for on-site testing of samples. Be that point-of-care within clinical settings or in-field testing/identification wherever these psychoactive substances are found. Finally, the successful multiplexed quantitative detection of mephedrone (4-MMC) and two of its main phase I metabolites, nor-mephedrone and 4-methylephedrine, by SERS in both water and human urine, demonstrates further the potential application of this approach for direct detection and quantification of multiple target analytes in human biofluids.

DATA AVAILABILITY

The raw data supporting the conclusions of this manuscript will be made available by the authors, without undue reservation, to any qualified researcher.

AUTHOR CONTRIBUTIONS

HM, OS, and RG designed the experiment. OS generated samples. HM and CJ undertook Raman. HM, AW, MC, AS, and CJ undertook SERS. HM and YX undertook data analysis. All interpreted the data. HM, YX, MC, AS, DE, OS, and RG wrote the manuscript.

FUNDING

RG is indebted to UK BBSRC (BB/L014823/1) for funding for Raman spectroscopy. HM thanks the University of Liverpool for funding and support.

SUPPLEMENTARY MATERIAL

The Supplementary Material for this article can be found online at: https://www.frontiersin.org/articles/10.3389/fchem.2019.00412/full#supplementary-material

REFERENCES

Ackermann, K. R., Henkel, T., and Popp, J. (2007). Quantitative online detection of low-concentrated drugs via a SERS microfluidic system. *ChemPhysChem* 8, 2665–2670. doi: 10.1002/cphc.200700554

Alharbi, O., Xu, Y., and Goodacre, R. (2015a). Detection and quantification of the opioid tramadol in urine using surface enhanced Raman scattering. *Analyst* 140, 5965–5970. doi: 10.1039/C5AN01177A

Alharbi, O., Xu, Y., and Goodacre, R. (2015b). Simultaneous multiplexed quantification of caffeine and its major metabolites theobromine and paraxanthine using surface-enhanced Raman scattering. *Analyt. Bioanalyt. Chem.* 407, 8253–8261. doi: 10.1007/s00216-015-9004-8

Balayssac, S., Retailleau, E., Bertrand, G., Escot, M.P., Martino, R., Malet-Martino, M., et al. (2014). Characterization of heroin samples by 1H NMR and 2D DOSY 1H NMR. *Foren. Sci. Int.* 234, 29–38. doi: 10.1016/j.forsciint.2013.10.025

Clayton, C. A., Hines, J. W., and Elkins, P. D. (1987). Detection limits with specified assurance probabilities. *Analyt. Chem.* 59, 2506–2514. doi: 10.1021/ac00147a014

D'Elia, V., Garcia, G. M., and Ruiz, C. G. (2015). Spectroscopic trends for the determination of illicit drugs in oral fluid. *Appl. Spectr. Rev.* 50, 775–796. doi: 10.1080/05704928.2015.1075206

Dong, R., Weng, S., Yang, L., and Liu, J. (2015). Detection and direct readout of drugs in human urine using dynamic surface-enhanced raman spectroscopy and support vector machines. *Analyt. Chem.* 87, 2937–2944. doi: 10.1021/acs.analchem.5b00137

Eilers, P. H. (2003). A perfect smoother. *Analyt. Chem.* 75, 3631–3636. doi: 10.1021/ac034173t

Elbardisy, H. M., García-Miranda Ferrari, A., Foster, C. W., Sutcliffe, O. B., Brownson, D. A. C., Belal, T. S., et al. (2019). Forensic electrochemistry: the electroanalytical sensing of mephedrone metabolites. *ACS Omega* 4, 1947–1954. doi: 10.1021/acsomega.8b02586

Faulds, K., Smith, W. E., Graham, D., and Lacey, R. J. (2002). Assessment of silver and gold substrates for the detection of amphetamine sulfate by surface enhanced Raman scattering (SERS). *Analyst* 127, 282–286. doi: 10.1039/b107318b

Geladi, P., and Kowalski, B. R. (1986). Partial least-squares regression: a tutorial. *Analyt. Chim. Acta* 185, 1–17. doi: 10.1016/0003-2670(86)80028-9

Goodacre, R., Graham, D., and Faulds, K. (2018). Recent developments in quantitative SERS: moving towards absolute quantification. *TrAC Trends Analyt. Chem.* 102, 359–368. doi: 10.1016/j.trac.2018.03.005

Green, A. R., King, M. V., Shortall, S. E., and Fone, K. C. (2014). The preclinical pharmacology of mephedrone; not just MDMA by another name. *Br. J. Pharmacol.* 171, 2251–2268. doi: 10.1111/bph.12628

Gromski, P. S., Muhamadali, H., Ellis, D. I., Xu, Y., Correa, E., Turner, M. L., et al. (2015). A tutorial review: metabolomics and partial least squares-discriminant analysis – a marriage of convenience or a shotgun wedding. *Analyt. Chim. Acta* 879, 10–23. doi: 10.1016/j.aca.2015.02.012

Han, Z., Liu, H., Meng, J., Yang, L., Liu, J., and Liu, J. (2015). Portable kit for identification and detection of drugs in human urine using surface-enhanced raman spectroscopy. *Analyt. Chem.* 87, 9500–9506. doi: 10.1021/acs.analchem.5b02899

Hillebrand, J., Olszewski, D., and Sedefov, R. (2010). Legal highs on the Internet. *Subst Use Misuse* 45, 330–340. doi: 10.3109/10826080903443628

Islam, S. K., Cheng, Y. P., Birke, R. L., Green, O., Kubic, T., and Lombardi, J. R. (2018). Rapid and sensitive detection of synthetic cannabinoids AMB-FUBINACA and α-PVP using surface enhanced Raman scattering (SERS). *Chem. Phys.* 506, 31–35. doi: 10.1016/j.chemphys.2018.03.028

Jones, L. E., Stewart, A., Peters, K. L., McNaul, M., Speers, S. J., Fletcher, N. C., et al. (2016). Infrared and Raman screening of seized novel psychoactive substances: a large scale study of >200 samples. *Analyst* 141, 902–909. doi: 10.1039/C5AN02326B

Khreit, O. I. G., Grant, M. H., Zhang, T., Henderson, C., Watson, D. G., and Sutcliffe, O. B. (2013). Elucidation of the Phase I and Phase II metabolic pathways of (±)-4′-methylmethcathinone (4-MMC) and (±)-4′-(trifluoromethyl)methcathinone (4-TFMMC) in rat liver hepatocytes using LC–MS and LC–MS2. *J. Pharmaceut. Biomed. Anal.* 72, 177–185. doi: 10.1016/j.jpba.2012.08.015

Lee, P. C., and Meisel, D. (1982). Adsorption and surface-enhanced raman of dyes on silver and gold sols. *J Phys Chem.* 86, 3391–3395. doi: 10.1021/j100214a025

Leopold, N., and Lendl, B. (2003). A new method for fast preparation of highly surface-enhanced raman scattering (SERS) active silver colloids at room temperature by reduction of silver nitrate with hydroxylamine hydrochloride. *J. Phys. Chem. B* 107, 5723–5727. doi: 10.1021/jp027460u

Mabbott, S., Alharbi, O., Groves, K., and Goodacre, R. (2015). Application of surface enhanced Raman scattering to the solution based detection of a popular legal high, 5,6-methylenedioxy-2-aminoindane (MDAI). *Analyst* 140, 4399–4406. doi: 10.1039/C5AN00591D

Mabbott, S., Eckmann, A., Casiraghi, C., and Goodacre, R. (2013). 2p or not 2p: tuppence-based SERS for the detection of illicit materials. *Analyst* 138, 118–122. doi: 10.1039/C2AN35974J

McKenzie, C., Sutcliffe, O. B., Read, K. D., Scullion, P., Epemolu, O., Fletcher, D., et al. (2018). Chemical synthesis, characterisation and in vitro and in vivo metabolism of the synthetic opioid MT-45 and its newly identified fluorinated analogue 2F-MT-45 with metabolite confirmation in urine samples from known drug users. *Foren. Toxicol.* 36, 359–374. doi: 10.1007/s11419-018-0413-1

Nguyen, T. A. H., Pham, T. N. M., Ta, T. T., Nguyen, X. T., Nguyen, T. L., Le, T. H. H., et al. (2015) Screening determination of four amphetamine-type drugs in street-grade illegal tablets and urine samples by portable capillary electrophoresis with contactless conductivity detection. *Sci. Justice* 55, 481–486. doi: 10.1016/j.scijus.2015.09.001

Olesti, E., Farré, M., Papaseit, E., Krotonoulas, A., Pujadas, M., de la Torre, R., et al. (2017). Pharmacokinetics of mephedrone and its metabolites in human by LC-MS/MS. *Aaps J.* 19, 1767–1778. doi: 10.1208/s12248-017-0132-2

Ortiz, M. C., Sarabia, L. A., Herrero, A., Sánchez, M. S., Sanz, M. B., Rueda, M. E., et al. (2003). Capability of detection of an analytical method evaluating false positive and false negative (ISO 11843) with partial least squares. *Chemometr. Intell. Lab. Syst.* 69, 21–33. doi: 10.1016/S0169-7439(03)00110-2

Penido, C., Pacheco, M. T. T., Lednev, I. K., and Silveira, L. (2016). Raman spectroscopy in forensic analysis: identification of cocaine and other illegal drugs of abuse. *J. Raman Spectrosc.* 47, 28–38. doi: 10.1002/jrs.4864

Poklis, A., Fitzgerald, R. L., Hall, K. V., and Saady, J. J. (1993). EMIT-d.a.u. monoclonal amphetamine/methamphetamine assay. II. Detection of methylenedioxyamphetamine (MDA) and methylenedioxymethamphetamine (MDMA). *Foren. Sci. Int.* 59, 63–70. doi: 10.1016/0379-0738(93)90312-X

Pozo, Ó. J., Ibáñez, M., Sancho, J. V., Lahoz-Beneytez, J., Farré, M., Papaseit, E., et al. (2015). Mass spectrometric evaluation of mephedrone *in vivo* human metabolism: identification of phase I and phase II metabolites, including a novel succinyl conjugate. *Drug Metabol. Disposition* 43, 248–257. doi: 10.1124/dmd.114.061416

Rauf, S., Zhang, L., Ali, A., Liu, Y., and Li, J. H. (2017). Label-free nanopore biosensor for rapid and highly sensitive cocaine detection in complex biological fluids. *Acs Sensors* 2, 227–234. doi: 10.1021/acssensors.6b00627

Risoluti, R., Materazzi, S., Gregori, A., and Ripani, L. (2016). Early detection of emerging street drugs by near infrared spectroscopy and chemometrics. *Talanta* 153, 407–413. doi: 10.1016/j.talanta.2016.02.044

Saar-Reismaa, P., Erme, E., Vaher, M., Kulp, M., Kaljurand, M., and Mazina-Šinkar, J. (2018). *In situ* determination of illegal drugs in oral fluid by portable capillary electrophoresis with deep UV excited fluorescence detection. *Analyt. Chem.* 90, 6253–6258. doi: 10.1021/acs.analchem.8b00911

Schulz, H., Baranska, M., Quilitzsch, R., and Schütze, W. (2004). Determination of alkaloids in capsules, milk and ethanolic extracts of poppy (Papaver somniferum L.) by ATR-FT-IR and FT-Raman spectroscopy. *Analyst* 129, 917–920. doi: 10.1039/B408930H

Stiles, P. L., Dieringer, J. A., Shah, N. C., and Van Duyne, R. P. (2008). Surface-enhanced Raman spectroscopy. *Annu. Rev. Anal. Chem.* 1, 601–626. doi: 10.1146/annurev.anchem.1.031207.112814

Subaihi, A., Almanqur, L., Muhamadali, H., AlMasoud, N., Ellis, D. I., Trivedi, D. K., et al. (2016). Rapid, accurate, and quantitative detection of propranolol in multiple human biofluids via surface-enhanced raman scattering. *Analyt. Chem.* 88, 10884–10892. doi: 10.1021/acs.analchem.6b02041

Subaihi, A., Muhamadali, H., Mutter, S. T., Blanch, E., Ellis, D. I., and Goodacre, R. (2017). Quantitative detection of codeine in human plasma using surface-enhanced Raman scattering via adaptation of the isotopic labelling principle. *Analyst* 142, 1099–1105. doi: 10.1039/C7AN00193B

Tracy, D. K., Wood, D. M., and Baumeister, D. (2017). Novel psychoactive substances: types, mechanisms of action, and effects. *BMJ* 356:i6848. doi: 10.1136/bmj.i6848

UNODC. (2018). *World Drug Report 2018*. [Online]. Available online at: https://www.unodc.org/wdr2018/prelaunch/WDR18_Booklet_1_EXSUM.pdf (accessed March 08, 2019].

Welter-Luedeke, J., and Maurer, H. H. (2016). New psychoactive substances: chemistry, pharmacology, metabolism, and detectability of amphetamine derivatives with modified ring systems. *Ther. Drug Monit.* 38, 4–11. doi: 10.1097/FTD.0000000000000240

Westerhuis, J. A., Hoefsloot, H. C. J., Smit, S., Vis, D. J., Smilde, A. K., van Velzen, E. J. J., et al. (2008). Assessment of PLSDA cross validation. *Metabolomics* 4, 81–89. doi: 10.1007/s11306-007-0099-6

Yu, B., Ge, M., Li, P., Xie, Q., and Yang, L. (2019). Development of surface-enhanced Raman spectroscopy application for determination of illicit drugs: towards a practical sensor. *Talanta* 191, 1–10. doi: 10.1016/j.talanta.2018.08.032

Yu, B. R., Li, P., Zhou, B. B., Tang, X. H., Li, S. F., and Yang, L. B. (2018). Sodium chloride crystal-induced SERS platform for controlled highly sensitive detection of illicit drugs. *Chem. Eur. J.* 24, 4800–4804. doi: 10.1002/chem.201800487

Zeiri, L., Bronk, B. V., Shabtai, Y., Czégé, J., and Efrima, S. (2002). Silver metal induced surface enhanced Raman of bacteria. *Colloids Surf. A* 208, 357–362. doi: 10.1016/S0927-7757(02)00162-0

Conflict of Interest Statement: The authors declare that the research was conducted in the absence of any commercial or financial relationships that could be construed as a potential conflict of interest.

frontiers in Chemistry

HYPOTHESIS AND THEORY
published: 16 July 2019
doi: 10.3389/fchem.2019.00470

Modeling Surface-Enhanced Spectroscopy With Perturbation Theory

Niclas S. Mueller* and Stephanie Reich

Department of Physics, Freie Universität Berlin, Berlin, Germany

Theoretical modeling of surface-enhanced Raman scattering (SERS) is of central importance for unraveling the interplay of underlying processes and a predictive design of SERS substrates. In this work we model the plasmonic enhancement mechanism of SERS with perturbation theory. We consider the excitation of plasmonic modes as an integral part of the Raman process and model SERS as higher-order Raman scattering. Additional resonances appear in the Raman cross section which correspond to the excitation of plasmons at the wavelengths of the incident and the Raman-scattered light. The analytic expression for the Raman cross section can be used to explain the outcome of resonance Raman measurements on SERS analytes as we demonstrate by comparison to experimental data. We also implement the theory to calculate the optical absorption cross section of plasmonic nanoparticles. From a comparison to experimental cross sections, we show that the coupling matrix elements need to be renormalized by a factor that accounts for the depolarization by the bound electrons and interband transitions in order to obtain the correct magnitude. With model calculations we demonstrate that interference of different scattering channels is key to understand the excitation energy dependence of the SERS enhancement for enhancement factors below 10^3.

Keywords: surface-enhanced Raman spectroscopy (SERS), plasmonics, perturbation theory, second quantization formalism, optical interference

OPEN ACCESS

Edited by:
Ivano Alessandri,
University of Brescia, Italy

Reviewed by:
Lingxin Chen,
Yantai Institute of Coastal Zone Research (CAS), China
Mikolaj Kajetan Schmidt,
Macquarie University, Australia

****Correspondence:***
Niclas S. Mueller
niclasm@physik.fu-berlin.de

Specialty section:
This article was submitted to Analytical Chemistry, a section of the journal Frontiers in Chemistry

Received: *07 March 2019*
Accepted: *19 June 2019*
Published: *16 July 2019*

Citation:
Mueller NS and Reich S (2019) Modeling Surface-Enhanced Spectroscopy With Perturbation Theory. Front. Chem. 7:470. doi: 10.3389/fchem.2019.00470

1. INTRODUCTION

Surface-enhanced Raman scattering (SERS) is the giant increase in the Raman cross section of a molecule close to a metallic nanostructure (Fleischmann et al., 1974). The local enhancement can exceed ten orders of magnitude making SERS an ideal tool for analytical chemistry that can be even applied for single-molecule detection (Kneipp et al., 1997; Nie and Emory, 1997; Sharma et al., 2012; Wang et al., 2013). The enhancement arises from an interplay of several mechanisms that act simultaneously. There is a general agreement that the strongest enhancement mechanism is the excitation of localized surface plasmon resonances in noble metal nanostructures (Ru and Etchegoin, 2009; Ding et al., 2017). The collective oscillation of conduction electrons leads to intense electromagnetic near fields close to the metal surface that drive the Raman process. The largest enhancement arises from so-called electromagnetic hot spots that occur in the nanometer gaps between plasmonic nanoparticles with a local field intensity that can be five orders of magnitude larger than that of the incident light. Besides plasmonic enhancement, the SERS intensity is affected by chemical enhancement which encompasses a number of effects that concern the chemical interaction of the molecule with the metal surface (Jensen et al., 2008). The metal-molecule interaction can lead to hybridized or charge transfer states that introduce new resonances in the SERS cross section or the molecular resonances can be shifted which may lead to an increase or decrease of the SERS intensity (Osawa et al., 1994; Morton and Jensen, 2009; Darby et al., 2015; Hu et al., 2015; Sevinc et al., 2016). A successful design of SERS substrates depends critically on our understanding of the underlying enhancement mechanisms and a predictive theoretical modeling.

Even though the phenomenon of SERS was discovered more than 40 years ago there are many aspects that remain not fully understood (Moskovits, 2013). Due to the multitude of involved processes it is a challenge to predict the outcome of a SERS experiment, such as the magnitude of the enhancement and its excitation energy dependence. For many years the focus has been on developing microscopic theories for the chemical enhancement mechanism which give insight into the interaction of a molecule with a metal surface and its effect on the Raman spectrum (Jensen et al., 2008; Lombardi and Birke, 2008; Galperin et al., 2009; Hu et al., 2015). The plasmonic enhancement mechanism, on the other hand, is usually modeled with a purely electromagnetic enhancement factor, which is known as the theory of electromagnetic enhancement (Ru and Etchegoin, 2009; Ding et al., 2017). This macroscopic approach is a powerful tool for designing SERS substrates with large enhancement factors but lacks microscopic insight into the different scattering processes underlying SERS. Recently, there has been renewed interest in plasmonic enhancement and in developing microscopic theories that complement the EM enhancement model and expand it to include quantum mechanical effects, such as electron tunneling, optomechanical backaction and non locality (Pustovit and Shahbazyan, 2006; Davis et al., 2010; Roelli et al., 2016; Schmidt et al., 2016; Kamandar Dezfouli and Hughes, 2017; Neuman et al., 2018).

Based on the microscopic theory of Raman scattering we suggested to describe SERS as higher-order Raman (HORa) scattering and developed a theory that treats the plasmonic excitation as a part of the Raman process (Mueller et al., 2016). The localized surface plasmon resonances were included in the Raman cross section in the same way as the molecular resonances. Considering the excitations of the plasmon and of the molecular transitions as subsequent steps of the Raman process allowed us to derive selection rules for SERS with group theory (Jorio et al., 2017). On the experimental side, we designed SERS substrates that allowed to measure exclusively the plasmonic enhancement of the Raman cross section (Heeg et al., 2013, 2014; Mueller et al., 2017b; Wasserroth et al., 2018). The approach of describing SERS as higher-order Raman scattering gives an intuitive picture of what happens in the various steps of the Raman transition (absorption of light by plasmon, electronic excitation by the plasmonic near field, vibronic coupling and so forth). We therefore argued that it should be an excellent tool to fit experimental data and extract information like the strength of light-matter coupling and the energy of the plasmonic resonance, but have not performed such an analysis.

Here we revisit the theory of SERS as higher-order Raman scattering and draw the comparison to experiments. We discuss how the analytic expression for the SERS cross section is used to interpret the excitation energy dependence of the enhancement in experiments. By treating the localized surface plasmon as a quasi-particle we derive analytic expressions for the coupling matrix elements. We account for the depolarization by bound electrons and interband transitions in the interaction Hamiltonians. These contributions were omitted in our previous work that, therefore, overestimated SERS enhancement factors. We calculate the optical absorption cross section of gold and silver nanoparticles as intermediate steps in the Raman process. The excellent agreement with experiments supports the quantitative predictions of our theory. Based on model calculations for a molecule close to a silver nanoparticle we demonstrate that interference between different scattering processes can strongly affect the excitation energy dependence of the SERS enhancement. Our theory leads to the same expression for the plasmonic enhancement in SERS as the commonly used electromagnetic enhancement. In addition, it is used to extract experimental data on the plasmonic system from Raman spectroscopy without requiring a detailed knowledge of the geometry of the plasmonic nanostructure as an input parameter.

2. SERS AS HIGHER-ORDER RAMAN SCATTERING

The theory of surface-enhanced Raman scattering as a higher-order Raman process was introduced in Mueller et al. (2016) and will be reviewed in this section in order to set a theoretical basis for the rest of this paper. The implementation is based on the microscopic theory of Raman scattering which uses perturbation theory to calculate the Raman scattering cross section (Long, 2002; Yu and Cardona, 2010). The main idea is to consider the plasmonic excitation, similar to the molecular excitation, as a step in the Raman scattering process. SERS is therefore described as a higher-order Raman process and the plasmonic resonances appear in the Raman cross section.

We consider a plasmon-enhanced Raman process as illustrated in **Figure 1A** that consists of the following steps: (1) The incoming laser light ω_L excites a localized surface plasmon ω_pl. (2) The plasmonic nanostructure couples via its optical near field to a nearby molecule and induces a transition from the vibronic ground state g to an intermediate state i. The intermediate state can be also a virtual state. (3) The molecule relaxes to a final vibronic state f and excites again the localized surface plasmon. (4) Finally, the Raman-scattered light ω_S is emitted by the plasmonic nanostructure (Mack et al., 2017; Raab et al., 2017). The plasmon-enhanced Raman process can be also illustrated by the Feynman diagram in **Figure 1B**. Each vertex of the diagram corresponds to one of the four steps of the Raman process. Additionally, there are three other relevant scattering processes that take place simultaneously; see **Figure 1C**: The processes where only the incoming light (i) or only the Raman-scattered light (ii) couples to the localized surface plasmon and the Raman process without plasmonic enhancement (iii).

Following Martin and Falicov (1975) and Yu and Cardona (2010) the Feynman diagrams can be translated into Raman scattering amplitudes with perturbation theory.

$$K^{w,w',i}_{\text{pl}-\text{pl}}(\omega_{\text{L}}) = \frac{\mathcal{M}^{w'}_{\text{pt}-\text{pl}}\mathcal{M}^{w',i}_{\text{pl}-\text{vib}}\mathcal{M}^{w,i}_{\text{vib}-\text{pl}}\mathcal{M}^{w}_{\text{pl}-\text{pt}}}{\hbar^3(\omega_{\text{L}} - \omega^{\text{vib}}_f - \omega_{w'} - \text{i}\gamma_{w'})(\omega_{\text{L}} - \omega^{\text{vib}}_i - \text{i}\gamma^{\text{vib}}_i)(\omega_{\text{L}} - \omega_w - \text{i}\gamma_w)} \tag{1}$$

corresponds to the Feynman diagram in **Figure 1B**,

$$K^{w,i}_{\text{pl}-\text{pt}}(\omega_{\text{L}}) = \frac{\mathcal{M}^{i}_{\text{pt}-\text{vib}}\mathcal{M}^{w,i}_{\text{vib}-\text{pl}}\mathcal{M}^{w}_{\text{pl}-\text{pt}}}{\hbar^2(\omega_{\text{L}} - \omega^{\text{vib}}_i - \text{i}\gamma^{\text{vib}}_i)(\omega_{\text{L}} - \omega_w - \text{i}\gamma_w)} \tag{2}$$

to **Figure 1C** (i),

$$K^{w,i}_{\text{pt}-\text{pl}}(\omega_{\text{L}}) = \frac{\mathcal{M}^{w}_{\text{pt}-\text{pl}}\mathcal{M}^{w,i}_{\text{pl}-\text{vib}}\mathcal{M}^{i}_{\text{vib}-\text{pt}}}{\hbar^2(\omega_{\text{L}} - \omega^{\text{vib}}_f - \omega_w - \text{i}\gamma_w)(\omega_{\text{L}} - \omega^{\text{vib}}_i - \text{i}\gamma^{\text{vib}}_i)} \tag{3}$$

to **Figure 1C** (ii) and

$$K^{i}_{\text{pt}-\text{pt}}(\omega_{\text{L}}) = \frac{\mathcal{M}^{i}_{\text{pt}-\text{vib}}\mathcal{M}^{i}_{\text{vib}-\text{pt}}}{\hbar(\omega_{\text{L}} - \omega^{\text{vib}}_i - \text{i}\gamma^{\text{vib}}_i)} \tag{4}$$

to **Figure 1C** (iii). $\hbar\omega^{\text{vib}}_i$ and $\hbar\omega^{\text{vib}}_f$ are the energies of the vibronic molecular states and $\hbar\omega_w$ and $\hbar\omega_{w'}$ are the energies of two plasmon modes w and w'. The energy of the molecular ground state $\hbar\omega^{\text{vib}}_g$ was referenced to zero. $\gamma^{\text{vib}}_i = \hbar/\tau^{\text{vib}}_i$, $\gamma_w = \hbar/\tau_w$ and $\gamma_{w'} = \hbar/\tau_{w'}$ are the respective inverse life times τ^{vib}_i, τ_w and $\tau_{w'}$ of the excitations. The matrix elements $\mathcal{M}_{i-j}$ correspond to the vertices of the Feynman diagrams and describe the coupling strength of the photon-plasmon (pt-pl), plasmon-molecule (pl-vib) and photon-molecule (pt-vib) interactions. We will derive explicit expressions below.

The energy terms in the denominators correspond to plasmonic and molecular resonances and generate the excitation energy dependence of the Raman cross section. When the incoming light matches the energy $\hbar\omega_w$ of a plasmon mode, the real part of the corresponding energy term vanishes which leads to a resonance of the Raman cross section with spectral width $2\gamma_w$. In the following we will term this "incoming plasmonic Raman resonance" because the incoming light matches a plasmon mode. Similarly an outgoing plasmonic Raman resonance occurs for $\omega_{\text{L}} - \omega^{\text{vib}}_f = \omega_{w'}$, i.e., when the energy of the Raman-scattered light matches that of the plasmon mode. Furthermore, a molecular Raman resonance occurs when the incoming light matches a vibronic state i. The excitation of a virtual state is described by the off-resonant excitation of the vibronic state i. The resonances will have Lorentzian line shape. We will discuss the applicability of this approximation for plasmonic excitations below.

The Raman scattering rate that is relevant for the intensity that arrives at the detector can be calculated with the Fermi Golden Rule as

$$\Gamma(\omega_{\text{L}}) = \sum_f \left| \sum_{w,w',i} K^{w,w',i}_{\text{SERS}}(\omega_{\text{L}}) \right|^2 \frac{2\gamma_{\text{vib}}}{\hbar^2\left[(\omega_{\text{L}} - \omega^{\text{vib}}_f)^2 + (\gamma^{\text{vib}}_f)^2\right]}, \tag{5}$$

where $K^{w,w',i}_{\text{SERS}} = K^{w,w',i}_{\text{pl}-\text{pl}} + K^{w,i}_{\text{pl}-\text{pt}} + K^{w,i}_{\text{pt}-\text{pl}} + K^{i}_{\text{pt}-\text{pt}}$. γ^{vib}_f is the inverse lifetime of the final vibronic state and corresponds to the spectral width $2\gamma^{\text{vib}}_f$ of the vibrational mode in the Raman spectrum. All Raman amplitudes that lead to the same final state f are summed before calculating the absolute square; i.e., summation over w, w' and i in Equation (5). The different scattering channels might interfere constructively or destructively which will be discussed below. In a SERS experiment one typically divides the measured intensity of a Raman mode by a reference to calculate an enhancement factor

$$\text{EF}(\omega_{\text{L}}) = \frac{\left|\sum_{w,w',i} K^{w,w',i}_{\text{SERS}}(\omega_{\text{L}})\right|^2}{\left|\sum_i K^{i}_{\text{ref}}(\omega_{\text{L}})\right|^2}, \tag{6}$$

where $K^{i}_{\text{ref}}(\omega_{\text{L}})$ is given by an expression similar to Equation (4). The enhancement factor can be only written in this way when referencing to the intensity of the same Raman mode. In experiments the measured Raman intensity of the SERS analyte is typically divided by the intensity of the same analyte in solution (Le Ru and Etchegoin, 2013). The different dielectric environment might shift the molecular resonance of the SERS analyte with respect to that of the reference. In this case the energies of the intermediate molecular states $\hbar\omega^{\text{vib}}_i$ that appear in K_{SERS} and K_{ref} are different. On the other hand, if the molecular states of the SERS analyte and the reference are identical all terms related to the molecular resonance cancel and Equation (6) simplifies to

$$\begin{aligned}\text{EF}(\omega_{\text{L}}) = \Bigg| &\frac{\tilde{\mathcal{M}}_1\tilde{\mathcal{M}}_2}{\hbar^2(\omega_{\text{L}} - \omega_{\text{vib}} - \omega_{\text{pl}} - \text{i}\gamma_{\text{pl}})(\omega_{\text{L}} - \omega_{\text{pl}} - \text{i}\gamma_{\text{pl}})} \\ &+ \frac{\tilde{\mathcal{M}}_1}{\hbar(\omega_{\text{L}} - \omega_{\text{pl}} - \text{i}\gamma_{\text{pl}})} \\ &+ \frac{\tilde{\mathcal{M}}_2}{\hbar(\omega_{\text{L}} - \omega_{\text{vib}} - \omega_{\text{pl}} - \text{i}\gamma_{\text{pl}})} + 1 \Bigg|^2,\end{aligned} \tag{7}$$

where $\tilde{\mathcal{M}}_1$ and $\tilde{\mathcal{M}}_2$ are coupling factors that describe the strength of the incoming and the outgoing plasmonic Raman resonances (Mueller et al., 2016). Additionally we have assumed that only one plasmon mode ω_{pl} is excited and set $\omega_{\text{vib}} \equiv \omega^{\text{vib}}_f$. Equation (7) is a purely plasmonic enhancement factor of the SERS cross section. The enhancement at the incoming plasmonic Raman

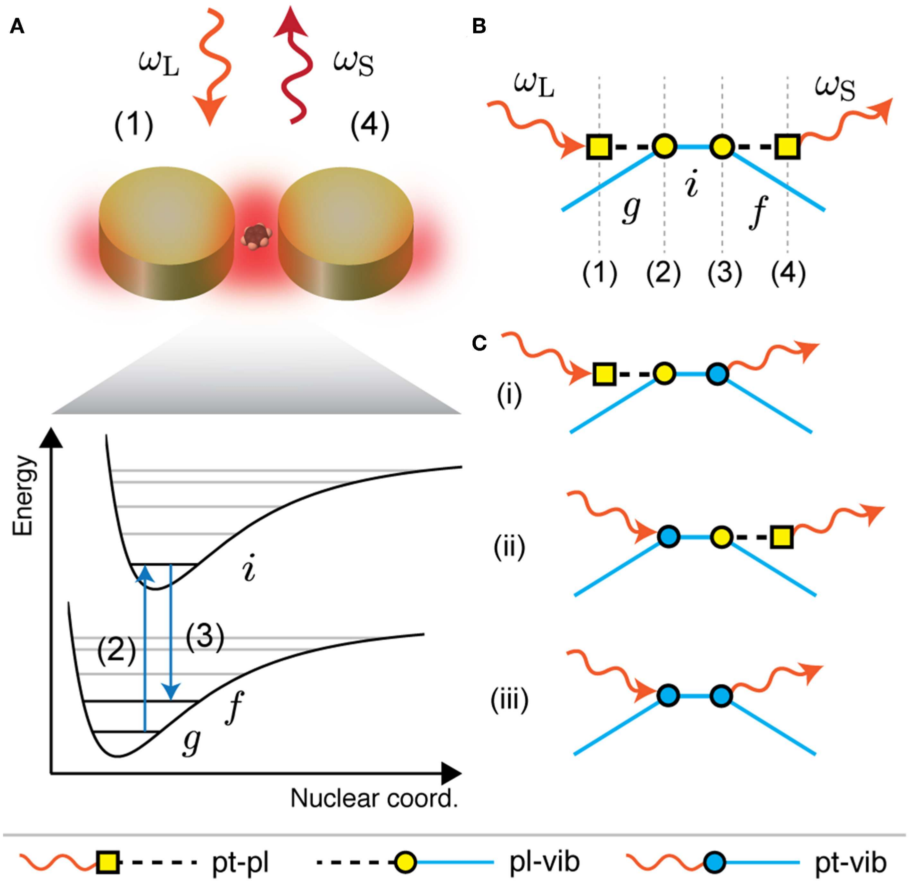

FIGURE 1 | SERS as higher-order Raman scattering. **(A)** Sketch of a plasmon-enhanced Raman process relevant for SERS. The steps are: (1) excitation of a plasmon by the incoming light ω_L; (2) molecular transition from ground state g to intermediate state i by coupling to the plasmonic near field; (3) molecular relaxation to final state f and excitation of the plasmon; (4) emission of Raman-scattered light ω_S by the plasmon. **(B)** Plasmon-enhanced Raman process in **(A)** illustrated as a Feynman diagram which corresponds to fourth-order perturbation theory. **(C)** Feynman diagrams of three other scattering processes that are relevant for SERS, i.e., (i) only the incoming light or (ii) only the Raman-scattered light couples to the plasmon and (iii) the Raman process without plasmonic enhancement.

resonance is

$$\mathrm{EF}(\omega_{\mathrm{pl}}) = \frac{(\tilde{\mathcal{M}}_1^2 + \hbar^2\gamma_{\mathrm{pl}}^2)\left[\tilde{\mathcal{M}}_2^2 - 2\,\hbar\,\omega_{\mathrm{vib}}\tilde{\mathcal{M}}_2 + \hbar^2(\omega_{\mathrm{vib}}^2 + \gamma_{\mathrm{pl}}^2)\right]}{\hbar^4\gamma_{\mathrm{pl}}^2(\omega_{\mathrm{vib}}^2 + \gamma_{\mathrm{pl}}^2)} \tag{8}$$

and the enhancement at the outgoing plasmonic Raman resonance is

$$\mathrm{EF}(\omega_{\mathrm{pl}}{+}\omega_{\mathrm{vib}}) = \frac{(\tilde{\mathcal{M}}_2^2 + \hbar^2\gamma_{\mathrm{pl}}^2)\left[\tilde{\mathcal{M}}_1^2 + 2\,\hbar\,\omega_{\mathrm{vib}}\tilde{\mathcal{M}}_1 + \hbar^2(\omega_{\mathrm{vib}}^2 + \gamma_{\mathrm{pl}}^2)\right]}{\hbar^4\gamma_{\mathrm{pl}}^2(\omega_{\mathrm{vib}}^2 + \gamma_{\mathrm{pl}}^2)}. \tag{9}$$

We will demonstrate below that the enhancement at the incoming- and outgoing plasmonic Raman resonances can differ significantly because of inteference between different scattering channels.

In previous works we have designed SERS experiments which allow to extract the plasmonic enhancement of the SERS cross section (Heeg et al., 2013, 2014; Mueller et al., 2017b; Wasserroth et al., 2018). For this we used carbon nanostructures as SERS analytes, i.e., graphene, carbon nanotubes and carbon nanotubes filled with molecules. These structures have a Raman response that is strong enough to be detected in the absence of plasmonic enhancement. The experiments were designed in such a way that the Raman intensities with and without the plasmonic nanostructure could be compared directly. In **Figure 2** we show the excitation-energy dependent SERS enhancement for graphene deposited on top of a gold nanodimer (Wasserroth et al., 2018). The enhancement was measured for the two prominent Raman modes of graphene, the carbon-carbon stretching G mode ($\hbar\omega_G = 0.19$ eV) and the overtone of the ring-breathing mode 2D ($\hbar\omega_{2D} \approx 0.3$ eV). An exemplary SERS spectrum (red) and a reference spectrum recorded away from the plasmonic nanodimer (black) are shown in **Figure 2A**. The enhanced Raman modes are shifted with respect to the reference because of strain that is induced in the graphene lattice by the nanodimer (Mueller et al., 2017a). By using tunable laser excitation we measured the excitation energy dependence of the

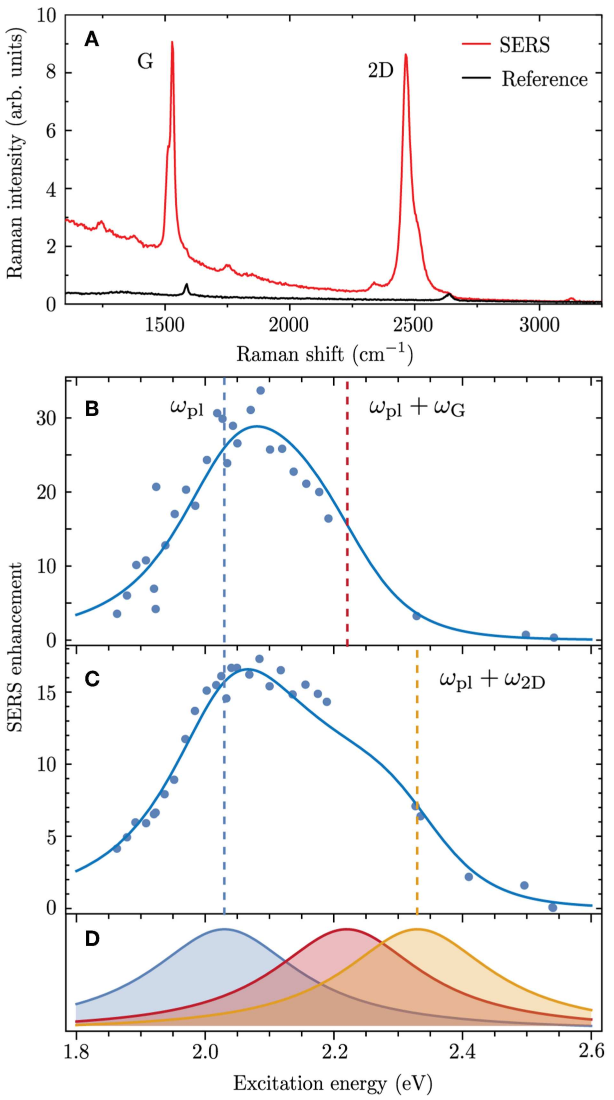

FIGURE 2 | (A) SERS spectrum of graphene deposited on top of a gold nanodimer (red) and reference spectrum without the gold nanodimer (black) for $\hbar\omega_{\mathrm{L}} = 1.94$ eV. **(B,C)** Excitation energy dependence of the SERS enhancement measured for **(B)** the Raman G mode and **(C)** the 2D mode (data from Wasserroth et al., 2018). Solid lines are a fit to the experimental data with Equation (7) using $\hbar\omega_{\mathrm{pl}} = 2.03$ eV, $\hbar\gamma_{\mathrm{pl}} = 140$ meV and $\tilde{\mathcal{M}}_1 = \tilde{\mathcal{M}}_2 = -1.5$ eV for the G mode and $\tilde{\mathcal{M}}_1 = \tilde{\mathcal{M}}_2 = -1.52$ eV for the 2D mode. The Raman shifts $\hbar\omega_{\mathrm{G}} = 0.19$ eV and $\hbar\omega_{\mathrm{2D}} \approx 0.3$ eV were obtained from the experimental spectra. The incoming ($\omega_{\mathrm{L}} = \omega_{\mathrm{pl}}$) and outgoing ($\omega_{\mathrm{L}} = \omega_{\mathrm{pl}} + \omega_f^{\mathrm{vib}}$) plasmonic Raman resonances are indicated as dashed lines. The enhancement factor in Equation (7) was divided by a factor of 230 as it gives a local enhancement while the experimental data are a global enhancement (see Wasserroth et al., 2018 for details). **(D)** Normalized incoming (blue) and outgoing plasmonic Raman resonances (red for G mode and orange for 2D mode) which constitute the resonance profiles in **(B,C)**.

plasmonic enhancement which is plotted for the G mode in **Figure 2B** and for the 2D mode in **Figure 2C**.

The excitation energy dependence of the SERS enhancement can be interpreted with Equation (7) using $\tilde{\mathcal{M}}_1$, $\tilde{\mathcal{M}}_2$, ω_{pl} and γ_{pl} as fitting parameters. The fits are illustrated as solid lines in **Figures 2B,C** and match excellently the experimental data. The corresponding incoming and outgoing plasmonic Raman resonances are illustrated in **Figure 2D**. The excitation energy dependence of the SERS enhancement is narrower than the sum of the two resonances as it mainly arises from their product. An asymmetry appears because of interference between different scattering channels, which will be discussed in detail below. Generally we observed that the outgoing Raman resonance is weaker than the incoming Raman resonance.

3. INTERACTION HAMILTONIANS

The description of surface-enhanced Raman scattering as higher-order Raman scattering considers the excitation of the localized surface plasmon by the incoming light and the coupling of the plasmon to the molecule as two subsequent steps of the Raman process. This requires to treat the localized surface plasmon as a quasiparticle. In the following we derive analytic expressions for the coupling matrix elements based on a quantization of the localized surface plasmon. We use the same interaction Hamiltonians to describe the incoming scattering pathway (absorption of light by plasmon, excitation of vibronic transition in molecule by plasmonic near field) and the outgoing scattering pathway (excitation of plasmon by molecule, emission of Raman scattered light by plasmonic nanostructure). We demonstrated in Mueller et al. (2016) that this is a good approximation in the backscattering geometry; see also Ausman and Schatz (2009) and Ausman and Schatz (2012).

3.1. Quantization of the Localized Surface Plasmon

To quantize the localized surface plasmon resonances of a metallic nanoparticle, we use a jellium model which assumes a density $\mathcal{N}$ of free electrons that move in the presence of a uniform positively charged background (Gerchikov et al., 2002; Weick et al., 2005; Finazzi and Ciccacci, 2012). The center-of-mass Hamiltonian describing the collective motion of the electrons is given by

$$\hat{\mathcal{H}}_{\mathrm{pl}} = \frac{\mathcal{N} V_{\mathrm{p}}}{2} \sum_w \left(\frac{1}{m} \hat{\Pi}_w^2 + m\omega_w^2 \hat{\Psi}_w^2 \right), \tag{10}$$

where V_{p} is the volume of the metallic nanoparticle. $\hat{\Psi}_w$ and $\hat{\Pi}_w$ are canonical position and momentum coordinates that are written in terms of creation and annihilation operators $\hat{b}_w^\dagger$ and $\hat{b}_w$ of a plasmon mode w as

$$\hat{\Psi}_w = \sqrt{\frac{\hbar}{2m\mathcal{N} V_{\mathrm{p}} \omega_w}} (\hat{b}_w^\dagger + \hat{b}_w) \tag{11}$$

and

$$\hat{\Pi}_w = \mathrm{i} \sqrt{\frac{m\,\hbar\,\omega_w}{2\mathcal{N} V_{\mathrm{p}}}} (\hat{b}_w^\dagger - \hat{b}_w). \tag{12}$$

Using the bosonic commutation relations

$$[\hat{b}_w, \hat{b}_{w'}^\dagger] = \delta_{w,w'} \tag{13}$$

the Hamiltonian in Equation (10) can be rewritten as

$$\hat{\mathcal{H}}_{\rm pl} = \sum_w \hbar\omega_w \hat{b}_w^\dagger \hat{b}_w + \frac{1}{2}. \tag{14}$$

The plasmonic Hamiltonian may be written in this way when initially ignoring losses; otherwise the plasmonic modes are ill-defined (Waks and Sridharan, 2010; Finazzi and Ciccacci, 2012). We account for the decay by using complex energies $\omega_w + i\gamma_w$ in the energy denominators of Equations (1–3) as is common practice within the microscopic theory of Raman scattering (Long, 2002; Yu and Cardona, 2010). The Hamiltonian in Equation (14) can also be applied for oligomers or arrays of plasmonic nanoparticles (Brandstetter-Kunc et al., 2015, 2016; Lamowski et al., 2018). In this case $\hat{b}_w$ corresponds to the operator of the hybridized plasmon modes w of the coupled nanoparticles and is given by a Bogoliubov transformation of the single nanoparticle operators.

3.2. Plasmon-Photon Interaction

In the presence of an external light field, the plasmonic Hamiltonian in Equation (10) has to be modified by the Peierl's substitution $\hat{\Pi}_w \rightarrow \hat{\Pi}_w + e\hat{A}_w$ which leads to the minimal coupling Hamiltonian

$$\hat{\mathcal{H}}_{\rm pl-pt} = \frac{e\mathcal{N}V_{\rm p}}{m}\sum_w \hat{\Pi}_w \hat{A}_w. \tag{15}$$

$\hat{A}_w$ is a projection of the vector potential $\hat{\mathbf{A}}_{\rm pt}$ of the external light field onto a plasmonic mode w. It can be calculated with a volume integral approach as Finazzi and Ciccacci (2012)

$$\hat{A}_w = C_{\rm LF}\int_{V_{\rm p}} d\mathbf{r}'\ \hat{\mathbf{A}}_{\rm pt}(\mathbf{r}',\omega_w)\cdot\mathbf{q}_w(\mathbf{r}'), \tag{16}$$

where $\mathbf{q}_w(\mathbf{r})$ is the eigenvector of a plasmon mode w which has to fulfill the normalization condition (Yu et al., 2017)

$$\int_{V_p} d\mathbf{r}\int_{V_p} d\mathbf{r}'\mathbf{q}_w(\mathbf{r})\cdot\mathbf{q}_{w'}(\mathbf{r}') = \delta_{w,w'}. \tag{17}$$

$C_{\rm LF}$ is a local field correction factor which accounts for the difference between the microscopic light field that couples to the plasmonic mode $\mathbf{q}_w(\mathbf{r})$ and the incident macroscopic light field $\hat{\mathbf{A}}_{\rm pt}$ (Onsager, 1936; de Vries and Lagendijk, 1998; Dolgaleva and Boyd, 2012). For a single nanoparticle it is given by

$$C_{\rm LF} = \frac{\epsilon_m\omega_w^2}{L\omega_p^2}, \tag{18}$$

where L is a depolarization factor that accounts for the shape of the nanoparticle, $\omega_p = \sqrt{\mathcal{N}e^2/\epsilon_0 m}$ is the plasma frequency of the metal and ϵ_m is the dielectric constant of the surrounding medium; see **Appendix** for details. We note that this correction factor was not included in Mueller et al. (2016) which lead to an overestimation of the SERS enhancement calculated from the coupling matrix elements.

To derive an explicit expression for the photon-plasmon interaction Hamiltonian, we express the vector potential of the light field with second quantization as Ho and Kumar (1993); Loudon (2000)

$$\hat{\mathbf{A}}_{\rm pt}(\mathbf{r},\omega_{\rm pt}) = \tilde{A}_{\rm pt}\boldsymbol{\varepsilon}_{\rm pt}\left(\hat{a}_{\rm pt}e^{i\mathbf{k}_{\rm pt}\cdot\mathbf{r}} + \hat{a}_{\rm pt}^\dagger e^{-i\mathbf{k}_{\rm pt}\cdot\mathbf{r}}\right), \tag{19}$$

where we considered for simplicity only one wavevector $\mathbf{k}_{\rm pt}$ and polarization $\boldsymbol{\varepsilon}_{\rm pt}$. The amplitude of the light field is $\tilde{A}_{\rm pt} = \sqrt{\hbar/2\omega_{\rm pt}V_{\rm R}\epsilon_0\epsilon_{\rm m}}$ with a normalization volume $V_{\rm R}$ and the frequency of the light field $\omega_{\rm pt}$. By using Equations (15), (12), (16), and (19) and dropping the counter-rotating terms the interaction Hamiltonian is given by

$$\hat{\mathcal{H}}_{\rm pl-pt} = ie\hbar\sqrt{\frac{\mathcal{N}V_{\rm p}}{4mV_{\rm R}\epsilon_0\epsilon_m}}\sum_w\left(\varepsilon_w^{\rm pt}\hat{a}_{\rm pt}\hat{b}_w^\dagger - (\varepsilon_w^{\rm pt})^*\hat{a}_{\rm pt}^\dagger\hat{b}_w\right), \tag{20}$$

where

$$\varepsilon_w^{\rm pt} = C_{\rm LF}\int_{V_{\rm p}} d\mathbf{r}'\boldsymbol{\varepsilon}_{\rm pt}\cdot\mathbf{q}_w(\mathbf{r}')e^{i\mathbf{k}_{\rm pt}\cdot\mathbf{r}'} \tag{21}$$

is a factor that gives the selection rules for the interaction of light with plasmonic modes w.

To discuss the applicability of the interaction Hamiltonian in Equation (20) we will first calculate the optical absorption cross section of plasmonic nanoparticles and draw a comparison to experimental data.

The absorption of a plasmon mode with frequency $\omega_{\rm pl}$ and spectral width $2\gamma_{\rm pl}$ is given by the cross section

$$\sigma_{\rm abs}(\omega_{\rm L}) = \frac{2V_{\rm R}\sqrt{\epsilon_m}}{cn_{\rm pt}\hbar^2}|\mathcal{M}_{\rm pl-pt}|^2\frac{\gamma_{\rm pl}}{(\omega_{\rm L}-\omega_{\rm pl})^2+\gamma_{\rm pl}^2}, \tag{22}$$

with the coupling matrix element

$$\mathcal{M}_{\rm pl-pt} = \langle 1_{\rm pl}, n_{\rm pt}-1|\mathcal{H}_{\rm pl-pt}|0_{\rm pl}, n_{\rm pt}\rangle. \tag{23}$$

The absorption cross section is obtained by dividing the plasmon excitation rate (Fermi Golden Rule)

$$\Gamma_{\rm pl} = \frac{2}{\hbar^2}|\mathcal{M}_{\rm pl-pt}|^2\frac{\gamma_{\rm pl}}{(\omega_{\rm L}-\omega_{\rm pl})^2+\gamma_{\rm pl}^2} \tag{24}$$

by the photon flux of the incident light field $|\langle n_{\rm pt}|\hat{\mathbf{S}}|n_{\rm pt}\rangle| = n_{\rm pt}c/V_{\rm R}\sqrt{\epsilon_m}$, where $\hat{\mathbf{S}}$ is the Poynting vector. We assumed a Lorentzian line shape of the plasmon resonance as in the SERS scattering amplitudes in Equations (1)–(3).

The plasmonic properties of small nanoparticles are well described by the point dipole approximation and the plasmon eigenvector of a dipole mode is given by

$$\mathbf{q}_{\rm pl}(\mathbf{r}) = \boldsymbol{\varepsilon}_{\rm pl}\delta(\mathbf{r}-\mathbf{r}_{\rm pl}), \tag{25}$$

where $\boldsymbol{\varepsilon}_{\rm pl}$ is the polarization and $\mathbf{r}_{\rm pl}$ is the position of the particle center. For larger nanoparticles the eigenvectors may be calculated with Mie theory as we demonstrated in Mueller et al.

(2016). Using Equations (18) and (20)–(25) the absorption cross section of a plasmonic nanoparticle can be expressed as

$$\sigma_{\mathrm{abs}}(\omega_{\mathrm{L}}) = \frac{\epsilon_m^{3/2} V_{\mathrm{p}} \omega_{\mathrm{pl}}^4}{2cL^2\omega_p^2} \frac{\gamma_{\mathrm{pl}}}{(\omega_{\mathrm{L}} - \omega_{\mathrm{pl}})^2 + \gamma_{\mathrm{pl}}^2}. \tag{26}$$

The absorption cross section as a function of energy can be measured with optical modulation spectroscopy (Crut et al., 2014). In **Figure 3** we compare the absorption cross section from Equation (26) with experimental data for spherical silver and gold nanoparticles and a gold nanorod from Lombardi et al. (2012), Billaud et al. (2007), and Muskens et al. (2006). By using ω_{pl} and γ_{pl} as fitting parameters and the particle volume V_{p} measured in experiments we obtain perfect agreement with the magnitude and energy dependence of the experimental cross sections. In the case of the gold nanosphere the theory underestimates the cross section for energies larger than 2.5 eV. The asymmetry in the excitation energy dependence appears because of interband transitions which is not captured by the Lorentzian line profile in Equation (26). On the other hand, the excellent agreement of the magnitudes shows that the local field correction factor in Equation (18) correctly accounts for the optical properties of gold and silver at the energies $\hbar\omega_{\mathrm{pl}}$ of the localized surface plasmon resonances. The plasmon-photon interaction Hamiltonian in Equation (20) therefore gives the correct oscillator strength and will be used below to calculate the SERS enhancement for a molecule close to a plasmonic nanoparticle.

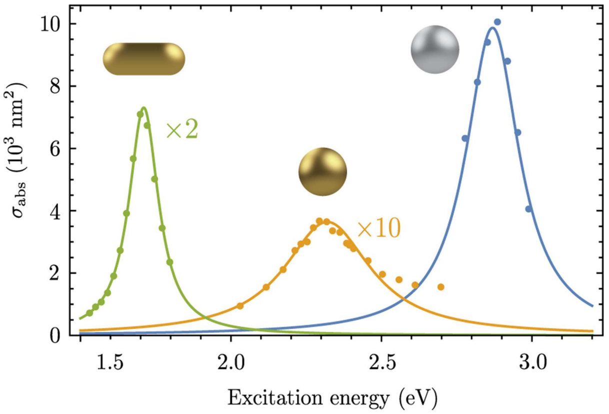

FIGURE 3 | Experimental and calculated (Equation 26) optical absorption cross sections for a gold nanorod (green, Lombardi et al., 2012), a gold nanosphere (orange, Billaud et al., 2007) and a silver nanosphere (blue, Muskens et al., 2006). The nanoparticle volume V_{p} was taken from the experimental works. The following parameters were used to reproduce the experimental spectra: $\hbar\omega_{\mathrm{pl}} = 1.71$ eV, $\hbar\gamma_{\mathrm{pl}} = 60$ meV, $\epsilon_m = 2.02$ and $L = 0.12$ for the Au nanorod; $\hbar\omega_{\mathrm{pl}} = 2.32$ eV, $\hbar\gamma_{\mathrm{pl}} = 175$ meV, $\epsilon_m = 1.96$ and $L = 1/3$ for the Au nanosphere; $\hbar\omega_{\mathrm{pl}} = 2.87$ eV, $\hbar\gamma_{\mathrm{pl}} = 108$ meV, $\epsilon_m = 2.31$ and $L = 1/3$ for the Ag nanosphere.

3.3. Plasmon-Molecule Interaction

We consider the coupling of the plasmonic nanostructure to a molecule with vibronic states as illustrated in **Figure 1A**. We assume that the interaction is of dipolar nature and use the interaction Hamiltonian (Waks and Sridharan, 2010)

$$\hat{\mathcal{H}}_{\mathrm{pl-vib}} = -\hat{\boldsymbol{\mu}} \cdot \hat{\mathbf{E}}_{\mathrm{LSP}}(\mathbf{r}), \tag{27}$$

where $\hat{\mathbf{E}}_{\mathrm{LSP}}(\mathbf{r})$ is the electric field generated by the plasmonic nanostructure and

$$\hat{\boldsymbol{\mu}} = \sum_{m,n} \boldsymbol{\mu}_{mn} |n\rangle\langle m| \tag{28}$$

is a generic transition operator for the dipole transitions of the molecule. The matrix element $\boldsymbol{\mu}_{mn}$ gives the transition probability from a vibronic state $|m\rangle$ to a state $|n\rangle$. The point dipole approximation for the molecule is justified as long as the plasmonic near field $\hat{\mathbf{E}}_{\mathrm{LSP}}(\mathbf{r})$ is approximately constant over the size of the molecule, which is a good approximation for metal-molecule distances much larger than the size of the molecule. For smaller distances, surface roughness and atomic scale protrusions of the metallic nanostructure become important which can be modeled by including field-dependent terms to the permanent molecular dipole in Equation (28) or by a quantum-mechanical modeling of the molecular states (Ayars et al., 2000; Jensen et al., 2008; Neuman et al., 2018).

We calculate the electric near field $\mathbf{E}_{\mathrm{LSP}}(\mathbf{r}) = -\nabla_{\mathbf{r}}\phi_{\mathrm{pl}}(\mathbf{r})$ of the plasmonic nanostructure within the electrostatic approximation as the gradient of the scalar potential

$$\phi_{\mathrm{pl}}(\mathbf{r}) = -\frac{1}{\epsilon_0\epsilon_m} \int_{V_{\mathrm{p}}} \mathrm{d}\mathbf{r}' \rho(\mathbf{r}') G_0(\mathbf{r}, \mathbf{r}'). \tag{29}$$

$G_0(\mathbf{r}, \mathbf{r}')$ is a Green function that gives the field distribution outside the plasmonic nanoparticle and $\rho(\mathbf{r})$ is the electric charge density (Novotny and Hecht, 2012). In order to obtain a quantized expression for the plasmonic near field we express the charge density $\rho(\mathbf{r}) = -\mathcal{N}eC_{\mathrm{LF}}\nabla_{\mathbf{r}} \cdot \mathbf{s}(\mathbf{r})$ in terms of a microscopic displacement $\mathbf{s}(\mathbf{r})$ of the charges inside the nanoparticle. It was shown in Finazzi and Ciccacci (2012) that a projection of the charge displacement onto the plasmonic eigenvectors can be substituted by the generalized position operator as

$$\int_{V_{\mathrm{p}}} \mathrm{d}\mathbf{r}' \, \mathbf{s}(\mathbf{r}') \cdot \mathbf{q}_w(\mathbf{r}') \rightarrow \hat{\Psi}_w. \tag{30}$$

By using the normalization condition for the plasmonic eigenvectors in Equation (17), the plasmonic near field can be written as

$$\hat{\mathbf{E}}_w(\mathbf{r}) = -\frac{\mathcal{N}eV_p}{\epsilon_0\epsilon_m} \hat{\Psi}_w \mathbf{G}_w(\mathbf{r}), \tag{31}$$

with

$$\mathbf{G}_w(\mathbf{r}) = C_{\mathrm{LF}}\nabla_{\mathbf{r}} \int_{V_{\mathrm{p}}} \mathrm{d}\mathbf{r}' \mathbf{q}_w(\mathbf{r}') \cdot \nabla_{\mathbf{r}'} G_0(\mathbf{r}, \mathbf{r}'). \tag{32}$$

The position dependence and polarization of the plasmonic near field is entirely contained in $\mathbf{G}_w(\mathbf{r})$ and $\hat{\Psi}_w$ contains plasmonic creation and annihilation operators; see Equation (11). Based on Equations (27) and (31) we obtain

$$\mathcal{H}_{\text{pl}-\text{vib}} = \sum_{w} \frac{e}{\epsilon_0 \epsilon_m} \sqrt{\frac{\hbar \mathcal{N} V_p}{2 m \omega_w}} (\hat{b}_w^{\dagger} + \hat{b}_w) \hat{\boldsymbol{\mu}} \cdot \mathbf{G}_w(\mathbf{r}) \qquad (33)$$

for the plasmon-molecule interaction Hamiltonian.

Finally we also consider the direct coupling of the incident light to the molecular transition dipole, which is described by the interaction Hamiltonian $\hat{\mathcal{H}}_{\text{pt}-\text{vib}} = -\hat{\boldsymbol{\mu}} \cdot \hat{\mathbf{E}}_{\text{pt}}(\mathbf{r})$. From Equation (19) and $\hat{\mathbf{E}}_{\text{pt}}(\mathbf{r}) = -\partial \hat{\mathbf{A}}_{\text{pt}}(\mathbf{r})/\partial t$ we obtain the explicit expression

$$\hat{\mathcal{H}}_{\text{pt}-\text{vib}} = -\mathrm{i} \sqrt{\frac{\hbar \omega_{\text{pt}}}{2 V_{\text{R}} \epsilon_0 \epsilon_{\text{m}}}} \hat{\boldsymbol{\mu}} \cdot \boldsymbol{\varepsilon}_{\text{pt}} \left(\hat{a}_{\text{pt}} \mathrm{e}^{\mathrm{i}\mathbf{k}_{\text{pt}} \cdot \mathbf{r}} - \hat{a}_{\text{pt}}^{\dagger} \mathrm{e}^{-\mathrm{i}\mathbf{k}_{\text{pt}} \cdot \mathbf{r}} \right). \qquad (34)$$

4. SERS ENHANCEMENT BY A SILVER NANOSPHERE

In order to discuss the magnitude and excitation energy dependence of the plasmonic enhancement we calculate the enhancement of the SERS cross section for a molecule next to a silver nanoparticle. We consider a SERS experiment in which the same molecule is used as SERS analyte and reference and the molecular resonance is not perturbed by the metal surface; see e.g., Mueller et al. (2017b). In this case the SERS enhancement is given by the plasmonic enhancement factor in Equation (7). From the analytic expressions for the interaction Hamiltonians above we calculate the coupling factors as.

$$\tilde{\mathcal{M}}_1 = \tilde{\mathcal{M}}_2 = -\frac{\hbar \omega_p^2 V_{\text{p}}}{2 \epsilon_m \omega_{\text{pl}}} \varepsilon_{\text{pl}}^{\text{pt}} \frac{\mathbf{e}_{\text{mol}} \cdot \mathbf{G}_{\text{pl}}(\mathbf{r})}{\mathbf{e}_{\text{mol}} \cdot \boldsymbol{\varepsilon}_{\text{pt}}}, \qquad (35)$$

where "pl" refers to the dipolar plasmon resonance of the silver nanoparticle. $\mathbf{e}_{\text{mol}}$ is a unit vector along the transition dipole of the molecule. The coupling factors $\tilde{\mathcal{M}}_1$ and $\tilde{\mathcal{M}}_2$ are only equal for a Raman process where $\boldsymbol{\mu}_{gi} \parallel \boldsymbol{\mu}_{if}$. For the more general case of a Raman tensor with off-diagonal elements $\mathbf{e}_{\text{mol}}$ may differ in $\tilde{\mathcal{M}}_1$ and $\tilde{\mathcal{M}}_2$.

In the following, we consider the spherical silver nanoparticle for which we calculated the absorption cross section in **Figure 3** with radius $r_{\text{NP}} = 15.5$ nm. As this nanoparticle is small compared to the wavelength of the incident light (350–500 nm), we calculate the plasmonic eigenvector of the dipole mode with the point dipole approximation; see Equation (25). That way we obtain $\varepsilon_{\text{pl}}^{\text{pt}} = C_{\text{LF}}$ and

$$\mathbf{G}_{\text{pl}}(\mathbf{r}) = \frac{C_{\text{LF}}}{4\pi |\mathbf{r}|^3} \left(3 \frac{(\boldsymbol{\varepsilon}_{\text{pt}} \cdot \mathbf{r})\mathbf{r}}{|\mathbf{r}|^2} - \boldsymbol{\varepsilon}_{\text{pt}} \right). \qquad (36)$$

The coupling factors $\tilde{\mathcal{M}}_1$ and $\tilde{\mathcal{M}}_2$ are, within the approximations made here, real valued quantities and take negative values for the places of strongest field enhancement. This nicely agrees with the assumptions that were made to explain the experimental SERS resonance profiles in **Figure 2**.

In **Figure 4** we calculate the plasmonic SERS enhancement for a molecule close to the silver nanoparticle. We assume a molecular transition dipole parallel to the polarization of the incident light field and to the plasmonic near field. This configuration leads to the largest enhancement. The excitation energy dependence of the SERS enhancement is plotted in **Figure 4** for different distances of the molecule to the silver nanoparticle. We consider a Raman shift of $\hbar\omega_{\text{vib}} = 0.3$ eV which is larger than the spectral width $2\gamma_{\text{pl}} \approx 0.2$ eV of the plasmon resonance. In this case the incoming and outgoing Raman resonances are visible as distinct and overlapping peaks in the SERS enhancement. When the molecular dipole is placed on the surface of the silver nanoparticle the Raman cross section is enhanced by a factor of 2×10^4 (**Figure 4A**, $d = 0$, solid line). The incoming and outgoing plasmonic Raman resonances provide almost the same enhancement with a slight dominance of the incoming Raman resonance. The resonance profile looks strikingly different when the molecule is moved away from the metal surface. When the metal-molecule distance equals the nanoparticle radius ($d = r_{\text{NP}}$) the enhancement occurs only at the incoming plasmonic Raman resonance with a factor of $\sim$20 while the outgoing plasmonic Raman resonance is entirely missing. For an even larger distance of $d = 2r_{\text{NP}}$ the incoming and outgoing resonances obtain a Fano-like profile and only the incoming resonance provides a modest enhancement of 2.8. In the following we refer to these three cases as the regimes of strong, intermediate and weak plasmonic enhancement.

The difference in enhancement at the incoming and outgoing plasmonic Raman resonances occurs because of interference between the scattering channels that are illustrated as Feynman diagrams in **Figures 1B,C** (i)–(iii). These scattering processes have the same final state, i.e., a molecular vibration ω_f^{vib} is excited and the Raman-scattered light $\omega_{\text{L}} - \omega_f^{\text{vib}}$ is emitted. The corresponding Raman amplitudes are therefore summed in Equation (6) before calculating the absolute square and the different terms can add constructively or destructively. When only considering the process in **Figure 1B**, where the incoming- and the Raman-scattered light couple to the plasmon, both Raman resonances provide the same enhancement (dashed lines in **Figure 4A**). This process is the dominant contribution in the regime of strong plasmonic enhancement, i.e., for $d \approx r_{\text{NP}}$. In the intermediate enhancement regime the scattering processes in **Figure 1C** (i) and (ii), where the plasmon resonance enhances either the incoming or the Raman-scattered light, have to be taken into account to explain the SERS resonance profile. The Raman amplitudes of the different scattering processes add constructively at the incoming plasmonic Raman resonance and cancel each other at the outgoing plasmonic Raman resonance. In the weak enhancement regime the Raman process without plasmonic enhancement (**Figure 1C** (iii)] becomes important as the enhancement is close to one.

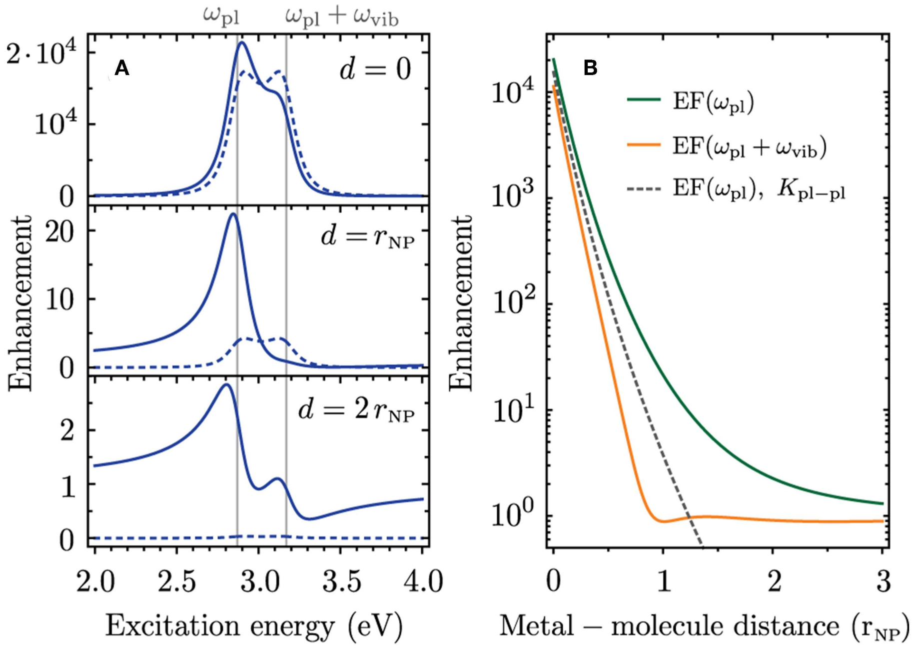

FIGURE 4 | Plasmonic enhancement of the Raman cross section for a molecule close to a silver nanoparticle with properties similar to those in **Figure 3**, i.e., an Ag nanosphere with radius $r_{\rm NP}=15.5$ nm, $\hbar\omega_{\rm pl}=2.87$ eV, $\hbar\gamma_{\rm pl}=108$ meV and $\epsilon_{\rm m}=2.31$. We place the Ag nanosphere center at the origin, consider $\boldsymbol{\varepsilon}_{\rm pl},\mathbf{e}_{\rm mol}\parallel x$ and move the molecule along the x axis. **(A)** Excitation energy dependence of the enhancement for three distances d of the molecule to the metal surface. **(B)** Enhancement at $\omega_{\rm pl}$ (incoming plasmonic Raman resonance, green) and $\omega_{\rm pl}+\omega_{\rm vib}$ (outgoing plasmonic Raman resonance, orange) as a function of metal-molecule distance. Dashed lines show the enhancement when only $K_{\rm pl-pl}$ is used to calculate the enhancement factor.

The contribution from the process in **Figure 1B** is negligible in this case.

In **Figure 4B** we plot the enhancement at the energies of the incoming and Raman-scattered light as a function of metal-molecule distance. The enhancement from the scattering process in **Figure 1B** is plotted as a dashed line for comparison. A constructive interference at the incoming plasmonic Raman resonance and destructive interference at the outgoing plasmonic Raman resonance occurs for all metal-molecule distances. The difference in enhancement is largest around $d=2r_{\rm NP}$. More generally the effect of interference between different scattering channels is most pronounced when $\tilde{\mathcal{M}}_1=\tilde{\mathcal{M}}_2=-\hbar\,\omega_{\rm vib}$, which corresponds to the intermediate enhancement regime with enhancement factors of 10^1-10^2. The effect is clearly irrelevant for single-molecule SERS which requires enhancement factors on the order of 10^7-10^9 (Ru and Etchegoin, 2009). On the other hand, the intermediate enhancement regime becomes important when a spatially extended film of molecules or a two-dimensional material is coupled to a plasmonic nanostructure (McFarland et al., 2005; Heeg et al., 2013). Furthermore, the enhancement factors in tip-enhanced Raman scattering (TERS) are typically in the intermediate enhancement regime (Beams et al., 2014; Wang et al., 2017). The constructive interference between different scattering pathways can strongly increase the enhancement at a specific excitation energy making TERS sensitive to near-field coupling.

5. COMPARISON TO THEORY OF ELECTROMAGNETIC ENHANCEMENT

The plasmonic enhancement in SERS is commonly estimated by a theory that treats that plasmonic nanostructure as a nanoscale antenna which increases the local light intensity (Ru and Etchegoin, 2009; Ding et al., 2017). The enhancement of the Raman intensity for a molecule at position **r** is given by

$$\mathrm{EF}_{\rm EM}(\mathbf{r},\omega)=\frac{|\mathbf{E}_{\rm loc}(\mathbf{r},\omega)|^2}{|\mathbf{E}_0(\mathbf{r},\omega)|^2}\frac{|\mathbf{E}_{\rm loc}(\mathbf{r},\omega-\omega_{\rm vib})|^2}{|\mathbf{E}_0(\mathbf{r},\omega-\omega_{\rm vib})|^2}, \tag{37}$$

where $\mathbf{E}_{\rm loc}$ is the local electric field amplitude and $\mathbf{E}_0$ the amplitude of the incoming light field without enhancement. This theory of electromagnetic (EM) enhancement is a powerful tool for the design of plasmonic nanostructures with strong SERS enhancement (Ding et al., 2017). The local electric field enhancement can be calculated for complicated nanostructure geometries with numerical techniques (Solís et al., 2014). On the other hand, a precise knowledge of the nanostructure geometry is required to interpret the outcome of a SERS experiment and molecular resonances are not included in the enhancement factor. Our approach benefits from microscopic insight into the scattering processes underlying SERS and can be used to extract the spectral properties of the plasmonic and molecular resonances from SERS profiles. In the following we will show that both theories predict the same plasmonic enhancement and the

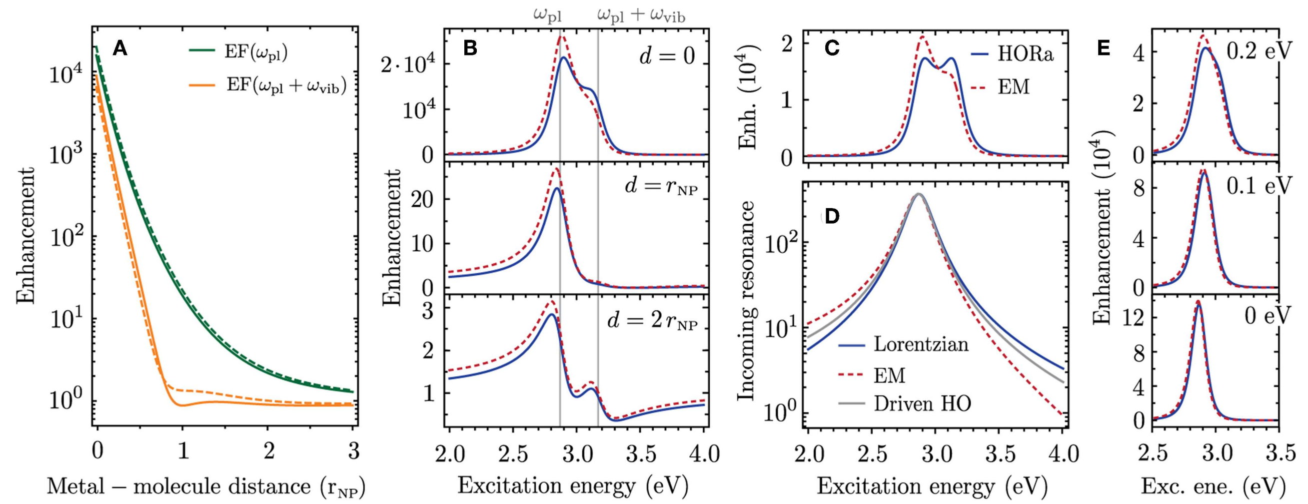

FIGURE 5 | Comparison of enhancement factors from higher-order Raman approach (HORa, solid lines) and electromagnetic enhancement theory (EM, dashed lines). The parameters are the same as in **Figure 4**. **(A)** Enhancement at the incoming- and outgoing plasmonic Raman resonance as a function of metal-molecule distance. **(B)** Excitation energy dependence of the enhancement for three metal-molecule distances. **(C)** Enhancement for $d = 0$ when only considering the scattering process where the incoming- and Raman-scattered light couples to the plasmon. **(D)** Enhancement provided by the incoming plasmonic Raman resonance for a Lorentzian line profile as in the HORa approach (blue solid line), for the EM enhancement theory (red dashed line) and for the resonance of a driven harmonic oscillator (gray solid line). **(E)** Enhancement profiles for different Raman shifts given in the insets.

enhancement factor in Equation (37) can be rewritten into an expression that is formally equivalent to Equation (7).

An important aspect that is disregarded when writing the electromagnetic enhancement factor as in Equation (37) is that only the electric field component along the molecular transition dipole contributes to the enhancement. We therefore project the local electric field vectors onto the transition dipoles $\boldsymbol{\mu}_{gi}$ and $\boldsymbol{\mu}_{if}$ that are relevant for the Raman process (see **Figure 1A**). By expressing the local electric field $\mathbf{E}_{\mathrm{loc}}$ as the sum of the plasmonic near field $\mathbf{E}_{\mathrm{pl}}$ and the incident light field $\mathbf{E}_0$ we obtain

$$\mathrm{EF}_{\mathrm{EM}}(\mathbf{r},\omega) = |1 + f_{\mathrm{in}}(\mathbf{r},\omega)|^2 |1 + f_{\mathrm{out}}(\mathbf{r},\omega)|^2, \tag{38}$$

with

$$f_{\mathrm{in}}(\mathbf{r},\omega) = \frac{\boldsymbol{\mu}_{gi} \cdot \mathbf{E}_{\mathrm{pl}}(\mathbf{r},\omega)}{\boldsymbol{\mu}_{gi} \cdot \mathbf{E}_0(\mathbf{r},\omega)} \tag{39}$$

and

$$f_{\mathrm{out}}(\mathbf{r},\omega) = \frac{\boldsymbol{\mu}_{if} \cdot \mathbf{E}_{\mathrm{pl}}(\mathbf{r},\omega - \omega_{\mathrm{vib}})}{\boldsymbol{\mu}_{if} \cdot \mathbf{E}_0(\mathbf{r},\omega - \omega_{\mathrm{vib}})}. \tag{40}$$

This enhancement factor can be rewritten as

$$\mathrm{EF}_{\mathrm{EM}}(\mathbf{r},\omega) = |f_{\mathrm{in}}(\mathbf{r},\omega) f_{\mathrm{out}}(\mathbf{r},\omega) + f_{\mathrm{in}}(\mathbf{r},\omega) + f_{\mathrm{out}}(\mathbf{r},\omega) + 1|^2, \tag{41}$$

which is formally equivalent with the plasmonic enhancement factor from our microscopic approach in Equation (7). The four terms can be identified with the scattering processes in **Figures 1B,C** (i)–(iii).

In order to compare the enhancement predicted by the two theories we repeat the model calculations in **Figure 4** based on the enhancement factor in Equation (41). Within the quasi-static approximation the plasmonic near field of the silver nanoparticle is

$$\mathbf{E}_{\mathrm{pl}}(\mathbf{r},\omega) = \frac{1}{4\pi\epsilon_0|\mathbf{r}|^3}\left(3\frac{(\mathbf{p}_{\mathrm{pl}}(\mathbf{r},\omega)\cdot\mathbf{r})\mathbf{r}}{|\mathbf{r}|^2} - \mathbf{p}_{\mathrm{pl}}(\mathbf{r},\omega)\right), \tag{42}$$

with the plasmonic dipole moment

$$\mathbf{p}_{\mathrm{pl}}(\mathbf{r},\omega) = \alpha(\omega) E_0 \boldsymbol{\varepsilon}_{\mathrm{pt}} \delta(\mathbf{r}), \tag{43}$$

and the polarizability of the nanosphere

$$\alpha(\omega) = 4\pi\epsilon_0\epsilon_{\mathrm{m}} r_{\mathrm{NP}}^3 \frac{\epsilon_{\mathrm{Ag}}(\omega) - \epsilon_{\mathrm{m}}}{\epsilon_{\mathrm{Ag}}(\omega) + 2\epsilon_{\mathrm{m}}}. \tag{44}$$

We use a Drude model for the dielectric function of silver $\epsilon_{\mathrm{Ag}}(\omega)$ from Yang et al. (2015) and include a phenomenological surface broadening term to reproduce the experimentally determined spectral width of the plasmon resonance (see Muskens et al., 2006). In **Figure 5A** we compare the enhancement factors at the incoming and outgoing plasmonic Raman resonances as a function of metal-molecule distance. There is good agreement of the enhancement predicted by our microscopic approach (HORa, solid lines) and the electromagnetic enhancement model (EM, dashed lines). The weaker enhancement at the outgoing resonance is also predicted by the electromagnetic enhancement factor. When calculating the resonance profiles for different metal-molecule distances we obtain overall good agreement between both theories for all enhancement regimes (**Figure 5B**).

Upon a closer look it appears that the difference in enhancement at the incoming and outgoing plasmonic Raman resonances is even more pronounced for the EM enhancement model. To explain this small discrepancy we calculate the enhancement profiles for the case when only the scattering process in **Figure 1B** is considered; see **Figure 5C**. While the HORa theory predicts in this case two overlapping Raman resonances of equal intensity, the enhancement profile from the EM enhancement theory remains asymmetric. This asymmetry cannot be explained by interference between different scattering channels but is attributed to an intrinsic asymmetry of the plasmon resonance; see **Figure 5D**. It is only visible on a logarithmic scale and negligible in the absorption spectra in **Figure 3**. However, when multiplying two resonances that are spectrally displaced by the Raman shift, as is the case in **Figure 5C**, the asymmetry becomes important.

As our microscopic model is based on higher-order perturbation theory the plasmonic and molecular resonances have a symmetric Lorentzian line profile (blue line in **Figure 5D**). The asymmetry of the plasmonic resonance from the EM model arises for two reasons. First, when considering the localized surface plasmon as a driven and damped harmonic oscillator the Lorentzian energy denominators in Equation (7) have to be replaced by Zuloaga and Nordlander (2011)

$$\frac{1}{\omega-\omega_{\mathrm{pl}}+\mathrm{i}\gamma_{\mathrm{pl}}} \rightarrow \frac{2\omega_{\mathrm{pl}}}{\omega^2-\omega_{\mathrm{pl}}^2+2\mathrm{i}\gamma_{\mathrm{pl}}\omega}, \tag{45}$$

which leads to a slight asymmetry of the plasmon resonance (gray line in **Figure 5D**). Second, the depolarization by the bound electrons which we modeled with a local field correction factor C_{LF} is wavelength dependent and increases toward shorter wavelength. In this work we derived an analytic expression that is strictly only valid at the plasmon resonance [Equation (18)]. How to incorporate the wavelength dependent damping and depolarization when quantizing a localized surface plasmon oscillation is a matter of ongoing research and will be key to fully capture the energy dependence of the SERS enhancement. On the other hand, the differences in the enhancement profiles from EM and HORa only occur when the Raman shift is larger than the spectral width of the plasmon. For smaller Raman shifts the incoming and outgoing plasmonic Raman resonances cannot be spectrally resolved and there is excellent agreement between the enhancement profiles from both theories (**Figure 5E**).

6. CONCLUSIONS

In conclusion we presented a microscopic model of the plasmonic enhancement mechanism in SERS which is based on perturbation theory. The main idea of our approach is to treat the plasmonic excitation as an integral part of the Raman scattering process. This leads to a description of SERS as higher-order Raman scattering. We derived analytic expressions for the Raman scattering amplitudes that can be used to study the interplay of plasmonic and molecular resonances or the interference between different scattering channels. As the properties of the plasmonic and molecular resonances, such as frequency, spectral width and oscillator strength, appear as explicit parameters in the theoretical framework, it can be used for the interpretation of experimental data.

Based on a quantization of the localized surface plasmon we derived analytic expressions for all coupling matrix elements that describe the oscillator strength of the material excitations and lead to selection rules for SERS. We demonstrated that a local field correction factor must be included in the quantization model of the plasmon in order to reproduce the experimental absorption cross sections of plasmonic nanoparticles. This was not considered in our previous work (Mueller et al., 2016) and lead to an overestimation of the SERS enhancement factor. With model calculations for a molecule close to a silver nanoparticle we showed that interference between different scattering channels can strongly affect the excitation energy dependence of the SERS enhancement. This effect is most relevant in the intermediate enhancement regime with enhancement factors of $10-10^3$ and is therefore particularly important when plasmonic nanostructures are coupled to spatially extended materials. We showed that the plasmonic enhancement obtained from our microscopic approach is overall in good agreement with that predicted by the commonly used theory of EM enhancement. While the EM enhancement theory is a powerful tool to design SERS substrates with strong plasmonic enhancement our approach gives microscopic insight, serves well in fitting experimental data, and can be used to study the interplay of different scattering channels underlying SERS.

DATA AVAILABILITY

All datasets generated for this study are included in the manuscript and/or the supplementary files.

AUTHOR CONTRIBUTIONS

Both authors contributed in multiple ways to the research presented in this manuscript.

ACKNOWLEDGMENTS

This work was supported by the European Research Council under grant DarkSERS (772108). NM acknowledges Deutsche Telekom Stiftung for financial support. We acknowledge support by the Open Access Publication Initiative of Freie Universität Berlin.

REFERENCES

Ausman, L., and Schatz, G. (2012). "Dipole re-radiation effects in surface enhanced raman scattering," in *The Mie Theory, volume 169 of* Springer Series in Optical Sciences, eds W. Hergert and T. Wriedt (Berlin; Heidelberg: Springer), 135–155.

Ausman, L. K., and Schatz, G. C. (2009). On the importance of incorporating dipole reradiation in the modeling of surface enhanced raman scattering from spheres. *J. Chem. Phys.* 131:084708. doi: 10.1063/1.3211969

Ayars, E. J., Hallen, H. D., and Jahncke, C. L. (2000). Electric field gradient effects in raman spectroscopy. *Phys. Rev. Lett.* 85, 4180–4183. doi: 10.1103/PhysRevLett.85.4180

Beams, R., Cançado, L. G., Oh, S.-H., Jorio, A., and Novotny, L. (2014). Spatial coherence in near-field raman scattering. *Phys. Rev. Lett.* 113:186101. doi: 10.1103/PhysRevLett.113.186101

Billaud, P., Huntzinger, J.-R., Cottancin, E., Lermé, J., Pellarin, M., Arnaud, L., et al. (2007). Optical extinction spectroscopy of single silver nanoparticles. *Eur. Phys. J. D* 43, 271–274. doi: 10.1140/epjd/e2007-00112-y

Bohren, C., and Huffman, D. R. (1998). *Absorption and Scattering of Light by Small Particles*. Weinheim: Wiley Science Paperback Series. doi: 10.1002/9783527618156

Brandstetter-Kunc, A., Weick, G., Downing, C. A., Weinmann, D., and Jalabert, R. A. (2016). Nonradiative limitations to plasmon propagation in chains of metallic nanoparticles. *Phys. Rev. B* 94:205432. doi: 10.1103/PhysRevB.94.205432

Brandstetter-Kunc, A., Weick, G., Weinmann, D., and Jalabert, R. A. (2015). Decay of dark and bright plasmonic modes in a metallic nanoparticle dimer. *Phys. Rev. B* 91:035431. doi: 10.1103/PhysRevB.91.035431

Crut, A., Maioli, P., Del Fatti, N., and Vallée, F. (2014). Optical absorption and scattering spectroscopies of single nano-objects. *Chem. Soc. Rev.* 43, 3921–3956. doi: 10.1039/c3cs60367a

Darby, B. L., Auguié, B., Meyer, M., Pantoja, A. E., and Le Ru, E. C. (2015). Modified optical absorption of molecules on metallic nanoparticles at sub-monolayer coverage. *Nat. Photon.* 10:40. doi: 10.1038/nphoton.2015.205

Davis, T. J., Gómez, D. E., and Vernon, K. C. (2010). Evanescent coupling between a raman-active molecule and surface plasmons in ensembles of metallic nanoparticles. *Phys. Rev. B* 82:205434. doi: 10.1103/PhysRevB.82.205434

de Vries, P., and Lagendijk, A. (1998). Resonant scattering and spontaneous emission in dielectrics: Microscopic derivation of local-field effects. *Phys. Rev. Lett.* 81, 1381–1384. doi: 10.1103/PhysRevLett.81.1381

Ding, S. Y., You, E. M., Tian, Z. Q., and Moskovits, M. (2017). Electromagnetic theories of surface-enhanced raman spectroscopy. *Chem. Soc. Rev.* 46, 4042–4076. doi: 10.1039/C7CS00238F

Dolgaleva, K., and Boyd, R. W. (2012). Local-field effects in nanostructured photonic materials. *Adv. Opt. Photon.* 4, 1–77. doi: 10.1364/AOP.4.000001

Finazzi, M., and Ciccacci, F. (2012). Plasmon-photon interaction in metal nanoparticles: second-quantization perturbative approach. *Phys. Rev. B* 86:035428. doi: 10.1103/PhysRevB.86.035428

Fleischmann, M., Hendra, P., and McQuillan, A. (1974). Raman spectra of pyridine adsorbed at a silver electrode. *Chem. Phys. Lett.* 26, 163–166. doi: 10.1016/0009-2614(74)85388-1

Galperin, M., Ratner, M. A., and Nitzan, A. (2009). Raman scattering in current-carrying molecular junctions. *J. Chem. Phys.* 130:144109. doi: 10.1063/1.3109900

Gerchikov, L. G., Guet, C., and Ipatov, A. N. (2002). Multiple plasmons and anharmonic effects in small metallic clusters. *Phys. Rev. A* 66:053202. doi: 10.1103/PhysRevA.66.053202

Heeg, S., Fernandez-Garcia, R., Oikonomou, A., Schedin, F., Narula, R., Maier, S. A., et al. (2013). Polarized plasmonic enhancement by au nanostructures probed through raman scattering of suspended graphene. *Nano Lett.* 13, 301–308. doi: 10.1021/nl3041542

Heeg, S., Oikonomou, A., Fernandez-Garcia, R., Lehmann, C., Maier, S. A., Vijayaraghavan, A., et al. (2014). Plasmon-enhanced raman scattering by carbon nanotubes optically coupled with near-field cavities. *Nano Lett.* 14, 1762–1768. doi: 10.1021/nl404229w

Ho, S.-T., and Kumar, P. (1993). Quantum optics in a dielectric: macroscopic electromagnetic-field and medium operators for a linear dispersive lossy medium—a microscopic derivation of the operators and their commutation relations. *J. Opt. Soc. Am. B* 10, 1620–1636. doi: 10.1364/JOSAB.10.001620

Hu, W., Duan, S., Zhang, G., Ma, Y., Tian, G., and Luo, Y. (2015). Quasi-analytical approach for modeling of surface-enhanced raman scattering. *J. Phys. Chem. C* 119, 28992–28998. doi: 10.1021/acs.jpcc.5b09793

Jensen, L., Aikens, C. M., and Schatz, G. C. (2008). Electronic structure methods for studying surface-enhanced raman scattering. *Chem. Soc. Rev.* 37, 1061–1073. doi: 10.1039/b706023h

Jorio, A., Mueller, N. S., and Reich, S. (2017). Symmetry-derived selection rules for plasmon-enhanced raman scattering. *Phys. Rev. B* 95:155409. doi: 10.1103/PhysRevB.95.155409

Kamandar Dezfouli, M., and Hughes, S. (2017). Quantum optics model of surface-enhanced raman spectroscopy for arbitrarily shaped plasmonic resonators. *ACS Photon.* 4, 1245–1256. doi: 10.1021/acsphotonics.7b00157

Kneipp, K., Wang, Y., Kneipp, H., Perelman, L. T., Itzkan, I., Dasari, R. R., et al. (1997). Single molecule detection using surface-enhanced raman scattering (sers). *Phys. Rev. Lett.* 78, 1667–1670. doi: 10.1103/PhysRevLett.78.1667

Lamowski, S., Mann, C.-R., Hellbach, F., Mariani, E., Weick, G., and Pauly, F. (2018). Plasmon polaritons in cubic lattices of spherical metallic nanoparticles. *Phys. Rev. B* 97:125409. doi: 10.1103/PhysRevB.97.125409

Le Ru, E. C., and Etchegoin, P. G. (2013). Quantifying sers enhancements. *MRS Bull.* 38, 631–640. doi: 10.1557/mrs.2013.158

Lombardi, A., Loumaigne, M., Crut, A., Maioli, P., Del Fatti, N., Vallée, F., et al. (2012). Surface plasmon resonance properties of single elongated nano-objects: gold nanobipyramids and nanorods. *Langmuir* 28, 9027–9033. doi: 10.1021/la300210h

Lombardi, J. R., and Birke, R. L. (2008). A unified approach to surface-enhanced raman spectroscopy. *J. Phys. Chem. C* 112, 5605–5617. doi: 10.1021/jp800167v

Long, D. A. (2002). *The Raman Effect: A Unified Theory of Raman Scattering by Molecules*. Weinheim: John Wiley & Sons, Ltd.

Loudon, R. (2000). *The Quantum Theory of Light, 3rd Edn*. Oxford: Oxford University Press.

Mack, D. L., Cortés, E., Giannini, V., Török, P., Roschuk, T., and Maier, S. A. (2017). Decoupling absorption and emission processes in super-resolution localization of emitters in a plasmonic hotspot. *Nat. Comm.* 8:14513. doi: 10.1038/ncomms14513

Martin, R. M., and Falicov, L. M. (1975). *Resonant Raman Scattering*. Berlin; Heidelberg: Springer.

McFarland, A. D., Young, M. A., Dieringer, J. A., and Van Duyne, R. P. (2005). Wavelength-scanned surface-enhanced raman excitation spectroscopy. *J. Phys. Chem. B* 109, 11279–11285. doi: 10.1021/jp050508u

Morton, S. M., and Jensen, L. (2009). Understanding the moleculesurface chemical coupling in sers. *J. Am. Chem. Soc.* 131, 4090–4098. doi: 10.1021/ja809143c

Moskovits, M. (2013). Persistent misconceptions regarding sers. *Phys. Chem. Chem. Phys.* 15, 5301–5311. doi: 10.1039/c2cp44030j

Mueller, N. S., Heeg, S., Alvarez, M. P., Kusch, P., Wasserroth, S., Clark, N., et al. (2017a). Evaluating arbitrary strain configurations and doping in graphene with raman spectroscopy. *2D Mater.* 5:015016. doi: 10.1088/2053-1583/aa90b3

Mueller, N. S., Heeg, S., Kusch, P., Gaufrés, E., Tang, N. Y., Hübner, U., et al. (2017b). Plasmonic enhancement of sers measured on molecules in carbon nanotubes. *Faraday Discuss.* 205, 85–103. doi: 10.1039/C7FD00127D

Mueller, N. S., Heeg, S., and Reich, S. (2016). Surface-enhanced raman scattering as a higher-order raman process. *Phys. Rev. A* 94:023813. doi: 10.1103/PhysRevA.94.023813

Muskens, O., Christofilos, D., Fatti, N. D., and Vallée, F. (2006). Optical response of a single noble metal nanoparticle. *J. Opt. A* 8, S264–S272. doi: 10.1088/1464-4258/8/4/S28

Neuman, T., Esteban, R., Casanova, D., Garcí-a-Vidal, F. J., and Aizpurua, J. (2018). Coupling of molecular emitters and plasmonic cavities beyond the point-dipole approximation. *Nano Lett.* 18, 2358–2364. doi: 10.1021/acs.nanolett.7b05297

Nie, S., and Emory, S. R. (1997). Probing single molecules and single nanoparticles by surface-enhanced raman scattering. *Science* 275, 1102–1106. doi: 10.1126/science.275.5303.1102

Novotny, L., and Hecht, B. (2012). *Principles of Nano-Optics, 2nd Edn*. Cambridge, UK: Cambridge University Press.

Onsager, L. (1936). Electric moments of molecules in liquids. *J. Am. Chem. Soc.* 58, 1486–1493. doi: 10.1021/ja01299a050

Osawa, M., Matsuda, N., Yoshii, K., and Uchida, I. (1994). Charge transfer resonance raman process in surface-enhanced raman scattering from p-aminothiophenol adsorbed on silver: Herzberg-teller contribution. *J. Phys. Chem.* 98, 12702–12707. doi: 10.1021/j100099a038

Pustovit, V. N., and Shahbazyan, T. V. (2006). Microscopic theory of surface-enhanced raman scattering in noble-metal nanoparticles. *Phys. Rev. B* 73:085408. doi: 10.1103/PhysRevB.73.085408

Raab, M., Vietz, C., Daniel Stefani, F., Pedro Acuna, G., and Tinnefeld, P. (2017). Shifting molecular localization by plasmonic coupling in a single-molecule mirage. *Nat. Comm.* 8:13966. doi: 10.1038/ncomms13966

Roelli, P., Galland, C., Piro, N., and Kippenberg, T. J. (2016). Molecular cavity optomechanics as a theory of plasmon-enhanced raman scattering. *Nat. Nanotechnol.* 11, 164–169. doi: 10.1038/nnano.2015.264

Ru, E. C. L., and Etchegoin, P. G. (2009). *Principles of Surface-Enhanced Raman Spectroscopy*. Amsterdam: Elsevier.

Schmidt, M. K., Esteban, R., González-Tudela, A., Giedke, G., and Aizpurua, J. (2016). Quantum mechanical description of raman scattering from molecules in plasmonic cavities. *ACS Nano* 10, 6291–6298. doi: 10.1021/acsnano.6b02484

Sevinc, P. C., Dhital, B., Govind Rao, V., Wang, Y., and Lu, H. P. (2016). Probing electric field effect on covalent interactions at a molecule-semiconductor interface. *J. Am. Chem. Soc.* 138, 1536–1542. doi: 10.1021/jacs.5b10253

Sharma, B., Frontiera, R. R., Henry, A.-I., Ringe, E., and Duyne, R. P. V. (2012). Sers: materials, applications, and the future. *Mater. Today* 15, 16–25. doi: 10.1016/S1369-7021(12)70017-2

Solís, D. M., Taboada, J. M., Obelleiro, F., Liz-Marzán, L. M., and García de Abajo, F. J. (2014). Toward ultimate nanoplasmonics modeling. *ACS Nano* 8, 7559–7570. doi: 10.1021/nn5037703

Waks, E., and Sridharan, D. (2010). Cavity qed treatment of interactions between a metal nanoparticle and a dipole emitter. *Phys. Rev. A* 82:043845. doi: 10.1103/PhysRevA.82.043845

Wang, X., Huang, S. C., Huang, T. X., Su, H. S., Zhong, J. H., Zeng, Z. C., et al. (2017). Tip-enhanced raman spectroscopy for surfaces and interfaces. *Chem. Soc. Rev.* 46, 4020–4041. doi: 10.1039/C7CS00206H

Wang, Y., Yan, B., and Chen, L. (2013). Sers tags: novel optical nanoprobes for bioanalysis. *Chem. Rev.* 113, 1391–1428. doi: 10.1021/cr300120g

Wasserroth, S., Bisswanger, T., Mueller, N. S., Kusch, P., Heeg, S., Clark, N., et al. (2018). Graphene as a local probe to investigate near-field properties of plasmonic nanostructures. *Phys. Rev. B* 97:155417. doi: 10.1103/PhysRevB.97.155417

Weick, G., Molina, R. A., Weinmann, D., and Jalabert, R. A. (2005). Lifetime of the first and second collective excitations in metallic nanoparticles. *Phys. Rev. B* 72:115410. doi: 10.1103/PhysRevB.72.115410

Yang, H. U., D'Archangel, J., Sundheimer, M. L., Tucker, E., Boreman, G. D., and Raschke, M. B. (2015). Optical dielectric function of silver. *Phys. Rev. B* 91:235137. doi: 10.1103/PhysRevB.91.235137

Yu, P. Y., and Cardona, M. (2010). *Fundamentals of Semiconductors: Physics and Materials Properties, 4th Edn*. Berlin: Springer.

Yu, R., Liz-Marzán, L. M., and García de Abajo, F. J. (2017). Universal analytical modeling of plasmonic nanoparticles. *Chem. Soc. Rev.* 46, 6710–6724. doi: 10.1039/C6CS00919K

Zuloaga, J., and Nordlander, P. (2011). On the energy shift between near-field and far-field peak intensities in localized plasmon systems. *Nano Lett.* 11, 1280–1283. doi: 10.1021/nl1043242

Conflict of Interest Statement: The authors declare that the research was conducted in the absence of any commercial or financial relationships that could be construed as a potential conflict of interest.

APPENDIX

Local Field Correction Factor

As demonstrated above, a local field correction factor C_{LF} must be included in our microscopic theory to reproduce the experimental absorption cross sections of plasmonic nanoparticles (see **Figure 3**). In this appendix we will derive the general expression for C_{LF} in Equation (18).

Due to the normalization of the plasmon eigenvectors (Equation 17) all prefactors that accounted for the coupling to an external light field are not included. The plasmon eigenvector $\mathbf{q}_w$ describes the microscopic oscillation of free charges inside the nanoparticle. The incident light field is described by a macroscopic amplitude $\hat{\mathbf{A}}_{\text{pt}}(\mathbf{r})$ which differs from the microscopic amplitude inside the nanoparticle because of a depolarization of the incident light field by the bound electrons of the metal. This can be modeled by considering a plasmonic point dipole inside a spherical nanoparticle with a dielectric function ϵ_b that accounts for the effect of the bound charges and interband transitions (Lamowski et al., 2018). The amplitude of the light field inside the nanoparticle is given within the quasi-static approximation by Bohren and Huffman (1998)

$$\mathbf{A}_{\text{pt}}^{\text{int}} = \frac{3\epsilon_m}{\epsilon_b + 2\epsilon_m}\mathbf{A}_{\text{pt}}. \tag{A1}$$

The factor $3\epsilon_m/(\epsilon_b + 2\epsilon_m)$ is known as a local field correction factor and might take different forms depending on the considered geometry (Onsager, 1936; de Vries and Lagendijk, 1998; Dolgaleva and Boyd, 2012). It must be also included in $\hat{\mathcal{H}}_{\text{pl-vib}}$ when calculating the quantized electric field of the plasmon in Equations (31) and (32).

To obtain a more general expression we consider a nanoparticle with an ellipsoidal shape. Using a Drude model for the electromagnetic response of the metal, the dipolar plasmon resonance occurs at Bohren and Huffman (1998) and Ru and Etchegoin (2009)

$$\omega_{\text{pl}} = \frac{\omega_{\text{p}}}{\sqrt{\epsilon_b + \epsilon_m(1/L - 1)}}, \tag{A2}$$

where L is a shape-dependend depolarization factor which is $1/3$ for a nanosphere (for explicit expressions see Bohren and Huffman, 1998; Ru and Etchegoin, 2009). The amplitude of the incident light field inside the nanoparticle is given by

$$\mathbf{A}_{\text{pt}}^{\text{int}} = \frac{\epsilon_m}{L\epsilon_b + \epsilon_m(1 - L)}\mathbf{A}_{\text{pt}}. \tag{A3}$$

Using Equation (A2) we obtain the local field correction factor

$$C_{\text{LF}} = \frac{\epsilon_m \omega_{\text{pl}}^2}{L\omega_p^2}. \tag{A4}$$

As this factor only contains the bulk plasma frequency of the metal ω_{p}, the dielectric constant of the environment ϵ_m and the plasmon frequency ω_{pl} it can be used for any dipolar plasmon mode of a single nanoparticle.

frontiers
in Chemistry

ORIGINAL RESEARCH
published: 20 August 2019
doi: 10.3389/fchem.2019.00582

Study of Chemical Enhancement Mechanism in Non-plasmonic Surface Enhanced Raman Spectroscopy (SERS)

Jayeong Kim[1], Yujin Jang[1], Nam-Jung Kim[2], Heehun Kim[2], Gyu-Chul Yi[2], Yukyung Shin[3], Myung Hwa Kim[3] and Seokhyun Yoon[1]*

[1] Department of Physics, Ewha Womans University, Seoul, South Korea, [2] Department of Physics and Astronomy, Institute of Applied Physics, Research Institute of Advanced Materials, Seoul National University, Seoul, South Korea, [3] Department of Chemistry and Nanoscience, Ewha Womans University, Seoul, South Korea

Surface enhanced Raman spectroscopy (SERS) has been intensively investigated during the past decades for its enormous electromagnetic field enhancement near the nanoscale metallic surfaces. Chemical enhancement of SERS, however, remains rather elusive despite intensive research efforts, mainly due to the relatively complex enhancing factors and inconsistent experimental results. To study details of chemical enhancement mechanism, we prepared various low dimensional semiconductor substrates such as ZnO and GaN that were fabricated via metal organic chemical vapor deposition process. We used three kinds of molecules (4-MPY, 4-MBA, 4-ATP) as analytes to measure SERS spectra under non-plasmonic conditions to understand charge transfer mechanisms between a substrate and analyte molecules leading to chemical enhancement. We observed that there is a preferential route for charge transfer responsible for chemical enhancement, that is, there exists a dominant enhancement process in non-plasmonic SERS. To further confirm our idea of charge transfer mechanism, we used a combination of 2-dimensional transition metal dichalcogenide substrates and analyte molecules. We also observed significant enhancement of Raman signal from molecules adsorbed on 2-dimensional transition metal dichalcogenide surface that is completely consistent with our previous results. We also discuss crucial factors for increasing enhancement factors for chemical enhancement without involving plasmonic resonance.

Keywords: surface enhanced Raman scattering, chemical enhancement, enhancement mechanism, charge transfer, semiconductor microstructure

OPEN ACCESS

Edited by:
Ivano Alessandri,
University of Brescia, Italy

Reviewed by:
Lingxin Chen,
Yantai Institute of Coastal Zone Research, Chinese Academy of Sciences (CAS), China
Huawen Wu,
Lam Research, United States

***Correspondence:**
Seokhyun Yoon
syoon@ewha.ac.kr

Specialty section:
This article was submitted to Analytical Chemistry, a section of the journal Frontiers in Chemistry

Received: *15 March 2019*
Accepted: *02 August 2019*
Published: *20 August 2019*

Citation:
Kim J, Jang Y, Kim N-J, Kim H, Yi G-C, Shin Y, Kim MH and Yoon S (2019) Study of Chemical Enhancement Mechanism in Non-plasmonic Surface Enhanced Raman Spectroscopy (SERS). Front. Chem. 7:582. doi: 10.3389/fchem.2019.00582

INTRODUCTION

Since its first observation and following explanation by pioneers (Fleischmann et al., 1974; Jeanmaire and Van Duyne, 1977; Moskovits, 1985; Otto, 1991; Smith and Dent, 2005; Stiles et al., 2008; Schlücker, 2014), surface enhanced Raman spectroscopy (SERS) has been a subject of intense research in various disciplines, especially in analytical chemistry utilizing its very high sensitivity that might overcome main disadvantage of the signal weakness of Raman scattering spectroscopy (Chan et al., 2003; Haynes and Van Duyne, 2003; Tian and Ren, 2004; Haynes et al., 2005; Zhang et al., 2005, 2008; Le Ru et al., 2008; Wang et al., 2010). It is reported that SERS enhancement factor (EF) can be as high as 10^{12} in some cases (David et al., 2010) indicating that unprecedented area of analyses such as Raman fingerprinting of a very small amount of materials, even of a single molecule may be possible, and hence enormous research efforts have been exerted over the decades (Kneipp et al., 1997; Nie and Emory, 1997; Stiles et al., 2008). Recent applications of SERS include, for example, employing various nanostructured materials (Wang Y. et al., 2012; Jin, 2013; Li et al., 2013, 2017; Xu et al., 2013; Lin et al., 2015; Bakan et al., 2016; Wang et al., 2016; Chowdhury et al., 2018; Yu et al., 2019). SERS is also very interesting because it inherently involves light-matter interaction in small scale where quantum mechanical effects might be crucial. In this regard, SERS attracts attention from research communities that emphasize basic research and that are rather application-oriented as well.

By now, it is well-accepted that the largest contribution for the EF is coming from so-called electromagnetic mechanism. In the electromagnetic mechanism, it is explained that the Raman signal enhancement occurs as a result of surface plasmonic resonance, i.e., when the energy of the laser excitation is close to the surface plasmon energy of a substrate which is often made of noble metal, Raman response is strongly enhanced. Obviously there should be another mechanism to explain SERS results that depend not only on substrates but also analyte molecules, which is referred to as chemical mechanism (Wang X. et al., 2012; Alessandri and Lombardi, 2016). As a matter of fact, chemical enhancement (CE) is rather inclusive nomenclature than a specific phenomenon that comes from a definite origin. For example, CE includes several different transitions/processes. In case of a metal substrate, the charge transfer transition between highest occupied molecular orbital (HOMO) of analyte molecules and the fermi level of metal is most relevant. For dielectric substrates, charge transfer transition between either HOMO of molecules and the conduction band (CB) edge of substrate material or valence band (VB) of substrate material and lowest unoccupied molecular orbital (LUMO) of molecules is crucial. Moreover, electronic transition from HOMO to LUMO or transition between VB and CB of substrate material can also contribute to the enhancement of Raman signal by resonance processes that lead to surface enhanced resonance Raman spectroscopy (SERRS). All of the above effects can contribute to enhancement of Raman response and tracking the exact origin of a particular enhancement is not always trivial. Even though there is some guidance from theoretical side (Lombardi and Birke, 2007, 2012, 2014), at this point, if possible, experimental ways to single out the main effect for CE is needed. With this information, we can have better understanding of chemical enhancement mechanism and we can establish microscopic theory of CE.

In this study, we used compound III-V semiconductor (ZnO and GaN) microstructure and 2-dimensional transition metal dichalcogenide (WS_2) as substrates to study charge transfer (CT) transitions and their influence on enhanced Raman spectra. By using semiconductor materials as substrates, we could safely exclude surface plasmon resonance as the origin of Raman enhancement in our measurements. Another advantage of using semiconductor materials is that we can fully use current state-of-art semiconductor technology for preparing substrates. For example, ZnO and GaN microstructures we used can be made rather easily by following well-defined procedures resulting good reproducibility and the manufacturing cost is not high (Kim et al., 2012; Park et al., 2015). It is well-known that ZnO (Zhao et al., 2012), GaN (Jewett et al., 2012), and WS_2 (Goldman et al., 2015) are biocompatible so together with easy and highly reproducible fabrication make semiconducting materials as quite promising SERS substrates with wide applicability. We observed clear SERS effects from all combinations of our samples but there is indication that the enhancement is asymmetric, that is, there might be a preferential route of charge transfer between substrates and analytes for exhibiting large EF. We suggest that there can be a dominant enhancement mechanism in CE that can lead us to design combinations of materials showing maximal Raman enhancement effect.

EXPERIMENTAL

Fabrication of SERS Substrate Samples

The position-controlled ZnO microwalls are grown on chemical vapor deposition (CVD) graphene films through the catalyst-free CVD process. We obtained ZnO microwall growth selectivity by depositing a silicon dioxide (SiO_2) growth mask on the graphene films and patterning hole array on the growth mask layer using E-beam lithography and etching techniques. Dimensional parameters including the heights and diameters of microwalls can be controlled by modifying the lithographic pattern mask or varying the growth parameters of catalyst-free CVD process. In this work, highly oriented and ordered ZnO mircrowalls with an outer diameter of 4 μm and a height of 4 μm were typically employed. For GaN substrates, GaN layers were over-grown laterally from pre-fabricated ZnO microstructures using a similar MOVPE process with tri-methyl gallium and ammonia as sources. The detailed process for growing ZnO/GaN microstructure is described in previous reports (Kim et al., 2012, 2019; Park et al., 2015).

The vertically aligned single crystalline tungsten disulfide WS_2 nanosheets was synthesized via the chemical vapor deposition (CVD) method on a Si wafer. The process to form the WS_2 were as follows. First of all, the quartz boat with tungsten hexachloride (WCl_6, Sigma-Aldrich) was placed in the center of the quartz tube and another quartz boat with sulfur powder (Sigma-Aldrich, 99.98%) was held 14.5 cm distant from it. The Si substrate was placed face-down above the quartz boat with tungsten hexachloride. Before the chemical reaction, flushing the quartz tube by carrier gas helium (He, 99.999%) for 10 min by 400 sccm (standard cubic centimeter per minute) to remove impure gases in quartz tube. When the flushing was finished, the furnace was heated up to 550 through the speed rate of 26 per minute condition and kept the temperature at 550°C for 20 min. The carrier gas, helium (He) was flowed by 10 sccm for the whole process since heating up the furnace. After finishing the chemical reaction, stop flowing carrier gas was off at the same time. The furnace was turned off after chemical reaction and cooled down gradually until to room temperature.

Preparation for SERS Measurement Samples—Molecule Deposition

We prepared SERS samples by two methods of immersing and drop casting. For ZnO substrates, we immersed the substrates in molecular solution with 10^{-4}M concentration for 2 h, and washed with deionized water. We used three different molecules (4-MPY, 4-MBA, 4-ATP) for the molecular solution for each ZnO substrates. For GaN substrates, we deposited the molecules (4-MPY, 4-MBA, 4-ATP) by drop casting as follows. 10 μL of 10^{-3} M 4-Mpy solution was prepared and was divided into 4 equal droppings of 2.5 μLs each that was dropped on a substrate and was left dried naturally. We also using drop casting method for depositing R6G molecules on WS_2 nanoflower structure.

SERS Measurements

Room temperature Raman scattering spectra of ZnO and GaN microstructure samples with 3 different molecules (4-MPY, 4-MBA, 4-ATP) adsorbed and R6G adsorbed WS_2 samples were measured by using a McPherson 207 spectrometer equipped with a nitrogen-cooled charge-coupled-device (CCD) array detector. The ZnO microstructure samples were excited with 532.0 nm (2.33 eV) DPSS (diode-pumped solid state) laser, focused to ∼1 μm diameter spot using a microscope objective (x50). The GaN microstructure samples were excited with 514.5 nm (2.41 eV) Ar+ ion laser, also focused to ∼1 μm diameter spot using a microscope objective (x50). The WS_2 samples were excited with three different

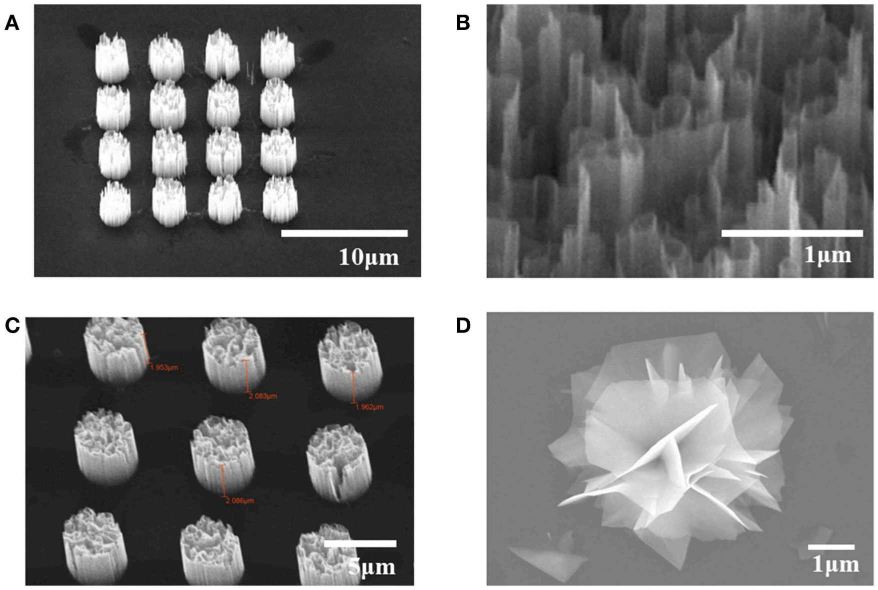

FIGURE 1 | SEM images of **(A)** GaN microrod array **(B)** nanowall structure in a microrod **(C)** ZnO microrod array **(D)** CVD grown WS_2 nanoflower.

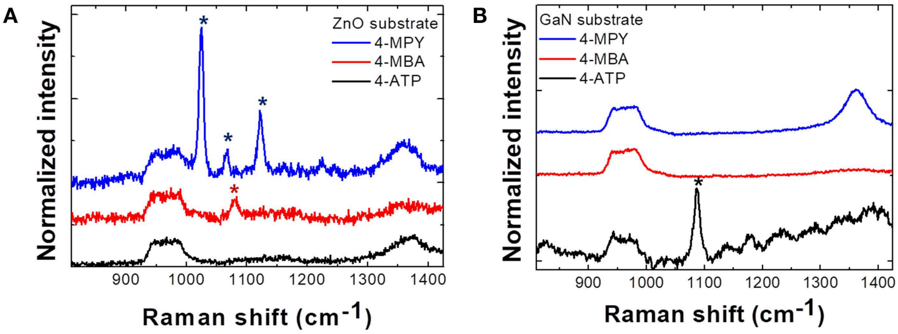

FIGURE 2 | Raman spectra of three different molecules (4-MPY, 4-MBA, 4-ATP) adsorbed on **(A)** ZnO microrod array substrate and **(B)** GaN microrod array substrate. Phonon intensity in each spectrum is normalized to Si phonon (520 cm^{-1}) intensity. Raman peaks of 4-MPY and 4-MBA molecules are enhanced only on the ZnO substrate and Raman peak of 4-ATP molecules is enhanced only on the GaN substrate. *Indicates the peak positions of each molecules (4-MPY, 4-MBA, 4-ATP).

excitation wavelengths, 488.0 nm (2.54 eV), 532.0 nm, 632.8 nm (1.96 eV). The excitation power was kept <0.2 mW to avoid laser heating.

RESULTS AND DISCUSSIONS

Figure 1 shows scanning electron microscope (SEM) images of samples we used. **Figure 1A** is a picture of highly oriented GaN microrod array. **Figure 1B** shows the maze-like structure inside each GaN microrods, which provides large surface area. **Figure 1C** is highly oriented ZnO microrod array and **Figure 1D** shows a WS_2 "nanoflower" flake structure. The samples we used exhibit high crystalline quality with little defects and display excellent optical characteristics, as shown in previous reports (Kim et al., 2012, 2017, 2019; Park et al., 2015).

Figure 2 illustrates Raman spectra from (a) ZnO and (b) GaN semiconductor microrod arrays. From the spectra it is clear that the enhancement of Raman signal is quite selective with respect to the combinations of adsorbed molecules and substrates. In ZnO substrates, only 4-MPY shows clearly enhanced response and signal from 4-ATP is enhanced only on GaN substrates. This can be explained by CE, that is, the Raman signal of analyte molecules is strongly enhanced when the laser excitation energy matches with the CT transition energy between substrates and analyte molecules. This point will be discussed further with explanations of **Figure 4**.

In **Figure 3**, excitation wavelength dependence of Raman spectra of R6G molecules adsorbed on CVD grown WS_2 nanoflower substrates is shown. It is clear that signal is strongly enhanced when the excitation energy is 2.33 eV (532.0 nm), is significantly weaker but still observable for 1.96 eV (632.8 nm) excitation, and is not observable under 2.54 eV (488.0 nm) illumination. As a matter of fact, there are numerous works reporting that there is a SERS like effect from TMDC materials (Sun et al., 2014; Lee et al., 2016; Muehlethaler et al., 2016; Miao et al., 2018; Zheng et al., 2018). Our observation can again be explained by CE that is related with light induced charge transfer transition between substrates and analytes. Thus, the selective Raman enhancement of analyte molecules is not just a characteristic for III–V semiconductor microstructures but also is observed in two-dimensional transition metal dichalcogenide (TMDC) materials suggesting that it is rather universal phenomenon in molecule-semiconductor system.

Energy band schematics and relevant electronic energy diagrams are shown in **Figure 4**. For CE, there are four energy scales that need to be considered. The first is the molecular transition from HOMO to LUMO, related with "A-term" in Herzberg-Teller (HT) treatment (Albrecht, 1961; Schatz and Ratner, 2002), the second is a charge transfer transition from molecular HOMO to CB of semiconductor substrates (B-term in HT picture), the third is a charge transfer transition from the VB of semiconductor substrates to molecular LUMO (HT's C-term), and the fourth is the band or excitonic transition from VB to CB of semiconductor substrates. From our previous work, we can safely exclude the HOMO to LUMO transition and the VB to CB transition as main cause for Raman enhancement (Kim et al., 2019). Our results can rather be explained by transitions described by either HT's B- or C-term and resulting enhancement. In Lombardi and Birke's pioneering work they explained the chemical enhancement mechanism of SERS by resonance process of which the relevant energy is the difference between either HOMO and CB (B-term) or VB to LUMO (C-term) where light induced charge transfer transition can occur (Lombardi and Birke, 2014). In their theory, however, there is no a priori difference between B- and C-terms, that is, large enhancement can occur due to any of the two processes and there would be no preference or advantage from one process over another. There can be even more pathways for charge transfer such as transition involving the surface state of semiconductor, charge transfer complex, and/or excitonic states, for example (Kneipp et al., 2018). In any of those current approaches, there is no dominant process over other ones.

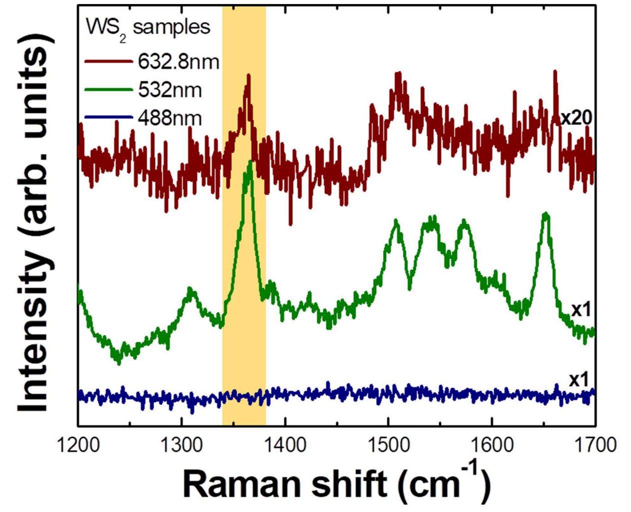

FIGURE 3 | Wavelength dependent Raman spectra of R6G molecules adsorbed on CVD grown WS_2 nanoflower substrate measured with 3 different excitation lasers. Phonon intensity in each spectrum is normalized to Si phonon (520 cm^{-1}) intensity. The largest enhancement is observed at 532.0 nm excitation and significantly weaker but observable enhancement is observed at 632.8 nm excitation. No observable enhancement is seen under 488.0 nm illumination.

Recently, we reported that there might be a preferential route for CE by observing selective enhancement that strongly depends on the relative positions of each energy level (Kim et al., 2019). Interestingly, the EF calculated for a transition due to C-term (transition from VB to LUMO) was found to be at least 100 times larger than that for a transition due to B-term (transition from HOMO to CB) suggesting that utilizing a charge transfer from semiconductor substrates to molecular LUMO would be more efficient way to attain large EF in chemical enhancement. From **Figure 4A**, we can see that how charges are transferred for each molecule. When energy excitation energy of 2.33 eV is applied to ZnO and molecules, charge transfer transition can only be caused by C-term for 4-MPY (denoted by blue arrow) and B-term for 4-MBA (denoted by red arrow), respectively.

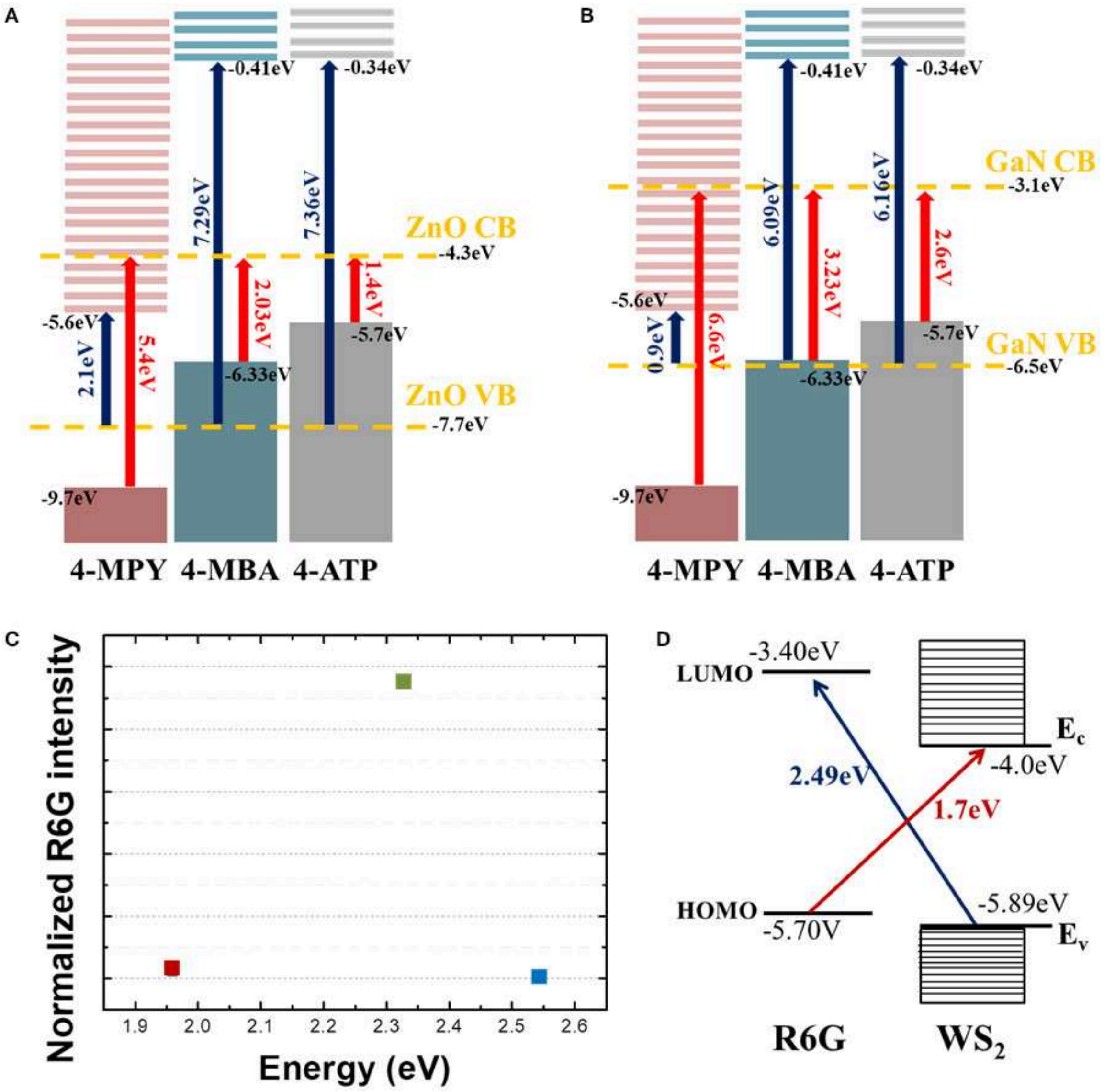

FIGURE 4 | Energy level diagrams of three molecules (4-MPY, 4-MBA, 4-ATP) with **(A)** ZnO and **(B)** GaN. Bands of each semiconductor are denoted by yellow dashed lines. All vertical arrows indicate possible charge transfer routes between molecules and semiconductor substrates. Blue arrows denote charge transfer transition from semiconductor valence band (VB) to LUMO of molecules, and red arrows denote charge transfer transition from HOMO of molecules to semiconductor conduction band (CB). **(C)** Normalized (to Si phonon intensity) intensity of R6G 1368 cm^{-1} mode with three different excitation laser wavelengths. **(D)** Energy level schematics of R6G and WS_2. The red arrow denotes a charge transfer route from HOMO of R6G to WS_2 CB, and the blue arrow denotes a charge transfer route from WS_2 VB to LUMO of R6G.

The other way, red arrow (B-term) for 4-MPY and blue arrow (C-term) for 4-MBA, of transition cannot occur with 2.33 eV excitation. If we compare Raman intensities associated with charge transfer, C-term related one (4-MPY) is much larger than B-term related one (4-MBA). Similarly, charge transfer between GaN substrate and molecules can only occur through B-term for 4-ATP (**Figure 4B**) with 2.41 eV excitation. This agrees well with our experimental results shown in **Figures 2A,B**. This observation of asymmetric enhancement is also evident from the R6G on WS_2 as shown in **Figures 4C,D**. **Figure 4C** shows the normalized R6G intensity to Si phonon intensity as a function of excitation energy. Comparing this with the energy band diagram of R6G and WS_2 in **Figure 4D**, we can see that large enhancement at 2.33 eV observed in **Figure 3** is associated with C-term (blue arrow in **Figure 4D**). The much weaker enhancement at 1.96 eV observed in **Figure 3** is due to B-term (red arrow in **Figure 4D**).

Our current observations from three different material systems are completely consistent with our previous reports (Shin et al., 2014; Kim et al., 2019). That is, chemical enhancement seems to occur asymmetrically. Stronger enhancement with larger EF is associated with charge transfer transition from semiconductor substrates to analyte molecules. More work need to be done before we completely understand why there seems to be a dominant route showing a larger EF for CE, but possible cause would be associated with density of states, existence of excitonic levels, coordination and/or orientation of molecules on the surface of substrates, for example. Since CE is caused by "borrowing intensity" from transitions of various origins, it is not always easy to single out which one is the most relevant or irrelevant to Raman enhancement. From our measurements, we could suggest that the most important transition for attaining larger EF is C-term related one. In other words, the dominant process for chemical SERS effect is associated with charge transfer transition from semiconductor VB to molecular LUMO.

CONCLUSIONS

We measured Raman response from adsorbed molecules on III–V semiconductor microstructures and thin TMDC materials. In non-plasmonic condition where the energy of excitation laser is far from that of surface plasmon of substrates SERS is thought to be associated with charge transfer transitions, that is referred to as chemical enhancement. In theoretical prediction, there is no preferential route or dominant channel for chemical enhancement, however, we found that the charge transfer transition from semiconductor substrates to molecular LUMO may play a role as an efficient or a dominant process for attaining a large EF. We observed the above results in two independent systems, one in III–V compound semiconductor microstructure and the other in thin TMDC materials. Our finding can provide important information for understanding chemical SERS effects microscopically.

DATA AVAILABILITY

All datasets generated for this study are included in the manuscript and/or the supplementary files.

AUTHOR CONTRIBUTIONS

JK carried out most of the experimental work and analyses and drafted the paper. YJ helped with the experimental work and analyses. N-JK contributed initial design of the study. HK and G-CY wrote sections of the manuscript and provided the III–V semiconductor microrod array samples. YS and MK wrote sections of the manuscript and provided the TMDC samples. SY designed the project and wrote the paper. All authors have approved the final version of the manuscript.

FUNDING

This work was supported by Basic Science Research Program (NRF-2016R1D1A1B01009032, NRF-2016R1D1A1B03934962, NRF-2018R1A6A1A03025340) through the National Research Foundation of Korea (NRF). This work at SNU was also supported by Global Research Laboratory Program (2015K1A1A2033332), through the National Research Foundation of Korea (NRF) funded by the Ministry of Science, ICT.

REFERENCES

Albrecht, A. C. (1961). On the theory of Raman intensities. *J. Chem. Phys.* 34, 1476–1484. doi: 10.1063/1.1701032

Alessandri, I., and Lombardi, J. R. (2016). Enhanced Raman scattering with dielectrics. *Chem. Rev.* 116, 14921–14981. doi: 10.1021/acs.chemrev.6b00365

Bakan, G., Ayas, S., Ozgur, E., Celebi, K., and Dana, A. (2016). Thermally tunable ultrasensitive infrared absorption spectroscopy platforms based on thin phase-change films. *ACS Sens.* 1, 1403–1407. doi: 10.1021/acssensors.6b00591

Chan, S., Kwon, S., Koo, T.-W., Lee, L. P., and Berlin, A. A. (2003). Surface-enhanced Raman scattering of small molecules from silver-coated silicon nanopores. *Adv. Mater.* 15, 1595–1598. doi: 10.1002/adma.200305149

Chowdhury, A. K. M. R. H., Tan, B., and Venkatakrishnan, K. (2018). SERS active 3D interconnected nanocarbon web towards non-plasmonic *in-vitro* sensing of HeLa cells and fibroblasts. *ACS Appl. Mater. Interfaces.* 10, 35715–35733. doi: 10.1021/acsami.8b10308

David, C., Guillot, N., Shen, H., Toury, T., and de la Chapelle, M. L. (2010). SERS detection of biomolecules using lithographed nanoparticles towards a reproducible SERS biosensor. *Nanotechnology* 21:475501. doi: 10.1088/0957-4484/21/47/475501

Fleischmann, M., Hendra, P. J., and McQuillan, A. J. (1974). Raman spectra of pyridine adsorbed at a silver electrode. *Chem. Phys. Lett.* 26, 163–166. doi: 10.1016/0009-2614(74)85388-1

Goldman, E. B., Zak, A., Tenne, R., Kartvelishvily, E., Levin-Zaidman, S., Neumann, Y., et al. (2015). Biocompatibility of Tungsten disulfide inorganic nanotubes and fullerene-like nanoparticles with salivary gland cells. *Tissue Eng Part A* 21, 1013–1023. doi: 10.1089/ten.tea.2014.0163

Haynes, C. L., McFarland, A. D., and Van Duyne, R. P. (2005). Surface-enhanced: Raman spectroscopy. *Anal. Chem.* 77, 338–346. doi: 10.1021/ac053456d

Haynes, C. L., and Van Duyne, R. P. (2003). Dichroic optical properties of extended nanostructures fabricated using angle-resolved nanosphere lithography. *Nano Lett.* 3, 939–943. doi: 10.1021/nl0342287

Jeanmaire, D. L., and Van Duyne, R. P. (1977). Surface raman spectroelectrochemistry: part I. Heterocyclic, aromatic, and aliphatic amines adsorbed on the anodized silver electrode. *J. Electroanal. Chem. Interfac. Electrochem.* 84, 1–20. doi: 10.1016/S0022-0728(77)80224-6

Jewett, S. A., Makowski, M. S., Andrews, B., Manfra, M. J., and Ivanisevic, A. (2012). Gallium nitride is biocompatible and non-toxic before and after functionalization with peptides. *Acta Biomater.* 8, 728–733. doi: 10.1016/j.actbio.2011.09.038

Jin, Y. (2013). Multifunctional compact hybrid au nanoshells: a new generation of nanoplasmonic probes for biosensing, imaging, and controlled release. *Acc. Chem. Res.* 47, 138–148. doi: 10.1021/ar400086e

Kim, N. J., Kim, J., Park, J. B., Kim, H., Yi, G. C., and Yoon, S. (2019). Direct observation of quantum tunnelling charge transfers between molecules and semiconductors for SERS. *Nanoscale* 11, 45–49. doi: 10.1039/C8NR08389D

Kim, S., Yu, H. K., Yoon, S., Lee, N.-S., and Kim, M. H. (2017). Growth of two-dimensional rhenium disufide (ReS_2) nanosheets with a few layers at low temperature. *CrystEngComm.* 19, 5341–5345. doi: 10.1039/C7CE00926G

Kim, Y. J., Yoo, H., Lee, C. H., Park, J. B., Baek, H., Kim, M., et al. (2012). Position- and morphology-controlled ZnO nanostructures grown on graphene layers. *Adv. Mater.* 24, 5565–5569. doi: 10.1002/adma.201201966

Kneipp, K., Ozaki, Y., and Tian, Z. Q. (2018). *Recent Developments in Plasmon-Suppoted Raman Spectroscopy: 45 Years of Enhanced Raman Signals*. London: World Scientific.

Kneipp, K., Wang, Y., Kneipp, H., Perelman, L. T., Itzkan, I., Dasari, R. R., et al. (1997). Single molecule detection using Surface-Enhanced Raman Scattering (SERS). *Phys. Rev. Lett.* 78, 1667–1670. doi: 10.1103/PhysRevLett.78.1667

Le Ru, E. C., Meyer, M., Blackie, E., and Etchegoin, P. G. (2008). Advanced aspects of electromagnetic SERS enhancement factors at a hot spot. *J. Raman Spectrosc*. 39, 1127–1134. doi: 10.1002/jrs.1945

Lee, Y., Kim, H., Lee, J., Yu, S. H., Hwang, E., Lee, C., et al. (2016). Enhanced Raman scattering of rhodamine 6G films on two-dimensional transition metal dichalcogenides correlated to photoinduced charge transfer. *Chem. Mater*. 28, 180–187. doi: 10.1021/acs.chemmater.5b03714

Li, B., Zhang, W., Chen, L., and Lin, B. (2013). A fast and low-cost spray method for prototyping and depositing surface-enhanced Raman scattering arrays on microfluidic paper based device. *Electrophoresis* 34, 2162–2168. doi: 10.1002/elps.201300138

Li, K., Hogan, N. J., Kale, M. J., Halas, N. J., Nordlander, P., and Christopher, P. (2017). Balancing near-field enhancement, absorption, and scattering for effective antenna–reactor plasmonic photocatalysis. *Nano Lett*. 17, 3710–3717. doi: 10.1021/acs.nanolett.7b00992

Lin, M., Wang, Y., Sun, X., Wang, W., and Chen, L. (2015). "Elastic" property of mesoporous silica shell: for dynamic surface enhanced raman scattering ability monitoring of growing noble metal nanostructures via a simplified spatially confined growth method. *ACS Appl. Mater. Interfaces*. 7, 7516–7525. doi: 10.1021/acsami.5b01077

Lombardi, J. R., and Birke, R. L. (2007). Time-dependent picture of the charge-transfer contributions to surface enhanced Raman spectroscopy. *J. Chem. Phys*. 126:244709. doi: 10.1063/1.2748386

Lombardi, J. R., and Birke, R. L. (2012). The theory of surface-enhanced Raman scattering. *J. Chem. Phys*. 136:144704. doi: 10.1063/1.3698292

Lombardi, J. R., and Birke, R. L. (2014). Theory of surface-enhanced Raman scattering in semiconductors. *J. Chem. Phys. C* 118, 11120–11130. doi: 10.1021/jp5020675

Miao, P., Qin, J. K., Shen, Y., Su, H., Dai, J., Song, B., et al. (2018). Unraveling the raman enhancement mechanism on 1T'-Phase ReS2 nanosheets. *Small* 14:1704079. doi: 10.1002/smll.201704079

Moskovits, M. (1985). Surface-enhanced spectroscopy. *Rev. Mod. Phys.* 57, 783–826. doi: 10.1103/RevModPhys.57.783

Muehlethaler, C., Considine, C. R., Menon, V., Lin, W. C., Lee, Y. H., and Lombardi, J. R. (2016). Ultrahigh Raman enhancement on monolayer MoS_2. *ACS Photonics* 3, 1164–1169. doi: 10.1021/acsphotonics.6b00213

Nie, S., and Emory S. R. (1997). Probing single molecules and single nanoparticles by surface-enhanced Raman scattering. *Science* 275, 1102–1106. doi: 10.1126/science.275.5303.1102

Otto, A. (1991). Surface-enhanced Raman scattering of adsorbates. *J. Raman Specrtoscosc*. 22, 743–752. doi: 10.1002/jrs.1250221204

Park, S. I., Tchoe, Y., Baek, H., Heo, J., Hyun, J. K., Jo, J., et al. (2015). Growth and optical characteristics of high-quality ZnO thin films on graphene layers. *APL Mater*. 3:016103. doi: 10.1063/1.4905488

Schatz, G. C., and Ratner, M. A. (2002). *Quantum Mechanics in Chemistry*. Dover.

Schlücker, S. (2014). Surface-enhanced Raman spectroscopy: concepts and chemical applications. *Angew. Chem. Int. Ed*. 53, 4756–4795. doi: 10.1002/anie.201205748

Shin, H. Y., Shim, E. L., Choi, Y. J., Park, J. H., and Yoon, S. (2014). Giant enhancement of the Raman response due to one-dimensional ZnO nanostructures. *Nanoscale* 6, 14622–14626. doi: 10.1039/C4NR04527K

Smith, E., and Dent, G. (2005). *Modern Raman Spectroscopy*. Chichester: John Wiley and Sons.

Stiles, P. L., Dieringer, J. A., Shah, N. C., and Van Duyne, R. P. (2008). Surface-enhanced Raman spectroscopy. *Annu. Rev. Anal. Chem*. 1, 601–626. doi: 10.1146/annurev.anchem.1.031207.112814

Sun, L., Hu, H., Zhan, D., Yan, J., Liu, L., Teguh, J. S., et al. (2014). Plasma modified MoS_2 nanoflakes for surface enhanced Raman scattering. *Small* 10, 1090–1095. doi: 10.1002/smll.201300798

Tian, Z. Q., and Ren, B. (2004). Adsorption and reaction at electrochemical interfaces as probed by surface-enhanced Raman spectroscopy. *Annu. Rev. Phys. Chem*. 55, 197–229. doi: 10.1146/annurev.physchem.54.011002.103833

Wang, X., Shi, W., She, G., and Mu, L. (2012). Surface-Enhanced Raman Scattering (SERS) on transition metal and semiconductor nanostructures. *Phys. Chem. Chem. Phys*. 14, 5891–5901. doi: 10.1039/c2cp40080d

Wang, X. T., Shi, W. S., She, G. W., Mu, L. X., and Lee, S. T. (2010). High-performance surface-enhanced Raman scattering sensors based on Ag nanoparticles-coated Si nanowire arrays for quantitative detection of pesticides. *Appl. Phys. Lett*. 96:053104. doi: 10.1063/1.3300837

Wang, Y., Wang, Y., Wang, W., Sun, K., and Chen, L. (2016). Reporter-embedded SERS tags from gold nanorod seeds: selective immobilization of reporter molecules at the tip of nanorods. *ACS Appl. Mater. Interfaces*. 8, 28105–28115. doi: 10.1021/acsami.6b04216

Wang, Y., Yan, B., and Chen, L. (2012). SERS tags: novel optical nanoprobes for bioanalysis. *Chem. Rev*. 113, 1391–1428. doi: 10.1021/cr300120g

Xu, B., Chen, P., Zhou, S., Hong, Z., Hao, J., and Qiu, J. (2013). Enhanced broadband near-infrared luminescence in Bi-doped glasses by co-doping with Ag. *J. Appl. Phys*. 113:183506. doi: 10.1063/1.4804256

Yu, Q., Wang, Y., Mei, R., Yin, Y., You, J., and Chen, L. (2019). Polystyrene encapsulated SERS tags as promising standard tools: simple and universal in synthesis, highly sensitive and ultrastable for bioimaging. *Anal. Chem*. 91, 5270–5277. doi: 10.1021/acs.analchem.9b00038

Zhang, B., Wang, H., Lu, L., Ai, K., Zhang, G., and Cheng, X. (2008). Large-area silver-coated silicon nanowire arrays for molecular sensing using Surface-enhanced Raman spectroscopy. *Adv. Funct. Mater*. 18, 2348–2355. doi: 10.1002/adfm.200800153

Zhang, X., Young, M. A., Lyandres, O., and Van Duyne, R. P. (2005). Rapid detection of an anthrax biomarker by Surface-enhanced Raman spectroscopy. *J. Am. Chem. Soc.* 127, 4484–4489. doi: 10.1021/ja043623b

Zhao, L.-H., Zhang, R., Zhang, J., and Sun, S.-Q. (2012). Synthesis and characterization of biocompatible ZnO nanoparticles. *CrystEngComm*. 14, 945–950. doi: 10.1039/C1CE05621B

Zheng, G., Zhang, P., Zhang, S., Peng, Y., Huang, L., Zhang, L., et al. (2018). SERS effect of selectively adsorbed dyes by hydrothermally-produced MoS_2 nanosheets. *N. J. Chem*. 42, 18906–18912. doi: 10.1039/C8NJ03837F

Conflict of Interest Statement: The authors declare that the research was conducted in the absence of any commercial or financial relationships that could be construed as a potential conflict of interest.

frontiers in Chemistry

ORIGINAL RESEARCH
published: 24 September 2019
doi: 10.3389/fchem.2019.00647

Plasmon Enhanced Fluorescence and Raman Scattering by [Au-Ag Alloy NP Cluster]@SiO$_2$ Core-Shell Nanostructure

Chengyun Zhang[†], *Tingting Zhang*[†], *Zhenglong Zhang** *and Hairong Zheng**

School of Physics and Information Technology, Shaanxi Normal University, Xi'an, China

Silica-shell coated noble metal nanoparticles have shown a good performance in surface enhanced fluorescence and Raman scattering. However, silica-shell coated single noble nanoparticle cannot effectively enhance the optical signal due to the relative weak near-field enhancement. In this paper, [Au-Ag alloy NP cluster]@SiO$_2$ core-shell nanostructure is employed to achieve the effective electric field enhancement. With the specific structure, simultaneous Raman scattering and fluorescence emission enhancement is obtained, and the enhancement comparison of fluorescence emission with Raman scattering in different type agglomeration of metal NPs is investigated *in-situ*. With different thickness of SiO$_2$ shell, the optimized Raman and fluorescence enhancement systems are obtained, respectively, and corresponding study of power dependence are investigated in detail. The selectively enhanced Raman and fluorescence can be realized via controlling the shell thickness and laser power. Our work provides a non-polarization dependent [metal NP cluster]@SiO$_2$ system, which may have a promising application in portable chemical and biochemistry detecting.

Keywords: plasmon enhanced spectroscopy, raman scattering, fluorescence, core-shell structure, Au-Ag alloy NP cluster

Edited by:
Ivano Alessandri,
University of Brescia, Italy

Reviewed by:
Aihua Liu,
Qingdao University, China
Nicolò Bontempi,
Catholic University of the Sacred Heart, Italy

***Correspondence:**
Zhenglong Zhang
zlzhang@snnu.edu.cn
Hairong Zheng
hrzheng@snnu.edu.cn

[†] *These authors have contributed equally to this work*

Specialty section:
This article was submitted to Analytical Chemistry, a section of the journal Frontiers in Chemistry

Received: *19 April 2019*
Accepted: *10 September 2019*
Published: *24 September 2019*

Citation:
Zhang C, Zhang T, Zhang Z and Zheng H (2019) Plasmon Enhanced Fluorescence and Raman Scattering by [Au-Ag Alloy NP Cluster]@SiO$_2$ Core-Shell Nanostructure. Front. Chem. 7:647. doi: 10.3389/fchem.2019.00647

INTRODUCTION

Nobel metal based nanoparticles (NPs), such as silver or gold NPs, have shown a great potential in plasmon sensor (Homola et al., 1999; Chen and Ming, 2012; Rosman et al., 2013), catalyst (Christopher et al., 2011; Han et al., 2015; Vadai et al., 2018; Zhang et al., 2018), biotherapy (Wang et al., 2014), and signal enhancement (Li et al., 2010; Ando et al., 2011; Wang and Kong, 2015) because of the abundant tunable surface plasmon resonance (SPR) peak in wide-range spectrum. The position of the SPR peak can be easily controlled through changing the morphology and material of the NPs (Liu et al., 2017). However, for pure Ag or Au NPs, it is hard to manipulate the SPR wavelength, especially at the wavelength of 400–530 nm (Liu et al., 2011; Li et al., 2017), which limits its application to some extent. Bimetallic Au-Ag alloy NPs provide a solution to the fault of the SPR wavelength, which can keep the morphology and size of metal NPs unchanged (Kuladeep et al., 2012; Rioux et al., 2014). Moreover, the Au-Ag alloy has congregated the advantages of Au and Ag, such as high chemical stability (Gao et al., 2014) and good photocatalytic properties (Tsukamoto et al., 2012; Han et al., 2016), and it is considered to be a promising candidate in metal material.

For years, many researches have been focused on plasmonic NPs enhancement of the optical signal (Ming et al., 2009; Schietinger et al., 2010; Ding et al., 2016), which is utilizing the near-field generated by the plasmonic NPs. The property of the Electricmagnetic (EM) field generated by the NPs is highly dependent on the morphology of the NPs and the features of the incident light (Sherry et al., 2005; Talley et al., 2005; Hao et al., 2007). For certain isolated NP structures, the enhancement of the near-field is highly dependent on the polarization of the incident light and the size of the NPs (Nie and Emory, 1997; Mia et al., 2019), and the effect of the enhancement is relatively lower compared with the cluster structure. For the cluster structure, the aggregation of the small particles generates lots of the hot spot, which effectively improves the intensity of the surrounding EM field (Adams et al., 2012). Furthermore, the cluster structure also has a low dependency to the polarization variation of the incident light, which simplifies the experimental condition, making it a more efficient enhancement system.

In this paper, different agglomeration types of Au-Ag alloy NPs are employed to investigate the enhancement effect of the fluorescence and Raman signal. Three different thickness levels of the SiO_2 layer are coated on the alloy NPs and clusters to explore the optimized enhancement system for the fluorescence and Raman signal, respectively. The power dependence of the fluorescence and Raman signal are also studied on [Au-Ag alloy NP cluster]@SiO_2 core-shell nanostructure with different shell thickness. This work offers a convenient non-polarization dependent Au-Ag alloy cluster system to enhance both the fluorescence emission and Raman scattering, which have the promising application potential in portable chemical or biochemistry detecting.

EXPERIMENT

Sodium citrate reduction method (Lee and Meisel, 1982) are used in synthesizing citrate-reduced Au-Ag alloy NPs. First, Aqueous solution of $AgNO_3$ (99.8%) and $HAuCl_4 \cdot 4H_2O$, (99%) are added in proportion into boiled deionized water and keeping reaction for 10 min, then the reductant Sodium citrate (99%) is added and heating is continued for 15 min. Finally, isolated alloy NPs can be obtained after centrifugation (8,000 r/min) and washing with deionized water. We can get the alloy clusters by washing with ethyl alcohol and increasing the rpm (12,000 r/min) during a repeating washing-centrifuging cycle. It should be noted that centrifugal speed and washing solution need to be controlled in order to control the dispersion of the obtained NPs.

The modified Stöber method (Lu et al., 2002; Lessard-Viger et al., 2009) is used to coat the SiO_2 shell on Au-Ag alloy NPs or clusters. The obtained Au-Ag alloy NPs (clusters) are dissolved in isopropyl alcohol (99.7%) and heated to 40°C. Then deionized water, ammonium hydroxide (25%) and tetraethyl orthosilicate (28.5%) are added into the colloid and keeping reaction for 3.5 h with continuous stirring. The amount of silica precursor (tetraethyl orthosilicate) is important to the thickness of the silica shell. After washing with ethanol and deionized water, the obtained core-shell structures are dispersed in deionized water and mixed with probe molecules (Rh6G). Then the mixture solution after ultrasonic agitation was left to stand in the dark for 2 days at room temperature, in order to achieve a uniformly coated fluorophore molecule on the surface of the shell. The excess molecule in the solution can be removed by washing several times.

RESULTS AND DISCUSSION

With different ratios of the Au and Ag content, the SPR peak can be easily tuned from 400 to 530 nm (**Figure 1A**). The 1:1 ratio of the Au and Ag is chosen in the following parts, and corresponding elemental distribution is obtained through the energy dispersive X-ray (EDX) elemental mapping. As shown in **Figures 1B–D**, the elemental mapping image (**Figures 1B–D**) of Au-Ag alloy NPs shows that the ratio of the Au and Ag content is 1:1. Besides, the morphology of the obtained isolated Au-Ag alloy NPs, Au-Ag alloy NP clusters, [isolated Au-Ag alloy NP]@SiO_2 and [Au-Ag alloy NP cluster]@SiO_2 core-shell structure are characterized with TEM. As shown in **Figure 2A**, the uniform-sized Au-Ag alloy isolated nanospheres are synthesized with high dispersity. The thickness controllable SiO_2 layer can be evenly coated on the surface of the Au-Ag alloy nanospheres (**Figure 2B**). **Figure 2C** shows the morphology of the Au-Ag alloy cluster which is composed with the uniform sized Au-Ag alloy nanospheres, and corresponding SiO_2 coated structure is shown in **Figure 2D**. Meanwhile, the different thickness of the SiO_2 layer can also be selectively coated on the cluster.

In order to evaluate the ability of the enhancement on Raman scattering and fluorescence emission of different system, Rh6G molecule is chosen as a fluorescence/Raman detecting molecule, which is uniformly absorbed on the surface of SiO_2 layer. Here we choose [isolated Au-Ag alloy NP]@SiO_2 system (**Figure 2A**) to compare with the [Au-Ag alloy NP cluster]@SiO_2 system (**Figure 2C**). Both above systems are coated with Rh6G in same concentration. Surface enhanced Raman scattering (SERS) and surface enhanced fluorescence (SEF) spectra were investigated with quantitative core-shell particles system. The number of molecules absorbed on the surface of the SiO_2 is different due to the different surface area. Thus, all the spectra are normalized with the surface area, and signal intensity is from the per unit area of the surface.

Three different levels of thickness (2, 8, and 15 nm) of SiO_2 shell are selectively chosen to investigate the sensitivity of SERS/SEF effect. SEF spectra of single [isolated Au-Ag alloy NP]@SiO_2 (**Figure 3A**) and multiple tightly distributed shell isolated core-shell NPs (**Figure 3B**) with different shell thickness is shown in **Figures 3C,D**. It is obvious that the fluorescence signal is effectively enhanced in the core-shell system, especially for the 8 nm SiO_2 coated system. However, no obvious SERS signal could be detected in both two spectra, which means that the Raman scattering cannot be effectively enhanced and observed by the above single Au-Ag alloy NPs@SiO_2 shell isolated NP or multiple tightly distributed shell isolated core-shell NPs.

Figure 4 shows the enhancement effect of Raman and fluorescence signal of the [Au-Ag alloy NP cluster]@SiO_2 system. As shown in **Figures 4A–C**, three different thickness levels of the

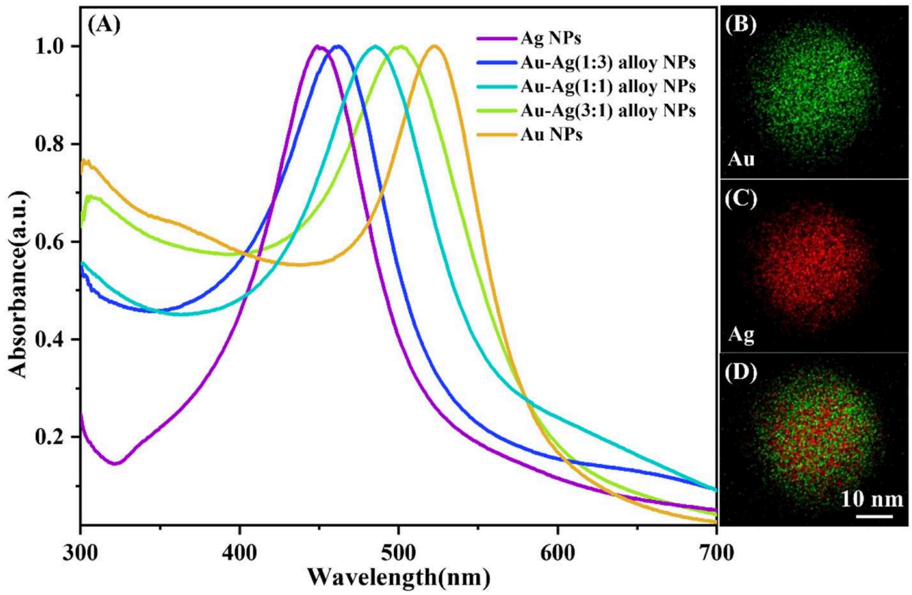

FIGURE 1 | (A) Absorption spectra of pure Au and Ag nanospheres, and bimetallic Au-Ag alloy nanospheres with different ratio of gold to silver 1:3, 1:1, and 3:1. STEM-EDX elemental mapping image of Au-Ag alloy NP with the ratio of gold to silver 1:1, where the green represents Au **(B)**, red represents Ag **(C)**, and the merged image **(D)** from single Au-Ag alloy nanoparticle.

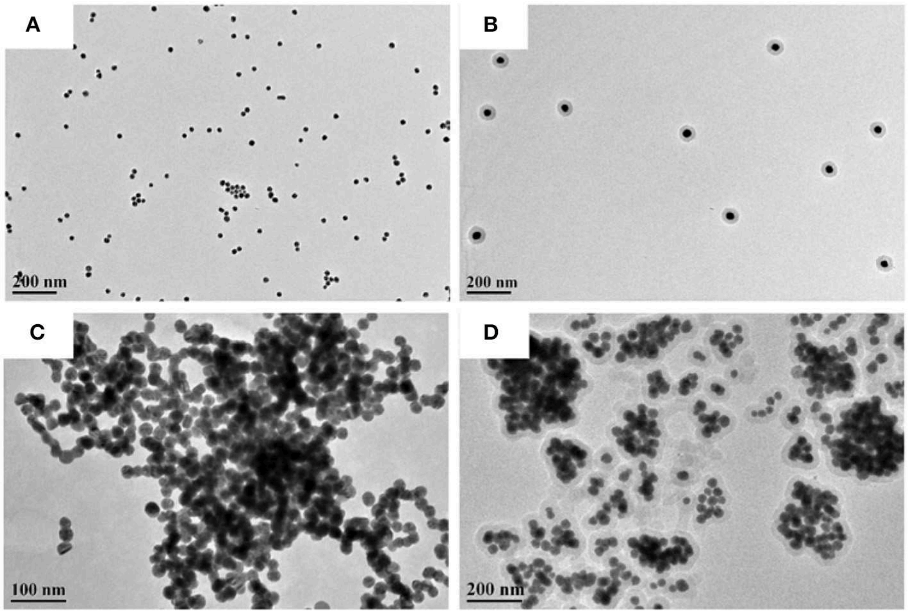

FIGURE 2 | TEM images of **(A)** isolated Au-Ag alloy NPs. **(B)** [isolated Au-Ag alloy NP]@SiO_2. **(C)** Au-Ag alloy NP cluster. **(D)** [Au-Ag alloy NP cluster]@SiO_2.

SiO_2 layer (2, 8, and 15 nm) are evenly coated on the Au-Ag alloy cluster. **Figures 4D–F** show the power-dependence *in-situ* spectra of the corresponding samples shown in **Figures 4A–C**. When the thickness of the SiO_2 is 2 nm (**Figure 4D**), both Raman and fluorescence signal are obviously enhanced by the system. As the laser power decreases, the intensity of the Raman scattering and fluorescence emission have obvious damping, but the Raman signal can still be clearly observed under the lowest power excitation, which results in the high intensity EM field generated by the alloy cluster. When comparing to the spectra of **Figures 4E**,**F** that were obtained from the cluster coated with thicker SiO_2, the fluorescence intensity of the cluster

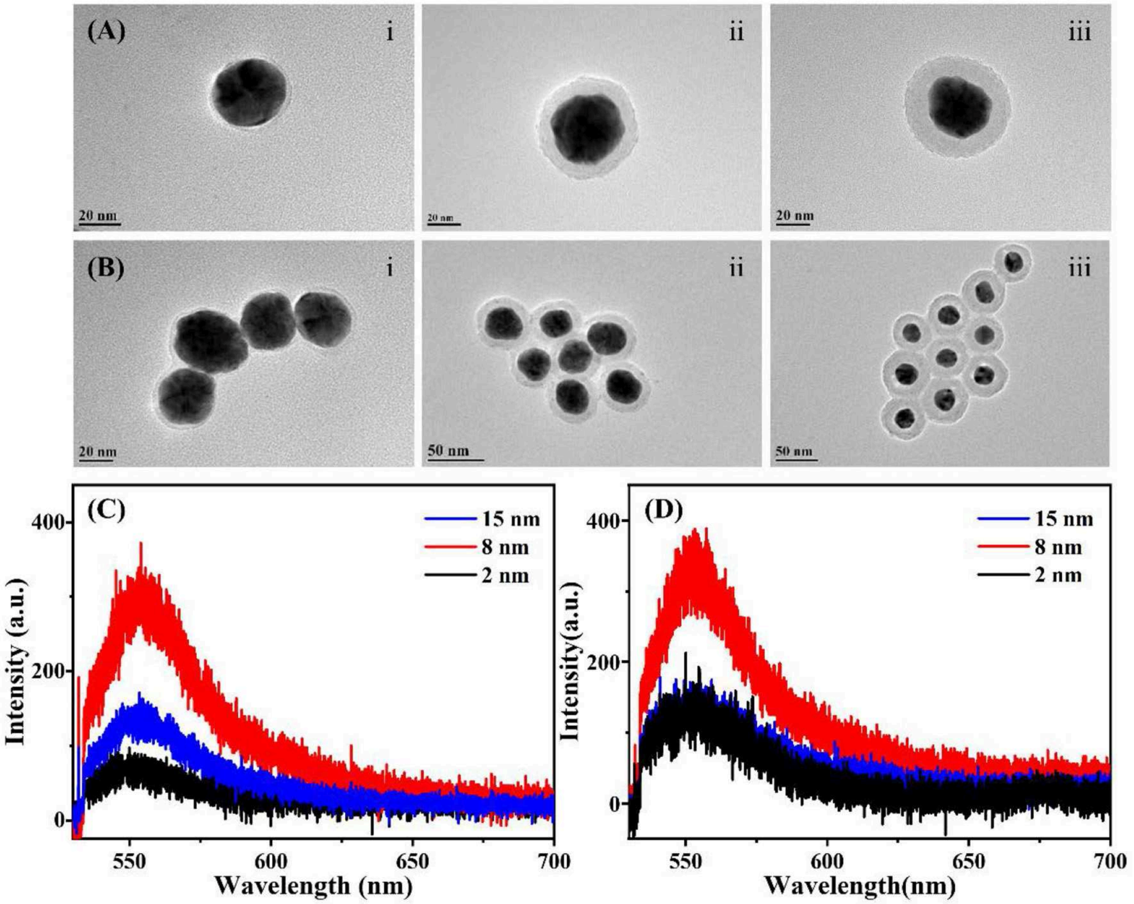

FIGURE 3 | TEM images and SEF spectra of Au-Ag alloy@SiO_2 shell isolated system with different thickness of SiO_2 layer. **(A)** [Isolated Au-Ag alloy NP]@SiO_2 with the SiO_2 layer of 2 nm (i); 8 nm (ii); 15 nm (iii), respectively. **(B)** Aggregated [isolated Au-Ag alloy NP]@SiO_2 core-shell structure with the SiO_2 layer of 2 nm (i); 8 nm (ii); 15 nm (iii), respectively. **(C)** SEF spectra of the single [isolated Au-Ag alloy NP]@SiO_2 core-shell NP with different SiO_2 layer shown in **(A)**. **(D)** SEF spectra of a certain number of closely arranged core-shell NPs with different SiO_2 layer shown in **(B)**.

coated with 2 nm SiO_2 is obviously lower under the same power laser excitation, which is attributed to the quenching effect of SPR. When the molecules are located in the vicinity of the plasmonic metal NPs, the fluorescence emission intensity will be affected by many factors, such as the enhanced local field and the energy transfer between the molecule and plasmonic metal and the field. In general, the local EM field brings with it the enhancement effect of the excitation of molecules, while the effect of energy exchange between metal and molecules on SEF will change from quenching to enhancement with an increase of spacing (Zhang et al., 2016). The EM fields are confined at the surface of the shell, as its spatially inhomogeneous distribution is dramatically decayed with increased thickness of the SiO_2, and the overall SEF results is dependent on the competition effects between the excitation enhancement and quenching effect. Alloy NP cluster coated with 8 nm SiO_2 shows the best enhancement effect on the fluorescence of the Rh6G molecular (**Figure 4E**). For the optimized shell thickness (8 nm) of SEF, it is interesting that the SERS signal cannot be observed under the relative high-power excitation, due to the ultra-high enhanced fluorescence emission that may cover the SERS signal. Thus, it can be seen that the Raman scattering can only be obviously observed between the power of 0.9×10^5 and 3×10^5 W with the 8 nm shell. Moreover, as for the [Au-Ag alloy NP cluster]@SiO_2 with 15 nm silica layer, because the EM enhancement is too weak at the surface of shell far away from the cluster, both the Raman and fluorescence signal cannot be effectively enhanced.

Comparing the influence of the SiO_2 layer to the SERS/SEF intensity under different power excitation, Raman scattering and fluorescence emission intensity of the Rh6G molecules are obtained from the per unit area of the molecules adsorbed on the surface of the SiO_2. **Figure 5** shows the relation between the fluorescence (Raman) intensity and the laser power of different thickness of SiO_2 coated Au-Ag NP cluster. As shown in **Figure 5A**, due to the fluorescence quenching effect with thin shell (2 nm) and the far distance with the EM enhanced field with thicker shell (15 nm), Au-Ag alloy NP

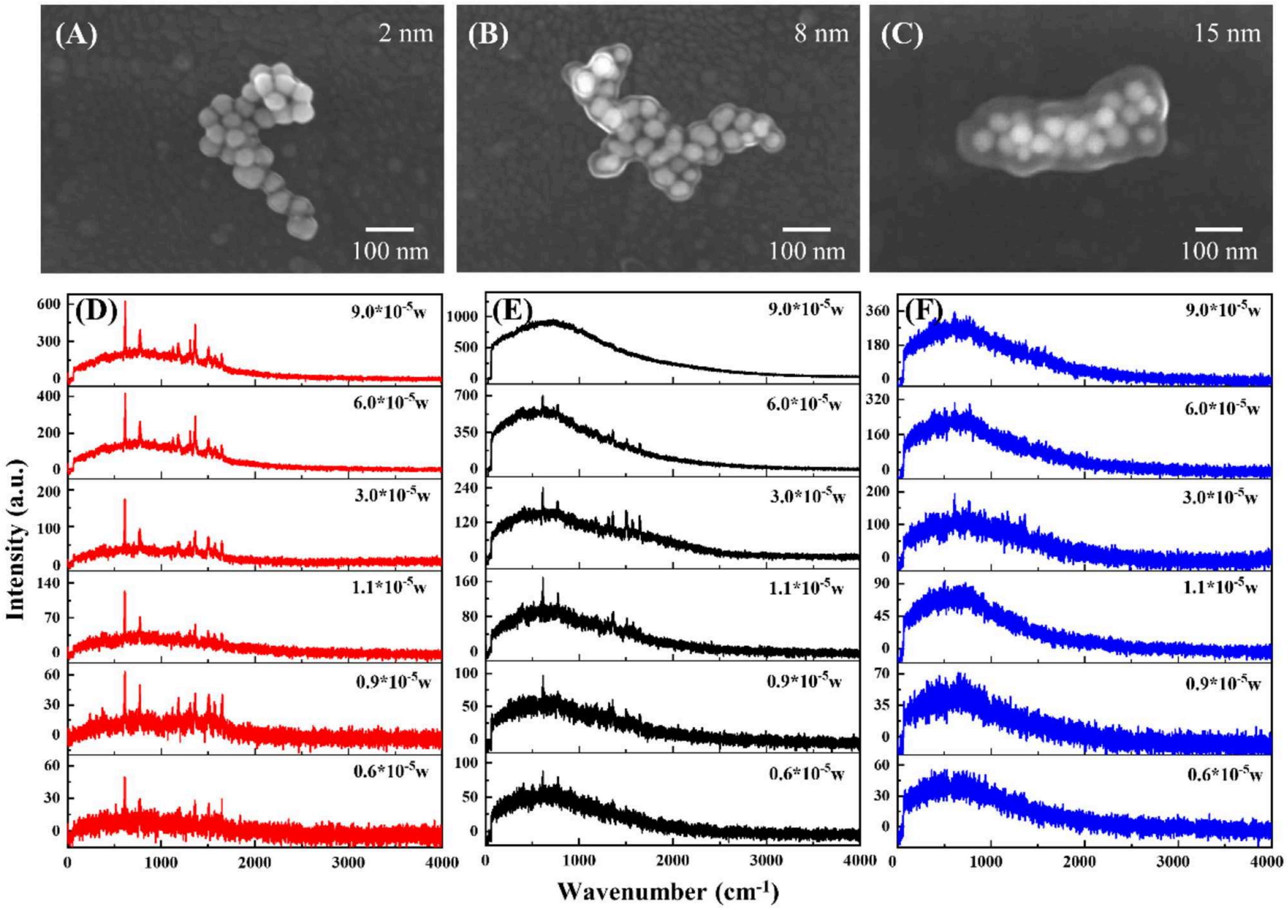

FIGURE 4 | SEM images of [Au-Ag alloy NP cluster]@SiO$_2$ core-shell nanostructure with the SiO$_2$ layer of 2 nm **(A)**, 8nm **(B)** and 15 nm **(C)**, respectively. Raman spectra of [Au-Ag alloy NP cluster]@SiO$_2$ under different laser power excitation with the SiO$_2$ layer of 2 nm **(D)**, 8 nm **(E)** and 15 nm **(F)**, respectively.

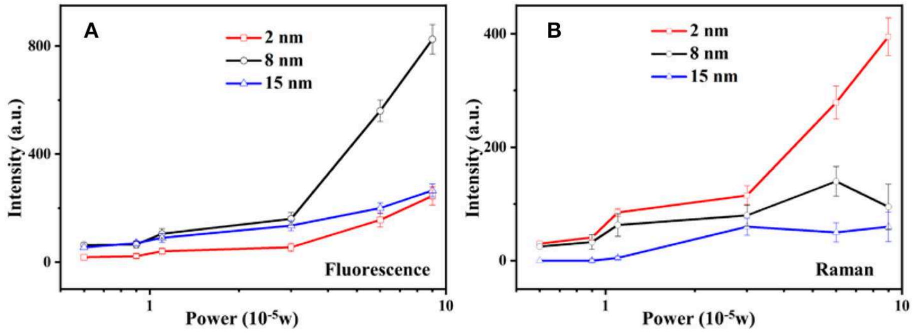

FIGURE 5 | Power dependence of the intensity of SEF **(A)** and SERS **(B)** with [Au-Ag alloy NP cluster]@SiO$_2$ core-shell structure.

cluster coated with 8 nm silica shell is the optimized system for the fluorescence enhancement. **Figure 5B** indicates the relation between the Raman intensity and the laser power. Different from the fluorescence emission, the intensity of Raman scattering demonstrates a positive correlation to the intensity of the biquadrate of the EM field ($|E|^4$). Thus, NP cluster coated with 2 nm silica shell shows the great performance in SERS. Nevertheless, in core-shell structure, to get the high quality of the SERS signal, the influence of fluorescence has to be excluded due to the fluorescence signal coverage to the Raman signal. The alloy NP cluster coated with 8 nm shows a great performance in fluorescence enhancement, which means it is unsuitable for the SERS enhancement system. The anticlimactic intensity of the Raman scattering at the largest power excitation, shown as the black line, results in the competition between the fluorescence and Raman signal.

CONCLUSION

Isolated Au-Ag alloy NPs and Au-Ag alloy NP clusters are employed to investigate and compare the enhancement effect of the fluorescence and Raman signal. Rh6G molecular with the same concentration are absorbed on three different thickness levels of the SiO_2 layer which is coated on the Au-Ag alloy NPs and clusters. Under the same power laser excitation, the single [isolated Au-Ag alloy NP]@SiO_2 particle and their aggregates cannot effectively enhance the Raman scattering of the adsorbed molecular. However, as seen from the strong near-field enhancement of the alloy NP cluster, both 2 and 8 nm SiO_2 coated cluster system can obviously enhance the Raman signal, and Au-Ag alloy NP cluster with 8 nm silica shell shows the best performance in fluorescence enhancement. This work offers a convenient non-polarization dependent Au-Ag alloy NP cluster system to enhance both the fluorescence and Raman signal, which have promising application potentials in portable chemical or biochemical detection.

DATA AVAILABILITY STATEMENT

All datasets generated for this study are included in the manuscript/supplementary files.

AUTHOR CONTRIBUTIONS

CZ and HZ conceived the idea. CZ did the experiment and the measurement. CZ and TZ discussed and analyzed the results. TZ and CZ wrote the paper. All the authors revised the paper.

FUNDING

This work was supported by the National Natural Science Foundation of China (Grant 11574190), the Fundamental Research Funds for the Central Universities (GK201701008, No. 2017TS013, 2018CSLZ001).

REFERENCES

Adams, S. M., Campione, S., Caldwell, J. D., Bezares, F. J., Culbertson, J. C., Capolino, F., et al. (2012). Non-lithographic SERS substrates: tailoring surface chemistry for Au nanoparticle cluster assembly. *Small* 8, 2239–2249. doi: 10.1002/smll.201102708

Ando, J., Fujita, K., Smith, N. I., and Kawata, S. (2011). Dynamic SERS imaging of cellular transport pathways with endocytosed gold nanoparticles. *Nano Lett.* 11, 5344–5348. doi: 10.1021/nl202877r

Chen, Y., and Ming, H. (2012). Review of surface plasmon resonance and localized surface plasmon resonance sensor. *Photonic Sens.* 2, 37–49. doi: 10.1007/s13320-011-0051-2

Christopher, P., Xin, H., and Linic, S. (2011). Visible-light-enhanced catalytic oxidation reactions on plasmonic silver nanostructures. *Nat. Chem.* 3:467. doi: 10.1038/nchem.1032

Ding, S.-Y., Yi, J., Li, J.-F., Ren, B., Wu, D.-Y., Panneerselvam, R., et al. (2016). Nanostructure-based plasmon-enhanced Raman spectroscopy for surface analysis of materials. *Nat. Rev. Mater.* 1:16021. doi: 10.1038/natrevmats.2016.21

Gao, C., Hu, Y., Wang, M., Chi, M., and Yin, Y. (2014). Fully alloyed Ag/Au nanospheres: combining the plasmonic property of Ag with the stability of Au. *J. Am. Chem. Soc.* 136, 7474–7479. doi: 10.1021/ja502890c

Han, L., Li, C., Zhang, T., Lang, Q., and Liu, A. (2015). Au@Ag heterogeneous nanorods as nanozyme interfaces with peroxidase-like activity and their application for one-pot analysis of glucose at nearly neutral pH. *ACS Appl. Mater. Interfaces* 7, 14463–14470. doi: 10.1021/acsami.5b03591

Han, Q., Zhang, C., Gao, W., Han, Z., Liu, T., Li, C., et al. (2016). Ag-Au alloy nanoparticles: synthesis and *in situ* monitoring SERS of plasmonic catalysis. *Sens. Actu. B Chem.* 231, 609–614. doi: 10.1016/j.snb.2016.03.068

Hao, F., Nehl, C. L., Hafner, J. H., and Nordlander, P. (2007). Plasmon resonances of a gold nanostar. *Nano Lett.* 7, 729–732. doi: 10.1021/nl062969c

Homola, J., Yee, S. S., and Gauglitz, G. (1999). Surface plasmon resonance sensors: review. *Sens. Actu. B Chem.* 54, 3–15. doi: 10.1016/S0925-4005(98)00321-9

Kuladeep, R., Jyothi, L., Alee, K. S., Deepak, K. L. N., and Rao, D. N. (2012). Laser-assisted synthesis of Au-Ag alloy nanoparticles with tunable surface plasmon resonance frequency. *Opt. Mater. Exp.* 2, 161–172. doi: 10.1364/OME.2.000161

Lee, P., and Meisel, D. (1982). Adsorption and surface-enhanced Raman of dyes on silver and gold sols. *J. Phys. Chem.* 86, 3391–3395.

Lessard-Viger, M., Rioux, M., Rainville, L., and Boudreau, D. (2009). FRET enhancement in multilayer core–shell nanoparticles. *Nano Lett.* 9, 3066–3071. doi: 10.1021/nl901553u

Li, C., Wang, C., Han, Q., Wu, Y., and Zheng, H. (2017). Investigation on optical properties of Ag–Au alloy nanoparticles. *Plasmonics* 12, 1373–1379. doi: 10.1007/s11468-016-0396-x

Li, J. F., Huang, Y. F., Ding, Y., Yang, Z. L., Li, S. B., Zhou, X. S., et al. (2010). Shell-isolated nanoparticle-enhanced Raman spectroscopy. *Nature* 464:392. doi: 10.1038/nature08907

Liu, A., Wang, G., Wang, F., and Zhang, Y. (2017). Gold nanostructures with near-infrared plasmonic resonance: Synthesis and surface functionalization. *Coord. Chem. Rev.* 336, 28–42. https://doi.org/10.1016/j.ccr.2016.12.019

Liu, S., Chen, G., Prasad, P. N., and Swihart, M. T. (2011). Synthesis of Monodisperse Au, Ag, and Au–Ag Alloy nanoparticles with tunable size and surface plasmon resonance frequency. *Chem. Mater.* 23, 4098–4101. doi: 10.1021/cm201343k

Lu, Y., Yin, Y., Mayers, B. T., and Xia, Y. (2002). Modifying the surface properties of superparamagnetic iron oxide nanoparticles through a sol–gel approach. *Nano Lett.* 2, 183–186. doi: 10.1021/nl015681q

Mia, X., Wang, Y., Li, R., Sun, M., Zhang, Z., and Zheng, H. (2019). Multiple surface plasmon resonances enhanced nonlinear optical microscopy. *Nanophotonics* 8, 487–493. doi: 10.1515/nanoph-2018-0231

Ming, T., Zhao, L., Yang, Z., Chen, H., Sun, L., Wang, J., et al. (2009). Strong polarization dependence of plasmon-enhanced fluorescence on single gold nanorods. *Nano Lett.* 9, 3896–3903. doi: 10.1021/nl902095q

Nie, S., and Emory, S. R. (1997). Probing single molecules and single nanoparticles by surface-enhanced raman scattering. *Science* 275, 1102–1106. doi: 10.1126/science.275.5303.1102

Rioux, D., Vallières, S., Besner, S., Muñoz, P., Mazur, E., and Meunier, M. (2014). An analytic model for the dielectric function of Au, Ag, and their Alloys. *Adv. Opt. Mater.* 2, 176–182. doi: 10.1002/adom.201300457

Rosman, C., Prasad, J., Neiser, A., Henkel, A., Edgar, J., and Sönnichsen, C. (2013). Multiplexed plasmon sensor for rapid label-free analyte detection. *Nano Lett.* 13, 3243–3247. doi: 10.1021/nl401354f

Schietinger, S., Aichele, T., Wang, H.-Q., Nann, T., and Benson, O. (2010). Plasmon-enhanced upconversion in single $NaYF4:Yb^{3+}/Er^{3+}$ codoped nanocrystals. *Nano Lett.* 10, 134–138. doi: 10.1021/nl903046r

Sherry, L. J., Chang, S.-H., Schatz, G. C., Van Duyne, R. P., Wiley, B. J., and Xia, Y. (2005). Localized surface plasmon resonance spectroscopy of single silver nanocubes. *Nano Lett.* 5, 2034–2038. doi: 10.1021/nl0515753

Talley, C. E., Jackson, J. B., Oubre, C., Grady, N. K., Hollars, C. W., Lane, S. M., et al. (2005). Surface-enhanced raman scattering from individual Au nanoparticles and nanoparticle dimer substrates. *Nano Lett.* 5, 1569–1574. doi: 10.1021/nl050928v

Tsukamoto, D., Shiro, A., Shiraishi, Y., Sugano, Y., Ichikawa, S., Tanaka, S., et al. (2012). Photocatalytic H_2O_2 production from Ethanol/O_2 system using TiO_2 Loaded with Au–Ag bimetallic alloy nanoparticles. *ACS Catal.* 2, 599–603. doi: 10.1021/cs2006873

Vadai, M., Angell, D. K., Hayee, F., Sytwu, K., and Dionne, J. A. (2018). *In-situ* observation of plasmon-controlled photocatalytic dehydrogenation of individual palladium nanoparticles. *Nat. Commun.* 9:4658. doi: 10.1038/s41467-018-07108-x

Wang, F., Liu, P., Sun, L., Li, C., Petrenko, V. A., and Liu, A. (2014). Bio-mimetic nanostructure self-assembled from Au@Ag heterogeneous nanorods and phage fusion proteins for targeted tumor optical detection and photothermal therapy. *Sci. Rep.* 4:6808. doi: 10.1038/srep06808

Wang, X. A., and Kong, X. (2015). Review of recent progress of plasmonic materials and nano-structures for surface-enhanced raman scattering. *Materials* 8, 3024–3052. doi: 10.3390/ma8063024

Zhang, C., Han, Q., Li, C., Zhang, M., Yan, L., and Zheng, H. (2016). Metal-enhanced fluorescence of single shell-isolated alloy metal nanoparticle. *Appl. Opt.* 55, 9131–9136. doi: 10.1364/AO.55.009131

Zhang, X., Li, X., Reish, M. E., Zhang, D., Su, N. Q., Gutiérrez, Y., et al. (2018). Plasmon-enhanced catalysis: distinguishing thermal and nonthermal effects. *Nano Lett.* 18, 1714–1723. doi: 10.1021/acs.nanolett.7b04776

Conflict of Interest: The authors declare that the research was conducted in the absence of any commercial or financial relationships that could be construed as a potential conflict of interest.

frontiers in Chemistry

ORIGINAL RESEARCH
published: 25 October 2019
doi: 10.3389/fchem.2019.00706

A Surface-Enhanced Raman Spectral Library of Important Drugs Associated With Point-of-Care and Field Applications

Stuart Farquharson*, Carl Brouillette, Wayne Smith and Chetan Shende

Real-Time Analyzers, Inc., Middletown, CT, United States

During the past decade, the ability of surface-enhanced Raman spectroscopy (SERS) to measure extremely low concentrations, such as mg/L and below, and the availability of hand-held Raman spectrometers, has led to a significant growth in the number and variety of applications of SERS to real-world problems. Most of these applications involve the measurement of drugs, such as quantifying medication in patients, identifying illicit drugs in impaired drivers, and more recently, identifying drugs used as weapons. Similar to Raman spectroscopy, most of the point-of-care and field applications involve the identification of the drug to determine the course of action. However, unlike Raman spectroscopy, spectral libraries are not readily available to perform the necessary identification. In a large part, this is due to the uniqueness of the commercially available SERS substrates, each of which can produce different spectra for the same drug. In an effort to overcome this limitation, we have measured numerous drugs using the most common, and readily available SERS material and hand-held Raman analyzers, specifically gold colloids and analyzers using 785 nm laser excitation. Here we present the spectra of some 39 drugs of current interest, such as buprenorphine, delta-9 tetrahydrocannabinol, and fentanyl, which we hope will aid in the development of current and future SERS drug analysis applications.

Keywords: opioids, buprenorphine, cannabis, fentanyl, SERS, drug analysis, trace analysis, spectral library

OPEN ACCESS

Edited by:
John Lombardi,
City College of New York (CUNY),
United States

Reviewed by:
Hui Xu,
Ludong University, China
Lingxin Chen,
Yantai Institute of Coastal Zone Research (CAS), China

****Correspondence:***
Stuart Farquharson
stu@rta.biz

Specialty section:
This article was submitted to Analytical Chemistry,
a section of the journal
Frontiers in Chemistry

Received: *23 May 2019*
Accepted: *08 October 2019*
Published: *25 October 2019*

Citation:
Farquharson S, Brouillette C, Smith W and Shende C (2019) A Surface-Enhanced Raman Spectral Library of Important Drugs Associated With Point-of-Care and Field Applications. Front. Chem. 7:706.
doi: 10.3389/fchem.2019.00706

INTRODUCTION

One of the most important applications of analytical chemistry is the analysis of drugs. Raman spectroscopy became an important tool for this application in its ability to quantify active and inactive pharmaceutical ingredients in manufactured products beginning in the 1990s (Tensmeyer and Heathman, 1989; Tudor et al., 1990; Cutmore and Skett, 1993; Petty et al., 1996; McCreery et al., 1998; Fini, 2004), and its ability to identify illicit and counterfeit products sold over the internet in the past two decades (Ryder et al., 1999; Carter et al., 2000; Bell et al., 2004; de Veij et al., 2008; Sacré et al., 2010; Lanzarotta et al., 2017). However, three significant events have occurred in the past 5 years that require the analysis of trace amounts of drugs. First, the over prescription of opioids contributed to 63,000 overdose fatalities in 2016 (Media Relations, 2018). Second, fentanyl is illegally entering the USA (U.S. Customs and Border Protection, 2019), where it is added to cocaine and heroin, contributing to approximately one third of the 2016 drug-related fatalities (Jones et al., 2018), and as of 2019 it is considered a form of terrorism by the USA Department of

Homeland Security (DHS) (Hoffman et al., 2019). Third, the legalization of marijuana for medical, as well as recreational use in many states (Sanders, 2018) and cannabidiol for purported health benefits (Kelman and Sharp, 2018), has led to their ever increasing legal and illegal use in everyday products, such as food, beverages, and oils (Sanders, 2019). In the first case, ambulance and hospital physicians need methods to rapidly identify and quantify opioids in overdose patients. In the second case the DHS needs simple and fast methods to detect fentanyl in merchandise entering the country. In the third case the Food and Drug Administration needs methods to verify the identity and quantity of cannabinoids in medical, recreational, as well as new food and beverage products. The ability of surface-enhanced Raman spectroscopy (SERS) to measure extremely low concentrations, such as mg/L and below, could soon be the method of choice for these trace drug analysis needs.

The potential of SERS to perform such analyses began with the measurement of nitrogen- and sulfur-containing drugs in the late 1980s and early 1990s (Torres and Winefordner, 1987; Sutherland et al., 1990). The first forensic samples were measured at the turn of the century (Perez et al., 1998; Angel et al., 1999; Sägmüller et al., 2001; Faulds et al., 2002; Pînzaru et al., 2004; Ryder, 2005), followed quickly by measurement of drugs in body fluids (Perez et al., 1998; Farquharson and Lee, 2000; Trachta et al., 2004a). We began measuring chemotherapy and illicit drugs in saliva a few years later (Farquharson et al., 2005, 2011; Shende et al., 2005; Inscore et al., 2011; Dana et al., 2015), and more recently, measuring opioid treatment drugs in the saliva of USA military veterans (Farquharson et al., 2017, 2019), as well as fentanyl in saliva and blood (Shende et al., 2019).

During the development of these applications we noticed a lack of SERS publications for these and other drugs of interest. Furthermore, most of the available spectra were obtained using author-unique substrates and various excitation wavelengths that resulted in spectra that are incomparable. Therefore, we measured 39 drugs of interest using the most common and readily available SERS-active material, gold colloids, and using the most common excitation wavelength of portable Raman spectrometers, 785 nm. Here we present a spectral library of numerous opioids, illicit and treatment drugs, as well as some important metabolites, which would be suitable for identification of samples using either field or point-of-care Raman spectrometers.

MATERIALS AND METHODS

All solvents and chemicals used to prepare samples and colloids were obtained from Sigma-Aldrich (St. Louis, MO). The drugs used to prepare the spectral library were purchased as 1 mg/mL acetonitrile or methanol certified forensic samples obtained from Cerilliant Corp (Round Rock, TX). Drug samples were prepared by diluting the forensic samples by a factor of 5 in HPLC grade water and then added to an equal volume of colloid to make 0.1 mg/mL (100 ppm) initial concentrations, which were in some cases further diluted with water (see figure captions). The gold colloids used for SERS were synthesized following a modified Lee-Meisel method (Lee and Meisel, 1982). Briefly, a solution of 0.005 M $HAuCl_4$ (100 mL), was slowly added to 300 mL of 0.02 M $NaBH_4$ in an ice bath. A solution of 1% polyvinyl alcohol (50 mL) was added and refluxed for 1 h. 0.5 M NaCl was used as an aggregating agent. The solutions were placed in 2 mL glass vials from Glass Vials Company (Hanover, MD) and then measured using ∼30 mW of 785 nm laser excitation with an in-house Raman spectrometer and collection software (RTA LabRaman and Vista). Each presented spectrum is the average of five 1-s integrations. In some cases a glass sample vial spectrum was subtracted to flatten the baseline between 1,100 and 1,700 cm^{-1}. All spectral peaks are given to the nearest 5 cm^{-1}.

RESULTS AND DISCUSSION

The spectra are, in general, presented in the following order: opioids, synthetic opioids, stimulants, sedatives, cannabinoids, and common drugs. A basic background is provided for each drug to provide a framework for why its analysis at low concentrations is important. Each figure, as best possible, contains three drugs that share the same basic chemical structure so that their spectra can be compared.

Opioids

In simplest terms opioids influence the release and uptake of neurotransmitters at one or more of the delta-, mu-, kappa-, and zeta-opioid receptors (Corbett et al., 2006), involved in the reward (pleasure) pathway in the brain and the pain pathway in both the brain and spinal cord. The opioids have structures similar to the neurotransmitter dopamine associated with the reward pathway and the neuropeptide endorphins associated with the pain pathway, allowing them to bind to sites on the end of neurons. The effectiveness of the various opioids is also a function of their lipophilicity, the ability to pass through the blood-brain barrier, and their reactivity with the neuron sites associated with the release and uptake of these and other neurotransmitters and neuropeptides. These abilities make opioids ideal for treating depression and pain. Unfortunately, the activity level of these neural chemical and biochemical interactions diminish with repeated opioid use, such that greater amounts are needed to achieve previous levels of pleasure and/or pain relief, which can lead to addiction and dependence.

While the pain relieving powers of opium have been known for thousands of years, the primary active drugs, morphine and codeine, were not isolated until the early 1800s (Courtwright, 2009; Newton, 2015). Today these two natural drugs are used to produce a wide range of semi-synthetic opioid medicines, such as hydrocodone, hydromorphone, oxycodone, and oxymorphone, treatment medicines, such as buprenorphine and naloxone, and the illicit drug heroin. More recently, much more powerful opioids have been synthesized, such as fentanyl and carfentanil.

Heroin is a Schedule I drug, as it does not have any accepted medical use and it has a high potential for abuse (Brandán, 2018). Heroin use resulted in nearly 16,000 deaths in the USA in 2017 (NIH, 2019). It is synthesized by acetylation of morphine, and the product usually contains some 6-acetylcodeine, due to the presence of codeine in the starting solution, as an impurity

(O'Neal et al., 2001). 6-acetylcodeine measured in urine is often used to distinguish between heroin use and prescription opioid use (Staub et al., 2001).

The SERS of heroin, morphine, and 6-acetylecodeine are dominated by peaks at 530, 625–630, 1,215–1,225, 1,270–1,275, 1,440–1,445, and 1,600–1,610 cm^{-1} (**Figure 1**). Based on their similar Raman spectra (Rana et al., 2010; Gardner et al., 2013), these peaks are assigned to c-ring out-of-plane bending plus a- and c-ring CH bending, a-ring C = CH out-of-plane bending, c-ring CCC out-of-plane bending, c-ring CC stretching, d-ring CH_2 scissoring, and c-ring CC stretching. These drugs can be differentiated primarily by their peak intensities between 1,200 and 1,400 cm^{-1}. It is worth noting that the SERS of morphine presented here on gold has many of the same peaks as that reported for silver (Rana et al., 2010). However, the relative intensities are substantially different, likely due to the fact that morphine is protonated at pH 7 at very low concentrations in water [pKa_1 is 8.21 (Lide, 1997)] and attracted more to electronegative gold than electropositive silver, affecting the orientation on the metal surface and interaction with the plasmon field. Furthermore, these orientation-induced spectral differences would challenge the ability of library search-and-match software.

Codeine, hydrocodone, and oxycodone are Schedule II drugs usually prescribed in combination with nonsteroidal anti-inflammatory drugs, such as acetaminophen, aspirin, and ibuprofen, to treat varying degrees of pain. Oxycodone, sold as OxyContin, is currently the most abused opioid, and resulted in ~6,000 deaths in 2017 (Hedegaard et al., 2018; Pergolizzi et al., 2018). The SERS of codeine, hydrocodone, and oxycodone are also dominated by similar peaks at 510–530, 620–640, 1,275, 1,435, and 1,595–1,605 cm^{-1}, and assigned to the same vibrational modes (**Figure 2**) (Rana et al., 2010). Substitution at the juncture of the c, b, and d rings influences the intensity of the CC and CCC bending modes. The drugs also have unique spectral features in the low frequency region between 500 and 850 cm^{-1}, such as the c-ring CH out-of-plane bending mode at 535, 510, and 530 cm^{-1} for the three drugs, respectively. Again, spectral differences were obtained on silver (Rana et al., 2010).

Hydromorphone and oxymorphone are two additional Schedule II opioids used to treat pain, and often prescribed to alleviate pain due to cancer (Sloan, 2008; Pigni et al., 2011). The latter drug has proven highly addictive, and was removed from the market in 2017 at the request of the Food and Drug Administration (Peddicord, 2017).

Not all opioids are used to treat pain and depression, some are used to treat opioid addiction. For example, the chemical structures of naltrexone, naloxone and buprenorphine, are very similar to the above described drugs, and can compete for or block the opioid receptor sites (**Figures 3**, **4**). Naltrexone also has a much greater affinity for opioid sites than morphine, while not generating the euphoria of addicting opioids (Melichar et al., 2003), and is used to treat opioid addiction and overdose patients (Comer et al., 2006; Lynn and Galinkin, 2018). Hydromorphone, oxymorphone, and naltrexone, like codeine and morphine, contain SERS peaks at 625–635, 1,205–1,210, 1,270, 1,445–1,450, and 1,610–1,615 cm^{-1}, and can be assigned to the same vibrational modes. They also have peaks at 485–490, 750, a single or double at 820, 1,030, a shoulder at 1,570, and a weak peak at 1,675–1,695 cm^{-1}, assigned to a-/c-CH bending, out-of-plane C = O bending (Rana et al., 2010), c-ring CH bending, CH_2 rocking, e-ring CN stretch (Socrates, 2001), and a c-ring C = C stretch (Rana et al., 2010). It is worth noting that the spectra of oxymorphone and naltrexone are nearly identical, suggesting that the methylcyclopropane functional group is either non-SERS-active, or directed away from the gold surface due to the attraction of the OH groups. The primary difference between the spectra of these two drugs is the relative peak intensities.

Naloxone is a prescription opioid treatment drug that has opioid site-blocking ability and minimal side-affects similar to naltrexone. However, its high lipophilicity allows it to rapidly pass through the blood-brain barrier, and when taken intravenously can arrest the effects of opioids in 2–5 min (Milne and Jhamandas, 1984). Consequently, it has become the drug of choice for emergency rooms and first responders to treat people who have overdosed, especially those taking fentanyl (Walsh, 2014). As of this year, a nasal spray has been approved for use (Meyer, 2019).

Buprenorphine, a Schedule III drug with a modest potential for abuse, is one of the most successful opioid treatment medications, approved for use in 1981 (Sadock et al., 2012). It has a substantially higher affinity to the mu-opioid receptor, involved in both the reward and pain pathways, but only partially activates the receptor, while it suppresses the kappa-opioid receptor and the associated psychological depression (Khroyan et al., 2015). It is 20–30 times as strong as morphine in relieving pain (DEA, 2013). Furthermore, its low lipophilicity allows it to stay in the cerebrospinal fluid, and coupled with its mean metabolic half-life of 36 h, it provides long-lasting effects that have made it the drug treatment of choice for substance use disorders (Arias and Kranzler, 2008; Urbano et al., 2014). For long term treatment of patients, buprenorphine is combined with naloxone, sold as Suboxone, to prevent the patient from transferring their addiction to buprenorphine (Yassen et al., 2007). One of the challenges in treating patients is compliance. Patients may give into withdrawal symptoms, and re-initiate opioid use. Recently, it has been shown that buprenorphine and its metabolite, norbuprenorphine, can be detected by SERS in saliva (Farquharson et al., 2017, 2019), while other studies indicate that their relative concentrations could be used to determine the time of dosing (Kronstrand et al., 2008).

Naloxone, buprenorphine, and norbuprenorphine, like morphine, contain SERS peaks at 630–640, 810–839, 1,205–1,220, and 1,595–1,620 cm^{-1}, and can be assigned to the same vibrational modes. The spectra of these drugs are unique in the 475–900 cm^{-1} and 1,550–1,650 cm^{-1} regions. While the structures and hence SERS share a lot of similarity for all of these natural and semi-synthetic opioids, spectral search and match software should easily distinguish which one might be in a sample (Farquharson et al., 2011), especially if the search focuses on the 475 to 850 cm^{-1} and the 1,175–1,375 cm^{-1} regions. However, quantifying mixtures would be difficult at best.

Methadone and meperidine, Schedule II drugs, were two of the first fully synthetic opioids, developed in the 1930s

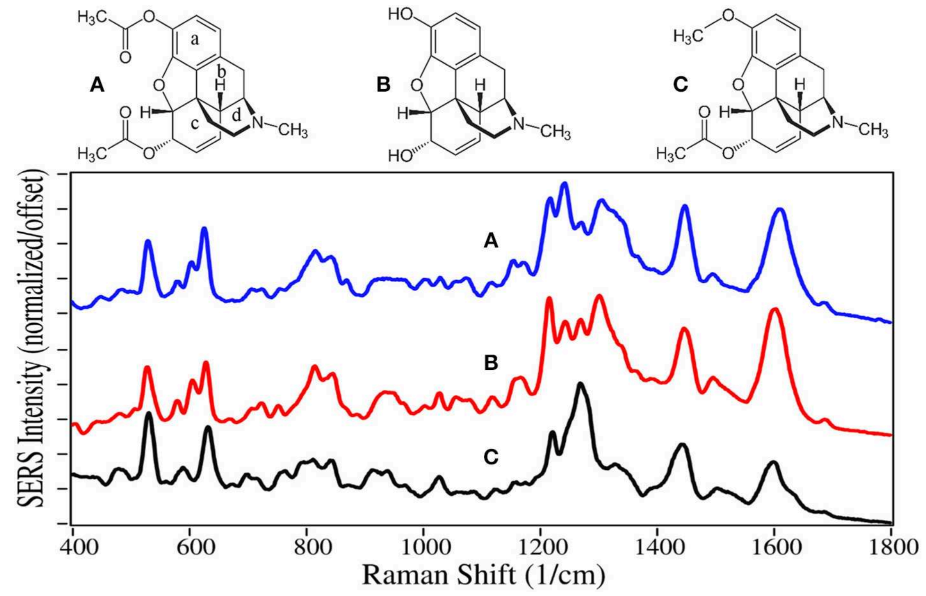

FIGURE 1 | Structures and 10 ppm SERS of **(A)** heroin, **(B)** morphine, and **(C)** 6-acetylcodeine.

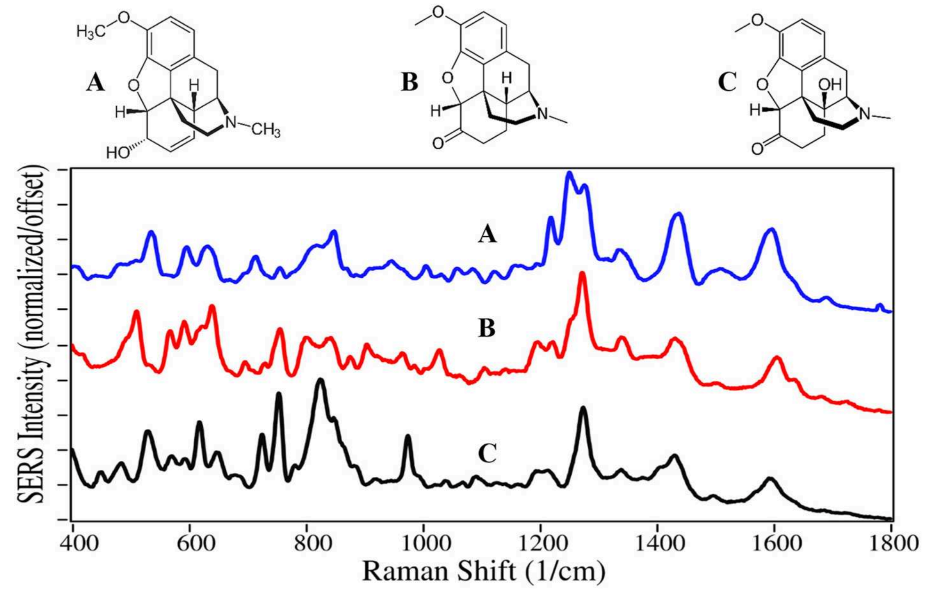

FIGURE 2 | Structures and 100 ppm SERS of **(A)** codeine, **(B)** hydrocodone, and **(C)** oxycodone.

to overcome shortages of codeine, morphine and their semi-synthetic products. While methadone interacts with opioid receptors to alleviate pain, it is primarily used today for opioid maintenance therapy, as it is slow acting with a mean elimination half-life of 22 h (Eap et al., 1999). Meperidine, also known as pethidine and sold as Demerol, was the drug of choice to treat pain during the middle of the last century. However, it was discovered that its metabolite, norpethidine, was toxic (Stone et al., 1993), and it has been replaced by safer drugs. Methylphenidate has a structure nearly identical to meperidine, but has a significantly different pharmacology. It blocks the reuptake of dopamine and norepinephrine by neuron receptors (Kimko et al., 1999), and consequently acts as a stimulant. It is sold as Ritalin to treat attention deficit hyperactivity disorder (ADHD), and has been highly prescribed in the USA during the first part of this century (Pharmaceutical Society, 2015).

Methadone, meperidine, and methylphenadate are all dominated by the symmetric and asymmetric phenyl ring

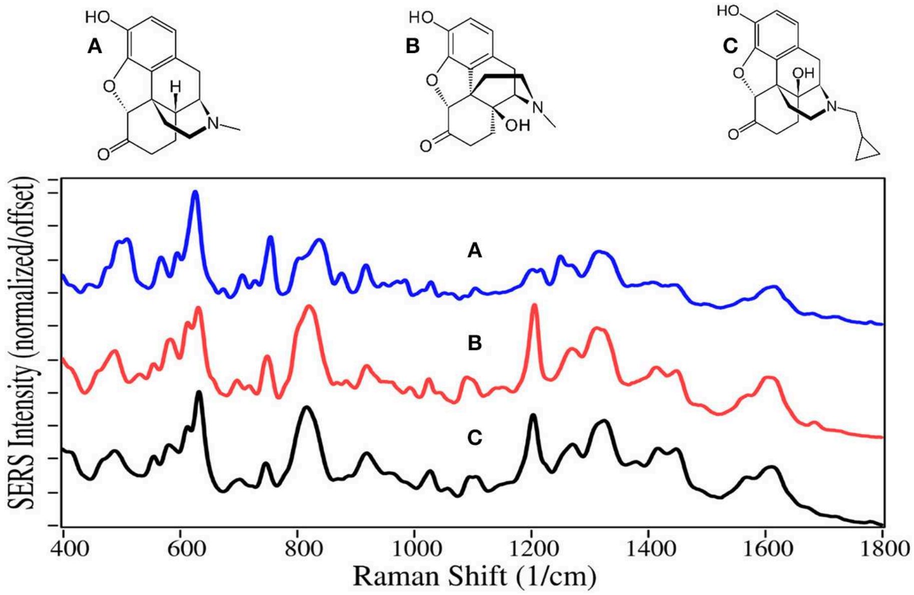

FIGURE 3 | Structures and 100 ppm SERS of **(A)** hydromorphone, **(B)** oxymorphone, and **(C)** naltrexone.

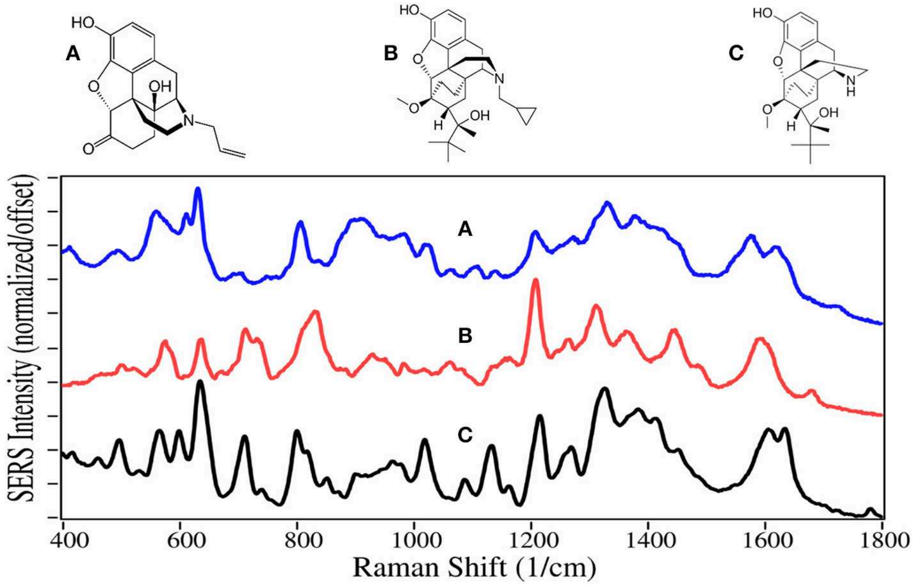

FIGURE 4 | Structures and 100 ppm SERS of **(A)** naloxone, **(B)** buprenorphine, and **(C)** norbuprenorphine.

breathing modes at 1,000 and 1,025–1,035 cm^{-1}, and to some extent the trigonal phenyl ring breathing mode at 1,595–1,600 cm^{-1} (**Figure 5**) (Dollish et al., 1974; Carter et al., 2000). All three drugs have a peak at 910–915 cm^{-1} due to CNC stretching (Stanley, 2014). The same assignments have been given for SERS of methadone, except for the 1,660 cm^{-1} peak, which is assigned to a tertiary amine mode (Stanley, 2014), as opposed to a carbonyl mode that was very intense on silver (Trachta et al., 2004a). While meperidine and methylphenidate have nearly identical structures, the former appears to interact with the gold more strongly having more intense peaks, with many of the same peaks as the normal Raman spectrum (Angel et al., 1999).

In 1960, fentanyl, a Schedule II drug, was synthesized by Paul Janssen by modifying the structure of meperidine to make it more lipophilic so it would rapidly cross the blood-brain barrier, and consequently make its ability to ease pain more powerful (Stanley, 2014). He succeeded in making a drug ∼100 times more potent than morphine. Today fentanyl is widely used as an

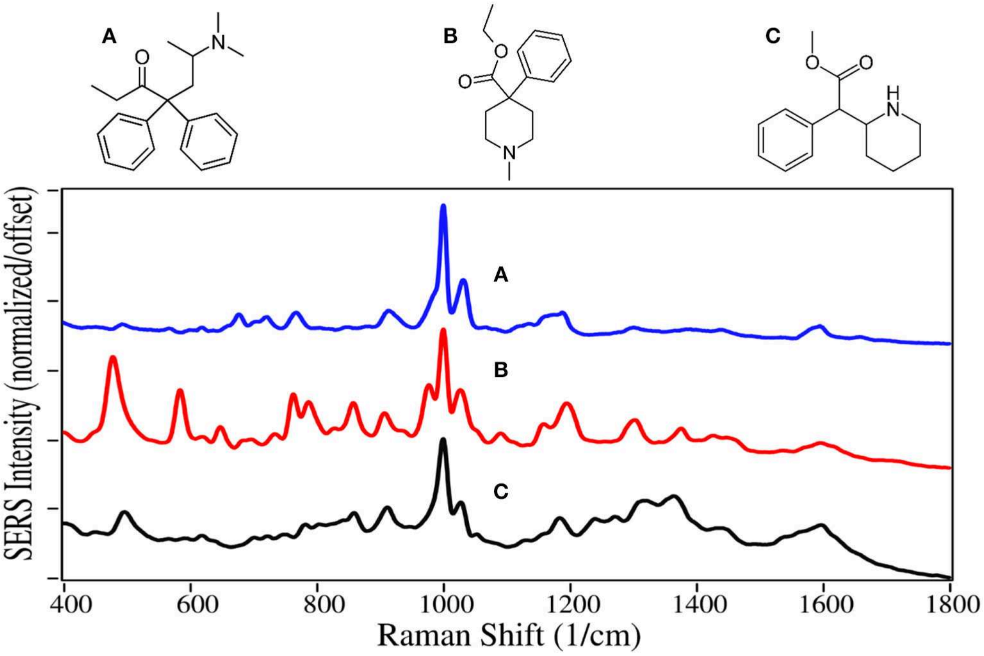

FIGURE 5 | Structures and 100 ppm SERS of **(A)** methadone, **(B)** meperidine, and **(C)** methylphenidate.

anesthetic during surgery, which may include a benzodiazepine sedative, and naloxone after surgery to arrest fentanyl's effects (Comer et al., 2006). Unfortunately, it has become a recreational drug typically mixed with heroin, 250 pounds of which were seized at the Mexican border earlier this year (U.S. Customs and Border Protection, 2019). In 2016 it was responsible for ∼20,000 overdose deaths in the USA (Jones et al., 2018). Furthermore, it and its analogs carfentanil and remifentanil, are considered weapons of war, as the latter two were used by the Russian military to incapacitate rebels in a Moscow theater (Wax et al., 2003; Riches et al., 2012). In 2016 Canadian authorities seized 1 kg of carfentanil sent from China, equivalent to 50 million lethal doses (Kinetz and Butler, 2016). Fortunately, the Chinese government has since banned its sale. While carfentanil's use is limited to tranquilizing animals, remifentanil is used in surgery similar to fentanyl.

SERS for all of these drugs are dominated by the symmetric and asymmetric phenyl ring breathing modes at 1,000 and 1,025–1,035 cm^{-1}, and a modest trigonal phenyl ring breathing mode at 1,595–1,600 cm^{-1} (**Figure 6**) (Stanley, 2014; Leonard et al., 2017). All three drugs also have peaks at 590–620, 830 to 870, and 1,310–1,320 cm^{-1}, which are assigned to a CCC phenyl bending mode (Hummel and Unterwald, 2002), a piperidine C-C mode or out-of-plane phenyl CH stretch, and a piperidine CH mode (Stanley, 2014). While the spectra are very similar, each has several unique features for identification.

Stimulants

This class of drugs also acts upon the central nervous system, primarily by preventing the uptake of the dopamine, serotonin, and norepinephrine (adrenaline) neurotransmitters. This causes their accumulation in the synaptic gap, and thereby continuously stimulates the reward and cognitive (alertness) pathways (Hummel and Unterwald, 2002), and increases blood pressure and heart rate (Zimmerman, 2012). Consequently, these drugs can be highly addictive and dangerous.

Cocaine is a natural product isolated from the coca plant, and has chemical functional groups similar to natural and synthetic opioids, and as such affects the central nervous system as described above. It is the second most used illegal drug in the world behind cannabis (Karila et al., 2014). Approximately 15 million people in the USA use cocaine yearly (Pomara et al., 2012), which resulted in ∼14,000 fatalities in 2017. The primary metabolite of cocaine is benzoylecgonine, which is used to test for cocaine use, as it is present in urine for as long as a week (Schindler and Goldberg, 2012). In contrast, cocaethylene is often tested for in autopsy, since it is produced when cocaine and alcohol are used together, a combination that increases the chance of death by "18 to 25 fold" compared to cocaine taken by itself (Andrews, 1997; Pennings et al., 2002).

Cocaine, benzoylecgonine, and cocaethylene are also dominated by the symmetric and asymmetric phenyl ring breathing modes at 995–1,000 and 1,015–1,020 cm^{-1}, and to some extent the trigonal phenyl ring breathing mode at 1,595–1,600 cm^{-1} (**Figure 7**). Another intense mode appears at 885–890 cm^{-1} due to the tropine ring stretch (Carter et al., 2000; D'Elia et al., 2016). The primary difference in their spectra occur in the 800 to 900 cm^{-1} region due to the changes in the ester group, which also appears to influence the intensity of the weaker tropine modes between 1,300 and 1,400 cm^{-1}. It is also

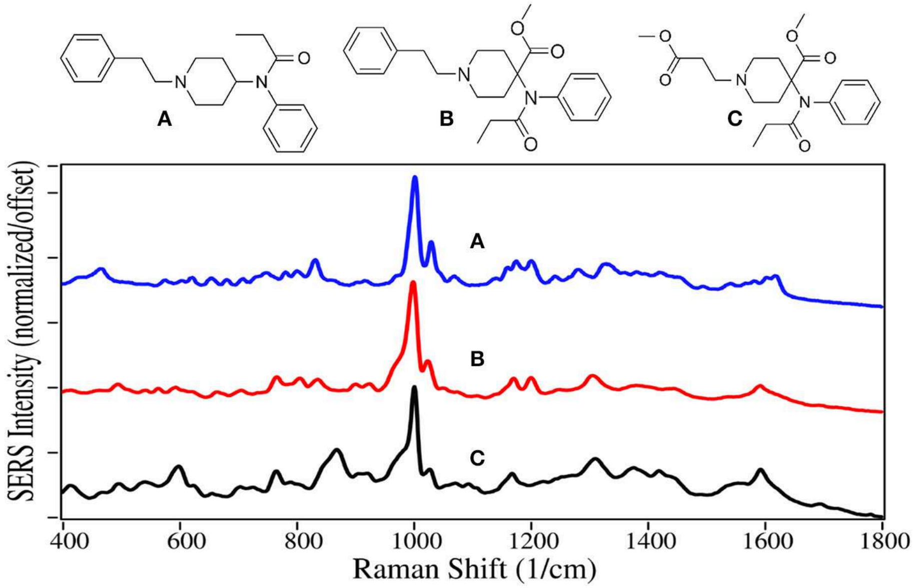

FIGURE 6 | Structures and 10 ppm SERS of **(A)** fentanyl, **(B)** carfentanil, and **(C)** remifentanil.

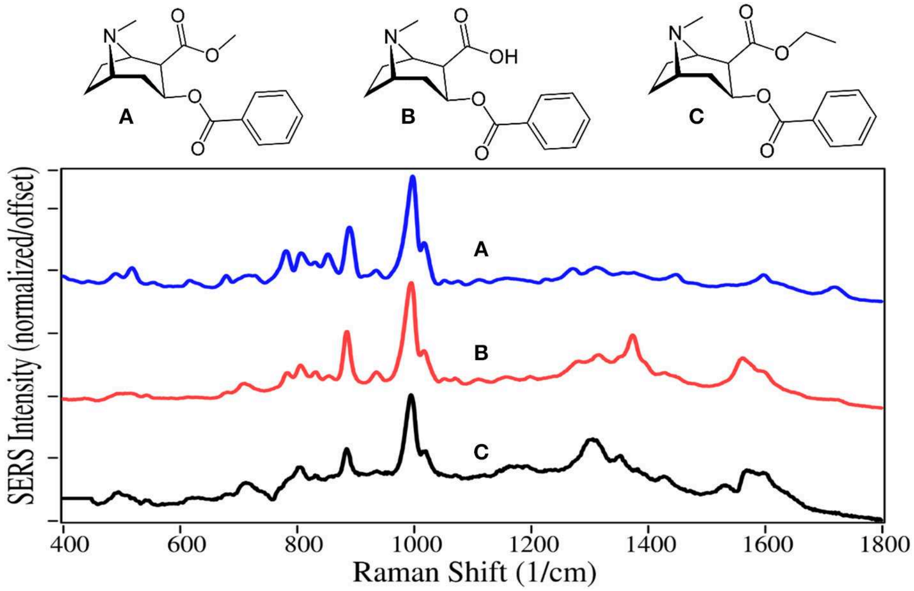

FIGURE 7 | Structures and 100 ppm SERS of **(A)** cocaine, **(B)** benzoylecgonine, and **(C)** cocaethylene.

worth noting that the 1,600 cm^{-1} trigonal phenyl ring breathing mode and ester carbonyl stretch at 1,720 cm^{-1} are more intense when measured with silver (Dana et al., 2015).

Amphetamine and methamphetamine are Schedule II synthetic drugs, while mephedrone is a Schedule I synthetic drug. All three have chemical structures similar to dopamine, serotonin and epinephrine, and much like cocaine, cause accumulation of these neurotransmitters in the synaptic gap stimulating the reward and cognitive pathways (Arnold, 2000). A 25/75% mixture of the amphetamine enantiomers, prescribed as Adderall, is used to treat ADHD (Bidwell et al., 2011). Amphetamine is also used to enhance athletic performance. While methamphetamine can also be used for these applications with deminished effect, it is primarily used as a recreational aphrodisiac. Mephedrone, also known as "bath salts" and "meow meow" (Glennon, 2014), is used as a recreational drug with effects similar to the amphetamines and cocaine.

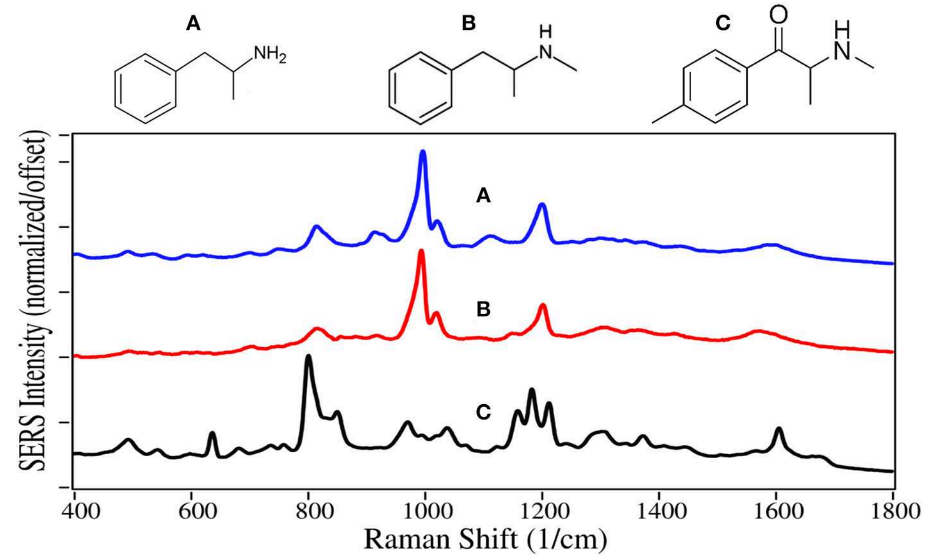

FIGURE 8 | Structures and 100 ppm SERS of **(A)** amphetamine, **(B)** methamphetamine, and **(C)** mephedrone.

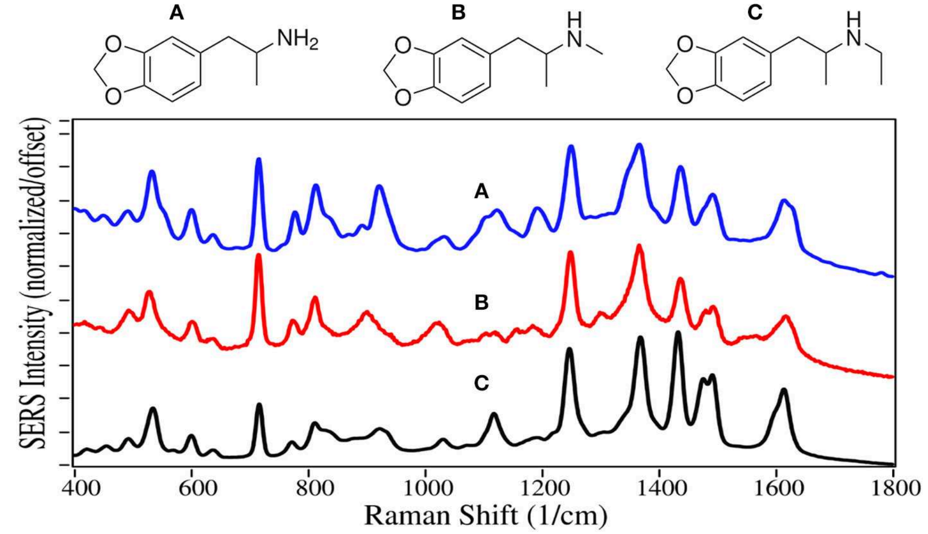

FIGURE 9 | Structures and 100 ppm SERS of **(A)** MDA, **(B)** MDMA, and **(C)** MDEA.

As with fentanyl and cocaine and their analogs, amphetamine and methamphetamine are dominated by the symmetric and asymmetric phenyl ring breathing modes at 995–1,000 and 1,020 cm^{-1}, and to some extent the trigonal phenyl ring breathing mode at 1,595–1,600 cm^{-1} (**Figure 8**) (Carter et al., 2000; Hargreaves, 2013). The peaks at 815–820 and 1,200 cm^{-1} are C-ring modes for the amphetamines, which are enhanced as the para-substituted C-ring-C modes for mephedrone (Carter et al., 2000). In contrast, the para-substituted benzene ring of mephedrone results in intense peaks at 805 and 1,215 cm^{-1}, and an asymmetric C-N-C stretch at 1,185 cm^{-1} and amide mode at 1,672 cm^{-1} (Milne and Jhamandas, 1984). Similar SERS has been reported for methamphetamine (Sägmüller et al., 2003) and mephedrone (Mabbott et al., 2013).

3,4-Methylenedioxyamphetamine (MDA) 3,4-Methylenedioxymethamphetamine (MDMA) and 3,4-Methylenedioxy-*N*-ethylamphetamine (MDEA) are all Schedule I drugs because they are used recreationally and have no medical value. All three drugs have structures similar to the amphetamines and dopamine, with the addition of a dioxole ring. They not only inhibit reuptake, but also enhance release of dopamine, serotonin and epinephrine, stimulating the reward and cognitive pathways. The result is enhanced euphoria and psychedelic effects for these drugs, also known as "the love drug," "ecstasy," and "Eve," respectively.

The SERS of MDA, MDMA and MDEA are very similar to each other with 7 intense peaks occurring at 530–535, 715–720, 1,250, 1,365–1,370, 1,430–1,435, 1,470–1,480, and 1,620 cm^{-1}, largely due to the dioxole ring alone or coupled with the phenyl ring (**Figure 9**). The first 3 peaks dominate the normal Raman and SER spectra on silver (Bell et al., 2000; Lombardi et al., 2013), but the remaining peaks, while present, are of much lower relative intensity.

Sedatives

Most sedatives are benzodiazepines, which increase the effect of the neurotransmitter gamma-aminobutyric acid, which in turn increases the flow of chloride ions into the neuronal cell (Derry et al., 2004). This increases the neuron's chemical potential, such that it is less likely to fire, reducing both brain and spinal cord function (Date et al., 1984), making the user tired.

Diazepam, temazepam, and oxazepam are Schedule IV drugs primarily used to treat anxiety and sleeplessness. Diazepam easily

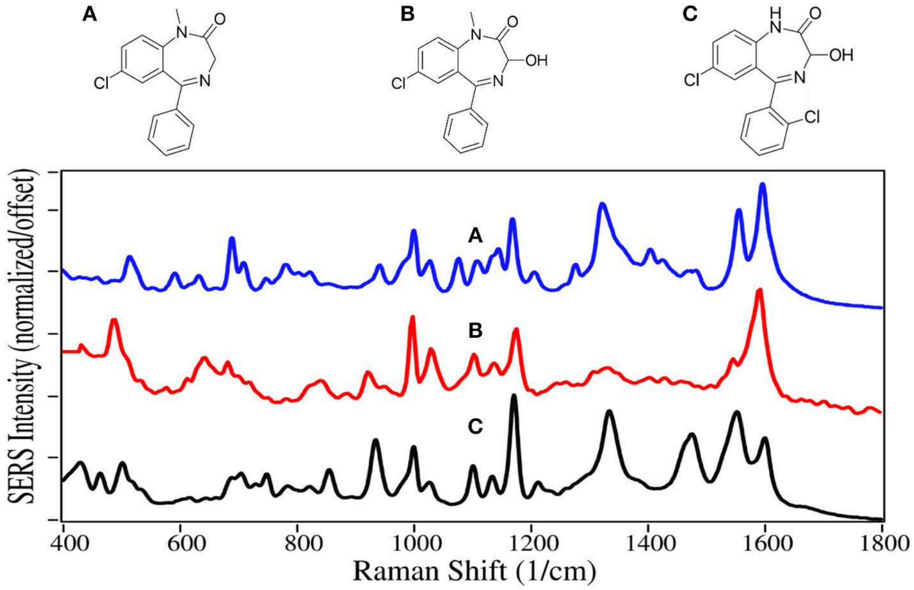

FIGURE 10 | Structures and 100 ppm SERS of **(A)** diazepam, **(B)** temazepam, and **(C)** oxazepam.

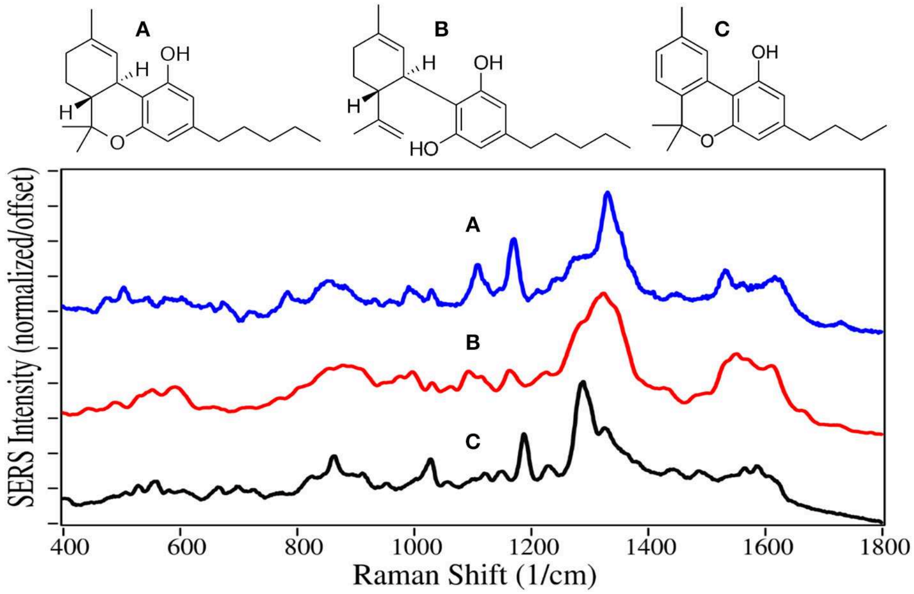

FIGURE 11 | Structures and 10 ppm SERS of **(A)** tetrahydrocannabinol, **(B)** cannabidiol, and **(C)** cannabinol.

crosses the blood-brain barrier, and has a long half-life of 30 to 56 h (Oelschläger, 1989). It was first marketed in 1963 as Valium, and rapidly became the highest prescribed drug in the USA (Calcaterra and Barrow, 2014). Temazepam is largley prescribed for people having trouble sleeping, while oxazepam is more for people who have trouble staying asleep. Both drugs are less powerful with shorter half-lives than diazepam. Since the reward pathway is not engaged by these drugs, they are not addicting, but dependence can occur, particularly when combined with alcohol (Poulos and Zack, 2004). In 2017 there were 11,500 deaths due to overdose, many involving automobile accidents (Smink et al., 2010).

The benzodiazepines are dominated by the 7-membered diazapine and phenyl ring modes. The former modes at 935–945, 1,170, and 1,590–1,600 cm^{-1} are due to ring stretching, C-H deformation, and ring stretching, respectively (**Figure 10**) (Neville et al., 1995). Diazepam and Oxazepam have phenyl modes at ∼1,000, 1,030, 1,325–1,335, and 1,555 cm^{-1}, whereas temazepam is missing the 1,330 and 1,555 cm^{-1} due to the chlorine substitution that reduces the symmetryof these

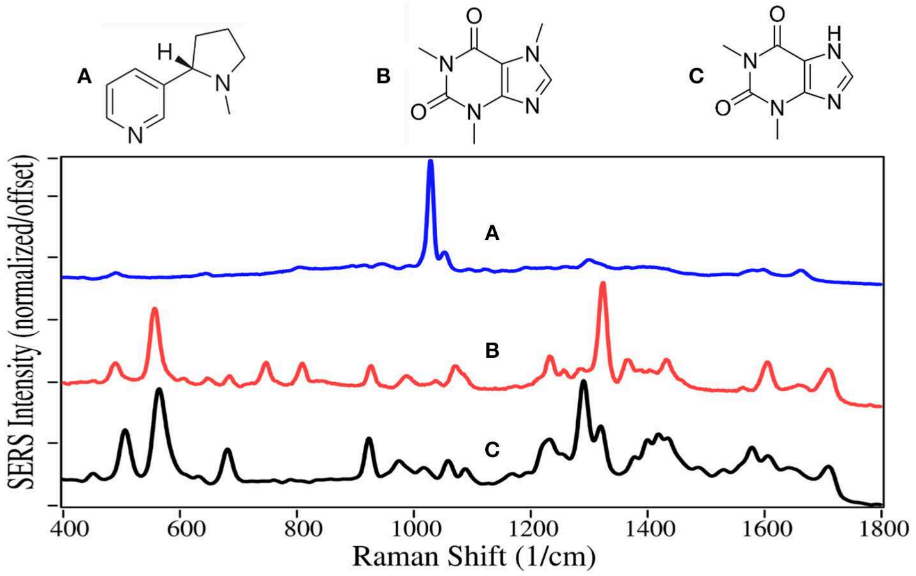

FIGURE 12 | Structures and 100 ppm SERS of **(A)** nicotine, **(B)** caffeine, and **(C)** theophylline.

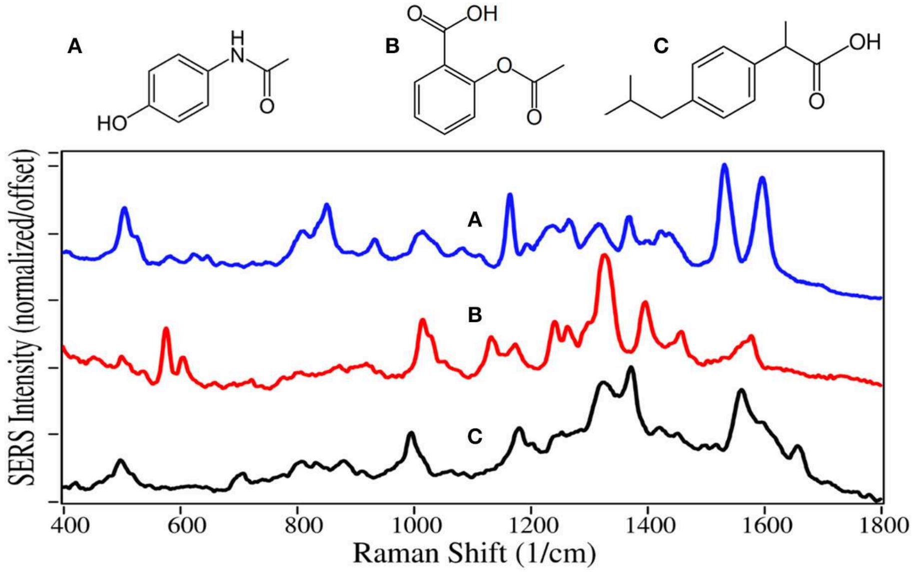

FIGURE 13 | Structures and 100 ppm SERS of **(A)** acetaminophen, **(B)** aspirin, and **(C)** ibuprofen.

TABLE 1 | Similar characteristic and unique SERS peaks for the 39 drugs measured using gold colloids and 785 nm excitation (see text for assignments).

Drug, References	**Similar characteristic peaks, cm^{-1} (see text for assignments)**											**Unique peaks**
Spectral regions	**500**	**600**	**700**	**800**	**900**	**1,000**	**1,100**	**1,200**	**1,300**	**1,400**	**1,600**	**1,700**	
Heroin (Gardner et al., 2013)	530	625						1,220		1,450	1,610		1,240
Morphine (Rana et al., 2010)	530	630						1,215		1,445	1,605		1,300
6-Acetylcodiene*	530	630						1,225		1,445	1,600		1,270
Codeine (Rana et al., 2010)								1,275		1,435	1,595		535
Hydrocodone (Rana et al., 2010)								1,275		1,435	1,605		510
Oxycodone*								1,275		1,435	1,595		975
Hydromorphone* (Milne and Jhamandas, 1984)		625	755						1,320		1,615		835
Oxymorphone* (Milne and Jhamandas, 1984)		630	750						1,320		1,610		1,685
Naltrexone* (Milne and Jhamandas, 1984)		635	750						1,325		1,610		1,110
Naloxone* (Milne and Jhamandas, 1984)		630		810				1,275					1,725
Buprenorphine		640		830						1,445	1,595		1,680
Norbuprenorphine* (Milne and Jhamandas, 1984)		635		800							1,605		1,020
Methadone (Stanley, 2014)					915	1,000	1,190				1,595		675
Meperidine (Stanley, 2014)					910	1,000	1,195				1,600		585
Methylphenidate (Stanley, 2014)					910	1,000	1,185				1,600		495
Fentanyl (Hummel and Unterwald, 2002)						1,000, 1,030							465, 830
Carfentanil (Hummel and Unterwald, 2002)						1,000, 1,025							765
Remifentanil*						1,000, 1,025							600, 1,700
Cocaine (Carter et al., 2000)				890		1,000, 1,015							1,450
Benzoylecgonine*				885		995, 1,020							1,375
Cocaethylene*				890		1,000, 1,020							1,310
Amphetamine (Sägmüller et al., 2003)				815		1,000, 1,020		1,200					1,595
Methamphetamine (Sägmüller et al., 2003)				820		995, 1,020		1,200					1,570
Mephedrone*	*												805, 1,185
MDA (Derry et al., 2004)	530		720					1,250	1,370	1,435	1,620		1,195
MDMA (Derry et al., 2004)	530		720					1,250	1,365	1,435	1,615		1,025
MDME (Derry et al., 2004)	535		715					1,250	1,365	1,435	1,615		1,120
Diazepam (Cinta et al., 1999)					945	1,000	1,170				1,595		690
Temazepam (Cinta et al., 1999)					940	1,000	1,180				1,590		490
Oxazepam (Cinta et al., 1999)					935	1,000	1,175				1,600		1,475
Tetrahydrocannabinol (Sivashanmugan et al., 2019)							1,170						1,532
Cannabidiol*							1,170	1,290					1,345, 1,665

(Continued)

TABLE 1 | Continued

Drug, References	Similar characteristic peaks, cm^{-1} (see text for assignments)												Unique peaks
Spectral regions	**500**	**600**	**700**	**800**	**900**	**1,000**	**1,100**	**1,200**	**1,300**	**1,400**	**1,600**	**1,700**	
Cannabinol*								1,290					1,190
Nicotine (Pavel et al., 2003)	*												1,030, 1,660
Caffeine (Ricciotti and FitzGerald, 2011)					925			1,235	1,325		1,605	1,710	510, 1,290
Theophylline*					925			1,235	1,320		1,605	1,710	1,290
Acetaminophen (Vueba et al., 2008)									1,320				505, 1,535
Aspirin (Gemperline, 2006)									1,325				580, 1,400
Ibuprofen* (Vueba et al., 2008)									1,325				1,660

**Assignments based on similar drugs in this study.*

***The structure and spectra for this drug was different from any other.*

vibrations. The SERS are similar to the normal Raman spectra of these drugs (Shende et al., 2014), as well as the SERS using silver (Cinta et al., 1999; Trachta et al., 2004b).

Other Drugs

Delta-9 Tetrahydrocannabinol (THC), first isolated in 1964 (Pertwee, 2006), is the main psychoactive component of cannabis. Its C_{22} structure, similar to the C_{22} fatty acid neurotransmitter anandamide, allows it to bind and partially activate both the cannabinoid receptors located in the central nervous system and those in cells of the immune system. THC also indirectly influences the mu- and gamma-opioid receptors (Mechoulam and Fride, 1995). These actions result in modest euphoria, relaxation, and for some users, anxiety. Cannabidiol (CBD) represents 40% of the oil extracted from cannabis, making it economical for use in products (Hazekamp, 2018). However, it is not psychoactive (Iseger and Bossong, 2015), and the only verified medical use is the treatment of severe forms of epilepsy (FDA, 2018). Cannabinol (CBN) provides the same effects as THC, but to a lesser extent. It is also the primary metabolite of THC, and often tested in body fluids to determine use of either. Currently, 47 states allow medical use to varying degrees, and 10 states allow recreational use (Media Relations, 2018; State Medical Marijuana Laws, 2018).

The phenyl ring peak intensities, despite being weak, appear for THC, CBD and CBN at 1,000, 1,030, and 1,610–1,615 cm^{-1}, although the former two relative peak intensities for CBN are reversed (**Figure 11**). Peaks at 855 and 864 cm^{-1} for THC and CBN are assigned to stretching of the middle tetrahydropyran ring (Milne and Jhamandas, 1984; Stanley, 2014). Weak intensity peaks at 1,095–1,110 and 1,165–1,190 cm^{-1} are assigned to C-C stretching of the alkane chain for CBN, and C-C stretching of the rings, respectively, while a peak at 1,530–1,565 cm^{-1} is assigned to C = C stretching. The 1,250 to 1,350 cm^{-1} is the most interesting spectral region with two peaks at ∼1,290 and 1,330 cm^{-1}, both assigned to CH deformation modes. The latter peak appears to have significant contribution from the two CHs at the junction of the cyclohexene and tetrahydropyran rings. The same intensity difference has been observed for THC and CBN for their Raman spectra (Fedchak, 2014). While SERS of these drugs on gold are similar to Raman spectra, their SERS using silver are considerably different (Yüksel et al., 2016; Sivashanmugan et al., 2019).

Nicotine and caffeine are two of the oldest drugs, used as stimulants, and are largely unregulated. They are primarily produced by extraction from tobacco plants and coffee beans, respectively. Nicotine binds to acetylcholine receptors in the brain releasing several neurotransmitters, in particular dopamine (Malenka et al., 2009), and appears to also cause the release of natural opioids (Kishioka et al., 2014). It thus activates the reward pathway in the brain, making it highly addictive (Stolerman and Jarvis, 1995). The availability of traditional cigarettes and now e-cigarettes makes nicotine one of the most abused drugs (Sajja et al., 2016). Traditional cigarettes have been the dominant cause of lung cancer, and a major contributor to heart disease for the past 50 years (Nicotine, 2014). The intent of e-cigarettes, or vaping, was to reduce these horrendous side-effects. Unfortunately, vaping has grown rapidly among high school students to 21% in 2016 (Surgeon General, 2016), potentially leading to an even greater number of nicotine addicts.

Caffeine is legal in most of the world and is the most consumed psychoactive drug. Its mechanism is somewhat different than other stimulants, in that its molecular structure is similar to adenosine, and it binds to the adenosine receptors, but does not slow the release of neurotransmitters that regulate breathing, heart rate and blood pressure in the medulla oblongata (Fisone et al., 2004). Theophylline, which is also extracted from coffee beans, is structurally similar to caffeine, and it also binds to the adenosine receptors (Daly et al., 1987). It is mostly used to treat asthma and other respiratory conditions.

The SERS of nicotine is dominated by the symmetric pyridine ring breathing mode at 1,030 cm^{-1}, which also produces peaks at 645, 1,055, and 1,595 cm^{-1}, assigned to in-plane ring, trigonal ring breathing modes (**Figure 12**) (Milne and Jhamandas, 1984). These peaks are all the same in both Raman and SERS (Barber et al., 1994). However, the relative intensities more closely match Raman than SERS using silver (Itoh and Bell, 2017). The SERS of caffeine and theophylline are dominated by two peaks, one at

555–570 cm^{-1}, the other at 1,290 and 1,320 cm^{-1}, assigned to pyrimidine ring breathing and imidazole ring trigonal stretching, for theophylline and caffeine, respectively (Pavel et al., 2003). The shift in frequency is due to the methyl group on the imidazole ring for caffeine. The following peaks occur for both drugs, 490–510, 925, 1,235, 1,605, and 1,710 cm^{-1} assigned to an in-plane ring-ring deformation, deformation of both rings, HCN bending, C-C stretching, and in-phase C = O stretching. The SERS for theophylline is very similar to that reported for caffeine (Ricciotti and FitzGerald, 2011).

Acetaminophen, aspirin and ibuprofen inhibit cyclooxygenase from producing the prostaglandin hormones that are local messengers of pain, fever and inflammation (Day and Graham, 2004; Ricciotti and FitzGerald, 2011). However, acetaminophen only inhibits cyclooxygenase in the brain, and consequently, is not an anti-inflammatory. Aspirin also inhibits clotting by keeping blood platelets from sticking together. Each of the three drugs are often combined with other drugs, such as prescription opioids to aid in reducing pain. These three drugs are the most common medication used to treat pain in the world (WHO, 2015). Unfortunately, the high use of acetaminophen led to ∼1,200 overdose deaths in the USA in 2016 (Hedegaard et al., 2018). Acetaminophen, aspirin, and ibuprofen were the 38th, 35th, and 17th most prescribed drugs in the USA in 2016, respectively (ClinCalc, 2019).

The SERS of acetaminophen has peaks at 810, 855, 1,235, 1,320, 1,535, and 1,610 cm^{-1}, which are assigned to CNC ring stretching, ring breathing, C-C ring stretching, amide III, and amide II modes, respectively (**Figure 13**) (Diniz et al., 2004). Aspirin and ibuprofen have the typical phenyl peaks at 1,000–1,015, 1,325, and 1,580–1,595 cm^{-1}. In addition to the 1,325 cm^{-1} peaks, they have intense peaks at 1,400 and 1,375 cm^{-1}, respectively, possibly due to COO stretching (El-Shahawy, 1988; Vueba et al., 2008). Ibuprofen also has a carboxylic acid C = O peak at 1,660 cm^{-1}, notably absent for aspirin. While the acetaminophen spectrum matches the Raman spectrum, the SERS of aspirin and ibuprofen are significantly different, especially their relative peak intensities. This is likely due to their different chemical interactions with gold and the resultant orientation.

The SERS peaks, according to wavenumber, for the 39 drugs are summarized in **Table 1** in terms of vibrations common to each drug type, as well as 1 or 2 unique vibrations that could be used to identify and differentiate the drugs within each group. The peaks are arranged in columns such that vibrations can be compared across the entire set of 39 spectra. The references used to make the vibrational assignments are also included. However, for many drugs, the assignments were based on functional groups common to a referenced drug, as well as the measured peak wavenumber and intensity. It is worth noting that many spectral analysis algorithms can be used to both identify an unknown substance and quantify simple mixtures (Gemperline, 2006). These algorithms have been used to identify unknown drugs (Farquharson et al., 2011), and in some cases determine relative concentrations in mixtures (Farquharson et al., 2017).

CONCLUSIONS

The SER spectra presented here are intended to aid researchers develop substrates, and companies develop products useful to first responders, police officers, medical point-of-care personnel, and military personnel. While a simple set of spectra have been presented, there are several important variables that can influence the actual measured spectra. We have attempted to eliminate two variables; laser wavelength and plasmonic metal type. However, sample concentration and pH can also significantly change the spectra. In most cases, the peaks will be at the same wavenumbers, but with different intensities. Buffers can be used to control the latter. The most challenging variable is the medium that the sample might be found. This includes numerous surface types, ranging from soil to clothing to illicit lab benches, numerous sample types, powders or liquids with other chemicals, and numerous body fluids from saliva to urine. Care must be taken in assessing the final analysis.

DATA AVAILABILITY STATEMENT

All datasets generated for this study are included in the manuscript/supplementary files.

AUTHOR CONTRIBUTIONS

SF directed the work and wrote this publication. CB designed the Raman analyzer used for these measurements. WS wrote the software to measure and analyse the spectra. CS prepared the gold nanoparticles and measured all of the drugs presented in this publication.

FUNDING

This work was funded in part by National Institute of Health, National Institute of Drug Abuse (2R44DA032178-02), and the Department of Defense, Chemical and Biological Defense (W911QY19C0008).

ACKNOWLEDGMENTS

The authors are grateful to Drs. Albert Arias and Jennifer Newcomb for their helpful discussions regarding buprenorphine treatment of veterans suffering from post-traumatic stress disorder.

REFERENCES

Andrews, P. (1997). Cocaethylene toxicity. *J. Addict. Dis.* 16, 75–84. doi: 10.1300/J069v16n03_08

Angel, S. M., Carter, J. C., Stratis, D. N., Marquardt, B. J., and Brewer, W. E. (1999). Some new uses for filtered fiber-optic Raman probes: *in situ* drug identification and *in situ* and remote Raman imaging. *J. Raman Spectrosc.* 30, 795–805.

Arias, A. J., and Kranzler, H. R. (2008). Treatment of co-occurring alcohol and other drug use disorders. *Alcohol Res. Health* 31, 155–167.

Arnold, L. E. (2000). Methyiphenidate vs amphetamine: comparative review. *J. Atten. Disord.* 3, 200–211. doi: 10.1177/108705470000300403

Barber, E., List, M. S., Haas, J. W., and Wachter, E. A. (1994). Determination of nicotine by surface-enhanced Raman scattering (SERS). *Appl. Spectrosc.* 48, 1423–1427. doi: 10.1366/0003702944027985

Bell, S. E., Burns, D. T., Dennis, A. C., and Speers, J. S. (2000). Rapid analysis of ecstasy and related phenethylamines in seized tablets by Raman spectroscopy. *Analyst* 125, 541–544. doi: 10.1039/a908091k

Bell, S. E. J., Beattie, J. R., McGarvey, J. J., Peters, K. L., Sirimuthu, N. M. S., and Speers, S. J. (2004). Development of sampling methods for Raman analysis of solid dosage forms of therapeutic and illicit drugs. *J. Raman Spectrosc.* 35, 409–417. doi: 10.1002/jrs.1160

Bidwell, L. C., McClernon, F. J., and Kollins, S. H. (2011). Cognitive enhancers for the treatment of ADHD. *Pharmacol. Biochem. Behav.* 99, 262–274. doi: 10.1016/j.pbb.2011.05.002

Brandán, S. A. (2018). Understanding the potency of heroin against morphine and cocaine. *Int. J. Sci. Res. Methods* 10, 97–140.

Calcaterra, N. E., and Barrow, J. C. (2014). Classics in chemical neuroscience: diazepam (valium). *ACS Chem. Neurosci.* 5, 253–260. doi: 10.1021/cn5000056

Carter, J. C., Brewer, W. E., and Angel, S. M. (2000). Raman spectroscopy for the *in situ* identification of cocaine and selected adulterants. *Appl. Spectrosc.* 54, 1876–1881. doi: 10.1366/0003702001949014

Cinta, S., Iliescu, T., Astilean, S., David, L., Cozar, O., and Kiefer, W. (1999). 1,4-Benzodiazepine drugs adsorption on the Ag colloidal surface. *J. Mol. Struc.* 482/483, 685–688. doi: 10.1016/S0022-2860(99)00025-3

ClinCalc (2019). *The Top 300 of 2019*. Available online at: clincalc.com

Comer, S. D., Sullivan, M. A., Yu, E., Rothenberg, J. L., Kleber, H. D., Kampman, K., et al. (2006). Injectable, sustained-release naltrexone for the treatment of opioid dependence: a randomized, placebo-controlled trial. *Arch. Gen. Psychiatry* 63, 210–218. doi: 10.1001/archpsyc.63.2.210

Corbett, A. D., Henderson, G., McKnight, A. T., and Paterson, S. J. (2006). 75 years of opioid research: the exciting but vain quest for the Holy Grail. *Br. J. Pharmacol.* 147, S153–S162. doi: 10.1038/sj.bjp.0706435

Courtwright, D. T. (2009). *Forces of Habit Drugs and the Making of the Modern World*. Cambridge: Harvard University Press.

Cutmore, E. A., and Skett, P. W. (1993). Application of Fourier transform Raman spectroscopy to a range of compounds of pharmaceutical interest. *Spectrochim. Acta* 49A, 809–818. doi: 10.1016/0584-8539(93)80105-J

Daly, J. W., Jacobson, K. A., and Ukena, D. (1987). Adenosine receptors: development of selective agonists and antagonists. *Prog. Clin. Biol. Res.* 230, 41–63.

Dana, K., Shende, C., Huang, H., and Farquharson, S. (2015). Rapid analysis of cocaine in saliva by surface-enhanced Raman spectroscopy. *Anal. Bioanal. Tech* 6, 1–5. doi: 10.4172/2155-9872.1000289

Date, S. K., Hemavathi, K. G., and Gulati, O. D. (1984). Investigation of the muscle relaxant activity of nitrazepam. *Arch. Int. Pharmacodyn. Ther.* 272, 129–139.

Day, R. O., and Graham, G. G. (2004). The Vascular Effects of COX-2 selective inhibitors. *Aust. Prescr.* 27, 142–145. doi: 10.18773/austprescr.2004.119

de Veij, M., Deneckere, A., Vandenabeele, P., de Kaste, D., and Moens, L. (2008). Detection of counterfeit Viagra with Raman spectroscopy. *J. Pharm. Biomed. Anal.* 2008, 303–309. doi: 10.1016/j.jpba.2007.10.021

DEA (2013). *Bupronorphine*. Available online at: www.deadiversion.usdoj.gov/drug_chem_info/bupronorphine.pdf

D'Elia, V., Montalvo, G., and García Ruiz, C. (2016). Analysis of street cocaine samples in nasal fluid by Raman spectroscopy. *Talanta* 154, 367–373. doi: 10.1016/j.talanta.2016.03.077

Derry, J. M., Dunn, S. M., and Davies, M. (2004). Identification of a residue in the gamma-aminobutyric acid type A receptor alpha subunit that differentially affects diazepam-sensitive and -insensitive benzodiazepine site binding. *J. Neurochem.* 88, 1431–1438. doi: 10.1046/j.1471-4159.2003.02264.x

Diniz, J. E. M., Borges, R. S., and Alves, C. A. N. (2004). DFT study for paracetamol and 3,5-disubstituted analogues. *J. Mol. Struct. Theochem.* 673, 93–99. doi: 10.1016/j.theochem.2003.12.002

Dollish, F. R., Fately, W. G., and Bentley, F. F. (1974). *Characteristic Raman Frequencies of Organic Compounds*. Oxford: Wiley Interscience.

Eap, C. B., Déglon, J. J., and Baumann, P. (1999). Pharmacokinetics and pharmacogenetics of methadone: clinical relevance. *Heroin. Add. Rel. Clin. Probl.* 1, 19–34.

El-Shahawy, S. A. (1988). Spectroscopic structural studies of salicylic acid, salicylamide and aspirin. *Spectrochim. Acta* 44A, 903–907. doi: 10.1016/0584-8539(88)80007-2

Farquharson, S., Dana, K., Shende, C., Gladding, Z., Newcomb, J., Dascher, J., et al. (2017). Rapid identification of buprenorphine in patient saliva. *J. Anal. Bioanal. Tech.* 8:368. doi: 10.4172/2155-9872.1000368

Farquharson, S., and Lee, Y. H. (2000). Trace drug analysis by surface-enhanced Raman spectroscopy. *Proc. SPIE* 4200, 89–95. doi: 10.1117/12.411716

Farquharson, S., Shende, C., Inscore, F., Maksymiuk, P., and Gift, A. (2005). Analysis of 5-fluorouracil in saliva using surface-enhanced Raman spectroscopy. *J. Raman Spectrosc.* 36, 208–212. doi: 10.1002/jrs.1277

Farquharson, S., Shende, C., Newcomb, J., Dascher, J., Petrakis, I. L., and Arias, A. J. (2019). Analysis of treatment drugs in saliva of USA Military veterans treated for substance-use disorders using supported liquid extraction and surface-enhanced Raman spectral analysis. *J. Anal. Bioanal. Tech.* 144, 5449–5454. doi: 10.1039/c9an01087d

Farquharson, S., Shende, C., Sengupta, A., Huang, H., and Inscore, F. (2011). Rapid detection and identification of overdose drugs in saliva by surface-enhanced Raman scattering using fused gold colloids. *Pharmaceutics* 3, 425–439. doi: 10.3390/pharmaceutics3030425

Faulds, K., Smith, W. E., Graham, D., and Lacey, R. J. (2002). Assessment of silver and gold substrates for the detection of amphetamine sulfate by surface enhanced Raman scattering (SERS). *Analyst* 127:282. doi: 10.1039/b107318b

FDA (2018). *FDA Approves First Drug Comprised of an Active Ingredient Derived from Marijuana to Treat Rare, Severe Forms of Epilepsy*.

Fedchak, S. (2014). *Presumptive Field Testing Using Portable Raman Spectroscopy. Report No. 244564*. Department of Justice.

Fini, G. (2004). Applications of Raman spectroscopy to pharmacy. J Raman Spectrosc, 35, 335–337 (also see references therein). doi: 10.1002/jrs.1161

Fisone, G., Borgkvist, A., and Usiello, A. (2004). Caffeine as a psychomotor stimulant: mechanism of action. *CLMS* 61, 857–872. doi: 10.1007/s00018-003-3269-3

Gardner, C. M., Hargreaves, M. D., Wang, P., and Shen, Y. (2013). *Heroin Detection by Raman Spectroscopy from Impure Compositions Comprising an Interfering Fluorescent Contaminant*.

Gemperline, P. (2006). *Practical Guide to Chemometrics, 2nd Edn*. Boca Raton, FL: Taylor and Francis Group CRC Press.

Glennon, R. A. (2014). Bath salts, mephedrone, and methylenedioxypyrovalerone as emerging illicit drugs that will need targeted therapeutic intervention. Adv. *Pharmacol.* 69, 581–620. doi: 10.1016/B978-0-12-420118-7.00015-9

Hargreaves, M. D. (2013). *Infrared and Raman Spectroscopy in Forensic Science*. eds J. M. Chalmers, H. G. M. Edwards, and M. D. Hargreaves. West Sussex: Wiley.

Hazekamp, A. (2018). The trouble with CBD oil. *Med. Can. Cannabinoids* 1, 65–72. doi: 10.1159/000489287

Hedegaard, H., Bastian, B. A., Trinidad, J. P., Spencer, M., and Warner, M. (2018). *Drugs Most Frequently Involved in drug Overdose Deaths: United States, 2011–2016. Nat Vital Stat Reports, 67*.

Hoffman, P., Verrico, J., and Bluestein, M. (2019). *News Release: Multi-agency Partnership Launches $1.55M Challenge for New Solutions to Detect Opioids*. Department of Homeland Security.

Hummel, M., and Unterwald, E. M. (2002). D1 dopamine receptor: a putative neurochemical and behavioral link to cocaine action. *J. Cell Physiol.* 191, 17–27. doi: 10.1002/jcp.10078

Inscore, F., Shende, C., Sengupta, A., Huang, H., and Farquharson, S. (2011). Detection of drugs of abuse in saliva by SERS. *Appl. Spectrosc.* 65, 1004–1008. doi: 10.1366/11-06310

Iseger, T. A., and Bossong, M. G. (2015). A systematic review of the antipsychotic properties of cannabidiol in humans. *Schizophr. Res.* 162, 153–161. doi: 10.1016/j.schres.2015.01.033

Itoh, N., and Bell, S. E. (2017). High dilution surface-enhanced Raman spectroscopy for rapid determination of nicotine in e-liquids for electronic cigarettes. *Analyst* 142, 994–998. doi: 10.1039/C6AN02286C

Jones, C. M., Einstein, E. B., and Compton, W. M. (2018). Changes in synthetic opioid involvement in drug overdose deaths in the United States, 2010–2016. *JAMA* 319, 1819–1821. doi: 10.1001/jama.2018.2844

Karila, L., Zarmdini, R., Petit, A., Lafaye, G., Lowenstein, W., and Reynaud, M. (2014). Cocaine addiction: current data for the clinician. *Presse Med.* 43, 9–17. doi: 10.1016/j.lpm.2013.01.069

Kelman, B., and Sharp, A. (2018). *Trump Signs Farm Bill and Legalizes Hemp, Cannabidiol*. USA Today.

Khroyan, T. V., Wu, J., Polgar, W. E., Cami-Kobeci, G., Fotaki, N., Husbands, S. M., et al. (2015). BU08073 a buprenorphine analogue with partial agonist activity at μ-receptors *in vitro* but long-lasting opioid antagonist activity *in vivo* in mice. *Br. J. Pharmacol.* 172, 668–680. doi: 10.1111/bph.12796

Kimko, H. C., Cross, J. T., and Abernethy, D. R. (1999). Pharmacokinetics and clinical effectiveness of methylphenidate. *Clin. Pharmacokinet.* 37, 457–470. doi: 10.2165/00003088-199937060-00002

Kinetz, E., and Butler, D. (2016). Chemical Weapon for Sale: China's Unregulated Narcotic. New York, NY: AP News.

Kishioka, S., Kiguchi, N., Kobayashi, Y., and Saika, F. (2014). Nicotine effects and the endogenous opioid system. *J. Pharm. Sci.* 125, 117–124. doi: 10.1254/jphs.14R03CP

Kronstrand, R., Nyström, I., Andersson, M., Gunnarsson, L., Hägg, S., Josefsson, M., et al. (2008). Urinary detection times and metabolite/parent compound ratios after a single dose of buprenorphine. *J. Anal. Toxicol.* 32, 586–593. doi: 10.1093/jat/32.8.586

Lanzarotta, A., Lorenz, L., JaCinta, S., and Flurer, C. (2017). Development and implementation of a Pass/Fail field-friendly method for detecting sildenafil in suspect pharmaceutical tablets using a handheld Raman spectrometer and silver colloids. *J. Pharma Biomed. Anal.* 146, 420–425. doi: 10.1016/j.jpba.2017.09.005

Lee, P. C., and Meisel, D. (1982). Adsorption and surface-enhanced Raman of dyes on silver and gold sols. *J. Phys. Chem.* 86, 3391–3395. doi: 10.1021/j100214a025

Leonard, J., Haddad, A., Green, O., Birke, R. L., Kubic, T., Kocak, A., et al. (2017). SERS, Raman, and DFT analyses of fentanyl and carfentanil: toward detection of trace samples. *J. Raman Spectrosc.* 48, 1323–1329. doi: 10.1002/jrs.5220

Lide, D. R. (1997). *Handbook of Chemistry and Physics, 77th Edn*. New York, NY: CRC Press.

Lombardi, J. R., Leona, M., Buzzini, P., and Antoci, P. (2013). *Development of Advanced Raman Spectroscopy Methods and Databases for the Evaluation of Trace Evidence and the Examination of Questioned Documents. Report No. 242324. Department of Justice*.

Lynn, R. R., and Galinkin, J. L. (2018). Naloxone dosage for opioid reversal: current evidence and clinical implications. *Ther. Adv. Drug Saf.* 9, 63–88. doi: 10.1177/2042098617744161

Mabbott, S., Correa, E., Cowcher, D. P., Allwood, J. W., and Goodacre, R. (2013). Optimization of parameters for the quantitative surface-enhanced raman scattering detection of mephedrone using a fractional factorial design and a portable Raman spectrometer. *Anal. Chem.* 85, 923–931. doi: 10.1021/ac302542r

Malenka, R. C., Nestler, E. J., and Hyman, S. E. (2009). "Chapter 9: autonomic nervous system," in *Molecular Neuropharmacology: A Foundation for Clinical Neuroscience, 2nd Edn*, eds A. Sydor and R. Y. Brown. New York, McGraw-Hill Medical, 234–244.

McCreery, R. L., Horn, A. J., Spencer, J., and Jefferson, E. (1998). Noninvasive identification of materials inside USP vials with Raman spectroscopy and a Raman spectral library. *Pharm. Sci.* 87, 1–8. doi: 10.1021/js970330q

Mechoulam, R., and Fride, E. (1995). "The unpaved road to the endogenous brain cannabinoid ligands, the anandamides," in *Cannabinoid Receptors*, ed RG Pertwee (Boston, MA: Academic Press), 233–258.

Media Relations (2018). *U.S. drug overdose deaths continue to rise; increase fueled by synthetic opioids*. CDC. Available online at: www.cdc.gov/media/releases/2018/p0329-drug-overdose-deaths.html

Melichar, J. K., Nutt, D. J., and Malizia, A. L. (2003). Naloxone displacement at opioid receptor sites measured in vivo in the human brain. *Eur. J. Pharmacol.* 459, 217–219. doi: 10.1016/S0014-2999(02)02872-8

Meyer, L. (2019). *FDA Approves First Generic Naloxone Nasal Spray to Treat Opioid Overdose*. FDA News Release.

Milne, B., and Jhamandas, K. (1984). Naloxone: new therapeutic roles. *Can. Anaesth. Soc. J.* 31, 272–278. doi: 10.1007/BF03007888

Neville, G. A., Beckstead, H. D., and Shurvell, H. F. (1995). A Fourier transform-Raman and IR vibrational study of flurazepam base and the mono- and di-hydrochloride salts. *J. Pharm. Sci.* 84, 179–184. doi: 10.1002/jps.2600840211

Newton, D. E. (2015). *Prescription Drug Abuse: A Reference Handbook*. Santa Barbara, CA: CLIO and LLC.

Nicotine (2014). Chapter 5, "Nicotine. The Health Consequences of Smoking—50 Years of Progress: A Report of the Surgeon General, Surgeon General of the United States. National Center for Chronic Disease Prevention and Health Promotion Office on Smoking Health.

NIH (2019). *Overdose Death Rates*. NIH National Institute on Drug Abuse. Available online at: www.drugabuse.gov/related-topics/trends-statistics/overdose-death-rates

Oelschläger, H. (1989). Chemical and pharmacologic aspects of benzodiazepines. *Schweiz. Rundsch. Med. Prax.* 78, 766–772.

O'Neal, C. L., Poklis, A., and Lichtman, A. H. (2001). Acetylcodeine, an impurity of illicitly manufactured heroin, elicits convulsions, antinociception, and locomotor stimulation in mice. *Drug Alcohol. Depend.* 65, 37–43. doi: 10.1016/S0376-8716(01)00145-4

Pînzaru, S. C., Pavel, I., Leopold, N., and Kiefer, W. (2004). Identification and characterization of pharmaceuticals using Raman and surface-enhanced Raman Scattering. *J. Raman Spectrosc.* 35, 338–346. doi: 10.1002/jrs.1153

Pavel, I., Szeghalmi, A., Moigno, D., Cîntă, S., and Kiefe, W. (2003). Theoretical and pH Dependent surface enhanced Raman spectroscopy study on caffeine. *Biopolymers* 72, 25–37. doi: 10.1002/bip.10248

Peddicord, S. (2017). *FDA Requests Removal of Opana ER for Risks Related to Abuse*. FDA News Release.

Pennings, E. J., Leccese, A. P., and Wolff, F. A. (2002). Effects of concurrent use of alcohol and cocaine. *Addiction* 97, 773–783. doi: 10.1046/j.1360-0443.2002.00158.x

Perez, R., Ruperez, A., and Laserna, J. J. (1998). Evaluation of silver substrates for surface-enhanced Raman detection of drugs banned in sport practices. *Anal. Chim. Acta* 376, 225–263. doi: 10.1016/S0003-2670(98)00519-4

Pergolizzi, J. V., Taylor, R., LeQuang, J. A., and Raffa, R. B. (2018). Managing severe pain and abuse potential: the potential impact of a new abuse-deterrent formulation oxycodone/naltrexone extended-release product. *J. Pain Res.* 11, 301–311. doi: 10.2147/JPR.S127602

Pertwee, R. G. (2006). Cannabinoid pharmacology: the first 66 years. *Br. J. Pharmacol.* 147, S163–S171. doi: 10.1038/sj.bjp.0706406

Petty, C. J., Bugay, D. E., Findlay, W. P., and Rodriguez, C. (1996). Application of FT-Raman spectroscopy in the pharmaceutical industry. *Spectroscopy* 11, 41–45.

Pharmaceutical Society (2015). *Narcotics Monitoring Board Reports 66% Increase in Global Consumption of Methylphenidate*.

Pigni, A., Brunelli, C., and Caraceni, A. (2011). The role of hydromorphone in cancer pain treatment: a systematic review. *Palliat. Med.* 25, 471–477. doi: 10.1177/0269216310387962

Pomara, C., Cassano, T., D'Errico, S., Bello, S., Romano, A. D., Riezzo, I., et al. (2012). Data available on the extent of cocaine use and dependence: biochemistry, pharmacologic effects and global burden of disease of cocaine abusers. *Curr. Med. Chem.* 19:5647. doi: 10.2174/092986712803988811

Poulos, C. X., and Zack, M. (2004). Low-dose diazepam primes motivation for alcohol and alcohol-related semantic networks in problem drinkers. *Behav. Pharmacol.* 15, 503–512. doi: 10.1097/00008877-200411000-00006

Rana, V., Canamares, M. V., Kubic, T., Leona, M., and Lombardi, J. R. (2010). Surface-enhanced Raman spectroscopy for trace identification of controlled substances: morphine, codeine, and hydrocodone. *J. Forensic Sci.* 56, 200–207. doi: 10.1111/j.1556-4029.2010.01562.x

Ricciotti, E., and FitzGerald, G. A. (2011). Prostaglandins and inflammation. *Arterioscler. Thromb. Vasc. Biol.* 31, 986–1000. doi: 10.1161/ATVBAHA.110.207449

Riches, J. R., Read, R. W., Black, R. M., Cooper, N. J., and Timperley, C. M. (2012). Analysis of clothing and urine from Moscow theatre siege casualties reveals carfentanil and remifentanil use. *J. Anal. Toxicol.* 36, 647–656. doi: 10.1093/jat/bks078

Ryder, A. G. (2005). Surface enhanced Raman scattering for narcotic detection and application to chemical biology. *Curr. Opin. Chem. Biol.* 9, 489–493. doi: 10.1016/j.cbpa.2005.07.001

Ryder, A. G., O'Connor, G. M., and Glynn, T. J. (1999). Identifications and quantitative measurements of narcotics in solid mixtures using near-IR Raman spectroscopy and multivariate analysis. *J. Forensic Sci.* 44, 1013–1019. doi: 10.1520/JFS12031J

Sacré, P. Y., Deconinck, E., De Beer, T., Courselle, P., Vancauwenberghe, R., Chiap, P., et al. (2010). Comparison and combination of spectroscopic techniques for the detection of counterfeit medicines. *J. Pharm. Biomed. Anal.* 53, 445–453. doi: 10.1016/j.jpba.2010.05.012

Sadock, B. J., Sadock, V. A., and Sussman, N. (2012). *Kaplan & Sadock's Pocket Handbook of Psychiatric Drug Treatment, 5th Ed*. Philadelphia, PA: Lippincott Williams and Wilkins.

Sägmüller, B., Schwarze, B., Brehm, G., and Schneider, S. (2001). Application of SERS spectroscopy to the identification of (3,4-methylenedioxy)amphetamine in forensic samples utilizing matrix stabilized silver halides. *Analyst* 126, 2066–2071. doi: 10.1039/b105321n

Sägmüller, B., Schwarze, B., Brehm, G., Trachta, G., and Schneid, S. (2003). Identification of illicit drugs by a combination of liquid chromatography and surface-enhanced Raman scattering spectroscopy. *J. Mol. Struct.* 661/662, 279–290. doi: 10.1016/S0022-2860(03)00507-6

Sajja, R. K., Rahman, S., and Cucullo, L. (2016). Drugs of abuse and blood-brain barrier endothelial dysfunction: a focus on the role of oxidative stress. *J. Cereb. Blood Flow Metab.* 36, 539–554. doi: 10.1177/0271678X15616978

Sanders, L. (2018). *Marijuana Legalization 2018: Which States Might Consider Cannabis Laws this Year?* Newsweek.

Sanders, L. (2019). The allure of CBD. *Sci. News* 2019, 14–18. doi: 10.1049/et.2019.0120

Schindler, C. W., and Goldberg, S. R. (2012). Accelerating cocaine metabolism as an approach to the treatment of cocaine abuse and toxicity. *Future Med. Chem.* 4, 163–175. doi: 10.4155/fmc.11.181

Shende, C., Brouillette, C., and Farquharson, S. (2019). Detection of fentanyl in saliva and blood in 5-minutes by SERS using a lateral flow strip. *Analyst* 144, 5449–5454. doi: 10.1039/C9AN01087D

Shende, C., Inscore, F., Gift, A., Maksymiuk, P., and Farquharson, S. (2005). Ten-minute analysis of drugs and metabolites in saliva by surface-enhanced Raman spectroscopy. *Proc. SPIE* 6007, 165–171. doi: 10.1117/12.633281

Shende, C. S., Huang, H., and Farquharson, S. (2014). Detection of illicit drugs in impaired driver saliva by a field-usable SERS analyzer. *Proc SPIE* 9107, 1–8. doi: 10.1117/12.2054284

Sivashanmugan, K., Squire, K., Tan, A., Zhao, Y., Kraai, J. A., Rorrer, G. L., et al. (2019). Trace detection of tetrahydrocannabinol in body fluid via surface-enhanced Raman scattering and principal component analysis. *ACS Sens.* 4, 1109–1117. doi: 10.1021/acssensors.9b00476

Sloan, P. (2008). Review of oral oxymorphone in the management of pain. *Ther. Clin. Risk Manag.* 4, 777–787. doi: 10.2147/TCRM.S1784

Smink, B. E., Egberts, A. C., Lusthof, K. J., Uges, D. R., and de Gier, J. J. (2010). The relationship between benzodiazepine use and traffic accidents: a systematic literature review. *CNS Drugs* 24, 639–653. doi: 10.2165/11533170-000000000-00000

Socrates, G. (2001). *Infrared and Raman Characteristic Group Frequencies, 3rd Edn*. New York, NY: John Wiley and Sons.

Stanley, T. H. (2014). The fentanyl story. *J. Pain* 12, 1215–1226. doi: 10.1016/j.jpain.2014.08.010

State Medical Marijuana Laws (2018). *National Conference of State Legislatures*. Available online at: http://www.ncsl.org/research/health/state-medical-marijuana-laws.aspx

Staub, C., Marset, M., Mino, A., and Mangin, P. (2001). Detection of acetylcodeine in urine as an indicator of illicit heroin use: method validation and results of a pilot study. *Clin. Chem.* 47, 301–307. Available online at: http://citeseerx.ist.psu.edu/viewdoc/download?doi=10.1.1.528.6309&rep=rep1&type=pdf

Stolerman, I. P., and Jarvis, M. J. (1995). The scientific case that nicotine is addictive. *Psychopharmacology* 117, 2–10; discussion 14–20. doi: 10.1007/BF02245088

Stone, P. A., Macintyre, P. E., and Jarvis, D. A. (1993). Norpethidine toxicity and patient controlled analgesia. *Br. J. Anaesth.* 71, 738–740. doi: 10.1093/bja/71.5.738

Surgeon General (2016). *E-cigarette Use among Youth and Young Adults: A Report of the Surgeon General*. Washington, DC: US Department of Health and Human Services, Centers for Disease Control and Prevention.

Sutherland, W. S., Laserna, J. J., Angebranndt, M. J., and Winefordner, J. D. (1990). Surface-enhanced Raman analysis of sulfa drugs on colloidal silver dispersion. *Anal. Chem.* 62, 689–693. doi: 10.1021/ac00206a008

Tensmeyer, L. G., and Heathman, M. A. (1989). Analytical applications of Raman spectroscopy in the pharmaceutical field. *Trends Anal. Chem.* 8, 19–24. doi: 10.1016/0165-9936(89)80009-3

Torres, E. L., and Winefordner, J. D. (1987). Trace determination of nitrogen-containing drugs by surface enhanced Raman scattering spectrometry on silver colloids. *Anal. Chem.* 59, 1626–1632. doi: 10.1021/ac00140a010

Trachta, G., Schwarze, B., Brehm, G., Schneider, S., Hennemann, M., and Clark, T. (2004a). Near-infrared Fourier transform surface-enhanced Raman scattering spectroscopy of 1,4-benzodiazepine drugs employing gold films over nanospheres. *J. Raman Spectrosc.* 35, 368–383. doi: 10.1002/jrs.1154

Trachta, G., Schwarze, B., Sagmuller, B., Brehm, G., and Schneider, S. (2004b). Combination of high-performance liquid chromatography and SERS detection applied to the analysis of drugs in human blood and urine. *J. Mol. Struct.* 693, 175–185. doi: 10.1016/j.molstruc.2004.02.034

Tudor, A. M., Melia, C. D., Binns, J. S., and Hendra, P. J. (1990). The application of Fourier transform Raman spectroscopy to the analysis of pharmaceuticals and biomaterials. *J. Pharmaceut. Biomed. Anal.* 8, 717–720. doi: 10.1016/0731-7085(90)80109-3

U.S. Customs and Border Protection (2019). *CBP Officers Seize Largest Amount of Fentanyl in CBP History*. Available online at: www.cbp.gov/newsroom/local-media-release/cbp-officers-seize-largest-amount-fentanyl-cbp-history

Urbano, M., Guerrero, M., Rosen, H., and Roberts, E. (2014). Antagonists of the kappa opioid receptor. *Bioorg. Med. Chem. Lett.* 24, 2021–2032. doi: 10.1016/j.bmcl.2014.03.040

Vueba, M. L., Pina, M. E., and Batista de Carvalho, L. A. (2008). Conformational stability of ibuprofen: assessed by DFT calculations and optical vibrational spectroscopy. *J. Pharm. Sci.* 97, 845–859. doi: 10.1002/jps.21007

Walsh, S. (2014). *FDA Approves New Hand-held Auto-injector to Reverse Opioid Overdose*. FDA News Release.

Wax, P. M., Becker, C. E., and Curry, S. C. (2003). Unexpected "Gas" Casualties in Moscow: a medical toxicology perspective. *Ann. Emerg. Med.* 42, 700–705. doi: 10.1067/mem.2003.148

WHO. (2015). *WHO Model List of Essential Medicines*. Geneva: World Health Organization.

Yassen, A., Olofsen, E., van Dorp, E., Sarton, E., Teppema, L., Danhof, M., et al. (2007). Mechanism-based pharmacokinetic-pharmacodynamic modelling of the reversal of buprenorphine-induced respiratory depression by naloxone: a study in healthy volunteers. *Clin. Pharmacokinet.* 46, 965–980. doi: 10.2165/00003088-200746110-00004

Yüksel, S., Schwenke, A. M., Soliveri, G., Ardizzone, S., Weber, K., Cialla-May, D., et al. (2016). Trace detection of tetrahydrocannabinol (THC) with a SERS-based capillary platform prepared by the *in situ* microwave synthesis of AgNPs. *Anal. Chim. Acta* 939, 93–100. doi: 10.1016/j.aca.2016.08.033

Zimmerman, J. L. (2012). Cocaine intoxication. *Crit. Care Clin.* 28, 517–526. doi: 10.1016/j.ccc.2012.07.003

Conflict of Interest: All authors were employed at Real-Time Analyzers, Inc. when this work was performed.

ORIGINAL RESEARCH
published: 10 January 2020
doi: 10.3389/fchem.2019.00888

Polycaprolactone-Based, Porous $CaCO_3$ and Ag Nanoparticle Modified Scaffolds as a SERS Platform With Molecule-Specific Adsorption

Mariia Saveleva [1,2†], ***Ekaterina Prikhozhdenko*** [3†], ***Dmitry Gorin*** [4], ***Andre G. Skirtach*** [1*], ***Alexey Yashchenok*** [4*] **and** ***Bogdan Parakhonskiy*** [1*]

[1] Department of Biotechnology, Ghent University, Ghent, Belgium, [2] Education and Research Institute of Nanostructures and Biosystems, Saratov State University, Saratov, Russia, [3] Department of Nano- and Biomedical Technologies, Saratov State University, Saratov, Russia, [4] Skoltech Center for Photonics and Quantum Materials, Skolkovo Institute of Science and Technology, Moscow, Russia

Surface-enhanced Raman scattering (SERS) is a high-performance technique allowing detection of extremely low concentrations of analytes. For such applications, fibrous polymeric matrices decorated with plasmonic metal nanostructures can be used as flexible SERS substrates for analysis of analytes in many application. In this study, a three-dimensional SERS substrate consisting of a $CaCO_3$-mineralized electrospun (ES) polycaprolactone (PCL) fibrous matrix decorated with silver (Ag) nanoparticles is developed. Such modification of the fibrous substrate allows achieving a significant increase of the SERS signal amplification. Functionalization of fibers by porous $CaCO_3$ (vaterite) and Ag nanoparticles provides an effective approach of selective adsorption of biomolecules and their precise detection by SERS. This new SERS substrate represents a promising biosensor platform with selectivity to low and high molecular weight molecules.

Keywords: SERS, Raman, calcium carbonate, silver nanoparticles, vaterite

OPEN ACCESS

Edited by:
Ivano Alessandri,
University of Brescia, Italy

Reviewed by:
Chih-Ching Huang,
National Taiwan Ocean University, Taiwan
Irene Vassalini,
University of Brescia, Italy

****Correspondence:***
Andre G. Skirtach
andre.skirtach@ugent.be
Alexey Yashchenok
a.yashchenok@skoltech.ru
Bogdan Parakhonskiy
bogdan.parakhonskiy@ugent.be

[†] These authors have contributed equally to this work

Specialty section:
This article was submitted to Analytical Chemistry, a section of the journal Frontiers in Chemistry

Received: *27 April 2019*
Accepted: *10 December 2019*
Published: *10 January 2020*

Citation:
Saveleva M, Prikhozhdenko E, Gorin D, Skirtach AG, Yashchenok A and Parakhonskiy B (2020) Polycaprolactone-Based, Porous $CaCO_3$ and Ag Nanoparticle Modified Scaffolds as a SERS Platform With Molecule-Specific Adsorption. Front. Chem. 7:888. doi: 10.3389/fchem.2019.00888

INTRODUCTION

Raman spectroscopy is an analytical method, which provides information about molecular spectra and enables identification of chemical species. It is important in many areas, including biomedicine for early diagnosis and monitoring of diseases. However, Raman scattering signals are very weak. One of the most effective methods to enhance them is surface-enhanced Raman scattering (SERS), carried out by means of adsorption of silver, gold, etc. nanoparticles or nanostructures (Xu et al., 2014; Morrissey et al., 2015). In particular, strong amplification of electromagnetic fields of up to 10^{11} can be achieved within an interparticle junction (a "hot spot" area) or around them (Rycenga et al., 2012; Wang et al., 2014). Substantial efforts have been made for fabricating effective SERS platforms for environmental sensing (Bontempi et al., 2016), molecule detection by warped optical areas (Mao et al., 2018), ultrabright SERS sensors with embedded Raman tags (Jin et al., 2017), various types of dual-mode optical probes (Alvarez-Puebla et al., 2018), waveguide-based on-chip amplification (Raza et al., 2018), vertically aligned ZnO nanorod SERS substrates (Jue et al., 2019), fiber-based SERS probe (Kwak et al., 2019). Properties of nanoparticles and substrates play a crucial role in tuning SERS signal (Wi et al., 2012; Yashchenok et al., 2012; Kodiyath et al., 2013; Lin and Tang, 2015; López-Puente et al., 2015) as well as their distribution on the chip

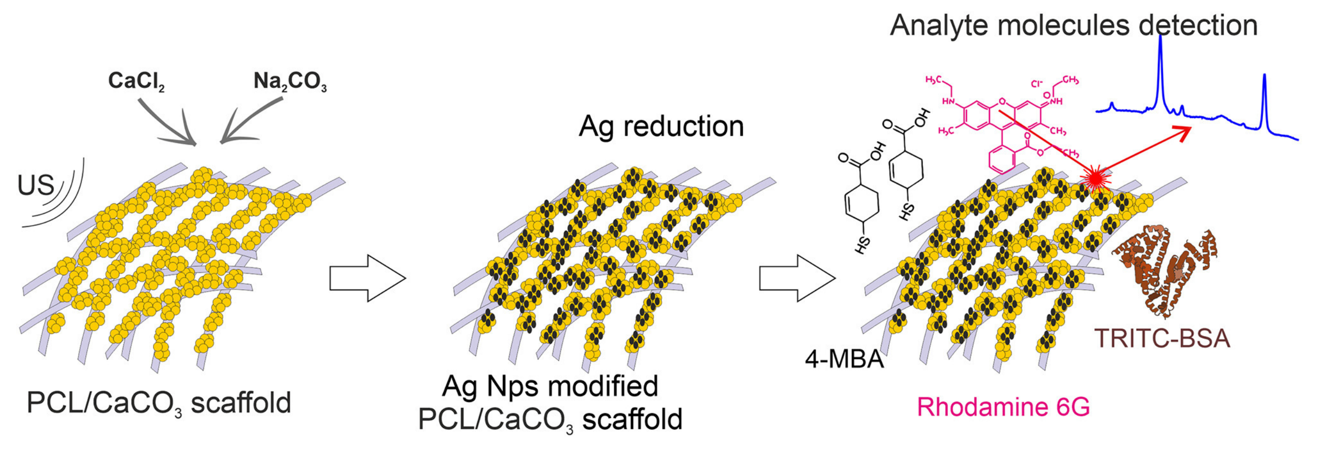

GRAPHICAL ABSTRACT | SERS platform for molecules with different ways of adsorption.

(Zalduendo et al., 2018). Furthermore, SERS has been applied in cell biology (Kneipp et al., 2006; Yashchenok et al., 2013; Krafft et al., 2017), where development of new super resolution methods should further contribute to localization of molecules. Porous colloidal particles of calcium carbonate or hydroxyapatite can be used for accumulation of analyte molecules in pores and thus increase the signal amplification, as it was demonstrated for adsorption of gold nanoparticles on their surface (Yashchenok et al., 2012). Furthermore, silver nanoparticles adsorbed onto calcium carbonate matrices have been demonstrated to substantially improve the SERS signal (Parakhonskiy et al., 2014; Kamyshinsky et al., 2019). Concentration of silver nanoparticles can be controlled either by adsorption conditions (Parakhonskiy et al., 2010) or direct synthesis (Hering et al., 2008; Parakhonskiy et al., 2010). The following functionalization them with magnetic nanoparticles will prove a possibility to move such SERS platforms under the magnetic field (Parakhonskiy et al., 2019). In addition, porous calcium carbonate particles have been shown to prolong the stability and detection capability of silver nanoparticles (Markina et al., 2018). An appropriate platform for deposition of such particles are scaffolds, for which electrospinning (ES) appears to be a very attractive fabrication technique (Prikhozhdenko et al., 2016; Saveleva et al., 2017; Chernozem et al., 2019).

Electrospinning is a simple and versatile technique capable of spinning fibers with diameters down to tens of nanometers. A variety of ES scaffolds with proper functionalization can be assembled for SERS. Indeed, ES nanofibers were shown to be an effective SERS substrate, because of a high surface to volume ratio and special optical properties achieved through the addition of metal or oxide nanoparticles (Severyukhina et al., 2015; Chen et al., 2017; Chamuah et al., 2018; Celebioglu et al., 2019; Restaino and White, 2019). The amplification of the signal, the impregnation of electrospun scaffolds with metal nanoparticles could enhance its optical, mechanical and morphological properties. The flexibility of the selection of polymers for ES allows producing electrospun scaffolds composed of biocompatible and environmentally friendly materials relevant for biomedical applications, including tissue engineering. Polycaprolactone (PCL) is attractive to ES, because it is non-toxic, chemically stable material available at a low cost. However, it is rather hydrophobic, which makes it challenging for biomedical applications. One solution to this problem is the surface functionalization of a scaffold to control its hydrophobic-hydrophilic (Duque Sánchez et al., 2016). The formation of hydrophilic inorganic porous bioceramic based coatings (for example, calcium phosphates CaP, calcium carbonates CaCO$_3$, mesoporous silica) on a scaffold surface allows enhancing surface properties along with endowing of the additional functionality of drug delivery capability (Vallet-Regí et al., 2011; Savelyeva et al., 2017; Ivanov et al., 2019). The recently developed method of mineralization of the electrospun PCL scaffold with the CaCO$_3$ porous ceramic microparticles allows obtaining homogeneous coatings in the vaterite phase overall fibrous electrospun scaffold by the *in situ* ultrasound-assisted CaCO$_3$ syntheses at the surface of fibers (Savelyeva et al., 2017). Such biocompatible highly porous vaterite coating endows a scaffold with the following advantages: capability of encapsulating and targeted delivery of functional molecules and nanoparticles (including metal and metal oxide ones for SERS applications), and bioactivity (particularly, stimulating cell adhesion and increasing the surface hydrophilization; Saveleva et al., 2018; Ivanov et al., 2019).

Another aspect that appears to be important in SERS is the attachment of molecules—indeed, attached molecules have been reported to enable both stability and a high level of amplification (Wuytens et al., 2017).

In the present study, we design novel materials, which possess the functionalities of selective sorption of macro- and small- molecules along with amplification of their Raman signals for the detection. We hypothesized that electrospun PCL scaffolds sequentially modified with porous CaCO$_3$ and silver Ag nanoparticles will provide selective sorption of the macro- and micromolecules and efficient amplification of the Raman signal by SERS. Ag nanoparticles were synthesized using two different methods: by *in-situ* reduction by the Tollen's reagents and by a similar reaction conducted in the presence of silver oxide, which is associated with hampering the SERS signal. Furthermore, such a comparison allows us to trace the influence of the oxidation on the SERS signal amplification.

MATERIALS AND METHODS

Preparation of Mineralized Scaffolds PCL/$CaCO_3$

The formation (electrospinning) of fibrous polymeric PCL scaffolds and subsequent mineralization of electrospun polymeric fibrous scaffold was performed by using approaches introduced previously in (Savelyeva et al., 2017).

Modification of Scaffolds With Ag

Using clear Tollen's reagent: the 1 × 1 cm sample of scaffolds (PCL and mineralized PCL/$CaCO_3$) were placed in 5 mL of Tollen's reagent [a mixture of 0.5 M $AgNO_3$ (Sigma-Aldrich, Germany) and 0.5 M NH_4OH (ChemReactiv, Russia) in a volume ratio is 1:1] for 10 min for adsorption of Tollen's complex on the surface of scaffold. After this, the scaffold was placed in a 40% solution of D-glucose for 10 min, then was washed with deionized water and dried at 40°C for 20 min.

Using Tollen's reagent containing 50% of silver oxide: the 1 × 1 cm sample of scaffolds (PCL and mineralized PCL/$CaCO_3$) were placed in 5 mL of Tollen's reagent (0.5 M $AgNO_3$: 0.5 M NH_4OH in volume ratio 2:1) for 10 min for adsorption of silver oxides from solution on the surface of the scaffold. After this, the scaffold was placed in a 40% solution of D-glucose for 10 min, then was washed with deionized water and dried at 40°C for 20 min.

The Adsorption of the Low and High Molecular Weight Molecuels

A solution of tetramethylrhodamine-bovine serum albumin (TRITC-BSA, 0.5 mg/ml, Sigma-Aldrich) was used as source as macromolecular with relatively high molecular weight (Mw = 70 kDA). A solution of Rhodamine 6G (Rh6G, 0.5 mg/ml, Sigma-Altrich) was used as low molecular weight substance (Mw = 479 Da) for loading and Raman studies. For confocal studies a solution of photosensitizer "Photosens"® (Russia) (Phs), representing a mixture of sulfonated aluminum phthalocyanines with various degrees of sulfonation (0.5 mg/mL), was used as a source of macromolecules.

For Raman and loading efficiency studies scaffolds with various modifications were immersed for 5 min in the solution of TRITC-BSA with initial concentration (Cini) 0.5 mg/ml in the solution with Rh6G with initial concentration (Cini = 0.5 mg/ml). After this the concentration of molecules in solution (Csn) were analyzed via UV-Vis spectrophotometry at appropriate wavelengths (567 nm for TRITC-BSA and 567 nm for Rh6G), and the Loading Efficiency (LE) was calculated using the following equation:

$$\text{LE} = (\text{Cini–Csn})/\text{Cini}^{*}100\% \qquad (1)$$

The mixture of TRITC-BSA and Phs was prepared in a 1:1 ratio (by volume) with initial concentrations: Cini(Phs) = 05 mg/ml and Cini(TRITC-BSA) = 0.5 mg/ml. The scaffold was immersed in the mixture and fixed in such position for 5 min for adsorption of molecules. The concentration of the molecules in solution was measured via UV-vis spectrophotometry (UVIKON XL Secomam), in an appropriate wavelength (567 for TRITC-BSA and 670 for Photosens). Loading efficiency was estimated via Equation (1). All LE ware calculated based on statistic of 5 samples.

Characterization Methods

The scanning electron microscopy of scaffolds was performed in the manner as described in (Savelyeva et al., 2017). Raman and SERS measurements were carried out using Renishaw inVia (UK) spectrometer with a 785-nm laser irradiated through a 50× objective (Leica N PLAN 0.5 N.A.).

4-mercaptobenzoic acid (4-MBA, Sigma Aldrich, Germany) ethanol solutions (10^{-3}, 10^{-4}, and 10^{-5} M) were used as analyte. Prior to Raman and SERS measurements, all substrates (5 × 5 mm size) were put into 4-MBA solution (1 mL) for 20 min and then washed with ethanol. Raman spectra of 4-MBA (10^{-3} M) on PCL and mineralized PCL/$CaCO_3$ were recorded with 10 mW laser power and were scanned for 5 s per spectrum. SERS maps (20 × 20 μm) of 4-MBA with concentrations 10^{-3}, 10^{-4}, and 10^{-5} M were recorded with 10 μW laser power and 5 s per spectrum. Enhancement factors (EF) were calculated according to the formula:

$$EF = \frac{I_{SERS}}{I_{Raman}} \cdot \frac{p_{Raman}}{p_{SERS}} \cdot \frac{c_{Raman}}{c_{SERS}}, \qquad (2)$$

where I —the intensity of the 1,580 cm^{-1} line for SERS spectra (I_{SERS}) and that of the control analyte (I_{Raman}); p—laser power for SERS spectra (pSERS) and control analyte (p_{Raman}); c — the concentration (of 4-MBA) for SERS spectra (c_{SERS}) and control analyte (c_{Raman}). SERS data were represented as box-and-whiskers diagrams with the interquartile range 1.5 and no outliers plotted for SERS intensities.

TRITC-BSA or Rhodamine 6G water solution (0.5 mg/ml) was used as analyte which models high molecular weight molecule (protein) and low molecular weight molecule which was loaded like described above (Section The Adsorption of Low and High Weight Molecules). Raman spectra of analyte on PCL, mineralized PCL, functionalized with silver were recorded with laser power 0.5 mW 0.1 s per spectrum and with 50 mW 0.1 s per not functionalize with silver. SERS maps (20 × 20 μm). The enhancement factor was estimated via formula (2) were the intensity I—the intensity of the 1,513 cm^{-1} line.

RESULTS

The Ag nanoparticles (AgNP) were synthesized by two methods: (1) from the clear Tollens reagent (produced with and denoted as Ag) and (2) the Tollens reagent mixed with silver oxide (produced with and denoted as Ag/AgO). Subsequently, their adsorption has been studied on scaffolds possessing porous $CaCO_3$ (and referred to as $CaCO_3$ mineralized) and those without $CaCO_3$ (referred to as non-mineralized) scaffolds. That allows to investigate the influence of $CaCO_3$ mineralization of PCL scaffolds on adsorption of Ag nanoparticles synthesized by the above mentioned two methods, **Figure 1**. This study is

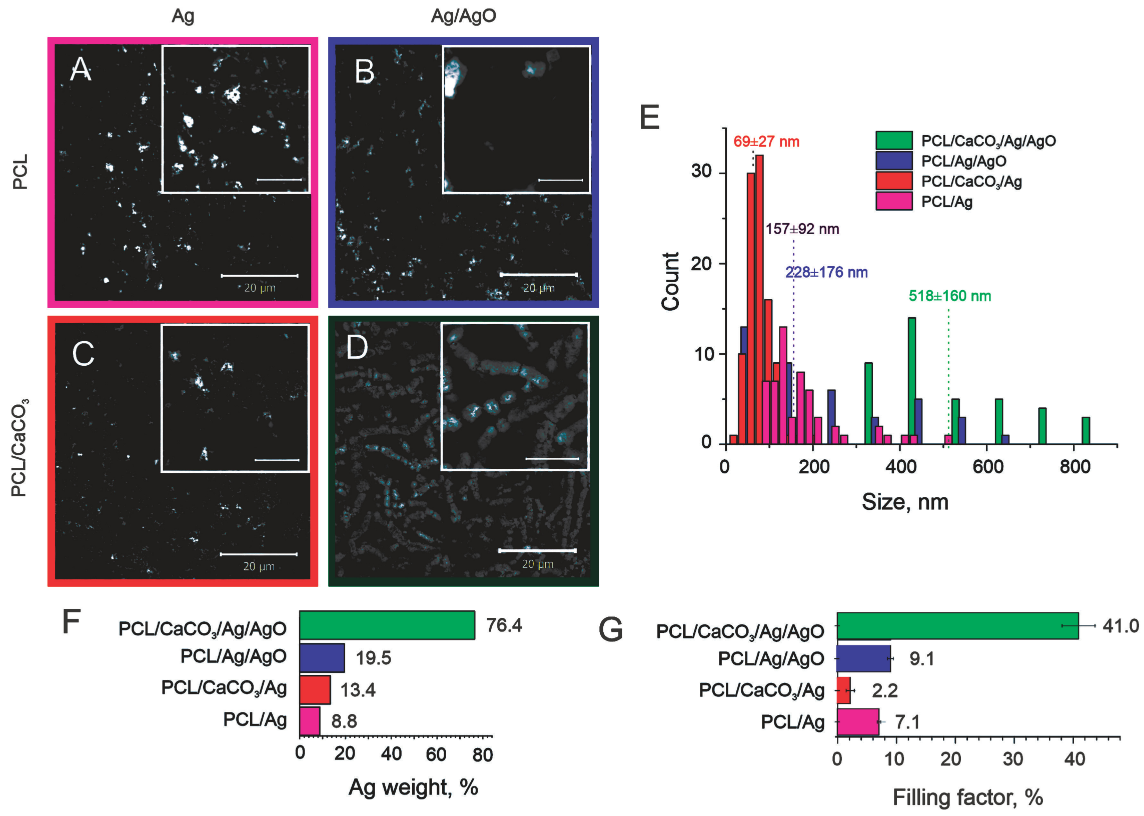

FIGURE 1 | SEM images of the Ag reduction on non-mineralized PCL fibers **(A,B)** and mineralized PCL-$CaCO_3$ scaffolds **(C,D)** after Ag reduction from the clear Tollen's reagent **(A,C)** and the reagent containing the Tollen's reagent with 50% of silver oxides **(B,D)**. The scale bars in inset images are 5 μm. **(E)** The size distribution of silver nanoparticles adsorbed on various scaffolds. **(F)** The silver content (weight percent) obtained via EDX analysis. **(G)** The filling factor of silver nanoparticles in various PCL scaffolds.

relevant, because the concentration, sizes, and the aggregation state of Ag nanoparticles determine the strength of the SERS amplification.

SEM images demonstrating adsorption of Ag and Ag/AgO on PCL scaffolds are shown in **Figures 1A,B**, respectively. Functionalization of non-woven PCL nanofibers was also carried out with $CaCO_3$. SEM images of the morphology of PCL scaffolds mineralized with $CaCO_3$ after subsequent reduction of Ag and Ag/AgO are shown in **Figures 1C,D**, respectively. Aggregation of nanoparticles leads to a higher SERS amplification; therefore, the aggregation state of nanoparticles is compared in the scaffolds before, **Figure 1A** (Ag on PCL), and after, **Figure 1C** (Ag on PCL/$CaCO_3$), $CaCO_3$ deposition. It can be seen from these images that in the former case a more agglomerated pattern of Ag particles is observed—calcium carbonate, thus, has not promoted the aggregate formation. $CaCO_3$ affects adsorption of Ag/AgO, which is found to be higher (in weight percent) on PCL/$CaCO_3$ scaffolds than that on PCL, **Figure 1D**.

We further present data on the sizes of nanoparticles (**Figure 1E**), the overall weight of adsorbed silver NP (**Figure 1F**) and their filling factor (**Figure 1G**), determined as the ratio of the sum of cross-sections of all individual nanoparticles to the total area (Skirtach et al., 2005). The average sizes of adsorbed Ag nanoparticles depend on the mineralization with $CaCO_3$, in which case it is almost two times lower. Specifically, AgNP adsorbed from the Tollen's reagent were obtained in the size range of ∼ 70 ± 30 nm for the mineralized scaffolds, while they were ∼ 160 ± 90 nm for the non-mineralized scaffolds, **Figure 1E**. The size difference is thus by a factor of more than 2. In contrast to data obtained with the Tollen's reagent only (Ag), the size of AgNP obtained from the mixture of Tollen's agent and Ag/AgO the average size of AgNP is also higher by the factor of ∼2, but in this case, the size of AgNP is ∼520 ± 160 nm for mineralized with $CaCO_3$ scaffolds versus 230 ± 180 nm for non-mineralized ones.

To define and match the SERS performance of different scaffolds, we used 4-mercaptobenzoic (4-MBA) acid as an analyte. 4-MBA has a high affinity to silver nanoparticles through the thiol group. But, there was no signal of 4-MBA (10^{-3} M) on PCL scaffolds without $CaCO_3$ (**Figure 2A**, the violet and bottom line), while all of the present peaks correspond to PCL (Kotula et al., 2017). After the mineralization procedure, there was an additional peak at 1,583 cm^{-1} corresponding to the 4-MBA $\nu(C–C)_{ring}$ mode (Orendorff et al., 2005). This peak intensity was used as 4-MBA Raman intensity for further EF calculations. The average SERS scattering intensities and the EF at 1,580 cm^{-1} are shown in **Figures 2B–E** and in a **Table S1**.

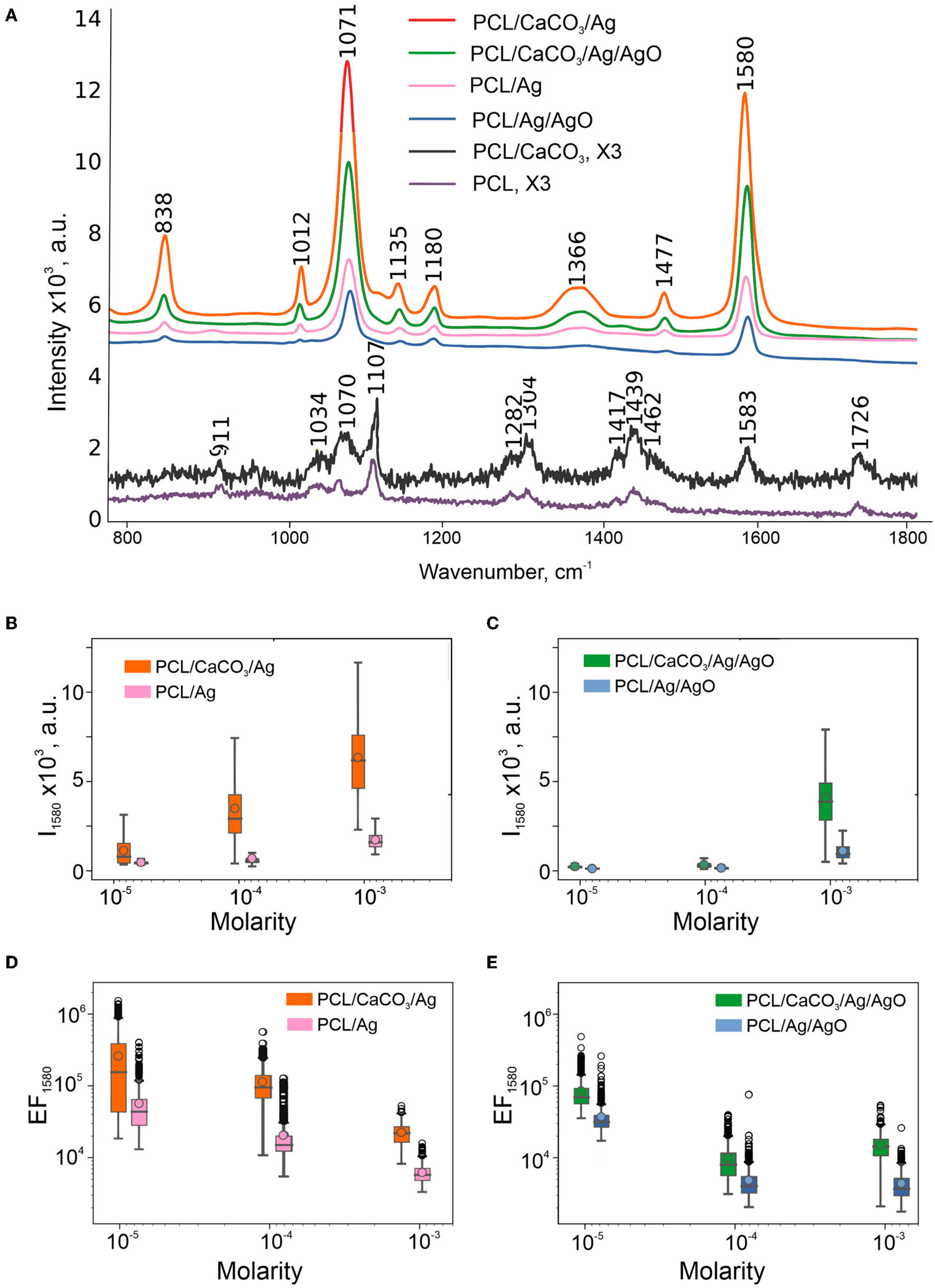

FIGURE 2 | SERS performance of obtained scaffolds: Average spectra of 4-MBA (10^{-3} M) on SERS-substrates calculated from maps 20 × 20 μm and multiplied by 3 spectra on PCL, PCL/$CaCO_3$ fibers **(A)**. Box-and-whiskers plots of intensity at 1,580 cm^{-1} of SERS substrates without **(B)** and with 50% of silver oxides **(C)**. Data on SERS substrates without $CaCO_3$ are shown in the insets. Enhancement factors calculated from these intensities according to the formula in Section Characterization Methods are shown in the log scale **(D,E)**.

To reveal the difference between specificity of molecule adsorption TRITC-BSA (Mw = 70 kDa) and Rh6G (Mw = 479 Da) as large and small molecule have been chosen. Both of these molecules have the same mechanism of adsorption–the physical sorption on the surface of the scaffold. It was found that the loading efficiency (LE) were much higher for Rh6G (40%) than for TRITC-BSA (24–30%). The presence of silver nanoparticles (AgNPs) on PCL scaffold increase large molecule sorption for non-mineralized scaffolds (PCL, PCL/Ag).

The SERS spectra revealed several peaks of Rh6G in the region between 500 cm^{-1} and 1,700 cm^{-1} (**Figures 3A,B**). The most intense peaks at 1,314, 1,363, 1,512, and 1,651 cm^{-1} are assigned to C-C aromatic stretching. The SERS spectra of TRITC-BSA displayed three peaks of BSA at 1,203, 1,453, and 1,654 cm^{-1}, which are assigned to Amide III, CH_2 bending and Amide I, respectively. Two peaks at 1,363 and 1,513 cm^{-1}, representing a contribution from TRITC, are also detected for SERS spectra of TRITC-BSA. The enhancement factor (**Figures 3C,D**) of both analyzed molecules (TRITC-BSA and Rh6G) was estimated using the intensity at 1,513 cm^{-1} which corresponds to C-C aromatic stretching peak of Rh6G. Comparison of Enhancement factor showed that the scaffolds without AgNP demonstrate the Raman signal intensity <50, as with high laser power (50 mW) On the other hand, the samples modified with AgNP (PCL/Ag and PCL/$CaCO_3$/Ag) demonstrate the SERS effect with the signal intensity of up to 10^5 that for Rh6G and up to 500 for TRITC-BSA. Peculiarly, there is no significant difference (based on ANOVA tests) between signal amplification on modified and non-modified by calcium carbonate samples. Eventually, this means that macro roughness due to AgNP is a dominant factor for adsorption of small and large molecules regardless of the size of molecules.

Ensuing study of the sorption process was carried out using fluorescence microscopy. Here, we have used TRITC-BSA as a large molecule, while Photosens (Phs) is used as a small molecule. The molecular weight of Phs is 574.9 Da, which is comparable to that of Rh6G (479.2 Da). However, Photosens has a strong fluorescence signal at a different wavelength (with the emission maximum at around 689 nm). Our results reveal that it is possible to recognize both of these molecules using confocal fluorescence microscopy (**Figure 4**).

Confocal microscopy images (**Figures 4A–D**) complemented by a same images split by different fluorescent channels (**Figures S3–S6**) demonstrate the distribution of small and large molecules in various scaffolds. Significant differences can be observed between mineralized and non-mineralized scaffolds, along with the obvious influence of the presence of Ag particles on the separation performance of molecules. In the case of the non-mineralized scaffold without $CaCO_3$ and Ag, no separation and no characteristic aspects can be revealed from the image. Mineralized scaffold PCL/$CaCO_3$ exhibits the

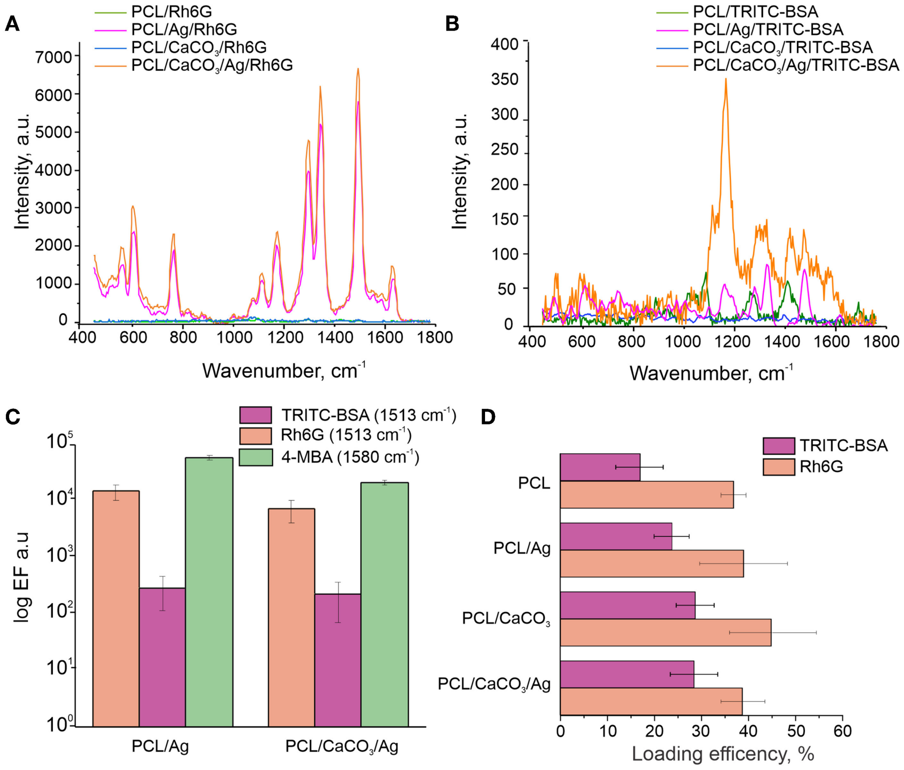

FIGURE 3 | Raman spectra of the Rh6G **(A)** and TRITC-BSA **(B)** on various scaffolds. **(C)** Comparison of the enhancement factor of the C-C aromatic stretching peak (1,513 cm^{-1}) for TRITC-BSA and Rh6G and at 1,580 cm^{-1} for 4-MBA in log scale. **(D)** The loading efficiency (LE) for TRITC-BSA (pink) and Rh6G (orange).

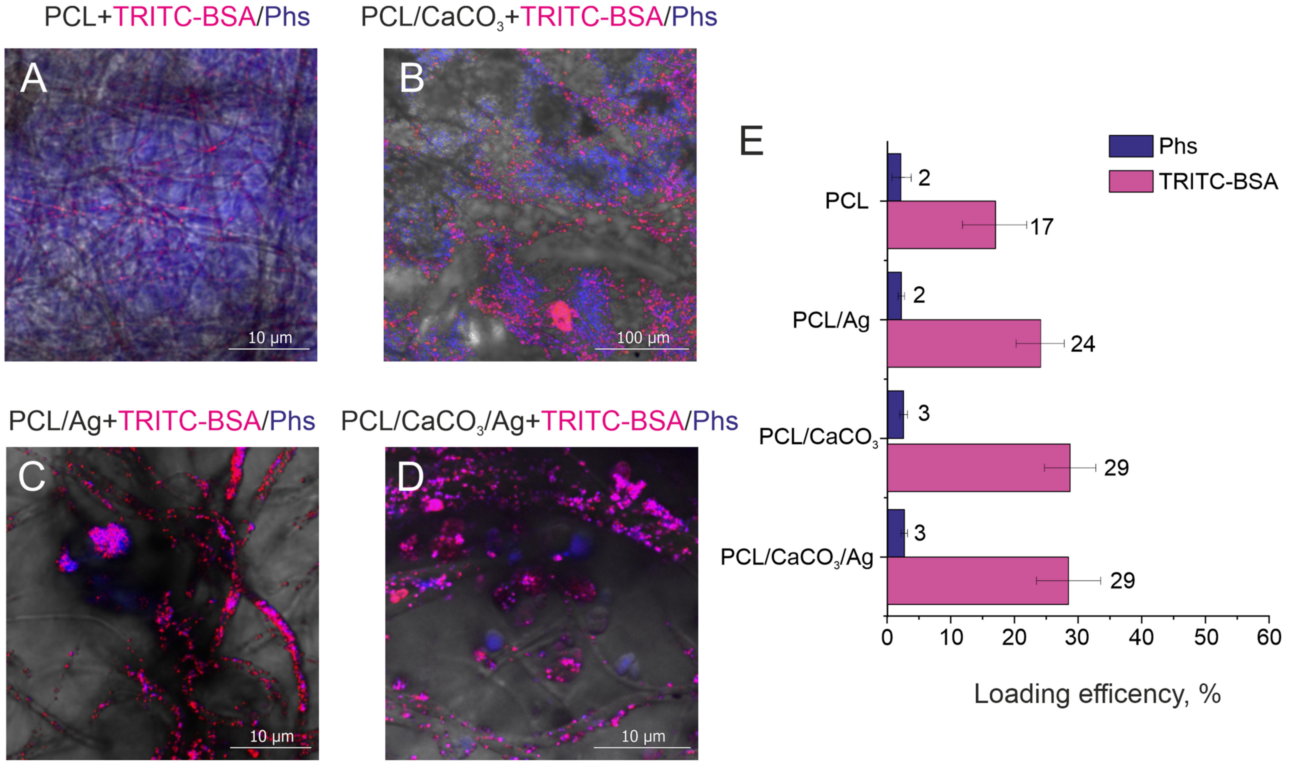

FIGURE 4 | Confocal images of different scaffolds **(A)** polycaprolactone, **(B)** PCL/CaCO$_3$. **(C)** PCL/Ag, and **(D)** PCL/CaCO$_3$ matrix after Ag immersed in a mixture of Photosens and TRITC –BSA. **(E)** The loading efficiency for different scaffolds for Phs (blue) and TRITC-BSA (pink).

conspicuous separation of Phs and TRITC-BSA pronounced in selective adsorption of small Phs molecules by vaterite coating and accumulation of TRITC-BSA macromolecules as aggregates at the surface of vaterite-coated fibers without adsorption. The decoration of scaffolds with Ag particles suppressed the adsorption of small molecules by vaterite due to Ag filling of adsorption sites of CaCO$_3$. In this case, molecules distribution expressed in the form of molecules clusters and aggregates on the surface of the fibers—this idea confirmed by a study of the sorption molecules (**Figure 4E**). Small molecule better adsorbed on porous vaterite structure. Due to the method sensitivity for small molecule sorption has a higher deviation than for TRITC BSA. Vaterite has a significant increase in the loading capacity of TRITC-BSA as well, but silver nanoparticles don't provide any significant effect on the sorption efficiency.

Therefore, the modification of the scaffold by porous particles resulted in a significant (2 times) increase of the sorption of the large molecule and a slight increase of the sorption of a small molecule. The functionalization of the silver nanoparticles, which can provide the SERS amplification, but it doesn't significantly influence the loading properties of modified scaffolds.

DISCUSSION

The presence of a vaterite coating leads to both an increase of the hydrophilization of a surface and to an increase of the surface area and porosity, which influence the formation of Ag nanoparticles. Analysis of SEM images in combination with EDX data shows that the scaffolds coated with porous vaterite coating, while using the Tollens reagent without additional oxide let to the formation of smallest silver nanoparticles (~70 nm) (**Figures 1A–D**). It should be noted that the space confinement of the pores of calcium carbonate particles pose constrictions for AgNPs particle growth leading to their narrow size distribution. In the case of non-porous scaffolds, i.e., pure PCL, the Ag particles grow mostly in the solution followed with the adsorption on the PCL structure. Such an increase in a confined volume leads to the formation of much larger particles with sizes ~160 nm ± 90 nm. We note that the presence of silver oxide in the reaction mixture serves as a template for additional growth of the seeds for the Ag reduction. In this case, the particle size increases significantly up to 230 nm for PCL scaffolds and up to 520 nm for PCL/CaCO$_3$. It can be noted that for PCL/CaCO$_3$/Ag + 50% AgO and PCL/Ag + 50% AgO the filling factor as well as the Ag element content increase significantly. Moreover, in the case of vaterite-coated scaffolds, almost total coverage of the scaffolds with Ag is achieved.

Furthermore, the filling factor varies in the scaffolds from 2% till 40% and it is substantially higher for non-mineralized scaffolds (~7.1) in comparison to that for CaCO$_3$ mineralized ones (~2.2) (**Figure 1G**). In the case of the Tollen's reagent containing 50% of silver oxide (Ag/AgO), the difference in Ag particle contents for not-mineralized and mineralized scaffolds can be observed from SEM images and EDX results (**Figures 1A–D**) together with **Figures S1, S2**. The Ag filling factor is higher by ∼4 times for mineralized scaffolds in comparison with that for the non-mineralized scaffolds, **Figure 1G**. More specifically, the Ag content is 76.4 wt.% in the mineralized scaffolds, while it is only 19.5 wt.% in the case of the non-mineralized scaffolds. The X-ray element maps confirm the larger Ag content and the denser distribution of Ag particles in the mineralized scaffold in comparison with the non-mineralized scaffold in the case of using Ag/AgO nanoparticles.

Even though the Ag content (or in other words the filling factor) is much higher on fibers of scaffolds with AgO, the SERS EFs are observed to be higher on PCL/Ag and PCL/$CaCO_3$/Ag without AgO (**Figures 2B–E**). Lower SERS EFs can be assigned to 2 factors: (1) the presence of silver oxide film resulting in a poor adsorption of the 4-MBA due to S atoms and carboxyl groups, and (2) plasmon damping on dielectric oxide films. For this reason, investigation of scaffolds with AgO is not further pursued.

We further investigate the SERS amplification comparing PCL, PCL/$CaCO_3$, PCL/Ag, and PCL/$CaCO_3$/Ag scaffolds. The following molecules have been used as analytes: (a) TRITC BSA (higher molecular weight molecule); (b) 4-MBA (small molecule, which is chemically cross-linked with the silver nanoparticles); and (c) Rh6G (small molecule, which is physically adsorbed to the surface). The discussion begins with scaffold adsorption of 4-MBA molecule—this process is referred to as chemisorption, i.e., in this case 4-MBA adsorption on the Ag surface via carboxyl groups and S atoms. The sorption efficiency depends on the filling factor of Ag nanoparticles and for PCL/Ag scaffolds the amount of the adsorbed molecules is 3 times higher than that for PCL/Ag/$CaCO_3$. Furthermore, chemical adsorption of molecules is higher for mineralized PCL scaffolds (PCL/$CaCO_3$ and PCL/$CaCO_3$/Ag) in comparison with that for non-mineralized scaffolds (PCL, PCL/Ag), as demonstrated by the appearance of the peak in the Raman spectrum of chemically adsorbed 4-MBA of PCL/$CaCO_3$ scaffold without silver nanoparticles (**Figure 3A**). At higher concentrations of 4-MBA, the Raman signal intensity is higher compared to that at a lower concentration, **Figures 2B,C**, but the EF of SERS has an inverse dependence on concentration. Indeed one can see in **Figures 2D,E** that the EF of SERS (calculated by Equation 1) at 10^{-3} M is about 10–15 times lower than that at 10^{-3} M of 4-MBA. This is presumably due to the saturation of the sorption of 4-MBA molecules on the scaffolds. The SERS signal on PCL/$CaCO_3$/Ag substrates has the mean EF of 2.8×10^5 with EF of 1.6×10^6 in "hot spots."

It is essential to note that even though the filling factor is higher for PCL/Ag (without $CaCO_3$) than that for PCL/$CaCO_3$/Ag, the SERS effect is stronger for the latter sample (PCL/$CaCO_3$/Ag). It could be because of a higher amount of smaller nanoparticles (70 nm with $CaCO_3$ vs. 160 nm without $CaCO_3$, **Figures 1A,C,E**) provides a better distribution of Ag nanoparticles for SERS amplification. This is achieved by creating nanometer sized gaps between Ag nanoparticles, which essentially facilitate the SERS amplification.

On the other hand, the loading efficiency of molecules, which are physically adsorpbed on scaffold structures depends on the surface area and roughness of scaffolds as well as on the shape and size of to be analyzed molecules. For the following fluorescenct molecules: TRITC-BSA, Rh6G, Phs it is possible to directly measure their loading efficiency (Equation 1). First of all, we probe the spatial distribution of adsorbed small and large molecules on PCL and PCL/$CaCO_3$ scaffolds functionalized with Ag nanoparticles. For this purpose, a pair of biomedically relevant molecules TRITC-BSA (a high-molecular weight protein BSA labeled with TRITC) and Photosens® (Phs) (photodynamic drug) molecules is chosen due to a non-overlapping nature of their fluorescent signals. Functionalization of PCL scaffolds with $CaCO_3$ and AgNP is shown in our study to be useful for concentrating molecules. Indeed, **Figure 4** shows images of PCL nanofibers after incubation in a solution containing these two molecules. It should be noted that the typical pore sizes of vaterite ranges from 30 to 90 nm, which limits incorporation of larger molecules, while smaller ones would more effectively penetrate inside the vaterite interior (Parakhonskiy et al., 2012). At the same time, large molecules would not penetrate inside the vaterite pores as efficiently as the small ones, and they would be adsorbed only at the external vaterite surface.

The scaffold modification by Ag has a significant influence on the adsorption of all molecules. In this regard and based on the confocal image analysis, it is observed that in the case of scaffolds without Ag small molecules penetrate inside the vaterite pores, while large molecules are adsorbed on the surface and are clustered in between the vaterite structures. In the case of Ag-decorated scaffolds, Ag nanoparticles fill the vaterite pores, blocking them and decreasing the sorption of small molecules. As a result, small molecules, Phs, are clustered similarly to large molecules (proteins in this case). The same effect is obtained for another pair of small and large molecules: Rh6G and TRITC-BSA, respectively (**Figure 3D**). The loading efficiency of the modified PCL scaffolds by calcium carbonate and/or AgNP provides a better sorption of large and small molecules than the non-modified scaffolds. The SERS signal amplification of TRITC-BSA is lower than that for either of the small molecules: 4-MBA and for Rh6G (**Figure 3C**). The scaffolds with AgNP provide amplification for Rh6G up 10^5 which are comparable with the amplification ($5*10^5$) of chemically bound 4-MBA, but in the case of physical sorption functionalization of the scaffold with the calcium carbonate don't give any advantage.

We further investigate SERS effect of the TRITC BSA induced by the C-C aromatic stretching of the rhodamine part of the molecule, because BSA has a low scattering cross section compared to that of rhodamine. For large molecule TRITC-BSA, the SERS amplification is not so significant, just 500 times with respect to the samples without AgNPs. It can occur due to three reasons: (1) smaller number of molecules providing C-C aromatic stretching because of: (a) an inefficient sorption of TRITC-BSA in comparison to that for Rh6G, and (b) the grafting ratio of TRITC on BSA is only 0.5 M per 1 M of BSA; (2) the presence of the BSA prevents an efficient contact of C-C atoms with Ag nanoparticles.

Nanostructures including electrospun scaffolds composed of such biocompatible materials as polycaprolactone, chitosan, polyurethane, polycaprolactone, etc., are identified here as an effective SERS amplification platform. Their modification, for example, by inorganic nanoparticles leading to the so-called hybrid (Saveleva et al., 2019) structures or scaffolds makes them a unique platform, where the porosity and the concentration or the filling factor of the metal nanoparticles can be controlled. Furthermore, their uniqueness lies in a possibility to adsorb molecules—a property, which has been identified as a very important factor enabling high and stable amplification (Wuytens et al., 2017). This principle, demonstrated in this work for porous materials in combination with their adsorption of molecules, resulted in significant amplification of the surface-enhanced Raman signals relevant for detection of a wide range of molecules.

CONCLUSION AND PERSPECTIVES

Polycaprolactone scaffolds, mineralized in this work by both calcium carbonate in the form of vaterite and Ag nanoparticles in the vaterite pores, are shown to be an effective SERS platform for dual- and molecularly selective detection. The SERS effect is provided by silver nanoparticles in a combination with a high specific adsorption facilitated by the porous structure of vaterite. The mineralization of the scaffolds by vaterite is found to play a key role in the silver nanoparticle formation, and it has led to a more homogeneous coverage of AgNP with the sizes ∼70 nm. It is found in our studies that the SERS amplification for both TRITC-BSA and Rhodamine 6G strongly depends on the presence of Ag nanoparticles, because the latter provides not only the SERS amplification, but they also form a rough surface, on which molecules can attach better. The SERS amplification is found to be better for Rhodamine 6G (up to 10^5) than for TRITC-BSA (up to 10^3) assigned to a larger concentration of adsorbed Rhodamine 6G molecules and, most likely, their closer location to Ag nanoparticles. The SERS amplification signal of TRITC-BSA, monitored by the C-C aromatic stretching corresponding to the peak provided by TRITC functionalization, is worse than that for Rhodamine 6G. This is attributed to the presence of protein (BSA), which would prevent a close proximity of Rhodamine of TRITC-BSA to Ag nanoparticles. 4-MBA molecules, attached to scaffolds functionalized with Ag nanoparticles, have produced a good SERS amplification respect to the Rh6G and TRITC-BSA molecule. On the other hand, the amount of cross-linked 4-MBA is proportional to Ag nanoparticles, which directly give rise to the SERS signal amplification and which grow significantly better on Ag nanoparticles. It is also found in our studies that the presence of silver oxide in the reaction mixture significantly decreases the enhancement factor. Strong SERS magnification factors coupled with possibilities to probe molecular specific adsorption are characteristic features of these new scaffolds.

DATA AVAILABILITY STATEMENT

All datasets generated for this study are included in the article/**Supplementary Material**.

AUTHOR CONTRIBUTIONS

MS and EP contributed to writing and performed experiments, on which this work is based. DG, AY, BP, and AS have organized work and led some of research directions, on which this work is based.

FUNDING

This research was supported by the Special Research Fund (BOF) of Ghent University (01IO3618, BAS094-18, BOF14/IOP/003) and FWO-Vlaanderen (G043219, 1524618N, G0D7115N).

ACKNOWLEDGMENTS

We thank the Special Research Fund (BOF) of Ghent University and FWO Flanders for support. BP is a FWO Flanders post-doctoral fellow. AY thanks the Russia-platform of Ghent University for support with the visiting fellowship.

SUPPLEMENTARY MATERIAL

The Supplementary Material for this article can be found online at: https://www.frontiersin.org/articles/10.3389/fchem.2019.00888/full#supplementary-material

REFERENCES

Alvarez-Puebla, R. A., Pazos-Perez, N., and Guerrini, L. (2018). SERS-fluorescent encoded particles as dual-mode optical probes. *Appl. Mater. Today* 13, 1–14. doi: 10.1016/j.apmt.2018.07.007

Bontempi, N., Carletti, L., De Angelis, C., and Alessandri, I. (2016). Plasmon-free SERS detection of environmental CO_2 on TiO_2 surfaces. *Nanoscale* 8, 3226–3231. doi: 10.1039/c5nr08380j

Celebioglu, A., Topuz, F., Yildiz, Z. I., and Uyar, T. (2019). One-step green synthesis of antibacterial silver nanoparticles embedded in electrospun cyclodextrin nanofibers. *Carbohydr. Polym.* 207, 471–479. doi: 10.1016/j.carbpol.2018.12.008

Chamuah, N., Bhuyan, N., Das, P. P., Ojah, N., Choudhary, A. J., Medhi, T., et al. (2018). Gold-coated electrospun PVA nanofibers as SERS substrate for detection of pesticides. *Sensors Actuators B Chem.* 273, 710–717. doi: 10.1016/j.snb.2018.06.079

Chen, C., Tang, Y., Branislav, V., and Fei, Y. (2017). Electrospun polymer nanofibers decorated with noble metal nanoparticles for chemical sensing. *Nanoscale Res. Lett.* 12:451. doi: 10.1186/s11671-017-2216-4

Chernozem, R. V., Surmeneva, M. A., Shkarina, S. N., Loza, K., Epple, M., Ulbricht, M., et al. (2019). Piezoelectric 3-D fibrous poly(3-hydroxybutyrate)-based scaffolds ultrasound-mineralized with calcium carbonate for bone tissue engineering: inorganic phase formation, osteoblast cell adhesion, and proliferation. *ACS Appl. Mater.* Interfaces 11, 19522–19533. doi: 10.1021/acsami.9b04936

Duque Sánchez, L., Brack, N., Postma, A., Pigram, P. J., and Meagher, L. (2016). Surface modification of electrospun fibres for biomedical applications:

a focus on radical polymerization methods. *Biomaterials* 106, 24–45. doi: 10.1016/j.biomaterials.2016.08.011

Hering, K. K., Möller, R., Fritzsche, W., and Popp, J. (2008). Microarray-based detection of dye-labeled DNA by SERRS using particles formed by enzymatic silver deposition. *ChemPhysChem*. 9, 867–872. doi: 10.1002/cphc.200700591

Ivanov, A. N., Saveleva, M. S., Kurtukova, M. O., Kustodov, S. V., Gladkova, E., Blinnikova, V. V., et al. (2019). Particularities of bone regeneration in rats after implantation of polycaprolactone scaffold mineralized with vaterite with adsorbed tannic acid. *Bull. Exp. Biol. Med*. 167, 275–278. doi: 10.1007/s10517-019-04508-x

Jin, X., Khlebtsov, B. N., Khanadeev, V. A., Khlebtsov, N. G., and Ye, J. (2017). Rational design of ultrabright SERS probes with embedded reporters for bioimaging and photothermal therapy. *ACS Appl. Mater. Interfaces* 9, 30387–30397. doi: 10.1021/acsami.7b08733

Jue, M., Lee, S., Paulson, B., Namgoong, J.-M., Yu, H., Kim, G., et al. (2019). Optimization of ZnO nanorod-based surface enhanced Raman scattering substrates for bio-applications. *Nanomaterials* 9:447. doi: 10.3390/nano9030447

Kamyshinsky, R., Marchenko, I., Parakhonskiy, B. V., Yashchenok, A., Chesnokov, Y., Mikhutkin, A., et al. (2019). Composite materials based on Ag nanoparticles in situ synthesized on the vaterite porous matrices. *Nanotechnology* 30:035603. doi: 10.1088/1361-6528/aaea38

Kneipp, K., Kneipp, H., and Kneipp, J. (2006). Surface-enhanced raman scattering in local optical fields of silver and gold nanoaggregates s from single-molecule raman spectroscopy to ultrasensitive probing in live cells single-molecule Raman scattering in local. *Acc. Chem. Res*. 39, 443–450. doi: 10.1021/ar050107x

Kodiyath, R., Malak, S. T., Combs, Z. A., Koenig, T., Mahmoud, M. A., El-Sayed, M. A., et al. (2013). Assemblies of silver nanocubes for highly sensitive SERS chemical vapor detection. *J. Mater. Chem. A* 1, 2777–2788. doi: 10.1039/c2ta00867j

Kotula, A. P., Snyder, C. R., and Migler, K. B. (2017). Determining conformational order and crystallinity in polycaprolactone via Raman spectroscopy. *Polymer* 117, 1–10. doi: 10.1016/j.polymer.2017.04.006

Krafft, C., Schmitt, M., Schie, I. W., Cialla-May, D., Matthäus, C., Bocklitz, T., et al. (2017). Label-free molecular imaging of biological cells and tissues by linear and nonlinear raman spectroscopic approaches. *Angew. Chemie Int. Ed*. 56, 4392–4430. doi: 10.1002/anie.201607604

Kwak, J., Lee, W., Kim, J.-B., Bae, S.-I., and Jeong, K.-H. (2019). Fiber-optic plasmonic probe with nanogap-rich Au nanoislands for on-site surface-enhanced Raman spectroscopy using repeated solid-state dewetting. *J. Biomed. Opt*. 24, 1–6. doi: 10.1117/1.JBO.24.3.037001

Lin, Y.-W., Tang, C. (2015). Electrochemical synthesis and deposition of surface-enhanced Raman scattering-active silver microstructures on a screen-printed carbon electrode. *J. Phys. Chem. C* 119, 24865–24874. doi: 10.1021/acs.jpcc.5b08375

López-Puente, V., Angelomé, P. C., Soler-Illia, G. J. A. A., Liz-Marzán, L. M. (2015). Selective SERS sensing modulated by functionalized mesoporous films. *ACS Appl. Mater. Interfaces* 7, 25633–25640. doi: 10.1021/acsami.5b10543

Mao, P., Liu, C., Favraud, G., Chen, Q., Han, M., Fratalocchi, A., et al. (2018). Broadband single molecule SERS detection designed by warped optical spaces. *Nat. Commun*. 9:5428. doi: 10.1038/s41467-018-07869-5

Markina, N. E., Volkova, E. K., Zakharevich, A. M., Goryacheva, I. Y., and Markin, A. V. (2018). SERS detection of ceftriaxone and sulfadimethoxine using copper nanoparticles temporally protected by porous calcium carbonate. *Microchim. Acta*. 185:481. doi: 10.1007/s00604-018-3018-9

Morrissey, J. J., Kharasch, E. D., Fei, M., Tian, L., Tadepalli, S., and Singamaneni, S. (2015). Bio-enabled gold superstructures with built-in and accessible electromagnetic hotspots. *Adv. Healthc. Mater*. 4, 1502–1509. doi: 10.1002/adhm.201500227

Orendorff, C. J., Gole, A., Sau, T. K., and Murphy, C. J. (2005). Surface-enhanced Raman spectroscopy of self-assembled monolayers: sandwich architecture and nanoparticle shape dependence. *Anal. Chem*. 77, 3261–3266. doi: 10.1021/ac048176x

Parakhonskiy, B. V., Abalymov, A., Ivanova, A., Khalenkow, D., and Skirtach, A. (2019). Magnetic, and silver nanoparticle functionalized calcium carbonate particles—dual functionality of versatile, movable delivery carriers which can surface-enhance Raman signals. *J. Appl. Phys*. 126:203102. doi: 10.1063/1.5111973

Parakhonskiy, B. V., Bedard, M. F., Bukreeva, T. V., Sukhorukov, G. B., Möhwald, H., and Skirtach, A. G. (2010). Nanoparticles on polyelectrolytes at low concentration: controlling concentration and size. *J. Phys. Chem. C* 114, 1996–2002. doi: 10.1021/jp904564v

Parakhonskiy, B. V., Haase, A., and Antolini, R. (2012). Sub-micrometer vaterite containers: synthesis, substance loading, and release. *Angew. Chemie Int. Ed*. 51, 1195–1197. doi: 10.1002/anie.201104316

Parakhonskiy, B. V., Svenskaya, Y. I., Yashchenok, A. M., Fattah, H. A., Inozemtseva, O. A., Tessarolo, F., et al. (2014). Size controlled hydroxyapatite and calcium carbonate particles: Synthesis and their application as templates for SERS platform. *Colloids Surfaces B Biointerfaces* 118, 243–248. doi: 10.1016/j.colsurfb.2014.03.053

Prikhozhdenko, E. S., Atkin, V. S., Parakhonskiy, B. V., Rybkin, I. A., Lapanje, A., Sukhorukov, D. A., et al. (2016). New post-processing method of preparing nanofibrous SERS substrates with a high density of silver nanoparticles. *RSC Adv*. 6, 84505–84511. doi: 10.1039/C6RA18636J

Raza, A., Clemmen, S., Wuytens, P., Muneeb, M., Van Daele, M., Dendooven, J., et al. (2018). ALD assisted nanoplasmonic slot waveguide for on-chip enhanced Raman spectroscopy. *APL Photonics* 3:116105. doi: 10.1063/1.5048266

Restaino, S. M., and White, I. M. (2019). A critical review of flexible and porous SERS sensors for analytical chemistry at the point-of-sample. *Anal. Chim. Acta*. 1060, 17–29. doi: 10.1016/j.aca.2018.11.057

Rycenga, M., Langille, M. R., Personick, M. L., Ozel, T., and Mirkin, C. A. (2012). Chemically isolating hot spots on concave nanocubes. *Nano Lett*. 12, 6218–6222. doi: 10.1021/nl3032235

Saveleva, M. S., Eftekhari, K., Abalymov, A., Douglas, T. E. L., Volodkin, D., Parakhonskiy, B. V., et al. (2019). Hierarchy of hybrid materials—the place of inorganics-in-organics in it, their composition and applications. *Front. Chem*. 7:179. doi: 10.3389/fchem.2019.00179

Saveleva, M. S., Ivanov, A. N., Kurtukova, M. O., Atkin, V. S., Ivanova, A. G., Lyubun, G. P., et al. (2018). Hybrid PCL/$CaCO_3$ scaffolds with capabilities of carrying biologically active molecules: synthesis, loading and *in vivo* applications. *Mater. Sci. Eng. C* 85, 57–67. doi: 10.1016/j.msec.2017.12.019

Saveleva, M. S., Lengert, E. V., Gorin, D. A., Parakhonskiy, B. V., Skirtach, A. G., et al. (2017). Polymeric and lipid membranes—from spheres to flat membranes and vice versa. *Membranes* 7:44. doi: 10.3390/membranes7030044

Savelyeva, M. S., Abalymov, A. A., Lyubun, G. P., Vidyasheva, I. V., Yashchenok, A. M., Douglas, T. E. L., et al. (2017). Vaterite coatings on electrospun polymeric fibers for biomedical applications. *J. Biomed. Mater. Res. Part A* 105, 94–103. doi: 10.1002/jbm.a.35870

Severyukhina, A. N., Parakhonskiy, B. V., Prikhozhdenko, E. S., Gorin, D. A., Sukhorukov, G. B., Möhwald, H., et al. (2015). Nanoplasmonic chitosan nanofibers as effective SERS substrate for detection of small molecules. *ACS Appl. Mater. Interfaces* 7, 15466–15473. doi: 10.1021/acsami.5b03696

Skirtach, A. G., Dejugnat, C., Braun, D., Susha, A. S., Rogach, A. L., Parak, W. J., et al. (2005). The role of metal nanoparticles in remote release of encapsulated materials. *Nano Lett*. 5, 1371–1377. doi: 10.1021/nl050693n

Vallet-Regí, M., Colilla, M., and González, B. (2011). Medical applications of organic-inorganic hybrid materials within the field of silica-based bioceramics. *Chem. Soc. Rev*. 40, 596–607. doi: 10.1039/c0cs00025f

Wang, Y., Polavarapu, L., and Liz-Marzán, L. M. (2014). Reduced graphene oxide-supported gold nanostars for improved SERS sensing and drug delivery. *ACS Appl. Mater. Interfaces* 6, 21798–21805. doi: 10.1021/am501382y

Wi, J.-S., Tominaka, S., Uosaki, K., and Nagao, T. (2012). Porous gold nanodisks with multiple internal hot spots. *Phys. Chem. Chem. Phys*. 14, 9131–9136. doi: 10.1039/c2cp40578d

Wuytens, P. C., Demol, H., Turk, N., Gevaert, K., Skirtach, A. G., Lamkanfi, M., et al. (2017). Gold nanodome SERS platform for label-free detection of protease activity. *Faraday Discuss*. 205, 345–361. doi: 10.1039/C7FD00124J

Xu, L. J., Zong, C., Zheng, X. S., Hu, P., Feng, J. M., and Ren, B. (2014). Label-free detection of native proteins by surface-enhanced Raman spectroscopy using iodide-modified nanoparticles. *Anal. Chem*. 86, 2238–2245. doi: 10.1021/ac403974n

Yashchenok, A. M., Borisova, D., Parakhonskiy, B. V., Masic, A., Pinchasik, B.-E., Möhwald, H., et al. (2012). Nanoplasmonic smooth silica versus porous calcium carbonate bead biosensors for detection of biomarkers. *Ann. Phys*. 524, 723–732. doi: 10.1002/andp.201200158

Yashchenok, A. M., Masic, A., Gorin, D. A., Shim, B. S., Kotov, N. A., Fratzl, P., et al. (2013). Nanoengineered colloidal probes for Raman-based detection of biomolecules inside living cells. *Small* 9, 351–356. doi: 10.1002/smll.201201494

Zalduendo, M. M., Langer, J., Giner-Casares, J. J., Halac, E. B., Soler-Illia, G. J. A. A., Liz-Marzán, L. M., et al. (2018). Au nanoparticles–mesoporous TiO_2 thin films composites as SERS sensors: a systematic performance analysis. *J. Phys. Chem. C* 122, 13095–13105. doi: 10.1021/acs.jpcc.8b01444

Conflict of Interest: The authors declare that the research was conducted in the absence of any commercial or financial relationships that could be construed as a potential conflict of interest.

Advantages of publishing in Frontiers

OPEN ACCESS
Articles are free to read
for greatest visibility
and readership

FAST PUBLICATION
Around 90 days
from submission
to decision

HIGH QUALITY PEER-REVIEW
Rigorous, collaborative,
and constructive
peer-review

TRANSPARENT PEER-REVIEW
Editors and reviewers
acknowledged by name
on published articles

Frontiers
Avenue du Tribunal-Fédéral 34
1005 Lausanne | Switzerland

Visit us: www.frontiersin.org
Contact us: info@frontiersin.org | +41 21 510 17 00

REPRODUCIBILITY OF RESEARCH
Support open data
and methods to enhance
research reproducibility

DIGITAL PUBLISHING
Articles designed
for optimal readership
across devices

FOLLOW US
@frontiersin

IMPACT METRICS
Advanced article metrics
track visibility across
digital media

EXTENSIVE PROMOTION
Marketing
and promotion
of impactful research

LOOP RESEARCH NETWORK
Our network
increases your
article's readership